AAAS

Science

9 OCTOBER 2025

Seeking ghost flowers in Japanese forests **p. 122**

Cholesterol in T cells affects uptake of dietary lipids **pp. 128 & 149**

The evolving regulatory landscape for AI in China **p. 132**



Eclipsing the Sun

A unique cosmic event shows an influence of light on bird behavior **p. 152**



BII | Science | Prize for Innovation

Bring Science to Life

Behind every life-changing solution is an entrepreneurial scientist – a creative mind who developed an idea in the lab and dared to carry it out into the world.

To encourage more scientists to translate their research, BioInnovation Institute (BII) and *Science* are collaborating to host an annual award.

Up to three winners will have their essays published in *Science* magazine and will be invited into BII's entrepreneurial ecosystem. In addition, the Grand Prize winner will receive a prize of USD 25,000, and each finalist will receive USD 10,000 at a grand award ceremony in Copenhagen, Denmark.

Xiaojing Gao, Grand Prize winner 2025
For his work on developing an innovative programmable RNA sensor and molecular tools to improve mRNA vector therapeutics.

BII BioInnovation Institute Science

Apply before November 1, 2025
bii.dk/community/prizes

CONTENTS

9 OCTOBER 2025
VOLUME 390 | ISSUE 6769



122 *Monotropastrum kirishimense* is a newly recognized species of nonphotosynthetic flower that draws sustenance from fungi on the forest floor.

PHOTOS: KENJI SUETSUGU

EDITORIAL

111 Free global access to climate and weather data must continue —P. Taalas

NEWS

112 Research on immune system's 'police' garners Nobel
Three scientists honored for revealing how regulatory T cells prevent autoimmune disease —C. Offord

113 Quantum effects in circuits honored with Physics Nobel
Breakthrough paved the way to many of today's budding quantum computers —A. Cho

114 First approved drug for mitochondrial disease raises hopes for more
Researchers are testing multiple treatments for the rare genetic conditions —M. Leslie

116 Long-lived gamma ray burst puzzles astronomers
Some theorists think unusual event could be a black hole devouring a star from within —D. Clery

118 AI-generated 'participants' can lead social science experiments astray
Data produced by "silicon samples" vary with researchers' exact choice of models, prompts, and settings, study finds —C. O'Grady

119 Science teachers scramble as U.S. climate resources vanish
As government websites go dark, some nonprofits are trying to provide classroom materials —G. Cabico

FEATURES

122 Seeking ghosts
A Japanese botanist is revealing the secrets of plants that have given up photosynthesis —D. Normile

COMMENTARY

PERSPECTIVES

126 Longevity steps on the cGAS
A DNA repair function in a cytosolic sensor demonstrates a potential role in naked mole-rat longevity —J . C. Martinez *et al.*
RESEARCH SUMMARY p. 150

128 A tripartite alliance for dietary fat absorption
Microbes, immune cells, and enterocytes interact to regulate the intake of lipids in the mouse gut —R. Burkhardt and J. Ecker
RESEARCH SUMMARY p. 149

129 Natural directed evolution in gut microbiota
Bacteria undergo rapid genetic changes that are selected by alterations in the human gut environment —B. G. Paul and J. J. Mekalanos
RESEARCH SUMMARY p. 151

131 A light switch for a hidden order
Circularly polarized light provides a direct control of ferroaxiality —Z. He and G. Khalsa
RESEARCH ARTICLE p. 195

POLICY FORUM

132 China's emerging regulation toward an open future for AI
Legislation proposals seek to bring certainty, clarification, harmonization, and simplification —Y. Zhu *et al.*

BOOKS ET AL.

136 The lithium dilemma
A social scientist questions the importance of a key mineral in "green" technology —S. H. Ali

137 The complicated legacy of antibiotics
Antimicrobial drugs changed everything, but misuse and resistance have been constant companions —A. R. Glynn



Senior leaders from Morgan State University and elected officials attend the ground-breaking ceremony for Morgan's new Science Center. Pictured (left to right): Dean Paul Tchounwou, Baltimore Mayor Brandon Scott, Maryland Governor Wes Moore, Morgan President David Wilson, Congressman Kweisi Mfume, and Provost Hongtao Yu.

Growing the future with Morgan State University

With more than 30 new academic programs, soaring enrollment, and a brand-new science center in the works, Morgan is bursting at the seams.

As Morgan State University sets its sights on R1, top-tier research university status, it is adding academic programs and breaking ground on new buildings. And students are noticing, enrolling at record numbers for the historically Black research university located in Baltimore, Maryland.

"As we ascend toward R1 classification, we remain steadfast in our commitment to producing the leaders, innovators, and researchers who will shape tomorrow while staying grounded in our mission, our roots, and our enduring legacy of growing the future and leading the world," says David K. Wilson, president of Morgan State University. Since 2020, Morgan has added more than 30 new academic programs, expanding to over 150 offerings, including a master's program in neuroscience and a bachelor's program in coastal science and policy. Among Maryland institutions, Morgan was the first to offer programs in advanced computing, interior design, and mechatronics—a field that combines mechanics, electronics, and computing to support automated manufacturing processes.

To better equip students for today's job market, Morgan developed 18 new interdisciplinary degree programs called Morgan Completes You. Launched in 2021, this collection of programs helps students who already have college credits finish their degrees and learn in-demand skills. Morgan Completes You offers adult learners and working professionals the opportunity to earn degrees at the bachelor's, master's, and doctoral levels.

Morgan also wants to educate the educators, especially those who are former federal workers and career changers with science and math degrees, through the Transitioning to Teaching program. Launched in 2025, the initiative addresses the growing teacher shortage in K-12 classrooms and turns the recent federal government layoffs into an opportunity. Candidates can earn a one-year Master of Arts in teaching and participate in a new alternative certification program.

Students are attending Morgan in unprecedented numbers. During the 2024-2025 school year, the university experienced a 9.4% increase in enrollment over the previous year, with its largest freshman class of over 2,300 students from 41 states. Enrollment has risen for four consecutive years to a current tally of over 11,000 students, exceeding the university's goal of 10,000 students 6 years earlier than targeted. This past academic year, Morgan posted its largest graduate enrollment with over 1,700 students and awarded a record 93 doctorates, surpassing the R1 benchmark of 70.

"Our growth in recent years is a testament to our buy-in to President Wilson's vision of transforming Morgan," says Hongtao Yu, provost and senior vice president for academic affairs. "We will continue to stay aligned to our core values while reaching new milestones and breaking new ground."

With so many new programs and students, classroom and lab space can quickly become an issue. Rising to the challenge, Morgan has just broken ground on a cutting-edge, seven-story, 246,000 square-foot science center. The state-of-the-art, $337-million facility will boost research capacity and further increases Morgan's more than $1 billion in infrastructure investments over the past 10 years. In addition, the university has recently renovated its dorms and has built new off-campus apartments to ensure housing options for the growing student body. And Morgan isn't stopping there, with plans for major investments over the next decade that have already begun.

"As we continue to strive to attain R1 status as a 'very high research' university, we must ensure that our students are provided the best facilities and resources, which speaks to our recent infrastructure investments," says Willie E. May, vice president, division of research and economic development.

Sponsored by

MORGAN STATE UNIVERSITY

GROWING THE FUTURE • LEADING THE WORLD

PHOTO: PROVIDED BY MORGAN STATE UNIVERSITY



178
Greater noctule bats (*Nyctalus lasiopterus*) locate, catch, and consume migrating birds in flight

LETTERS

138 EU's global investments put biodiversity at risk
—C. Grilo *et al.*

138 Strategic foundations of science diplomacy
—M. H. Ivanova *et al.*

139 Science diplomacy is a tool, not a currency
—K. Montgomery and I. Wiggins

REVIEWS

REVIEW SUMMARY

140 Exoplanets
Constraining exoplanet interiors using observations of their atmospheres
—T. Lichtenberg *et al.*

RESEARCH

HIGHLIGHTS

141 From *Science* and other journals

RESEARCH SUMMARIES

144 Molecular biology
mRNA initiation and termination are spatially coordinated
—E. Calvo-Roitberg *et al.*

145 Metabolism
Acidosis orchestrates adaptations of energy metabolism in tumors
—S. Groessl *et al.*

146 Cancer
MTAP deficiency confers resistance to cytosolic nucleic acid sensing and STING agonists —J.-M. Hsu *et al.*

147 Yeast genetics
A genome-to-proteome map reveals how natural variants drive proteome diversity and shape fitness
—C. M. Jakobson *et al.*

148 Transposon
Mechanism of DNA targeting by human LINE-1 —W. Jin *et al.*

149 Immunology
T cell cholesterol transport links intestinal immune responses to dietary lipid absorption
—Y. Gao *et al.*
PERSPECTIVE p. 128

150 Aging
A cGAS-mediated mechanism in naked mole-rats potentiates DNA repair and delays aging —Y. Chen *et al.*
PERSPECTIVE p. 126

151 Microbiome
Targeted protein evolution in the gut microbiome by diversity-generating retroelements
—B. R. Macadangdang *et al.*
PERSPECTIVE p. 129

RESEARCH ARTICLES

152 Animal behavior
Total solar eclipse triggers dawn behavior in birds: Insights from acoustic recordings and community science —L. A. Aguilar *et al.*
PODCAST

156 Cell biology
Ubiquitin-mediated mitophagy regulates the inheritance of mitochondrial DNA mutations
—M. Frison *et al.*

164 Kidney disease
Reversible compromise of physiological resilience by accumulation of heteroplasmic mtDNA mutations —H. Huang *et al.*

173 Optics
Wavefront shaping enables high-power multimode fiber amplifier with output focus —S. Rothe *et al.*

178 Predation
Greater noctule bats prey on and consume passerines in flight
—L. Stidsholt *et al.*

182 Carbon offsets
Tropical forest carbon offsets deliver partial gains amid persistent over-crediting
—Y. Tang *et al.*

188 Hormone sensors
SALICYLIC ACID SENSOR1 reveals the propagation of an SA hormone surge during plant pathogen advance —B. Tang *et al.*

195 Ferroic materials
Photo-induced nonvolatile rewritable ferroaxial switching
—Z. Zeng *et al.*
PERSPECTIVE p. 131

199 Batteries
Anion sublattice design enables superionic conductivity in crystalline oxyhalides —F. Zhao *et al.*

WORKING LIFE

210 Learning from my stutter
—P. Deak

110 *Science* Staff
205 *Science* Careers

ON THE COVER



As the Moon eclipsed the Sun on 8 April 2024, birds like these rock pigeons (*Columba livia*) took note. For most birds, changes in light are used to appropriately time their behavior. Leveraging nature's own experiment, scientists and the public joined forces to show how different species responded to sudden midafternoon darkness followed by a new "dawn." See page 152. Photo: Christopher Everett

ON THE PODCAST

How birds reacted to a solar eclipse, and keeping wildfire smoke out of wine

PHOTO: ELENA TENA

Science **serves as a forum for discussion of important issues related to the advancement of science by publishing material on which a consensus has been reached as well as including the presentation of minority or conflicting points of view. Accordingly, all articles published in *Science*—including editorials, news, commentary, and book reviews—are signed and reflect the individual views of the authors and not official points of view adopted by AAAS or the institutions with which the authors are affiliated.** *Science* (ISSN 0036-8075) is published weekly on Thursday, except last week in December, by the American Association for the Advancement of Science, 1200 New York Avenue, NW, Washington, DC 20005. Periodicals mail postage (publication No. 484460) paid at Washington, DC, and additional mailing offices. Copyright © 2025 by the American Association for the Advancement of Science. The title *Science* is a registered trademark of the AAAS. Domestic individual membership, including subscription (12 months): $165 ($74 allocated to subscription). Domestic institutional subscription (51 issues): $2865; Foreign postage extra: Air assist delivery: $135. First class, airmail, student, and emeritus rates on request. Canadian rates with GST available upon request, GST #125488122. Publications Mail Agreement Number 1069624. **Printed in the U.S.A. Change of address:** Allow 4 weeks, giving old and new addresses and 8-digit account number. **Postmaster:** Send change of address to AAAS, P.O. Box 96178, Washington, DC 20090–6178. **Single-copy sales:** $15 each plus shipping and handling available from backissues.science.org; bulk rate on request. **Authorization to reproduce** material for internal or personal use under circumstances not falling within the fair use provisions of the Copyright Act can be obtained through the Copyright Clearance Center (CCC), www.copyright.com. The identification code for *Science* is 0036-8075. *Science* is indexed in the *Reader's Guide to Periodical Literature* and in several specialized indexes.

Science AAAS

EDITOR-IN-CHIEF **Holden Thorp**, hthorp@aaas.org

EXECUTIVE EDITOR Valda Vinson

EDITORS, RESEARCH Sacha Vignieri, Jake S. Yeston **EDITOR, COMMENTARY** Lisa D. Chong

DEPUTY EXECUTIVE EDITOR Lauren Kmec

DEPUTY EDITORS Stella M. Hurtley (UK), Phillip D. Szuromi **SENIOR EDITORS** Caroline Ash (UK), Michael A. Funk, Angela Hessler, Di Jiang, Priscilla N. Kelly, Marc S. Lavine (Canada), Sarah Lempriere (UK), Mattia Maroso, Yevgeniya Nusinovich, Ian S. Osborne (UK), Joana Osório (UK), L. Bryan Ray, H. Jesse Smith, Keith T. Smith (UK), Jelena Stajic, Peter Stern (UK), Yury V. Suleymanov, Valerie B. Thompson, Brad Wible **ASSOCIATE EDITORS** Jack Huang, Sumin Jin, Bianca Lopez, Sarah Ross (UK), Madeleine Seale (UK), Corinne Simonti, Ekeoma Uzogara **SENIOR LETTERS EDITOR** Jennifer Sills **NEWSLETTER EDITOR** Christie Wilcox **RESEARCH & DATA ANALYST** Jessica L. Slater **LEAD CONTENT PRODUCTION EDITORS** Chris Filiatreau, Harry Jach **SR. CONTENT PRODUCTION EDITOR** Amelia Beyna **CONTENT PRODUCTION EDITORS** Anne Abraham, Robert French, Julia Haber-Katris, Nida Masiulis, Abigail Shashikanth, Suzanne M. White **SENIOR PROGRAM ASSOCIATE** Maryrose Madrid **EDITORIAL MANAGER** Joi S. Granger **EDITORIAL ASSOCIATES** Aneera Dobbins, Lisa Johnson, Jerry Richardson, Anita Wynn **SENIOR EDITORIAL COORDINATORS** Alexander Kief, Ronmel Navas, Isabel Schnaidt, Alice Whaley (UK), Brian White **EDITORIAL COORDINATORS** Samuel Bates, Clair Goodhead (UK), Kat Kirkman, Daniel Young **ADMINISTRATIVE COORDINATOR** Karalee P. Rogers **ASI DIRECTOR, OPERATIONS** Janet Clements (UK) **ASI OFFICE MANAGER** Carly Hayward (UK) **ASI SR. OFFICE ADMINISTRATORS** Simon Brignell (UK), Jessica Waldock (UK) **COMMUNICATIONS DIRECTOR** Meagan Phelan **DEPUTY DIRECTOR** Matthew Wright **SENIOR WRITERS** Walter Beckwith, Joseph Cariz, Abigail Eisenstadt **WRITER** Mahathi Ramaswamy **SENIOR COMMUNICATIONS ASSOCIATES** Zachary Graber, Sarah Woods **COMMUNICATIONS ASSOCIATES** Kiara Brooks, Haley Riley, Mackenzie Williams

NEWS EDITOR Tim Appenzeller

NEWS MANAGING EDITOR John Travis **INTERNATIONAL EDITOR** David Malakoff **DEPUTY NEWS EDITORS** Rachel Bernstein, Martin Enserink, David Grimm, Eric Hand, Michael Price, Kelly Servick, Matt Warren (Europe) **SENIOR CORRESPONDENTS** Daniel Clery (UK), Jon Cohen, Jeffrey Mervis **ASSOCIATE EDITORS** Michael Greshko, Katie Langin **NEWS REPORTERS** Jeffrey Brainard, Adrian Cho, Phie Jacobs, Jocelyn Kaiser, Rodrigo Pérez Ortega (Mexico City), Robert F. Service, Erik Stokstad, Paul Voosen, Meredith Wadman **CONSULTING EDITOR** Elizabeth Culotta **CONTRIBUTING CORRESPONDENTS** Vaishnavi Chandrashekhar, Dan Charles, Warren Cornwall, Andrew Curry (Berlin), Ann Gibbons, Kai Kupferschmidt (Berlin), Andrew Lawler, Mitch Leslie, Virginia Morell, Dennis Normile (Tokyo), Catherine Offord, Cathleen O'Grady, Elisabeth Pain (Careers), Charles Piller, Zack Savitsky, Richard Stone (Senior Asia Correspondent), Gretchen Vogel (Berlin), Lizzie Wade (Mexico City) **INTERNS** Nazeefa Ahmed, Annika Inampudi **COPY EDITORS** Julia Cole (Senior Copy Editor), Hannah Knighton, Cyra Master (Copy Chief) **ADMINISTRATIVE SUPPORT** Meagan Weiland

CREATIVE DIRECTOR Beth Rakouskas

DESIGN MANAGING EDITOR Chrystal Smith **GRAPHICS MANAGING EDITOR** Chris Bickel **PHOTOGRAPHY MANAGING EDITOR** Emily Petersen **MULTIMEDIA MANAGING PRODUCER** Kevin McLean **DIGITAL DIRECTOR** Kara Estelle-Powers **DESIGN EDITOR** Marcy Atarod **DESIGNER** Noelle Jessup **SENIOR SCIENTIFIC ILLUSTRATOR** Noelle Burgess **SCIENTIFIC ILLUSTRATORS** Austin Fisher, Kellie Holoski, Ashley Mastin **SENIOR GRAPHICS EDITOR** Monica Hersher **GRAPHICS EDITOR** Veronica Penney **SENIOR PHOTO EDITOR** Charles Borst **PHOTO EDITOR** Elizabeth Billman **SENIOR PODCAST PRODUCER** Sarah Crespi **SENIOR VIDEO PRODUCER** Meagan Cantwell **SOCIAL MEDIA STRATEGIST** Jessica Hubbard **SOCIAL MEDIA PRODUCER** Sabrina Jenkins **WEB DESIGNER** Jennie Pajerowski

CHIEF EXECUTIVE OFFICER AND EXECUTIVE PUBLISHER

Sudip Parikh

PUBLISHER, SCIENCE FAMILY OF JOURNALS Bill Moran

DIRECTOR, BUSINESS OPERATIONS & ANALYSIS Eric Knott **MANAGER, BUSINESS OPERATIONS** Jessica Tierney **SENIOR MANAGER, BUSINESS ANALYSIS** Cory Lipman **BUSINESS ANALYSTS** Kurt Ennis, Maggie Clark, Isacco Fusi **BUSINESS OPERATIONS ADMINISTRATOR** Taylor Fisher **DIGITAL SPECIALIST** Marissa Zuckerman **SENIOR PRODUCTION MANAGER** Jason Hillman **SENIOR MANAGER, PUBLISHING AND CONTENT SYSTEMS** Marcus Spiegler **CONTENT OPERATIONS MANAGER** Rebecca Doshi **PUBLISHING PLATFORM MANAGER** Jessica Loayza **PUBLISHING SYSTEMS SPECIALIST, PROJECT COORDINATOR** Jacob Hedrick **SENIOR PRODUCTION SPECIALIST** Kristin Wowk **PRODUCTION SPECIALISTS** Kelsey Cartelli, Audrey Diggs **SPECIAL PROJECTS ASSOCIATE** Shantel Agnew

MARKETING DIRECTOR Sharice Collins **ASSOCIATE DIRECTOR, MARKETING** Justin Sawyers **GLOBAL MARKETING MANAGER** Allison Pritchard **ASSOCIATE DIRECTOR, MARKETING SYSTEMS & STRATEGY** Aimee Aponte **SENIOR MARKETING MANAGER** Shawana Arnold **MARKETING MANAGER** Ashley Evans **MARKETING ASSOCIATES** Hugues Beaulieu, Ashley Hylton, Lorena Chirinos Rodriguez, Jenna Voris **MARKETING ASSISTANT** Courtney Ford **SENIOR DESIGNER** Kim Huynh

DIRECTOR AND SENIOR EDITOR, CUSTOM PUBLISHING Erika Gebel Berg **ADVERTISING PRODUCTION OPERATIONS MANAGER** Deborah Tompkins **DESIGNER, CUSTOM PUBLISHING** Jeremy Huntsinger **SENIOR TRAFFIC ASSOCIATE** Christine Hall

DIRECTOR, PRODUCT MANAGEMENT Kris Bishop **PRODUCT DEVELOPMENT MANAGER** Scott Chernoff **ASSOCIATE DIRECTOR, PUBLISHING INTELLIGENCE** Rasmus Andersen **SR. PRODUCT ASSOCIATE** Robert Koepke **PRODUCT ASSOCIATES** Caroline Breul, Anne Mason

ASSOCIATE DIRECTOR, INSTITUTIONAL LICENSING MARKETING Kess Knight **ASSOCIATE DIRECTOR, INSTITUTIONAL LICENSING SALES** Ryan Rexroth **INSTITUTIONAL LICENSING MANAGER** Nazim Mohammedi, Claudia Paulsen-Young **SENIOR MANAGER, INSTITUTIONAL LICENSING OPERATIONS** Judy Lillibridge **MANAGER, RENEWAL & RETENTION** Lana Guz **SYSTEMS & OPERATIONS ANALYST** Ben Teincuff **FULFILLMENT ANALYST** Aminta Reyes

ASSOCIATE DIRECTOR, INTERNATIONAL Roger Goncalves **ASSOCIATE DIRECTOR, US ADVERTISING** Stephanie O'Connor **US MID WEST, MID ATLANTIC AND SOUTH EAST SALES MANAGER** Chris Hoag **DIRECTOR, OUTREACH AND STRATEGIC PARTNERSHIPS, ASIA** Shoupeng Liu **SALES REP, ROW** Sarah Lelarge **SALES ADMIN ASSISTANT, ROW** Victoria Glasbey **DIRECTOR OF GLOBAL COLLABORATION AND ACADEMIC PUBLISHING RELATIONS, ASIA** Xiaoying Chu **ASSOCIATE DIRECTOR, INTERNATIONAL COLLABORATION** Grace Yao **SALES MANAGER** Danny Zhao **MARKETING MANAGER** Kilo Lan **ASCA CORPORATION, JAPAN** Rie Rambelli (Tokyo), Miyuki Tani (Osaka)

DIRECTOR, COPYRIGHT, LICENSING AND SPECIAL PROJECTS Emilie David **RIGHTS AND PERMISSIONS ASSOCIATE** Elizabeth Sandler **LICENSING ASSOCIATE** Virginia Warren **RIGHTS AND LICENSING COORDINATOR** Dana James **CONTRACT SUPPORT SPECIALIST** Michael Wheeler

EDITORIAL
science_editors@aaas.org

NEWS
science_news@aaas.org

INFORMATION FOR AUTHORS
science.org/authors/
science-information-authors

REPRINTS AND PERMISSIONS
science.org/help/
reprints-and-permissions

MULTIMEDIA CONTACTS
SciencePodcast@aaas.org
ScienceVideo@aaas.org

MEDIA CONTACTS
scipak@aaas.org

PRODUCT ADVERTISING & CUSTOM PUBLISHING
advertising.science.org
science_advertising@aaas.org

CLASSIFIED ADVERTISING
advertising.science.org/
science-careers
advertise@sciencecareers.org

JOB POSTING CUSTOMER SERVICE
employers.sciencecareers.org
support@sciencecareers.org

MEMBERSHIP AND INDIVIDUAL SUBSCRIPTIONS
science.org/subscriptions

MEMBER BENEFITS
aaas.org/membership/
benefits

INSTITUTIONAL SALES AND SITE LICENSES
science.org/librarian

AAAS BOARD OF DIRECTORS

CHAIR Joseph S. Francisco

IMMEDIATE PAST PRESIDENT
Willie E. May

PRESIDENT
Theresa A. Maldonado

PRESIDENT-ELECT
Marina Picciotto

TREASURER Carolyn N. Ainslie

COUNCIL CHAIR
Ichiro Nishimura

CHIEF EXECUTIVE OFFICER
Sudip Parikh

BOARD
Mark Dingfield
Morton Ann Gernsbacher
Kathleen Hall Jamieson
Jane Maienschein
Babak Parviz
Gabriela Popescu
Juan S. Ramírez Lugo
Susan M. Rosenberg
Vassiliki Betty Smocovitis
Roger Wakimoto

BOARD OF REVIEWING EDITORS (Statistics board members indicated with **S**)

Erin Adams, *U. of Chicago*
Takuzo Aida, *U. of Tokyo*
Leslie Aiello, *Wenner-Gren Fdn.*
Anastassia Alexandrova, *UCLA*
Mohammed AlQuraishi, *Columbia U.*
James Analytis, *UC Berkeley*
Paola Arlotta, *Harvard U.*
Madan Babu, *St. Jude*
Jennifer Balch, *U. of Colorado*
Nenad Ban, *ETH Zürich*
Carolina Barillas-Mury, *NIH, NIAID*
Christopher Barratt, *U. of Dundee*
François Barthelat, *U. of Colorado Boulder*
Franz Bauer, *Universidad de Tarapacá*
Andreas Baumler, *UC Davis*
Carlo Beenakker, *Leiden U.*
Sarah Bergbreiter, *Carnegie Mellon U.*
Kiros T. Berhane, *Columbia U.*
Aude Bernheim, *Inst. Pasteur*
Joseph J. Berry, *NREL*
Dominique Bonnet, *Francis Crick Inst.*
Chris Bowler, *École Normale Supérieure*
Ian Boyd, *U. of St. Andrews*
Malcolm Brenner, *Baylor Coll. of Med.*
Ron Brookmeyer, *UCLA* (**S**)
Christian Büchel, *UKE Hamburg*
Johannes Buchner, *TUM*
Dennis Burton, *Scripps Res.*
Carter Tribley Butts, *UC Irvine*
György Buzsáki, *NYU School of Med.*
Annmarie Carlton, *UC Irvine*
Jane Carlton, *Johns Hopkins U.*
Pedro Carvalho, *U. of Oxford*
Simon Cauchemez, *Inst. Pasteur*
Ling-Ling Chen, *SIBCB, CAS*
Hilde Cheroutre, *La Jolla Inst.*
Wendy Cho, *UIUC*
Ib Chorkendorff, *Denmark TU*
Chunaram Choudhary, *København U.*
Karlene Cimprich, *Stanford U.*
Laura Colgin, *UT Austin*
James J. Collins, *MIT*
Robert Cook-Deegan, *Arizona State U.*
Carolyn Coyne, *Duke U.*
Roberta Croce, *VU Amsterdam*
Ismaila Dabo, *Penn State U.*
Jeff L. Dangl, *UNC*
Nicolas Dauphas, *U. of Chicago*
Claude Desplan, *NYU*
Sandra Díaz, *U. Nacional de Córdoba*
Samuel Díaz-Muñoz, *UC Davis*
Ulrike Diebold, *TU Wien*
Stefanie Dimmeler, *Goethe-U. Frankfurt*
Hong Ding, *Inst. of Physics, CAS*
Dennis Discher, *UPenn*
Jennifer A. Doudna, *UC Berkeley*
Ruth Drdla-Schutting, *Med. U. Vienna*
Raissa M. D'Souza, *UC Davis*
Bruce Dunn, *UCLA*
William Dunphy, *Caltech*
Scott Edwards, *Harvard U.*
Todd A. Ehlers, *U. of Glasgow*
Tobias Erb, *MPS, MPI Terrestrial Microbiology*
Beate Escher, *UFZ & U. of Tübingen*
Barry Everitt, *U. of Cambridge*
Vanessa Ezenwa, *U. of Georgia*
Toren Finkel, *U. of Pitt. Med. Ctr.*
Natascha Förster Schreiber, *MPI Extraterrestrial Phys.*
Serita Frey, *U. of New Hampshire*
Elaine Fuchs, *Rockefeller U.*
Caixia Gao, *Inst. of Genetics and Developmental Bio., CAS*
Daniel Geschwind, *UCLA*
Lindsey Gillson, *U. of Cape Town*
Alemu Gonsamo Gosa, *McMaster U.*
Simon Greenhill, *U. of Auckland*
Gillian Griffiths, *U. of Cambridge*
Nicolas Gruber, *ETH Zürich*
Hua Guo, *U. of New Mexico*
Taekjip Ha, *Johns Hopkins U.*
Daniel Haber, *Mass. General Hos..*
Hamida Hammad, *VIB IRC*
Brian Hare, *Duke U.*
Wolf-Dietrich Hardt, *ETH Zürich*
Kelley Harris, *U. of Wash*
Carl-Philipp Heisenberg, *IST Austria*
Emiel Hensen, *TU Eindhoven*
Christoph Hess, *U. of Basel & U. of Cambridge*
Brian Hie, *Stanford U.*
Heather Hickman, *NIAID, NIH*
Janneke Hille Ris Lambers, *ETH Zürich*
Kai-Uwe Hinrichs, *U. of Bremen*
Pinshane Huang, *UIUC*
Christina Hulbe, *U. of Otago, New Zealand*
Randall Hulet, *Rice U.*
Gwyneth Ingram, *ENS Lyon*
Darrell Irvine, *Scripps Res.*
Erich Jarvis, *Rockefeller U.*
Peter Jonas, *IST Austria*
Sheena Josselyn, *U. of Toronto*
Matt Kaeberlein, *U. of Wash.*
Daniel Kammen, *UC Berkeley*
Kisuk Kang, *Seoul Nat. U.*
Vedika Khemani, *Stanford U.*
V. Narry Kim, *Seoul Nat. U.*
Nancy Knowlton, *Smithsonian*
Etienne Koechlin, *École Normale Supérieure*
Alex L. Kolodkin, *Johns Hopkins U.*
LaShanda Korley, *U. of Delaware*
Paul Kubes, *U. of Calgary*
Deborah Kurrasch, *U of Calgary*
Laura Lackner, *Northwestern U.*
Mitchell A. Lazar, *UPenn*
Hedwig Lee, *Duke U.*
Fei Li, *Xi'an Jiaotong U.*
Jianyu Li, *McGill U.*
Ryan Lively, *Georgia Tech*
Luis Liz-Marzán, *CIC biomaGUNE*
Omar Lizardo, *UCLA*
Jonathan Losos, *WUSTL*
Ke Lu, *Inst. of Metal Res., CAS*
Christian Lüscher, *U. of Geneva*
Jean Lynch-Stieglitz, *Georgia Tech*
David Lyons, *U. of Edinburgh*
Fabienne Mackay, *QIMR Berghofer*
Vidya Madhavan, *UIUC*
Anne Magurran, *U. of St. Andrews*
Asifa Majid, *U. of Oxford*
Oscar Marín, *King's Coll. London*
Matthew Marinella, *Arizona State U.*
Charles Marshall, *UC Berkeley*
Christopher Marx, *U. of Idaho*
Geraldine Masson, *CNRS*
Jennifer McElwain, *Trinity College Dublin*
Scott McIntosh, *NCAR*
Rodrigo Medellín, *U. Nacional Autónoma de México*
Mayank Mehta, *UCLA*
C. Jessica Metcalf, *Princeton U.*
Tom Misteli, *NCI, NIH*
Jeffery Molkentin, *Cincinnati Children's Hospital Medical Center*
Alison Motsinger-Reif, *NIEHS, NIH* (**S**)
Rosa Moysés, *U. of São Paulo School of Medicine*
Carey Nadell, *Dartmouth College*
Thi Hoang Duong Nguyen, *MRC LMB*
Helga Nowotny, *Vienna Sci. & Tech. Fund*
Pilar Ossorio, *U. of Wisconsin*
Andrew Oswald, *U. of Warwick*
Isabella Pagano, *Istituto Nazionale di Astrofisica*
Giovanni Parmigiani, *Dana-Farber* (**S**)
Zak Page, *UT Austin*
Sergiu Pasca, *Stanford U.*
Julie Pfeiffer, *UT Southwestern Med. Ctr.*
Philip Phillips, *UIUC*
Matthieu Piel, *Inst. Curie*
Pierre Paoletti, *Ecole Normale Supérieure, Paris*
Kathrin Plath, *UCLA*
Martin Plenio, *Ulm U.*
Katherine Pollard, *UCSF*
Elvira Poloczanska, *Alfred-Wegener-Inst.*
Julia Pongratz, *Ludwig Maximilians U.*
Philippe Poulin, *CNRS*
Suzie Pun, *U. of Wash*
Lei Stanley Qi, *Stanford U.*
Simona Radutoiu, *Aarhus U.*
Maanasa Raghavan, *U. of Chicago*
Trevor Robbins, *U. of Cambridge*
Adrienne Roeder, *Cornell U.*
Joeri Rogelj, *Imperial Coll. London*
John Rubenstein, *SickKids*
Yvette Running Horse Collin, *Toulouse U.*
Mike Ryan, *UT Austin*
Alberto Salleo, *Stanford U.*
Miquel Salmeron, *Lawrence Berkeley Nat. Lab*
Nitin Samarth, *Penn State U.*
Erica Ollmann Saphire, *La Jolla Inst.*
Joachim Saur, *U. zu Köln*
Alexander Schier, *Harvard U.*
Wolfram Schlenker, *Columbia U.*
Susannah Scott, *UC Santa Barbara*
Anuj Shah, *U. of Chicago*
Vladimir Shalaev, *Purdue U.*
Jie Shan, *Cornell U.*
Jay Shendure, *U. of Wash.*
Steve Sherwood, *U. of New South Wales*
Ken Shirasu, *RIKEN CSRS*
Robert Siliciano, *JHU School of Med.*
Emma Slack, *ETH Zürich & U. of Oxford*
Richard Smith, *UNC* (**S**)
Ivan Soltesz, *Stanford U.*
John Speakman, *U. of Aberdeen*
Allan C. Spradling, *Carnegie Institution for Sci.*
V. S. Subrahmanian, *Northwestern U.*
Sandip Sukhtankar, *U. of Virginia*
Naomi Tague, *UC Santa Barbara*
A. Alec Talin, *Sandia Natl. Labs*
Patrick Tan, *Duke-NUS Med. School*
Sarah Teichmann, *Wellcome Sanger Inst.*
Dörthe Tetzlaff, *Leibniz Institute of Freshwater Ecology and Inland Fisheries*
Amanda Thomas, *UC Davis*
Rocio Titiunik, *Princeton U.*
Shubha Tole, *Tata Inst. of Fundamental Res.*
Maria-Elena Torres Padilla, *Helmholtz Zentrum München*
Kimani Toussaint, *Brown U.*
Barbara Treutlein, *ETH Zürich*
Li-Huei Tsai, *MIT*
Jason Tylianakis, *U. of Canterbury*
Matthew Vander Heiden, *MIT*
Jo Van Ginderachter, *VIB, U. of Ghent*
Ivo Vankelecom, *KU Leuven*
Henrique Veiga-Fernandes, *Champalimaud Fdn.*
Reinhilde Veugelers, *KU Leuven*
Elizabeth Villa, *UC San Diego*
Bert Vogelstein, *Johns Hopkins U.*
David Wallach, *Weizmann Inst.*
Jane-Ling Wang, *UC Davis* (**S**)
Jessica Ware, *Amer. Mus. of Natural Hist.*
David Waxman, *Fudan U.*
Alex Webb, *U. of Cambridge*
Chris Wikle, *U. of Missouri* (**S**)
Ian A. Wilson, *Scripps Res.* (**S**)
Marjorie Weber, *U. of Michigan*
Sylvia Wirth, *ISC Marc Jeannerod*
Hao Wu, *Harvard U.*
Amir Yacoby, *Harvard U.*
Benjamin Youngblood, *St. Jude*
Yu Xie, *Princeton U.*
Kenneth Zaret, *UPenn School of Med.*
Lidong Zhao, *Beihang U.*
Bing Zhu, *Inst. of Biophysics, CAS*
Xiaowei Zhuang, *Harvard U.*
Maria Zuber, *MIT*

Free global access to climate and weather data must continue

Petteri Taalas

Last month at the 80th session of the United Nations, the call to be "better together" was especially appropriate for discussions on the Early Warnings for All global initiative. About half the world's countries now have multihazard weather alert systems, and disaster-related mortality is considerably lower in countries with such warning capacities. But much more is needed to achieve the 2027 goal of ensuring that everyone on Earth is protected from extreme and hazardous weather events. This will require the continued free sharing of data and the improvement of observation systems and weather service facilities.

The World Meteorological Organization (WMO) and its predecessor, the International Meteorological Organization, have been promoting the free global exchange of weather observations since the mid-19th century and have agreed-upon standards for instrument technologies. Without sharing internationally standardized data, weather forecasts and early warning systems would not be feasible. Associated with this, international collaborations have sustained vital observing networks for the atmosphere, oceans, and land. For example, the Global Climate Observing System, established by the WMO, the United Nations, and the International Science Council, supports a network of satellites and other on-site monitoring systems to provide a comprehensive view of Earth's climate.

Without sharing...data, weather forecasts and early warning systems would not be feasible.

The collection and free dissemination of such data are needed to understand and predict weather events, assess risks and underlying causes, and guide regional and global climate adaptation and mitigation efforts. Yet, there have been threats to this long-standing approach of data sharing. The United States has been a pioneer in the free exchange and availability of climate data for decades. However, current and future cuts to atmospheric service agencies such as the US National Oceanic and Atmospheric Administration (NOAA) are matters of concern. Meteorologists and scientists worldwide rely on NOAA systems and data for weather forecasting and long-term climate predictions. Degrading NOAA will jeopardize the accurate and spatially detailed information that guide weather forecasting agencies around the world. For example, the US provides roughly a quarter of the meteorological satellite information used worldwide by weather agencies. It is therefore vital to continue the current NOAA practices.

There also have been attempts to commercialize atmospheric and meteorological data, driven by meteorological satellite data providers. Such initiatives would ruin global weather forecasting systems and harm poorer countries lacking the financial means to buy the essential data. In the past, almost all Western European countries regulated the use of publicly funded weather observations for commercial purposes. National weather services were charging private companies for observational data and other information. Even satellite data from the European Space Agency were sold, which severely limited the use of its observations. Fortunately, two decades ago, the European Union changed environmental and atmospheric policies, making such data and related modeling software codes and satellite algorithms freely available to anyone. In Finland, an academic study showed that the economic value of free meteorological data is more than 20-fold the earnings of Finnish Meteorological Institute data sales. The government has since increased the institute's budget to support free data to compensate for revenue loss by data sales and to cover data release service costs.

Thanks to a new WMO data policy in 2021, larger amounts of meteorological and atmospheric data are released for free use by all 193 WMO member states and territories. This has led to improvements in the quality and quantity of weather services worldwide and has also enhanced the socioeconomic value of the basic weather observations. Moving forward, half a billion dollars is planned for investment in a Systematic Observations Financing program, supported by Northern European countries, the United States, Australia, and New Zealand, to improve weather observations in less developed countries.

Climate change and weather extremes affect everyone, everywhere. Countries should not retreat from supporting the early warning systems and related technologies that save lives. The free exchange of observational data and weather-related information has been foundational for governments to prepare for heat waves, droughts, floods, wildfires, and hurricanes, among other weather hazards, that cause widespread destruction, damage, and loss of life. Countries rely on each other for data, knowledge, and collective planning. If this trust and collaboration are broken, then we are all in danger. □

Petteri Taalas is the director general of the Finnish Meteorological Institute, Helsinki, Finland. He served as the secretary-general of the World Meteorological Organization (2016–2023). petteri.taalas@fmi.fi

10.1126/science.aec8146



Mary Brunkow is overcome with emotion at her Seattle home after a photographer told her she had won a Nobel Prize.

PHOTO: LINDSEY WASSON/AP

NOBEL PRIZES

Research on immune system's 'police' garners Nobel

Three scientists honored for revealing how regulatory T cells prevent autoimmune disease **CATHERINE OFFORD**

WINNERS

MARY BRUNKOW, Institute for Systems Biology

FRED RAMSDELL, Sonoma Biotherapeutics

SHIMON SAKAGUCHI, University of Osaka

Three scientists have won this year's Nobel Prize in Physiology or Medicine for disentangling how the immune system distinguishes friend from foe.

Shimon Sakaguchi of the University of Osaka, Mary Brunkow of the Institute for Systems Biology in Seattle, and Fred Ramsdell of San Francisco–based Sonoma Biotherapeutics revealed some of the mechanisms that prevent accidental attacks by the immune system against the body's own cells—and showed how autoimmune diseases arise when that process goes awry. The work has led to the development of experimental treatments for cancer and autoimmune disease.

The recognition for their work, announced at a Stockholm press conference on 6 October, is "richly deserved," says Carola Vinuesa, who studies autoimmunity at the Francis Crick Institute. "Their pioneering research uncovered one of the immune system's most critical regulatory mechanisms."

The immune system protects the body from invading microbes with the help of white blood cells known as T cells. Each T cell carries specific receptors that—when things work as they should—recognize proteins from hostile microbes and other threats and help launch an attack against them. However, the body also makes some T cells that carry receptors recognizing the body's own cells. If left unchecked, they can trigger autoimmune diseases such as lupus and type 1 diabetes.

By the 1990s, scientists knew the body was able to prevent some of this friendly fire by eliminating self-recognizing cells during T cell development in an organ called the thymus. That mechanism is known as central immune tolerance.

But Sakaguchi, then at the Aichi Cancer Center Research Institute, found there was more to the story. Mice that have their thymus removed just after birth are prone to autoimmune diseases, but his lab discovered that injecting T cells from normal mice protected the recipients. This suggested the injected T cells could somehow eliminate self-recognizing cells.

Sakaguchi identified these protectors as a specific class of T cells that express a protein called CD25 on their surfaces. In a 1995 paper, his group described the cells, later known as regulatory T cells or Tregs, and suggested they stop other immune cells from reacting to the body's own tissues. The scientific community was initially skeptical, but Tregs have since been recognized as police officers of the immune system and an important part of what's known as peripheral immune tolerance. "Anyone who does not have an autoimmune disease, that's because of these regulatory T cells," says Markus Feuerer, an immunologist at the Leibniz Institute for Immunotherapy.

Meanwhile Brunkow and Ramsdell, then both at a U.S. biotech named Celltech Chiroscience, were studying "scurfy mice," which have an autoimmune disorder that causes flaky skin, an oversize spleen and lymph nodes, and a shortened life span. The condition only affects males, suggesting the mutation responsible is on the X chromosome. (Because males have only one X, mutations there go unchecked by a normal gene on a matching X.)

In a 2001 paper, they identified the gene that contained the mutation, called it *Foxp3*, and proposed it codes for a transcription factor, a type of protein that regulates gene expression. They also linked the human equivalent of the gene, *FOXP3*, to an

autoimmune disease called IPEX that causes symptoms like those of scurfy mice in boys.

The two groups' discoveries coalesced in subsequent work by Sakaguchi, who showed that *Foxp3* is important for the development of Tregs. The gene is expressed in these cells, and experiments showed other types of T cells can be transformed into Tregs by switching on *Foxp3* expression. Ramsdell's team would later find that scurfy mice lack Tregs. Work by other labs has since found altered *FOXP3* expression and defects in Treg function in human diseases, including type 1 diabetes and multiple sclerosis, although the cells' exact role remains unclear.

Building on the trio's discoveries, various groups have aimed to modulate Tregs for therapeutic purposes, resulting in more than 200 registered clinical trials involving the cells. "If you control the brakes to the immune system, it gives you the ability to turn the immune response up or to tone it down," says Adrian Liston, an immunologist at the University of Cambridge.

In some clinical trials, a compound made naturally in the body called interleukin-2—essentially "food for Tregs," Liston says—is given to try to boost the cells' activity in patients with autoimmune disease or in people who have received an organ transplant. Meanwhile, companies such as Sonoma, which Ramsdell co-founded, are developing engineered Tregs that might police autoimmunity more effectively. Other researchers hope to reduce or redirect Tregs' activity. In cancer, for example, "an excess of Tregs in the tumor microenvironment can suppress immune responses against cancer cells," Vinuesa says.

Immunologists applauded the Nobel committee's decision. "It's amazing news," says Holm Uhlig, a pediatrician at the University of Oxford who studies inflammatory bowel diseases and has collaborated with Ramsdell. "It just shows the contribution that the field has made." Immunologist Thomas Boehm of the Max Planck Institute of Biology says he is "particularly pleased that Mary Brunkow is being recognized because she has not always received the credit she deserves for her work."

At a press conference in Osaka, Sakaguchi said he was "surprised and honored." He thanked students and collaborators and acknowledged the broader efforts of the research field. "I was never working alone," he said. "I see this award as one that represents all of those people who have contributed to this research alongside me."

Sakaguchi was the only winner the Nobel committee was able to reach before it announced the prize. Ramsdell was reportedly on vacation in the Rocky Mountains at the time, and Brunkow heard the news from an AP photographer who went to her Seattle home early in the morning. She told AP she had not picked up her phone when the call from Stockholm came, explaining: "I saw a number from Sweden and thought: 'That's just, that's spam of some sort.'" □

With reporting by Kai Kupferschmidt and Dennis Normile.

NOBEL PRIZES

Quantum effects in circuits honored with Physics Nobel

Breakthrough paved the way to many of today's budding quantum computers **ADRIAN CHO**

The strange rules of quantum mechanics ordinarily hold sway only at subatomic scales. However, in 1985, three physicists coaxed distinctly quantum mechanical behavior out of a tiny electrical circuit—gigantic for the quantum realm. That feat paved the way for much of the current work on quantum computers. And this week it earned the Nobel Prize in Physics for John Clarke of the University of California, Berkeley; Michel Devoret of Yale University; and John Martinis of UC Santa Barbara.

In the 1980s, when the three worked in Clarke's UC Berkeley lab, "it was a big open question whether a macroscopic circuit would show quantum behavior at all," says Andreas Wallraff, a quantum physicist at ETH Zürich. Simon Storz, a quantum physicist also at ETH Zürich, marvels that the work could have led to the then unimagined field of quantum computing. "Its potential wasn't obvious at the time."

When cooled to near absolute zero, certain metals become superconductors, and a circuit built from them will carry a current with no resistance. Such flow arises when the electrons join in loosely associated pairs and those pairs condense into a single macroscopic wave. In Clarke's lab, where Devoret was a postdoc and Martinis was a graduate student, the trio demonstrated the existence of that macroscopic wave. They also proved it behaves quantum mechanically.

WINNERS

JOHN CLARKE, University of California, Berkeley

MICHEL DEVORET, Yale University

JOHN MARTINIS, University of California, Santa Barbara

To do that, they exploited an effect known as quantum tunneling, which was predicted in the 1920s and invoked to explain some radioactive decays. An insulating barrier in a superconducting wire normally stops the flow of electricity. If, however, the barrier is thin enough, then the quantum wave of electrons on either side can penetrate it and overlap inside it, allowing pairs of electrons to tunnel through and current to flow. British theorist Brian Josephson predicted the effect in superconductors in 1962, and it was soon observed in devices now known as Josephson junctions.

Still, those experiments did not show that the waves existed or behaved quantum mechanically. To do that, the laureates ran an additional "bias" current through a junction, which altered the relative energies of the waves on either side of the barrier. They then showed that as the temperature plummeted toward absolute zero, the unquenchable tunneling current varied as predicted by theory. By shining microwaves on the junction, they also showed that the wave has distinct higher energy states in which the tunneling current increased as predicted.

Today, superconducting circuits hosting such quantum waves are among the leading candidates for the quantum bits that power quantum computers, which should be able to solve certain problems that would overwhelm any conventional computer. In 2019, Martinis led a Google team when it claimed to perform the first computation a supercomputer couldn't match—although the claim was later disputed.

This year's prize does not, however, cite the rise of superconducting qubits, a development a few other researchers could also claim credit for, notes Stefan Filipp, a quantum physicist at the Technical University of Munich. Filipp wonders whether the Nobel committee "left the door open" for a future prize to honor superconducting qubits.

For his part, Clarke says the prize came "as the surprise of my life." During a press conference announcing the prize, he added, "It had never occurred to me that this [work] might the basis for a Nobel Prize." □

With reporting by Daniel Clery and Cathleen O'Grady.

IN OTHER NEWS

INSECT ETHICS

Scientists working with mice and other vertebrates are typically required to treat them humanely, such as by using anesthetics. But such rules rarely apply to insects and other invertebrates. Maybe that should change, say Bob Fischer, a philosopher at Texas State University, and Craig Perl, an entomologist at the University of Stirling. They are co-authors of a recent *PLOS ONE* study that found papers describing invertebrate studies often ignore welfare issues. "Entomologists tend to assume there's no reason to be concerned about insects, as though they're just little robots," Fisher says. "But when we [reviewed] the literature, we came to think that isn't so straightforward. We can't confidently say insects feel pain, but there is enough evidence that we think some precautionary measures make sense." Even if a scientist "doesn't think precautionary measures are warranted, it's still really important to report what they have and haven't done to insects in experiments," Perl says. Not reporting how insects died, for example, could affect reproducibility. "What we need," Fisher says, "is for scientists to collectively say: 'OK, this is an issue worth spending a little bit of time on.'"
—Phie Jacobs

BIOMEDICINE

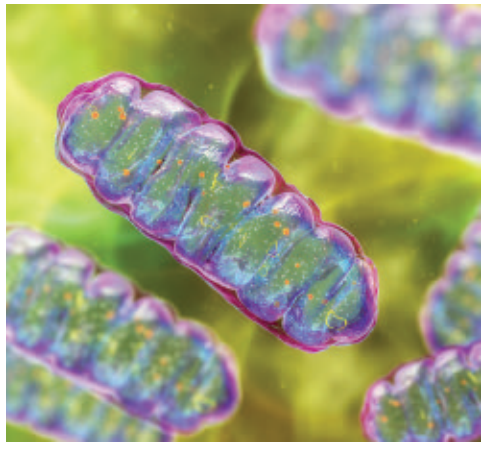
First approved drug for mitochondrial disease raises hopes for more

Researchers are testing multiple treatments for the rare genetic conditions

MITCH LESLIE

The thousands of mitochondria that populate a typical human cell are best known for generating ATP, life's chemical fuel. But these organelles also help cells synthesize key molecules, control calcium levels, manage stress, and perform other essential tasks. No wonder that when mutations cause mitochondria to malfunction, the consequences can be serious, ranging from fatigue and weakness to seizures and occasionally death.

Mitochondrial diseases have seemed intractable, but last month the Food and Drug Administration (FDA) OK'd the first treatment targeting a mitochondrial flaw. Called elamipretide, it aims to treat Barth syndrome, an extremely rare condition that kills some babies within their first year.



Mitochondria are known as cells' energy factories, but they have many other functions—and many ways to go wrong.

"This is a very important step for mitochondrial disease physicians and patients," says pediatric neurologist Mary Kay Koenig of the University of Texas Health Science Center at Houston. The decision shows that "this is a field where treatments are approvable."

The progress has been hard won, however, because the diseases have complex mechanisms and varied symptoms. Just a few weeks before, FDA rejected a therapy for another often-fatal mitochondrial disease, pyruvate dehydrogenase complex deficiency (PDCD), asking its manufacturer to run an additional clinical trial. Elamipretide, too, was rejected twice, and only greenlit after more than a year of back and forth with the manufacturer.

Still, mitochondrial disease researchers hope they are finally on a roll. FDA is currently considering another drug, MT1621, for an extremely rare mitochondrial disease known as thymidine kinase 2 deficiency (TK2d). "I'd be floored if it wasn't approved," Koenig says. At least seven other treatments for mitochondria-related illnesses are in clinical trials, and academic researchers and a host of new biotechs are pursuing more potential therapies. "There is an explosion of studies," says geneticist and clinical researcher Fernando Scaglia of Baylor College of Medicine. "We are excited."

Although mitochondrial diseases are numerous, all are rare. Barth syndrome affects about 150 people in the United States, and TK2d is even less common—only about 250 people in the world suffer from it. The most prevalent mitochondrial disease–causing mutation, a flaw in a gene necessary for the organelle to synthesize proteins, affects about 50,000 people in the U.S., Europe, and Japan, says Jan Smeitink, founder of the Netherlands-based biotech Khondrion.

One reason these genetic diseases are attracting more attention is that the organelles also falter in more common conditions, including several neurodegenerative illnesses, heart disease, and diabetes. Mitochondria can go awry in aging as well. Some companies are betting that if they develop a treatment for a rare mitochondrial mutation, it might also work for the more common—and therefore more lucrative—conditions.

Biotechs are encouraged because researchers now understand more about how mitochondrial flaws cause disease, which improves the odds of finding drug targets, says neurologist Robert Pitceathly of University College London. Doctors also have better tools for diagnosing the disorders, which could expand the market for a potential drug. Pursuing treatments is now "much more financially viable," Pitceathly says.

"For a long time, people were stuck because the diseases were so complex," says pediatrician and clinical geneticist Marni Falk of the Children's Hospital of Philadelphia. More than 350 genetic glitches in the mitochondria's own DNA, or the DNA in the nucleus that encodes some of their proteins, can trigger the illnesses, and they cause a panoply of health effects. Even among people with the same genetic flaw, symptoms, severity, and age of

PHOTO: KATERYNA KON/SCIENCE PHOTO LIBRARY

onset can vary widely. In addition, Koenig says, "A big challenge is how do you prove these drugs work." For instance, mitochondrial illnesses often cause fatigue, but showing objectively that a drug reduces fatigue is tricky.

The failed PDCD trial illustrates some of the challenges. Patients with the disease carry a lethargic mitochondrial enzyme and, as a result, accumulate large amounts of lactate, a metabolic waste product that can be harmful at high levels. The drug that endocrinologist Peter Stacpoole of the University of Florida and colleagues were testing, dichloroacetate (DCA), boosts the activity of the enzyme by blocking another enzyme that normally inhibits it.

By some measures the researchers used, DCA appeared to work. Patients' lactate levels fell, as did their risk of dying. Movement and coordination seemed to improve in those with the most severe symptoms. "We assumed [the trial] would result in approval," says Stacpoole, who has been working on DCA since he was an undergraduate chemistry major in 1969.

But for the trial's primary endpoint—its main effectiveness criterion—the researchers chose an assessment of the patients' condition by their parents or caregivers, who reported on symptoms such as weakness, fatigue, breathing difficulties, and sleep problems. These evaluations did not reveal benefits from the drug, leading to the FDA rejection. The study participants may have been too healthy, Stacpoole says. "Many of our patients were not sick enough to show changes." The new trial demanded by FDA to confirm the drug's effectiveness could cost $20 million to $40 million and take years, he notes.

Elamipretide, which treats Barth syndrome by shielding a molecule that is key for mitochondria to function, barely cleared the bar for approval. The drug did meet its endpoint—strengthening the muscle in the thigh that extends the lower leg—according to FDA's announcement. Still, the decision "comes with conditions," Scaglia says. The drug's manufacturer, Stealth BioTherapeutics, has to conduct a further study to confirm that the increase in the muscle strength helps patients. In addition, FDA only approved the drug for patients who weigh at least 30 kilograms, excluding newborns who may already be suffering from symptoms.

Two other clinical trials of mitochondrial disease drugs have adopted yet another endpoint. Pitceathly and Koenig are taking part in a phase 2 trial of the drug KL1333 in patients who have a range of mitochondrial conditions that lead to fatigue and muscle weakness. The drug hikes the amounts of a chemical called NAD+ that mitochondria require to produce ATP, delivering a shot of energy to cells. Researchers will measure whether KL1333 increases the number of times the patients can stand up from a sitting position in 30 seconds. "That is a good measure" because it gauges strength and endurance, Pitceathly says.

The so-called sit-to-stand test is also a key criterion for a phase 3 trial planned later this year to test Khondrion's drug sonlicromanol. The molecule, which Smeitink and colleagues developed, squelches harmful oxidants, prevents cells from killing themselves, and combats inflammation, a problem in mitochondrial diseases. Results from a phase 2 trial detailed earlier this year in the journal *Brain* suggest sonlicromanol boosts cognitive function and reduces fatigue in people with the most common mitochondrial mutation. The phase 3 trial will include patients with the same defect, Smeitink says.

Given the mixed record of drug candidates, mitochondrial disease researchers are tempering their hopes for future trials. But any stumbles would also help scientists home in on better therapies and better ways to evaluate them, Pitceathly says. "The more failures we have, the better we get." □



IMAGE: JOHN JAMES AUDUBON/WIKIMEDIA COMMONS

IN FOCUS

The last great auk, once lost, is found

Scientists have tracked down the remains of a female great auk strangled with her mate in 1844 by Icelanders bent on selling the skins to collectors. The large flightless birds stood no chance of escape and in the struggle their single egg was smashed. No one knew it at the time, but the two birds were likely the last of their species. Until recently, the whereabouts of their remains was a mystery. In 2017, researchers used DNA evidence to locate the male in a Belgian museum. Now, old-fashioned sleuthing and DNA testing have finally found its mate at the Museum of Natural History and Science in Cincinnati. The auks join a few other famous last survivors, sometimes called endlings, that persist in museums as grim mementos of loss. The last female great auk has been in storage at the Cincinnati museum since a renovation in 2016, but the new finding is an impetus to put the specimen on display again, said Heather Farrington, the museum's curator of zoology. "It's a tragic story," she said. "At the same time, we're really proud to care for it and maintain it for hopefully forever." —Erik Stokstad



ASTRONOMY

Long-lived gamma ray burst puzzles astronomers

Some theorists think unusual event could be a black hole devouring a star from within **DANIEL CLERY**

Typical gamma ray bursts occur when a large star collapses into a black hole, creating a beam of light.

Flashing from the distant cosmos, the searchlight beams of light called gamma ray bursts (GRBs) mark the brightest and most powerful cosmic blasts since the Big Bang, but they are short-lived. Triggered by the collapse of a giant star into a black hole, they last just seconds or minutes. So, on 2 July, when NASA's Fermi Gamma-ray Space Telescope detected a GRB that kept going for about 7 hours before fading, observers wondered whether they were witnessing an entirely new phenomenon.

"It basically just does not observationally look like any of the other things in that category that we've seen," says astrophysicist Daniel Perley of Liverpool John Moores University. In more than half a dozen preprints posted online last week, researchers describe watching the burst, known as GRB 250702B, as it unfolded across the electromagnetic spectrum, from gamma rays to radio waves. The papers also speculate that the unusual burst has an unusual source. One provocative idea is a black hole sinking into the heart of another star and tearing it apart from the inside.

GRBs were first detected in the 1960s by U.S. spy satellites looking for illicit nuclear weapons tests. It wasn't until the late '90s that astronomers linked them to supernovae, the explosions produced by dying, massive stars. When such a star runs out of fusion fuel, its core suddenly collapses into a black hole, and some material from the star's outer layers is swept into a disk. Swirling magnetic fields funnel some of that material into jets of plasma that fire out of the black hole's poles. As the jets barrel out at near–light-speed, they produce brief beams of gamma rays, the most energetic kind of light. If a beam happens to point toward Earth, a pulse of gamma rays dazzles observers.

When the Fermi Gamma-ray Space Telescope first saw GRB 250702B, astronomers thought the long-lasting gamma rays might have originated in a more sedate process in the Milky Way, appearing so bright only because their source is close to Earth. But Europe's Very Large Telescope and the Hubble Space Telescope soon found a faint infrared "afterglow" in a distant galaxy, which NASA's JWST observatory estimated to be billions of light-years away. The GRB signal also contained peculiar peaks, as if the light beam was pulsing. "It's very unusual in its duration, a bit unusual in its environment, and then this weird periodicity I think makes it stick out,"

PHOTO: A. ROQUETTE/ESO

says astrophysicist Brian Metzger of Columbia University, who like Perley was not involved in the studies. Several authors contacted by *Science* declined to comment for this story.

Based on that pulsing rhythm, some theorists speculate that GRB 250702B occurred when a star began to swing too close in its orbit around a similar-size black hole, allowing the black hole to strip off stellar material on each pass. The disk around the black hole, refueled on each orbit, could produce multiple bursts of gamma rays. Metzger sees problems with that scenario. "Even if the central engine was perfectly periodic, it's not so obvious that the gamma rays themselves should be," he says, noting that GRBs are "extremely messy."

Some researchers think the supermassive black holes lurking at the hearts of galaxies could also produce lengthy bursts of gamma rays. When a star strays too close to such a giant black hole it can be torn apart, producing a spectacular light show and, on occasion, a jet. This mechanism is thought to be responsible for a source, observed in 2011, that produced four gamma ray bursts over 2 days.

But that scenario can't explain GRB 250702B. Its afterglow was clearly not at the center of its galaxy, but farther out, leading some to propose a star destroyed by a midsize black hole, which could happen in the galactic suburbs. But the brightness of the gamma rays varied so quickly, roughly every second, that the source would have to be more compact.

That has led some theorists to consider perhaps the most unusual scenario of all: a black hole ripping up another star from within. This model starts with a stellar-mass black hole and a large star orbiting each other. When the star has burned up all its hydrogen fuel, it is left with a dense helium core and an outer envelope that swells up. That envelope can drag on the black hole, causing it to spiral in and ultimately fall into the helium core. Once there, it tears apart the core, which fuels a powerful, long-lived jet. "It's a GRB-like phenomenon, but it allows for the longer time scale," Perley says.

Perley says it's too soon to predict which explanation will rise to the top. "You can't say there's any consensus," he says. "We will need to wait and see how things sort out as these papers are refereed." But GRB 250702B is now fading into invisibility. Astronomers may have to live with the mystery until the next long-lived cataclysm provides more answers. □



THEY SAID IT

We need some large-scale solutions now. We know that neither the correction system nor the peer review system are geared up for the scale of the problem.

Jana Christopher, an imagery integrity analyst, commenting on 30 September in *Chemistry World* on research published last month in *Nature Nanotechnology*. It found scientists could not differentiate real nanomaterial images from artificial intelligence–generated fakes.

IN OTHER NEWS

NIH DIRECTORS FIRED Four institute directors at the National Institutes of Health (NIH) and another top agency official who had been in professional limbo since being placed on administrative leave in the spring have now been fired.

They are Jeanne Marrazzo, director of the National Institute of Allergy and Infectious Diseases (NIAID), who recently filed a federal whistleblower complaint that claims she was unlawfully removed for political reasons; Diana Bianchi, director of the National Institute of Child Health and Human Development; Eliseo Pérez-Stable, who directed the National Institute on Minority Health and Health Disparities; Shannon Zenk, director of the National Institute of Nursing Research; and NIH Deputy Director for Program Coordination, Planning, and Strategic Initiatives Tara Schwetz.

All received letters from NIH or the Department of Health and Human Services, its parent agency, in the past few weeks informing them that their appointments had expired or were being terminated.

"It's not surprising, but it's still incredibly disappointing," says Marrazzo, who was terminated as of 26 September. Leading $6.6 billion NIAID, which is NIH's second largest institute, was "an unbelievable privilege and kind of the job of my dreams," says the HIV prevention researcher. Her lawyer, Debra Katz, said in a statement: "Now, with her firing, there is no doubt she was removed from her position ... in retaliation for her protected whistleblower activity."

Although Marrazzo did not have an active research lab at NIH, the other three directors did—until now—employing a combined total of about 20 scientists and trainees. Pérez-Stable and Bianchi were told their positions as tenured senior investigators were ending, too.

Bianchi, a medical geneticist, headed a study of whether previously undetected cancers in pregnant people can be revealed by commercial prenatal blood tests that are designed to diagnose Down syndrome by looking for fetal DNA. It's unclear whether the study, which planned to enroll a total of 320 people, will reach that goal. —Jocelyn Kaiser

IN OTHER NEWS

UNIVERSITIES SPLIT ON TRUMP'S 'COMPACT' President Donald Trump's administration is offering nine elite U.S. universities a chance to sign a "compact for academic excellence" that it says would give them preference for federal grants if they agreed to limit foreign enrollment, freeze tuition, stay out of politics, and track what graduates earn so prospective students can assess value. Schools with "a strong readiness to champion this effort will be invited to the White House to finalize language," Secretary of Education Linda McMahon wrote to the colleges' presidents on 1 October. The offer has drawn divided reactions.

"We enthusiastically look forward to engaging with university officials and reviewing the compact immediately," said Kevin Eltife, chair of the University of Texas System Board of Regents, adding that he was honored that the state's flagship campus in Austin was "selected for potential funding advantages."

"Maybe the leaders of the University of Texas can live with these restrictions, but what about the ones imposed by the next administration?" said Jameel Jaffer of the Knight First Amendment Institute at Columbia University. "If universities normalize this, there may be no end to federal meddling." —Jeffrey Mervis



ILLUSTRATION: A. MASTIN/*SCIENCE*

ARTIFICIAL INTELLIGENCE

AI-generated 'participants' can lead social science experiments astray

Data produced by "silicon samples" vary with researchers' exact choice of models, prompts, and settings, study finds **CATHLEEN O'GRADY**

For behavioral scientists struggling to recruit enough subjects for their studies, artificial intelligence (AI) offers a tantalizing solution: artificial "participants" that can stand in for real people. Researchers have already reported that these so-called silicon samples produce humanlike responses in some surveys and experiments—and some even hope they could simulate the responses of minorities or other groups who are often underrepresented in studies.

But a new preprint calls for caution before researchers make the leap. Those who turn to AI samples face a dizzying array of choices—from which large language model (LLM) to use, to its settings, to precisely what information it is fed. According to the paper, posted to arXiv last month, these decisions can result in wide-ranging and even contradictory results—and no specific combination of choices produces data that best match human responses.

By studying the combined effect of researchers' decisions, the finding bolsters previous work that has studied the impact of individual choices, says Indira Sen, a computational social scientist at the University of Mannheim who was not involved with the study. "It definitely seems that this risk is very real."

Jamie Cummins, a metascientist at the University of Bern, began the work after peer reviewing a paper in which the authors had used silicon samples without describing important decisions they had made along the way.

To see how these decisions could affect a study's outcome, Cummins drew on existing data from human participants, feeding LLMs information about the participants and examining how closely the AI could predict their answers. He focused on two psychological measures that had been collected for 85 participants in the Attitudes, Identities, and Individual Differences data set: their gut-level preference for European Americans compared with African Americans, and their belief that the world is fundamentally fair.

Cummins varied which LLM he used to predict those responses (for example, ChatGPT or Deepseek) and how much demographic information he provided to the model about the participants it was meant to be aping. He also toyed with model settings such as "temperature," which dictates how creative or predictable a model's output is. The different combinations of settings multiplied quickly, leading to 252 different possible sets of choices.

Then, he checked how close the models had come to the human data, using various measures: If a human participant had the highest score on a given question, did its

silicon counterpart also have the highest score, or close to it? Did the overall data sets produced by the models and the humans look similar, with similar means and distributions of scores? And were the virtual participants' scores on the two scales weakly correlated, as human scores are?

He found that the 252 choice combinations produced a wide range of different outcomes. Some settings led models to more closely match the rankings of human participants, for instance, whereas others more closely matched the correlation between the measures. But no single combination of settings worked well across the board. "There doesn't appear to be one true answer," Cummins says. If two different researchers ran the same study in silicon samples, making different defensible choices, they could reach opposite conclusions, he says.

The finding "emphasizes how many choices we have as researchers and how these choices can subtly influence the results that we get out," says Benjamin Paaßen, a computer scientist at Bielefeld University whose own work has cautioned against using LLMs to simulate human responses. Although even the most optimistic proponents of silicon sampling still recommend checking results against human participants, Paaßen says, some studies might soon rely exclusively on LLM results. But "maybe one cannot rely on LLM-generated data as much as one might think."

Cummins is particularly uneasy at the idea of using agents to simulate the responses of vulnerable or hard-to-reach populations, such as older people, minorities, or people living in countries far removed from dominant Western cultures. Sen agrees this could be harmful, partly because these groups are often underrepresented in LLM training data. "It could really risk disenfranchising people, further reducing trust in science," she says.

Lisa Argyle, a political scientist at Purdue University, agrees that not every LLM or prompt is "equally capable of valid simulation"—but if researchers carefully check that their precise model, prompts, and settings are appropriate for a given task, they can still be valuable, she says. The paper would have been more convincing if it had tackled a data set where LLMs have already been shown to accurately mimic human responses, adds Suhaib Abdurahman, a social psychologist at the University of Southern California, because that would demonstrate that researcher choices can lead to poor outcomes even in data sets where LLMs had previously excelled.

Scientists haven't yet discussed the ethical issues surrounding silicon sampling in enough depth, Sen says, or settled on the situations where it might be appropriate to use them, such as pilot experiments or as a way to test-run surveys. "This seems like a good time to have those discussions, before the technology is ready." □

CLIMATE CHANGE

Science teachers scramble as U.S. climate resources vanish

As government websites go dark, some nonprofits are trying to provide classroom materials **GAEA CABICO**

When news broke that climate.gov was about to go dark in June, Jeffrey Grant scrambled to download as many graphs and data tables from the website as he could. The high school biology teacher had relied heavily on the U.S. National Oceanic and Atmospheric Administration (NOAA) website to teach students about climate change, showing data on carbon dioxide levels and asking the students to analyze trends and make connections like real climatologists. "Science is always expanding," says Grant, who works at Downers Grove North High School in Illinois. "So, it is important that I always provide them with the latest research. Otherwise, they just have to take my word for it."

Grant is not alone. As the school year kicked into gear this fall, educators across the country have been reworking lesson plans and searching for reliable sources of up-to-date scientific information. The URL climate.gov, which was shuttered after President Donald Trump's administration terminated 10 science communication and data visualization experts who maintained it, now redirects web users to a NOAA web page on climate that contains a fraction of the original information. A NOAA spokesperson says the move was "an effort to centralize and consolidate resources."

> **"It's absolutely critical that teachers continue to have access."**
> **Rebecca Lindsey**
> Former climate.gov program manager

Since taking office in January, Trump has moved to restrict climate change research and education and retreat from U.S. commitments to reducing greenhouse gas emissions. Last month, he told world leaders at the United Nations that climate change was "the greatest con job ever perpetrated." As part of the campaign, officials have deleted climate data sets used by scientists and the public or made them more difficult to reach.

Many science teachers depended on those resources. The Next Generation Science Standards, which were created by a consortium of states and nonprofit organizations to provide guidance on what K-12 students should know, recommend introducing humanmade climate change in fifth grade and weaving it through all science classes. But that may become increasingly difficult if teachers can't readily find the information they need. "The more time it takes for them to find those things, the less apt they're going to use it. So that's discouraging," Grant says.

The cuts go beyond climate.gov to sites explicitly designed for educators, such as the Climate Literacy and Energy Awareness Network (CLEAN), a University of Colorado Boulder project funded by NOAA. The program, which is home to more than 800 lessons and videos covering topics such as droughts, wildfires, energy efficiency, and climate anxiety for high school– and college-level courses, went into hibernation on 31 August after it was defunded. "It's not just a priority for NOAA anymore and not something that they see worthwhile to spend money on," says Gina Fiorile-Desranleau, a former CLEAN program coordinator who was laid off.

The lessons and videos remain on CLEAN's website. But unless new funding materializes, there will be no staff support to update the lessons with new data.

Breck Foster, a teacher at Lake Oswego High School in Oregon who weaves climate change into her social studies classes, says she has used disappearing resources as an

opportunity to teach about politics and science. "I've shown my students in real time as materials have been taken off the internet, materials that we have used. I've called attention to that not in a political way, but just to say this is what happens when any administration will have political changes," she says.

Some nonprofit organizations have been scrambling to fill the void. Margaret Wang-Aghania, executive director and co-founder of SubjectToClimate, a nonprofit that curates and develops free teaching materials, says her organization is spending a lot of time reworking lesson plans and finding replacement data—a strain for her small, 15-person team.

"As an organization, you always want to be moving forward—building and reaching more teachers—not backtracking and fixing these things," Wang-Aghania says. Right now, SubjectToClimate's resources are instead being utilized "just to maintain what we already have." For instance, the organization was forced to find a new data source for a lesson on sea level rise in January after a data set on ice thickness in Antarctica vanished from a government website.

Former NOAA employees hope to mitigate the loss of climate.gov. "We intend to restore all that content ... outside the federal domain, where it is safe from further political interference," says Rebecca Lindsey, former program manager of climate.gov. "It's absolutely critical that teachers continue to have access to that type of resource," she says.

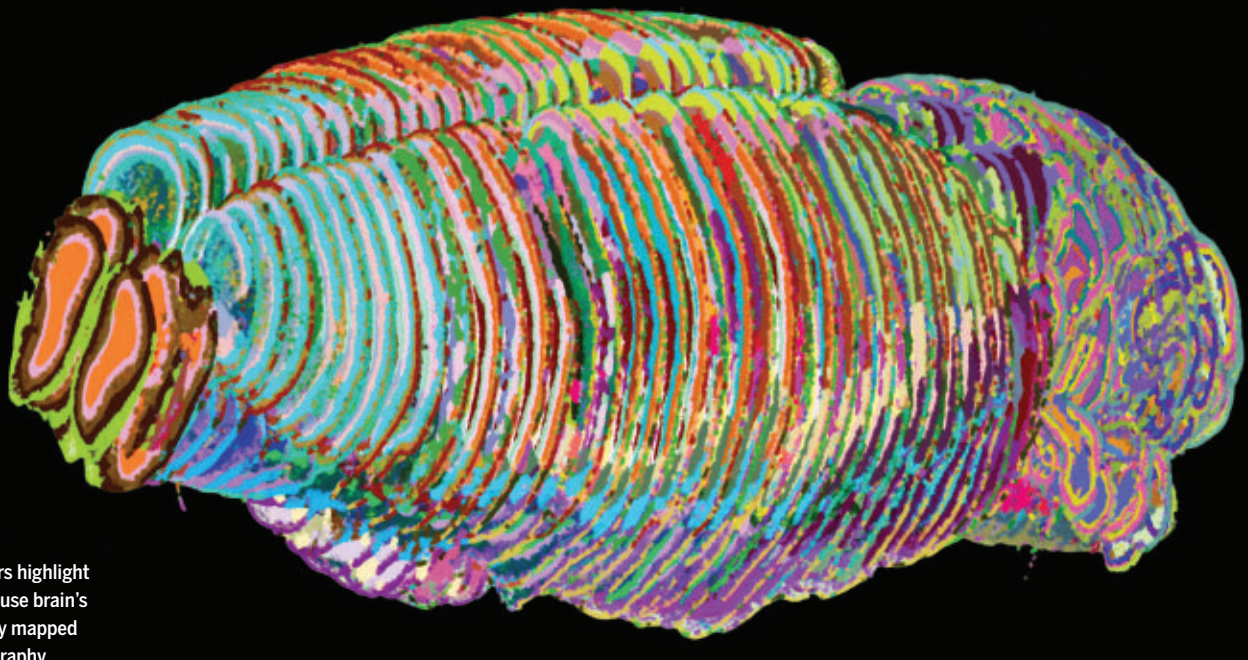
Lindsey's team is currently crowdfunding. If they can raise enough money, she says they will produce updates and new content and post the materials on climate.us, an independent, nongovernmental website. "To make smart, effective decisions about climate change, we need unbiased, uncensored information," she argues. □

Gaea Cabico is a journalist based in New York City.

IN FOCUS

AI maps the brain's neighborhoods

Unleash artificial intelligence (AI) on a catalog of all cell types in a mouse brain and voilà—you get one of the most granular brain visualizations to date: a vibrant patchwork highlighting 1300 brain regions and subregions, many previously uncharted. "It's like going from a map showing only continents and countries to one showing states and cities," says Bosiljka Tasic, director of molecular genetics at the Allen Institute for Brain Science. She and colleagues developed an AI tool called CellTransformer to make sense of vast data sets that record where millions of cells sit and which genes they express. Traditional methods for mapping the brain's cellular geography rely on hand-drawn, or annotated, atlases; CellTransformer's algorithms infer from so-called spatial transcriptomic data how cells are organized into functional neighborhoods. When researchers applied CellTransformer to the Allen Brain Cell Atlas, which documents nearly 4 million cells, it picked out known structures such as the hippocampus, but also hundreds of previously unannotated microregions, the team reported on 7 October in *Nature Communications*. Some appeared in areas that lack detailed maps, such as the midbrain reticular nucleus, suggesting the AI tool had found genuinely new patterns. —Richard Stone



Colors highlight a mouse brain's newly mapped geography.

IMAGE: UNIVERSITY OF CALIFORNIA SAN FRANCISCO


Science Podcast
AAAS
Stay curious, stay informed.
Tune into the *Science* Podcast for the latest from the world of science
LISTEN NOW
NEW EPISODES EVERY THURSDAY



SEEKING GHOSTS

A Japanese botanist is revealing the secrets of plants that have given up photosynthesis

DENNIS NORMILE

One day when Kenji Suetsugu was 4 or 5 years old, he went for a walk with his parents through the Kasugayama Primeval Forest near their home in Nara, one of Japan's ancient capitals. He recalls spotting a cluster of delicate, otherworldly flowers that looked like they were made of decorative milk glass, with translucent white stems and blossoms. They are called ghost flowers, he later learned. And unlike most plants, they don't rely on photosynthesis to survive, instead drawing carbon and nutrients from fungi buried in the soil. "I was moved by the existence of such a mysterious living thing," he says.

Now 37 and a botanist at Kobe University, Suetsugu has become one of the world's preeminent authorities on these unusual symbiotic plants, called mycoheterotrophs. Combining dogged fieldwork with old-school taxonomic studies and modern molecular technologies, he has produced some 250 papers since 2008 that have shed new light on these plants, tiny forest floor dwellers that typically bloom for just a few days once a year. His studies have overturned conventional ideas about how mycoheterotrophic plants pollinate and reproduce. He's also helped describe 30 previously unrecognized species found in Japan and overseas. And he is producing a children's book, illustrated with his own photographs, that he hopes will convey the joy of discovering new forms of life.

Botanist Kenji Suetsugu is enthusiastic about fieldwork, which often involves crawling along the forest floor in search of tiny flowers.

Colleagues marvel at Suetsugu's passion, persistence, and collegiality, which extends to working with a small army of ardent amateur botanists. In a world where hyperspecialization is common, the breadth of Suetsugu's research—involving plant taxonomy and systematics, entomology, plant physiology, reproductive ecology, and molecular biology—is "very refreshing," says Jeff Ollerton, an ecologist at the University of Northampton. Suetsugu's discoveries are "important in providing an element of wonder and curiosity about the natural world," says botanist Luiza Teixeira-Costa of the Meertens Institute and the Meise Botanic Garden. She hopes his example will "motivate the next generation of scientists."

IN ESSENCE, mycoheterotrophic plants are thieves. Found in forests worldwide, they entwine their roots with the threadlike hyphae of soil fungi. These fungi acquire carbon from trees and shrubs while providing nutrients in a mutually beneficial exchange. The mycoheterotrophs then steal some of that carbon from the fungi, instead of relying on sunlight and chlorophyll to power photosynthesis.

More than 33,000 plant species—including certain clubmosses, ferns, liverworts, and all orchids—are known to be initially mycoheterotrophic during germination and early development. Botanists have also identified about 600 species, nearly half of which are orchids, that have fully abandoned photosynthesis and depend on fungi throughout their

PHOTO: KATSUMI IWAHORI



PHOTO: KENJI SUETSUGU

lives. (An unknown number of species are partially mycoheterotrophic, drawing carbon from both photosynthesis and fungi, and may represent a transitional stage toward full mycoheterotrophy.)

Evolutionary biologists have found evidence that full mycoheterotrophy has evolved independently more than 40 times. The strategy could be an adaption to surviving in dense forests where light is scarce. But how mycoheterotrophy arises and persists is still a mystery—in part because the plants can be elusive. In Japan, Suetsugu says, "There has been very little research done on mycoheterotrophic plants." Ollerton says the same is true elsewhere in the world.

Suetsugu set out to fill that gap during his undergraduate and graduate studies at Kyoto University. A year after completing his Ph.D. in 2014, he joined Kobe University, becoming a full professor in 2022 at age 34. (He is still the youngest full professor on the university's Faculty of Science.) Today, Suetsugu's prodigious scientific output on mycoheterorophs makes him "the most productive author in the field of botany and pollination ecology," says Zong-Xin Ren, a botanist and a pollination ecologist at the Chinese Academy of Sciences's Kunming Institute of Botany.

In conversation, Suetsugu is reserved and chooses his words carefully, although he is prone to chuckle over amusing or philosophical questions. He is most at home in the field, where his "explorational" approach has enabled him to "discover things previously unknown," says Vincent Merckx, a botanist at the Naturalis Biodiversity Center.

Suetsugu's enthusiasm for fieldwork was readily apparent during a June research trip to the Kongō-Ikoma-Kisen Quasi-National Park just south of Osaka.

"THERE!" Suetsugu exclaimed, pointing through the window of a car crawling along a narrow road through a thick forest. A clutch of thumb-size pinkish blossoms, perched on spindly milk-white stems, barely poked above the dense leaf litter. With several cameras strapped around his neck, Suetsugu jumped from the car and crawled through the sparse underbrush. Then, confirmation: The flowers were specimens of the rare *Monotropastrum kirishimense*, a new species of orchid found only in western Japan, which he had identified in 2022.

Spotting *M. kirishimense* takes a bit of luck; studying it requires a lot of patience. The plants spend most of the year underground, and when the leafless, ghostly orchids do bloom the flowers last just a week or so.

It was long thought *M. kirishimense* was a variant of a different species, *M. humile*, which is common throughout Asia. But about 20 years ago, Suetsugu noted that

Monotropastrum humile

A childhood encounter with *M. humile*, an ethereal "ghost plant," led Kenji Suetsugu to his life's work: understanding how mycoheterotrophic plants came to eschew photosynthesis and instead rely on carbon and nutrients from soil fungi.





seemingly related orchids in Japan flowered at different times, making cross-pollination unlikely. Closer examination of the stems and roots of the plants revealed significant differences. The two plants also proved to be far apart genetically, and researchers found that *M. kirishimense* associates with a single fungus species that *M. humile* avoids. "We gradually accumulated morphological, ecological, and genetic evidence, which finally allowed us to describe it as a new species," Suetsugu says. Researchers have since documented only 10 populations of the new orchid, typically with fewer than 20 individuals each, earning it critically endangered status in Japan.

The 2-decade-long project, Ren says, "is an example of good science coming from patience."

PATIENCE HAS ALSO enabled Suetsugu to untangle the reproductive strategies of mycoheterotrophic plants. Many were thought to rely on the wind to scatter their seeds, which are often the size of dust particles. But skeptics argued that the short stature of the plants and the weak breezes in dense forests made wind dispersion chancy.

Suetsugu added some hard—and surprising—data to the debate by studying three species during their brief fruiting seasons. Over 4 years, he used motion-triggered cameras to collect 190 hours of nighttime observations of *Yoania amagiensis*, *Phacellanthus tubiflorus*, and *M. humile*. The videos revealed that camel crickets and ground beetles ate the plants' seed-laden fruits. Experiments back in the laboratory found that up to hundreds of viable seeds passed through the camel crickets; none survived ingestion by the ground beetles. Further investigation showed that a woody outer covering protects the seeds from cricket digestive fluids but not beetle chewing, Suetsugu reported in *New Phytologist* in 2017. Identifying camel crickets as crucial seed dispersers was "a remarkable discovery," Merckx says.

Suetsugu has used the same painstaking approach to identify other unexpected pollinators and seed dispersers. A camera trap caught a *Clubiona* spider feeding on the nectar of the orchid *Neottianthe cucullata* and moving between flowers with pollen clinging to its jaws. His group showed for the first time that two insects—camel crickets and ants—could both pollinate and disperse the seeds of a flowering plant. And lab experiments showed that 1-centimeter-long woodlice could consume the fruit of ghost flowers (*M. humile*) and defecate viable seeds, making the woodlice the world's smallest known seed dispersers.

Many mycoheterotrophic plants also self-pollinate, likely an evolutionary response to the dearth of pollinators in deep forests. But Suetsugu found that one orchid, *Stigmatodactylus sikokianus*, hedges its bets. Its flower is initially open, giving pollinators their chance. But after several days, the stigma, or female organ, collapses, bringing a minute, fingerlike appendage into contact with the flower's male organ and enabling pollen to reach the ovary. This "delayed selfing" likely evolved to assure reproduction while providing an opportunity for occasional cross-pollination to avoid potentially harmful inbreeding, Suetsugu says.

Merckx says such work has been groundbreaking. Before Suetsugu's studies, he says, "we knew little about how mycoheterotrophic plants are pollinated, because it is very difficult and time consuming to get any data."

PHOTOS: KENJI SUETSUGU



PHOTO: KENJI SUETSUGU

Stigmatodactylus sikokianus

The tiny orchid *S. sikokianus* (left) has a backup mechanism to ensure pollination. Its flower is initially open, giving pollinators an opportunity. But after several days, the stigma, or female organ, wilts, bringing a minute, fingerlike appendage into contact with the flower's male organ, enabling pollen to reach the ovary.

Thismia kobensis

T. kobensis (center) highlights the precarious existence of many mycoheterotrophic plants. The critically endangered Japanese species was thought extinct after development erased the habitat of the last known specimen in 1999. But in 2021, an amateur botanist chanced upon the plant 30 kilometers away. This one known population has fewer than two dozen individuals.

Spiranthes hachijoensis

Plants in the orchid genus *Spiranthes* are commonly called "ladies' tresses" because of how their tiny flowers spiral around the stems. Scientists long believed only one *Spiranthes* species existed in Japan until botanists noted some plants bloomed earlier than others. Ten years of study showed the early bloomers represented a new species, *S. hachijoensis* (right).

ONE SECRET TO Suetsugu's success is his ability to enlist and inspire others, says Merckx, a collaborator. His grad students "share his passion for nature and remarkable species," he says, noting the unusual plants and orchids they have growing on their lab benches. Suetsugu "seems to consider himself part of the team, rather than the leader," Merckx says.

That ethos extends to the dozens of amateur plant enthusiasts who cooperate with Suetsugu. In Japan, "there is just a small gap [in expertise] between amateurs and professionals," Suetsugu says. One example is retired high school biology teacher Masayuki Ishibashi, who contributed to identifying a new species in the orchid genus *Spiranthes*, commonly called ladies' tresses. Scientists long believed that only one species, *S. australis*, was found in Japan. But in the 2010s Ishibashi, who had taught himself plant morphology and mastered high-magnification photography, helped change that picture.

Working with Suetsugu, he and other researchers noted that some ladies' tresses in Japan bloomed much earlier than others. Other amateurs documented the plant growing in gardens and even balcony flowerpots around Japan and collected samples for morphological and molecular analyses. Ten years of investigation led to the identification of a new species, *S. hachijoensis*. The find "was like a dream come true," Ishibashi says.

Last year, a similar collaboration led to the discovery of a mycoheterotrophic flower that represents the first new genus of vascular plant—a category including all trees, grasses, ferns, and flowers—found in Japan since 1930. Yasunori Nakamura is a consulting plant ecologist who often spends days off searching for rare plants, which he "just loves." While on a hike in 2022, he stumbled upon what he thought was an unusual specimen of fairy lantern, in the *Thismiaceae* family. (The plant's equally whimsical common Japanese name is "raccoon dog's candlestick.")

Sample plants ended up in Suetsugu's lab, and their morphology and genetics led his team to conclude the plant represented a new genus, *Relictithismia*, and a new species, *R. kimotsukiensis*. The team, including co-author Nakamura, reported its finding in the *Journal of Plant Research* in 2024. "It was a nearly miraculous discovery," Nakamura says, given that only five individuals of the new species have been found in one location.

Out of consideration for amateur collaborators such as Nakamura, Suetsugu publishes most of his papers in open-access journals. That is "so people who aren't affiliated with a university can read them," he says.

SUETSUGU SAYS he plans to continue his current work but is also looking for new challenges to fill the long career likely still ahead of him. One interest is tracing in detail how carbon moves through the subterranean networks of plant roots and fungi. Those carbon flows, he hopes, will point to "the general principles that explain when, how, and why plants shift toward fungal dependence [and the] loss of photosynthesis."

Finding answers to such questions will likely take years, but Suetsugu's enthusiasm is undimmed. Although it's been more than 30 years since he first encountered the ghostly forest dwellers, he says "the sense of wonder [they] inspired has remained with me." □

With reporting by Elizabeth Pennisi.



MOLECULAR BIOLOGY

Longevity steps on the cGAS

A DNA repair function in a cytosolic sensor demonstrates a potential role in naked mole-rat longevity

John C. Martinez[1], Andrei Seluanov[1,2], Vera Gorbunova[1,2]

The first line of defense that cells have against foreign pathogens is an innate immune response. Cyclic guanosine monophosphate–adenosine monophosphate synthase (cGAS) plays a crucial role in this response by detecting pathogen-derived DNA or RNA in the cytosol of the host cell and initiating a signaling cascade that causes the transcription of genes encoding type I interferons (*1*). Increased inflammation is a hallmark of aging (*2*), and dysregulation of cGAS signaling during aging can drive debilitating inflammatory processes (*3*, *4*). Therefore, cGAS was proposed as a therapeutic target. However, although present in the cytosol, cGAS is predominantly bound to chromatin, and its role in the nucleus is unclear (*5*). On page 150 of this issue, Chen *et al.* (*6*) report that cGAS from the naked mole-rat has a distinct set of four mutations on its N terminus that promote DNA repair—a mechanism crucial to the organism's extreme longevity.

The naked mole-rat has a maximum life span of nearly 40 years, making it the longest-lived rodent, and is resistant to a wide range of age-related diseases, including cancer, neurodegeneration, and arthritis. Chen *et al.* assessed differences in cGAS activity between naked mole-rat, mouse, and human cells in culture. They showed that upon DNA damage, amino acid substitutions in naked mole-rat cGAS allow it to undergo reduced ubiquitination and degradation relative to mouse and human isoforms. This increased abundance of cGAS enhanced the interaction between the DNA repair factors FANCI and RAD50, which promoted homologous recombination. Homologous recombination is essential for the repair of double-strand breaks in DNA. The authors also found that depletion of naked mole-rat cGAS in cultured cells results in increased DNA damage. These results suggest that the observed amino acid differences in naked mole-rat cGAS enhance the chromatin binding capabilities of the protein, ultimately resulting in higher rates of DNA repair. Notably, this strengthened tethering of cGAS within the nucleus would be expected to result in dampened inflammation, which would be interesting to explore in future studies. Additionally, Chen *et al.* demonstrated that fruit flies (*Drosophila melanogaster*) that express a form of human cGAS bearing the four naked

PHOTO: NEIL BROMHALL/NPL/MINDEN PICTURES



The naked mole rat (*Heterocephalus glaber*) is the longest-lived rodent, with a maximum life span of nearly 40 years.

mole-rat mutations lived longer compared with flies that express human cGAS without the mutations. This result suggests that cGAS plays a role in the longevity of the naked mole-rat.

It is unclear what species other than the naked mole-rat gain from using cGAS in the nucleus. Previous studies in human and mouse cells have suggested that cGAS inhibits DNA repair and replication (*7*, *8*). This is consistent with cGAS playing a role in chromatin maintenance, whereas the removal of cGAS may unleash uncontrolled recombination or replication. Preliminary data from genetically modified mice lacking cGAS show derepression of transposable elements—"jumping genes" that can move from one location of the genome to another—that ultimately leads to increased inflammatory signaling and a shortened life span (*9*). Similar to the findings from Chen *et al.*, these findings indicate that cGAS is important in regulating chromatin organization and maintenance by protecting genomic integrity.

If naked mole-rat cGAS has been modified in a way that confers resistance to DNA damage, do other long-lived organisms alter their cGAS in a similar way? Several bat species also have enhanced longevity relative to mammals their size. Furthermore, in contrast to most mammals, these bats have an immune system that tolerates viruses (*10*)—the result of lineage-specific evolutionary adaptations on hundreds of proteins. These adaptations include a single-residue mutation in a phosphorylation site on stimulator of interferon genes (*STING*), which encodes a transmembrane protein that is downstream of cGAS and is important for initiating interferon production, as well as the complete loss of the *PYHIN* family of genes, which encode cytosolic sensors that recognize the same double-stranded nucleic acid substrates as cGAS (*11*, *12*).

But how is *cGAS* modified in bats? The *cGAS* gene is present in bats, and the evolutionary retention of the protein over the *PYHIN* sensors would suggest that *cGAS* may serve additional noncanonical roles outside of immune sensing or that it may serve as a more important immune regulator than the *PYHIN* sensors. Indeed, expanded phylogenetic analysis corroborates the importance of *cGAS*—there are homologs in both invertebrates and bacteria (*13*). However, analysis of amino acid differences between bat *cGAS* and that of other mammals uncovered a high rate of changes, including a region of extremely high divergence in the N terminus of cGAS (essential for innate immune activation) in Old World fruit bats (pteropodids), some of which exhibit enhanced longevity (*14*). Notably, these bats also have amino acid mutations within two of the three loops in cGAS that were previously identified as important for binding to nucleosomes, which are the basic building block of chromatin (*15*). The mutations have the potential to increase the interaction of cGAS and chromatin. Notably, one of the four amino acid mutations that was shown by Chen *et al.* to be necessary for naked mole-rat cGAS to enhance DNA repair (and is absent from both mouse and human cGAS), Glu^{511}→Lys, is also shared with pteropodids. Thus, evolutionary forces resulting in chromatin binding of cGAS, potentially through differing sets of mutations, could be a characteristic of long-lived species as a mechanism to facilitate DNA repair or avoid autoimmunity—a major component of the increased inflammation associated with aging.

The findings from Chen *et al.* describe an unexpected role for naked mole-rat cGAS in the nucleus that influences longevity. Further research will be required to establish the roles that cGAS may play in the nucleus in other organisms, both short- and long-lived, but the answer may be substantially more complex than originally predicted. □

REFERENCES AND NOTES

1. L. Sun, J. Wu, F. Du, X. Chen, Z. J. Chen, *Science* **339**, 786 (2013).
2. G. Kroemer *et al.*, *Cell* **188**, 2043 (2025).
3. M. Simon *et al.*, *Cell Metab.* **29**, 871 (2019).
4. M. F. Gulen *et al.*, *Nature* **620**, 374 (2023).
5. H. E. Volkman, S. Cambier, E. E. Gray, D. B. Stetson, *eLife* **8**, e47491 (2019).
6. Y. Chen *et al.*, *Science* **390**, eadp5056 (2025).
7. H. Liu *et al.*, *Nature* **563**, 131 (2018).
8. H. Chen *et al.*, *Sci. Adv.* **6**, eabb8941 (2020).
9. J. C. Martinez *et al.*, bioRxiv 10.1101/2024.10.10.617645 (2024).
10. V. Gorbunova, A. Seluanov, B. K. Kennedy, *Cell Metab.* **32**, 31 (2020).
11. J. Xie *et al.*, *Cell Host Microbe* **23**, 297 (2018).
12. G. Zhang *et al.*, *Science* **339**, 456 (2013).
13. J. M. Jenson, Z. J. Chen, *Mol. Cell* **84**, 120 (2024).
14. S. Tian *et al.*, *Sci. Adv.* **9**, eadd0141 (2023).
15. S. Michalski *et al.*, *Nature* **587**, 678 (2020).

ACKNOWLEDGMENTS

The authors acknowledge support by grants from the US National Institute on Aging, the Impetus Grant, and the Hevolution Foundation.

10.1126/science.aeb6125

[1]Department of Biology, University of Rochester, Rochester, NY, USA. [2]University of Rochester Medical Center, Rochester, NY, USA. Email: vera.gorbunova@rochester.edu; andrei.seluanov@rochester.edu

PHYSIOLOGY

A tripartite alliance for dietary fat absorption

Microbes, immune cells, and enterocytes interact to regulate the intake of lipids in the mouse gut

Ralph Burkhardt and **Josef Ecker**

Dietary lipids are a major daily source of calories in adult mammals. The textbook description of lipid absorption is straightforward: Lipids cross the layer of cells lining the gut (the intestinal epithelium) to move from inside the intestinal tract to the blood stream. On page 149 of this issue, Gao *et al.* (*1*) report that lipid absorption in mice also relies on communication between immune cells and specific intestinal epithelial cells (enterocytes). This relationship is influenced by the gut microbiota, a complex and diverse microbial ecosystem of the intestinal tract (*2*). Loss of the protein Aster-A in immune cells inhibits lipid absorption and protects mice against diet-induced obesity and its consequences, including adipose tissue inflammation and fatty liver. These findings are likely to be of major interest for research on therapies that target dietary fat absorption.

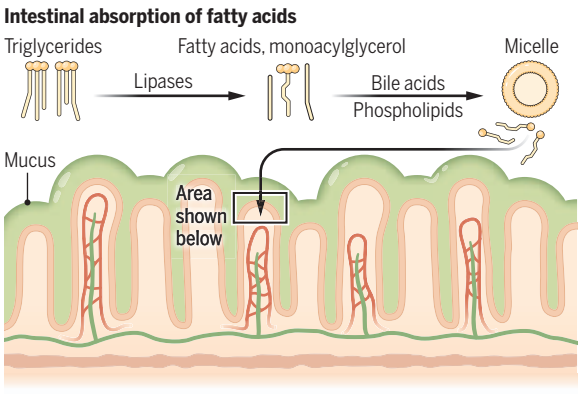
The intestinal epithelium is a physical and biochemical barrier that separates the space inside the gut—the intestinal lumen—from the host tissue (see the figure). Most dietary lipids are triglycerides, which are molecules composed of three fatty acids esterified to a single glycerol backbone. The entry of fatty acids into enterocytes depends on the activity of pancreatic lipase, an enzyme that breaks down triglycerides (*3*). Monoacylglycerols and free fatty acids are emulsified with bile acids and phospholipids, forming a spherical structure known as a micelle. The biophysical properties of the apical cell membrane of enterocytes, which faces the intestinal lumen, also influence lipid absorption. This membrane is under constant remodeling by enzymes of the lysophosphatidylcholine acyltransferase protein family, which change its phospholipid composition (*4*). The gut microbiota also plays a role in fatty acid uptake. Mice without gut microbes have higher levels of dietary polyunsaturated fatty acids in the circulation and peripheral tissues compared with mice with a naturally diverse microbiota (*5*). In humans, the presence of the commensal mucus-degrading bacterium *Akkermansia muciniphila* has been associated with reduced plasma lipid levels, fat storage, and obesity (*6*), although the mechanisms underlying these effects are unclear.

The inner layer of the intestinal tract is covered by the mucosa, which contains different regions. Immune cells, which sense microbial stimuli and initiate appropriate responses, can be found within the tissue of the lamina propria and in the Peyer's patches (*7*). Gao *et al.* observed that T helper 17 (T_H17) cells, a subset of $CD4^+$ T cells, express Aster-A, a protein involved in the nonvesicular shuttling of cholesterol from the plasma membrane to the endoplasmic reticulum within cells (*8*). Free cholesterol makes up ~50% of the total lipid content of the plasma membrane of mammalian cells (*9*). Some of this free-cholesterol pool, referred to as sequestered cholesterol, is required to maintain the membrane's biophysical properties, but another portion, referred to as accessible cholesterol, can be mobilized to other organelles (*10*). Gao *et al.* observed that T cell–specific deletion of Aster-A in mice reduced dietary lipid absorption in the small intestine and circulation, which suggests that cholesterol trafficking in immune cells influences lipid uptake by enterocytes. This link between immune cell homeostasis and intestinal lipid absorption is a surprising finding considering the intrinsic immune role of T_H17 cells in maintaining the integrity of the mucosa and preventing pathogens from entering the body.

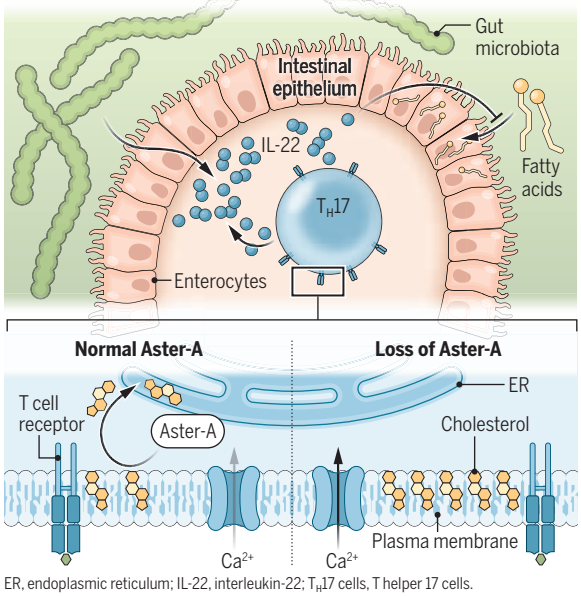
Potentially harmful substances (antigens) that enter the body are broken down into smaller components. These components are presented by major histocompatibility complex molecules on antigen-presenting cells and recognized by T cell receptors (TCRs) on T cells. High cholesterol levels in the plasma membrane stimulate TCR signaling, which affects T cell proliferation (*11*). Gao *et al.* observed that T cell activation increased the amount of accessible cholesterol available in the plasma membrane. However, Aster-A activity swiftly reduced the amount of this cholesterol in the membrane, which mitigated TCR signaling and the activation and expansion of T_H17 cells. Furthermore, the interaction between Aster-A and stromal interaction molecule 1 (STIM1), a protein that regulates calcium (Ca^{2+}) flux across the plasma membrane, was required for the movement of accessible cholesterol from the plasma membrane to the endoplasmic reticulum.

Regulation of dietary lipid intake

Triglycerides, the main type of dietary lipid, are broken down by lipase enzymes. Fatty acids are emulsified with bile acids and phospholipids, creating spherical structures called micelles. Fatty acids released by micelles are taken in by the enterocytes of the intestinal epithelium.



Microbes and the immune system control fatty acid intake
Gut microbes stimulate IL-22 production by immune cells. Aster-A shuttles cholesterol between the plasma membrane and the ER in T_H17 cells, which requires Ca^{2+} influx. Mice without Aster-A in T cells have an increased amount of free cholesterol in the plasma membrane, which stimulates T cell receptor signaling, IL-22 production, and T cell activation and proliferation. An enhanced immune response leads to reduced intestinal absorption of fatty acids by enterocytes and inhibits diet-induced obesity.



ER, endoplasmic reticulum; IL-22, interleukin-22; T_H17 cells, T helper 17 cells.

GRAPHIC: A. FISHER/*SCIENCE*

What is the role of the gut microbiota in this scenario? Gao *et al.* observed that interleukin-22 (IL-22), a cytokine involved in gut homeostasis and mucosal defense (*12*), acts as a signaling molecule between T cells and enterocytes to impair lipid absorption. Segmented filamentous bacteria of the gut microbiota can induce T cells to produce IL-22 (*13*). Gao *et al.* observed that mice treated with broad-spectrum antibiotics to induce dysbiosis had reduced expression of IL-22. Lipid uptake was restored in dysbiotic mice with a T cell–specific Aster-A deficiency.

The study of Gao *et al.* highlights the importance of the interplay between gut microbes, immune cells, and intestinal epithelial cells in the regulation of dietary fat absorption. The authors have worked out many elements of a complex signaling cascade underlying cell-to-cell communication. Aster-A controls the response of T_H17 cells to gut microbes. Loss of Aster-A in T_H17 cells increases the plasma membrane's accessible free-cholesterol content, enhancing TCR signaling and gut microbe–dependent IL-22 production. These processes then reduce intestinal absorption of dietary lipids in enterocytes and inhibit diet-induced obesity.

How lipid flux into enterocytes is altered by Aster-A in immune cells remains to be determined. It might involve intestinal fatty acid transporters such as CD36 in enterocytes (*3*), modification of the composition of the enterocyte's apical plasma membrane by lysophosphatidylcholine acyltransferases (*4*), or the emulsification process in the lumen of the small intestine.

For researchers in the cardiometabolic disease field, the finding that a loss of Aster-A confers resistance to diet-induced obesity, including fatty liver, could be of major interest. The discovery of drugs that target systemic lipid absorption is attracting considerable interest, as dietary lipids accumulate not only in adipocytes and hepatocytes but also in various cancer cells, including those in human colorectal tumors (*14*). In mice with hypercholesterolemia, excess cholesterol is deposited into the plasma membranes of T cells (*15*), potentially promoting immune-mediated diseases. In this case, the removal of cholesterol from the plasma membrane by Aster-A might have an anti-inflammatory role by dampening inflammatory responses.

It will be intriguing to explore to what extent the interplay between microbes, immune cells, and enterocytes that has been uncovered in mice also governs dietary lipid absorption in humans. Future studies may reveal the physiological importance of this signaling pathway in metabolism and inflammation and open avenues to new therapeutic strategies. □

REFERENCES AND NOTES

1. Y. Gao *et al.*, *Science* **390**, eadt4169 (2025).
2. R. Sender, S. Fuchs, R. Milo, *PLOS Biol.* **14**, e1002533 (2016).
3. M. M. Hussain, *Curr. Opin. Lipidol.* **25**, 200 (2014).
4. B. Wang *et al.*, *Cell Metab.* **23**, 492 (2016).
5. A. Kindt *et al.*, *Nat. Commun.* **9**, 3760 (2018).
6. P. D. Cani *et al.*, *Nat. Rev. Gastroenterol. Hepatol.* **19**, 625 (2022).
7. L. W. Peterson, D. Artis, *Nat. Rev. Immunol.* **14**, 141 (2014).
8. T. Naito *et al.*, *eLife* **8**, e51401 (2019).
9. G. van Meer, D. R. Voelker, G. W. Feigenson, *Nat. Rev. Mol. Cell Biol.* **9**, 112 (2008).
10. E. Ikonen, X. Zhou, *Dev. Cell* **56**, 1430 (2021).
11. W. Yang *et al.*, *Nature* **531**, 651 (2016).
12. M. Keir, Y. Yi, T. Lu, N. Ghilardi, *J. Exp. Med.* **217**, e20192195 (2020).
13. I. I. Ivanov *et al.*, *Cell* **139**, 485 (2009).
14. J. Ecker *et al.*, *Gastroenterology* **161**, 910 (2021).
15. A. H. Pollock *et al.*, *J. Immunol.* **196**, 3993 (2016).

ACKNOWLEDGMENTS

J.E. acknowledges support from Deutsche Forschungsgemeinschaft (DFG, German Research Foundation) project nos. 446175916 and 395357507 (SFB 1371, Microbiome Signatures).

10.1126/science.aeb5717

Institute of Clinical Chemistry and Laboratory Medicine, Functional Lipidomics and Metabolism Research, University Hospital Regensburg, Regensburg, Germany. Email: josef.ecker@ukr.de

MICROBIOLOGY

Natural directed evolution in gut microbiota

Bacteria undergo rapid genetic changes that are selected by alterations in the human gut environment

Blair G. Paul[1] and **John J. Mekalanos**[2]

Mutation is necessary for evolution, but the prevalent assumption is that most genes maintain a balance between change that supports development of new beneficial attributes and preservation of existing function. Interestingly, two different types of genes emerge when observing genomic variation across large datasets: core, slow-evolving ones, and fast-evolving genes that are presumably responding to environmental changes that lead to rapid adaptation. Microbial cells can tolerate some genetic plasticity but generally have active mechanisms to correct mutations rather than enhance their formation. On page 151 of this issue, Macadangdang *et al.* (*1*) describe genomic elements that hypermutate target genes in human gut bacteria. They found that species of the *Bacteroides* group actively swap these diversity-generating retroelements (DGRs). Successful recipient bacteria form distinct populations in which specific gene types have been hypermutated by a DGR. The study results strongly suggest that DGRs drive changes selected by perturbations of the gut environment.

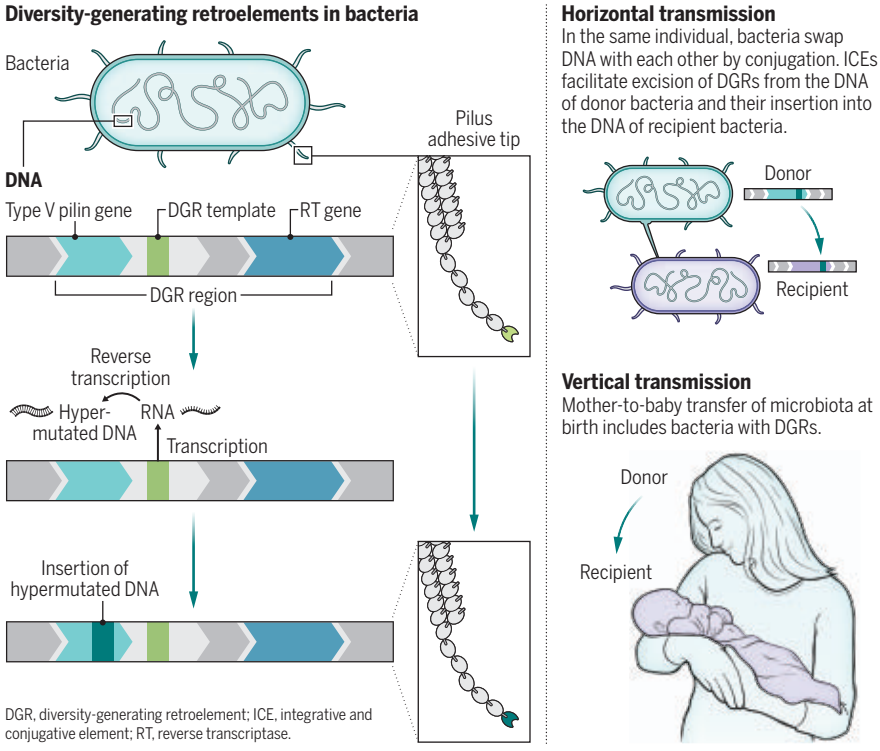
DGRs are remarkable elements that diversify their target protein's function through an error-prone mechanism that is mediated by reverse transcriptase, an enzyme that copies RNA into DNA (*2*). This molecular strategy drives protein diversity because the resulting DNA mutations tend to encode functionally different amino acids rather than the same amino acid or a shorter protein. The variation that DGR hypermutation can theoretically create by rewriting protein-coding DNA sequences is staggering. These elements pack variation into a short region of a target gene where such DNA sequence changes will still encode a viable and functional protein, and a single genome can have up to 14 DGR targets (*3*). Through their hypermutation, these targets maintain a form of potential evolution that exceeds 10e282 mutant variant combinations. This localized and highly diverse mutagenesis may repeat indefinitely during replication and selection.

Although DGRs were first discovered in bacteriophages (viruses that infect bacteria), they are also common in a diverse range of bacteria and archaea. For example, they are found in archaea from remote seafloor sediments, symbiotic microbes that colonize plant and animal hosts, and nano-sized microbes in groundwater (*4*–*6*). However, little was known about DGR biology and its evolutionary importance in the human microbiome.

Bacteria exchange genetic elements with each other in several ways (collectively called horizontal gene trans-

Driving diversity in gut microbiota

DGRs in a bacterial genome are retrotranscribed by RT in an error-prone process that causes hypermutation. The mutated DNA sequences insert themselves into target DNA regions such as genes encoding type V pilin proteins. These proteins are found at the adhesive tip of pili on the surface of bacterial cells.



DGR, diversity-generating retroelement; ICE, integrative and conjugative element; RT, reverse transcriptase.

fer), including a process known as conjugation. Macadangdang *et al.* developed computational and molecular tools to monitor the movement of integrative and conjugative elements (ICEs) encoding DGRs from the chromosomes of donor bacteria to the chromosomes of recipient bacteria. They applied these tools to bacteria from the gut of healthy humans and mice, as well as in vitro bacterial cultures. This approach provided convincing evidence that horizontal gene transfer of DGR elements occurs in complex communities of gut microbiota. The findings also indicated that the mutagenic activity of DGRs of several bacterial species is higher in vivo within the human gut than in bacteria grown in laboratory cultures, as well as in mice colonized with gut microbiota compared with germ-free mice.

Macadangdang *et al.* found that DGRs from the human gut microbiome are most abundant in *Bacteroides*-infecting phages. The genomes of these viruses can integrate into the chromosome of their host bacteria, where they are likely to hypermutate genes encoding key proteins involved in the recognition of receptors on bacterial cells. However, the authors also identified cellular DGRs, including a cluster that modifies type V pilin adhesins (see the figure). This group of proteins is found at the tip of type V pili, which are hair-like structures on the surface of bacterial cells that contribute to their adhesion and colonization of host tissues. Type V pilin adhesins are thought to bind to ligand molecules displayed by host cells, secreted components of the gut mucus (e.g., mucus glycoproteins), dietary substrates, and the surface polymers of other bacteria within biofilms (bacterial communities attached to surfaces, including living host tissues).

These findings advance previous observations indicating that DGR recruitment has cell-specific functions. In the bacterial species *Treponema denticola* (*7*), DGRs were reported to target the DNA that encodes a type of protein structural domain known as a C-type lectin (C-Lec) fold, which is involved in ligand binding. The protein encoded by this DGR target also had structural features of a lipoprotein, which suggested that it may be located on the bacterial surface and have extracellular functions. A later study in *Legionella pneumophila* reported the presence of hypervariable DGR target proteins on the surface of these bacterial cells (*8*).

As reported in other bacteria and archaea (*6*, *9*), the *Bacteroides* DGRs studied by Macadangdang *et al.* target regions encoding C-Lec–like folds located almost exclusively in the termini of proteins. In mammals, immunoglobulin is also a ligand-binding protein domain that accommodates hypervariation, and this mechanism underpins the central function of immunoglobulin in adaptive immunity. In bacteria and archaea, C-Lec might provide a similar solution to rapidly evade viruses that recognize pili receptors, bind common structures on other species of bacteria in biofilms, or target innate immune cells of the host. The variety of potential functional modules that could be fused to a hypervariable C-Lec domain is also exciting to consider. These include kinase domains that might have regulatory roles in response to C-Lec ligands. Macadangdang *et al.* also confirmed previous findings that proteins that correct errors in DNA replication, such as MutS, are involved in the modulation of DGR hypermutagenesis. Clearly, tunable diversity can drive evolutionary success.

In humans, the gut microbiome of the mother can be passed on to children (vertical transmission) and has an important influence on their risks for metabolic, immune, and neurological disorders (*10*). However, finding molecular signatures of selective genetic events in the human microbiome has not been easy. Macadangdang *et al.* used DGR targets as "signature tags" to mine vast genome datasets for selected traits in the human gut microbiome that are preferentially passed from mother to child. The idea that selection of DGR variants in a mother can influence the success of a bacterium in colonizing the mother's progeny, and then affect the child's health, is heady stuff to consider. This study could inform future work on the effect of the inheritance of maternal microbiota on child health. □

REFERENCES AND NOTES

1. B. Macadangdang *et al.*, *Science* **390**, eadv2111 (2025).
2. S. Handa *et al.*, *Nature* **638**, 1122 (2025).
3. H. Doré *et al.*, *Proc. Natl. Acad. Sci. U.S.A.* **121**, e2316469121 (2024).
4. B. G. Paul *et al.*, *Nat. Commun.* **6**, 6585 (2015).
5. B. G. Paul *et al.*, *Nat. Microbiol.* **2**, 17045 (2017).
6. S. Roux *et al.*, *Nat. Commun.* **12**, 3076 (2021).
7. J. Le Coq, P. Ghosh, *Proc. Natl. Acad. Sci. U.S.A.* **108**, 14649 (2011).
8. D. Arambula *et al.*, *Proc. Natl. Acad. Sci. U.S.A.* **110**, 8212 (2013).
9. L. Wu *et al.*, *Nucleic Acids Res.* **46**, 11 (2018).
10. V. Heidrich, M. Valles-Colomer, N. Segata, *Nat. Rev. Microbiol.* **23**, 568 (2025).

ACKNOWLEDGMENTS

This Perspective is dedicated to the memory of David Baltimore, codiscoverer of reverse transcriptase. The authors acknowledge support by the G. Unger Vetlesen Foundation and Owens Family Foundation (B.G.P.) and the Morningside Foundation (J.J.M.).

10.1126/science.aeb8597

[1]Bay Paul Center for Comparative Molecular Biology and Evolution, Marine Biological Laboratory, Woods Hole, MA, USA. [2]Department of Microbiology, Harvard Medical School, Boston, MA, USA . Email: bgpaul@mbl.edu; john_mekalanos@hms.harvard.edu

GRAPHIC: A. MASTIN/*SCIENCE*

CONDENSED MATTER PHYSICS

A light switch for a hidden order

Circularly polarized light provides a direct control of ferroaxiality

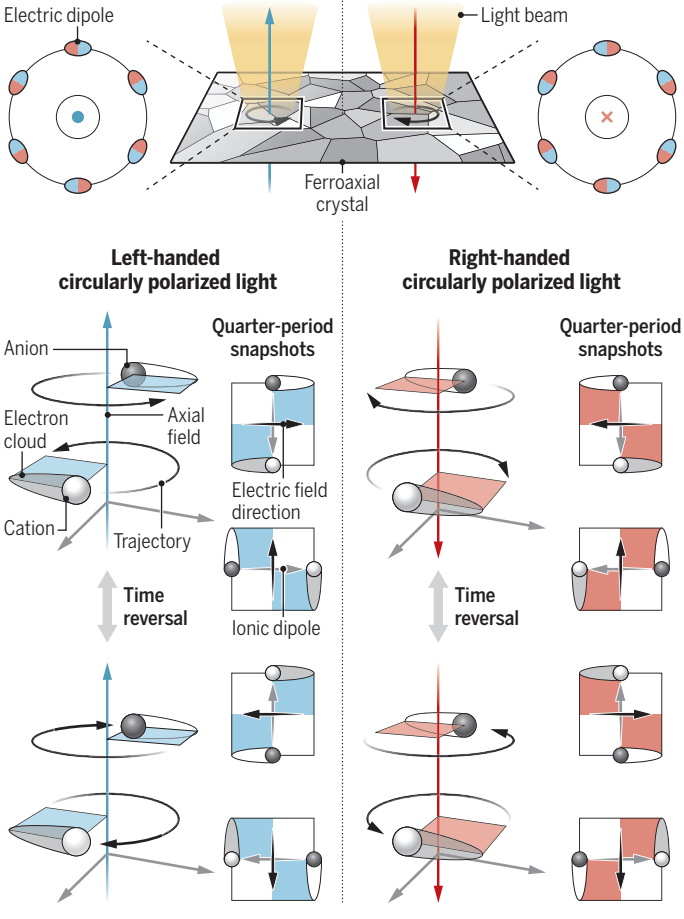
Zhiren He and **Guru Khalsa**

Fields control states of matter. For example, magnetic fields can flip the poles of a permanent magnet to store information in magnetic memory devices. An exception is ferroaxiality that is composed of loops of microscopic electric dipoles. This hidden order is insensitive to ordinary electric and magnetic fields. In fact, there is no natural conjugate field for direct control of ferroaxiality (*1*). On page 195 of this issue, Zeng *et al.* (*2*) report that circularly polarized light—a beam of light in which the electric field vector rotates in a circle—that is tuned to match an infrared-active lattice vibration creates a conjugate field for controlling ferroaxiality. This could expand the design space for multifunctional materials.

Electric dipole loops can describe ferroaxiality in a similar way to that of the current loops for a permanent magnet (ferromagnet). At low temperatures, the current loops align to produce regions (domains) of macroscopic magnetization, which can be switched with a sufficiently large magnetic fields. At high temperatures, these loops randomly orient or fluctuate to eliminate magnetization, shifting the material to the paramagnetic phase. Similarly, ferroaxial crystals exhibit ferroaxial domains and become para-axial at high temperatures. However, ferroaxiality couples very differently to fields compared with ferromagnetism. Magnetic moments (current loops) flip their orientation when time is reversed as magnetic fields do, but axial moments (electric dipole loops) remain fixed. Consequently, ferromagnetism responds to a magnetic field, but ferroaxiality does not. An axial conjugate field must mirror an electric dipole loop that is unchanged when reversing time.

Light controls ferroaxial order

Ferroaxial crystals have microscopic loops of electric dipoles (pairs of opposite charges separated by small distances). Atomic (lattice) vibrations resonating with circularly polarized light create a conjugate field in which electronic dipoles are aligned with, and ionic dipoles are oriented perpendicular to, the electric field of the light beam. The axial conjugate field, which is dictated by the light's handedness and is unchanged under time reversal, gives direct control of ferroaxiality.



GRAPHIC: A. FISHER/*SCIENCE*

Zeng *et al.* sent short pulses of circularly polarized light to excite an archetypal ferroaxial crystal, rubidium iron dimolybdate [$RbFe(MoO_4)_2$] near the para-axial–to–ferroaxial transition temperature. The electric field of the light was tuned to oscillate at the same frequency as the atomic vibrations inside the crystal (resonance). A subsequent light pulse measured the strength and orientation of ferroaxial order in the material (*3*, *4*). In the para-axial phase, the light induced a transient ferroaxial order that lasted only 1 picosecond (10^{-12} s). By contrast, in the ferroaxial phase, a single pulse above a fluence (energy per area) threshold deterministically switched the ferroaxial domains, which remained stable for hours. These domains were switched back to their previous states by applying a light pulse of opposite circular polarization. The field threshold and state reversibility are signatures of ferroic order, like ferromagnetism. Zeng *et al.* demonstrated the first direct, controlled manipulation of ferroaxial order, confirming a theoretical proposal of the axial conjugate field (*5*).

The conjugate field reported by Zeng *et al.* combined ionic and electronic motions. In response to the resonant, circular excitation with light, electrons and ions in the ferroaxial crystal moved in circles where electrons tracked the light's electric field while ions lagged behind it (see the figure). These created two perpendicular circulating dipoles that constitute the axial conjugate field. Tuning the light away from resonance aligned the circulating dipoles, creating a current loop akin to a magnetic field, which suppressed the ferroaxial response.

Ferroaxial order has been primarily studied in multiferroic materials in which states such as ferroelectricity and ferromagnetism coexist and can be coupled. Previously, ferroaxiality served as a bridge between ferroelectric polarization and chiral magnetic textures, facilitating control of magnetic states with electric fields (*6*, *7*). The work of Zeng *et al.* elevates ferroaxiality from a mediator of states to a new controllable state that is robust owing to its insensitivity to conventional fields. This could enable the development of multifunctional materials in which information can be encoded in electronic, magnetic, and ferroaxial degrees of freedom.

Key challenges remain, including mapping the kinetics of the ferroaxial switching, reducing the energy requirements, and scaling down the system size. Solving these issues may require alternative ferroaxial materials and conjugate fields, but the ability to directly manipulate ferroaxial order sets a foundation for future technologies. □

REFERENCES AND NOTES

1. J. Hlinka *et al.*, *Phys. Rev. Lett.* **116**, 177602 (2016).
2. Z. Zeng *et al.*, *Science* **390**, 195 (2025).
3. X. Luo *et al.*, *Phys. Rev. Lett.* **127**, 126401 (2021).
4. H. Yokota, T. Hayashida, D. Kitahara, T. Kimura, *npj Quantum Mater.* **7**, 106 (2022).
5. Z. He, G. Khalsa, *Phys. Rev. Res.* **6**, 043220 (2024).
6. R. D. Johnson *et al.*, *Phys. Rev. Lett.* **107**, 137205 (2011).
7. N. J. Perks *et al.*, *Nat. Commun.* **3**, 1277 (2012).

10.1126/science.aeb8208

Department of Physics, University of North Texas, Denton, TX, USA. Email: guru.khalsa@unt.

POLICY FORUM

ARTIFICIAL INTELLIGENCE

China's emerging regulation toward an open future for AI

Legislation proposals seek to bring certainty, clarification, harmonization, and simplification

Yue Zhu[1], Bo He[2], Hongyu Fu[3,4], Naying Hu[5], Shaoqing Wu[6], Taolue Zhang[1], Xinyi Liu[7], Gang Xu[1], Linghan Zhang[8], Hui Zhou[9]

Open-source artificial intelligence (AI) systems from China are gaining momentum worldwide. In parallel to these technical advances, China's AI regulation is also taking shape. But as this AI regulatory landscape is constantly evolving, already complicated, and awaiting more certainty, clarification, harmonization, and simplification are becoming more important than ever. An AI law that consolidates and improves existing laws, policies, and cases has the potential to be a solution. Although no official draft of such a law has been released in China yet, AI law experts in China have drafted two influential proposals, Model AI Law (v 3.0, with an article-by-article interpretation) and AI Law (Scholar's Proposal), that have become important references for understanding and researching China's AI regulation (*1*). We outline the current landscape, discuss both proposals, identify points for improvements of China's AI regulation, and conclude with an outlook on the regulatory future and global implications.

OVERVIEW OF CURRENT LANDSCAPE

Improved awareness and understanding of technical advancements and the regulatory landscape in China may assist global AI stakeholders—in particular, frontier AI scientists and engineers—not only in navigating this crucial jurisdiction but also in envisioning a globally inclusive technical and governance collaboration, particularly one that mitigates extreme AI risks (*2*). China has numerous AI-related laws and policies in effect (see the first table) as well as many algorithm filing requirements and judicial cases (*1*). Certain use cases of AI—including deep synthesis (often associated with "deepfake"), generative AI, and frontier models—are subject to filing requirements, in which an AI safety self-assessment shall be submitted for regulatory approval before providing service to end users. The assessment broadly covers content compliance, technical vulnerability, and misuse. There are five dimensions in content compliance, also called content safety, in China: upholding core socialist values, preventing discrimination and bias, respecting intellectual property (IP) rights, respecting personal rights, and increasing recognizability and reliability of generated contents. There have been more than 5600 filings (*3*). There have long been calls for filing requirements, especially content compliance ones, to be more transparent, efficient, and concretely workable—for example, providing clear and consistent feedback when a filing application is rejected, for domestic and foreign AI companies. National technical standards, specifically the "Cybersecurity Technology–Basic Security Requirements for Generative Artificial Intelligence Service" (no. GB/T 45654-2025), were recently released to provide detailed and often quantitative specifications for requirements.

A few other AI use cases—including autonomous vehicles, automated stock-trading, medical diagnosis, and meteorological service—are subject to sector-specific regulations (see the first table). Courts around China have adjudicated or are currently hearing a rapidly increasing number of AI-involved cases, especially regarding copyright, data privacy, deepfake, product safety, and unfair competition. Confronted with such technically and legally complex cases, courts face considerable challenges in delivering prompt conflict resolution that meets the expectations of the parties involved, such as copyright holders, and that is considered fair by all parties while also remaining future-proof amid the rapid evolution of AI.

China's highest legislative and administrative authorities, the National People's Congress (NPC) and the State Council, have officially stated that a legislation project on the healthy development of AI is ongoing (*1*). It has been publicly reported that the NPC is hearing from stakeholders regarding this project. The experts' proposals we discuss here (*1*) both advocate for consolidation and refinement for filing requirements, sector-specific regulation, and conflict resolution. Open-source AI in China, having already grown and flourished within its regulatory landscape, could further thrive under a coherent regulatory framework featuring a consolidated and refined AI law. Our interconnected narrative simultaneously examines how openness—a consensual goal explicitly acknowledged in pivotal laws and policy documents from regulators in China, the United States, the European Union, and other jurisdictions—is enabled within this landscape and how it can be further promoted through its improvement.

SIX PILLARS

There are six pillars, in our opinion, in China's emerging regulation, collectively acting as guide posts in an environment filled with technological and regulatory uncertainty, shaping a balanced approach to promote openness. For AI openness, we refer to a holistic approach that combines availability, documentation, and access (*4*), including life cycle transparency, functional accessibility, and genuine replicability, which enable the scientific community to thoroughly examine and use AI and to contribute to innovation, growth opportunity, and AI governance in the market. Imperfect, yet practically helpful, the six pillars hold prominent positions in our attempt to understand the coevolution of technology and policy. These principles are applicable to both private and public sectors. For the latter, administrative law requirements also should be considered. The scope of application for each pillar, often defined by technical terms such as deep synthesis or generative AI, is highly contextual and may overlap, conflict, or vary over time because of the controversial and evolving semantics of these terms.

The first pillar is the presumptive and clear-cut exemption of open-source AI. Many regulations, particularly the filing obligations, apply only to AI that provide services to end users. Merely open-sourcing an AI model through GitHub or Hugging Face, even a frontier one, will not trigger obligations. This does not prevent AI developers from voluntarily filing for registration, often to signal their capacity in AI safety and enhance attractiveness for downstream deployers who may then provide services to end users. This contrasts with the European Union (EU) AI Act, which does not grant exemption to open-source general-purpose models with systematic risks. It is now increasingly suggested, as exemplified in both expert's proposals, that a more cautious approach be taken for certain frontier models, considering possible extreme risks arising from open-sourcing which lacks due control and is thus vulnerable to dangerous misuse.

Principal laws and policies applicable to artificial intelligence (AI) in China

Field	Laws and policies	Examples of AI-related rules	Examples of detailed rules
Cyber, data, and content safety	Cyber Security Law (2016) and Data Security Law (2021)	Network, data, and content safety rules	Network Data Security Management Regulations (2024)
Product safety	Civil Law Code (2020)	Fault-based and non-fault liability rules	No AI-specific additional rules
Intellectual property (IP)	Trademark Law (2019), Patent Law (2020), and Copyright Law (2020)	Rules of IP protectability of AI-generated works	Guangdong Highest Court's Opinion on High-Quality IP Trial Work (2025)
Data protection	Cyber Security Law (2016) and Personal Information Protection Law (PIPL) (2021)	Rules of legal basis for personal data processing and data subject rights	Network Data Security Management Regulations (2024)
Discrimination and bias	Labor Law (2018), Education Law (2021), and PIPL (2021)	Rules of prohibition of discrimination in automated decision-making	Security Requirements for Automated Decision-Making (Draft standard)
Protection of special groups	Law on the Protection of Minors (2020), and Accessibility Law (2024)	Rule to develop minor's mode in certain app to prevent algorithm addiction	Guidelines for Establishment of Minors' Modes for Mobile Internet (2024)
Sector-specific regulations	Autonomous vehicles, program trading, medical diagnosis, meteorological service, judicial application, and environmental sustainability, for example	Rules specifying that program trading system shall have effective threshold management, abnormality monitoring, and error handling functions and more	Regulations on the Management of Program Trading in the Securities Market (2024), Measures for AI Meteorological Application Services (2025), and many others

The second pillar, complementary to the open-source exemption, is a presumptive exemption of AI scientific research. For example, as provided in Article 2 of the Interim Measures for the Management of Generative Artificial Intelligence Services, this measure does not apply where enterprises and educational and research institutions research, develop, and use generative AI technology but have not provided generative AI services to the domestic public. This is also a position explicitly and consensually taken in both experts' proposals. Nonetheless, there are now divergent opinions on whether research and development (R&D) activities of frontier AI shall be left unregulated. Several leading developers of frontier AI have expressed dedication to self-regulation, such as OpenAI's Preparedness Framework, Anthropic's Responsible Scaling Policy, and DeepMind's plan along its path to AGI. The effectiveness of these measures has yet to be independently verified. Similarly, there have been a few efforts to monitor and mitigate extreme risk in China at the industry level, including Safety Governance Framework, AI Safety Commitments, and AI Safety Benchmark (*5*, *6*). For example, the AI Safety Benchmark assesses instruction adherence and hallucination rate every quarter for a dozen models. However, compared with the AI safety commitments of leading developers that still lack independent verification, we argue that China's leading AI companies need to be even more transparent and evidence-based about their efforts to govern frontier models, particularly with regard to the nature and effectiveness of these efforts.

The third pillar is courts' deliberate and efficient adjudication of AI cases, particularly copyright cases that concern model pretraining and therefore can have substantial implications for AI development (*7*). This depth and efficiency are partially due to China's establishment of Internet Courts dedicated to frontier technology controversies. Generally, AI developers wait months, rather than years, for courts to issue a judgment. Consequently, there are currently dozens of adjudicated copyright cases in China, providing abundant resources for compliance. Most notably, in a judgment delivered in September 2024 by the Hangzhou Internet Court, the crucial pretraining issue was resolved, through dicta (a judge's opinion not necessary to resolve the controversy), as follows:

"Provided that the use of other people's works by generative AI in the data pretraining stage is for the purpose of learning from and analyzing the thoughts, feelings, linguistic features and characteristic styles expressed in previous works, and extracting the underlying rules, structures, patterns and trends from them in order to facilitate the subsequent transformative creation of new works, rather than reproducing the original expression of the works, it is held that data pretraining can be considered fair use in the absence of evidence to the contrary" (*8*).

Notably, in two recent rulings issued by the United States District Court for the Northern District of California (*Bartz v. Anthropic* and *Kadrey v. Meta*), similar conclusions were reached that the use of copyrighted data to train or "to iteratively map statistical relationships between every text fragment and every sequence of text fragments so that a completed [large language model] could receive new text inputs and return new text outputs..." (*Bartz v. Anthropic*, p. 11) may constitute fair use. However, this does not preclude AI companies from being held liable for copyright infringement for other uses of works. For example, Anthropic's fair use defense for creating a library containing more than 7 million pirated copies was denied (*Bartz v. Anthropic*, p. 18 and p. 30–31). On 25 September, preliminary approval was granted for a $1.5 billion settlement in *Bartz*, releasing Anthropic from liability for past use of works on a list.

Courts around China have publicly released more than a dozen judgments regarding other critical AI copyright issues, including AI-generated work copyrightability, intersection between copyright infringement and platform liability, and IP protection for model parameters. Nevertheless, achieving judicial efficiency in AI cases comes at a cost. There are a few justified concerns that we believe are internationally shared: lack of AI expertise, especially for low-level courts not dedicated to frontier technology controversies; rushing to a judgment that may soon become obsolete; conflicting judgments that reach facially different conclusions on copyright protectability (for example, see the 4th, 7th, 10th, and 12th cases listed in the second table); and courts' pro-innovation inclination in their judicial discretion that may unduly downplay protection of copyright and related rights.

In addition to the three pillars of exemptions and efficiency, the fourth to sixth pillars are made of restrictive rules. The fourth pillar is a decentralized, varied, and evolving approach to assessing a spectrum of AI-involved scientific research, from AI-assisted to fully automated. Particularly, in 2024 during the amending of the Degree Law that regulates academic integrity and degree conferral, an official draft version of the amendment once categorically regarded AI ghostwriting—a term that could be broadly interpreted to encompass all AI-assisted research execution and writing—as academic misconduct, but this provision was eliminated from the final amendment (*1*). A more contextualized ap-

Copyright cases and controversies in China

Case name	Case number	Time of judgment	Place of judgment	Case synopsis
Tencent v. Yingxun	(2019) Yue 0305 Min Chu 14010	December2019	Shenzhen Nanshan District People's Court	AI-generated work, hereby news article, can be protected by the Copyright Law
Mofa v. A Hangzhou company	(2022) Zhe 0192 Min Chu 9983	April 2023	Hangzhou Internet Court	Digital person can be protected by the Copyright Law, and its unlicensed use can constitute unfair competition
	(2023) Zhe 01 Min Zhong 4722	August 2023	Hangzhou Intermediate People's Court	
Four artists v. Xingyin Information Technology Co., Ltd. (RedNote), et al.	Not specified	Not applicable	Not applicable	Filing a lawsuit for copyright infringement concerning pretraining in the Beijing Internet Court in November 2023
Li v. Liu	(2023) Jing 0491 Min Chu 11279	November 2023	Beijing Internet Court	AI-generated work, hereby image generated by Stable Diffusion, can become a work protected by the Copyright Law
Chen v. A Shanghai company	(2024) Hu 0114 Min Chu 1326	April 2024	Shanghai Jiading District People's Court	Posting a video substantially similar to another, with only the faces therein altered by AI, may constitute copyright infringement
Shanghai Character License Administrative Co. Ltd (SCLA) v. Nianguang Network Tech	(2024) Yue 0192 Min Chu 113	February 2024	Guangzhou Internet Court	The famous Ultraman case, finding infringement for generating pictures substantially similar to copyrighted Ultraman image
Lin v. Hangzhou Gauss Inflatable Tech	(2024) Su 0581 Min Chu 6697	October 2024	Changshu People's Court	Copyright protectability of AI-generated image reaffirmed
SCLA v. A Shanghai company	(2024) Zhe 0192 Min Chu 1587	September 2024	Hangzhou Internet Court	AI service that hosts foundation model and low-rank adaptation can, in certain circumstances, contributorily infringe others' copyright
	(2024) Zhe 01 Min Zhong 10332	December 2024	Hangzhou Intermediate People's Court	
Tencent v. Baidu et al.	(2024) Xiang 0105 Min Chu 3790	October 2024	Changsha Kaifu District People's Court	AI-augmented video editing service can, in certain circumstances, directly infringe others' copyright
	(2024) Xiang 01 Min Chu 18114	December 2024	Changsha Intermediate People's Court	
Wang v. A Wuhan company	(2024) E 0192 Zhi Min Chu 968	January 2025	Wuhan Donghu New Technology Development Zone People's Court	Copyright protectability of AI-generated image reaffirmed
Douyin v. Yiruike	(2023) Jing 0105 Min Chu 71391	Not specified	Beijing Chaoyang District People's Court	Unlicensed use of others' model architecture and parameters can constitute unfair competition
	(2023) Jing 73 Min Zhong 3802	March 2025	Beijing Intellectual Property Court	
Feng v. Zhu and Dongshan	(2024) Su 0582 Min Chu 9015	March 2025	Zhangjiagang People's Court	Copyright protectability denied for AI-generated image due to insufficient human control over the expressive elements
	(2025) Su 05 Min Zhong 4840	April 2025	Suzhou Intermediate People's Court	

proach to regulating AI's various roles in scientific research is adopted by taking a more institution-specific, subject-specific, and fact-specific approach. Consequently, journals, academic associations, universities, and research institutions in China are currently taking drastically different stances concerning AI-involved research that range from complete bans, case-by-case evaluations, and AI considered irrelevant to encouragement. For example, as provided in the Guidelines for a Code of Conduct for Responsible Research issued by the Ministry of Science and Technology, the use of AI-generated content in scientific research should undergo verification and be disclosed comprehensively.

As the fifth pillar, in 2023 10 ministries, including the Ministry of Science and Technology of China, issued Trial Measures for Ethical Review of Science & Technology. Whenever researchers and developers engage in AI activities such as highly autonomous decision-making systems for specific scenarios, human-machine integration systems that notably affect individuals, and AI models and applications that substantially influence social discourse, they must fulfill a dual obligation of prior self-examination and review by ethical experts. The AI Ethics Governance Standardization Guide, published in 2023 by the national standardization authority, outlines 10 ethical principles: people-centeredness (preserving human well-being, dignity, autonomy, and freedom), sustainability, collaboration, privacy, fairness, sharing, security, safety, transparency, and accountability. These principles are both specified and elaborated on. The guide also provides a preliminary analytical framework, methodology, and case studies for addressing AI ethics in specific contexts (*9*). This stands in contrast to the EU AI Act, which integrates AI ethics principles into other specific requirements and no longer establishes a standalone set of AI ethics requirements.

Ethical review in China is still under development. Two aspects of progress are worth noting. The first is the gradual drafting and release of more detailed review guidelines and technical standards. Some local governments, enterprises, universities, and other institutions have gradually established ethical review committees. Ethical review and filing obligations may soon be harmonized to further alleviate compliance burden for AI companies. The second aspect comes from a judgment delivered by the Hangzhou Internet Court in August 2023. A developer of face-swapping AI was found to be criminally liable for violating the right to protection of the personal information of victims—whose identities remain unspecified owing to privacy concerns—by providing a service that swapped their faces with those of performers in pornographic films. The judgment also advised developers to embed technology ethics into the design and development stages to prevent future violations of the public's personal rights. The Supreme People's Court of China has also advocated in January 2025 that courts take serious consideration of science and technology ethics in deciding relevant cases (*10*).

The sixth pillar is that developers of certain AI systems can choose to participate in phased testing that gradually moves from closed sandbox

environments (a controlled experimentation and testing environment in the development and premarketing phase with a view to identify, isolate, and mitigate risks) to real-world conditions before being put into the market. For example, in 2022 the Pudong New Area of Shanghai enacted the first local regulation in China on promoting innovative applications of driverless vehicles, and the first batch of four licenses for road testing driverless Robotaxi was granted in 2024 (*11*). Recently, the Ministry of Industry and Information Technology and the State Administration for Market Supervision of China jointly released more concrete requirements for autonomous vehicle (AV) sandbox testing in the Notice on Further Strengthening the Management of Intelligent Networked Vehicle Product Access, Recall and Software Online Upgrade. As of July 2024, a total of 16,000 test licenses for AVs have been issued, and 32,000 km of roads nationwide have been opened for AV testing (*12*). All these contribute a rich and successful precedent for building an AI regulatory sandbox, as advocated for in various jurisdictions.

China's emerging AI regulation—a portfolio of exemptive laws, efficient adjudication, and experimentalist (pilot-first, phased implementation) requirements—collectively creates an innovation- and openness-friendly institutional environment for AI developers. AI developers enjoy considerable discretion in committing to resource-intensive and time-consuming AI research and collaborate through the international open-source community. Meanwhile, for AI extreme risks, multiple risk governance measures are in place. For R&D activities, they are often applied in a flexible and experimentalist manner, whereas for AI models, applications, and products that will be put into the market or provide services to end users, extensive laws and policies, including filing obligations, will apply. Numerous points for improving existing and future regulation are also proposed. As emphasized above, such as for foreign AI companies that are navigating China's AI regulatory landscape, clarification, harmonization, and simplification are the goals that need prioritizing and pursuing.

When considering implications of the six pillars, we should also consider potential setbacks. First, our discussions are largely illustrative and sometimes intuitive. More rigorous empirical studies are needed to assess the effects of existing AI regulations, as well as to draft an AI law. Also, throughout our discussion, we assume that AI openness is a worthy goal without providing further normative analysis, a view that we believe is widely held within the global AI community. However, there are also strong arguments against AI openness, particularly regarding concerns about AI safety, open-washing, and power concentration (*13*). We leave this disagreement for future debate. Importantly, all six pillars apply to the development and deployment activities not just of companies and academics but also of the government. We recognize that there are risks of government misuse of AI—for example, automated decision-making left unchecked in sensitive areas such as judicial decision-making—and we advocate for safeguarding individuals' rights and freedoms with regard to technological due process (*14*, *15*). This is a popular topic in both China and the United States and worthy of global attention.

In our opinion, this policy portfolio has a tangible positive impact on promoting the openness of frontier AI, as demonstrated by DeepSeek-R1, Wan 2.5, and other forthcoming frontier models. When these frontier models are deployed, meaning that end users may be subject to risk, those deploying them are obliged to assess and demonstrate the models' safety. Policies seek to maximize the freedom to pursue research for the AI research community while minimizing the risk to individuals and society whenever it may spill over outside the research community and affect end users. We are confident that this approach will be adhered to with China's ongoing AI legislation and that it has the potential to provide a productive, responsible, and well-balanced solution, accompanied by detailed context-specific rules and on-the-ground cases, for global AI governance. However, to have the potential fully unbridled, much work remains to be done to clarify ambiguity, harmonize inconsistency, and simplify byzantine regulation, mostly to be achieved through the ongoing AI legislation project.

Amid a time of open and near irreconcilable controversy concerning global AI governance, a promotive, pragmatic, and well-practiced solution is more important than ever. We advocate for an open future of AI not only because of its considerable local and global economic value, but also because in-depth global cooperation, for which openness has always and will always be necessary, is a prerequisite for the "urgently need[ed] national institutions and international governance to enforce standards preventing recklessness and misuse" by rapidly progressing frontier AI [(*2*), p. 844]. Countries now have a stronger than ever desire to accelerate AI R&D, which may make it difficult to negotiate full-fledged international governance. A solution that simultaneously promotes openness and innovation for AI can act as the most workable lowest common denominator for the global AI governance dialogue. In the meantime, China's AI regulation system, especially legislation on the healthy development of AI, will become better balanced, globally inclusive, and future proof by incorporating more ideas from international stakeholders in China and international dialogue involving China. □

REFERENCES AND NOTES

1. W. Wang *et al*., SSRN 5039316 [Preprint] (2025); https://papers.ssrn.com/sol3/papers.cfm?abstract_id=5039316.
2. Y. Bengio *et al*., *Science* **384**, 842 (2024).
3. DLaw Hub, "China algorithm filing statistics" (2025); https://s3zdtatd2r.feishu.cn/wiki/ANqLwe8NZirDzUkCw3icquZLnYd?table=blkGXb7JlXtDif8S.
4. A. Liesenfeld, M. Dingemanse, Proceedings of the 2024 ACM Conference on Fairness, Accountability, and Transparency, 10.1145/3630106.365900 (2024).
5. K. Elmgren, O. Guest, *Chinese AI Safety Institute Counterparts* (Insititute for AI Policy and Strategy, 2024); https://static1.squarespace.com/static/64edf8e7f2b10d716b5ba0e1/t/672261e1cb8fe024f2d10f9c/1730306539334/Chinese+AISI+Counterparts.pdf.
6. Artificial Intelligence Industry Alliance, Disclosure of practices on the artificial intelligence security and safety commitment (2025); https://aihub.caict.ac.cn/ai_security_and_safety_commitments
7. P. Samuelson, *Science* **381**, 158 (2023).
8. SCLA v. A Shanghai company (2025); https://mp.weixin.qq.com/s/4ZQ-qMwi82rzLPTyK7wqcg.
9. The National Artificial Intelligence Standardization General Working Group, the Artificial Intelligence Subcommittee of the National Information Technology Standardization Technical Committee, The AI Ethics Governance Standardization Guide (2023).
10. Supreme People's Court of China, "Supreme People's Court's announcement regarding the releasing of 'Opinions on securing technological innovation with high-quality trial services'" (2025); http://gongbao.court.gov.cn/Details/95026cfd9e4ff8a036c88683e66f51.html.
11. Shanghai government, "Shanghai Issues First License Plates for Driverless Vehicles" (2024); https://english.shanghai.gov.cn/en-Latest-WhatsNew/20240709/b237366f60204405bd47d1cb0f3ee5a8.html.
12. Xinhua News Agency, "16,000 test licenses for autonomous vehicles issued in China" (2024); https://www.chinadailyhk.com/hk/article/591613.
13. D. G. Widder, M. Whittaker, S. M. West, *Nature* **635**, 827 (2024).
14. D. K. Citron, *Wash. Univ. Law Rev*. **85**, 1249 (2008).
15. S. Yu, *Chinese J. Law* **45**, 91 (2023) [in Chinese].

ACKNOWLEDGMENTS

L.Z. is funded by United Nations Educational, Scientific, and Cultural Organization "Baseline Assessment Research of Artificial Intelligence in China, Japan and South Korea" project. L.Z. is a member of the Ministry of Public Security's Cybersecurity Legal Consultation Committee, Ministry of Industry and Information Technology's Information and Communication Science and Technology Committee. Y.Z., B.H., and H.Z. participated in the drafting of Model AI Law and its interpretations. B.H. participated in the drafting of Interim Measures for the Management of Generative Artificial Intelligence Services. L.Z. participated in the drafting of AI Law (Scholar's Proposal). S.W. and N.H. participated in the preparation and testing of AI Safety Commitments and AI Safety Benchmark.

10.1126/science.ady7922

[1]Tongji University Law School, Shanghai, China. [2]Research Center for Internet Law, China Academy of Information and Communication Technology, Beijing, China. [3]AI Governance Center of Aliresearch, Alibaba Group, Hangzhou, China. [4]School of Public Management, University of Electronic Science and Technology of China, Chengdu, China. [5]Artificial Intelligence Institute of China Academy of Information and Communication Technology, Beijing, China. [6]DeepSeek-AI, Beijing, China. [7]Institute of Scientific and Technical Information of China, Beijing, China. [8]China University of Political Science and Law, Beijing, China. [9]Faculty of Cyber and Information Law, Institute of Law, Chinese Academy of Social Sciences, Beijing, China. Email: yue_zhu@tongji.edu.cn (Y.Z.); xugang@tongji.edu.cn (G.X.); zl343@outlook.com (L.Z.); 13811511697@163.com (H.Z.)



BOOKS ET AL.

NATURAL RESOURCES

The lithium dilemma

A social scientist questions the importance of a key mineral in "green" technology

Saleem H. Ali



Thea Riofrancos
Norton, 2025.
288 pp.

EXTRACTION | The costs and impacts on communities of raw materials extraction have become a fertile research area for social scientists. Anthropologists, geographers, and political scientists have for decades questioned the economic orthodoxy regarding the "multiplier effect" of primary industries in charting development paths. Critical minerals for clean technologies have added an additional layer of complexity to this genre of scholarship, which suggests a trade-off between green innovations, such as electric cars or smart renewable grids, and the human cost to communities where resource extraction takes place. In *Extraction*, political scientist Thea Riofrancos takes readers to the heart of this trade-off with a focused analysis of lithium mining in Chile. Through her fieldwork in the vast lithium reserves of the Atacama Desert and the garden suburbs of the Chilean capital of Santiago, Riofrancos carefully describes the "geoeconomics" of lithium mining.

Lithium extraction delays due to protests and pushback mirror similar delays in other metal extraction projects. Yet we are reminded by the author that despite such delays, mining companies tripled the amount of metal they removed from the ground between 1970 and 2020. Riofrancos's training in political economy shines through in her nuanced analysis of state ownership of mineral assets under both the socialist Allende regime and the ostensibly capitalist Pinochet dictatorship, when the state-owned mining enterprise Codelco was consolidated.

A key insight regarding resource nationalism comes forth in the author's description of a recent debate held by the Chilean constitutional assembly in which members disagreed about the relative contributions of mining to development—an argument she describes as "at once relevant and outdated." While relevant in terms of Latin America's dependence on mineral exports rather than domestic value addition, the debate is outdated, she argues, because "political economy needed its complement of political ecology." The environmental impacts of such efforts and the role of science in constructing the arguments of political ecology are apparent in her description of how environmental experts and consultants connect with communities.

Lithium mined in the Atacama Desert fuels new technologies but comes with costs.

Of particular salience is how water availability—which is potentially affected by lithium mining—is defined in terms of salt content. While lithium companies try to argue that "brine" is not water, the scientific consensus around the value of brine in ecological viability holds sway for many communities. As a coastal country, Chile also has access to seawater, which is desalinated for some industrial purposes. Missing from Riofrancos's discussion is consideration of the impact of the efforts of the Antofagasta Minerals company to directly use seawater for some forms of mineral processing to reduce the pressure on groundwater resources in the Atacama (*1*).

The book's discussion of the Thacker Pass case study in Nevada and the Initiative for Responsible Mining Assurance has some overlap with Ernest Scheyder's 2024 book *The War Below* [previously reviewed in *Science* (*2*)]. However, Riofrancos provides more detailed referencing and academic rigor to the analysis while maintaining accessible prose. Yet she could have engaged further with some of the critiques of "resource curse" arguments supported by macroeconomic data analysis in the past decade (*3*).

Riofrancos ultimately has a broader ambition than just critiquing lithium extraction techniques, questioning the very forecasts that suggest the importance of and high demand for the mineral. In her final chapter, "Green Futures," she notes that the difference between best- and worst-case scenarios for lithium demand in 2050 is a staggering 92%—a disparity that depends on a range of assumptions around recycling, dematerialization, and redesigned transport systems. Technology and social behavior will need to converge quite dramatically for the best-case scenario to come to fruition, and countries such as Chile would need to establish alternative development pathways if minerals are removed from their economic development equation.

Despite conflicting opinions on its impacts, mining has been a key factor in allowing Chile to reduce its poverty indicators and improve a variety of human well-being indicators substantially (*4*). And although the notion of indigeneity in Chile has been historically questioned—more so than in other Latin American countries—there is still robust support for the rights of Indigenous communities to have a say in land management practices. Greater discussion of such considerations, alongside examples of successful community agreements that have been negotiated and well studied by social scientists, would have been illuminating.

Ultimately, the extraction dilemma for lithium and other elements as methods for meeting human "wants" versus "needs" will likely endure. Books like *Extraction* help us to remain vigilant about the costs of such choices. □

REFERENCES AND NOTES

1. L. A. Cisternas, E. D. Gálvez, *Miner. Process. Extr. Metall. Rev.* **39**, 18 (2018).
2. S. H. Ali, *Science* **383**, 374 (2024).
3. G. M. Nülle, G. A. Davis, *Miner. Econ.* **31**, 35 (2018).
4. C. Clark, E. A. Clark, *Challenging Neoliberalism: Globalization and the Economic Miracles in Chile and Taiwan* (Edward Elgar Publishing, 2016).

10.1126/science.ady8020

The reviewer is at the Department of Geography and Spatial Sciences, University of Delaware, Newark, DE, USA, and is a member of the United Nations International Resource Panel.
Email: saleem@alum.mit.edu

PHOTO: FREEDOM WANTED/ALAMY

MICROBIOLOGY

The complicated legacy of antibiotics

Antimicrobial drugs changed everything, but misuse and resistance have been constant companions

Audrey R. Glynn



Liam Shaw
Simon & Schuster, 2025. 352 pp.

DANGEROUS MIRACLE | The first antibiotic became commercially available less than 90 years ago, with resistance emerging almost immediately. In 2024, the United Nations General Assembly declared antibiotic resistance "one of the most urgent global health threats." The drugs are scientific marvels, argues British biologist Liam Shaw in his new book, *Dangerous Miracle*, but inseparable from capitalism, power struggles, and misuse. Shaw tells the story of antibiotics with clarity and flair, from penicillin's serendipitous discovery and wartime mobilization to the combination therapy that saved his own grandfather from tuberculosis. Throughout, he reminds readers that antibiotics are not abstractions: They have been a large factor in defining modern life.

The book is thoughtfully structured, opening with a prelude on the discovery of bacteria, followed by 10 chapters, each of which are devoted to a landmark antibiotic, and concluding with a call to action. Each drug profiled serves as a lens on scientific discovery and its entanglement with politics, economics, and culture. This format makes a sprawling history digestible and memorable, pulling together archival detail, industry history, and personal narrative.

Shaw excels at illustrating how science and politics collide. His account of broad-spectrum antibiotics captures what might be called the mid-20th century's "guns blazing" approach: a push to produce drugs that could kill nearly all bacteria, despite limited understanding of microbial ecology. In 1959, hospitals using broad-spectrum agents unexpectedly reported increased mortality from bacterial infections, and some scientists warned of their destructive impact on microbial flora. Yet drug companies promoted them as cure-alls and encouraged indiscriminate prescribing. This observation drives home the point that antibiotics were not just medical tools, they were commercial products shaped by marketing and profit motives.

Equally powerful is Shaw's discussion of antibiotic use in farming. After 1950, he reveals, antibiotics reshaped global meat production, first as US Food and Drug Administration–approved growth promoters and later by enabling concentrated animal feeding operations. "Antibiotics became a crucial cog in a vast new agricultural machine," Shaw writes, with animals "slaughtered on the altar of economic growth." What began in the United States soon spread worldwide, where antibiotics fueled unsanitary and inhumane but profitable modes of food production, with consequences we are still living with today.

The book also surprises in its cultural reach. Shaw writes, for example, that antibiotics used in tuberculosis sanatoriums sometimes triggered euphoria, leading to the serendipitous discovery of compounds first called "psychic energizer[s]" (later "antidepressants"). Another striking vignette reveals that penicillin-resistant *Staphylococcus aureus* nearly killed Elizabeth Taylor in 1960, halting production of the film *Cleopatra* until an emergency tracheotomy and methicillin saved her life.

Might antibiotics be outmoded? Shaw raises the question but does not linger on it. After recounting a dramatic case in which phage therapy saved a patient's life, he retreats to safer ground, stressing that antibiotics are easier to use than phages, and pivots to the promise of artificial intelligence–driven discovery. That path, however, depends on vast quantities of high-quality data, a massive challenge given the dearth of new antibiotic research. Other means of addressing bacterial infections are mentioned but not explored, leaving the reader without an appreciation for alternative approaches to tackling drug-resistant infections in the postantibiotic era.

In his conclusion, Shaw argues that "the system of patents that emerged over the twentieth century is killing antibiotics." His remedy is ambitious: an international public institute for antibiotic development, beginning with the wholesale public purchase of antimicrobial drugs now in commercial pipelines. In this framework, universities would waive intellectual property rights in exchange for public ownership, while generic manufacturers would produce the medicines under license at fair prices. Drawing inspiration from the CERN Large Hadron Collider and the International Space Station, Shaw envisions a globally funded, career-stable home for antibiotic researchers. Experts have dismissed this idea as utopian, yet others' proposed smaller-scale fixes, such as subscription models in which a government pays a fixed fee to pharmaceutical companies for unlimited access to new antibiotics, seem insufficient to match the scope of the crisis. Shaw's idea is worthy of serious debate, although I think it could be pushed even further: If the non–patent-driven system were to also encompass phages, microbiome-based interventions, and other alternatives, innovation in these areas might avoid the very traps that have stalled antibiotic pipelines.



Antibiotics are not only medical tools but also products shaped by economic drivers.

Overall, *Dangerous Miracle* succeeds brilliantly as an engaging and incisive history of antibiotics, capturing paradigm-shattering breakthroughs and political upheavals. Its call to rethink the patent system is essential. But the battle against antimicrobial resistance will require not only a reinvigoration of antibiotic research but also a broadening of our therapeutic imagination. As history, the book is a triumph. As a roadmap, it left me with questions—and perhaps that is the point. □

10.1126/science.aea3949

The reviewer is at the Innovative Genomics Institute, University of California, Berkeley, Berkeley, CA, USA. Email: audrey.glynn@berkeley.edu

PHOTO: LJUBAPHOTO/ISTOCK PHOTO



Road construction in Cameroon, where Europe's Global Gateway projects are underway, threatens ecosystems.

EU's global investments put biodiversity at risk

The Global Gateway initiative of the European Union (EU) aims to strengthen geopolitical influence through sustainable investments in energy, transport, health, education, and digital sectors, mobilizing up to €300 billion between 2021 and 2027 (*1*). Global Gateway supports sustainable development and the global energy transition but lacks sufficient biodiversity safeguards, putting hotspots such as sub-Saharan Africa and Southeast Asia at risk (*2*). To honor its commitment to halting biodiversity loss and achieving net biodiversity gain by 2030, the EU should update the initiative to include specific mechanisms that ensure biodiversity protection (*1*).

Of the 227 Global Gateway projects, 71% focus on climate, energy, and transport infrastructure (*1*). These sectors drive biodiversity loss through wildlife mortality, disturbance, and habitat fragmentation (*3*–*5*), potentially causing population declines (*6*) and putting threatened species at increased risk (*7*, *8*). Global Gateway projects include the 700-km Lobito railway, which cuts through key habitats in southern Africa for carnivores sensitive to linear infrastructures (*9*), and the 220-km Choir–Sainshand transmission line in Mongolia, which overlaps with breeding and stopover habitats of threatened bustards (*10*). It remains unclear whether Environmental and Social Impact Assessments are required for all Global Gateway projects because the initiative lacks a proactive and transparent framework of environmental requirements to guarantee comprehensive assessment across all projects.

To position the EU as a global leader in sustainable development, Global Gateway investments must incorporate robust and science-based safeguards. Every Global Gateway project should conduct standardized biodiversity risk screening, use transparent monitoring platforms that integrate habitat sensitivity and species vulnerability, and rigorously enforce Strategic Environmental Assessment and Environmental Impact Assessment standards. Collaboration among scientists, civic groups, and public authorities is essential, supported by capacity building and academic exchange for local professionals. Development of best-practice guidelines and ecological restoration tools would further enhance outcomes. By placing biodiversity at the core of Global Gateway initiatives, the EU can set a global standard for sustainable infrastructure development.

Clara Grilo[1,2,3], Pedro Beja[1,2,3], Joana Bernardino[1,2,3], Nuno Ferrand,[1,3] William F. Laurance[4], Anthony P. Clevenger[5]

[1]Research Centre in Biodiversity and Genetic Resources (CIBIO), Research Network in Biodiversity and Evolutionary Biology (InBIO), Universidade do Porto, Vairão, Portugal. [2]CIBIO/InBIO, Instituto Superior de Agronomia, Universidade de Lisboa, Lisboa, Portugal. [3]Program in Genomics, Biodiversity and Land Planning (BIOPOLIS)/CIBIO, Vairão, Portugal. [4]Centre for Tropical Environmental and Sustainability Science and College of Science and Engineering, James Cook University, Cairns, QLD, Australia. [5]Western Transportation Institute, Montana State University, Bozeman, MT, USA. Email: clara.grilo@cibio.up.pt

REFERENCES AND NOTES

1. European Commission, *Global Gateway Forum 2025*; https://commission.europa.eu/strategy-and-policy/priorities-2019-2024/stronger-europe-world/global-gateway_en.
2. S. Tagliapietra, *World Econ.* **47**, e13551 (2024).
3. D. Biasotto, A. Kindel, *Environ. Impact Assess. Rev.* **71**, 110 (2018).
4. C. B. Thaxter *et al.*, *Proc. R. Soc. B* **284**, 20170829 (2017).
5. R. van der Ree *et al.*, *Handbook of Road Ecology* (Wiley, 2015).
6. L. Fahrig *et al.*, *Biol. Conserv.* **73**, 177 (1995).
7. C. Palacín *et al.*, *Endanger. Species Res.* **30**, 73 (2016).
8. C. Grilo *et al.*, *Glob. Ecol. Biogeogr.* **30**, 2200 (2021).
9. I. Quintana *et al.*, *Sci. Rep.* **12**, 2902 (2022).
10. J. P. Silva *et al.*, *Bird Conserv. Int.* **33**, e30 (2023).

10.1126/science.adz8915

Strategic foundations of science diplomacy

In their Editorial "Rewiring science diplomacy" (21 August, 10.1126/science.aeb4815), V. C. Turekian and P. Gluckman offer a timely framework for rethinking science diplomacy in an era of renewed geopolitical competition. However, describing earlier efforts as merely "aspirational" risks underestimating their strategic value, and overemphasizing transactionalism could undermine the foundations of international cooperation.

The science diplomacy that took place after World War II and during the Cold War was not simply aspirational but highly strategic. It established notable and durable institutions, including the Antarctic Treaty System (*1*), the International Institute for Applied Systems Analysis (*2*), and the Montreal Protocol, that enabled science to effectively bridge political divides (*3*). These were important strategic achievements, grounded in efforts to build trust, institutions, and peace. Pragmatically, those efforts have focused on shared problem-solving and have reinforced institutions that translate scientific

PHOTO: WILLIAM F. LAURANCE

collaboration into informed decisions, which operate in the short to long term (*4*)—from climate action to biodiversity protection—even when political relations are strained.

A shift to a transactional approach is understandable in today's geopolitical environment, but it carries substantial risks. If science is reduced to a bargaining chip, cooperation becomes fragile, and countries with less leverage—particularly those in the Global South—will be marginalized. To be effective, transactional agreements must be anchored in frameworks that preserve open science (*5*) and sustain science as a global public good (*6*). Ultimately, science diplomacy must be grounded in the principles of transparency, inclusivity, and equity to sustain cooperation and adapt agreements, even in periods of geopolitical rivalry.

Small states provide vital lessons about building common interests. In the negotiations for a plastics treaty, Rwanda, Peru, and small island states advanced ambitious, equity-driven proposals. Their leadership helped build a coalition of more than 100 countries, demonstrating that principled, inclusive coalitions can counterbalance narrow, economic transactionalism and drive both national and global innovation (*7*).

Science diplomacy must remain a bridge, not only between rival powers but also across regions, disciplines, and generations. Effective transdisciplinary frameworks that incorporate science, including natural sciences, social sciences, humanities, and Indigenous knowledge, will balance near-term national interests with shared, long-term responsibilities (*4*). Transactional approaches have a place, but only when they reinforce, rather than replace, the trust on which science diplomacy depends.

The future of science diplomacy will depend on practitioners who can not only solve problems as they arise but also think strategically and build frameworks that endure. Science diplomats who are trained to move comfortably across these dimensions and who act with a strong sense of ethics will help facilitate the multilateral cooperation on which a globally interconnected civilization depends. With capacities to build common interests (*8*–*10*), science diplomacy as a "language of hope" [(*4*), p. viii] will continue to steady relations in difficult times and to inspire new forms of collective action.

Maria H. Ivanova[1,2,3], Paul Arthur Berkman[1,3,4,5], Zakri Abdul Hamid[1,3,5], Saleem H. Ali[1,6,7], Lawrence E. Susskind[1,4,8]

[1]Science Diplomacy Center, Inc., Falmouth, MA, USA. [2]School of Public Policy and Urban Affairs, Northeastern University, Boston, MA, USA. [3]International Science Council, Paris, France. [4]Program on Negotiation at Harvard Law School, Cambridge, MA, USA. [5]International Institute of Science Diplomacy and Sustainability, UCSI University, Kuala Lumpur, Malaysia. [6]Department of Geography and Spatial Sciences, University of Delaware, Newark, DE, USA. [7]United Nations University Institute for Water, Environment and Health, Richmond Hill, ON, Canada. [8]Department of Urban Studies and Planning, Massachusetts Institute of Technology, Cambridge, MA, USA. Email: pberkman@law.harvard.edu

REFERENCES AND NOTES

1. P. A. Berkman, *Science into Policy: Global Lessons from Antarctica* (Academic Press, 2001).
2. K. M. Lord, V. C. Turekian, *Science* **315**, 769 (2007).
3. L. E. Susskind, S. H. Ali, *Environmental Diplomacy: Negotiating More Effective Global Agreements* (Oxford Univ. Press, 2014).
4. P. A. Berkman, A. N. Vylegzhanin, O. R. Young, D. Balton, O. Øvretveit, Eds., *Building Common Interests in the Arctic Ocean with Global Inclusion*, vol. 2 of *Informed Decisionmaking for Sustainability*, P. A. Berkman, A. N. Vylegzhanin, Eds. (Springer, 2022).
5. UNESCO, "UNESCO Recommendation on Open Science" (2023); https://www.unesco.org/en/open-science/about.
6. International Science Council, "Science as a global public good" (2021); https://council.science/publications/science-as-a-global-public-good/.
7. M. Hillsdon, "Analysis: What can break the global deadlock over plastics?" *Reuters*, 20 August 2025.
8. G. H. Brundtland, "Report of the World Commission on Environment and Development: Our common future" (UN Document A/42/427, 1987); https://sustainabledevelopment.un.org/content/documents/5987our-common-future.pdf.
9. E. Ostrom, *Governing the Commons: The Evolution of Institutions for Collective Action* (Cambridge Univ. Press, 2015).
10. UNESCO, "UNESCO hosts global gathering to advance science diplomacy for peace" (2025); https://www.unesco.org/en/articles/unesco-hosts-global-gathering-advance-science-diplomacy-peace.

10.1126/science.aec1419

Science diplomacy is a tool, not a currency

In their Editorial "Rewiring science diplomacy" (21 August, 10.1126/science.aeb4815), V. C. Turekian and P. Gluckman argue that science diplomacy efforts must include a transactional approach to remain relevant and suggest that advancing national interest is a new feature of science diplomacy. We disagree.

Asserting that transactional approaches are new to any form of diplomacy—science diplomacy or otherwise—is incorrect and inaccurately implies that science diplomacy is a field unto itself rather than a tool of statecraft. The diplomatic objectives that the tool is used to advance can range from relational, to transactional, to altruistic. But national priorities, which can be seen as positive or negative, have always played a role. Advocating different modalities of science diplomacy risks presenting it as a practice with its own inherent values rather than a mechanism to advance scientific or diplomatic objectives.

As the popularity of the term "science diplomacy" has grown, so has confusion about what activities deserve the label (*1*). Overuse of the term can obscure the differences between science and diplomacy (*2*). Diplomatic objectives might be transactional, but scientific goals are not.

We agree with Turekian and Gluckman that clear frameworks are needed. We also acknowledge that past frameworks overemphasized shared global interests and underemphasized diplomacy that advances national interests. In response, many groups have published new or updated frameworks for science diplomacy, including the European Commission (*3*); the Geneva Science and Diplomacy Anticipator (GESDA) (*4*); the United Nations Educational, Scientific and Cultural Organization (UNESCO) (*5*); and our organizations—the American Association for the Advancement of Science (AAAS) (the publisher of *Science*) and the Royal Society (*6*).

In the current era, the fields of science and diplomacy have indeed fundamentally changed, and the geopolitical context is becoming increasingly fragmented, contested, and unstable. As our framework states, this era of disruption demands science diplomacy (*6*). Rather than overcategorizing science diplomacy or worrying about its relevance, scientists and diplomats should focus on using science diplomacy effectively as a tool to address challenges and seize opportunities. If these efforts are successful, science diplomacy will be relevant.

Kimberly Montgomery[1] and Ian Wiggins[2]

[1]Director of International Affairs and Science Diplomacy, American Association for the Advancement of Science, Washington, DC, USA. [2]Director of International Affairs, The Royal Society, London, UK. Email: kmontgomery@aaas.org

REFERENCES AND NOTES

1. E. Ledgerwood, S. Bunn, "Science Diplomacy," POST (UK Parliament, 2022).
2. "The future of science diplomacy," INGSA 2024 Conference, Kigali, Rwanda, 3 May 2024; https://royalsociety.org/-/media/about-us/international/science-diplomacy/ingsa-kigali-science-diplomacy-write-up-final.pdf.
3. European Commission: Directorate-General for Research and Innovation *et al*., *A European Framework for Science Diplomacy: Recommendations of the EU Science Diplomacy Working Groups*, R. Gjedssø Bertelsen *et al*., Eds. (Publications Office of the European Union, 2025)..
4. "Anticipatory science diplomacy: A framework for global action" (GESDA, 2025); https://www.gesda.global/wp-content/uploads/2025/08/GESDA_ASD_Paper_2025_28July__FINAL.pdf.
5. "Science diplomacy in a rapidly changing world: building peace in the minds of men and women," UNESCO Global Ministerial Dialogue on Science Diplomacy, Paris, France, 25 to 26 March 2025; https://articles.unesco.org/sites/default/files/medias/fichiers/2025/04/25-26%20March_UNESCO%20Global%20Ministerial%20Dialogue%20on%20Science%20Diplomacy_EN.pdf.
6. "Science diplomacy in an era of disruption" (Royal Society, AAAS, 2025); https://www.aaas.org/sites/default/files/2025-02/Final_Science%20diplomacy_15%20years%20on_report_WEB.pdf.

COMPETING INTERESTS

I.W. is a member of the International Science Council's Committee for Finance, Compliance, and Risk.

10.1126/science.aeb8644

REVIEW SUMMARY

EXOPLANETS

Constraining exoplanet interiors using observations of their atmospheres

Tim Lichtenberg*, Oliver Shorttle, Johanna Teske, Eliza M.-R. Kempton

Full article and list of author affiliations: https://doi.org/10.1126/science.ads3360

BACKGROUND: Extrasolar planets (exoplanets) orbit stars other than the Sun. Most of the ≈6000 known exoplanets were detected indirectly by studying how they affect the light emitted by their host stars. The principal observational signatures are the wobble that exoplanets induce in the star's radial velocity and the periodic dimming of the star's light as the exoplanet passes through our line of sight to their host star, which are known as transits. These techniques provide mass and radius measurements, respectively.

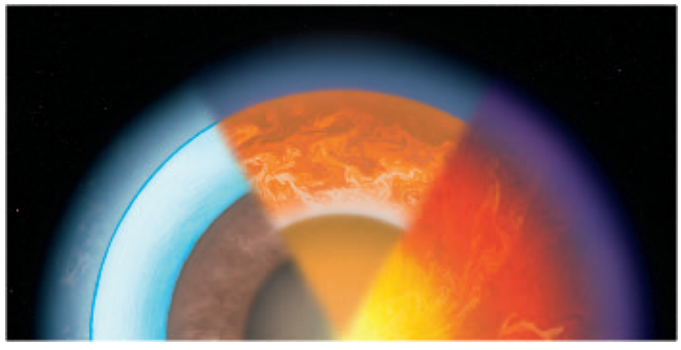
Observed exoplanets display a wider diversity than that of the planets in the Solar System. This includes their physical and chemical characteristics, orbital configurations, stellar irradiations, and compositions. Characterization of exoplanet properties is provided by astronomical observations. Interpreting those properties requires an understanding of planetary science, geophysics, geochemistry, atmospheric science, and astrobiology.

ADVANCES: Transit surveys by use of space telescopes have provided statistical insight into the population of exoplanets. Those surveys have found a common class of small exoplanets that is intermediate in size between Earth and Neptune and spans a large range in bulk densities, from close to Earth-like (super-Earths) to densities that necessitate large amounts of atmospheric volatiles (sub-Neptunes). These observations have allowed researchers to perform comparative planetology across a statistically meaningful sample of exoplanets.

Improved precision in transit and radial velocity observations has provided bulk density measurements for numerous exoplanets, which can be compared with interior structure and evolution models. Spectroscopic observations made with the JWST have provided some information on the atmospheric composition of low-mass exoplanets. These combined observations have shown a highly diverse population, including exoplanets composed of nearly pure iron, mixtures of rock and metal, and hydrogen-rich gas envelopes.

Most transiting exoplanets receive far more extreme irradiation from their host star than Solar System planets receive from the Sun. The resulting higher temperatures cause more material and energy exchange throughout the planet, blurring the distinction between segregated layers such as the atmosphere and rocky mantle. This interior-atmosphere exchange potentially allows the interior composition of a planet to be constrained by measuring the chemistry of its atmosphere. This indirect method could be used to study planetary geodynamics.

JWST spectra of several sub-Neptune exoplanets show evidence of chemical mixing between the upper atmospheric layers and the deep interiors. Spectroscopic observations of Earth-sized exoplanets orbiting low-mass stars show that they do not have thick atmospheric envelopes. However, several ultrashort-period super-Earths, with orbital timescales of <1 day, defy expectations of complete atmospheric evaporation: Their bulk densities necessitate either chemically undifferentiated interior structures or a high bulk abundance of volatile elements. In either case, this constrains the nature of interior-atmosphere exchange on these exoplanets.



Predicted interior structures of sub-Neptune exoplanets. Observed density and atmospheric constraints are interpreted in three scenarios, each with a gaseous envelope. (**Left**) Water worlds have a small metal core, rocky mantle, high-pressure ice layer, and possible liquid water ocean. (**Middle**) Gas dwarfs have a larger metal core and a magma ocean. (**Right**) Global supercritical regimes have no clear boundaries between layers. [Image: Mark A. Garlick]

OUTLOOK: Interpreting these results requires collaboration between researchers in exoplanet astronomy with those in planetary science, geophysics, and geochemistry. The limited astronomical data needs to be understood within laboratory-validated limits of material properties and thermodynamics. This approach will likely improve our understanding of how atmospheric escape, natal H/He envelopes, volatile accretion, and global-scale planetary magma oceans all interact to produce the properties of low-mass, highly irradiated exoplanets.

Upcoming facilities will perform wider and more detailed surveys to study planetary demographics across a larger temperature range. Future space telescopes are being designed to directly image temperate terrestrial exoplanets around Sun-like stars. This would provide the capability to investigate Earth-like exoplanets and assess their habitability. □

*Corresponding author. Email: tim.lichtenberg@rug.nl Cite this article as T. Lichtenberg *et al.*, *Science* **390**, eads3360 (2025). DOI: 10.1126/science.ads3360

EXOPLANETS

Constraining exoplanet interiors using observations of their atmospheres

Tim Lichtenberg[1]*, Oliver Shorttle[2,3], Johanna Teske[4,5], Eliza M.-R. Kempton[6,7]

Astronomical surveys have identified numerous exoplanets with bulk compositions that are unlike the planets of the Solar System, including rocky super-Earths and gas-enveloped sub-Neptunes. Observing the atmospheres of these objects provides information on the geological processes that influence their climates and surfaces. In this Review, we summarize the current understanding of these planets, including insights into the interaction between the atmosphere and interior based on observations made with the JWST. We describe the expected climatic and interior planetary regimes for planets with different density and stellar flux and how those regimes might be observationally distinguished. We also identify the observational, experimental, and theoretical innovations that will be required to characterize Earth-like exoplanets.

Observations of extrasolar planets (exoplanets)—which orbit stars other than the Sun—have increased our understanding of Earth and the Solar System (*1*, *2*). A great diversity of planetary mass, stellar irradiation, and planetary composition is evident among exoplanets, extending beyond the planets of the Solar System. Compared with exoplanetary systems, the Solar System architecture, with a Jupiter-like planet at a few astronomical units (au) distance from its host star, is unusual (*3*, *4*), but it is unclear whether Solar System–like terrestrial planets are equally rare (*5*).

Exoplanet observations, with both ground-based and space-based instruments, have advanced beyond simply detecting exoplanets to providing detailed characterization of statistically meaningful samples (Fig. 1). There are about 6000 known exoplanets, spanning wide ranges of radii, masses, orbital configurations, and host star types. The most commonly detected exoplanets are intermediate in size between Earth and Neptune, which have no Solar System counterpart (*6*). Such planets form two subpopulations (*7*, *8*): larger and less dense objects typically referred to as sub-Neptunes [≈2 to 4 Earth radii (R_{Earth})], and smaller, denser planets known as super-Earths ($\lesssim 1.6\ R_{\mathrm{Earth}}$). The gap between those groups (*7*), known as the radius valley, is populated by a less frequent group of planets with ambiguous nature. These different types of exoplanets experience geological processes at extremes of pressure, temperature, and states of matter. Experimentally grounded modeling frameworks are required to interpret the observed planetary properties (*5*, *9*).

Atmospheres provide the principal means of characterizing the detailed processes occurring on and within exoplanets (*10*). The atmospheres of gas giants grow by the accretion of hydrogen and helium gas (H/He hereafter) from the circumstellar disk during the planet formation process, forming a primary envelope. By contrast, low-mass exoplanets (similar to the terrestrial planets of the Solar System) have a secondary atmosphere, thought to be produced by material exchanged with the planet's deep interior through chemical reactions and transport of gases such as water (H_2O), carbon dioxide (CO_2), methane (CH_4), and sulfur dioxide (SO_2) into and out of the planetary mantle (ingassing and outgassing, respectively). These reactions couple the long-term climate and surface conditions of low-mass exoplanets to their interiors, establishing a connection that is distinct from that of gas giants (*5*, *10*).

It is unknown whether intermediate planets, such as sub-Neptunes and super-Earths, have primary envelopes or secondary atmospheres shaped by interior processes. The JWST is providing detailed spectroscopic studies of the atmospheres and surfaces of low-mass exoplanets, enabling the application of geological models to exoplanet data. Comparing those observations to models provides information about the planets' bulk composition, internal dynamics, and overall geophysical history, bringing insights into their geology. This requires constraining the surface and internal processes of exoplanets through atmospheric spectra, bulk density measurements, and host star compositions.

Measuring exoplanet density

The structure of a planet determines how its interior communicates with its surface and atmosphere. A planet's structure and composition depends on its density, which constrains whether it is mainly composed of high-density iron, moderate-density rock, or lower-density ice or gas. Density is determined by measuring a planet's mass [from radial velocities (RVs) or transit-timing variations] and radius (from transits). Short-period super-Earth masses have been measured to ~15% precision around bright low-mass stars (those classified as M dwarfs) and to ~25% around more massive Sun-like stars (*11*). Determining the masses of even smaller planets with RVs is limited by stellar variability (*12*).

Precise planetary radius measurements are provided by transits observed with space telescopes. The Kepler spacecraft, the Transiting Exoplanet Survey Satellite (TESS), and the CHaracterizing ExOPlanets Satellite (CHEOPS) have observed thousands of exoplanets and provided radii measurements with 10 to 15% precision, although many of those systems are too distant for detailed follow-up. Determining planet radii from transit depth measurements requires knowing the host star radius, for which the Gaia spacecraft (*13*) has provided stellar observations that enabled the precision of exoplanet host star radius determination to be improved by almost an order of magnitude (*14*).

Distinguishing distinct exoplanet populations

Precise exoplanet radius measurements demonstrated the bimodal radius distribution of sub-Neptunes and super-Earths discussed above. This bimodality was theoretically predicted (*15*–*17*) to arise from planets with dense, rocky interiors and an initial hydrogen-dominated primary envelope, some of which later lost their atmospheres because of stellar irradiation, producing the smaller and denser planets we observe. Alternative explanations for the loss of the primary atmosphere include rapid boil-off immediately after formation (*18*), long-lived photoevaporation (*19*), or internal luminosity–driven mass loss (*20*). These models predict that super-Earths are mostly bare rocks or have secondary atmospheres and that sub-Neptunes have similar interiors but retain overlying thick hydrogen-dominated envelopes. Specifically, the interiors of both types of planet are predicted to be mixtures of rock and iron because any wider diversity in composition would smear out the resulting bimodal radius distribution, muting the distinction between populations. These models of the bimodal distribution do not require migration of the planets from farther out in the protoplanetary disk to their current short orbital periods, although migration is typically predicted with planet-formation models (*21*).

[1]Kapteyn Astronomical Institute, University of Groningen, Groningen, Netherlands. [2]Department of Earth Sciences, University of Cambridge, Cambridge, UK. [3]Institute of Astronomy, University of Cambridge, Cambridge, UK. [4]Earth and Planets Laboratory, Carnegie Institution for Science, Washington, DC, USA. [5]The Observatories of the Carnegie Institution for Science, Pasadena, CA, USA. [6]Department of Astronomy and Astrophysics, University of Chicago, Chicago, IL, USA. [7]Department of Astronomy, University of Maryland, College Park, MD, USA. ***Corresponding author. Email: tim.lichtenberg@rug.nl**

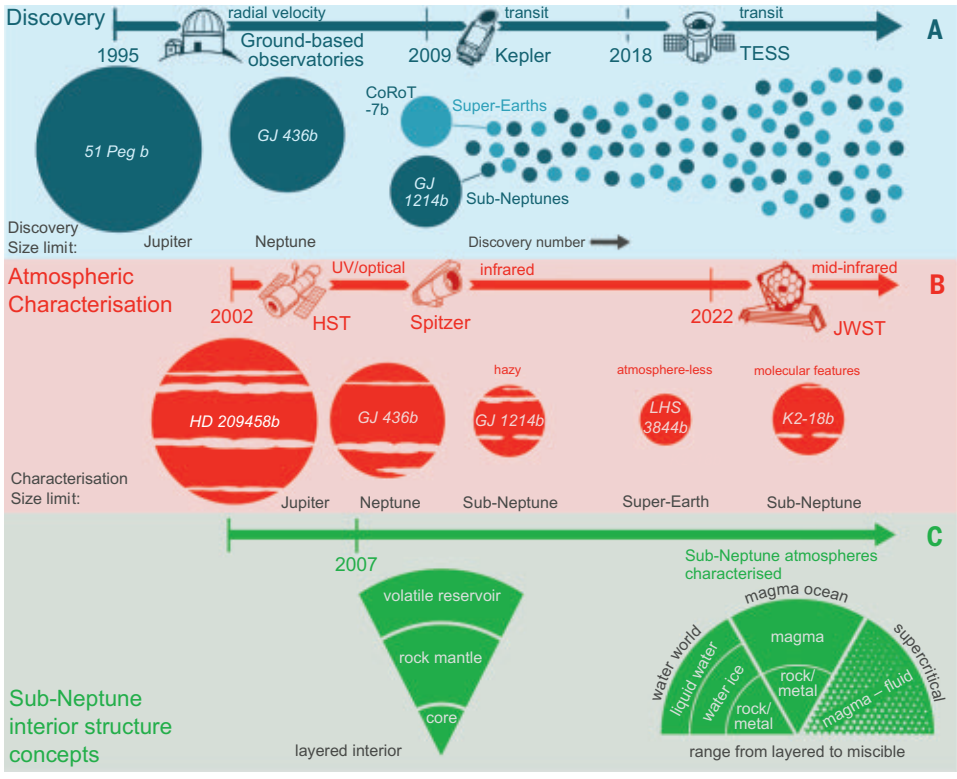


Fig. 1. Timeline of exoplanet detection and atmospheric characterization. (**A**) Symbol sizes schematically illustrate the sizes of exoplanets detected by each facility and the increasing numbers of super-Earths and sub-Neptune exoplanets found by using Kepler and TESS. (**B**) An equivalent illustration of the atmospheric characterization of exoplanets by use of space telescopes. (**C**) The conceptual interior structures of sub-Neptune exoplanets, with increasing complexity owing to improved characterization.

The radii and masses of the precisely characterized exoplanets are shown in Fig. 2, selected to have <3 R_{Earth} and <10 Earth masses. We used the planetary equilibrium temperature, defined as the theoretical temperature of blackbody emission in radiative equilibrium with the global heat redistribution (which is always lower than the substellar temperature of a tidally locked blackbody), to define four broad climate regimes within this parameter space (*5*). The onset of a runaway greenhouse effect, in which ocean H_2O is expected to evaporate in a feedback loop at increasing stellar irradiation (*22*, *23*), separates the regimes we label as temperate and bistable in Fig. 2. Models predict that any planets in the bistable regime that have substantial H_2O (in their atmosphere or on their surface) do not have a stable temperate climate but instead experience a super-runaway climate. In the super-runaway regime, radiative equilibrium is reached only after all oceans are evaporated and persists until atmospheric escape removes most of the atmosphere. However, variations in starting configuration (for example, the presence of an underlying magma or H_2O ocean) affect the predictions of climate models of this regime (*24*, *25*). At atmospheric pressures similar to the Solar System terrestrial planets, solid rock begins to melt at ≈1250 K, which we label as the lava planet regime. At even higher temperatures (≳ 1800 K), molten surfaces become increasingly vaporized, forming a thin veneer of gaseous magnesium (Mg), sodium (Na), and silicon (Si) around the planet, which we label as the rock vapor regime.

The measured mass and radius of an exoplanet can be reproduced by an entire family of structural models (*26*, *27*), so each exoplanet has multiple degenerate explanations with varying compositions and internal structures (*28*, *29*). For example, the lava world 55 Cancri e can be explained equally well with models of either 100% magnesium silicate ($MgSiO_3$) rock or by an Earth-like internal structure with a molten rock mantle (magma ocean) and ≈5 wt % bulk H_2O content (the latter is more than two orders of magnitudes greater than that of Earth) (*30*).

We also show in Fig. 2 a population of intermediate-density planets around ~2 R_{Earth} that span a wide range in temperature. These planets are rare around Sun-like stars (*7*) but have the potential to constrain models of the formation and evolution of small planets. Planet formation theory predicts that planets typically start accreting outside the H_2O ice line (the boundary of the region where solid H_2O ice can survive in the protoplanetary disk) (*21*), followed by migration into closer orbits (*31*, *32*). This process is predicted to produce at least some short-period planets that have incorporated volatile ice-rich solids (*33*, *34*). It is therefore possible that a fraction of the larger 1 to 3 R_{Earth} planets are highly H_2O-rich because they originated from the outer regions of their protoplanetary disk (*35*, *36*). However, high-molecular-weight volatiles [carbon-nitrogen-sulfur (C-N-S)–rich gas and ice compounds] in planet atmospheres could alternatively arise from preferential loss of hydrogen (H) from the atmosphere (*37*, *38*) or from chemical reactions between molten metal or silicate on the surface and a H/helium (He)–rich gaseous envelope (*39*–*41*).

These examples illustrate that mass and radius alone are not enough to distinguish between different exoplanet structures and bulk compositions. Additional information is required, which can be provided by measurements of the atmospheric composition.

Transmission spectroscopy of exoplanet atmospheres

Observations made with JWST have provided atmospheric composition measurements for a diverse range of exoplanets. Some of the molecular features observed in JWST transmission spectra of small (≈1.7 to 2.8 R_{Earth}) exoplanets are shown in Fig. 3. These transmission spectra record starlight that has been filtered through the exoplanet's atmosphere and are plotted in terms of scale height, the characteristic length scale of an atmosphere. The labeled features arise from absorption by H_2O, CH_4, and CO_2.

The strengths of these features constrain the relative abundances of the detected molecules, which Fig. 3 also shows are temperature dependent. This trend was previously identified by using Hubble Space Telescope (HST) observations (*42*), which showed weak spectral features in the 500 to 700 K equilibrium temperature range. This was interpreted as being due to cloud condensation or photochemical hazes produced by photolysis of CH_4, which is expected to be the dominant C-bearing species at those temperatures. At hotter temperatures, carbon monoxide (CO) is expected to be the dominant C-bearing species, so hazes are predicted to be less common. At cooler temperatures, the observations show little to no obscuration by aerosols (clouds or hazes)—for example, the spectra of K2-18 b (*43*, *44*) and TOI-270 d (*45*, *46*) in Fig. 3 are consistent with cloud-free atmospheres.

If small planets have atmospheres dominated by H/He, planets in the 500 to 700 K range are expected to show featureless transmission spectra owing to efficient cloud and haze formation. However, the

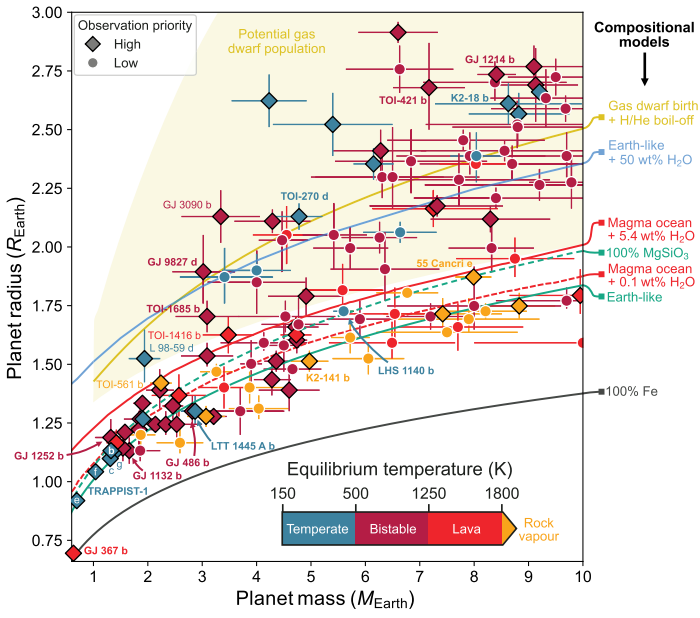


Fig. 2. Observed exoplanet masses and radii compared with compositional models. Radii [in Earth radii (R_{Earth})] are plotted as a function of mass [in Earth masses (M_{Earth})]. Colored symbols are observed exoplanets; we selected those with mass uncertainties <50% and radius uncertainties <30% from a data compilation (*136*). Symbol color indicates the equilibrium temperature, assuming full heat redistribution and zero albedo. Temperature thresholds in the color bar were chosen to reflect the regimes identified in Fig. 5. Curved lines are theoretical mass-radius relations for different compositions, as labeled (*30*, *31*, *137*). Diamonds are planets with high transmission spectroscopy metric (TSM) or emission spectroscopy metric (ESM), making them a high priority for observational characterization; we selected those with TSM > 90 if the planet radius ≥1.5 R_{Earth}, or TSM > 10 for smaller radii, or ESM > 7.5 (*138*). Some specific exoplanets are labeled; those in boldface are shown in Figs. 3 and 4. The shaded region is a gas dwarf model of sub-Neptunes (*137*), which assumes an Earth-like silicate mantle and iron core composition, surrounded by a H/He envelope accreted from the protoplanetary disk.

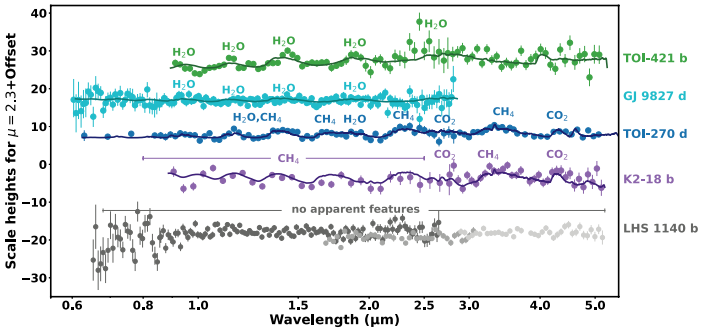


Fig. 3. Transmission spectra and atmospheric models for selected small exoplanets observed with JWST. Data points are the observed spectra of five example exoplanets discussed in the text, with vertical bars indicating the 1σ uncertainties. Thick solid lines indicate the best-fitting atmospheric model, as reported by each study. Colors indicate different exoplanets: green is TOI-421 b (*139*), cyan is GJ 9827 d (*47*), blue is TOI-270 d (*45*), purple is K2-18 b (*43*), and gray is LHS 1140 b (dark gray and light gray are from two different JWST instruments) (*140*, *141*). The planets are ordered from hottest (~920 K) to coldest (~225 K) equilibrium temperature, assuming zero albedo; they also have different masses and radii (Fig. 2). For comparison, the spectra are offset by a constant value and have been converted to atmospheric scale height, assuming a mean molecular weight (μ) of 2.3 g/mol. This weight is unlikely to be valid for all of these exoplanets, given their diversity of compositions. Labels and thin horizontal lines above each spectrum identify the molecules responsible for absorption features (which extend upward in this representation). The wavelength scale is logarithmic.

intermediate-temperature exoplanet GJ 9827 d provides a counterexample: Its spectrum is not featureless and provides no evidence of clouds. Instead, its spectrum is consistent with an H_2O-dominated atmosphere, with a volume mixing ratio >31% and an oxygen (O)/H mass ratio of ≈4. At this exoplanet's equilibrium temperature, H_2O is not expected to condense in the atmosphere or at the surface, and hydrogen should be well mixed with H_2O, so that the upper-atmosphere O/H is representative of deeper layers (*47*). This atmospheric observation breaks the degeneracy between models of cloudy atmospheres with low metallicity (low abundance of elements heavier than He) and atmospheres with a high mean molecular weight (expected to produce weak spectral features owing to small scale heights), indicating that GJ 9827 d is >20% H_2O by mass. This could arise if the planet formed from material with a high volatile ice/rock ratio (*31*–*33*). Alternatively, it is possible to produce a H_2O-rich atmosphere through geochemical interactions between a (perhaps primordial) hydrogen-rich atmosphere and the planet's magma ocean during planetary accretion (*40*, *48*–*50*). Determining the origin of volatiles in the atmospheres of small planets requires larger samples of exoplanets spanning the density-irradiation parameter space (*51*).

Two other planets shown in Fig. 3 provide evidence of mixing and interaction with some kind of surface underneath the atmosphere. The JWST spectrum of K2-18 b indicates the presence of CH_4 but not NH_3 (*43*), although atmosphere-only models of sub-Neptunes predict that both should be present at K2-18 b's temperature (~250 K). The low NH_3 abundance could either be explained by chemical dissolution of N-bearing species into an internal magma ocean (*52*, *53*) or H_2O ocean (*54*–*56*). The statistical significances of CO_2 and other atmospheric compounds in K2-18 b's atmosphere are disputed (*44*, *57*). The spectrum of TOI-270 d shows features of CH_4 and CO_2, which can be explained by an atmosphere with a high mean molecular weight. This finding is inconsistent with a distinct H/He layer above a metal- and rock-rich mantle (*45*). Instead, TOI-270 d's envelope could contain similar amounts of C- and O-rich volatiles and H/He mixed together in a supercritical phase. As with GJ 9827 d above, this scenario could arise from either interactions between a magma ocean and the atmosphere, or from an initial enrichment of volatile ices. These examples illustrate how JWST observations constrain interior-atmosphere interactions.

About a dozen other small exoplanets have featureless JWST transmission spectra, which could be due to atmospheres that are either (i) of sufficiently high mean molecular weight that features of individual species are below the JWST detection limit; (ii) blanketed by high-altitude clouds or hazes that mute molecular features; or (iii) not atmospheres at all, just a solid or liquid (magma) surface. Among these, scenario (ii) is a plausible explanation for most featureless transmission spectra. The higher-precision spectrum of the sub-Neptune GJ 1214 b is especially constraining: It indicates that both high-mean-molecular-weight and high-altitude aerosols act together, at least for this planet (*58*). Scenario (iii) is possible only for smaller planets with bulk densities that are consistent with no atmospheric envelope.

Featureless spectra also constrain the pressure of the cloud (or haze) top at a given atmospheric composition or metallicity. Atmospheric metallicities of ≳ 200 times that of the Sun are required to explain the lack of observed spectral features (*58*). Most of the small planets observed with JWST transmission spectra orbit M-dwarf stars, which have cool photospheres (the layer from which light is radiated) and a high prevalence of starspots (darker and cooler regions of strong magnetic activity that suppress convection). These factors can contaminate the planet transmission spectrum because an M-dwarf's photosphere is cool enough to also host H_2O, and the occulted part of the stellar disk could differ from the average stellar spectrum because of starspots. Several JWST transmission spectra

of small planets contain evidence of such contamination, particularly those of the Earth-sized planets orbiting the star TRAPPIST-1 (*59*). Therefore, transmission spectra are insufficient to determine whether these planets have atmospheres and what they are made of.

Eclipse spectroscopy of atmospheres and surfaces

Secondary eclipse spectroscopy compares observations immediately before and after the planet moves directly behind the host star. This approach has fewer issues with stellar contamination. It measures the dayside emission from the planet (the side that is facing the star), which for transiting planets is expected to be tidally locked to the host star (*60*, *61*). If the atmosphere is sufficiently dense, heat from the irradiated dayside can be circulated to the nightside, causing the dayside flux measured from eclipse observations to be lower than expected for a blackbody at the equilibrium temperature of the planet (*62*, *63*). Another method, which requires more telescope time, is to observe emission from a planet over its full orbit—a phase curve—which can constrain nightside emission attributable to atmospheric circulation (*63*, *64*). If there is no atmosphere, the dayside emission can provide information about the planet's surface composition, mineralogy, and geology (*9*).

Distinguishing planets with bare surfaces from those with atmospheres is not straightforward. In Fig. 4, we show the ratio of observed dayside brightness temperature (T_{day}), the blackbody temperature that would reproduce the observed emission intensity, to the theoretical maximum disk-integrated dayside temperature for a zero-albedo, zero–heat redistribution planet ($T_{day,max}$). That ratio is shown for 11 transiting rocky exoplanets measured by using JWST secondary eclipse observations, plotted as a function of the substellar temperature of a tidally locked planet with zero albedo at all wavelengths (T_{irr}). Most of the secondary eclipse observations (those with $T_{irr} \lesssim 2000$ K) are consistent with either low-albedo bare-rock surfaces (no atmosphere) or alternatively atmospheres with high mean molecular weight and surface pressures $\lesssim 10$ bar, with little heat redistribution by atmospheric circulation. This degeneracy is exacerbated by uncertainty in stellar spectral models (*65*), which are used to calculate the brightness temperatures (*66*, *67*), and possible interactions of secondary atmospheres with the interiors of planets, which could store a substantial amount of volatiles (*30*) and thus reduce the outgassed atmospheric envelope. There is no evidence for strong heat redistribution or thick cloud-free atmospheres in this observed sample; however, nor is it clear whether these rocky exoplanets orbiting M-dwarf stars have secondary atmospheres of $\lesssim 10$ bar surface pressure. Intense stellar x-ray and extreme ultraviolet radiation of M-dwarf stars gradually strips the gaseous atmosphere from orbiting planets, but the efficiency of this process is highly sensitive to the composition of the atmosphere (*68*).

Using atmospheres to study planetary interiors

Small and highly irradiated exoplanets are most likely to have had their atmospheres removed, allowing observations to directly probe their surfaces. Otherwise, mass exchange between the interior and surface of a planet is expected to be recorded in the composition of the atmosphere. The transport of mass and energy between the internal and external layers of planets is driven by the redistribution of heat provided by energy released during accretion, the decay of radioactive elements, tidal interactions, and stellar irradiation. The latter two heat sources are particularly relevant for short-period planets because they orbit close to their host stars.

The exchange of material between interiors and atmospheres imprints information about the interior of a planet in the chemistry of its atmosphere. Planetary interiors are at higher pressures and temperatures than those of their atmospheres. In the relative cold and low pressure of an atmosphere, the chemical reactions that occur in the interior are likely to be quenched, leaving long-lasting and detectable signs of disequilibrium chemistry. Such transport from lower atmospheric layers has been proposed to explain the presence of ammonia (NH_3) in the atmospheres of sub-Neptunes (*69*). This atmospheric disequilibrium could drive reactions between the transported material and the background atmospheres, leading to the sequestration of gases from an atmosphere into the deeper layers of the planet. This is analogous to atmospheric CO_2 and O_2 on Earth, which combine with liquid H_2O and rock to produce carbonates and oxides in Earth's crust and mantle (*70*). This forms part of a geological cycle, potentially returning these atoms to the atmosphere hundreds of millions of years later (*71*). Indications of interior-atmosphere exchange could be stronger if mass transport occurs across a compositional stratification inside a planet; for example, on Earth volcanic eruptions release SO_2 into the atmosphere, which react with H_2O vapor to form aerosols. The presence or absence of an atmospheric gas species can therefore provide insight into a planet's structure and dynamics.

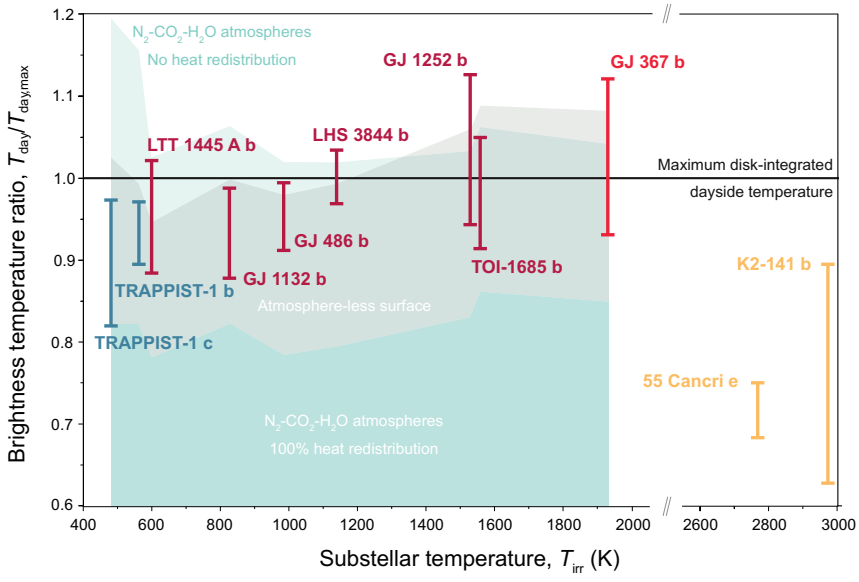


Fig. 4. Brightness temperature ratio from eclipse observations compared with theoretical models. Colored bars are the 1σ ranges of brightness temperatures (T_{day}) derived from eclipse observations, normalized to the theoretical maximum disk-integrated dayside temperature for a zero-albedo, zero-heat redistribution planet (solid black line). They are plotted as a function of the substellar temperature of a tidally locked planet with zero albedo at all wavelengths (T_{irr}). Bar colors indicate the equilibrium temperature categories defined in Fig. 2, calculated by using published methods (*66*) applied to eclipse depths and uncertainties from JWST and Spitzer emission observations as reported in the literature. Data sources are TRAPPIST-1 c (*142*,*143*), TRAPPIST-1 b (*142*,*144*,*145*), LTT 1445 A b (*146*), LHS 3844 b (*98*,*147*), GJ 1132 b (*148*), GJ 486 b (*149*), GJ 1252 b (*150*,*151*), TOI-1685 b (*67*,*152*), GJ 367 b (*153*), 55 Cancri e (*154*,*155*), and K2-141 b (*156*). Shaded regions indicate the ranges predicted by theoretical models for the specific exoplanets with red and blue bars (*64*); gray is a model of bare rock surfaces with no atmosphere. Cyan is a model of atmospheres with N_2-CO_2-H_2O compositions with 1 to 10 bar total surface pressure, with (top) no (light cyan) or (bottom) complete (dark cyan) day-to-night heat redistribution through atmospheric circulation.

The nature of interior-atmosphere exchange on a given planet depends on its geodynamic regime—the mode of mass and energy transport it experiences. Earth's mobile-lid geodynamic regime results in plate tectonics on its surface, but the origin of that regime is debated (*72*), and it is unclear which exoplanets experience similar geodynamics (*73*, *74*). Two factors probably set the long-term geodynamic processes on exoplanets: their density, which is a proxy for their composition, and their stellar irradiation (instellation), which determines their thermodynamics through the ratio of in- and outgoing energy fluxes. The combination of irradiation and composition, for a given mass of an exoplanet, provides a broad description of a planet's structure and dynamics because they determine the interfaces between interior layers and how material is transported between them. In Fig. 5, we schematically illustrate the predicted exoplanetary thermodynamic climate and interior regimes, as derived from laboratory measurements, observations, and empirical evidence in geochemistry, geophysics, climate science, planetary science, and astronomy (*5*, *9*, *10*). Those interfaces can be abrupt (for example, the rocky surfaces of terrestrial planets) or diffuse (for example, the edges of atmospheres). The pressure, temperature, and composition of matter on either side of each interface determine the rate of exchange of mass and energy between the layers. The predicted diversity of geodynamic regimes for planets across the density–instellation parameter space (Fig. 5) indicates how exoplanet interior structures can potentially be constrained by observing their atmospheres.

Super-Earths and terrestrial exoplanets

Planets close to an Earth-like composition (Fig. 2) are predicted to exhibit geodynamic processes that are familiar to planetary scientists, so we consider them first.

In the temperate regime (Fig. 5A), aqueous chemistry mediates the long-term atmospheric expression of interior-atmosphere exchange and regulates heat transport. Exchange between the atmosphere and the liquid-H_2O hydrosphere is expected to be rapid, by analogy to Earth's oceans, which ventilate in $\lesssim$ 5000 years and rapidly equilibrate with the atmosphere. On such planets, gases that readily dissolve in liquid H_2O, such as SO_2, are expected to be removed from the atmosphere within a few years (*75*) so are only transiently present after major inputs, such as large volcanic eruptions. Atmospheric CO_2 is depleted by H_2O-rock reactions, which can occur at sharp interfaces on exposed landmasses and at the base of the oceans. These reactions drive Earth's climate thermostat; we therefore expect that CO_2 would be present at low concentrations in the atmospheres of habitable terrestrial exoplanets (*76*–*78*). Planets in this regime would have low atmospheric abundances of some volatile species (including CO_2, SO_2, and H_2O) that are otherwise cosmochemically abundant.

At high irradiation, terrestrial planets are expected to experience a climate collapse (Fig. 5B, Venus-like). Evaporation of liquid H_2O oceans would produce a steam-rich atmosphere; the atmospheric H_2O is expected to then be photodissociated and the hydrogen lost to space (*79*, *80*). This runaway greenhouse scenario (*81*, *82*) appears to have occurred on Venus (*83*), either early (*22*) or late (*84*) in its history. The result is a planet with a dry and oxidized atmosphere with a high mean molecular weight, with an atmospheric chemistry dominated by C- and S-bearing species (*85*). On these planets, the atmosphere-to-surface interaction is mediated by reactions between gas and rock, which are less efficient than aqueous reactions at transferring material (*86*). In this regime, volcanic input to the atmosphere is potentially suppressed by two factors: First, a massive CO_2 atmosphere provides a high surface pressure that would resist degassing because gases are more soluble in magmas at higher pressure (*87*). Second, the geodynamic feedback from a hot and dry planetary surface is expected to lower overall volcanic activity by inhibiting plate tectonics (*88*). We expect planets in this regime to have wholly volcanically derived atmospheres, but of an ancient nature, and a clearly demarcated rock-atmosphere interface.

All rocky planets likely experience an early period with a magma ocean, as they dissipate the initial heat from their formation (*5*, *89*). However, highly irradiated rocky planets could be trapped in this state permanently (Fig. 5C, transcritical magma ocean). These planets would retain an atmosphere with a high mean molecular weight and that is H-poor owing to the same processes as in Venus-like climates, directly overlaying a molten mantle. Gas exchange with magma is far more efficient than with rock, and rapid convection within the magma itself would facilitate exchange between the atmosphere and interior (*90*–*92*). Because the interior is vastly more massive than the atmosphere in this regime, the resulting atmospheric chemistry would reflect the interior chemistry (*93*, *94*). For example, redox chemistry and the relative abundances of gas species would be dictated by their solubility in the magma (*25*, *87*). Depending on the instellation and atmospheric opacity, the magma ocean could extend down to the core-mantle boundary. Sufficiently massive atmospheres would become supercritical fluids at their base, leaving no clear boundary with the magma (*95*, *96*). In this regime, chemical exchange could in principle extend through the entire planet—including keeping the metal core in chemical equilibrium with the mantle and atmosphere (*39*, *41*). We expect planets in this regime to have atmospheres that directly reflect their interiors (*5*).

Atmosphere-stripped worlds

Planets with bulk densities similar to or greater than Earth's (below the 100% $MgSiO_3$ or Earth-like lines shown in Fig. 2) might have lost their initially accreted volatile species to space. The surfaces of such planets are directly subjected to intense stellar irradiation, which can drive their geodynamic and petrologic evolution into regimes that are unknown in the Solar System. Planets that completely lose their atmospheric volatile inventory are expected to be driven by tectonic and geological processes that span their lithosphere (Fig. 5D, bare rock). Energy transport across this layer is predicted to be dominated by the rheological properties of the mantle, internal energy sources, and irradiation. Bare-rock exoplanets that orbit close to their host star are likely to become tidally locked (*61*), producing alternative forms of geodynamic evolution that are driven by the strong day-night temperature contrast (*73*, *74*). The surface composition of these exoplanets could reflect their petrological past (*97*, *98*).

Atmosphere-less planets that are subject to intense irradiation (*90*) or strong tidal forces (*61*) from their host star are expected to have molten surfaces and interiors. These could potentially be observed as a global magma ocean or dayside magma pool (Fig. 5D, lava worlds). Energy and mass exchange in these systems is predicted to be highly dependent on the geometry and heat transport of the magma ocean or pool, its dynamical interaction with the underlying iron core, and the transition between magma and rock surface (magma ocean shorelines) across the day-night terminator (*99*, *100*). On these planets, the outgassing of refractory compounds is predicted to indicate the underlying magma composition and is potentially observable (*101*–*103*).

Sub-Neptunes: Water or magma worlds

The low bulk densities of sub-Neptune exoplanets imply the presence of substantial volatile envelopes (Fig. 5). The envelope could be composed of primary accreted H/He gas (*19*, *104*) or be H_2O-dominated from the planet having formed outside the H_2O ice line (*33*, *36*). The common feature of their interiors is that chemical exchange between silicates and volatiles happens at high pressure (equivalent to gigapascals or greater). This leads to different forms of mass and energy exchange than on terrestrial planets, producing different global dynamics and thermal histories (*105*, *106*).

For moderate pressures at the envelope-rock interface (<10 GPa) and low temperatures (≈1000 K, at low instellation) in a deep envelope of H_2O, it is predicted that rock is in contact with high-pressure H_2O

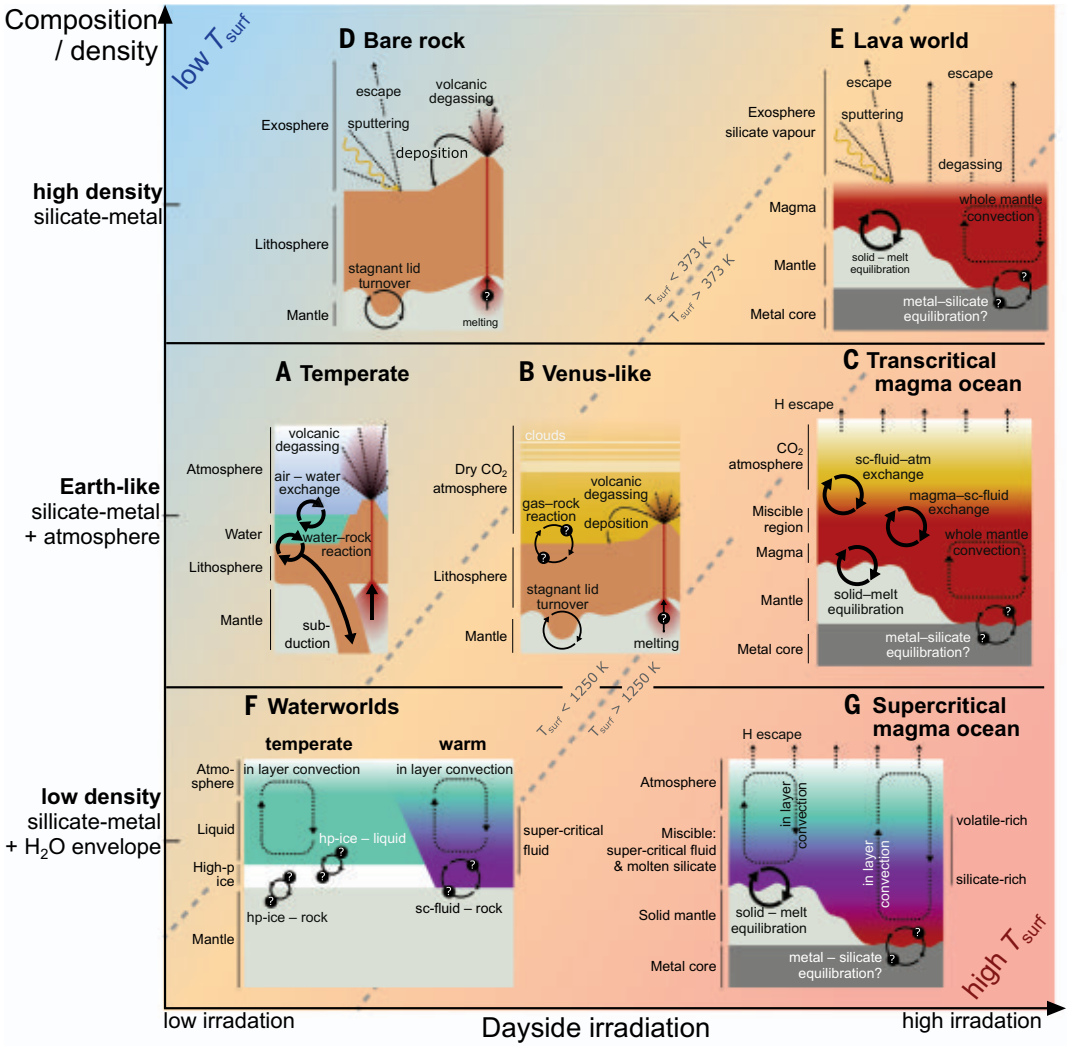


Fig. 5. Schematic illustration of the geodynamic regimes predicted for planets with different densities and dayside irradiations. (**A** to **G**) Seven regimes discussed in the text are illustrated at qualitative locations of density as a function of dayside irradiation by the host star. Each regime is represented by a schematic illustration of the processes that exchange mass and energy between planetary reservoirs; arrows indicate small (thin) or large (thick) fluxes; question marks indicate poorly constrained processes (for example, interactions between rock and high-pressure ice). Background color shading qualitatively indicates the expected temperature at the atmosphere-interior interface. In (A) to (G), the left axis indicates the structural interior layers of the planet, and colors indicate composition. The diagonal gray dashed lines indicate where the predicted surface temperature (T_{surf}; at the interface where the atmosphere or envelope contacts silicate material) equals those of boiling H_2O and silicate melting, labeled with their values at 1 bar atmospheric pressure. Thicker atmospheres produce higher surface temperatures for a given irradiation, shifting the irradiation at which a change in geodynamic regime occurs.

ice (Fig. 5F, temperate waterworlds). Energy transport out of the rocky interior would therefore be modulated by convection in the ice layer, at a rate that depends on the ice viscosity. The rheological properties of the ice are affected by its composition and the incorporation of other materials into the H_2O-ice structure. Transport of CO_2 across the high-pressure ice layer is predicted to be limited (*107*), whereas the solubility of silicate components in high-pressure ice is largely unknown. The chemical and geodynamic feedbacks between ice composition and the properties of the overlying ocean and atmosphere are also poorly understood (*108*).

At even moderate instellation, the insulating effect of a thick volatile envelope (whether composed of H_2O or H/He) causes the high-pressure H_2O and H layers to be in a supercritical fluid state (Fig. 5F, warm waterworlds). If the temperature is below the melting point of rock, this produces a sharp boundary beneath the supercritical H_2 or H_2 (*95*, *96*). The chemistry of reactions between supercritical fluids and rock is not well understood, including the kinetics and capacity for material transport (*109*). Because transitions in supercritical fluids are continuous, this regime could involve compositional stratification, with deeper fluids enriched in silicate components underlying more H_2O-rich layers above (*110*). This is expected to reduce the transport of mass and energy between the interior and atmosphere (*111*).

Higher levels of instellation produce molten rock at the base of the ice or gaseous envelope. Such a planet is predicted not to have any clearly defined internal layers (Fig. 5G, supercritical magma ocean) because molten silicate is miscible in high-pressure-fluids (*112*, *113*). This allows rapid reactions between the constituents, so that thermochemical equilibrium prevails throughout the continuous fluid envelope of the planet. Depending on the vertical extent of the supercritical regime (*96*), strong gradients in mean molecular weight of the fluid could occur, with a silicate-rich wet magma at depth and H_2O-rich material at shallower depths (lower pressures). Sub-Neptunes in this

regime are expected to have deep well-mixed supercritical atmospheres rather than stratified H_2O layers underlying H_2 (*95*, *114*). These compositional transitions affect heat and mass transport through the planet, but in this regime, the silicate interior becomes chemically coupled to the atmosphere, even if the silicate components rain out at much higher pressure levels (*115*). This is predicted to have consequences for the observed mass-radius relation (Fig. 2) (*112*) and upper-atmosphere abundances (*116*, *117*).

Interior-atmosphere exchange on hot exoplanets

Transit observations are biased toward detecting close-orbiting warm to hot exoplanets (Fig. 5, B, C, E, and G). These span transitions between planetary states that are predicted to show global chemical and energy exchange, a regime that is not present in the present-day inner Solar System but could reflect the Solar System planets in their early evolution, shortly after accretion (*89*). JWST spectroscopy (Fig. 3) can be interpreted as showing that the sub-Neptunes K2-18 b and TOI-270 d are either cold, H_2O ocean-bearing sub-Neptunes (*43*, *46*, *118*) or have a supercritical lower envelope and possible magma ocean surface (*52*, *53*, *119*). An analogous dichotomy of interpretations applies to Venus, which might have had a H_2O ocean in its early evolution (*84*) or instead lost its H_2O during a magma ocean and super-runaway greenhouse state that lasted hundreds of millions of years (*24*, *83*). Distinguishing between these options, for both Venus and sub-Neptune exoplanets, is necessary to determine whether the surfaces were ever habitable (*5*).

It remains uncertain how much of a planet's inventory of volatile elements can be stored in the interior during extended magma ocean phases (*25*, *30*, *120*). If interiors can efficiently remove volatiles from atmospheres, then volatiles could remain present on the surface at low levels for several billions of years rather than being rapidly lost to space (*30*, *106*, *121*). Efficient interior-atmosphere exchange would also strongly affect the atmospheric composition (*25*, *122*) so that itself influences the atmospheric loss rate (*68*, *123*). N- and S-bearing species are predicted to trace interaction with molten silicate mantles (*85*, *94*) but are also affected by liquid H_2O oceans (*55*, *75*).

Evolutionary considerations could provide a way to break this degeneracy for K2-18 b, TOI-270 d, GJ 9827 d, and similar exoplanets. The transition from a hot super-runaway regime to colder and potentially temperate climates is substantially different from the inverse (cold to hot) climate transition, owing to cloud feedbacks and volatile dissolution in magma oceans (*24*, *124*). Therefore, the initial conditions substantially affect the evolution of each planet (*91*, *121*). This climate transition is not symmetric (*25*), as had previously been assumed (*23*). Climate models of H_2- and H_2O-dominated atmospheres (*109*, *111*, *125*) indicate that super-runaway atmospheres have radiative, nonconvective layers in their interiors, which reduce energy transport across the atmosphere-interior interface. The evolutionary effect of this on low-mass exoplanets depends on their volatile composition and geochemical interactions with the underlying magma ocean (*94*, *124*). JWST observations of sub-Neptune exoplanets indicate that their atmospheres are composed of components with high mean molar weight, which are predicted to interact with the planetary interior.

More precise transit surveys, such as that planned for the PLATO (PLAnetary Transits and Oscillations of stars) space telescope (*126*), are required to empirically probe the radius-density transition that is predicted across the inner edge of the habitable zone (*51*, *127*). Such surveys could provide a statistical test of interior-atmosphere feedbacks on Earth-sized and super-Earth exoplanets. Additional spectroscopic observations are required to determine the C-N-S abundances in exoplanet atmospheres, which are affected by chemical and transport processes at the interface with the interior (*128*, *129*). The dominant carrier species and solubility of C-N-S compounds are poorly constrained under chemically reducing (H-rich) and high-pressure conditions (*87*). Experimental investigation of photochemical haze production and cloud particle properties in these regimes are necessary inputs for interpretative models (*130*, *131*). Progress will require interdisciplinary collaboration between astronomers, planetary scientists, and geoscientists, combining observational and experimental data with models of the energetic and chemical exchange across the interior-atmosphere interface.

Atmospheres on rocky exoplanets orbiting M-stars

There is experimental and theoretical evidence that atmospheres rapidly interact with magmatic and metallic liquids (*5*, *87*), which implies that planetary interiors have substantial capacity for storing volatile elements, particularly in the magma ocean and transition regimes (Fig. 5, C and G). It is unknown whether this also applies to Earth-sized rocky exoplanets. All observed transmission spectra of rocky exoplanets orbiting M-dwarf stars have been featureless (such as LHS 1140 b in Fig. 3), indicating that they do not have large gaseous envelopes. Eclipse measurements of those bodies are generally consistent with a blackbody at the expected equilibrium temperature; this is compatible with either bare rock or thin atmospheres ($\lesssim$ 10 bar) (Fig. 4). This implies that volatile escape to space is more rapid than volatile delivery to the gaseous envelope. Investigating this process as a function of orbital distance, stellar type, and planetary mass could potentially provide information on the prevalence of exoplanets with Earth-like atmospheres.

Connecting these results to planetary formation theory (*21*, *89*) will require spectroscopic observations of the emitting layer (whether it is an atmosphere or rocky surface) because the presence or absence of gaseous envelopes only indirectly reflects the interior volatile storage (*5*, *9*). It is debated whether statistical samples of transmission spectra or secondary eclipse spectra would provide better prospects for determining the prevalence of substantial atmospheres on these exoplanets (*59*, *63*, *66*), or if measuring the full phase curves of a smaller number of exoplanets would provide greater insight (*64*).

Prospects for Earth-like exoplanets

JWST can potentially constrain the link between the atmosphere and interiors of sub-Neptunes and super-Earths and the prevalence of volatile envelopes on rocky M-dwarf exoplanets. However, it is unlikely to provide similar understanding of Earth-like exoplanets. Upcoming exoplanet surveys will probe parameter spaces different to JWST's. PLATO (*126*) will provide long-baseline transit monitoring campaigns, but with only highly limited capabilities for atmospheric spectroscopy. The Nancy Grace Roman Space Telescope will use gravitational microlensing to search for exoplanets of one Earth mass and below (*132*), which is expected to constrain the mass function of exoplanets, but microlensing does not determine planet sizes. The Ariel space telescope will provide spectroscopic observations of a statistical sample of large gaseous exoplanets (*133*) but will have limited sensitivity for lower-mass exoplanets. Ground-based extremely large telescopes (ELTs), with diameters of 25 to 39 m, are expected to provide spectroscopic observations of a handful of nearby low-mass exoplanets. Each of these facilities are currently under construction.

Observing a statistical sample of Earth-like exoplanets orbiting a variety of host stars will require space-based survey facilities that are currently in their early planning stages, such as the Habitable Worlds Observatory (HWO) (*134*) and Large Interferometer for Exoplanets (LIFE) (*135*). These missions would provide observations of Earth-like planets around Sun-like stars that are analogous to the current exploration of M-dwarf rocky exoplanets with JWST, across optical to mid-infrared wavelengths. Insights gained from JWST observations will feed into the survey design of HWO and LIFE, including whether M-dwarf exoplanets should be a continued focus in the search of habitable conditions. Current exoplanet research therefore provides a path toward finding Earth-like exoplanets and determining their habitability.

REFERENCES AND NOTES

1. A. Wolszczan, D. A. Frail, A planetary system around the millisecond pulsar PSR1257 + 12. *Nature* **355**, 145–147 (1992). doi: 10.1038/355145a0
2. M. Mayor, D. Queloz, A Jupiter-mass companion to a solar-type star. *Nature* **378**, 355–359 (1995). doi: 10.1038/378355a0
3. R. B. Fernandes, G. D. Mulders, I. Pascucci, C. Mordasini, A. Emsenhuber, Hints for a turnover at the snow line in the giant planet occurrence rate. *Astrophys. J.* **874**, 81 (2019). doi: 10.3847/1538-4357/ab0300
4. W. Zhu, S. Dong, Exoplanet statistics and theoretical implications. *Annu. Rev. Astron. Astrophys.* **59**, 291–336 (2021). doi: 10.1146/annurev-astro-112420-020055
5. T. Lichtenberg, Y. Miguel, Super-Earths and Earth-like exoplanets. *Treat. Geochem.* **7**, 51–112 (2025). doi: 10.1016/B978-0-323-99762-1.00122-4
6. A. W. Howard *et al.*, Planet occurrence within 0.25 AU of solar-type stars from Kepler. *Astrophys. J. Suppl. Ser.* **201**, 15 (2012). doi: 10.1088/0067-0049/201/2/15
7. B. J. Fulton *et al.*, The California-Kepler Survey. III. A gap in the radius distribution of small planets. *Astron. J.* **154**, 109 (2017). doi: 10.3847/1538-3881/aa80eb
8. V. Van Eylen *et al.*, An asteroseismic view of the radius valley: Stripped cores, not born rocky. *Mon. Not. R. Astron. Soc.* **479**, 4786–4795 (2018). doi: 10.1093/mnras/sty1783
9. C. M. Guimond *et al.*, From stars to diverse mantles, melts, crusts, and atmospheres of rocky exoplanets. *Rev. Mineral. Geochem.* **90**, 259–300 (2024). doi: 10.2138/rmg.2024.90.08
10. E. M. R. Kempton, H. A. Knutson, Transiting exoplanet atmospheres in the era of JWST. *Rev. Mineral. Geochem.* **90**, 411–464 (2024). doi: 10.2138/rmg.2024.90.12
11. F. Pepe *et al.*, ESPRESSO at VLT. *Astron. Astrophys.* **645**, A96 (2021). doi: 10.1051/0004-6361/202038306
12. N. C. Hara, E. B. Ford, Statistical methods for exoplanet detection with radial velocities. *Annu. Rev. Stat. Appl.* **10**, 623–649 (2023). doi: 10.1146/annurev-statistics-033021-012225
13. A. Vallenari *et al.*, Gaia data release 3-summary of the content and survey properties. *Astron. Astrophys.* **674**, A1 (2023). doi: 10.1051/0004-6361/202243940
14. M. G. MacDougall *et al.*, The TESS-Keck Survey. XV. Precise properties of 108 TESS planets and their host stars. *Astron. J.* **166**, 33 (2023). doi: 10.3847/1538-3881/acd557
15. J. E. Owen, Y. Wu, Kepler planets: A tale of evaporation. *Astrophys. J.* **775**, 105 (2013). doi: 10.1088/0004-637X/775/2/105
16. E. D. Lopez, J. J. Fortney, The role of core mass in controlling evaporation: The Kepler radius distribution and the Kepler-36 density dichotomy. *Astrophys. J.* **776**, 2 (2013). doi: 10.1088/0004-637X/776/1/2
17. S. Jin *et al.*, Planetary population synthesis coupled with atmospheric escape: A statistical view of evaporation. *Astrophys. J.* **795**, 65 (2014). doi: 10.1088/0004-637X/795/1/65
18. Y. Tang, J. J. Fortney, R. Murray-Clay, Assessing core-powered mass loss in the context of early boil-off: Minimal long-lived mass loss for the sub-Neptune population. *Astrophys. J.* **976**, 221 (2024). doi: 10.3847/1538-4357/ad8567
19. J. E. Owen, Y. Wu, The evaporation valley in the Kepler planets. *Astrophys. J.* **847**, 29 (2017). doi: 10.3847/1538-4357/aa890a
20. S. Ginzburg, H. E. Schlichting, R. Sari, Core-powered mass-loss and the radius distribution of small exoplanets. *Mon. Not. R. Astron. Soc.* **476**, 759–765 (2018). doi: 10.1093/mnras/sty290
21. J. Drążkowska *et al.*, Planet formation theory in the era of ALMA and Kepler: From pebbles to exoplanets. in *Protostars and Planets VII*, S. Inutsuka, Y. Aikawa, T. Muto, K. Tomida, M. Tamura, Eds., *Astronomical Society of the Pacific Conference Series* (2023), vol. 534, p. 717.
22. K. Hamano, Y. Abe, H. Genda, Emergence of two types of terrestrial planet on solidification of magma ocean. *Nature* **497**, 607–610 (2013). doi: 10.1038/nature12163; pmid: 23719462
23. R. K. Kopparapu *et al.*, Habitable zones around main-sequence stars: New estimates. *Astrophys. J.* **765**, 131 (2013). doi: 10.1088/0004-637X/765/2/131
24. M. Turbet *et al.*, Day-night cloud asymmetry prevents early oceans on Venus but not on Earth. *Nature* **598**, 276–280 (2021). doi: 10.1038/s41586-021-03873-w; pmid: 34645997
25. I. D. Boer, H. Nicholls, T. Lichtenberg, Absence of a runaway greenhouse limit on lava planets. *Astrophys. J.* **987**, 172 (2025). doi: 10.3847/1538-4357/add69f
26. S. Seager, M. Kuchner, C. A. Hier-Majumder, B. Militzer, Mass-radius relationships for solid exoplanets. *Astrophys. J.* **669**, 1279–1297 (2007). doi: 10.1086/521346
27. D. Valencia, D. D. Sasselov, R. J. O'Connell, Detailed models of super-Earths: How well can we infer bulk properties? *Astrophys. J.* **665**, 1413–1420 (2007). doi: 10.1086/519554
28. L. A. Rogers, S. Seager, A framework for quantifying the degeneracies of exoplanet interior compositions. *Astrophys. J.* **712**, 974–991 (2010). doi: 10.1088/0004-637X/712/2/974
29. C. Dorn *et al.*, Can we constrain the interior structure of rocky exoplanets from mass and radius measurements? *Astron. Astrophys.* **577**, A83 (2015). doi: 10.1051/0004-6361/201424915
30. C. Dorn, T. Lichtenberg, Hidden water in magma ocean exoplanets. *Astrophys. J. Lett.* **922**, L4 (2021). doi: 10.3847/2041-8213/ac33af
31. L. Zeng *et al.*, Growth model interpretation of planet size distribution. *Proc. Natl. Acad. Sci. U.S.A.* **116**, 9723–9728 (2019). doi: 10.1073/pnas.1812905116; pmid: 31036661
32. T. Lichtenberg *et al.*, A water budget dichotomy of rocky protoplanets from $_{26}$Al-heating. *Nat. Astron.* **3**, 307–313 (2019). doi: 10.1038/s41550-018-0688-5
33. J. Venturini, O. M. Guilera, J. Haldemann, M. P. Ronco, C. Mordasini, The nature of the radius valley. *Astron. Astrophys.* **643**, L1 (2020). doi: 10.1051/0004-6361/202039141
34. A. Izidoro *et al.*, The exoplanet radius valley from gas-driven planet migration and breaking of resonant chains. *Astrophys. J. Lett.* **939**, L19 (2022). doi: 10.3847/2041-8213/ac990d
35. R. Luque, E. Pallé, Density, not radius, separates rocky and water-rich small planets orbiting M dwarf stars. *Science* **377**, 1211–1214 (2022). doi: 10.1126/science.abl7164; pmid: 36074855
36. R. Burn *et al.*, A radius valley between migrated steam worlds and evaporated rocky cores. *Nat. Astron.* **8**, 463–471 (2024). doi: 10.1038/s41550-023-02183-7; pmid: 38659612
37. H. Chen, L. A. Rogers, Evolutionary analysis of gaseous sub-Neptune-mass planets with MESA. *Astrophys. J.* **831**, 180 (2016). doi: 10.3847/0004-637X/831/2/180
38. I. Malsky, L. Rogers, E. M. R. Kempton, N. Marounina, Helium-enhanced planets along the upper edge of the radius valley. *Nat. Astron.* **7**, 57–66 (2023). doi: 10.1038/s41550-022-01823-8
39. T. Lichtenberg, Redox hysteresis of super-Earth exoplanets from magma ocean circulation. *Astrophys. J. Lett.* **914**, L4 (2021). doi: 10.3847/2041-8213/ac0146
40. E. S. Kite, L. Schaefer, Water on hot rocky exoplanets. *Astrophys. J. Lett.* **909**, L22 (2021). doi: 10.3847/2041-8213/abe7dc
41. H. E. Schlichting, E. D. Young, Chemical equilibrium between cores, mantles, and atmospheres of super-Earths and sub-Neptunes and implications for their compositions, interiors, and evolution. *Planet. Sci. J.* **3**, 127 (2022). doi: 10.3847/PSJ/ac68e6
42. J. Brande *et al.*, Clouds and clarity: Revisiting atmospheric feature trends in Neptune-size exoplanets. *Astrophys. J. Lett.* **961**, L23 (2024). doi: 10.3847/2041-8213/ad1b5c
43. N. Madhusudhan *et al.*, Carbon-bearing molecules in a possible Hycean atmosphere. *Astrophys. J. Lett.* **956**, L13 (2023). doi: 10.3847/2041-8213/acf577
44. R. Luque *et al.*, Insufficient evidence for DMS and DMDS in the atmosphere of K2-18 b. *Astron. Astrophys.* **700**, A284 (2025). doi: 10.1051/0004-6361/202555580
45. B. Benneke *et al.*, JWST Reveals CH4, CO2, and H2O in a Metal-rich Miscible Atmosphere on a Two-Earth-Radius Exoplanet. arXiv:2403.03325 [astro-ph.EP] (2024).
46. M. Holmberg, N. Madhusudhan, Possible Hycean conditions in the sub-Neptune TOI-270 d. *Astron. Astrophys.* **683**, L2 (2024). doi: 10.1051/0004-6361/202348238
47. C. Piaulet-Ghorayeb *et al.*, JWST/NIRISS reveals the water-rich "steam world" atmosphere of GJ 9827 d. *Astrophys. J. Lett.* **974**, L10 (2024). doi: 10.3847/2041-8213/ad6f00
48. M. Ikoma, H. Genda, Constraints on the mass of a habitable planet with water of nebular origin. *Astrophys. J.* **648**, 696–706 (2006). doi: 10.1086/505780
49. T. Kimura, M. Ikoma, Predicted diversity in water content of terrestrial exoplanets orbiting M dwarfs. *Nat. Astron.* **6**, 1296–1307 (2022). doi: 10.1038/s41550-022-01781-1
50. J. G. Rogers, H. E. Schlichting, E. D. Young, Fleeting but not forgotten: The imprint of escaping hydrogen atmospheres on super-Earth interiors. *Astrophys. J.* **970**, 47 (2024). doi: 10.3847/1538-4357/ad5287
51. M. Schlecker *et al.*, Bioverse: The habitable zone inner edge discontinuity as an imprint of runaway greenhouse climates on exoplanet demographics. *Planet. Sci. J.* **5**, 3 (2024). doi: 10.3847/PSJ/acf57f
52. O. Shorttle, S. Jordan, H. Nicholls, T. Lichtenberg, D. J. Bower, Distinguishing oceans of water from magma on mini-Neptune K2-18b. *Astrophys. J. Lett.* **962**, L8 (2024). doi: 10.3847/2041-8213/ad206e
53. C. R. Glein, X. Yu, C. N. Luu, Deciphering sub-Neptune atmospheres: New insights from geochemical models of TOI-270 d. *Astrophys. J.* **985**, 187 (2025). doi: 10.3847/1538-4357/adced4
54. X. Yu, J. I. Moses, J. J. Fortney, X. Zhang, How to identify exoplanet surfaces using atmospheric trace species in hydrogen-dominated atmospheres. *Astrophys. J.* **914**, 38 (2021). doi: 10.3847/1538-4357/abfdc7
55. R. Hu *et al.*, Unveiling shrouded oceans on temperate sub-Neptunes via transit signatures of solubility equilibria versus gas thermochemistry. *Astrophys. J. Lett.* **921**, L8 (2021). doi: 10.3847/2041-8213/ac1f92
56. S.-M. Tsai *et al.*, Inferring shallow surfaces on sub-Neptune exoplanets with JWST. *Astrophys. J. Lett.* **922**, L27 (2021). doi: 10.3847/2041-8213/ac399a
57. L. Welbanks *et al.*, The challenges of detecting gases in exoplanet atmospheres. arXiv:2504.21788 [astro-ph.EP] (2025).
58. P. Gao *et al.*, The hazy and metal-rich atmosphere of GJ 1214 b constrained by near- and mid-infrared transmission spectroscopy. *Astrophys. J.* **951**, 96 (2023). doi: 10.3847/1538-4357/acd16f
59. J. de Wit *et al.*, A roadmap for the atmospheric characterization of terrestrial exoplanets with JWST. *Nat. Astron.* **8**, 810–818 (2024). doi: 10.1038/s41550-024-02298-5
60. R. Barnes, Tidal locking of habitable exoplanets. *Celestial Mech. Dyn. Astron.* **129**, 509–536 (2017). doi: 10.1007/s10569-017-9783-7
61. M. Farhat, P. Auclair-Desrotour, G. Boué, T. Lichtenberg, J. Laskar, Tides on lava worlds: Application to close-in exoplanets and the early Earth–Moon system. *Astrophys. J.* **979**, 133 (2025). doi: 10.3847/1538-4357/ad9b93

62. M. Mansfield *et al.*, Identifying atmospheres on rocky exoplanets through inferred high albedo. *Astrophys. J.* **886**, 141 (2019). doi: 10.3847/1538-4357/ab4c90
63. D. D. B. Koll *et al.*, Identifying candidate atmospheres on rocky M dwarf planets via eclipse photometry. *Astrophys. J.* **886**, 140 (2019). doi: 10.3847/1538-4357/ab4c91
64. M. Hammond *et al.*, Reliable detections of atmospheres on rocky exoplanets with photometric JWST phase curves. *Astrophys. J. Lett.* **978**, L40 (2025). doi: 10.3847/2041-8213/ada0bc
65. J. Tayar, Z. R. Claytor, D. Huber, J. van Saders, A Guide to Realistic Uncertainties on the fundamental properties of solar-type exoplanet host stars. *Astrophys. J.* **927**, 31 (2022). doi: 10.3847/1538-4357/ac4bbc
66. B. P. Coy *et al.*, Population-level hypothesis testing with rocky planet emission data: A tentative trend in the brightness temperatures of M-Earths. *Astrophys. J.* **987**, 22 (2025). doi: 10.3847/1538-4357/add3f7
67. R. Luque *et al.*, A dark, bare rock for TOI-1685 b from a JWST NIRSpec G395H phase curve. *Astron. J.* **170**, 49 (2025). doi: 10.3847/1538-3881/addb40
68. R. D. Chatterjee, R. T. Pierrehumbert, Novel physics of escaping secondary atmospheres may shape the cosmic shoreline. arXiv:2412.05188 [astro-ph.EP] (2024).
69. J. Yang, R. Hu, Chemical mapping of temperate sub-Neptune atmospheres: Constraining the deep interior H_2O/H_2 ratio from the atmospheric CO_2/CH_4 ratio. *Astrophys. J. Lett.* **971**, L48 (2024). doi: 10.3847/2041-8213/ad6b25
70. N. H. Sleep, Evolution of the continental lithosphere. *Annu. Rev. Earth Planet. Sci.* **33**, 369–393 (2005). doi: 10.1146/annurev.earth.33.092203.122643
71. R. Dasgupta, M. M. Hirschmann, The deep carbon cycle and melting in Earth's interior. *Earth Planet. Sci. Lett.* **298**, 1–13 (2010). doi: 10.1016/j.epsl.2010.06.039
72. M. Brown, T. Johnson, N. J. Gardiner, Plate tectonics and the Archean Earth. *Annu. Rev. Earth Planet. Sci.* **48**, 291–320 (2020). doi: 10.1146/annurev-earth-081619-052705
73. T. G. Meier, D. J. Bower, T. Lichtenberg, P. J. Tackley, B.-O. Demory, Hemispheric tectonics on LHS 3844b. *Astrophys. J. Lett.* **908**, L48 (2021). doi: 10.3847/2041-8213/abe400
74. T. G. Meier *et al.*, Geodynamics of super-Earth GJ 486b. *J. Geophys. Res. Planets* **129**, e2024JE008491 (2024). doi: 10.1029/2024JE008491
75. K. Loftus, R. D. Wordsworth, C. V. Morley, Sulfate aerosol hazes and SO_2 gas as constraints on rocky exoplanets' surface liquid water. *Astrophys. J.* **887**, 231 (2019). doi: 10.3847/1538-4357/ab58cc
76. J. C. G. Walker, P. B. Hays, J. F. Kasting, A negative feedback mechanism for the long-term stabilization of the earth's surface temperature. *J. Geophys. Res.* **86**, 9776–9782 (1981). doi: 10.1029/JC086iC10p09776
77. B. J. Foley, The role of plate tectonic-climate coupling and exposed land area in the development of habitable climates on rocky planets. *Astrophys. J.* **812**, 36 (2015). doi: 10.1088/0004-637X/812/1/36
78. J. Krissansen-Totton, G. N. Arney, D. C. Catling, Constraining the climate and ocean pH of the early Earth with a geological carbon cycle model. *Proc. Natl. Acad. Sci. U.S.A.* **115**, 4105–4110 (2018). doi: 10.1073/pnas.1721296115; pmid: 29610313
79. R. Luger, R. Barnes, Extreme water loss and abiotic O_2 buildup on planets throughout the habitable zones of M dwarfs. *Astrobiology* **15**, 119–143 (2015). doi: 10.1089/ast.2014.1231; pmid: 25629240
80. L. Schaefer, R. D. Wordsworth, Z. Berta-Thompson, D. Sasselov, Predictions of the atmospheric composition of GJ 1132b. *Astrophys. J.* **829**, 63 (2016). doi: 10.3847/0004-637X/829/2/63
81. G. C. Simpson, On some studies in terrestrial radiation. *Q. J. R. Meteorol. Soc.* **2**, 73–73 (1928). doi: 10.1002/qj.49705522908
82. S. Nakajima, Y.-Y. Hayashi, Y. Abe, A study on the 'runaway greenhouse effect' with a one-dimensional radiative-convective equilibrium model. *J. Atmos. Sci.* **49**, 2256–2266 (1992). doi: 10.1175/1520-0469(1992)049<2256:ASOTGE>2.0.CO;2
83. T. Constantinou, O. Shorttle, P. B. Rimmer, A dry Venusian interior constrained by atmospheric chemistry. *Nat. Astron.* **9**, 189–198 (2024). doi: 10.1038/s41550-024-02414-5
84. M. J. Way *et al.*, Was Venus the first habitable world of our solar system? *Geophys. Res. Lett.* **43**, 8376–8383 (2016). doi: 10.1002/2016GL069790; pmid: 28408771
85. S. Jordan, O. Shorttle, P. B. Rimmer, Tracing the inner edge of the habitable zone with sulfur chemistry. *Sci. Adv.* **11**, eadp8105 (2025). doi: 10.1126/sciadv.adp8105; pmid: 39879310
86. X. Byrne, O. Shorttle, S. Jordan, P. B. Rimmer, Atmospheres as a window to rocky exoplanet surfaces. *Mon. Not. R. Astron. Soc.* **527**, 10748–10759 (2024). doi: 10.1093/mnras/stad3914
87. T.-A. Suer, C. Jackson, D. S. Grewal, C. Dalou, T. Lichtenberg, The distribution of volatile elements during rocky planet formation. *Front. Earth Sci.* **11**, 1159412 (2023). doi: 10.3389/feart.2023.1159412
88. F. Nimmo, D. McKenzie, Volcanism and tectonics on Venus. *Annu. Rev. Earth Planet. Sci.* **26**, 23–51 (1998). doi: 10.1146/annurev.earth.26.1.23
89. T. Lichtenberg, L. K. Schaefer, M. Nakajima, R. A. Fischer, Geophysical evolution during rocky planet formation in *Protostars and Planets VII*, S. Inutsuka, Y. Aikawa, T. Muto, K. Tomida, M. Tamura, Eds., *Astronomical Society of the Pacific Conference Series* (2023), vol. 534, p. 907.
90. E. S. Kite, B. Fegley Jr., L. Schaefer, E. Gaidos, Atmosphere-interior exchange on hot, rocky exoplanets. *Astrophys. J.* **828**, 80 (2016). doi: 10.3847/0004-637X/828/2/80
91. T. Lichtenberg *et al.*, Vertically resolved magma ocean-protoatmosphere evolution: H_2, H_2O, CO_2, CH_4, CO, O_2, and N_2 as primary absorbers. *J. Geophys. Res. Planets* **126**, JE006711 (2021). doi: 10.1029/2020JE006711; pmid: 33777608
92. D. J. Bower, K. Hakim, P. A. Sossi, P. Sanan, Retention of water in terrestrial magma oceans and carbon-rich early atmospheres. *Planet. Sci. J.* **3**, 93 (2022). doi: 10.3847/PSJ/ac5fb1
93. M. Maurice, R. Dasgupta, P. Hassanzadeh, Volatile atmospheres of lava worlds. *Astron. Astrophys.* **688**, A47 (2024). doi: 10.1051/0004-6361/202347749
94. H. Nicholls, R. T. Pierrehumbert, T. Lichtenberg, L. Soucasse, S. Smeets, Convective shutdown in the atmospheres of lava worlds. *Mon. Not. R. Astron. Soc.* **536**, 2957–2971 (2025). doi: 10.1093/mnras/stae2772
95. R. T. Pierrehumbert, The runaway greenhouse on sub-Neptune waterworlds. *Astrophys. J.* **944**, 20 (2023). doi: 10.3847/1538-4357/acafdf
96. E. D. Young, L. Stixrude, J. G. Rogers, H. E. Schlichting, S. P. Marcum, Phase equilibria of sub-Neptunes and super-Earths. *Planet. Sci. J.* **5**, 268 (2024). doi: 10.3847/PSJ/ad8c40
97. R. Hu, B. L. Ehlmann, S. Seager, Theoretical spectra of terrestrial exoplanet surfaces. *Astrophys. J.* **752**, 7 (2012). doi: 10.1088/0004-637X/752/1/7
98. L. Kreidberg *et al.*, Absence of a thick atmosphere on the terrestrial exoplanet LHS 3844b. *Nature* **573**, 87–90 (2019). doi: 10.1038/s41586-019-1497-4; pmid: 31427764
99. C.-É. Boukaré, N. B. Cowan, J. Badro, Deep two-phase, hemispherical magma oceans on lava planets. *Astrophys. J.* **936**, 148 (2022). doi: 10.3847/1538-4357/ac8792
100. T. G. Meier, D. J. Bower, T. Lichtenberg, M. Hammond, P. J. Tackley, Interior dynamics of super-Earth 55 Cancri e. *Astron. Astrophys.* **678**, A29 (2023). doi: 10.1051/0004-6361/202346950
101. A. A. A. Piette *et al.*, Rocky planet or water world? Observability of low-density lava world atmospheres. *Astrophys. J.* **954**, 29 (2023). doi: 10.3847/1538-4357/acdef2
102. M. Zilinskas, Y. Miguel, C. P. A. van Buchem, I. A. G. Snellen, Observability of silicates in volatile atmospheres of super-Earths and sub-Neptunes. *Astron. Astrophys.* **671**, A138 (2023). doi: 10.1051/0004-6361/202245521
103. A. S. Wolf, N. Jäggi, P. A. Sossi, D. J. Bower, VapoRock: Thermodynamics of vaporized silicate melts for modeling volcanic outgassing and magma ocean atmospheres. *Astrophys. J.* **947**, 64 (2023). doi: 10.3847/1538-4357/acbcc7
104. E. J. Lee, A. Karalis, D. P. Thorngren, Creating the radius gap without mass loss. *Astrophys. J.* **941**, 186 (2022). doi: 10.3847/1538-4357/ac9c66
105. A. Vazan, C. W. Ormel, L. Noack, C. Dominik, Contribution of the core to the thermal evolution of sub-Neptunes. *Astrophys. J.* **869**, 163 (2018). doi: 10.3847/1538-4357/aaef33
106. E. S. Kite, M. N. Barnett, Exoplanet secondary atmosphere loss and revival. *Proc. Natl. Acad. Sci. U.S.A.* **117**, 18264–18271 (2020). doi: 10.1073/pnas.2006177117; pmid: 32694204
107. A. Levi, A. Bansal, D. Sasselov, A high-pressure filled ice in the H_2O–CO_2–CH_4 system, with possible consequences for the CO_2–CH_4 biosignature pair. *Astrophys. J.* **944**, 209 (2023). doi: 10.3847/1538-4357/acb49a
108. B. Journaux *et al.*, Large ocean worlds with high-pressure ices. *Space Sci. Rev.* **216**, 7 (2020). doi: 10.1007/s11214-019-0633-7
109. H. Innes, S.-M. Tsai, R. T. Pierrehumbert, The runaway greenhouse effect on Hycean worlds. *Astrophys. J.* **953**, 168 (2023). doi: 10.3847/1538-4357/ace346
110. L. T. Elkins-Tanton, S. Seager, Ranges of atmospheric mass and composition of super-Earth exoplanets. *Astrophys. J.* **685**, 1237–1246 (2008). doi: 10.1086/591433
111. J. Leconte *et al.*, A 3D picture of moist-convection inhibition in hydrogen-rich atmospheres: Implications for K2-18 b. *Astron. Astrophys.* **686**, A131 (2024). doi: 10.1051/0004-6361/202348928
112. A. Vazan, R. Sari, R. Kessel, A new perspective on the interiors of ice-rich planets: Ice-rock mixture instead of ice on top of rock. *Astrophys. J.* **926**, 150 (2022). doi: 10.3847/1538-4357/ac458c
113. T. Kovačević, F. González-Cataldo, S. T. Stewart, B. Militzer, Miscibility of rock and ice in the interiors of water worlds. *Sci. Rep.* **12**, 13055 (2022). doi: 10.1038/s41598-022-16816-w; pmid: 35906271
114. M. C. Nixon *et al.*, New insights into the internal structure of GJ 1214 b informed by JWST. *Astrophys. J. Lett.* **970**, L28 (2024). doi: 10.3847/2041-8213/ad615b
115. A. Vazan, C. W. Ormel, Rocky sub-Neptunes formed by pebble accretion: Rain of rock from polluted envelopes. *Astron. Astrophys.* **676**, L8 (2023). doi: 10.1051/0004-6361/202346574
116. W. Misener, H. E. Schlichting, E. D. Young, Atmospheres as windows into sub-Neptune interiors: Coupled chemistry and structure of hydrogen-silane-water envelopes. *Mon. Not. R. Astron. Soc.* **524**, 981–992 (2023). doi: 10.1093/mnras/stad1910
117. Y. Ito, T. Kimura, K. Ohno, Y. Fujii, M. Ikoma, Monosilane worlds: Sub-Neptunes with atmospheres shaped by reduced magma oceans. *Astrophys. J.* **987**, 174 (2025). doi: 10.3847/1538-4357/add3fe
118. C. N. Luu *et al.*, Volatile-rich Sub-Neptunes as hydrothermal worlds: The case of K2-18 b. *Astrophys. J. Lett.* **977**, L51 (2024). doi: 10.3847/2041-8213/ad9eb1

119. N. F. Wogan *et al.*, JWST observations of K2-18b can be explained by a gas-rich mini-Neptune with no habitable surface. *Astrophys. J. Lett.* **963**, L7 (2024). doi: 10.3847/2041-8213/ad2616
120. H. Luo, C. Dorn, J. Deng, The interior as the dominant water reservoir in super-Earths and sub-Neptunes. *Nat. Astron.* **8**, 1399–1407 (2024). doi: 10.1038/s41550-024-02347-z
121. J. Krissansen-Totton, N. Wogan, M. Thompson, J. J. Fortney, The erosion of large primary atmospheres typically leaves behind substantial secondary atmospheres on temperate rocky planets. *Nat. Commun.* **15**, 8374 (2024). doi: 10.1038/s41467-024-52642-6; pmid: 39333519
122. H. Nicholls, T. Lichtenberg, D. J. Bower, R. Pierrehumbert, Magma ocean evolution at arbitrary redox state. *J. Geophys. Res. Planets* **129**, JE008576 (2024). doi: 10.1029/2024JE008576; pmid: 39722853
123. C. Cherubim *et al.*, An oxidation gradient straddling the small planet radius valley. *Astrophys. J.* **983**, 97 (2025). doi: 10.3847/1538-4357/adbca9
124. H. Nicholls *et al.*, Self-limited tidal heating and prolonged magma oceans in the L 98-59 system. *Mon. Not. R. Astron. Soc.* **541**, 2566–2584 (2025). doi: 10.1093/mnras/staf1167
125. F. Selsis, J. Leconte, M. Turbet, G. Chaverot, É. Bolmont, A cool runaway greenhouse without surface magma ocean. *Nature* **620**, 287–291 (2023). doi: 10.1038/s41586-023-06258-3; pmid: 37558846
126. H. Rauer *et al*, The PLATO mission. *Exp. Astron.* **59**, 26 (2025). doi: 10.1007/s10686-025-09985-9
127. M. Turbet, D. Ehrenreich, C. Lovis, E. Bolmont, T. Fauchez, The runaway greenhouse radius inflation effect. *Astron. Astrophys.* **628**, A12 (2019). doi: 10.1051/0004-6361/201935585
128. P. Liggins, S. Jordan, P. B. Rimmer, O. Shorttle, Growth and evolution of secondary volcanic atmospheres: 2. The importance of kinetics. *J. Geophys. Res. Planets* **128**, e2022JE007528 (2023). doi: 10.1029/2022JE007528
129. C. Brachmann, L. Noack, P. A. Baumeister, F. Sohl, Distinct types of CHON atmospheres and surface pressures depending on melt redox state and outgassing efficiency. *Icarus* **429**, 116450 (2025). doi: 10.1016/j.icarus.2024.116450
130. S. M. Hörst *et al.*, Haze production rates in super-Earth and mini-Neptune atmosphere experiments. *Nat. Astron.* **2**, 303–306 (2018). doi: 10.1038/s41550-018-0397-0
131. P. Gao, H. R. Wakeford, S. E. Moran, V. Parmentier, Aerosols in exoplanet atmospheres. *J. Geophys. Res. Planets* **126**, e2020JE006655 (2021). doi: 10.1029/2020JE006655
132. P. Tamburo, P. S. Muirhead, C. D. Dressing, Predicting the yield of small transiting exoplanets around mid-M and ultracool dwarfs in the Nancy Grace Roman Space Telescope Galactic Bulge Time Domain Survey. *Astron. J.* **165**, 251 (2023). doi: 10.3847/1538-3881/acd1de
133. G. Tinetti *et al.*, A chemical survey of exoplanets with ARIEL. *Exp. Astron.* **46**, 135–209 (2018). doi: 10.1007/s10686-018-9598-x
134. C. C. Stark *et al.*, Paths to robust exoplanet science yield margin for the Habitable Worlds Observatory. *J. Astron. Telesc. Instrum. Syst.* **10**, 034006–034006 (2024). doi: 10.1117/1.JATIS.10.3.034006
135. S. P. Quanz *et al.*, Large Interferometer For Exoplanets (LIFE). I. Improved exoplanet detection yield estimates for a large mid-infrared space-interferometer mission. *Astron. Astrophys.* **664**, A21 (2022). doi: 10.1051/0004-6361/202140366
136. L. Parc, F. Bouchy, J. Venturini, C. Dorn, R. Helled, From super-Earths to sub-Neptunes: Observational constraints and connections to theoretical models. *Astron. Astrophys.* **688**, A59 (2024). doi: 10.1051/0004-6361/202449911
137. J. G. Rogers, H. E. Schlichting, J. E. Owen, Conclusive evidence for a population of water worlds around M dwarfs remains elusive. *Astrophys. J. Lett.* **947**, L19 (2023). doi: 10.3847/2041-8213/acc86f
138. E. M. R. Kempton *et al.*, A framework for prioritizing the TESS planetary candidates most amenable to atmospheric characterization. *Publ. Astron. Soc. Pac.* **130**, 114401 (2018). doi: 10.1088/1538-3873/aadf6f
139. B. Davenport *et al.*, TOI-421 b: A hot sub-Neptune with a haze-free, low mean molecular weight atmosphere. *Astrophys. J. Lett.* **984**, L44 (2025). doi: 10.3847/2041-8213/adcd76
140. C. Cadieux *et al.*, Transmission spectroscopy of the habitable zone exoplanet LHS 1140 b with JWST/NIRISS. *Astrophys. J. Lett.* **970**, L2 (2024). doi: 10.3847/2041-8213/ad5afa
141. M. Damiano, A. Bello-Arufe, J. Yang, R. Hu, LHS 1140 b is a potentially habitable water world. *Astrophys. J. Lett.* **968**, L22 (2024). doi: 10.3847/2041-8213/ad5204
142. E. Agol *et al.*, Refining the transit-timing and photometric analysis of TRAPPIST-1: Masses, radii, densities, dynamics, and ephemerides. *Planet. Sci. J.* **2**, 1 (2021). doi: 10.3847/PSJ/abd022
143. S. Zieba *et al.*, No thick carbon dioxide atmosphere on the rocky exoplanet TRAPPIST-1 c. *Nature* **620**, 746–749 (2023). doi: 10.1038/s41586-023-06232-z; pmid: 37337068
144. T. P. Greene *et al.*, Thermal emission from the Earth-sized exoplanet TRAPPIST-1 b using JWST. *Nature* **618**, 39–42 (2023). doi: 10.1038/s41586-023-05951-7; pmid: 36972683
145. E. Ducrot *et al.*, Combined analysis of the 12.8 and 15 μm JWST/MIRI eclipse observations of TRAPPIST-1 b. *Nat. Astron.* **9**, 358–369 (2024). doi: 10.1038/s41550-024-02428-z
146. P. Wachiraphan *et al.*, The thermal emission spectrum of the nearby rocky exoplanet LTT 1445A b from JWST MIRI/LRS. *Astron. J.* **169**, 311 (2025). doi: 10.3847/1538-3881/adc990
147. R. Vanderspek *et al.*, TESS discovery of an ultra-short-period planet around the nearby M dwarf LHS 3844. *Astrophys. J. Lett.* **871**, L24 (2019). doi: 10.3847/2041-8213/aafb7a
148. Q. Xue *et al.*, JWST thermal emission of the terrestrial exoplanet GJ 1132b. *Astrophys. J. Lett.* **973**, L8 (2024). doi: 10.3847/2041-8213/ad72e9
149. M. Weiner Mansfield *et al.*, No thick atmosphere on the terrestrial exoplanet Gl 486b. *Astrophys. J. Lett.* **975**, L22 (2024). doi: 10.3847/2041-8213/ad8161
150. A. Shporer *et al.*, GJ 1252 b: A 1.2 $R_{\oplus}$. *Astrophys. J. Lett.* **890**, L7 (2020). doi: 10.3847/2041-8213/ab7020
151. I. J. M. Crossfield *et al.*, GJ 1252b: A hot terrestrial super-Earth with no atmosphere. *Astrophys. J. Lett.* **937**, L17 (2022). doi: 10.3847/2041-8213/ac886b
152. E. Goffo *et al.*, Company for the Ultra-high Density, Ultra-short period sub-Earth GJ 367 b: Discovery of two additional low-mass planets at 11.5 and 34 days. *Astrophys. J. Lett.* **955**, L3 (2023). doi: 10.3847/2041-8213/ace0c7
153. M. Zhang *et al.*, GJ 367b is a dark, hot, airless sub-Earth. *Astrophys. J. Lett.* **961**, L44 (2024). doi: 10.3847/2041-8213/ad1a07
154. R. Hu *et al.*, A secondary atmosphere on the rocky exoplanet 55 Cancri e. *Nature* **630**, 609–612 (2024). doi: 10.1038/s41586-024-07432-x; pmid: 38718834
155. J. A. Patel *et al.*, JWST reveals the rapid and strong day-side variability of 55 Cancri e. *Astron. Astrophys.* **690**, A159 (2024). doi: 10.1051/0004-6361/202450748
156. S. Zieba *et al.*, K2 and Spitzer phase curves of the rocky ultra-short-period planet K2-141 b hint at a tenuous rock vapor atmosphere. *Astron. Astrophys.* **664**, A79 (2022). doi: 10.1051/0004-6361/202142912

ACKNOWLEDGMENTS

T.L., J.T., and E.M.-R.K. acknowledge the Alfred P. Sloan Foundation's AEThER project (G202114194) for providing the opportunity to discuss the ideas in this Review in depth. **Funding:** T.L. acknowledges support from the Branco Weiss Foundation, the Netherlands eScience Center under grant NLESC.OEC.2023.017, and NASA's Nexus for Exoplanet System Science research coordination network (Alien Earths project, 80NSSC21K0593). O.S. acknowledges support from STFC grant UKRI1184. **Author contributions:** Conceptualization: T.L., O.S., J.T., E.M.-R.K. Data curation: T.L., J.T. Formal analysis: T.L., O.S., J.T., E.M.-R.K. Investigation: T.L., O.S., J.T., E.M.-R.K. Methodology: T.L., O.S., J.T. Visualization: T.L., O.S., J.T. Writing – original draft: T.L., O.S., J.T. Writing – review & editing: T.L., O.S., J.T., E.M.-R.K. **Competing interests:** There are no competing interests to declare. **Data and materials availability:** No new data were generated for this Review. **License information:** Copyright © 2025 the authors, some rights reserved; exclusive licensee American Association for the Advancement of Science. No claim to original US government works. https://www.science.org/about/science-licenses-journal-article-reuse. This research was funded in whole or in part by STFC (UKRI1184), a cOAlition S organization. The author will make the Author Accepted Manuscript (AAM) version available under a CC BY public copyright license.

Submitted 28 February 2025; accepted 28 August 2025

10.1126/science.ads3360

RESEARCH

IN *SCIENCE* JOURNALS

Edited by **Michael Funk**



PHOTO: DPA PICTURE ALLIANCE/ALAMY

OPTICS

Steadying the output of fiber lasers

High-power fiber lasers are used in a range of scientific fields in addition to their standard use for technology. However, increases in laser output power are limited by nonlinear effects that can damage the optical components and reduce the beam quality. Rothe *et al.* used a spatial wavefront-shaping technique for multimode fiber lasers that mitigates their detrimental processes, thus enabling output power to be increased appreciably while maintaining beam quality. —Ian S. Osborne *Science* p. 173, 10.1126/science.ady2226

Optical wavefront shaping can improve the performance of high-power fiber lasers such as those used for machining.

CELL BIOLOGY

Mitophagy removes mitochondrial mutants

Mitochondrial production of adenosine triphosphate (ATP) is essential for life and depends on the cooperation of mitochondrial DNA (mtDNA) with the nuclear genome, but little is known about the mechanisms ensuring nuclear-mtDNA compatibility. Frison *et al*. found that mitochondria harboring a mtDNA mutation evade mitochondrial quality control by inhibiting the ubiquitin proteasome system. In mouse models, restoring mitochondrial ubiquitination through ubiquitin-specific peptidase 30 (Usp30) loss increased purifying selection of mtDNA in early embryogenesis. In vitro, genetically or chemically inhibiting Usp30 reduced mutant burden by increasing ubiquitin-mediated mitochondrial autophagy. Usp30 thus provides a promising target to treat and prevent mtDNA disorders. —Stella M. Hurtley

Science p. 156, 10.1126/science.adr5438

PREDATION

Of bats and birds

Bats have evolved to be efficient aerial predators for a wide array of prey. Although most people think of them as insectivores, there are bats that eat mammals and amphibians and even birds. Three bat species have been recorded preying on birds, but how and when they do this has been mostly unknown. Stidsholt *et al*. monitored greater noctule bats in flight and found that individuals track migrating birds using echolocation and consume them on the wing. These observations suggest that these efficient aerial predators have also evolved to prey on migrating birds. —Sacha Vignieri

Science p. 178, 10.1126/science.adr2475

CARBON OFFSETS

Re-evaluating REDD+

Forest degradation is a major contributor to greenhouse gas emissions, such that forest protection projects are used as carbon offsets for greenhouse gas–producing activities in voluntary carbon markets. Recently, the effectiveness of carbon-offsetting programs such as REDD+ (Reducing Emissions from Deforestation and Degradation Plus) has been called into question, causing a decline in carbon offset values. Tang *et al*. addressed this question with updated analyses incorporating many projects and carefully chosen controls. Across 52 REDD+ Avoided Unplanned Deforestation projects from 12 countries in South America, Africa, and Southeast Asia, the authors found greater climate benefits than previous studies but low efficacy overall: Less than 20% of projects met their emissions targets. Project success and overestimation both varied considerably between countries. —Bianca Lopez

Science p. 182, 10.1126/science.adw4094

BATTERIES

Enabling faster lithium ion transport

Theoretical predictions have shown that crystalline structures with a lithium-hopping path of tetrahedral to tetrahedral are likely to display a higher lithium ionic conductivity than those with the more commonly observed tetrahedral-octahedral-tetrahedral diffusion pathway. Zhao *et al*. report on the synthesis, characterization, and electrochemical testing of a solid-state lithium tantalum oxychloride electrolyte with the formula $Li_3Ta_3O_4Cl_{10}$. The material has high ionic conductivity and low activation energy, even at lower temperatures. These properties are due to the mixed-anion chemistry, which enables facile lithium-ion migration pathways. The broad applicability of the mixed-anion strategy was validated using niobium and other cost-effective or earth-abundant elements to replace the tantalum, although with some decrease in conductivity. —Marc S. Lavine

Science p. 199, 10.1126/science.adt9678

HORMONE SENSORS

Detecting plant pathogen responses

Visualizing and quantifying the amount of a hormone within a cell can be achieved using fluorescence resonance energy transfer (FRET) sensors. These sensors involve a hormone binding to a pair of linked proteins, which then undergo conformational changes to alter the fluorescence emission ratio of two connected fluorescent proteins. Tang *et al*. have developed a FRET sensor for the plant hormone salicylic acid, which is primarily involved in activating immune responses. Using this sensor, the authors were able to visualize hormone levels with high sensitivity and spatial resolution at the cellular level and observed varied dynamics and patterns of salicylic acid up-regulation in response to bacterial infections. —Madeleine Seale

Science p. 188, 10.1126/science.adw7650

KIDNEY DISEASE

A vicious cycle in the kidneys

Both the nuclear genome and the mitochondrial genome accumulate mutations during each person's lifetime, and the same thing has been observed in mice. Of the major organs, the kidneys in particular have been reported to accumulate the largest number of mitochondrial mutations. By studying mouse models of acute and chronic kidney injury and patients with kidney disease, Huang *et al*. identified a vicious cycle in which accumulating mutations in the mitochondrial genome contribute to kidney injury, which in turn promotes the accumulation of further mutations, ultimately increasing the risk of fibrosis and chronic impairment. —Yevgeniya Nusinovich

Science p. 164, 10.1126/science.adk7978

DEVELOPMENTAL BIOLOGY

Hedgehog directs osteochondroma growth

Longitudinal bone growth occurs at plates located at the ends of bones. Hereditary multiple osteochondroma (HMO) causes benign bony tumors to form at the growth plates in children and leads to skeletal abnormalities that impair movement, impinge on nearby tissues, and cause chronic pain. In a mouse model of HMO, Catheline *et al*. found that the osteochondromas acquired a growth plate–like architecture as they emerged. Tumor outgrowth depended on the establishment of an ectopic growth axis orthogonal to that of the bone from which it emerged and involved Hedgehog signaling, which also drives normal bone growth. —Annalisa VanHook

Sci. Signal. (2025) 10.1126/scisignal.adu6357

IN OTHER JOURNALS

Edited by **Corinne Simonti** and **Jesse Smith**

PALEONTOLOGY

Seal paddling before seals

Today, tetrapods in the marine environment are mostly mammalian, but this is a relatively recent phenomenon, occurring after the end-Cretaceous expansion of mammals. Before this, tetrapod reptiles ruled the seas, with groups such as ichthyosaurs, mososaurs, and sauropterygians occurring in diverse forms. Renesto *et al*. describe a nearly complete fossil of the known sauropterygian *Lariosaurus* from the middle Triassic in Switzerland that was preserved with its skin nearly intact. The excellent preservation revealed that the species, long thought to have had both fore and aft flippers, actually had webbed forefeet. Further, its arms were elongated and well-muscled. These traits together suggest that it swam much like a seal or sea lion, using its forelegs for propulsion. —Sacha Vignieri

Swiss J. Palaeontol. (2025) 10.1186/s13358-025-00396-z

AGING

Beauty sleep for your brain

Difficulty sleeping not only prevents us from feeling refreshed but may also affect brain health; however, the relationship is poorly understood. Carvalho *et al.* longitudinally studied associations between insomnia, difficulty falling or staying asleep at least three times weekly over 3 months, and brain aging among adults over age 50. They found that chronic insomnia was associated with accelerated memory decline, brain aging, and a 40% increased risk of dementia. Although causal inferences cannot be drawn, the associations suggest that more research is needed to better understand how sleep may contribute to cognitive challenges later in life or if both are caused by a common factor. —Ekeoma Uzogara

Neurology (2025) 10.1212/WNL.0000000000214155

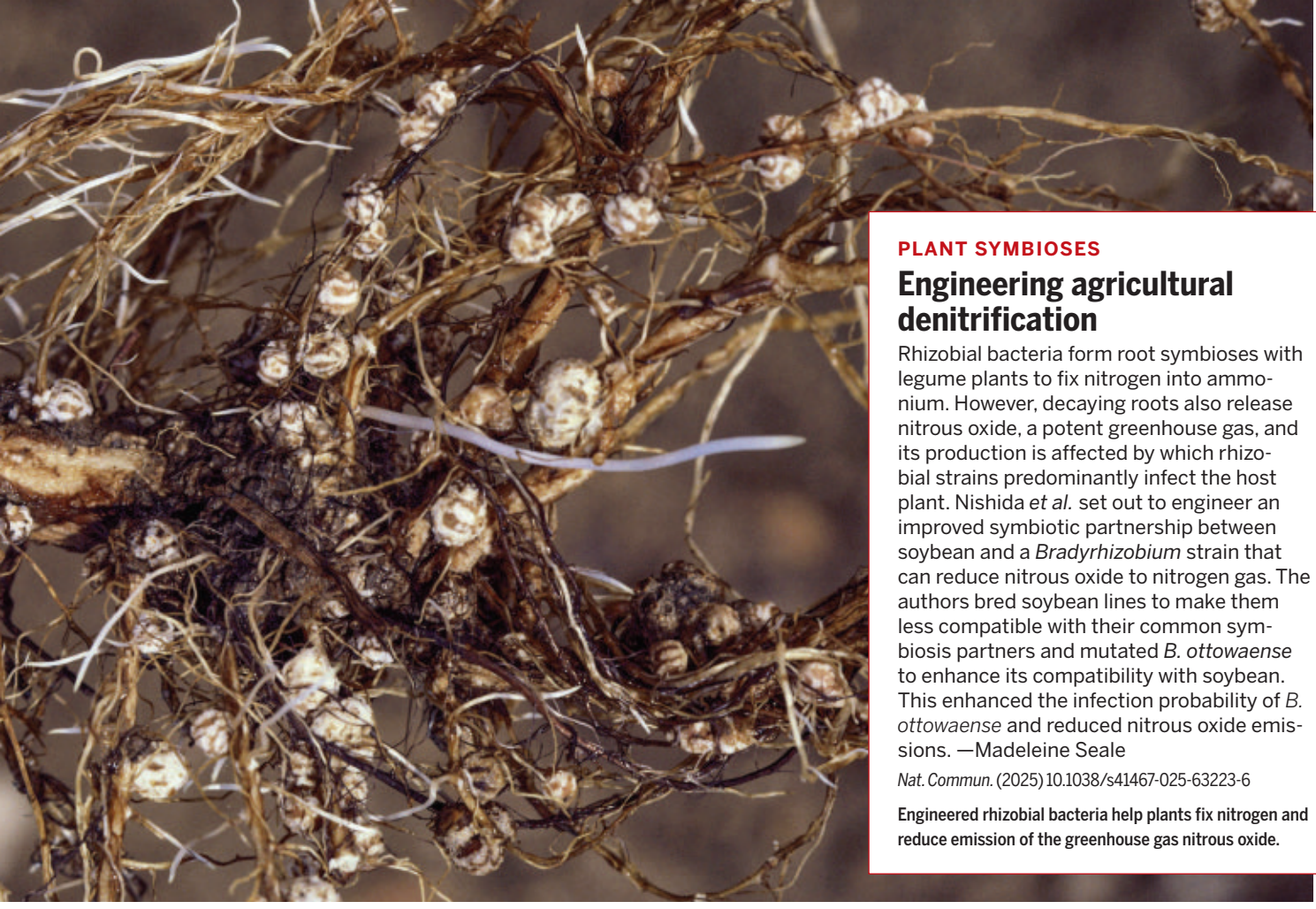


PHOTO: DAN GURAVICH/SCIENCE SOURCE

BEHAVIOR

Contagious violence

Witnessing violence increases the likelihood of perpetuating violent actions later in life. To understand the brain circuits underlying this behavior, Adjei *et al.* developed a model of socially transmitted aggression (STA) in mice and showed that male mice witnessing a familiar conspecific engaging in aggressive behavior increased their aggressivity later on. At the circuit level, this STA was mediated by the activation of excitatory neurons in the medial amygdala,



PLANT SYMBIOSES

Engineering agricultural denitrification

Rhizobial bacteria form root symbioses with legume plants to fix nitrogen into ammonium. However, decaying roots also release nitrous oxide, a potent greenhouse gas, and its production is affected by which rhizobial strains predominantly infect the host plant. Nishida *et al.* set out to engineer an improved symbiotic partnership between soybean and a *Bradyrhizobium* strain that can reduce nitrous oxide to nitrogen gas. The authors bred soybean lines to make them less compatible with their common symbiosis partners and mutated *B. ottowaense* to enhance its compatibility with soybean. This enhanced the infection probability of *B. ottowaense* and reduced nitrous oxide emissions. —Madeleine Seale

Nat. Commun. (2025) 10.1038/s41467-025-63223-6

Engineered rhizobial bacteria help plants fix nitrogen and reduce emission of the greenhouse gas nitrous oxide.

and silencing these neurons abolished STA. By contrast, STA was not observed in female animals or in male animals exposed to aggressive behavior perpetuated by an unfamiliar mouse. These results suggest potential targets for disorders associated with violent behaviors. —Mattia Maroso

J. Neurosci. (2025) 10.1523/JNEUROSCI.1018-25.2025

PHOTONICS

Shaping photonics with optical origami

Intricate three-dimensional (3D) photonic structures can be fabricated using techniques such as laser scribing and 3D printing. However, the fabrication processes can introduce defects and surface variability that can compromise optical functionality. Malhorta *et al.* worked with high-quality silica grown on a silicon substrate. After preparing layers of freely suspended silica layers by underetching, the authors showed that the application of laser pulses in the right place could be used to alter the local surface tension, resulting in accurate and controlled folding of the silica layer. The ability to form 3D structures with ultrasmooth silica could be used to develop high-quality photonic components for on-chip functionality. —Ian S. Osborne

Optica (2025) 10.1364/OPTICA.560597

SUPERCONDUCTIVITY

Spotting pockets

Elucidating the nature of the Fermi surface in cuprate superconductors at high temperatures could aid in our understanding of the pseudogap state. However, doing so remains experimentally challenging using conventional techniques such as quantum oscillation observations. Instead, Chan *et al.* looked for the so-called Yamaji effect, which manifests as a peak in the c-axis resistivity when the applied magnetic field is tilted. Performing angle-dependent magnetoresistivity measurements above the critical temperature in the cuprate $HgBa_2CuO_{4+\delta}$, the researchers observed such a peak, which was more prominent at higher magnetic fields. By comparing this against calculations, they concluded that the Fermi surface of this material features small pockets, presenting a valuable benchmark for theories of the pseudogap state. —Jelena Stajic

Nat. Phys. (2025) 10.1038/s41567-025-03032-2

BATTERY ELECTRODES

Lithium-deficient sintering lifts performance

Single-crystalline nickel-rich cathodes are attractive components for high-energy-density lithium-ion batteries. However, the relatively higher annealing temperatures required for these materials pose challenges in defect control, reducing battery capacity and rate performance. In contrast to previous doping- or coating-based strategies, Huang *et al.* delved into synthesis process control and showed that conducting high-temperature annealing with less than the required amount of lithium salt, followed by lower-temperature lithium supplementation, greatly reduced crystallographic defects and chemical heterogeneity by promoting the formation of locally ordered superlattices. These superlattices helped to improve the thermal stability and provided fast-conducting pathways for lithium-ion diffusion, which benefits the overall battery life span and rate capability, especially under extreme conditions. —Jack Huang

J. Am. Chem. Soc. (2025) 10.1021/jacs.5c00615

Edited by **Michael Funk**

EXOPLANETS

Atmospheres constrain exoplanet interiors

Exoplanet surveys have found objects that are far more diverse than the planets of the Solar System. Mass and radius measurements show exoplanets with densities consistent with pure iron, rock, and gas- or water-rich layers, but do not uniquely determine the interior structure of these bodies. Lichtenberg *et al*. reviewed how exoplanet atmospheres interact with the interior. They found that the transfer of energy and material between layers of an exoplanet affects the size and composition of its atmosphere in ways that are potentially observable. The authors discuss how atmospheric observations can be used to constrain exoplanet interiors. —Keith T. Smith

Science p. 140, 10.1126/science.ads3360

MOLECULAR BIOLOGY

Positional coordination of mRNA ends

The sites where RNA transcription begins and ends determine the full sequence of messenger RNA (mRNA) molecules and, consequently, the function of their encoded proteins. By analyzing both short- and long-read RNA-sequencing data across human tissues and other mammals, Calvo-Roitberg *et al*. revealed a coordinated relationship between transcription start and end sites that is dictated by the genomic order of alternative sites. This positional coupling, called the positional initiation-termination axis, is most prominent in long genes and is governed by the rate of RNA polymerase II elongation. These findings uncover a molecular mechanism that shapes mRNA diversity across tissues. —Di Jiang

Science p. 144, 10.1126/science.ado8279

METABOLISM

Acidosis supports tumor survival

To better understand how tumor cells respond in the stressful environments they encounter, Groessl *et al*. used CRISPR screens to evaluate genes that promote responses to metabolic stress and compared responses to metabolic stress in pancreatic tumor cells in vivo and in cell culture. Acidosis, a metabolic state known to occur in tumors, appeared to be a main factor affecting cell metabolism by decreasing activity of the protein kinase ERK (extracellular signal-regulated kinase). ERK suppression blunted the effects of oncogene activation on mitochondrial morphology and favored tumor growth by allowing the cells to adapt to metabolic stress. —L. Bryan Ray

Science p. 145, 10.1126/science.adp7603

CANCER

A hidden genetic block to STING therapy

Many cancers are resistant to immunotherapy because of poor immune cell infiltration. Activating the STING (stimulator of interferon genes) pathway is one way to encourage tumor immune cell infiltrates and positive therapeutic response. However, targeting the STING pathway has not yet succeeded in human trials despite encouraging results from experimental preclinical models. Hsu *et al*. report one possible reason: Many human cancers lose expression of a gene called *methylthioadenosine phosphorylase* (*MTAP*), which causes a block of the STING pathway, but MTAP deficiency is rare in animal models. The researchers found that targeting a related process, polyamine metabolism, with the existing drug DL-α-difluoromethylornithine could restore immune activity in MTAP-deleted cancers and reduce tumor growth. This approach may offer a new way to improve cancer treatment and patient selection for STING-based therapies. —Priscilla N. Kelly

Science p. 146, 10.1126/science.adl4089

YEAST GENETICS

Distant actors

It is difficult to determine the effects of genetic variants, even when studying less complex model organisms. Jakobson *et al*. crossed two strains of the yeast *Saccharomyces cerevisiae* and performed mass spectrometry and whole-genome sequencing on the F_6 progeny. Although these strains only differ by about 12,000 genetic variants, the authors identified nearly 6500 associations between genetic variants and protein levels. Nearly all (98%) of these variants acted in trans (>1 kilobase away from coding sequence) and many affected transcription factors, leading to downstream effects on many proteins. The results of this study represent a comprehensive atlas of variant protein dynamics in an important model organism. —Corinne Simonti

Science p. 147, 10.1126/ science.adu3198

TRANSPOSON

Mechanism of LINE-1 retrotransposition

Long interspersed nuclear element-1 (LINE-1) mobilizes by inserting into new genomic sites through its open reading frame 2 protein (ORF2p), which has endonuclease (EN) and reverse transcriptase (RT) activities. Jin *et al*. determined ORF2p's structure bound to an RNA-DNA hybrid in its RT site and a Y-shaped DNA on its surface. ORF2p binds double-stranded DNA without sequence specificity, and the single-stranded DNA path suggests dynamic EN positioning during cleavage. EN activity was strongly stimulated by forked or flap DNAs, indicating that ORF2p acts as a structure-selective endonuclease and explaining why LINE-1 mobilization predominantly occurs during DNA replication. —Di Jiang

Science p. 148, 10.1126/science.adu3433

IMMUNOLOGY

The cholesterol effect

Cholesterol is an important component of cell membranes and can be shuttled between different subcellular compartments through the action of proteins belonging to the Aster family. Gao *et al*. found that deleting Aster-A specifically in T cells inhibited the uptake of dietary fats and prevented diet-induced obesity in mice (see the Perspective by Burkhardt and Ecker). By regulating the abundance of cholesterol in the plasma membrane, Aster-A modulated T cell receptor signaling and differentiation. In the absence of Aster-A, CD4 T cells in the gut produced a cytokine, interleukin-22, which decreased the ability of intestinal epithelial cells to take up fatty acids from the diet. —Sarah H. Ross

Science p. 149, 10.1126/science.adt4169; see also p. 128, 10.1126/science.aeb5717

AGING

Long-lived rats reveal a secret

Somewhat lacking in good looks, the naked mole rat gets attention because it is very long lived and highly resistant to cancer. Chen *et al*. revealed a molecular mechanism that contributes to successful aging in these rodents: a

change in the enzyme cyclic guanosine monophosphate-adenosine monophosphate synthase (cGAS), which is known to sense cytosolic DNA and initiate immune defense responses (see the Perspective by Martinez *et al*.). Unlike human cGAS, which inhibits DNA repair by homologous recombination in the nucleus, the naked mole rat enzyme has four amino acid changes that allow it to enhance DNA repair, thus delaying aging and enhancing life span. —L. Bryan Ray

Science p. 150, 10.1126/science.adp5056; see also p. 126, 10.1126/science.aeb6125

MICROBIOME

Personalized protein diversity

The congregation of commensal organisms that sits within the human gut is strikingly individual. *Bacteroides* species are prominent, long-term constituents of the gut microbiome that also play host to diversity-generating retroelements (DGRs). DGRs produce extraordinary numbers of DNA sequence variants and variable protein sequences. Macadangdang *et al*. investigated the DGRs that specifically target bacterial adhesion proteins (pilins) without disrupting the scaffold of the adhesin (see the Perspective by Paul and Mekalanos). This arrangement maximizes the capacity and rate of bacterial diversification with minimal cost. Data from mother-baby pairs showed that the first of a lifelong experience of bacterial and DGR transfer occurs at birth, resulting in the transfer of *Bacteroides* variants that are specific to and stick with their new hosts. —Caroline Ash

Science p. 151, 10.1126/science.adv2111; see also p. 129, 10.1126/science.aeb8597

ANIMAL BEHAVIOR

Responding to light

The total solar eclipse that occurred across the central southern to northeastern parts of the US presented an opportunity to study the responses of animals to rapid changes in light. Aguilar *et al*. anticipated this event and created an app that observers could use to record bird behavior, receiving input from over 10,000 users. They combined these data with locally recorded vocalizations analyzed by the artificial neural network model BirdNET. Together, these analyses revealed that half of the species responded to the end of the eclipse by singing a dawn chorus despite the "night" lasting only a few minutes. Variation in species response also informs us about variation in sensitivity to light, with implications for the impacts of artificial light. —Sacha Vignieri

Science p. 152, 10.1126/science.adx3025

VACCINES

T cell receptor avidity assets

CD8 T cell responses are detected after SARS-CoV-2 messenger RNA (mRNA) vaccination, but how these vaccines shape the expansion of T cell clones is unclear. Kocher *et al*. characterized CD8 T cell responses in 29 individuals receiving three mRNA vaccinations before breakthrough infection. Using flow cytometry, ELISpot, single-cell RNA, and T cell receptor (TCR) sequencing analyses, as well as transgenic TCR re-expression, the authors examined the effects of TCR avidity on the expansion of T cell clones. Multiple vaccinations caused dynamic changes in the epitope-specific TCR repertoire, with TCR diversity being maintained over time. High-avidity TCRs were more likely to be maintained in stem-like T cell subsets, whereas clonal expansion was stochastic beyond an avidity threshold for recruitment into the immune response. These findings suggest that TCR avidity shapes the CD8 T cell response to mRNA vaccines. —Christiana N. Fogg

Sci. Immunol. (2025) 10.1126/sciimmunol.adu6730

FERROIC MATERIALS

Ferroaxial switching

Ferroics are important materials for applications in solid-state memory storage and ultrafast switching. Ferromagnetics and ferroelectrics have stray fields that can interfere with nearby memories, resulting in depolarization and ultimately limiting storage density. By contrast, in ferroaxial materials, the electric dipoles line up head to tail, forming vortices and thereby removing the stray fields. However, these vortex states have so far been difficult to control and switch. Zeng *et al*. demonstrated how single optical pulses can repeatedly switch a ferroaxial phase between two stable states (see the Perspective by He and Khalsa). The controlled switching between left and right helicity could be useful in developing a new platform for ultrafast information storage. —Ian S. Osborne

Science p. 195, 10.1126/science.adz5230; see also p. 131, 10.1126/science.aeb8208

CANCER

Longitudinally understanding GBM therapy

A major challenge in evaluating therapy responses to glioblastoma (GBM) is that longitudinal readouts are thought to be limited to clinical imaging with magnetic resonance imaging (MRI). Ling *et al.* challenged the idea that serial sampling of GBM is not feasible and report longitudinal tumor biopsy collection and multiomic readouts for two patients participating in a clinical trial of the oncolytic herpes simplex virus 1 (HSV1) CAN-3110. Samples from both study participants provided evidence for reshaping of the GBM tumor microenvironment in response to CAN-3110, including expansion of T cell responses, features that would not be apparent by traditional MRI. These results suggest a potential therapeutic benefit for CAN-3110 and demonstrate the feasibility of implementing longitudinal tumor sampling in GBM. —Courtney Malo

Sci. Transl. Med. (2025) 10.1126/scitranslmed.adv2881

RESEARCH ARTICLE SUMMARY

MOLECULAR BIOLOGY

mRNA initiation and termination are spatially coordinated

Ezequiel Calvo-Roitberg†, Christine L. Carroll†, GyeungYun Kim, Valeria Sanabria, Sergey V. Venev, Steven T. Mick, Joseph D. Paquette, Maritere Uriostegui-Arcos, Job Dekker, Ana Fiszbein*‡, Athma A. Pai*‡

Full article and list of author affiliations: https://doi.org/10.1126/science.ado8279

INTRODUCTION: Initiation and termination are key steps in the synthesis of mature mRNA molecules. Recent high-throughput analyses have suggested that most mRNA isoform diversity comes from the use of alternative initiation and termination sites. These choices can lead to variable protein conformations or different 5′ and 3′ untranslated regions that influence mRNA localization, translation efficiency, and stability. Thus far, these processing events have primarily been studied in isolation, with little insight into how decisions are coordinated across the transcript to govern the ultimate fate and function of mRNA molecules.

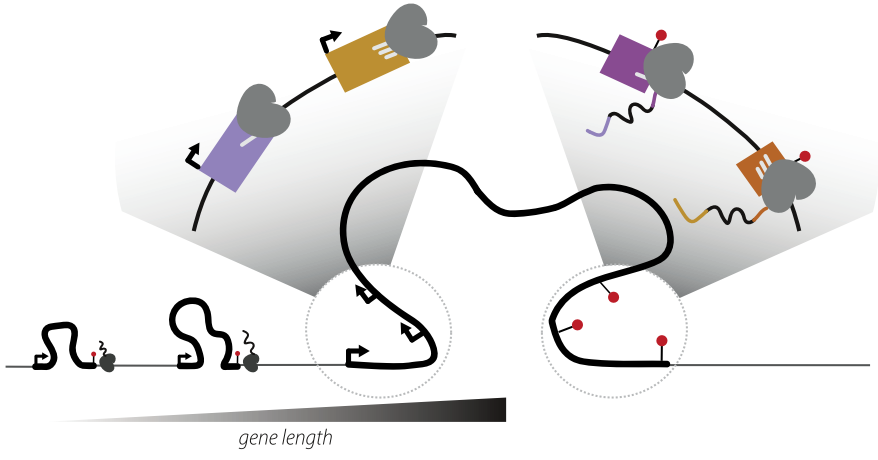
RATIONALE: Analyzing short-read RNA-sequencing (RNA-seq) data across human tissues, we observed that the numbers of alternative transcription start sites (TSSs) and alternative 3′ polyadenylation sites (PASs) are correlated across genes. This led us to hypothesize that genes may be structured to use these sites in a coordinated manner. We studied how alternative RNA processing decisions at the terminal ends of genes are coordinated, aiming to better understand the regulation of full-length RNA isoforms.

RESULTS: Through a systematic analysis of hundreds of long-read RNA-seq datasets across mammalian tissues, we find that mRNA initiation and termination site choice are directly coupled. Notably, this coupling is based on the order in which sites appear in the genome, with transcripts that start at an upstream TSS preferentially ending at an upstream PAS and those starting at a downstream TSS using a downstream PAS. This revealed a positional initiation termination axis (PITA), which governs coupled mRNA terminal end choices, independent of tissue- or context-specific regulation. Consistently, dCas9-CRISPR perturbations show that mRNA 5′ end choice directly influences mRNA 3′ end choice. PITA is strongly associated with the length of genomic features; PITA genes are longer and transcribed faster, have greater distances between alternative TSSs or PASs, and exhibit distinct chromatin features at TSSs. We see that the rate of RNA Polymerase II (RNAPII) elongation is dependent on where transcription begins, with downstream TSSs associated with faster RNAPII elongation. Overall, we found that PITA coupling depends on a combination of sustained RNAPII trafficking and progressively stronger alternative PAS sequences across longer genes. Specifically, slower RNAPII molecules originating at upstream TSSs are more likely to use weaker upstream PASs, whereas faster RNAPII molecules from downstream TSSs can reach stronger downstream PASs. Together, our data support a model integrating sequence and kinetic features to propose that full-length isoform expression is governed by RNAPII elongation rates within and across human genes.

CONCLUSION: This study reveals widespread ordinal coupling between alternative mRNA starts and ends across tissues and species. Our results suggest an interplay between mRNA processing and the evolution of gene architecture. By showing that PITA coupling is governed by transcription elongation dynamics, we extend the classical "window of opportunity" paradigm from splicing to full-length mRNA isoforms. This work lays the foundations for new areas of investigation into the spatial control of mRNA expression and co-transcriptional RNA processing. □

*Corresponding author. Email: anafisz@bu.edu (A.F.); athma.pai@umassmed.edu (A.A.P.)
†These authors contributed equally to this work. ‡These authors contributed equally to this work. **Cite this article as E. Calvo-Roitberg *et al.*, *Science* 390, eado8279 (2025). DOI: 10.1126/science.ado8279**

Transcription elongation rates drive the positional coordination of mRNA initiation and termination. RNAPII molecules initiating at downstream TSSs elongate faster throughout the gene, coupling the usage of these sites with downstream, stronger PASs in longer genes.



MOLECULAR BIOLOGY

mRNA initiation and termination are spatially coordinated

Ezequiel Calvo-Roitberg[1]†, Christine L. Carroll[2]†, GyeungYun Kim[2], Valeria Sanabria[1], Sergey V. Venev[3], Steven T. Mick[2], Joseph D. Paquette[1], Maritere Uriostegui-Arcos[2], Job Dekker[3,4], Ana Fiszbein[2,5]*‡, Athma A. Pai[1]*‡

Transcriptional initiation and termination decisions drive messenger RNA (mRNA) isoform diversity but the relationship between them remains poorly understood. By systematically profiling joint usage of transcription start and end sites, we observed that mRNA using upstream starts preferentially use upstream end sites and that the usage of downstream sites is similarly coupled. Our results suggest a positional initiation termination axis (PITA), in which usage of alternative terminal sites are coupled based on their genomic order. PITA is enriched in longer genes with distinct chromatin features. We find that mRNA 5′ start choice directly influences 3′ ends depending on RNA polymerase II trafficking speed. Our results indicate that spatial organization and transcriptional dynamics couple transcription initiation and mRNA 3′ end decisions to define mRNA isoform expression.

Mechanisms involved in mRNA processing are regulated by disparate molecular machineries and subjected to different global regulatory constraints to drive tissue- or context-specific transcriptomes (*1*). Thus, exon usage within mRNAs has historically been studied as independent events that contribute individually to the composition of full-length isoforms (*2*, *3*). However, increasing evidence suggests cooperative regulation by RNA processing mechanisms across a gene (*4*–*7*). Recent studies have found that factors involved in transcription, mRNA splicing, and cleavage and polyadenylation (CPA) may have distinct secondary roles in another step of RNA processing (*8*–*12*). These investigations have mostly focused on connections between splicing and either transcription initiation or CPA, with less known about direct connections between transcription initiation and CPA.

More than 70% of mammalian genes express alternative transcription start sites (TSSs) or polyadenylation sites (PASs) across cellular contexts (*4*, *13*, *14*), with four to five annotated TSSs and/or PASs per gene on average (*15*, *16*). Alternative mRNA terminal end usage underlies most variation in isoform usage across cells, tissue types, and cellular contexts (*4*, *17*–*19*). Alternative TSSs and PASs influence the composition and length of coding sequences and 5′ and 3′ untranslated regions (UTRs), respectively, with impacts on RNA stability, localization, and translation efficiency (*20*–*22*). Understanding whether and how these decisions are coordinated across the gene will inform the regulation of full-length isoforms, the proteins encoded by them, and effects on protein expression.

There are many shared regulatory features between the 5′ and 3′ ends of genes. For instance, RNA polymerase II (RNAPII) phosphorylation events required for promoter-proximal transcription elongation are also required for productive elongation at the end of the gene (*9*, *23*, *24*). RNAPII elongation rates can influence both alternative TSS and PAS usage based on the position of sites within genes (*25*–*31*). Decisions at the terminal ends of genes might also be spatially associated (*32*). Recent high-resolution measurement of chromatin conformation found dynamic loops anchored at TSSs and extruding through the body of the gene (*33*, *34*), suggesting that both two- and three-dimensional (2D and 3D, respectively) architecture may be important for mRNA synthesis. These findings all hint at spatiotemporal connections between transcription initiation and CPA.

We set out to answer two fundamental questions in RNA biology: Are transcription initiation and termination coregulated, and which mechanisms drive coordinated RNA processing? Through an analysis of genome-wide datasets across tissues, we find that genes have similar numbers of alternative sites at both their 5′ and 3′ ends and that there is a global bias toward coordinated usage of alternative TSSs and PASs based on their ordinal position within genes. Our analyses reveal a positional initiation termination axis (PITA) that intrinsically governs mRNA terminal end choices, independent of tissue- or context-specific regulation. We show that this coupling between transcription start and end sites is mostly driven by the dynamics of transcription.

Results

The selection of mRNA terminal (5′ and 3′) ends is a highly regulated process that often involves a choice between multiple alternative sites and exons (Fig. 1A). To understand the extent to which mRNA isoform diversity in genes is driven by the usage of alternative terminal exons, we systematically characterized the landscape of terminal exon usage across human cell types. We previously developed the hybrid-internal-terminal (HIT) index, a metric that uses RNA-sequencing (RNA-seq) data to identify and quantify the relative usage of alternative terminal exons across the genome (*35*). We applied the HIT index framework to 17,350 RNA-seq samples across 54 human tissues from the genotype tissue expression (GTEx) project (*36*) and identified 66,673 and 63,399 annotated alternative first and last exons, respectively, across all samples. The distributions of the number of first and last exons per gene were similar: The number of genes with one, two, three, etc. first exons closely matched the number of genes with only one, two, three, etc. last exons, respectively (Fig. 1B). Genes with alternative first exons (AFEs) are significantly more likely than expected to also use alternative last exons (ALEs) (hypergeometric test P-value $< 2.2 \times 10^{-16}$; fig. S1A).

Coordinated terminal exon usage based on ordinal position

This led us to speculate that genes might utilize similar numbers of first and last exons to jointly regulate the usage of terminal ends. Among genes with multiple AFEs and ALEs, there is a strong correlation between the expression of first and last exons within a gene, such that genes expressing two AFEs are more likely to use two ALEs, genes using three AFEs often use three ALEs, and so on (Fig. 1C, inset). Although the strength of this effect varies across tissues, 97.8% of samples showed positive correlations (Fig. 1C and fig. S1B) between quantities of first and last exons identified despite tissue-specific regulation of alternative terminal end usage. The presence of similar numbers of alternative sites at both gene ends suggests the potential for regulatory coupling of transcription and CPA decisions based on gene organization, so we next asked whether the usage of first and last exons was associated with their position within the gene. We measured exon usage with a percent spliced-in (PSI) value (*37*), which estimates the proportion of mRNA transcripts that include a specific terminal exon. As a baseline, genes that predominantly use a single first exon (PSI > 0.95) also tend to use a single last exon (fig. S1C). More broadly, we found that the usage of terminal exons with similar ordinal positions was correlated across genes (Fig. 1D). Specifically, increased usage of the most upstream AFE (AFE 1) was associated with increased usage of the most upstream ALE

[1]RNA Therapeutics Institute, University of Massachusetts Chan Medical School, Worcester, MA, USA. [2]Department of Biology, Boston University, Boston, MA, USA. [3]Department of Systems Biology, University of Massachusetts Chan Medical School, Worcester, MA, USA. [4]Howard Hughes Medical Institute, Chevy Chase, MD, USA. [5]Faculty of Computing & Data Sciences, Boston University, Boston, MA, USA. ***Corresponding authors. Email: anafisz@bu.edu (A.F.); athma.pai@umassmed.edu (A.A.P.)** †These authors contributed equally to this work. ‡These authors contributed equally to this work.

(ALE 1), AFE 2 usage positively correlated with ALE 2 usage, etc. Concordantly, we observed that usage of AFE 1 negatively correlated with usage of ALE 2, indicating a complex coupling relationship based on the ordinal positions of the terminal exons within genes. Restricting the analysis to genes that use exactly three AFEs and three ALEs confirmed this ordinal coupling pattern (Fig. 1D, inset), suggesting that not only are the number of terminal exons interconnected, but their usage is coupled as well. These findings indicate that gene architecture plays a pivotal role in determining coupling between terminal exons and thus regulating isoform diversity in genes.

PITA defines terminal exon coupling

The observed correlation of terminal exon usage could arise in one of two ways. Terminal sites may be directly coupled, whereby exons with similar ordinal positions co-occur on the same mRNA molecules (fig. S1D). Alternatively, coupling may be indirect, such that exons with similar ordinal positions are independently favored across transcripts, leading to apparent correlations in the short-read RNA-seq data. To distinguish between these possibilities and identify specific genes with coupled terminal end usage, we analyzed long-read isoform sequencing (Iso-Seq) data across human tissues and cells from the ENCODE Project (*38*, *39*) and evaluated whether terminal exons were coupled within the same molecules. Specifically, we wanted to quantify how often an mRNA that started at a particular TSS was likely to terminate at a PAS with a similar ordinal position. For example, after conditioning on full-length reads [methods, fig. S2; (*40*, *41*)], *MYO10* has 184 long mRNA reads in H9 cells, distributed across three TSSs and two primary PASs. Of the 128 reads that begin at the first TSS, 94% terminate at the first primary PAS and 59% of the remaining 56 reads, which start downstream of the first TSS, terminate at the second primary PAS (Fig. 2A). Thus, long reads from *MYO10* support direct coupling of terminal exons based on their ordinal position, consistent with evidence from short-read RNA-seq data. These observations support the existence of an

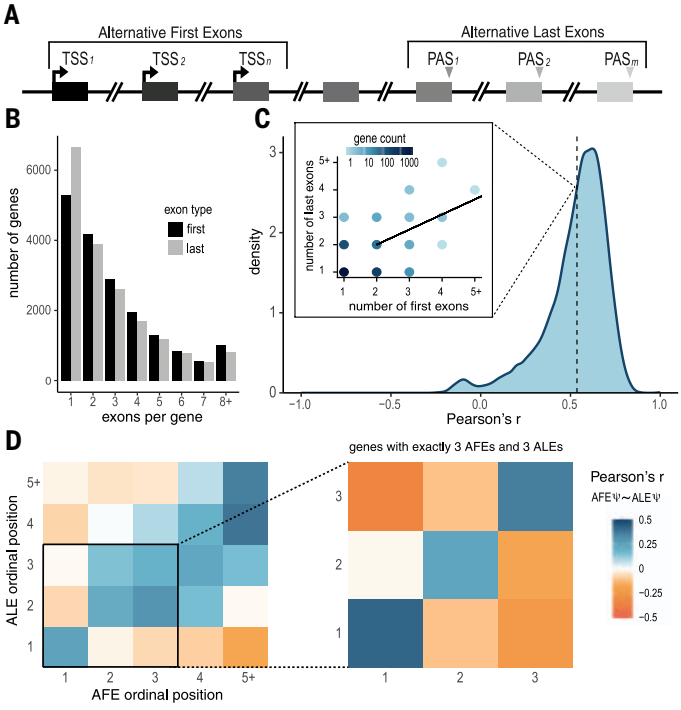


Fig. 1. A positional relationship between sites of mRNA initiation and termination in human genes. (**A**) Schematic of a gene with alternative start and end sites. AFEs (black/dark gray) and their respective TSSs are shown on the left and the ALEs (light gray) and their respective PASs are shown on the right. Exons are numbered by the order in which they appear in the direction of transcription (ordinal position). (**B**) The total number of protein coding genes (*y*-axis) that use a given number of annotated AFEs (black) or ALEs (gray), aggregated across all GTEx tissues. (**C**) Distribution of Pearson's r between the number of expressed AFEs and ALEs per gene in all GTEx samples (n = 17,350; mean r = 0.53). Inset shows a representative ovary sample, marked by the dashed line of the distribution plot, in which genes expressing n AFEs (*x*-axis) and n ALEs (*y*-axis) are depicted. Color intensity represents the number of genes exhibiting each unique AFE–ALE count combination. The trend line (black line) reflects the correlation between the number of expressed AFEs and ALEs in genes using multiple AFE and ALEs (Pearson's r = 0.55, *P*-value = 1.85×10^{-8}). (**D**) Heatmap of Pearson's r for pairwise correlations between the relative usage (Ψ) of AFEs and ALEs based on their ordinal position for genes with multiple first and last exons (left panel, n = 1,560,899 exons) and genes with exactly three AFEs and three ALEs (right panel, n = 63,811 exons).

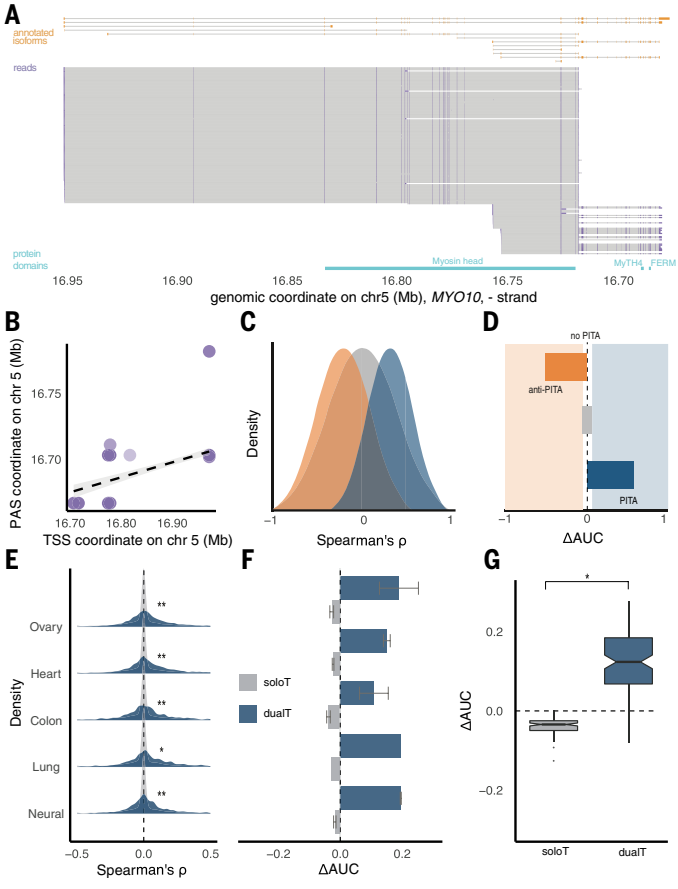


Fig. 2. Positional coupling of TSS-PAS usage occurs within individual mRNA molecules. (**A**) Annotated isoforms (top, orange), a subset of LRS reads (middle, purple with introns in thin black lines), and annotated protein domains (bottom, light blue) in H9 cells for MYO10. (**B**) Correlation between LRS read start (*x*-axis) and end coordinates (*y*-axis) for MYO10 (Spearman's ρ = 0.66). (**C**) Schematic of expected genome-wide distributions for Spearman's ρ showing possible shifts toward negative correlations (orange, anti-PITA), positive correlations (blue, PITA), or an unbiased distribution (gray, no PITA) using fictional data. (**D**) Schematic of expected ΔAUCs for the categories outlined in (C). ΔAUC is defined as $AUC_{\rho>0}$ to $AUC_{\rho<0}$. Distribution of Spearman's ρ (**E**) and the mean ΔAUC across samples (**F**) for solo termini genes (soloT, gray) and dual alternative termini genes (dualT, blue) in five human tissue types. K-S test, **P*-value < 10^{-8}; ** *P*-value < 10^{-16} for (E). (**G**) Distribution of ΔAUC values across 109 LRS samples for soloT (gray) and dualT genes (blue). *t*-test **P*-value < 10^{-16}.

intramolecular regulatory paradigm that we call PITA, which underlies the coupling of transcription initiation and CPA decisions.

To evaluate the extent to which intramolecular coupling of ordinal terminal exons occurs globally, we estimated a Spearman's ρ to look at the rank correlation between TSS and PAS positions across reads within a gene. *MYO10* has a Spearman's ρ of 0.66 (Fig. 2B). Since rank corresponds to the ordinal position across terminal sites, positive correlations indicate ordinal coupling (PITA) whereas negative correlations indicate coupling of exons according to inverse ordinal position (anti-PITA) (schematic of possible distributions shown in Fig. 2C). We then used area under the curve (ΔAUC) to quantify whether the distribution of Spearman's ρ per sample shifted away being centered around zero (methods), in which positive or negative ΔAUCs would again indicate genome-wide enrichments of PITA or anti-PITA genes, respectively (schematic of possible ΔAUCs shown in Fig. 2D).

When looking at genes that use multiple first exons and multiple PASs within a cell type [dual alternative termini (dualT)], we observed substantial enrichments of PITA genes across multiple human cells and tissues (shown for five tissues in Fig. 2, E and F). We considered genes that use only one first exon or one PAS within each sample [solo termini (soloT)] as a control that accounts for variability in long read start and end coordinates (fig. S3A) and observe that these genes consistently show weakly negative ΔAUCs, indicating that our observations are not due to biases in the metric or identification of terminal ends from long reads. These trends are also not biased by read depth (fig. S3B), gene expression (fig. S3C), read thresholds (fig. S3D), read length (fig. S3F), or other spurious correlations in the data (assessed with permutations, fig. S3E). Notably, the ΔAUCs are even more biased toward positive values when we calculated Pearson correlations using ordinal positions of sites rather than genomic coordinates of reads (fig. S3, G and H) and the enrichment remains across different thresholds for calculating the ΔAUC (fig. S3I). On average, the distribution of PITA coupling across genes is more similar between replicates than nonreplicates (fig. S3J). Finally, we observe a similar enrichment of PITA genes when we use data from orthogonal experimental approaches [transcript isoform sequencing (TIF-seq) and complementary DNA–polymerase chain reaction (cDNA-PCR) Nanopore sequencing datasets; fig. S4]. Overall, we observe that 80% of samples show evidence for greater than expected PITA coupling, with a 3 to 14% enrichment of PITA genes coupling across 109 Iso-Seq samples from 47 tissues and cell types (Fig. 2G) corresponding to 58 to 460 genes using conservative thresholds (methods). Together, our results suggest that there is direct coupling of terminal exon usage and we can identify genes that are enriched for coupled terminal exon usage. This relationship is biased toward coupled usage of terminal exons with similar ordinal positions in a gene (Fig. 3A).

PITA is independent of tissue-specific mRNA regulation

mRNA terminal ends are often regulated across tissues, with abundant tissue-specific usage of both TSSs and PASs. Indeed, 83% of genes expressed in the long-read dataset are regulated in a tissue-specific manner, such that they use distinct isoforms across tissues. It is also known that tissue- or context-specific regulation of alternative TSSs or PASs results in global shifts toward preferential usage of upstream or downstream sites (*20*, *42*–*46*). Even among dualT genes, there is usually one predominant isoform expressed, likely due to tissue-specific regulation of isoform usage and gene expression. When we control for this differential isoform usage and gene expression, the enrichment of PITA genes increases (9 to 23% enrichment; fig. S3B). Thus, PITA coupling within dualT genes is likely not a byproduct of global tissue-specific signatures, but rather an independent driver of full-length isoform usage. To investigate this regulatory paradigm further, we asked whether genes that show strong tissue-specific regulation of terminal sites also show PITA coupling across tissues. Specifically, we looked at genes that use unique termini within tissues but alternative TSSs and alternative PASs across tissues (tissue-dualT). For example, *DNJC11* expresses distinct TSSs and PASs across lung, induced pluripotent stem cells (iPSCs), and astrocyte cells (Fig. 3B). However, across cell types there is a significant correlation of *DNJC11* TSS and PAS usage, with the expressed isoforms showing a preference for PITA coupling (Spearman's $\rho = 0.92$). Using a tissue-ΔAUC metric in which Spearman's ρ is calculated using reads across tissues for tissue-dualT genes (methods), we observe an enrichment of PITA coupling that is stronger than that observed in most individual tissues (17 to 19% enrichment; Fig. 3C) corresponding to 982 genes showing cross-tissue PITA regulation. This observation suggests that PITA coupling is a pervasive phenomenon in which the coordination of transcript starts and ends might be influenced by gene architecture even when only one isoform is expressed per tissue or constitutively expressed within a cell type.

The preferential usage of PITA isoforms may enable the regulation of RNA or protein features related to the positioning of elements within a gene. For instance, if PITA coupling allows for the regulation of isoforms with specific functional significance, then PITA genes may show conserved features specifically at the terminal ends of transcripts. Consistent with this, the upstream and downstream TSS and PAS regions for dualT genes with PITA coupling are more conserved than similar regions for non-PITA or anti-PITA dualT genes (Fig. 3D). Furthermore, genes expressing PITA isoforms more often encode for a greater variety of protein domains than anti-PITA or non-PITA genes (methods, Fig. 3E), despite all of these genes containing similar numbers of domains on average (fig. S5, A and B). For instance, *MYO10* PITA isoforms starting at the upstream TSS are able to encode a myosin head domain whereas PITA isoforms starting at the downstream PAS are able to encode MyTH4 and FERM domains (Fig. 2A, bottom track). Together, these observations suggest that PITA coupling may help to shape mRNA function or proteome diversity through coordinated exon usage across the terminal ends of an isoform. Notably, we do not observe either increased conservation or protein domain diversity for genes with intertissue PITA coupling (fig. S5, C and D), suggesting that all tissue-dualT genes may already be under stronger functional constraints due to cell type–specific isoform regulation (*18*, *21*, *47*).

Alternative first exon usage directly influences last exon usage

These correlative analyses suggest a potential causal relationship between the ordinal, coupled usage of TSSs and alternative PASs. To directly test this, we used dCas9-CRISPR activation or interference approaches to perturb 27 specific AFEs across 16 genes. We achieved specific activation or repression for eight AFEs, and six of these perturbations changed downstream ALE expression in a manner consistent with PITA coupling. For example, activating AFE1 of *ZNF638* led to an increase in the expression of ALE1 and a concurrent decrease in the expression of both AFE2 and ALE2 (Fig. 3F, left). Similarly, activating AFE1 of *TP53* caused a comparable increase in the expression of ALE1, with no substantial changes in the expression of AFE2 or ALE2 (fig. S6A). Activation of AFE2 had similar effects for three genes: Activating AFE2 of the *MAST1* gene resulted in increased expression of ALE2 whereas both AFE1 and ALE1 decreased (Fig. 3F, middle) and activation of AFE2 in both *SYT9* and *LEPR* predominantly increased expression of ALE2 (fig. S6, B and C). Finally, repressing AFE2 of *SWI5* reduced the expression of ALE2 without considerably altering the expression of AFE1 or ALE1 (Fig. 3F, right). These results provide direct evidence that AFE choice can regulate ALE expression, supporting a model in which terminal exon usage is coordinated in an ordinal and functionally coupled manner.

Notably, perturbing the usage of PAS elements did not induce changes in AFE usage that are consistent with PITA coupling. Upon deletion of the downstream ALE in *ZNF638* [392 nucleotides (nt), fig. S6D], we observe substantial reductions in the expression of both ALE1 and ALE2 but a major increase in the expression of AFE1 (fig. S6E). This result

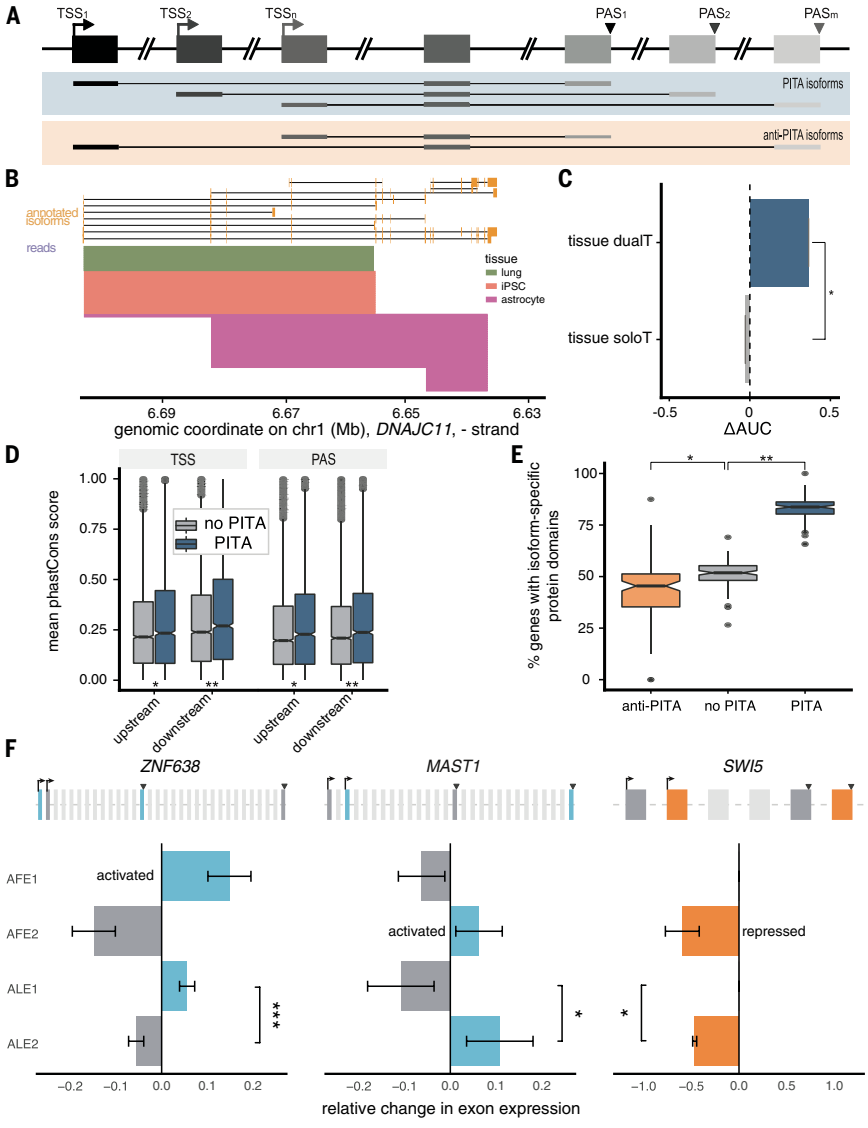


Fig. 3. Transcription start sites directly regulate transcript end site usage to govern the expression of functionally distinct isoforms. (**A**) Schematic of mRNA isoforms based on PITA classification. PITA isoforms preferentially use TSSs and PASs that are ordinally similar (light blue) whereas anti-PITA isoforms preferentially use ordinally different TSSs and PASs (light orange). (**B**) Annotated mRNA isoforms (orange) and a randomly subsampled proportion of reads for DNAJC11 in lungs (green), iPSCs (pink), and astrocytes (purple). (**C**) ΔAUC values for genes with dual alternative termini across tissues. Error bars represent standard error across 100 samples of reads across tissues. *t*-test **P*-value < 10^{-16}. (**D**) Conservation scores (mean phastCons score, *y*-axis) in a 400-nt region around each terminal site of the two most highly expressed isoforms for genes with dual alternative termini. K-S test **P*-value < 10^{-3}; ***P*-value < 10^{-7}. (**E**) Percentage of dual alternative termini genes (*y*-axis) whose isoforms overlap different annotated protein domains. *t*-test **P*-value < 10^{-7}; ***P*-value < 10^{-16}. (**F**) CRISPR modulation of a given first exon drives concordant changes in the corresponding last exon of the same ordinal position in three protein-coding genes expressed in HEK293T-A2 cells. Changes in exon expression were quantified relative to control samples (methods). Error bars depict the standard error of means. The *t*-test measured whether the corresponding last exon of the same ordinal position exhibited a larger directional change than the noncorresponding last exon. CRISPR activation of *ZNF638* AFE1 resulted in an increase in ALE1 (left); CRISPR activation of *MAST1* AFE2 resulted in an increase in ALE2 (middle); and CRISPR interference of *SWI5* AFE2 resulted in a decrease in ALE2 (right). **P*-value < 0.05, ***P*-value < 0.01, ****P*-value < 0.001.

indicates that PAS perturbations can influence AFE usage but that these regulatory effects are not involved in PITA coupling. These findings suggest that PITA represents a unidirectional regulatory mechanism by which alternative TSSs influence ordinally paired alternative PAS usage, but PAS usage does not drive PITA coupling.

PITA coupling depends on gene length

PITA coupling suggests that the architectures of genes are configured to enable coregulation of transcript start and end sites. This coupling involves long-distance coordination across transcription initiation and polyadenylation sites that are often separated by thousands to hundreds of thousands of base pairs in DNA space and hundreds to thousands of nucleotides in pre-mRNA space. Thus, we first evaluated whether the DNA or RNA distance between these sites was correlated with the strength of PITA coupling across genes. PITA coupling is more likely to occur in longer genes, defined as the total genomic length between the upstream most-expressed TSS and downstream most-expressed PAS (Fig. 4A). However, PITA coupling is not associated with the pre-mRNA length of the resulting isoforms (Fig. 4A) or the mRNA lengths of the isoforms expressed (estimated by average read length, methods and fig. S7A). This observation suggests that PITA coupling may be driven by transcriptional or co-transcriptional mechanisms and regulatory decisions.

A gene can be broken down into many regions, all of which contribute independently to the total length of a gene. To understand how the length of a gene may influence PITA coupling, we calculated the lengths of the regions involved in transcriptional regulation (interval between TSSs), in splicing regulation (interval between downstream-most TSS and upstream-most PAS), and in cleavage and polyadenylation regulation (interval between PASs). We find that both the TSS and PAS intervals are strongly associated with PITA, with longer intervals between alternative TSSs and alternative PASs leading to stronger PITA coupling (Fig. 4B). However, the length of the internal pre-mRNA interval is mostly not associated with the strength of PITA coupling, except for long genes in which the increased number of alternative TSSs and PASs limits the lengths of internal pre-mRNA intervals. To understand whether the TSS and PAS intervals were directly associated with PITA regulation, we used a comparative genomics approach and treated evolutionary changes as natural perturbations that vary gene length. Using Iso-Seq data from mouse tissues matched to the human tissues analyzed [ENCODE (*38*, *39*); methods], we identified species-specific PITA genes as described above (fig. S7, B and C). We find that genes only showing PITA coupling in human cells are, on average, significantly longer in the human genome than in the mouse genome and correspondingly, mouse-specific PITA genes are significantly longer in the mouse genome [Kolmogorov-Smirnov (K-S) test *P*-value < 0.001; Fig. 4C and fig. S7D]. Genes that show no PITA coupling in either species do not vary in gene length. This pattern of species-specific PITA genes having longer genomic intervals in the PITA species also holds for TSS and PAS intervals. The opposite is also true as genes with the largest difference in gene length or TSS and PAS interval lengths between species are enriched for species-specific PITA genes in species with longer lengths (fig. S7E). Together, these observations suggest that the strength of PITA coupling is directly associated with longer genomic distances.

Since PITA coupling shows a relationship with both TSS and PAS intervals, we wanted to understand whether certain genes were more

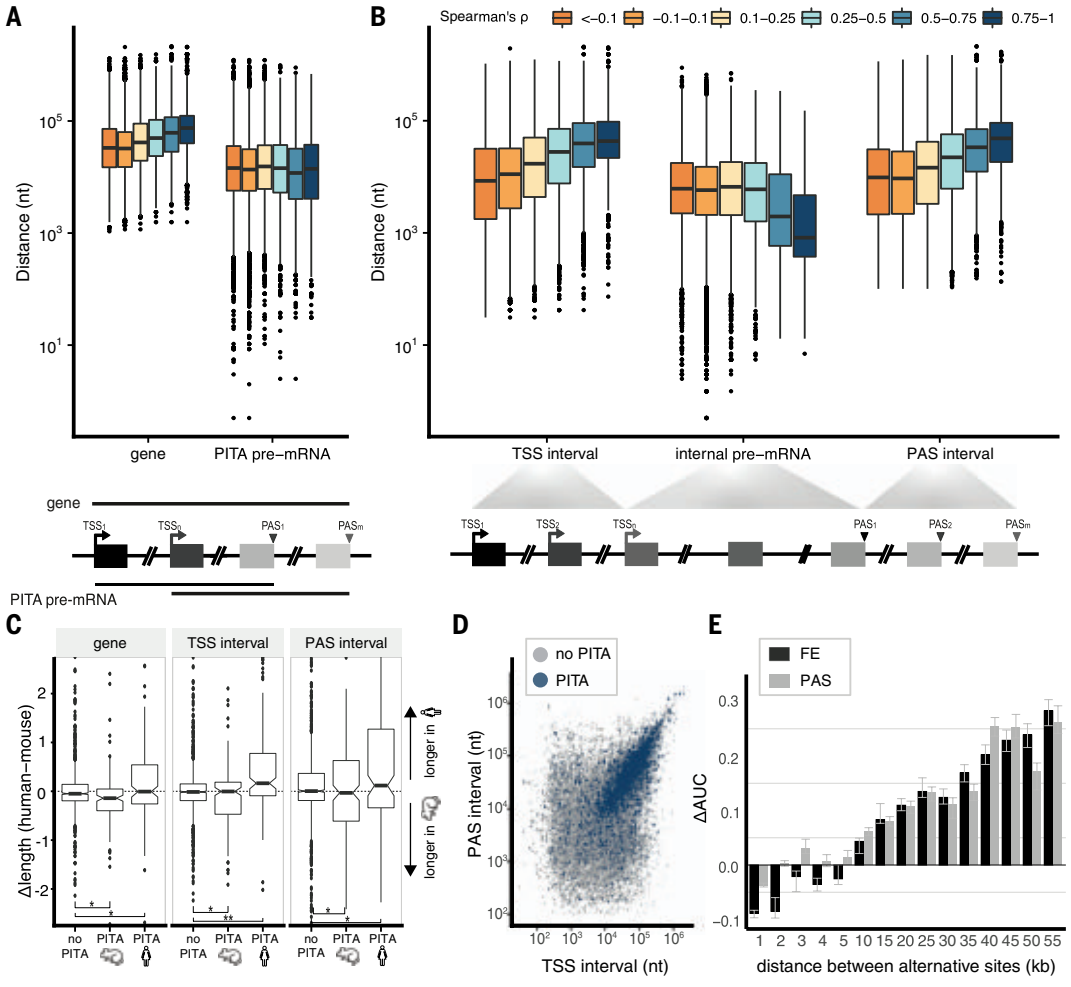


Fig. 4. PITA occurs more often in longer genes. (**A**) Distribution of the lengths (*y*-axis) of dual alternative termini genes (left) and PITA pre-mRNAs (right) for genes within bins of Spearman's ρ values (colors). (**B**) Distribution of the maximum distances (*y*-axis) between TSSs (left), the downstream-most TSS and upstream-most PAS (internal pre-mRNA, middle), and PASs (right) for dual alternative termini genes within varying bins of Spearman's ρ values (colors). (**C**) Distribution of the change in feature lengths between human and mouse orthologs (*y*-axis) for genes that are not PITA in either species, PITA only in mice, or PITA only in humans. To account for global differences in gene lengths between species, distances were first normalized by the mean distance within each species for each feature. K-S Test $*P$-value $< 10^{-3}$; $**P$-value $< 10^{-7}$. (**D**) Correlation between the TSS intervals (*x*-axis) and PAS intervals (*y*-axis) for dual alternative termini genes non-PITA genes (gray, Spearman's $\rho < 0.3$, Pearson's $r = 0.59$; P-value $< 2.2 \times 10^{-16}$) and PITA genes (blue, Spearman's $\rho \geq 0.3$, Pearson's $r = 0.82$; P-value $< 2.2 \times 10^{-16}$). (**E**) ΔAUC values binned by distances between FEs or PASs (black and gray, respectively) across pairwise comparisons between mRNA isoforms. Error bars represent bootstrapped 95% confidence intervals (CI).

likely to show an association with TSS intervals and others with PAS intervals. Given our initial observation that genes are more likely to have similar numbers of first and last exons and a correlation between gene length and terminal interval length (fig. S8, A and B), we first asked whether genes are also more likely to have similar transcription and CPA region intervals. Although TSS and PAS intervals are weakly correlated globally (Pearson's r = 0.59), this correlation is even stronger for PITA genes (Pearson's r = 0.82; Fig. 4D). The change in TSS interval length between human and mouse is also significantly correlated to the change in interspecies PAS interval length for human- and mouse-specific PITA genes (fig. S8C). Finally, we asked if there was a minimum distance between alternative sites at which PITA coupling is more likely to occur. PITA coupling is enriched when any two alternative TSSs or PASs are separated by at least 5 kb, regardless of whether the alternative PASs are present on the same exon or different exons (Fig. 4E and fig. S8D). Together, these observations suggest that there are selective pressures to coordinate the lengths of genomic regions that are involved in the regulation of alternative transcription and CPA.

Distinct promoter regions and 3D architecture around PITA-coupled TSSs and PASs

The association between PITA coupling and the lengths of genomic intervals suggests that PITA may be driven by mechanisms related to transcriptional regulation of PITA genes, including the relative positioning of regulatory elements at the beginning of genes (*34*). We hypothesized that alternative TSSs may have distinct regulatory patterns in PITA genes. To test this, we used ultradeep data from human embryonic stem (H1-ESC) and foreskin fibroblast (HFF) cells [4D Nucleome (*48*)] to estimate the positioning and strength of several promoter-defining marks such as chromatin accessibility, H3K4me3, CTCF binding, and 3D chromatin characteristics (measured by insulation strength from micro-capture (micro-C) data indicative of boundaries between structural chromatin domains). Upstream TSSs in both PITA and non-PITA genes are characterized by high chromatin accessibility, strong insulation, and well-positioned H3K4me3 and CTCF patterns (figs. S9A and S10A), regardless of the absolute or relative expression of the TSS. However, the presence of insulation and promoter-defining marks at downstream TSSs is correlated with the

relative usage of the TSS. This is especially true for signatures of chromatin domains, in which major TSSs (PSI > 0.5), including downstream TSSs, have equally strong insulation in both non-PITA and PITA genes whereas minor TSSs have insulation in PITA genes but not in non-PITA genes (figs. S9B and S10B). PITA genes also appear to have an additional insulation subdomain across the TSS interval, bounded by the upstream-most and downstream-most TSS (figs. S9C and S10C). By contrast, insulation at PASs appears to be less precisely positioned—likely because PASs are less well defined and more variable than TSSs between cells (*29*, *49*)—and therefore more difficult to capture at the same resolution as TSSs, as shown before (*50*). Together, these observations suggest that alternative TSSs in PITA genes may have distinct chromatin conformations that could facilitate downstream transcriptional dynamics.

Finally, we used ultradeep micro-C data (*48*, *51*) to investigate whether there is any evidence for specific localized physical interactions between the terminal ends of PITA or non-PITA genes and/or whether PITA genes display more global differences in chromatin conformation at the level of chromatin domains and domain boundaries, as compared with non-PITA genes (methods). To confidently distinguish signals across individual sites, these analyses were limited to ~150 and ~60 extremely long non-PITA and PITA genes, respectively, with at least 2.5 kb between alternative TSSs and PASs and a minimum gene length of 8 kb (methods). Previously, it has been shown by Hi-C that active TSSs and PASs display insulation (*32*): These loci prevent long-range chromatin interactions across them, leading to the formation of structural chromatin domains containing active genes from start to end, and demarcated by insulating boundaries (*32*, *34*, *50*, *52*). Consistently, we found that both non-PITA and PITA genes form structural domains defined across the entire gene, with insulation boundaries at upstream TSS and downstream PAS (figs. S9D and S10D). In addition, aggregate analyses suggest that PITA genes might form multiple overlapping structural domains whose boundaries are defined by relationships between the upstream TSS–upstream PAS and downstream TSS–downstream PAS pairs (figs. S9D and S10D), which could reflect or reinforce relationships between mRNA initiation, termination, and isoform expression.

RNAPII elongation rates mediate the relationship between mRNA ends

The length of a gene influences the total distance that RNAPII must travel to transcribe full-length mRNAs. The increased time necessary to transcribe these longer genes, with greater spacing between TSSs or PASs, may also create a coupling between transcriptional dynamics and the choice of alternative RNA processing sites. To test whether altered RNAPII elongation rates could directly influence PITA coupling, we analyzed publicly available RNA-seq data from human cells overexpressing RNAPII mutants that elongate either slower or faster than wild-type (WT) RNAPII, paired with a control line (Fig. 5A) (*53*). Although the slow RNAPII markedly disrupted the

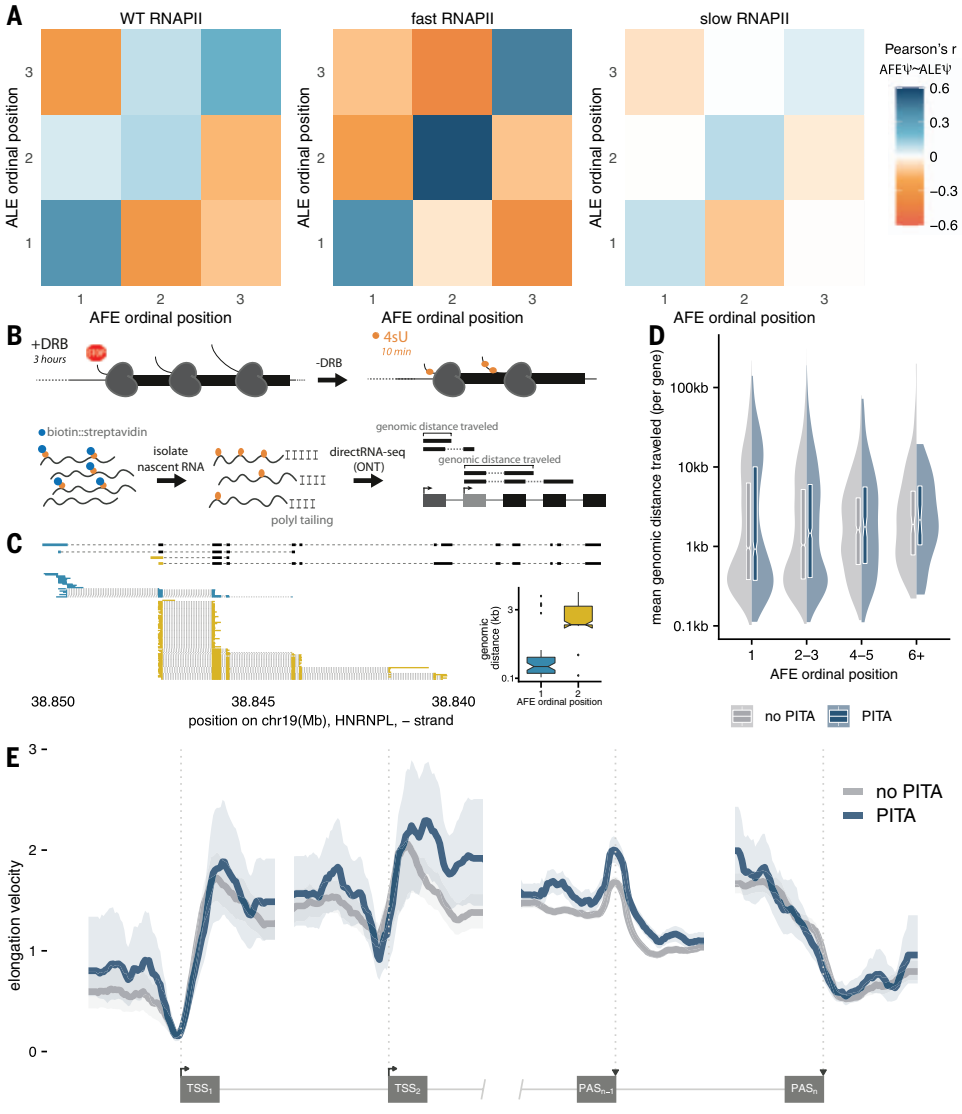


Fig. 5. RNA polymerase II elongation rate is associated with PITA. (**A**) Heatmaps of Pearson's r values for the pairwise correlations between the relative usage (Ψ) of a gene's AFEs and ALEs based on their ordinal position in HEK293T-A2 cells expressing for WT RNAPII (left, $n = 49$), rapidly elongating RNAPII (middle, R749H mutation, $n = 69$) and slowly elongating RNAPII (right, E1126C mutation, $n = 62$). All heatmaps show pairwise correlations for genes expressing exactly three AFEs and three AFEs. (**B**) Schematic of the 4sU-DRB-LRS protocol, which involves transcription blockage and then synchronization with DRB, followed by labeling of nascent RNA with 4sU for 10 min, then long-read library preparation using polyl tailing to facilitate direct RNA LRS. The bottom right schematic shows the estimation of genomic distances that the reads map to, which reflects the distance that RNAPII traveled from each TSS in the labeling period. (**C**) Direct RNA-seq for HNRNPL from long-read 4sUDRB-seq data in K562 cells. Shown are annotated isoforms (top, black) and LRS reads (middle, introns represented by thin gray lines) colored by whether they start in the first expressed AFE (blue) or the second expressed AFE (yellow). Inset shows the distributions of genomic distances across reads for each AFE. (**D**) Distribution of mean genomic distances for each gene, conditioned on reads starting in AFEs with increasing ordinal positions for no PITA (gray) and PITA genes (blue). Boxes show the median and 5 to 95% CI for each distribution. (**E**) Distribution of elongation velocities around upstream and downstream TSSs (left) and PASs (right) for no PITA (gray) and PITA (blue) genes. Elongation velocities are calculated using 50-nt bins across ± 5-kb windows around each site and smoothed with a sliding window approach for visualization (methods). Background density represents the CIs across genes.

correlated usage of ordinally similar terminal exons relative to the WT cells, the rapidly elongating RNAPII strengthened the enrichment of PITA coupling. This observation was consistent in an edited mouse cell line expressing the slow RNAPII mutation (fig. S11A) (*54*). This suggests that RNAPII elongation rates are crucial for coupling TSS-PAS interactions in long PITA genes.

To estimate gene-specific rates of RNAPII elongation, we used the ratio of transient transcriptome sequencing [(TT-seq), quantifying transcribed RNA] to mammalian native elongating transcript sequencing [(mNET-seq), quantifying actively transcribing RNAPIIs] data in K562 cells to calculate RNAPII elongation velocities, as described before (*55*, *56*). As has been observed previously (*57*), we observe that longer genes have faster RNAPII elongation velocities. Although PITA genes have significantly faster overall RNAPII elongation velocities relative to both non-PITA and anti-PITA genes (methods; K-S test P-value $< 1 \times 10^{-15}$, fig. S11B), they are not transcribed faster, on average, than expected based on their length (fig. S11C). When we look across different regions of the gene, however, we observe that PITA genes have increased elongation velocities in the middle of the gene body relative to non-PITA genes (fig. S11D).

These results suggest that long PITA genes may be elongated at an optimal rate that is crucial for enabling sustained RNAPII processivity until the end of the gene. Previous work has suggested that faster elongation rates lead to a global increase in the usage of more downstream PASs (*29*, *58*, *59*). Since PAS strength progressively increases across a gene body [i.e., upstream PASs are weaker than downstream PASs (*60*)], this is consistent with the "window of opportunity" model in which faster synthesis favors usage of stronger sites when weaker and stronger sites are in competition. Downstream PASs are stronger than upstream PASs in both PITA and non-PITA genes (fig. S11E). PITA coupling between TSSs and PASs suggests that alternative TSSs may have different elongation rates and, if the rate of elongation at the beginning of mRNA synthesis remains consistent throughout the gene, this may influence PAS usage at the 3′ end. Specifically, we hypothesized that RNAPII starting at downstream TSSs may elongate faster to promote usage of downstream PASs in PITA genes.

To estimate TSS-specific RNAPII elongation rates, we combined the previously described 4-thiouridine-DRB (4sUDRB-seq) (*61*) approach with long-read sequencing (LRS) of nascent RNA (Fig. 5B and methods). With this approach, we can infer TSS-specific elongation rates by estimating the distance that individual RNAPII molecules travel after transcription initiation using the total genomic distance between the read start and end coordinates. The mean distance that RNAPII molecules elongate from each TSS in the labeling period is highly correlated between two independent replicates (Pearson's r = 0.76, fig. S12A), providing confidence in the robustness of these measurements. Using these long read estimates, we asked about differences in elongation rate between TSSs within the same gene. For example, we observe that reads starting from the upstream TSS of *HNRNPL*, on average, map to a genomic distance of 821 nt whereas reads starting from the downstream TSS, on average, map to a genomic distance of 2606 nt (Fig. 5C). Globally, we observe that more downstream TSSs are associated with longer average genomic distances per gene and that this effect is more pronounced for PITA genes (Fig. 5D and fig. S12B). These results are consistent when performing LRS of cDNA and conditioning on the presence of a 5′ template switching oligo to obtain reads whose 5′ ends reflect TSSs with higher confidence (*40*) (fig. S12C).

Finally, to further characterize elongation rate differences between alternative sites, we again used elongation velocities across different regions of the gene. Although there is a minimal difference in elongation velocities between PITA and non-PITA genes around upstream TSSs, PITA genes are associated with higher elongation velocities at downstream TSSs (Fig. 5E). Promoter sequences do not appear to explain the faster elongation from downstream sites as these downstream promoters contain fewer core promoter elements (*62*) and are less likely to be predicted as active, especially in PITA genes (fig. S12, D and E). PITA genes also have higher elongation velocities around upstream PASs (Fig. 5E), likely leading to the reduced usage of these weaker PASs when RNAPII begins elongating from downstream TSSs. Our results indicate that the RNAPII elongation rate across a gene might be dependent on where the RNAPII started elongating. Specifically, downstream TSSs and upstream PASs are associated with faster RNAPII elongation rates, especially in PITA genes. Together, our observations indicate that a combination of spatial and kinetic mechanisms contribute to a relationship between pre-mRNA ends and ultimate expression of mRNA isoforms (Fig. 6).

Discussion

We observed widespread coordination between mRNA initiation and termination. A recent report in *Drosophila* tissues and human organoids showed that "dominant promoters" can be associated with usage of one or multiple polyadenylation sites (*7*). We find little overlap between PITA genes and genes with "dominant promoters" (fig. S4, B to D), suggesting that these regulatory paradigms may or may not be mutually exclusive.

Previous work has also shown intriguing associations between TSS, internal exon, and PAS usage (*1*, *4*, *14*, *63*). Biochemical and genetic evidence indicates that components of the splicing and CPA machinery, as well as auxiliary regulatory factors, are loaded onto the C-terminal domain of RNAPII at the time of transcription initiation to facilitate co-transcriptional RNA processing (*11*, *64*, *65*). Transcription and co-transcriptionally loaded factors can also influence splicing (*66*, *67*), the recruitment of transcription factors (*68*, *69*), and the usage of premature PASs (*8*). Studies have found connections between skipped exons and either TSSs or PASs over evolutionary timescales (*5*, *70*), cancer, cellular transitions (*31*), and across tissues (*7*, *14*). Our observations of direct TSS-PAS coupling add to this complex and coordinated regulatory landscape driving isoform usage. Although preliminary evidence points to the possibility of interconnections between skipped exon usage and TSS-PAS coregulation (*7*), it remains to be seen to what extent PITA coupling also drives the composition of internal exons in an isoform.

Despite past and present work, it remains unclear what molecular forces drive these correlations. Previous studies have suggested that transcriptional enhancers and elongation factors contribute to the regulation of alternative PASs by binding to upstream enhancer elements (*71*) or by playing a role in recruiting PAS machinery (*11*). However, these features do not explain the pairing of TSS-PAS sites in an

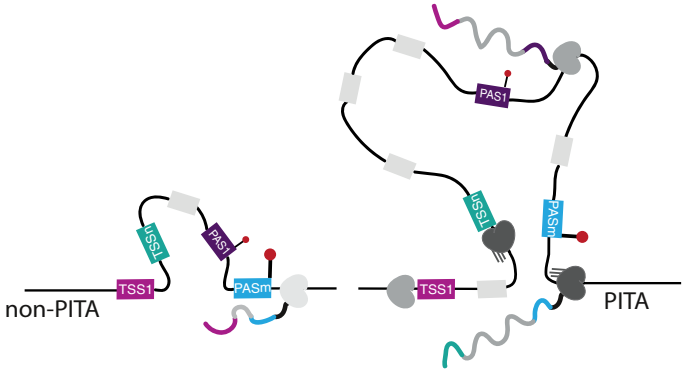


Fig. 6. Spatial organization and kinetic mechanisms drive the ordinal coupling of mRNA initiation and termination in PITA genes. Our results support a model in which longer PITA genes (right) exhibit faster elongation rates when transcription initiates at downstream TSSs. Faster RNAPII trafficking persists through upstream weaker PASs, leading to skipping of these sites in favor of downstream stronger PASs.

ordinal fashion across a gene. Consistent with our observations, previous literature has suggested the involvement of chromatin domains in constraining RNAPII directionality (*72*), particularly by insulation domains that encompass an entire gene.

We show that the rate of RNAPII elongation is dependent on where transcription begins and that downstream TSSs are associated with faster rates of RNAPII elongation, especially for longer PITA genes. This is consistent with our previous work showing stronger activity in downstream promoters, despite weaker promoter sequences (*62*). Our results suggest a model by which RNAPII molecules starting at downstream TSSs elongate faster throughout the gene and are more likely to reach a downstream PAS. This aligns with the "window of opportunity" model for RNA processing and suggests the existence of an optimal RNAPII elongation rate for RNA processing events (*53*). Although the window of opportunity model is classically used to describe the regulation of individual RNA processing sites on a pre-mRNA molecule, PITA coupling suggests that the expression of full-length isoforms may also be governed by differences in elongation rates within and across genes.

Our results also indicate that spatial organization and kinetic mechanisms jointly influence the coupled regulation of mRNA processing events across a gene. It is possible that these relationships exist to maintain efficient transcriptional environments and that PITA coupling is a by-product of these regulatory fluctuations. Insulated subdomains may structure chromatin to place specific regions within cellular subcompartments enriched for transcription and/or splicing machinery, which recent work has indicated may promote RNAPII processivity and recycling across multiple rounds of transcription (*33*, *73*–*76*). 3D architecture may be especially important for efficient CPA as it would bring RNAPII in contact with kinases that phosphorylate RNAPII to initiate transcription and elongation. The same phosphorylation marks are also necessary for CPA, but it has been seen that phosphorylation levels diminish across a gene (*9*), potentially setting an intrinsic limit on the productive elongation distance of RNAPII. However, our analyses are unable to infer any causality or directionality between these processes and so it is possible that chromatin conformations influence RNAPII processivity or recycling, or vice versa.

Recent evidence indicates that longer and more highly expressed genes in human cells are more likely to form cohesin-mediated extrusion loops that are bounded by transcription start and end sites (*33*). Thus, there might be a minimum genomic interval required between TSSs and between PASs to establish paired insulation across TSSs and PASs in mammalian genomes. However, it is unclear whether the first evolutionary determinant of PITA coupling is the regulation of terminal site usage, the distance between terminal sites, or the dynamics of RNAPII in the region. Our results would support the hypothesis that the change in genomic lengths across the gene would be accompanied by (and perhaps driven by) changes in RNAPII elongation rates.

PITA coupling represents paired mRNA 5′ and 3′ end usage that influences ultimate isoform compositions, adding complexity to the promoter-centric view of mRNA isoform regulation. This intricate interplay of gene regulatory mechanisms may be further modulated by tissue-specific factors that increase the specific usage of terminal sites. Understanding these and additional regulators of coupled mRNA terminal site usage will be key to revealing how cells fine-tune isoform expression and define their identities.

Materials and methods

Short-read RNA sequencing analysis

RNA-sequencing data from 17,350 tissue samples spanning 54 tissue sites from GTEx Version 8 were downloaded through dbGaP under study accession number phs000424.v8.p2. RNA-seq data from RNAPII mutant cell lines was downloaded from the NCBI Gene Expression Omnibus (GSE63375). RNA-seq data from mouse data was downloaded from the NCBI Gene Expression Omnibus (GSE127741). A detailed description of short read sequencing samples used can be found in table S1. For all short-read sequencing data, reads were mapped to genome assembly GRCh38.p14 for human or GRCm38.95 for mouse, using STAR v2.7.1a (*77*). Resulting bam files were processed using the HIT index pipeline to classify and quantify first and last exon usage (*35*). For exon classification, we utilized conservative parameters on all short read data analyzed, with a HIT_identity_parameters.txt file as follows: *# |HITindex| threshold for calling terminal exons [0.0, 1.0] HITterminal 1.0, # |HITindex| threshold for calling hybrid exons [0.0, 1.0] HIThybrid 0.5, # bootstrapping p-value threshold for HITindex significance [0.0, 1.0], HITpval 1, # confidence interval to use for HITindex significance (none, 0.75, 0.95, 0.95), HIT_CI none, # probability threshold for medium confidence with generative model [0.0, 1.0], prob_med 0.8, # probability threshold for high confidence with generative model [0.0, 1.0], prob_high 0.8.* Given the high sequencing depth in GTEx data, we raised the minimum threshold for the number of reads for confidence in HITindex classification ('—readnum' argument) to 10 for all GTEx samples.

PacBio long read sequencing analysis

Fastq files from PacBio reads were downloaded from the ENCODE Project data portal (https://www.encodeproject.org/) (*38*), including 113 human samples from 47 tissues and cell types and 130 mouse samples from 9 tissues (detailed in table S1). cDNA-PCR PacBio sequencing data for human organoids was downloaded from the Gene Expression Omnibus (GSE203583). LRS data was mapped to the hg38 human or mm38 reference genome using minimap2 (*78*) following the developers' recommended parameters: *-ax splice:hq -uf* and *-ax splice* for PacBio and cDNA-PCR reads respectively. Reads were divided into multiple split features to define exons using *bedtools bamtobed (79)* and assigned to overlapping genes. Only primary alignments and reads with all features assigned to the same gene were kept for downstream analyses. A detailed description of the long read sequencing samples can be found in table S1.

To retain full length reads, we then conditioned on reads whose 5′ end was within 20 nt of an empirically determined first exon identified in the full set of GTEx v8 samples (*36*) for human and a subset of ENCODE samples (*80*) for mouse, processed by the HITindex pipeline, and whose 3′ end was within 50nt of an experimentally verified human or mouse PAS in the polyASite 2.0 database (*81*). More than 80% of PacBio reads passed these filtering criteria (*40*). In addition, fully unspliced reads or reads whose 5′ and 3′ end mapped to the same exon were discarded.

TIF-seq analysis

Processed TIF-seq2 data containing the coordinates and counts of transcript start-end pairs from K562 cells was downloaded from the Gene Expression Omnibus (GSE140912). Each start and end site was intersected with all human genes and pairs which met the following criteria were retained for downstream analyses: (1) both termini aligned to the same gene, (2) the start feature was within 20 nt of an empirically derived first exon (as identified above), and (3) the end feature was within 50nt of an experimentally verified human PASs.

Identifying PITA genes

To identify PITA genes, only genes with at least 10 reads from PacBio Iso-seq and isoforms with at least 2 reads were considered. Genes were classified having dual alternative or solo termini by assessing the total number of first exon and polyA peaks used in each sample. Dual alternative termini genes were defined as those using at least two first exons and at least two polyA peaks, while solo termini genes were using only one first exon or polyA peak (but reads could exhibit variations in start and end coordinates, due to minor technical or biological fluctuations in the exact nucleotide positions defining the read boundaries, fig. S3A). All mapped reads per gene per sample were used to calculate a Spearman's

ρ between the start and end coordinates of the reads. Genes were classified as anti-PITA, no PITA or PITA using Spearman's ρ thresholds of $\rho \leq -0.2$, $-0.2 > \rho < 0.2$, or $\rho \geq 0.2$ respectively.

To quantify the enrichment of PITA genes, we first calculated an area under the curve for positive and negative Spearman's ρs using the *density.default* function in R to calculate AUCs using n = 512 and cut = 3. Only samples with more than 1000 genes were considered for the analysis. ΔAUCs were calculated by computing $AUC_{\rho>0} - AUC_{\rho<0}$.

Intertissue PITA genes

To identify intertissue PITA genes, we define tissue-dual alternative termini genes as those classified as solo termini in individual tissues. To avoid tissue-specific gene expression biases, we performed 100 sampling iterations, selecting two reads per isoform per gene per tissue-dual alternative termini, and then calculated the Spearman's ρ between the start and end coordinates of the reads for all the sampled reads across tissues. Genes were then re-classified as solo or dual alternative termini genes based on the number of first exons and polyA peaks used across tissues.

Calculating genomic distances

Genomic distances were calculated using estimated coordinates for first exons and polyA peaks (as described above) for the following intervals: (1) gene length: $PAS_n - TSS_1$, (2) pre-mRNA length of PITA isoforms: $PAS_1 - TSS_1$ and $PAS_n - TSS_n$, (3) TSS interval: $TSS_n - TSS_1$, (4) internal pre-mRNA interval: $PAS_1 - TSS_n$ only calculated when TSS_n is upstream of PAS_1, (5) PAS interval: $PAS_n - PAS_1$.

Identifying dominant promoters with the LATER pipeline

To identify dominant promoters as defined in Alfonso-Gonzalez *et al.* (*7*), the LATER pipeline (https://github.com/hilgers-lab/LATER) was applied to unfiltered human PacBio and cDNA-PCR samples following with recommended parameters (*7*). Genes were classified as having promoter dominance when promoter usage was higher than 0.2 and end dominance when PAS usage was higher than 0.6 (*7*).

Analysis of protein domains

Genomic coordinates for protein domains were obtained through the InterPro portal (*82*). Dual alternative termini genes were overlapped with the annotated protein domains. The proportion of genes in which different isoforms overlap different protein domains was calculated for the pre-mRNA regions of isoforms with support from more than 2 reads.

Conservation analysis

For conservation analyses, we considered the two highest expressed isoforms [most long-read sequencing (LRS) reads] from the tissue with the highest Spearman's ρ. Genes with Spearman's $\rho > 0.2$ were considered to be PITA genes and all others were used as a control set. The transcript start and end coordinates from the two isoforms were ordered by genomic position and the conservation in a 400 nt genomic region centered around each site was analyzed. Conservation scores were obtained by applying the *bigWigAverageOverBed* tool from *ucsctools* to extract the mean phastCons score for each region using a hg38 phastCons (100 mammal alignment) bigwig file downloaded from the UCSC database (*83*, *84*).

CRISPR-a and CRISPR-i experiments

HEK293T-A2 cells were cultured in Dulbecco's modified Eagle's medium (DMEM, Gibco #11965118) containing D-Glucose (4.5 g/L), L-Glutamine and 10% fetal bovine serum (FBS, Gibco #A31406-02) (*85*). Cells were seeded into 6-well plates and transiently transfected ~16 hours later, at ~80% confluency, using lipofectamine3000 (Invitrogen #L3000001). CRISPR activation experiments were carried out by transfecting empty UniSAM (Addgene #99866) vector as a control or UniSAM vector containing an sgRNA targeting the 400 bp region upstream of the intended first exon target (*86*). CRISPR interference experiments were carried out by transfecting a dCas9 vector (Addgene #159086) as a control, or the dCas9 vector containing an sgRNA targeting the 400 bp region downstream of the intended first exon target. All transfections consisted of 3 biological replicates. 48 hours post-transfection, total RNA was extracted using RNeasy Mini Kit (Qiagen #74104) according to the manufacturer's instructions. For *LEPR*, assessment of relative exon usage was performed using qPCR. Briefly, reverse transcription was performed in a reaction mix containing 1 μg of total RNA, using Maxima H Minus First Strand cDNA Synthesis Kit (Thermo Fisher Scientific, #K1652) according to the manufacturer's instructions. Quantitative PCR analyses were performed with SYBR green labeling (Thermo Fisher Scientific Maxima SYBR Green/ROX qPCR Master Mix (2X), #K0222) on the QuantStudio 5 Real-Time PCR System (Applied Biosystems #A28574). For the 7 remaining genes, relative exon usage was assessed from RNA-seq data, which was performed in two batches. For the first batch of genes (*SWI5*, *SYT9*, *TP53*, and control RNA), RNA was sequenced by first doing a polyA enrichment with the NEBNext® Poly(A) mRNA Magnetic Isolation Module (NEB #E7490L) followed by the NEBNext® Ultra II Directional RNA Library Prep Kit for Illumina (#E7760L). Libraries were sequenced on a NextSeq2000. For the second batch (*MAST1*, *ZNF638*, and control RNA), extracted RNA was sent to Novogene Corporation for polyA enriched mRNA library preparation and high-throughput sequencing on a NovaSeq 6000 with 150nt paired-end reads. Raw fastq files were processed as described in the short-read RNA sequencing analysis method section and analyzed using the HITindex pipeline to estimate relative terminal exon usage. Samples were compared to control RNA sequenced within the same batch. All gRNA oligos and qPCR primers for the CRISPR-a or CRISPR-i experiments are listed in table S2.

Estimating polyadenylation site strengths

APARENT2 (*60*) was used to estimate PAS strength for all reported human PAS in the polyASite 2.0 database (*87*) using a 200nt window centered about the middle of each peak and the pre-trained *aparent_all_libs_resnet_no_clinvar_wt_ep_5_var_batch_size_inference_mode_no_drop* model. Logits were calculated as $\ln\left(\frac{APARENT2\ score}{1-APARENT2\ score}\right)$.

Polyadenylation site deletion experiments

We ran APARENT2 as described above across the last exon of *ZNF638* to find the downstream most PAS. We designed two sgRNAs targeting the region flanking the PAS (one upstream and one downstream). Two hundred thousand HEK293T-A2 cells were electroporated using the Neon Transfection System (Thermo-Fisher #MPK5000) with 60pmol of sgRNAs plus 20pmol of SpyCas9. After three days, the cells were diluted to a limiting dilution of 0.25 cells per well to isolate individual clones. Each individual clone was validated using PCR and looking at the size of resulting products using capillary electrophoresis (fig. S6D). We selected the clone with the highest proportion of deleted alleles. Sequences for the sgRNAs and primers are available in table S2.

Analyses of micro-C and epigenetics data

Tier 1 micro-C ultradeep datasets for HFFc6 4DNFI9FVHJZQ and H1-ESC 4DNFI9GMP2J8 were downloaded from the 4DN Portal (*48*, *88*) as multi-resolution cooler files (*89*) and used for analysis of interaction landscapes around PITA and no PITA genes. Using HFFc6 and H1-ESCs PacBio data for genes with at least 10 reads and isoforms with at least 2 reads were considered. We selected the most upstream and downstream FE and polyA peak coordinates for genes using multiple FE and PAS. To ensure all selected sites could be clearly visualized on micro-C heatmaps at 500bp resolution, we only used PITA and non-PITA genes with a minimum distance of 2kb between all selected sites and a gene length of 8kb. We obtained 175 and 57 control and PITA genes, respectively, for H1-ESCs and 133 and 63 control and PITA

genes, respectively, for HFF. Average aggregated interaction profiles around genes (rescaled meta-gene pileups) were generated using coolpup.py (*90*) as follows: regions of interest were extended 100% up- and down-stream (flanking) and corresponding observed/expected matrices were extracted from microC (cooler-files) at 500 bp resolution, rescaled to 200*200 pixels, matrices corresponding to negatively stranded genes were "flipped", and averaged. Insulation profiles were calculated genome-wide for both microC datasets at 250 bp resolution using insulation window size of 2500 bp using *cooltools* (*91*) and stored as bigwig files. Stackups of relevant epigenetic features/tracks [insulation, ATAC-seq, H3K4me3 ChIP-seq, CTCF ChIP-seq (*51*)] were generated by extracting bigwig signal binned into 200 bins for each genomic interval ($TSS_{1,n}$, $PAS_{1,n}$ flanked with 7500 bp upstream and downstream) using pyBBI package (*92*) (https://zenodo.org/records/10382981). Insulation profiles for each genomic interval were normalized by subtracting mean flanking signal (50 upstream most and 50 downstream most bins) as in (*50*).

Calculation of RNAPII elongation velocities

TT-seq and mNET-seq datasets from K562 cells were downloaded from the Gene Expression Omnibus (GSE148433 and GSE159633, respectively, detailed in table S1). For both TT-seq and mNET-seq datasets, initial read trimming was performed using *cutadapt* (*93*) with parameters *–minimum-length 25*, *–quality-cutoff 25*, and *–overlap 12*. The adapter sequences -a AGATCGGAAGAGCACACGTCTGAACTCCAGTCA and -A AGATCGGAAGAGCGTCGTGTAGGGAAAGAGTGT were removed from TT-seq reads and -a TGGAATTCTCGGGTGCCAAGGAACTCCAGTCAC and -A AGATCGTCGGACTGTAGAACTCTGAAC were removed from mNET-seq reads. Both trimmed datasets were then aligned to the human reference genome GRCh38.v43 using STAR (*77*), with alignment parameters–*quantMode GeneCounts*, *–outSAMtype BAM SortedByCoordinate*, *–outFilterType BySJout*, *–outFilterMultimapNmax 1*, *–alignSJoverhangMin 8*, *–alignSJDBoverhangMin 1*, *–outFilterMismatchNmax 999*, *–outFilterMismatchNoverLmax 0.02*, *–alignIntronMin 20*, *–alignIntronMax 1000000*, and *–alignMatesGapMax 1000000*. Spike-in reads were aligned to the yeast reference genome S.cerevisiae.R64 and ERCC synthetic spiked-in sequences as described in (*94*), for the purpose of normalization of TT-seq counts and mNET-seq counts, respectively. RNAPII elongation velocities were calculated by dividing the amount of transcribed RNA (TT-seq coverage) by the density of transcribing RNAPII (mNET-seq reads), as described previously (*55*, *56*). For each gene, the mean elongation velocity across replicates was used for downstream analyses. Elongation velocities around alternative TSSs and PASs were estimated by calculating the mean enrichment and confidence intervals of TT-seq and mNET-seq reads in 100 bins across a 10 kb window centered on each TSS/PAS. Genes with (1) mean normalized read counts < 0.05 or > 0.95 and (2) less than 5 kb spacing between upstream and downstream TSSs or PASs were excluded from further analyses. Elongation velocity for each bin was calculated by dividing TT-seq signal by mNET-seq signal, and the distribution of elongation velocity across the region was smoothed using a sliding window approach with 10-bin windows before final visualization.

Estimation of TSS-specific elongation rates

K562 cells (ATCC #CCL-243) were grown at 37°C, 5% CO2 using Gibco RPMI-1640 medium (+ glutamine) (Gibco #11875119) supplemented with 10% heat-inactivated FBS (Thermo Fisher Scientific #A5256801) and Penicillin/Streptomycin (Gibco #15140122). Cells were treated cells with 100uM 5,6-Dichlorobenzimidazole 1-beta-D-ribofuranoside (DRB, Sigma Aldrich #D1916) for 3 hours. During the last 5 min of DRB treatment, 4-thio-uridine (4sU; ThermoFisher #J60679.MD) was added to a final concentration of 1mM (as described in (*61*)). After washing with PBS (Gibco #10010049), cells were resuspended in media containing 1mM 4sU for 10 min and spun down at 1000 RCF for 2 min in DNA low binding falcon tubes. The pellet was resuspended in Trizol (Thermo Fisher Scientific #15596018) and flash frozen in liquid nitrogen. RNA was extracted using Trizol-Chloroform and the aqueous phase was cleaned up using RNA Clean & Concentrator-100 columns (Zymo Research #R1019). 4sU pulldowns were performed with MTSEA biotin-XX (*95*), followed by RNAseH-based (Biosearch Technologies #H39500) ribosomal RNA depletion using custom probes targeted to mammalian rRNA sequences (*96*).

For direct RNA sequencing, polyinosine (polyI) tails were added as follows: 300ng of RNA was heated at 80C for 2 min, then mixed with a solution containing 0.5mM Tris-HCl pH 7 (Fisher Scientific #BP1756-100), 0.5 mM ITP (Sigma Aldrich #I0879-50MG), SUPERase. In 1 unit/ul (Invitrogen #AM2696), 2 ul of yeast polymerase and yeast polyA polymerase buffer (Thermo isher Scientific #74225Z25KU) and incubated at 37C for 40 min (as described in (*97*). The direct RNA nanopore library protocol (SQK-RNA004) was performed using manufacturer's instructions with one modification to replace the standard reverse transcription adapter (RTA) with a custom poly(C) splinted adapter (*97*). Libraries were sequenced on a GridION machine (GXB02310) with RNA flow cells (FLO-MIN00RA). rRNA reads were removed from fastq files using SortMeRNA (*98*) and the remaining reads were mapped to GRCh38.95 using minimap2/2.24 (*78*) with the following parameters: -ax splice -uf -k14. Uniquely aligned reads whose 5′ end overlapped an annotated AFEs and 3′ end did not overlap an annotated PAS peak were used for downstream analysis since they likely represent complete molecules that had not yet finished transcription. Genes with at least 10 reads and isoforms with at least 2 reads were retained for further analysis, as described above.

For cDNA sequencing, samples followed the same protocol as described above until polyI tailing. After polyI tailing, the RNA was reverse transcribed with the Takara Bio SMARTer® PCR cDNA Synthesis Kit (Takara Bio #634926) using a custom sequence for the 3′ end adapter [as described in (*99*)]: TGAGTCGGCAGAGAACTGGCGAANNNNNN-NNNNCCCCCCCCC. PCR was then conducted using the Takara Bio Advantage 2 PCR kit (Takara Bio #639207) and the custom PCR primer TGAGTCGGCAGAGAACTGGCGAA. The cDNA nanopore library protocol (SQK-LSK114) was used to prepare libraries that were sequenced on a GridION (GXB02310) machine using FLO-MIN114 flow cells (R10) (Oxford Nanopore Technologies #FLO-MIN114). Prior to rRNA read removal, fastq files were processed with Porechop (https://github.com/rrwick/Porechop) to identify and trim 5′ and 3′ adapters in the reads. To select for complete molecules, reads were retained only if they had the proper adapter at the 5′ end of the read. rRNA reads were removed as described above and remaining reads were mapped with minimap2/2.24 with these parameters: -ax splice. Downstream analysis steps were conducted as described above.

Promoter prediction, GC content, and CpG island analysis

K562 control RNA-seq data was downloaded from the Gene Expression Omnibus (GSE148433, under accession numbers SRR11521575 and SRR11521576). The data was processed using the HIT index pipeline to characterize multi-promoter genes and assign ordinal position to each promoter. To assess promoter properties, the sequences of expressed promoters were extracted from 275 nt upstream and 50 nt downstream of each transcription start site using the *bedtools getfasta* function. The iProEP promoter prediction algorithm was employed to predict the inherent presence of a promoter in the extracted sequences (*100*). The presence of CpG islands was determined using a 200 bp window moving across the extracted sequences. A CpG island was defined based on the observed/expected CpG value and a GC content greater than 50%, as described in Kim *et al.* (*62*).

REFERENCES AND NOTES

1. A. Joglekar *et al.*, Single-cell long-read mRNA isoform regulation is pervasive across mammalian brain regions, cell types, and development. bioRxiv 2023.04.02.535281 [Preprint] (2023); doi: 10.1101/2023.04.02.535281

2. T. W. Nilsen, B. R. Graveley, Expansion of the eukaryotic proteome by alternative splicing. *Nature* **463**, 457–463 (2010). doi: 10.1038/nature08909; pmid: 20110989
3. B. Tian, J. L. Manley, Alternative polyadenylation of mRNA precursors. *Nat. Rev.* **18**, 18–30 (2017). doi: 10.1038/nrm.2016.116; pmid: 20110989
4. S. Y. Anvar *et al.*, Full-length mRNA sequencing uncovers a widespread coupling between transcription initiation and mRNA processing. *Genome Biol.* **19**, 46 (2018). doi: 10.1186/s13059-018-1418-0; pmid: 29598823
5. A. Fiszbein, K. S. Krick, B. E. Begg, C. B. Burge, Exon-Mediated Activation of Transcription Starts. *Cell* **179**, 1551–1565.e17 (2019). doi: 10.1016/j.cell.2019.11.002; pmid: 31787377
6. S. A. Hardwick *et al.*, Single-nuclei isoform RNA sequencing unlocks barcoded exon connectivity in frozen brain tissue. *Nat. Biotechnol.* **40**, 1082–1092 (2022). doi: 10.1038/s41587-022-01231-3; pmid: 35256815
7. C. Alfonso-Gonzalez *et al.*, Sites of transcription initiation drive mRNA isoform selection. *Cell* **186**, 2438–2455.e22 (2023). doi: 10.1016/j.cell.2023.04.012; pmid: 37178687
8. D. Kaida *et al.*, U1 snRNP protects pre-mRNAs from premature cleavage and polyadenylation. *Nature* **468**, 664–668 (2010). doi: 10.1038/nature09479; pmid: 20881964
9. C. Laitem *et al.*, CDK9 inhibitors define elongation checkpoints at both ends of RNA polymerase II-transcribed genes. *Nat. Struct. Mol. Biol.* **22**, 396–403 (2015). doi: 10.1038/nsmb.3000; pmid: 25849141
10. L. Caizzi *et al.*, Efficient RNA polymerase II pause release requires U2 snRNP function Efficient RNA polymerase II pause release requires U2 snRNP function. *Mol. Cell* **81**, p1920–1934.e9 (2021). doi: 10.1016/j.molcel.2021.02.016; pmid: 33689748
11. T. Nagaike *et al.*, Transcriptional activators enhance polyadenylation of mRNA precursors. *Mol. Cell* **41**, 409–418 (2011). doi: 10.1016/j.molcel.2011.01.022; pmid: 21329879
12. Y. E. Guo *et al.*, Pol II phosphorylation regulates a switch between transcriptional and splicing condensates. *Nature* **572**, 543–548 (2019). doi: 10.1038/s41586-019-1464-0; pmid: 31391587
13. S. A. Shabalina, A. Y. Ogurtsov, N. A. Spiridonov, E. V. Koonin, Evolution at protein ends: Major contribution of alternative transcription initiation and termination to the transcriptome and proteome diversity in mammals. *Nucleic Acids Res.* **42**, 7132–7144 (2014). doi: 10.1093/nar/gku342; pmid: 24792168
14. E. T. Wang *et al.*, Alternative isoform regulation in human tissue transcriptomes. *Nature* **456**, 470–476 (2008). doi: 10.1038/nature07509; pmid: 18978772
15. A. R. Forrest *et al.*, A promoter-level mammalian expression atlas. *Nature* **507**, 462–470 (2014). doi: 10.1038/nature13182; pmid: 24670764
16. E. K. Stroup, Z. Ji, Deep learning of human polyadenylation sites at nucleotide resolution reveals molecular determinants of site usage and relevance in disease. *Nat. Commun.* **14**, 7378 (2023). doi: 10.1038/s41467-023-43266-3; pmid: 37968271
17. A. Reyes, W. Huber, Alternative start and termination sites of transcription drive most transcript isoform differences across human tissues. *Nucleic Acids Res.* **46**, 582–592 (2018). doi: 10.1093/nar/gkx1165; pmid: 29202200
18. S. Pal *et al.*, Alternative transcription exceeds alternative splicing in generating the transcriptome diversity of cerebellar development. *Genome Res.* **21**, 1260–1272 (2011). doi: 10.1101/gr.120535.111; pmid: 21712398
19. A. A. Pai, F. Luca, Environmental influences on RNA processing: Biochemical, molecular and genetic regulators of cellular response. *Wiley Interdiscip. Rev. RNA* **10**, e1503 (2019). doi: 10.1002/wrna.1503; pmid: 30216698
20. J. M. Taliaferro *et al.*, Distal Alternative Last Exons Localize mRNAs to Neural Projections. *Mol. Cell* **61**, 821–833 (2016). doi: 10.1016/j.molcel.2016.01.020; pmid: 26907613
21. S. Lianoglou, V. Garg, J. L. Yang, C. S. Leslie, C. Mayr, Ubiquitously transcribed genes use alternative polyadenylation to achieve tissue-specific expression. *Genes Dev.* **27**, 2380–2396 (2013). doi: 10.1101/gad.229328.113; pmid: 24145798
22. D. C. Di Giammartino, K. Nishida, J. L. Manley, Mechanisms and consequences of alternative polyadenylation. *Mol. Cell* **43**, 853–866 (2011). doi: 10.1016/j.molcel.2011.08.017; pmid: 21925375
23. P. K. Parua, S. Kalan, B. Benjamin, M. Sansó, R. P. Fisher, Distinct Cdk9-phosphatase switches act at the beginning and end of elongation by RNA polymerase II. *Nat. Commun.* **11**, 4338 (2020). doi: 10.1038/s41467-020-18173-6; pmid: 32859893
24. P. K. Parua *et al.*, A Cdk9-PP1 switch regulates the elongation-termination transition of RNA polymerase II. *Nature* **558**, 460–464 (2018). doi: 10.1038/s41586-018-0214-z; pmid: 29899453
25. C. D. Kaplan, H. Jin, I. L. Zhang, A. Belyanin, Dissection of Pol II trigger loop function and Pol II activity-dependent control of start site selection in vivo. *PLOS Genet.* **8**, e1002627 (2012). doi: 10.1371/journal.pgen.1002627; pmid: 22511879
26. H. Braberg *et al.*, From structure to systems: High-resolution, quantitative genetic analysis of RNA polymerase II. *Cell* **154**, 775–788 (2013). doi: 10.1016/j.cell.2013.07.033; pmid: 23932120
27. C. Qiu *et al.*, Universal promoter scanning by Pol II during transcription initiation in Saccharomyces cerevisiae. *Genome Biol.* **21**, 132 (2020). doi: 10.1186/s13059-020-02040-0; pmid: 32487207
28. J. V. Geisberg, Z. Moqtaderi, K. Struhl, The transcriptional elongation rate regulates alternative polyadenylation in yeast. *eLife* **9**, e59810 (2020). doi: 10.7554/eLife.59810; pmid: 32845240
29. J. V. Geisberg *et al.*, Nucleotide-level linkage of transcriptional elongation and polyadenylation. *eLife* **11**, e83153 (2022). doi: 10.7554/eLife.83153; pmid: 36421680
30. M. A. Cortazar *et al.*, Control of RNA Pol II Speed by PNUTS-PP1 and Spt5 Dephosphorylation Facilitates Termination by a "Sitting Duck Torpedo" Mechanism. *Mol. Cell* **76**, 896–908.e4 (2019). doi: 10.1016/j.molcel.2019.09.031; pmid: 31677974
31. R. Goering *et al.*, LABRAT reveals association of alternative polyadenylation with transcript localization, RNA binding protein expression, transcription speed, and cancer survival. doi: 10.1101/2020.10.05.326702
32. M. J. Rowley *et al.*, Condensin II Counteracts Cohesin and RNA Polymerase II in the Establishment of 3D Chromatin Organization. *Cell Rep.* **26**, 2890–2903.e3 (2019). doi: 10.1016/j.celrep.2019.01.116; pmid: 30865881
33. H. Wu, J. Zhang, L. Tan, X. Sunney Xie, Extruding transcription elongation loops observed in high-resolution single-cell 3D genomes. bioRxiv 2023.02.18.529096 [Preprint] (2023); doi: 10.1101/2023.02.18.529096.
34. S. Leidescher *et al.*, Spatial organization of transcribed eukaryotic genes. *Nat. Cell Biol.* **24**, 327–339 (2022). doi: 10.1038/s41556-022-00847-6; pmid: 35177821
35. A. Fiszbein *et al.*, Widespread occurrence of hybrid internal-terminal exons in human transcriptomes. *Sci Adv.* **8**, eabk1752 (2022). doi: 10.1126/sciadv.abk1752; pmid: 35044812
36. F. Aguet *et al.*, The GTEx Consortium atlas of genetic regulatory effects across human tissues. *Science* **369**, 1318–1330 (2020). doi: 10.1126/science.aaz1776; pmid: 32913098
37. Y. Katz, E. T. Wang, E. M. Airoldi, C. B. Burge, Analysis and design of RNA sequencing experiments for identifying isoform regulation. *Nat. Methods* **7**, 1009–1015 (2010). doi: 10.1038/nmeth.1528; pmid: 21057496
38. Y. Luo *et al.*, New developments on the Encyclopedia of DNA Elements (ENCODE) data portal. *Nucleic Acids Res.* **48**, D882–D889 (2020). doi: 10.1093/nar/gkz1062; pmid: 31713622
39. F. Reese *et al.*, The ENCODE4 long-read RNA-seq collection reveals distinct classes of transcript structure diversity. bioRxiv 2023.05.15.540865 [Preprint] (2023); doi: 10.1101/2023.05.15.540865.
40. E. Calvo-Roitberg, R. F. Daniels, A. A. Pai, Challenges in identifying mRNA transcript starts and ends from long-read sequencing data. *Genome Res.* **34**, 1719–1734 (2024). doi: 10.1101/2023.07.26.550536; pmid: 37546743
41. X. Dong *et al.*, Benchmarking long-read RNA-sequencing analysis tools using in silico mixtures. *Nat. Methods* **20**, 1810–1821 (2023). doi: 10.1038/s41592-023-02026-3; pmid: 37783886
42. C. Mayr, D. P. Bartel, Widespread shortening of 3'UTRs by alternative cleavage and polyadenylation activates oncogenes in cancer cells. *Cell* **138**, 673–684 (2009). doi: 10.1016/j.cell.2009.06.016; pmid: 19703394
43. R. Sandberg, J. R. Neilson, A. Sarma, P. A. Sharp, C. B. Burge, Proliferating cells express mRNAs with shortened 3′ untranslated regions and fewer microRNA target sites. *Science* **320**, 1643–1647 (2008). doi: 10.1126/science.1155390; pmid: 18566288
44. Z. Ji, J. Y. Lee, Z. Pan, B. Jiang, B. Tian, Progressive lengthening of 3′ untranslated regions of mRNAs by alternative polyadenylation during mouse embryonic development. *Proc. Natl. Acad. Sci. U.S.A.* **106**, 7028–7033 (2009). doi: 10.1073/pnas.0900028106; pmid: 19372383
45. R. Hou, C.-C. Hon, Y. Huang, CamoTSS: analysis of alternative transcription start sites for cellular phenotypes and regulatory patterns from 5' scRNA-seq data. *Nat. Commun.* **14**, 7240 (2023). doi: 10.1038/s41467-023-42636-1; pmid: 37945584
46. A. L. Richards *et al.*, Environmental perturbations lead to extensive directional shifts in RNA processing. *PLOS Genet.* **13**, e1006995 (2017). doi: 10.1371/journal.pgen.1006995; pmid: 29023442
47. M. Tajnik *et al.*, Intergenic Alu exonisation facilitates the evolution of tissue-specific transcript ends. *Nucleic Acids Res.* **43**, 10492–10505 (2015). pmid: 26400176
48. N. Krietenstein *et al.*, Ultrastructural Details of Mammalian Chromosome Architecture. *Mol. Cell* **78**, 554–565.e7 (2020). doi: 10.1016/j.molcel.2020.03.003; pmid: 32213324
49. B. Schwalb *et al.*, TT-seq maps the human transient transcriptome. *Science* **352**, 1225–1228 (2016). doi: 10.1126/science.aad9841; pmid: 27257258
50. A.-L. Valton *et al.*, A cohesin traffic pattern genetically linked to gene regulation. *Nat. Struct. Mol. Biol.* **29**, 1239–1251 (2022). doi: 10.1038/s41594-022-00890-9; pmid: 36482254
51. B. Akgol Oksuz *et al.*, Systematic evaluation of chromosome conformation capture assays. *Nat. Methods* **18**, 1046–1055 (2021). doi: 10.1038/s41592-021-01248-7; pmid: 34480151
52. B. Bonev *et al.*, Multiscale 3D Genome Rewiring during Mouse Neural Development. *Cell* **171**, 557–572.e24 (2017). doi: 10.1016/j.cell.2017.09.043; pmid: 29053968
53. N. Fong *et al.*, Pre-mRNA splicing is facilitated by an optimal RNA polymerase II elongation rate. *Genes Dev.* **28**, 2663–2676 (2014). doi: 10.1101/gad.252106.114; pmid: 25452276
54. M. M. Maslon *et al.*, A slow transcription rate causes embryonic lethality and perturbs kinetic coupling of neuronal genes. *EMBO J.* **38**, e101244 (2019). doi: 10.15252/embj.2018101244; pmid: 30988016
55. K. Žumer *et al.*, Two distinct mechanisms of RNA polymerase II elongation stimulation in vivo. *Mol. Cell* **81**, 3096–3109.e8 (2021). doi: 10.1016/j.molcel.2021.05.028; pmid: 34146481

56. L. Caizzi *et al.*, Efficient RNA polymerase II pause release requires U2 snRNP function. *Mol. Cell* **81**, 1920–1934.e9 (2021). doi: 10.1016/j.molcel.2021.02.016; pmid: 33689748
57. A. Veloso *et al.*, Rate of elongation by RNA polymerase II is associated with specific gene features and epigenetic modifications. *Genome Res.* **24**, 896–905 (2014). doi: 10.1101/gr.171405.113; pmid: 24714810
58. A. Khitun *et al.*, Elongation rate of RNA polymerase II affects pausing patterns across 3′ UTRs. *J. Biol. Chem.* **299**, 105289 (2023). doi: 10.1016/j.jbc.2023.105289; pmid: 37748648
59. J. V. Geisberg, Z. Moqtaderi, K. Struhl, Chromatin regulates alternative polyadenylation via the RNA polymerase II elongation rate. *Proc. Natl. Acad. Sci. U.S.A.* **121**, e2405827121 (2024). doi: 10.1073/pnas.2405827121; pmid: 38748572
60. J. Linder, S. E. Koplik, A. Kundaje, G. Seelig, Deciphering the impact of genetic variation on human polyadenylation using APARENT2. *Genome Biol.* **23**, 232 (2022). doi: 10.1186/s13059-022-02799-4; pmid: 36335397
61. G. Fuchs *et al.*, 4sUDRB-seq: Measuring genomewide transcriptional elongation rates and initiation frequencies within cells. *Genome Biol.* **15**, R69 (2014). doi: 10.1186/gb-2014-15-5-r69; pmid: 24887486
62. G. Kim, C. L. Carroll, Z. P. Wakefield, M. Tuncay, A. Fiszbein, U1 snRNP regulates alternative promoter activity by inhibiting premature polyadenylation. *Mol. Cell* **85**, 1968–1981.e7 (2025). doi: 10.1016/j.molcel.2025.04.021; pmid: 40378830
63. Z. Zhang, B. Bae, W. H. Cuddleston, P. Miura, Coordination of alternative splicing and alternative polyadenylation revealed by targeted long read sequencing. *Nat. Commun.* **14**, 5506 (2023). doi: 10.1038/s41467-023-41207-8; pmid: 37679364
64. K. Glover-Cutter, S. Kim, J. Espinosa, D. L. Bentley, RNA polymerase II pauses and associates with pre-mRNA processing factors at both ends of genes. *Nat. Struct. Mol. Biol.* **15**, 71–78 (2008). doi: 10.1038/nsmb1352; pmid: 18157150
65. H. Takahashi *et al.*, The role of Mediator and Little Elongation Complex in transcription termination. *Nat. Commun.* **11**, 1063 (2020). doi: 10.1038/s41467-020-14849-1; pmid: 32102997
66. F. Ullah, S. Jabeen, M. Salton, A. S. N. Reddy, A. Ben-Hur, Evidence for the role of transcription factors in the co-transcriptional regulation of intron retention. *Genome Biol.* **24**, 53 (2023). doi: 10.1186/s13059-023-02885-1; pmid: 36949544
67. M. Thompson *et al.*, Splicing in a single neuron is coordinately controlled by RNA binding proteins and transcription factors. *eLife* **8**, e46726 (2019). doi: 10.7554/eLife.46726; pmid: 31322498
68. K. Y. Kwek *et al.*, U1 snRNA associates with TFIIH and regulates transcriptional initiation. *Nat. Struct. Biol.* **9**, 800–805 (2002). doi: 10.1038/nsb862; pmid: 12389039
69. M. Uriostegui-Arcos, S. T. Mick, Z. Shi, R. Rahman, A. Fiszbein, Splicing activates transcription from weak promoters upstream of alternative exons. *Nat. Commun.* **14**, 3435 (2023). doi: 10.1038/s41467-023-39200-2; pmid: 37301863
70. A. Bergfort, K. M. Neugebauer, The promoter as a trip navigator: Guiding alternative polyadenylation site destinations. *Mol. Cell* **83**, 2395–2397 (2023). doi: 10.1016/j.molcel.2023.06.022; pmid: 37478824
71. B. Kwon *et al.*, Enhancers regulate 3′ end processing activity to control expression of alternative 3′UTR isoforms. *Nat. Commun.* **13**, 2709 (2022). doi: 10.1038/s41467-022-30525-y; pmid: 35581194
72. M. M. Ibrahim *et al.*, Determinants of promoter and enhancer transcription directionality in metazoans. *Nat. Commun.* **9**, 4472 (2018). doi: 10.1038/s41467-018-06962-z; pmid: 30367057
73. L. Han *et al.*, Concentration and length dependence of DNA looping in transcriptional regulation. *PLOS ONE* **4**, e5621 (2009). doi: 10.1371/journal.pone.0005621; pmid: 19479049
74. L. Chen *et al.*, R-ChIP Using Inactive RNase H Reveals Dynamic Coupling of R-loops with Transcriptional Pausing at Gene Promoters. *Mol. Cell* **68**, 745–757.e5 (2017). doi: 10.1016/j.molcel.2017.10.008; pmid: 29104020
75. A. M. Moabbi, N. Agarwal, B. El Kaderi, A. Ansari, Role for gene looping in intron-mediated enhancement of transcription. *Proc. Natl. Acad. Sci. U.S.A.* **109**, 8505–8510 (2012). doi: 10.1073/pnas.1112400109; pmid: 22586116
76. N. Agarwal, A. Ansari, Enhancement of Transcription by a Splicing-Competent Intron Is Dependent on Promoter Directionality. *PLOS Genet.* **12**, e1006047 (2016). doi: 10.1371/journal.pgen.1006047; pmid: 27152651
77. A. Dobin *et al.*, STAR: Ultrafast universal RNA-seq aligner. *Bioinformatics* **29**, 15–21 (2013). doi: 10.1093/bioinformatics/bts635; pmid: 23104886
78. H. Li, New strategies to improve minimap2 alignment accuracy. *Bioinformatics* **37**, 4572–4574 (2021). doi: 10.1093/bioinformatics/btab705; pmid: 34623391
79. A. R. Quinlan, I. M. Hall, BEDTools: A flexible suite of utilities for comparing genomic features. *Bioinformatics* **26**, 841–842 (2010). doi: 10.1093/bioinformatics/btq033; pmid: 20110278
80. S. Lin *et al.*, Comparison of the transcriptional landscapes between human and mouse tissues. *Proc. Natl. Acad. Sci. U.S.A.* **111**, 17224–17229 (2014). doi: 10.1073/pnas.1413624111; pmid: 25413365
81. C. J. Herrmann *et al.*, PolyASite 2.0: A consolidated atlas of polyadenylation sites from 3′ end sequencing. *Nucleic Acids Res.* **48**, D174–D179 (2020). doi: 10.1093/nar/gkz918; pmid: 31617559
82. T. Paysan-Lafosse *et al.*, InterPro in 2022. *Nucleic Acids Res.* **51**, D418–D427 (2023). doi: 10.1093/nar/gkac993; pmid: 36350672
83. A. Siepel *et al.*, Evolutionarily conserved elements in vertebrate, insect, worm, and yeast genomes. *Genome Res.* **15**, 1034–1050 (2005). doi: 10.1101/gr.3715005; pmid: 16024819
84. B. J. Raney *et al.*, The UCSC Genome Browser database: 2024 update. *Nucleic Acids Res.* **52**, D1082–D1088 (2024). doi: 10.1093/nar/gkad987; pmid: 37953330
85. P. Khandelia, K. Yap, E. V. Makeyev, Streamlined platform for short hairpin RNA interference and transgenesis in cultured mammalian cells. *Proc. Natl. Acad. Sci. U.S.A.* **108**, 12799–12804 (2011). doi: 10.1073/pnas.1103532108; pmid: 21768390
86. A. Fidanza *et al.*, An all-in-one UniSam vector system for efficient gene activation. *Sci. Rep.* **7**, 6394 (2017). doi: 10.1038/s41598-017-06468-6; pmid: 28743878
87. C. J. Herrmann *et al.*, PolyASite 2.0: A Consolidated Atlas of Polyadenylation Sites from 3′ End Sequencing. *Nucleic Acids Res* **8**, D174–D179 (2020). doi: 10.1093/nar/gkz918; pmid: 31617559
88. S. B. Reiff *et al.*, The 4D Nucleome Data Portal as a resource for searching and visualizing curated nucleomics data. *Nat. Commun.* **13**, 2365 (2022). doi: 10.1038/s41467-022-29697-4; pmid: 35501320
89. N. Abdennur, L. A. Mirny, Cooler: Scalable storage for Hi-C data and other genomically labeled arrays. *Bioinformatics* **36**, 311–316 (2020). doi: 10.1093/bioinformatics/btz540; pmid: 31290943
90. I. M. Flyamer, R. S. Illingworth, W. A. Bickmore, Coolpup.py: Versatile pile-up analysis of Hi-C data. *Bioinformatics* **36**, 2980–2985 (2020). doi: 10.1093/bioinformatics/btaa073; pmid: 32003791
91. Open2C *et al.*, Cooltools: enabling high-resolution Hi-C analysis in Python. bioRxiv 2022.10.31.514564 [Preprint] (2022); doi: 10.1101/2022.10.31.514564v1.
92. W. J. Kent, A. S. Zweig, G. Barber, A. S. Hinrichs, D. Karolchik, BigWig and BigBed: Enabling browsing of large distributed datasets. *Bioinformatics* **26**, 2204–2207 (2010). doi: 10.1093/bioinformatics/btq351; pmid: 20639541
93. M. Martin, Cutadapt removes adapter sequences from high-throughput sequencing reads. *EMBnet. J.* **17**, 10–12 (2011). doi: 10.14806/ej.17.1.200
94. L. Wachutka, L. Caizzi, J. Gagneur, P. Cramer, Global donor and acceptor splicing site kinetics in human cells. *eLife* **8**, e45056 (2019). doi: 10.7554/eLife.45056; pmid: 31025937
95. E. E. Duffy *et al.*, Tracking Distinct RNA Populations Using Efficient and Reversible Covalent Chemistry. *Mol. Cell* **59**, 858–866 (2015). doi: 10.1016/j.molcel.2015.07.023; pmid: 26340425
96. Z. Zhang, W. E. Theurkauf, Z. Weng, P. D. Zamore, Strand-specific libraries for high throughput RNA sequencing (RNA-Seq) prepared without poly(A) selection. *Silence* **3**, 9 (2012). doi: 10.1186/1758-907X-3-9; pmid: 23273270
97. H. L. Drexler *et al.*, Revealing nascent RNA processing dynamics with nano-COP. *Nat. Protoc.* **16**, 1343–1375 (2021). doi: 10.1038/s41596-020-00469-y; pmid: 33514943
98. E. Kopylova, L. Noé, H. Touzet, SortMeRNA: Fast and accurate filtering of ribosomal RNAs in metatranscriptomic data. *Bioinformatics* **28**, 3211–3217 (2012). doi: 10.1093/bioinformatics/bts611; pmid: 23071270
99. I. Legnini, J. Alles, N. Karaiskos, S. Ayoub, N. Rajewsky, FLAM-seq: Full-length mRNA sequencing reveals principles of poly(A) tail length control. *Nat. Methods* **16**, 879–886 (2019). doi: 10.1038/s41592-019-0503-y; pmid: 31384046
100. H.-Y. Lai *et al.*, IProEP: A computational predictor for predicting promoter. *Mol. Ther. Nucleic Acids* **17**, 337–346 (2019). doi: 10.1016/j.omtn.2019.05.028; pmid: 31299595
101. E. Calvo-Roitberg *et al.*, mRNA initiation and termination are spatially coordinated, Version v2, Zenodo (2025); https://doi.org/10.5281/zenodo.15837772.

ACKNOWLEDGMENTS

We thank Z.P. Wakefield for providing a curated list of human transcription start sites; H. Cheng and E. Sontheimer for discussions on CRISPR deletion experiments and the gift of SpyCas9 RNP; M. Walhout for suggesting the interspecies comparative analyses; P. Zamore for discussions; and the Fiszbein and Pai labs for helpful discussions and comments. **Funding:** This work was funded by the following: National Institutes of Health grants R35GM133762 and R01HG012967 (to A.A.P.); National Institutes of Health grant R35GM147254 and National Science Foundation grant CAREER2339464 (to A.F.); National Institutes of Health grants R01HG003143 and UM1HG011536 (to J.D.) **Author contributions:** Conceptualization: A.F. and A.A.P.; Methodology: E.C.-R., C.L.C., V.S., A.F., and A.A.P.; Formal Analysis: E.C.-R., C.L.C., G.Y.K., V.S., S.V.V., and S.T.M.; Investigation: E.C.-R., C.L.C., V.S., J.D.P., and M.U.-A.; Visualization: E.C.-R., C.L.C., G.Y.K., V.S., S.V.V., A.F., and A.A.P.; Funding acquisition: J.D., A.F., and A.A.P.; Project administration: A.F. and A.A.P.; Supervision: J.D., A.F., and A.A.P.; Writing – original draft: A.F. and A.A.P.; Writing – review & editing: E.C.-R., C.L.C., J.D., A.F., and A.A.P.; **Competing interests:** J.D. is an investigator of the Howard Hughes Medical Institute. J.D. is also an inventor on patent application US 12,146,186 B2, held by the University of Massachusetts Chan Medical School, Harvard College, the Whitehead Institute for Biomedical Research, and the Massachusetts Institute of Technology, which covers Hi-C technology. **Data and materials availability:** All code used for analysis in this manuscript is archived at Zenodo (*101*). Analyses of short and long-read sequencing datasets is detailed at https://github.com/thepailab/mrna_initiation_termination. Code for microC-related analyses is available at https://github.com/dekkerlab/pita_project. Sequencing data for CRISPRa/CRISPRi and DRB-4sU-LRS are available under the GSE294979 and GSE294980 accession numbers, respectively. **License information:** Copyright © 2025 the authors, some rights reserved; exclusive licensee American Association for the Advancement of Science. No claim to original US government works. https://www.science.org/content/page/science-licenses-journal-article-reuse

SUPPLEMENTARY MATERIALS

science.org/doi/10.1126/science.ado8279
Materials and Methods; Figs. S1 to S12; Tables S1 and S2; MDAR Reproducibility Checklist
Submitted 22 February 2024; resubmitted 25 April 2025; accepted 9 July 2025
10.1126/science.ado8279

RESEARCH ARTICLE SUMMARY

METABOLISM

Acidosis orchestrates adaptations of energy metabolism in tumors

Sven Groessl†, Robert Kalis†, Marteinn T. Snaebjornsson, Leon Wambach, Jakob Haider, Florian Andersch, Almut Schulze, Wilhelm Palm*, Johannes Zuber*

Full article and list of author affiliations: https://doi.org/10.1126/science.adp7603

INTRODUCTION: Malignant tumors expose cancer cells to diverse metabolic stresses, such as nutrient shortages, hypoxia, acidosis, and accumulation of metabolic by-products. To survive and grow in such harsh environments, cancer cells rely on metabolic adaptability and stress resilience. Although responses to individual stresses have been characterized in reductionist systems, it remains unclear how cancer cells adapt to complex metabolic challenges in tumors.

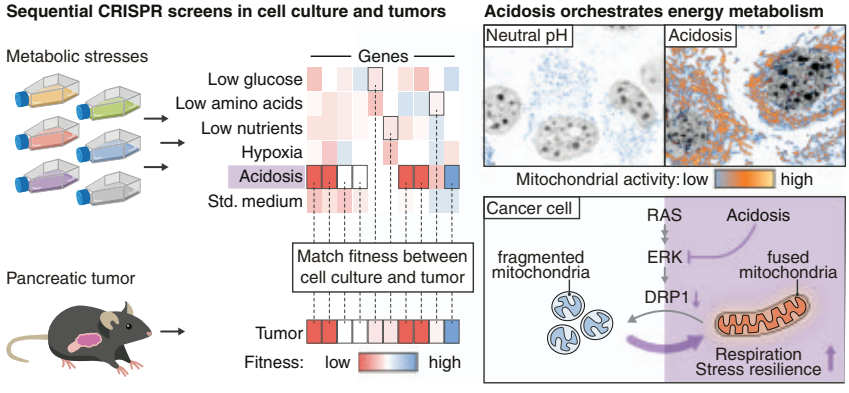
RATIONALE: To characterize the integrated adaptation of cancer cells to complex metabolic stresses, we devised a sequential CRISPR-based screening approach in a mouse model of pancreatic ductal adenocarcinoma: We conducted genome-wide screens to systematically identify genes affecting the fitness of cancer cells—their ability to survive and proliferate—under defined metabolic stress conditions in cell culture. We then probed the relevance of these fitness genes through focused screens in pancreatic tumors. Comparative analyses of cell culture–based and in vivo screens unveiled dominant environmental stresses and metabolic adaptations in tumors.

RESULTS: Genome-wide CRISPR screens under defined metabolic stresses revealed stress-specific changes in fitness gene profiles. The fitness gene profile of pancreatic tumors differed markedly from that in standard cell culture. Tumor effects were best recapitulated in cell culture by lactic acid accumulation, which was fully attributable to environmental acidosis. Exposing cells to combinations of different stresses revealed that acidosis could override fitness defects caused by various forms of starvation. The response of cancer cells to acidosis was characterized by a shift in energy metabolism from a glycolytic to a respiratory state, accompanied by profound changes in mitochondrial morphology and function. Mechanistically, acidosis suppressed extracellular signal–regulated kinase (ERK) mitogen-activated protein kinase (MAPK) signaling, which is commonly hyperactivated in cancer, thereby abrogating oncogene-induced activation of the mitochondrial fission factor, dynamin-related protein 1 (DRP1). The resulting inhibition of mitochondrial fragmentation triggered the formation of fused mitochondrial networks, promoting the usage of alternative bioenergetic substrates and enhancing mitochondrial respiration. Genetically enforcing the fragmentation of mitochondria prevented acidosis-induced changes in mitochondrial metabolism and suppressed cancer cell growth in acidic tumors.

CONCLUSION: Through sequential CRISPR screens relating hundreds of fitness genes under defined metabolic stresses in cell culture and in complex tumors, we identify acidosis as a dominant environmental factor that shapes cancer cell metabolism. By triggering the formation of fused mitochondria and enhancing mitochondrial respiration, acidosis sustains cancer cell bioenergetics and proliferation under nutrient-limiting conditions. These findings reconcile conflicting views on mitochondrial morphology and metabolism in cancer: Mitochondrial fragmentation is not a static consequence of oncogenic signaling but a dynamic process governed by pH-dependent regulation of ERK activity. This interplay between environmental pH and a key oncogenic signaling pathway directs a metabolic shift from glycolysis to respiration, which grants cancer cells metabolic flexibility and stress resilience. Thus, rather than being merely a by-product of cancer metabolism, acidosis orchestrates bioenergetic adaptations to complex metabolic stresses in tumors. □

*Corresponding author. Email: w.palm@dkfz-heidelberg.de (W.P.); johannes.zuber@imp.ac.at (J.Z.) †These authors contributed equally to this work. **Cite this article as S. Groessl *et al.*, *Science* 390, eadp7603 (2025). DOI: 10.1126/science.adp7603**

Acidosis controls bioenergetics and stress adaptation in tumors. Sequential CRISPR screens under defined metabolic stresses in cell culture and in pancreatic tumors identify acidosis as a dominant environmental factor in tumors. Acidosis triggers the formation of fused mitochondria, thus enhancing mitochondrial metabolism and stress resilience. Acidosis exerts these effects by suppressing cytoplasmic ERK activity, thereby abrogating oncogene-driven activation of the mitochondrial fission factor DRP1. Std. medium, standard medium.



METABOLISM

Acidosis orchestrates adaptations of energy metabolism in tumors

Sven Groessl[1,2]†, Robert Kalis[3,4]†, Marteinn T. Snaebjornsson[5], Leon Wambach[1], Jakob Haider[3], Florian Andersch[3], Almut Schulze[5], Wilhelm Palm[1]*, Johannes Zuber[3,6]*

Malignant tumors are characterized by diverse metabolic stresses, including nutrient shortages, hypoxia, and buildup of metabolic by-products. To understand how cancer cells adapt to such challenges, we conducted sequential CRISPR screens to identify genes that affect cellular fitness under specific metabolic stress conditions in cell culture and to then probe their relevance in pancreatic tumors. Comparative analyses of hundreds of fitness genes revealed that cancer metabolism in vivo was shaped by bioenergetic adaptations to tumor acidosis. Mechanistically, acidosis suppressed cytoplasmic activity of extracellular signal–regulated kinase (ERK), thereby preventing oncogene-induced mitochondrial fragmentation and promoting fused mitochondria. The resulting boost in mitochondrial respiration supported cancer cell adaptations to various metabolic stresses. Thus, acidosis is an environmental factor that alters energy metabolism to promote stress resilience in cancer.

Altered metabolism is a central characteristic of tumors. By dysregulating conventional pathways of nutrient uptake and usage, cancer cells enhance energy production and macromolecular synthesis to grow at pathologically increased rates (*1*–*3*). One widely documented metabolic program of cancer cells is aerobic glycolysis, also referred to as the Warburg effect, in which most glucose is converted to lactate despite the presence of oxygen (*4*–*6*). Alternatively, glucose-derived carbons can be fully oxidized in the mitochondrial tricarboxylic acid (TCA) cycle to power the respiratory chain, yielding large quantities of adenosine triphosphate (ATP) (*1*, *7*). Although glycolysis and mitochondrial respiration are central bioenergetic pathways, the factors that dictate the preference of cancer cells for either program remain incompletely understood.

Poor tumor perfusion and increased metabolic activity of cancer cells give rise to harsh microenvironments that are characterized by oxygen and nutrient deficiencies, buildup of metabolic by-products, and extracellular acidification (*2*, *8*). To adapt to these metabolic stresses, cancer cells alter their metabolic activities and exploit alternative nutrients (*1*, *7*, *9*). For example, cancer cells cope with fluctuating nutrient supply by adjusting the balance between glycolytic and oxidative metabolism and by supplying the TCA cycle with a range of carbon sources (*10*–*15*). Recently, metabolomics studies have quantified altered metabolite concentrations in tumors and tumor interstitial fluids (*16*–*21*), and isotope tracer–based flux analyses have delineated metabolic activities of cancer cells in vivo (*12*–*15*, *22*, *23*). In a complementary approach, cell culture–based genetic screens have identified metabolic pathways required for cancer cell growth under specific metabolic stresses (*24*–*29*). However, metabolite measurements do not directly establish functional relevance, and genetic screens have focused on individual stresses. Thus, which metabolic factors shape cancer cell metabolism in complex tumor microenvironments with multiple concurrent stresses remains unresolved.

To dissect the impact of different metabolic stresses and resulting cancer cell adaptations in vivo, we performed a series of genome-wide CRISPR screens to characterize genes that affect the fitness of cancer cells—their ability to survive and proliferate—under defined stress conditions in cell culture and, subsequently, determined the in vivo relevance of these genes using focused CRISPR screens in pancreatic tumors (fig. S1A). Comparative analyses of these sequential screens revealed metabolic dependencies of cancer cells in vivo and functionally linked these to specific metabolic stresses. Acidosis emerged as a dominant environmental factor in tumors, controlling mitochondrial morphology to alter energy metabolism and thus enabling cancer cell growth in stressful environments.

Results

Systematic identification of genes that affect cancer cell fitness under specific metabolic stresses

To systematically identify genes underlying cancer cell adaptations to metabolic stresses, we performed genome-wide CRISPR loss-of-function screens in a genetically engineered mouse model of pancreatic adenocarcinoma, a tumor type characterized by pronounced metabolic stress (*30*). Embryonic pancreatic progenitor carcinoma 2 (EPP2) cells (*31*) were engineered to harbor doxycycline-inducible Cas9 (iCas9), which provided stringent temporal control over CRISPR-based genome editing in cell culture and in tumors (fig. S1, B to E). To conduct screens under defined metabolic perturbations, we established cell culture conditions that recapitulated various stresses observed in tumors: low glucose, low nonessential amino acids (NEAA), low glucose with low amino acids, hypoxia, and lactic acid accumulation. To ensure comparable stress exposure, these conditions were adjusted to support similar proliferation rates (Fig. 1A). Upon transduction with the Vienna genome-wide single-guide RNA (sgRNA) library (*32*) and induction of Cas9 expression, the resulting pool of gene-edited cells was grown under various metabolic stress conditions or in standard medium, Dulbecco's modified Eagle's medium with Ham's F-12 nutrient mixture (DMEM/F-12). After 12 population doublings, changes in sgRNA abundance in the different culture conditions were quantified by next-generation sequencing to identify genes whose depletion affected cancer cell fitness.

In all conditions, sgRNAs targeting common essential genes were strongly decreased, confirming a high quality and dynamic range of our CRISPR screens (Fig. 1B). Comparisons between screens revealed numerous genes whose depletion affected cancer cell fitness only under specific stress conditions (Fig. 1C). On the basis of principal components analysis (PCA), these stress-specific fitness effects were relatively similar under various forms of nutrient deprivation, whereas hypoxia or lactic acid induced distinctive changes (Fig. 1D). Notably, only very few stress-specific fitness genes displayed changes in mRNA abundance under the respective stress condition, whereas transcriptionally altered genes rarely scored in the corresponding CRISPR screen (fig. S2A). Thus, transcriptional regulation poorly predicts functional involvement in metabolic stress adaptations.

Stress-specific fitness genes included various metabolic enzymes and components of the respiratory chain, nutrient sensing, and stress signaling pathways (Fig. 1E), which were validated by competitive cell proliferation assays (fig. S2B). Context-specific functions of these metabolic processes were also apparent in pathway-level analyses of our screening data (fig. S2C). For example, respiratory chain components were essential under both glucose starvation and lactic acid supplementation, whereas their depletion was tolerated under hypoxia and nonessential–amino acid starvation. By contrast, glycolytic enzymes were dispensable in lactic acid but essential in other stress conditions. Most differential fitness effects were observed in only one or two metabolic conditions (Fig. 1, C and E). Thus, cancer cells appear to adapt to different metabolic perturbations through distinct pathways rather than through a common stress response.

[1]Division of Cell Signaling and Metabolism, German Cancer Research Center (DKFZ) and DKFZ-ZMBH Alliance, Heidelberg, Germany. [2]Faculty of Biosciences, University of Heidelberg, Heidelberg, Germany. [3]Research Institute of Molecular Pathology (IMP), Vienna BioCenter (VBC), Vienna, Austria. [4]VBC PhD Program, Doctoral School of the University at Vienna and Medical University of Vienna, Vienna BioCenter (VBC), Vienna, Austria. [5]Division of Tumor Metabolism and Microenvironment, German Cancer Research Center (DKFZ) and DKFZ-ZMBH Alliance, Heidelberg, Germany. [6]Medical University of Vienna, Vienna BioCenter (VBC), Vienna, Austria. ***Corresponding author. Email: w.palm@dkfz-heidelberg.de (W.P.); johannes.zuber@imp.ac.at (J.Z.)** †These authors contributed equally to this work.

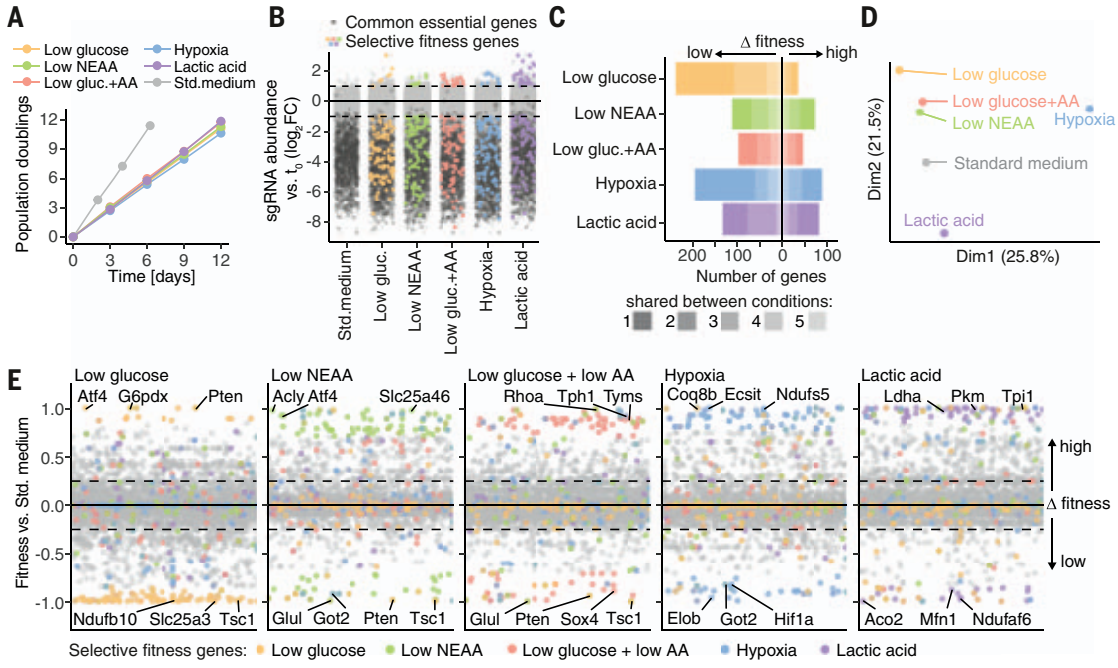


Fig. 1. Genome-wide CRISPR screens identify distinctive gene fitness effects in different metabolic stress conditions. (**A**) Population doublings of pancreatic cancer EPP2-iCas9 cells during genome-wide CRISPR screens in standard medium (DMEM/F-12), lactic acidosis (20 mM lactic acid, pH 6.7), hypoxia (0.8% O_2), low nonessential amino acids (40% NEAA), low glucose (25% glucose), or low glucose + low amino acids (AA) (50% glucose, 50% AA). (**B**) Gene-level changes in sgRNA abundance in CRISPR screens versus t_0. Increased and decreased sgRNA abundance indicates increased and decreased cell fitness, respectively, resulting from the corresponding gene depletion. Dashed lines indicate significance [|$\log_2$ fold change ($\log_2$FC)| > 1]. Common essential genes (*63*) and stress-specific fitness genes are highlighted. (**C**) Distinct and shared fitness genes in CRISPR screens. Selective fitness genes were defined as |$\log_2$ fold change > 2| relative to standard medium. (**D**) PCA of sgRNA abundance from CRISPR screens. (**E**) Gene knockout fitness in CRISPR screens relative to standard medium. The top 100 selective fitness genes, ranked by false discovery rate, of each condition are highlighted.

Tumor acidosis shapes the metabolic dependencies of cancer cells in vivo

To determine the relevance of stress-specific fitness genes in a disease-relevant tumor environment, we constructed a focused sgRNA library targeting 771 genes showing differential fitness effects in our cell culture screens (fig. S3A). EPP2-iCas9 cells were transduced with this stress-specific library and transplanted into the pancreases of mice. CRISPR editing was induced upon tumor formation, and tumors were harvested 9 days later to analyze sgRNA abundance changes. In parallel, we conducted focused cell culture screens in all metabolic stress conditions from the genome-wide screens, low fetal bovine serum (FBS) to approximate in vivo growth factor abundance, and human plasma–like medium (HPLM) (*25*) to approximate plasma metabolite concentrations.

The CRISPR screens in pancreatic tumors displayed a full representation of neutral control sgRNAs and a consistent depletion of sgRNAs targeting common essential genes (fig. S3, B and C), indicating that our tumor model and sgRNA library size were suitable for fitness screening in vivo. Comparison of cancer cells growing in tumors or under standard cell culture conditions revealed notable differences (Fig. 2A). For instance, depletion of Kirsten rat sarcoma viral oncogene homolog (Kras), a driving oncogene in our pancreatic cancer model, as well as other components of growth factor–dependent signaling pathways, led to mild fitness defects in standard cell culture but severely compromised cancer cell fitness in tumors. Cancer cells growing in tumors also showed an increased dependence on mitochondrial respiration. Conversely, depletion of glycolytic genes was tolerated in tumors but strongly decreased cancer cell fitness in standard cell culture. Thus, distinct genes affect cancer cell fitness in tumors and in standard cell culture, including components of oncogenic signaling and central energy metabolism.

To determine which environmental stresses affected cancer cells in vivo, we compared our screens to associate fitness gene effects in tumors with those induced by specific cell culture stresses (fig. S3D). For example, Kras was highly essential in tumors, which was recapitulated in cell culture by lowering FBS concentrations (Fig. 2, B and C, and fig. S3E), indicating that supraphysiological growth factor concentrations in standard medium mask the functional impact of this oncogene. Conversely, lactate dehydrogenase A (Ldha), a key enzyme downstream of glycolysis, was largely nonessential in tumors, which was recapitulated in cell culture by supplementing medium with lactic acid (Fig. 2, B and C, and fig. S3F). We conducted analogous comparisons between tumors and the various cell culture stresses for hundreds of fitness genes. The fitness gene effects observed in tumors were best recapitulated in cell culture by the addition of lactic acid, overall and for individual metabolic pathways (Fig. 2D). Similarly, tumor transcriptomes were best approximated by the transcriptional profiles of cells cultured in lactic acid (fig. S3G). Thus, we propose that lactic acid accumulation is a key environmental factor that shapes the metabolism of cancer cells in vivo.

Acidosis promotes stress resilience of cancer cells

Lactic acid provides reduced carbons as a potential nutrient source and acidifies the environment (*8*, *33*). To distinguish between these effects, we supplemented medium with sodium lactate, which does not alter pH, or induced acidosis with hydrochloric acid or adjustment of the bicarbonate buffer (Fig. 3, A and B, and fig. S4, A and B). Parallel screens with our stress-specific sgRNA library identified similar fitness gene profiles in standard medium with or without lactate supplementation (Fig. 3C and fig. S4C). By contrast, the effects of lactic acid were recapitulated by acidosis. For instance, depletion of the glycolytic enzyme aldolase A (Aldoa) stalled proliferation of EPP2 cells in standard medium both with and without lactate but was tolerated under acidosis (Fig. 3D and fig. S4, D and E). Acidosis also rendered

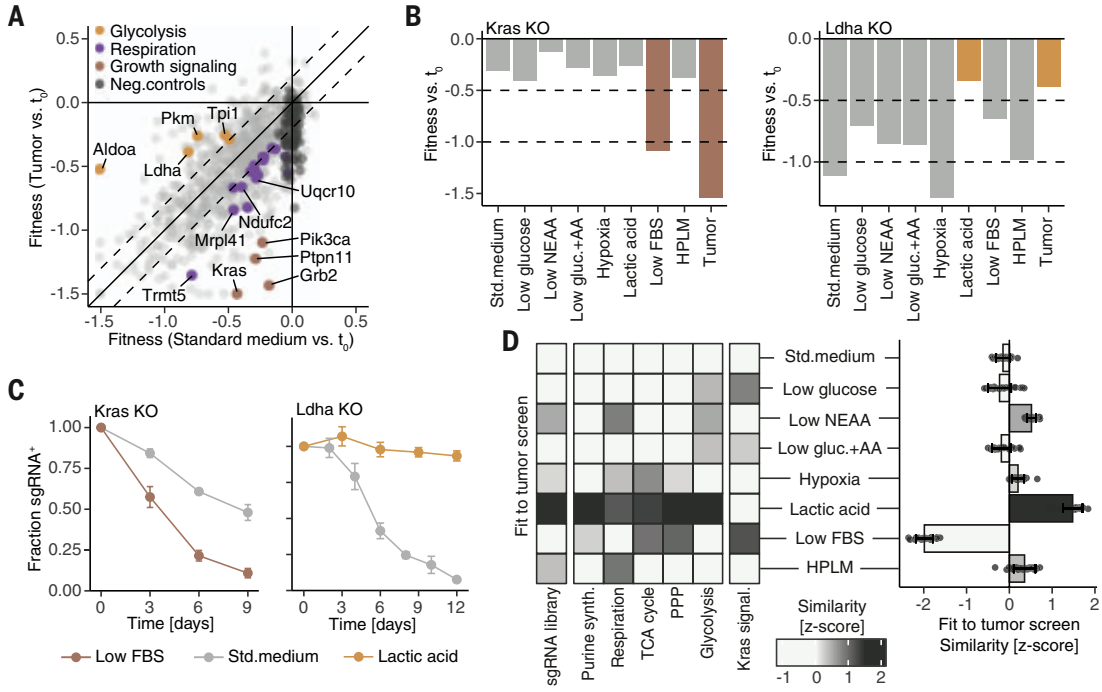


Fig. 2. Sequential cell culture—tumor CRISPR screens identify lactic acid accumulation as key metabolic factor in tumors. (**A**) Gene knockout fitness in standard medium versus pancreatic tumors in focused CRISPR screens with a stress-specific sgRNA library, shown as normalized $\log_2$ fold changes. Negative controls are sgRNAs targeting olfactory receptor genes. (**B**) Fitness of EPP2 cells with Kras or Ldha depletion (KO) across different screening conditions, shown as normalized $\log_2$ fold changes. Tumor phenotypes and best-matching cell culture stresses are highlighted. (**C**) Competitive proliferation assay of EPP2 cells with Kras depletion (KO) in low FBS (0.5%) or with Ldha depletion in lactic acidosis (20 mM lactic acid, pH 6.7). Data are represented as means ± SDs ($n = 3$). (**D**) Similarity scores (z-scores) of gene fitness effects in focused CRISPR screens between cell culture stresses and pancreatic tumors for the stress-specific sgRNA library and indicated pathways. In the right panel, each dot represents a tumor replicate. PPP, pentose phosphate pathway.

cells resistant to depletion of several other glycolytic enzymes and to pharmacological inhibition of glycolysis (fig. S4, F to H). Conversely, depletion of NADH dehydrogenase 1 subunit C2 (Ndufc2)—a respiratory chain complex 1I component—or pharmacological inhibition of complex I severely compromised fitness under acidosis but was tolerated at neutral pH (Fig. 3D and fig. S4, H to J). Similar effects were observed in the mouse pancreatic cancer cell line KRPC and in several human cancer cell lines (pancreatic MIA PaCa-2, Panc 10.05, and colorectal RKO) (fig. S4K). Consistently, acidosis, but not lactate supplementation, approximated the tumor phenotypes, including the increased dependence on respiration and decreased reliance on glycolysis (Fig. 3, E and F).

Our genetic analyses indicated that acidosis had a dominant impact on cancer cell phenotypes in vivo, which was unexpected because cells likely experience multiple stresses in tumors simultaneously. To better understand how cancer cells adapt, we conducted parallel fitness screens in EPP2 cells subjected to acidosis and glucose deprivation, alone or in combination (Fig. 3G and fig. S5A). Various genes were selectively essential when cells were cultured in a low concentration of glucose—for instance, the endoplasmic reticulum stress sensor Perk (Eif2ak3), lipoyltransferase 1 (Lipt1), and the glucose transporter Glut1 (Slc2a1) (Fig. 3H). Subjecting cells to a combination of glucose deprivation and acidosis, however, abolished the low-glucose–specific phenotypes (Fig. 3, H and I, and fig. S5B). Similarly, acidosis alleviated the selective fitness effects resulting from deprivation of nonessential amino acids (fig. S5, C to F) or FBS (fig. S5G). By contrast, combining glucose deprivation and hypoxia did not alleviate the effects from either stress but rather produced additive phenotypes (fig. S5H). Overall, these findings support the notion that an acidic environment increases cancer cell resilience to various metabolic stresses.

Acidosis shifts cancer cell bioenergetics from glycolysis to mitochondrial respiration

Our screens and validation studies revealed metabolic changes in response to acidosis, in particular a shift in the dependence from glycolysis to mitochondrial respiration (fig. S6). To investigate whether acidosis promoted the adaptation to glucose starvation, we limited glucose to concentrations that did not support proliferation at neutral pH. Acidifying the medium enabled EPP2 cells to proliferate at similar rates in both low and high concentrations of glucose (Fig. 4A). Likewise, medium acidification progressively restored proliferation in several other mouse and human cancer cell lines under glucose-restricted conditions (Fig. 4B). Thus, acidosis supports cancer cell proliferation when glucose is scarce.

Multiple glycolytic enzymes have reduced activity at an acidic pH (*34*). Consistently, exposing cancer cells to acidosis decreased glycolytic activity and lactate production (fig. S7A) and, hence, extracellular acidification rate (fig. S7, B and C). Although the glycolysis inhibitor 2-deoxyglucose (2DG) reduced cellular ATP in standard medium, acidosis-induced suppression of glycolysis had no effect on ATP abundance (Fig. 4C and fig. S7D). Rather, cells maintained ATP concentrations under acidosis even when treated with 2DG. By contrast, inhibition of mitochondrial respiration with rotenone and antimycin A led to a stronger reduction of cellular ATP under acidosis than at neutral pH (Fig. 4C and fig. S7, D and E). Thus, we investigated whether acidosis affected mitochondrial metabolism. We monitored mitochondrial membrane potential with the potentiometric dye tetramethylrhodamine methyl ester (TMRM) and measured oxygen consumption in a Seahorse Analyzer. In several cancer cell lines, acidosis increased mitochondrial membrane potential (Fig. 4, D and E, and fig. S7, F and G) as well as oxygen consumption rates (Fig. 4F and fig. S7H). Thus, acidosis appears to support ATP production independently of glycolysis by enhancing mitochondrial respiration.

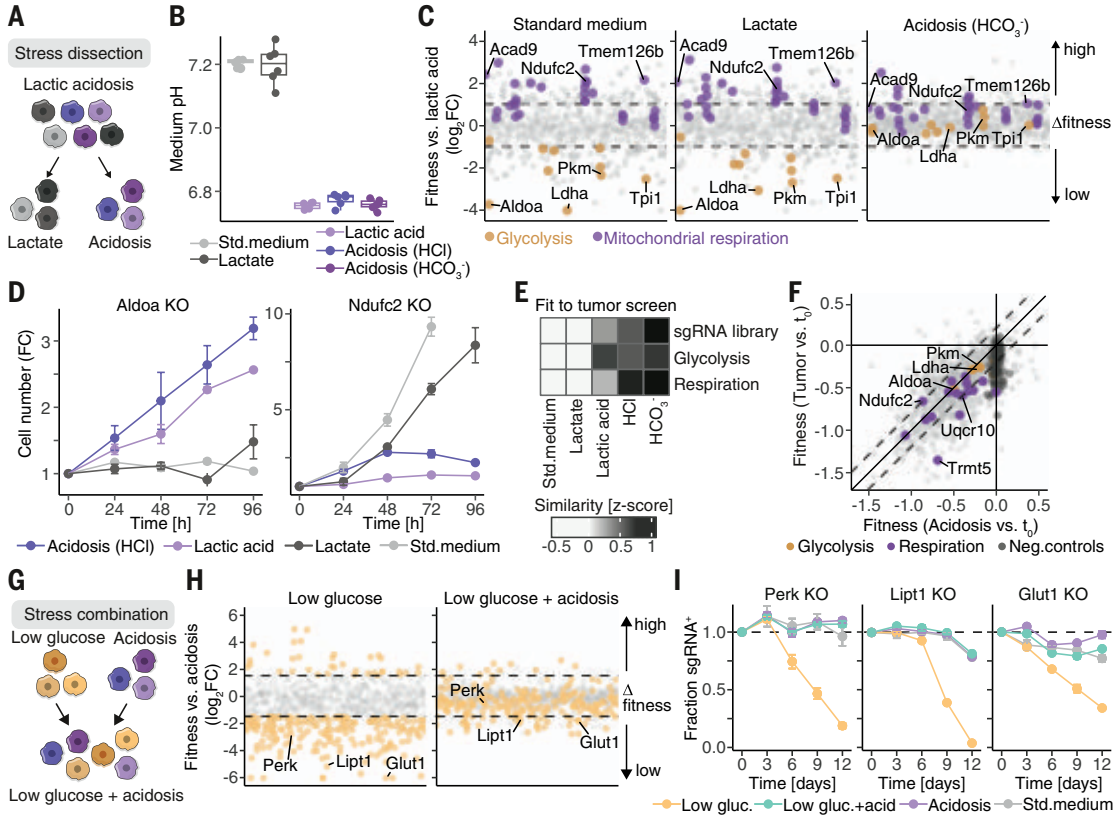


Fig. 3. Acidosis enhances the resilience of cancer cells to metabolic stress. (**A**) Schematic of stress dissection CRISPR screens for lactic acidosis. (**B**) Medium pH of cells grown in standard medium supplemented with lactic acid (20 mM, pH 6.7), hydrochloric acid (20 mM HCl, pH 6.7), low bicarbonate (0.2 g/liter HCO_3^-, pH 6.7), or sodium lactate (20 mM, pH 7.4). In further experiments, acidosis (pH 6.7) was induced by HCl (20 mM) if not indicated otherwise. (**C**) Gene knockout fitness in focused CRISPR screens with the stress-specific sgRNA library in standard medium, lactate, and acidosis (low HCO_3^-) relative to lactic acid. (**D**) Proliferation of cells with Aldoa or Ndufc2 depletion (KO) in lactic acid, acidosis, lactate, or standard medium. (**E**) Similarity scores (*z*-scores) of gene fitness effects in focused CRISPR screens between different cell culture conditions and pancreatic tumors for the stress-specific sgRNA library and indicated pathways. (**F**) Gene knockout fitness in acidosis (low HCO_3^-, pH 6.7) versus pancreatic tumors in focused CRISPR screens, shown as normalized $\log_2$ fold changes. Negative controls are sgRNAs targeting olfactory receptor genes. (**G**) Schematic of stress combination CRISPR screens for low glucose and acidosis. (**H**) Gene knockout fitness in focused CRISPR screens with the stress-specific sgRNA library in low glucose or low glucose + acidosis relative to acidosis. Low-glucose–specific fitness genes are highlighted. (**I**) Competitive proliferation of cells with depletion (KO) of Perk (Eif2ak3), Lipt1, or Glut1 (Slc2a1) in low glucose ± acidosis or standard medium. In (B), (D), and (I), data are represented as means ± SDs [$n = 6$ in (B); $n = 3$ in (D) and (I)]. All experiments were with EPP2 cells.

The respiratory chain is powered by chemical energy released through oxidation of various bioenergetic substrates in the TCA cycle. To monitor TCA cycle activity, we traced ^{13}C incorporation from isotope-labeled nutrients in EPP2 and RKO cells (Fig. 4G). Whereas at neutral pH, glucose-derived carbons readily labeled TCA cycle intermediates, TCA cycle labeling from glucose was strongly decreased under acidosis (Fig. 4H). Rather, TCA cycle intermediates now showed increased labeling from palmitate, acetate, and glutamine (Fig. 4H and fig. S7I), consistent with previous observations (*35*, *36*). Consequently, acidosis increased oxygen consumption when cells were supplied with palmitate, acetate, or glutamine but not glucose (fig. S7J). Thus, under acidosis, cancer cells appear to compensate for decreased glucose metabolism by increasing the use of alternative bioenergetic substrates for respiration.

Acidosis suppresses oncogene-induced fragmentation of mitochondria

To understand how acidosis enhances mitochondrial metabolism, we analyzed the mitochondrial proteome. Acidosis did not change the abundance of respiratory chain components or other mitochondrial proteins (fig. S8, A to C), indicating that acidosis does not alter mitochondrial biogenesis. The morphology of mitochondria can change between fragmented organelles and tubular networks (*37*). In standard medium, mitochondria were highly fragmented (Fig. 5, A to C, and fig. S8, D and E), which is typical for cancer cell lines under these culture conditions (*38*). By contrast, under acidosis, mitochondria formed extended tubular networks in multiple cancer cell lines. Various metabolic perturbations have been reported to exert opposing effects on mitochondrial morphology, inducing the formation of either fragmented or fused organelles (*39*–*43*). However, the pH-dependent reorganization of mitochondrial morphology was not affected by limiting concentrations of glucose or inhibition of glycolysis or glutaminolysis (fig. S8, F and G, and fig. S9, A and B). Thus, environmental pH is a key regulator of mitochondrial morphology in different metabolic contexts.

Mitochondrial morphology is dynamically regulated by fusion and fission events. Mitochondrial inner and outer membrane fusion are executed by optic atrophy 1 (OPA1) and mitofusin 1/2 (MFN1/2), respectively, whereas mitochondrial fission is mediated by dynamin-related protein 1 (DRP1) (*37*). Acidosis-induced mitochondrial fusion was abrogated by loss of OPA1 or MFN1 (fig. S9, C and D). Conversely, loss of DRP1 induced tubular mitochondria at neutral pH, which was not further enhanced by acidosis. Thus, acidosis-induced changes in mitochondrial morphology depend on the canonical fusion and fission machinery. Monitoring the mixing of two mitochondrial populations

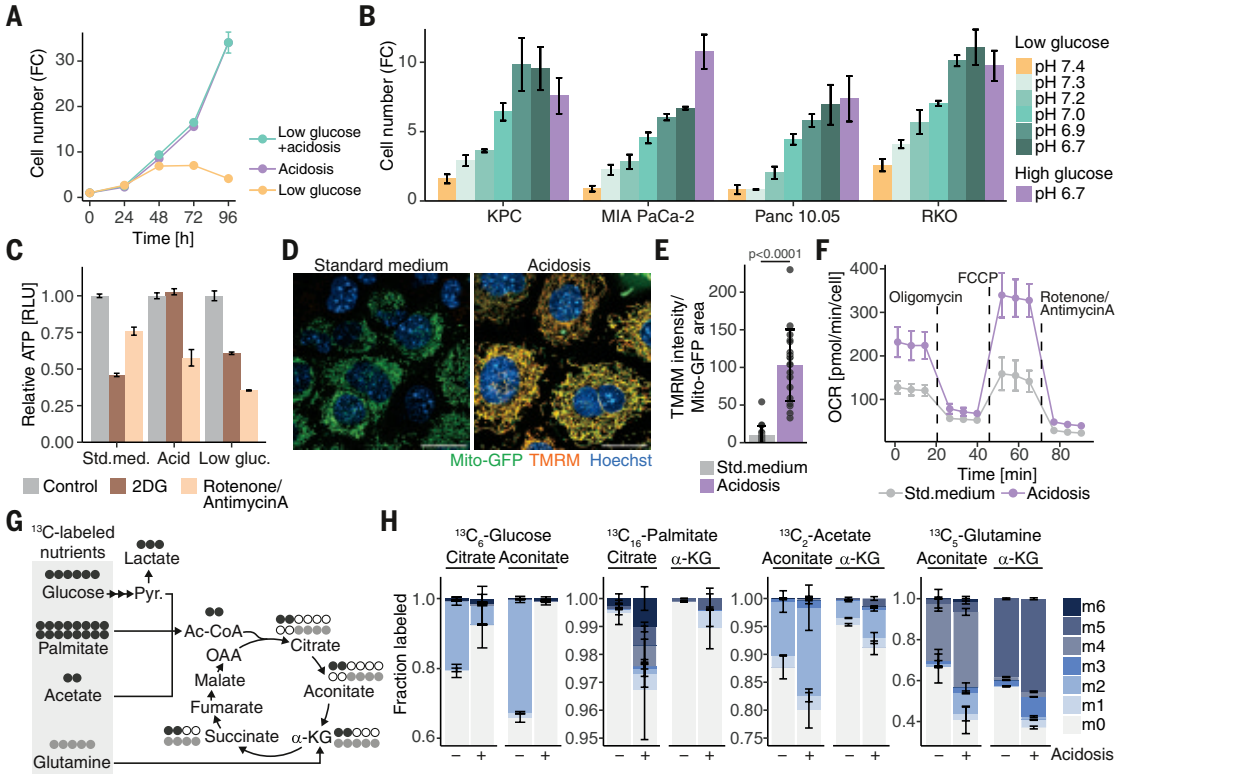


Fig. 4. Acidosis triggers a bioenergetic shift from a glycolytic to a respiratory state. (**A**) Proliferation of EPP2 cells in low glucose and/or acidosis. (**B**) Relative cell numbers of KPC, MIA PaCa-2, Panc 10.05, and RKO cells after 4 days of proliferation in low glucose and increasing acidosis (pH 7.4 to 6.7). (**C**) Relative ATP abundance in EPP2 cells after 48 hours of acidosis, low glucose, or standard medium and 2 hours of treatment with 2DG (10 mM) or rotenone + antimycin A (10 μM each). (**D**) Mitochondrial membrane potential in KPC cells expressing mito-GFP after 24 hours of acidosis or standard medium, assessed by TMRM imaging. Scale bars, 20 μm. (**E**) Quantification of TMRM intensity of (D). (**F**) Oxygen consumption rate (OCR) of EPP2 cells after 24 hours of acidosis or standard medium. OCR was measured upon sequential injection of oligomycin (0.5 μM), carbonyl cyanide *p*-trifluoromethoxyphenylhydrazone (FCCP) (1 μM), and rotenone + antimycin A (0.5 μM each). (**G**) Schematic of ^{13}C isotope tracing using different TCA cycle substrates. Ac-CoA, acetyl coenzyme A; α-KG, α-ketoglutarate; OAA, oxaloacetate. (**H**) Fractional enrichment of intracellular citrate, aconitate, or α-KG in RKO cells after 24 hours of acidosis or standard medium. Cells were labeled with $^{13}C_6$-glucose (10 min), $^{13}C_{16}$-palmitate (16 hours), $^{13}C_2$-acetate (16 hours), or $^{13}C_5$ glutamine (1 hour). In (A) to (C), (E), (F), and (H), data are represented as means ± SDs [$n = 3$ in (A) to (C) and (H); $n = 20$ fields of view in (E); $n = 4$ in (F)].

labeled with either green or red fluorescent proteins over time (*44*) revealed that acidosis did not alter mitochondrial fusion rates (fig. S9, E to H). Rather, acidosis decreased the abundance of mitochondrial DRP1 foci (Fig. 5, D and E), which assemble at sites of fission (*45*). Mitochondrial recruitment of DRP1 to initiate fission is triggered by phosphorylation on S616 (*46*–*48*). Acidosis strongly reduced DRP1 S616 phosphorylation (Fig. 5F and fig. S10A), which coincided with the appearance of fused mitochondria in several human and mouse cancer cell lines (Fig. 5G and fig. S10B). Expressing phosphomimetic constitutively active DRP1 S616D, however, blocked the acidosis-induced formation of tubular mitochondria (Fig. 5, H and I). Thus, acidosis suppresses mitochondrial fission through loss of DRP1 S616 phosphorylation, resulting in unopposed mitochondrial fusion.

To determine how acidosis suppressed DRP1, we identified the kinase responsible for DRP1 activation at neutral pH. Pharmacologic inhibition of kinases implicated in DRP1 regulation (*39*, *46*, *48*, *49*) revealed that DRP1 S616 phosphorylation was largely abrogated by inhibition of extracellular signal–regulated kinase (ERK) or its upstream activator, MAP-ERK kinase (MEK) (Fig. 5, J and K). These kinases are part of the RAF-MEK-ERK mitogen-activated protein kinase (MAPK) pathway, a key effector of RAS oncogenes that is commonly hyperactivated in cancer and implicated as a driver of mitochondrial fragmentation (*47*, *48*). Indeed, pharmacological inhibition of MEK or genetic depletion of ERK1/2 triggered mitochondrial fusion in cancer cells (fig. S10, C to F), whereas expression of hyperactive $Kras^{G12D}$ in nontransformed mouse embryonic fibroblasts (MEFs) led to mitochondrial fragmentation (Fig. 5, L and M). Exposing RAS-transformed MEFs to acidosis, however, reverted mitochondrial morphology from highly fragmented organelles back to tubular networks.

Because acidosis could counteract RAS-induced mitochondrial fragmentation, we investigated whether acidosis regulated RAS-ERK MAPK signaling. Acidosis led to a decrease in phosphorylated active ERK and a corresponding loss of DRP1 S616 phosphorylation in multiple cancer cell lines (Fig. 5N). Fractionation experiments revealed that acidosis decreased phospho-ERK in the cytosol, whereas nuclear ERK was largely unaffected (fig. S11, A and B). Accordingly, acidosis had no overt effect on the transcriptional output of ERK signaling (fig. S11C). To determine whether cytoplasmic ERK suppression was required for DRP1 inactivation under acidosis, we sustained ERK activity by expressing constitutively active MEK^{DD}. Under acidosis, constitutive ERK signaling prevented DRP1 dephosphorylation, abrogated mitochondrial fusion (Fig. 5, O to Q, and fig. S11, D to G), and compromised cell proliferation (Fig. 5R and fig. S11H). This suggests that acidosis triggers mitochondrial fusion by somehow suppressing cytosolic ERK, the dominant driver of DRP1 phosphorylation and mitochondrial fragmentation in cancer.

Tumor acidosis reprograms energy metabolism in cancer cells

Next, we determined whether the changes in mitochondrial morphology were relevant for the acidosis-induced changes of mitochondrial

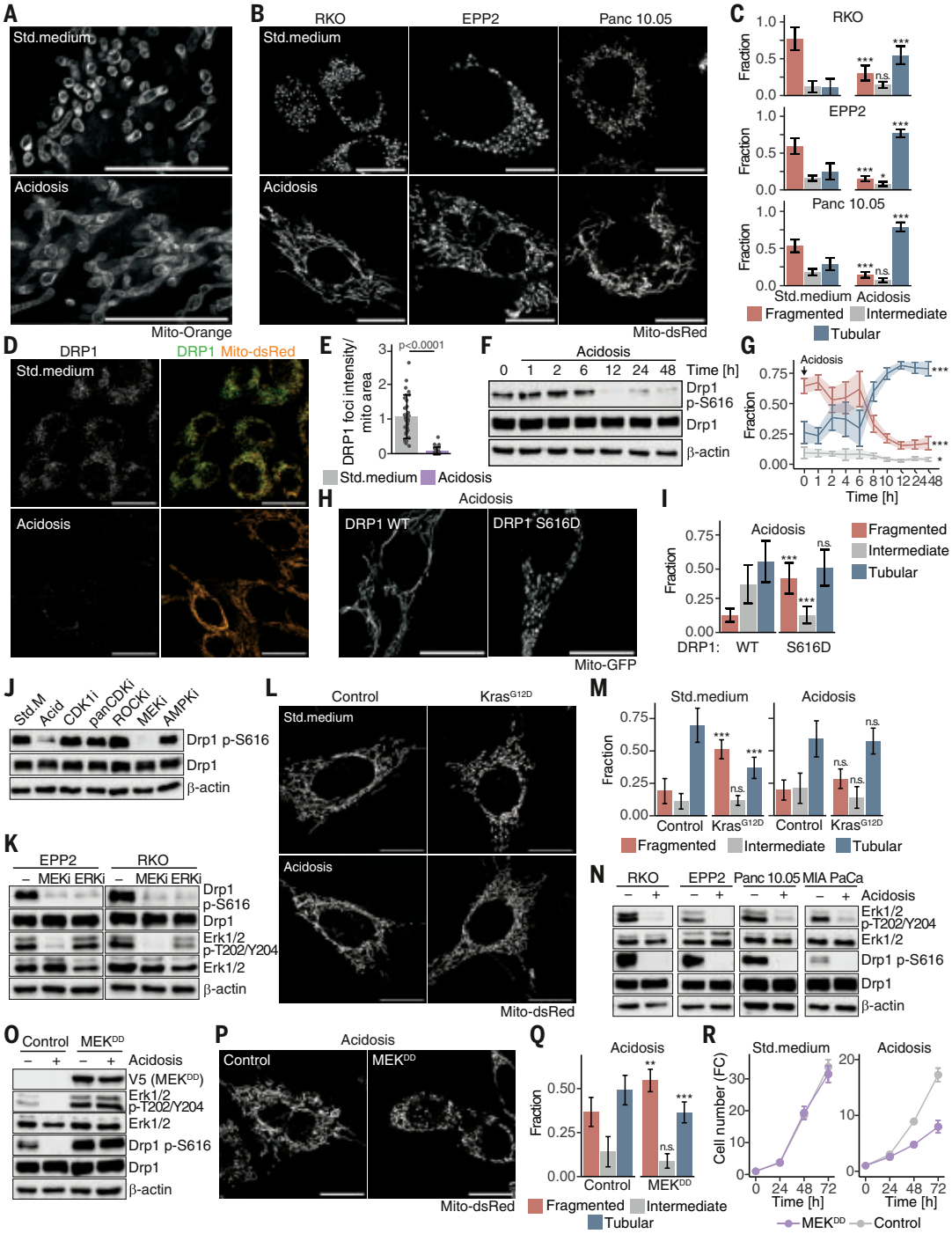


Fig. 5. Acidosis suppresses mitochondrial fragmentation in cancer cells. (**A** and **B**) Mitochondrial morphology after 24 hours of acidosis. (A) RKO cells, analyzed by super-resolution microscopy of mito-orange; (B) RKO, EPP2, and Panc 10.05 cells, analyzed by mito-dsRed imaging. (**C**) Quantification of mitochondrial morphology of (B). (**D**) DRP1 localization in RKO cells after 24 hours of acidosis, analyzed by immunofluorescence. (**E**) Quantification of DRP1 foci as in (D). (**F**) Change in Drp1 phosphorylation in RKO cells after indicated times in acidosis, analyzed by immunoblotting. S, serine. (**G**) Mitochondrial morphology in RKO cells over time in acidosis, analyzed by mito-dsRed imaging. (**H**) Mitochondrial morphology in RKO cells expressing DRP1 wild type (WT) or S616D after 24 hours of acidosis, analyzed by mito-GFP imaging. D, aspartic acid. (**I**) Quantification of mitochondrial morphology of (H). (**J** and **K**) Change in Drp1 phosphorylation after 48 hours of treatments, analyzed by immunoblotting. (J) EPP2 cells treated with acidosis or inhibitors against CDK1 (60 nM Ro-3306), panCDK (5 μM PHA793887), ROCK (10 μM Y-27632), MEK (1 μM mirdametinib), or AMPK (10 μM Compound C); (K) EPP2 and RKO cells treated with inhibitors against MEK (1 μM mirdametinib) or ERK (1 μM SCH772984). T, threonine; Y, tyrosine. (**L**) Mitochondrial morphology in $Kras^{G12D}$ and control MEFs after 24 hours of acidosis, analyzed by mito-dsRed imaging. G, glycine. (**M**) Quantification of mitochondrial morphology of (L). (**N**) Change in Drp1 and Erk1/2 phosphorylation in RKO, EPP2, Panc 10.05, and MIA PaCa-2 cells after 48 hours of acidosis, analyzed by immunoblotting. (**O**) Change in Drp1 and Erk1/2 phosphorylation in EPP2 cells expressing MEK^{DD} after 48 hours of acidosis, analyzed by immunoblotting. (**P**) Mitochondrial morphology in EPP2 cells expressing MEK^{DD} after 24 hours of acidosis, analyzed by mito-dsRed imaging. (**Q**) Quantification of mitochondrial morphology of (P). (**R**) Proliferation of EPP2 cells expressing MEK^{DD} in acidosis. Scale bars, 10 μm (A) and 20 μm [(B), (D), (H), (L), and (P)]. In (C), (G), (I), (M), and (Q), mitochondrial length was classified into fragmented (<1 μm), intermediate (1 to 2 μm), or tubular (>2 μm). In (C), (E), (G), (I), (M), (Q), and (R), data are represented as means ± SDs [$n = 10$ to 40 fields of view in (C), (E), (G), (I), (M), and (Q); $n = 3$ in (R)]. For mitochondrial length, statistical tests were performed in each group between manipulation and control or standard medium.

metabolism. Acidosis did not increase labeling of TCA cycle intermediates from ^{13}C glutamine when mitochondrial fragmentation was enforced by OPA1 depletion (fig. S12A) or upon short acid exposure when mitochondria were still fragmented (fig. S12, B and C). Consistently, depletion of OPA1 or MFN1 suppressed the acidosis-induced increases in mitochondrial membrane potential (Fig. 6A and fig. S12D) and respiration (Fig. 6B) and suppressed cell proliferation in acidic medium (Fig. 6C). By contrast, enforcing mitochondrial fusion by depletion of DRP1 had no effect. At neutral pH, depletion of OPA1, MFN1, or DRP1 had no effect on membrane potential (Fig. 6A and fig. S12D), respiration (Fig. 6B), or cell proliferation (Fig. 6C). Thus, whereas fragmented and fused mitochondria sustained bioenergetics in standard medium, mitochondrial fusion was required for bioenergetic adaptations to acidosis.

To investigate the relevance of mitochondrial morphology and metabolism in vivo, we developed a multicolor competition assay based on coexpressing distinct sgRNAs and fluorescent proteins, which enabled tracking the growth of cancer cell populations with distinct gene depletions within the same tumor. We conducted competition assays between cells in which we suppressed glycolysis (Pkm or Ldha depletion), mitochondrial respiration (Ndufc2 depletion), mitochondrial fusion (Opa1 depletion), or proliferation (DNA replication factor Rpa3 depletion). Pancreatic tumors from EPP2 cells acidified to pH ~6.7, in good agreement with the cell culture acidosis conditions (Fig. 6D). In these tumors, depletion of Ndufc2 or Opa1 reduced cancer cell fitness, whereas depletion of Pkm or Ldha was tolerated, similar to the acidosis phenotypes in cell culture (Fig. 6E). By contrast, cells depended on glycolytic enzymes instead of mitochondrial fusion and respiration when cultured in standard medium or hypoxia, and they depended on both glycolysis and respiration when cultured in low-glucose medium. Comparable results were obtained in pancreatic tumors from KPC cells (Fig. 6, F and G) and in subcutaneous tumors of a mouse lung cancer model (fig. S13A). Thus, an acidic environment, both in tumors and in cell culture, shifts the dependence of cancer cells from glycolysis to mitochondrial fusion and respiration.

To directly test the impact of pH alterations in vivo, we manipulated tumor acidification. We deleted Ldha, which suppressed acid excretion by cancer cells in culture (fig. S13B) and led to the formation of less acidic tumors (Fig. 6H). We generated tumors from Ldha-deficient or control cells containing a small number of cells transduced with sgRNAs of interest. In acidic control tumors, Ndufc2 and Opa1 were essential, whereas Pkm was not (Fig. 6I). Conversely, when cancer cells grew in less acidic tumors, Pkm became essential, whereas loss of Ndufc2 or Opa1 was

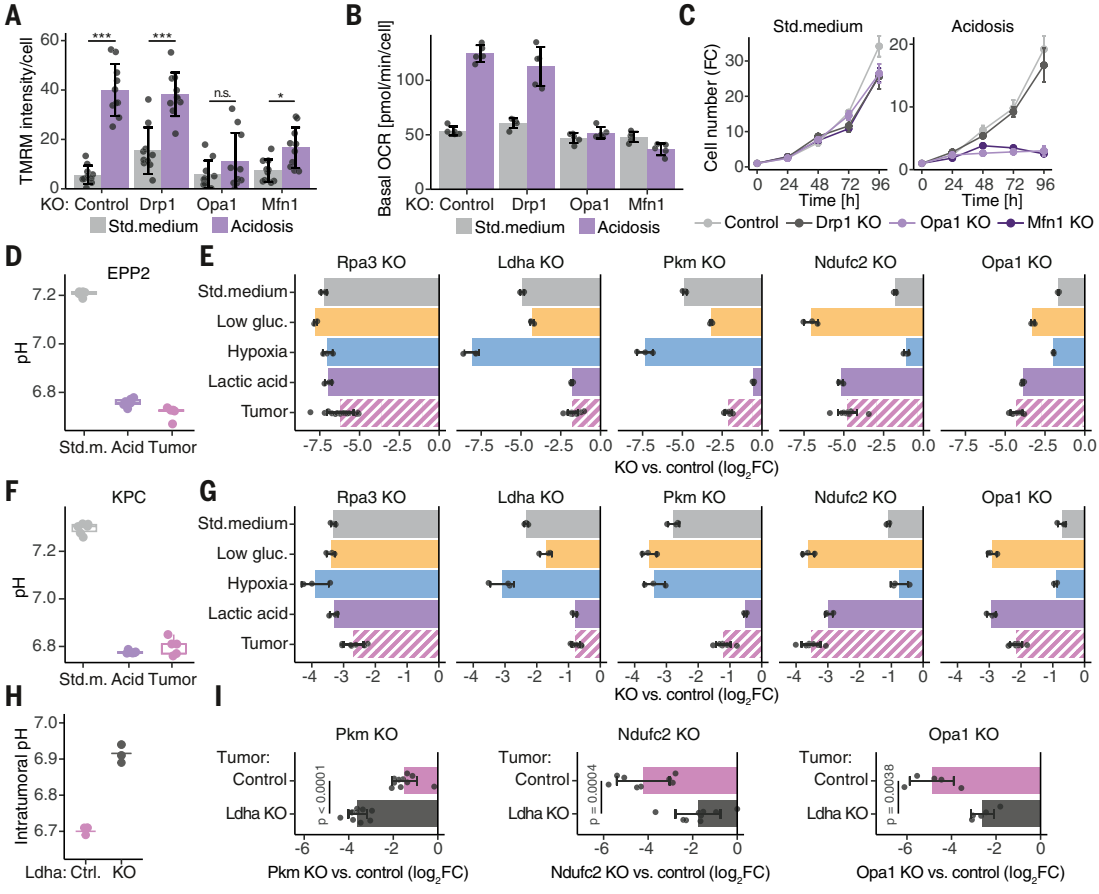


Fig. 6. Acidosis orchestrates energy metabolism in tumors. (**A**) Quantification of mitochondrial membrane potential in KPC cells with Drp1, Opa1, or Mfn1 depletion (KO) after 24 hours of acidosis, assessed by TMRM imaging. (**B**) Basal OCR in KPC cells with Drp1, Opa1, or Mfn1 depletion (KO) after 24 hours of acidosis. (**C**) Proliferation of KPC cells with Drp1, Opa1, or Mfn1 depletion (KO) in acidosis (pH 6.9). (**D** to **G**) Cells with indicated gene depletions (KO) in different cell culture stresses or in tumors after transplantation into the pancreas of *Rag2*$^{-/-}$ B6 mice. EPP2 (D) and KPC (F) cell culture medium and tumor pH. EPP2 (E) and KPC (G) competitive cell proliferation assays, analyzed by quantification of relative changes in sgRNA abundance after 12 population doublings in culture or 15 days of tumor growth. (**H**) pH of tumors generated by EPP2 cells with Ldha depletion (KO) or control cells at day 14 after transplantation into the pancreas. (**I**) Competitive cell proliferation assay of EPP2 cells with indicated gene depletions (KO) in the context of Ldha-depleted or control tumors in *Rag2*$^{-/-}$ B6 mice. Relative changes in sgRNA abundance were quantified after 15 days of tumor growth. *P* values were calculated with a two-tailed unpaired *t* test with Welch correction. In (A) to (I), data are represented as means ± SDs [$n = 10$ fields of view in (A); $n = 5$ in (B); $n = 3$ in (C); $n = 3$ in (D), (F), and (H); in (E), (G), and (I), cell culture $n = 3$, and tumor $n = 5$ to 10].

tolerated. These results indicate that the balance between mitochondrial respiration and glycolysis in cancer cells is dictated by tumor pH.

Discussion

By integrating CRISPR screens under defined cell culture stress conditions and in tumors, our study characterizes metabolic adaptations in cancer. Our cell culture–based screens expand findings from studies investigating individual stress conditions (*24*, *26*–*28*) and enable systematic comparisons of various metabolic stresses. The screens in pancreatic tumors reveal differences compared with standard cell culture conditions, which contrasts with recent studies reporting a high concordance of metabolic dependencies in cell culture and subcutaneous pancreatic tumors (*50*, *51*). This may be due to differences between subcutaneous implantation and transplantation to the original organ site. Moreover, whereas constitutive Cas9 systems report fitness effects during cell culture and transplantation, our inducible system enables gene depletion in established tumors; and our in vivo screen was based on the unbiased identification of fitness genes through cell culture–based screens in specific stress conditions. More generally, CRISPR screens that relate gene functions in tissues to defined cell culture conditions offer a promising approach for deciphering complex in vivo environments.

Tumors are complex metabolic environments where multiple stresses manifest simultaneously. How cancer cells adapt is a nontrivial problem—for example, hypoxia promotes glycolysis, whereas glucose starvation enhances mitochondrial respiration. Although our screens confirm contextual phenotypes under various cell culture conditions, they establish acidosis as a dominant determinant of cancer cell metabolism in vivo. By shifting energy metabolism to a respiratory state, acidosis promotes ATP production independently of glycolysis and abrogates the effects of glucose starvation. Accordingly, various genes that are essential during glucose starvation at neutral pH become dispensable under acidosis, including glucose transporters, glycolytic enzymes, and the glycosylation sensor, Perk. This switch in energy metabolism was triggered through medium acidification but not through the addition of lactate, although lactate is a TCA cycle substrate (*14*, *15*) and an activator of the electron transport chain (*52*). Acidosis conceivably synergizes with lactate to enhance mitochondrial bioenergetics, but because lactic acid is not the only contributor to tumor acidification (*53*, *54*), the impact of acidosis likely extends beyond areas where lactic acid accumulates.

Mechanistically, we show that acidosis suppresses DRP1-mediated mitochondrial fission, triggering the formation of tubular mitochondrial networks and enhancing mitochondrial metabolism. Opposing changes in mitochondrial morphology occur in response to various metabolic stresses, and mitochondrial morphology has context-dependent effects on respiration and ATP production (*37*, *39*–*43*, *55*–*57*), which raises the question of how mitochondrial morphology relates to cellular metabolism and stress adaptation. In cancer, mitochondrial fragmentation is potently triggered by oncogenic RAS-ERK MAPK signaling through activation of DRP1 (*47*, *48*). Our results demonstrate, however, that acidosis fully reverses oncogene-induced mitochondrial fragmentation through suppression of cytosolic ERK. Although we observe little impact of mitochondrial morphology on cellular bioenergetics at neutral pH, mitochondrial fusion becomes essential for cancer cell growth in acidic culture conditions and tumor environments. Thus, environmental pH dictates the dependence of cellular energy production on mitochondrial fusion.

The role of mitochondria in cancer is controversial: Mitochondrial fragmentation downstream of oncogenic RAS-ERK MAPK signaling has been suggested to enhance aerobic glycolysis as a result of mitochondrial dysfunction (*47*, *48*, *58*), reminiscent of the original explanation of the Warburg effect (*4*–*6*). However, cancer cells retain and often depend on functional mitochondria (*59*–*62*). Our results reveal that mitochondrial fragmentation is not a static consequence of oncogenic RAS-ERK MAPK signaling but a dynamic process that is governed by pH. Although this cross-talk between oncogenic signaling and metabolism retains bioenergetic flexibility, our findings indicate that therapeutic inhibition of RAS-ERK MAPK signaling may promote mitochondrial fusion and, thereby, an oxidative state that has been associated with therapy-resistant persister cells (*61*, *62*). In addition to supporting glycolysis-independent ATP production and thereby freeing scarce glucose resources for other demands, acidosis confers resilience to a range of metabolic stresses. Even beyond central carbon metabolism, many gene fitness effects observed in vivo can be recapitulated in cell culture by adjusting the medium's pH to tumor-relevant values. Thus, rather than merely being a by-product of cancer metabolism, acidosis orchestrates bioenergetic adaptations to complex metabolic stresses in tumors.

Materials and methods are available in the supplementary materials.

REFERENCES AND NOTES

1. L. W. S. Finley, What is cancer metabolism? *Cell* **186**, 1670–1688 (2023). doi: 10.1016/j.cell.2023.01.038; pmid: 36858045
2. A. Muir, L. V. Danai, M. G. Vander Heiden, Microenvironmental regulation of cancer cell metabolism: Implications for experimental design and translational studies. *Dis. Model. Mech.* **11**, dmm035758 (2018). doi: 10.1242/dmm.035758; pmid: 30104199
3. N. N. Pavlova, J. Zhu, C. B. Thompson, The hallmarks of cancer metabolism: Still emerging. *Cell Metab.* **34**, 355–377 (2022). doi: 10.1016/j.cmet.2022.01.007; pmid: 35123658
4. M. V. Liberti, J. W. Locasale, The Warburg Effect: How Does it Benefit Cancer Cells? *Trends Biochem. Sci.* **41**, 211–218 (2016). doi: 10.1016/j.tibs.2015.12.001; pmid: 26778478
5. R. J. DeBerardinis, N. S. Chandel, We need to talk about the Warburg effect. *Nat. Metab.* **2**, 127–129 (2020). doi: 10.1038/s42255-020-0172-2; pmid: 32694689
6. S. M. Fendt, 100 years of the Warburg effect: A cancer metabolism endeavor. *Cell* **187**, 3824–3828 (2024). doi: 10.1016/j.cell.2024.06.026; pmid: 39059359
7. R. J. DeBerardinis, N. S. Chandel, Fundamentals of cancer metabolism. *Sci. Adv.* **2**, e1600200 (2016). doi: 10.1126/sciadv.1600200; pmid: 27386546
8. E. Boedtkjer, S. F. Pedersen, The Acidic Tumor Microenvironment as a Driver of Cancer. *Annu. Rev. Physiol.* **82**, 103–126 (2020). doi: 10.1146/annurev-physiol-021119-034627; pmid: 31730395
9. W. Palm, C. B. Thompson, Nutrient acquisition strategies of mammalian cells. *Nature* **546**, 234–242 (2017). doi: 10.1038/nature22379; pmid: 28593971
10. S. M. Davidson *et al.*, Environment Impacts the Metabolic Dependencies of Ras-Driven Non-Small Cell Lung Cancer. *Cell Metab.* **23**, 517–528 (2016). doi: 10.1016/j.cmet.2016.01.007; pmid: 26853747
11. M. O. Yuneva *et al.*, The metabolic profile of tumors depends on both the responsible genetic lesion and tissue type. *Cell Metab.* **15**, 157–170 (2012). doi: 10.1016/j.cmet.2011.12.015; pmid: 22326218
12. T. Mashimo *et al.*, Acetate is a bioenergetic substrate for human glioblastoma and brain metastases. *Cell* **159**, 1603–1614 (2014). doi: 10.1016/j.cell.2014.11.025; pmid: 25525878
13. B. Faubert *et al.*, Lactate Metabolism in Human Lung Tumors. *Cell* **171**, 358–371.e9 (2017). doi: 10.1016/j.cell.2017.09.019; pmid: 28985563
14. S. Hui *et al.*, Glucose feeds the TCA cycle via circulating lactate. *Nature* **551**, 115–118 (2017). doi: 10.1038/nature24057; pmid: 29045397
15. C. T. Hensley *et al.*, Metabolic Heterogeneity in Human Lung Tumors. *Cell* **164**, 681–694 (2016). doi: 10.1016/j.cell.2015.12.034; pmid: 26853473
16. K. L. Abbott *et al.*, Metabolite profiling of human renal cell carcinoma reveals tissue-origin dominance in nutrient availability. *eLife* **13**, RP95652 (2024). doi: 10.7554/eLife.95652; pmid: 38787918
17. J. J. Kamphorst *et al.*, Human pancreatic cancer tumors are nutrient poor and tumor cells actively scavenge extracellular protein. *Cancer Res.* **75**, 544–553 (2015). doi: 10.1158/0008-5472.CAN-14-2211; pmid: 25644265
18. M. S. Lee *et al.*, Ornithine aminotransferase supports polyamine synthesis in pancreatic cancer. *Nature* **616**, 339–347 (2023). doi: 10.1038/s41586-023-05891-2; pmid: 36991126
19. D. R. Schmidt *et al.*, Metabolomics in cancer research and emerging applications in clinical oncology. *CA Cancer J. Clin.* **71**, 333–358 (2021). doi: 10.3322/caac.21670; pmid: 33982817
20. A. Sreekumar *et al.*, Metabolomic profiles delineate potential role for sarcosine in prostate cancer progression. *Nature* **457**, 910–914 (2009). doi: 10.1038/nature07762; pmid: 19212411
21. M. R. Sullivan *et al.*, Quantification of microenvironmental metabolites in murine cancers reveals determinants of tumor nutrient availability. *eLife* **8**, e44235 (2019). doi: 10.7554/eLife.44235; pmid: 30990168
22. M. Rossi *et al.*, PHGDH heterogeneity potentiates cancer cell dissemination and metastasis. *Nature* **605**, 747–753 (2022). doi: 10.1038/s41586-022-04758-2; pmid: 35585241
23. S. Rabinovich *et al.*, Diversion of aspartate in ASS1-deficient tumours fosters *de novo* pyrimidine synthesis. *Nature* **527**, 379–383 (2015). doi: 10.1038/nature15529; pmid: 26560030

24. J. Michl *et al.*, CRISPR-Cas9 screen identifies oxidative phosphorylation as essential for cancer cell survival at low extracellular pH. *Cell Rep.* **38**, 110493 (2022). doi: 10.1016/j.celrep.2022.110493; pmid: 35263578
25. N. J. Rossiter *et al.*, CRISPR screens in physiologic medium reveal conditionally essential genes in human cells. *Cell Metab.* **33**, 1248–1263.e9 (2021). doi: 10.1016/j.cmet.2021.02.005; pmid: 33651980
26. C. Pechincha *et al.*, Lysosomal enzyme trafficking factor LYSET enables nutritional usage of extracellular proteins. *Science* **378**, eabn5637 (2022). doi: 10.1126/science.abn5637; pmid: 36074822
27. I. H. Jain *et al.*, Genetic Screen for Cell Fitness in High or Low Oxygen Highlights Mitochondrial and Lipid Metabolism. *Cell* **181**, 716–727.e11 (2020). doi: 10.1016/j.cell.2020.03.029; pmid: 32259488
28. K. Birsoy *et al.*, Metabolic determinants of cancer cell sensitivity to glucose limitation and biguanides. *Nature* **508**, 108–112 (2014). doi: 10.1038/nature13110; pmid: 24670634
29. J. Zhang *et al.*, Asparagine plays a critical role in regulating cellular adaptation to glutamine depletion. *Mol. Cell* **56**, 205–218 (2014). doi: 10.1016/j.molcel.2014.08.018; pmid: 25242145
30. C. J. Halbrook, C. A. Lyssiotis, M. Pasca di Magliano, A. Maitra, Pancreatic cancer: Advances and challenges. *Cell* **186**, 1729–1754 (2023). doi: 10.1016/j.cell.2023.02.014; pmid: 37059070
31. P. Rathert *et al.*, Transcriptional plasticity promotes primary and acquired resistance to BET inhibition. *Nature* **525**, 543–547 (2015). doi: 10.1038/nature14898; pmid: 26367798
32. G. Michlits *et al.*, Multilayered VBC score predicts sgRNAs that efficiently generate loss-of-function alleles. *Nat. Methods* **17**, 708–716 (2020). doi: 10.1038/s41592-020-0850-8; pmid: 32514112
33. J. D. Rabinowitz, S. Enerbäck, Lactate: The ugly duckling of energy metabolism. *Nat. Metab.* **2**, 566–571 (2020). doi: 10.1038/s42255-020-0243-4; pmid: 32694798
34. J. Xie *et al.*, Beyond Warburg effect – Dual metabolic nature of cancer cells. *Sci. Rep.* **4**, 4927 (2014). doi: 10.1038/srep04927; pmid: 24820099
35. C. Corbet *et al.*, Acidosis Drives the Reprogramming of Fatty Acid Metabolism in Cancer Cells through Changes in Mitochondrial and Histone Acetylation. *Cell Metab.* **24**, 311–323 (2016). doi: 10.1016/j.cmet.2016.07.003; pmid: 27508876
36. G. LaMonte *et al.*, Acidosis induces reprogramming of cellular metabolism to mitigate oxidative stress. *Cancer Metab.* **1**, 23 (2013). doi: 10.1186/2049-3002-1-23; pmid: 24359630
37. M. Giacomello, A. Pyakurel, C. Glytsou, L. Scorrano, The cell biology of mitochondrial membrane dynamics. *Nat. Rev. Mol. Cell Biol.* **21**, 204–224 (2020). doi: 10.1038/s41580-020-0210-7; pmid: 32071438
38. D. Senft, Z. A. Ronai, Regulators of mitochondrial dynamics in cancer. *Curr. Opin. Cell Biol.* **39**, 43–52 (2016). doi: 10.1016/j.ceb.2016.02.001; pmid: 26896558
39. E. Q. Toyama *et al.*, AMP-activated protein kinase mediates mitochondrial fission in response to energy stress. *Science* **351**, 275–281 (2016). doi: 10.1126/science.aab4138; pmid: 26816379
40. N. Martinez-Lopez *et al.*, mTORC2–NDRG1–CDC42 axis couples fasting to mitochondrial fission. *Nat. Cell Biol.* **25**, 989–1003 (2023). doi: 10.1038/s41556-023-01163-3; pmid: 37386153
41. A. S. Rambold, B. Kostelecky, N. Elia, J. Lippincott-Schwartz, Tubular network formation protects mitochondria from autophagosomal degradation during nutrient starvation. *Proc. Natl. Acad. Sci. U.S.A.* **108**, 10190–10195 (2011). doi: 10.1073/pnas.1107402108; pmid: 21646527
42. M. Khacho *et al.*, Acidosis overrides oxygen deprivation to maintain mitochondrial function and cell survival. *Nat. Commun.* **5**, 3550 (2014). doi: 10.1038/ncomms4550; pmid: 24686499
43. L. C. Gomes, G. Di Benedetto, L. Scorrano, During autophagy mitochondria elongate, are spared from degradation and sustain cell viability. *Nat. Cell Biol.* **13**, 589–598 (2011). doi: 10.1038/ncb2220; pmid: 21478857
44. Y. Mattenberger, D. I. James, J. C. Martinou, Fusion of mitochondria in mammalian cells is dependent on the mitochondrial inner membrane potential and independent of microtubules or actin. *FEBS Lett.* **538**, 53–59 (2003). doi: 10.1016/S0014-5793(03)00124-8; pmid: 12633852
45. E. Smirnova, L. Griparic, D. L. Shurland, A. M. van der Bliek, Dynamin-related protein Drp1 is required for mitochondrial division in mammalian cells. *Mol. Biol. Cell* **12**, 2245–2256 (2001). doi: 10.1091/mbc.12.8.2245; pmid: 11514614
46. N. Taguchi, N. Ishihara, A. Jofuku, T. Oka, K. Mihara, Mitotic phosphorylation of dynamin-related GTPase Drp1 participates in mitochondrial fission. *J. Biol. Chem.* **282**, 11521–11529 (2007). doi: 10.1074/jbc.M607279200; pmid: 17301055
47. M. N. Serasinghe *et al.*, Mitochondrial division is requisite to RAS-induced transformation and targeted by oncogenic MAPK pathway inhibitors. *Mol. Cell* **57**, 521–536 (2015). doi: 10.1016/j.molcel.2015.01.003; pmid: 25658204
48. J. A. Kashatus *et al.*, Erk2 phosphorylation of Drp1 promotes mitochondrial fission and MAPK-driven tumor growth. *Mol. Cell* **57**, 537–551 (2015). doi: 10.1016/j.molcel.2015.01.002; pmid: 25658205
49. C. S. Brand, V. P. Tan, J. H. Brown, S. Miyamoto, RhoA regulates Drp1 mediated mitochondrial fission through ROCK to protect cardiomyocytes. *Cell. Signal.* **50**, 48–57 (2018). doi: 10.1016/j.cellsig.2018.06.012; pmid: 29953931
50. D. E. Biancur *et al.*, Functional Genomics Identifies Metabolic Vulnerabilities in Pancreatic Cancer. *Cell Metab.* **33**, 199–210.e8 (2021). doi: 10.1016/j.cmet.2020.10.018; pmid: 33152323
51. X. G. Zhu *et al.*, Functional Genomics *In Vivo* Reveal Metabolic Dependencies of Pancreatic Cancer Cells. *Cell Metab.* **33**, 211–221.e6 (2021). doi: 10.1016/j.cmet.2020.10.017; pmid: 33152324
52. X. Cai *et al.*, Lactate activates the mitochondrial electron transport chain independently of its metabolism. *Mol. Cell* **83**, 3904–3920.e7 (2023). doi: 10.1016/j.molcel.2023.09.034; pmid: 37879334
53. K. Newell, A. Franchi, J. Pouysségur, I. Tannock, Studies with glycolysis-deficient cells suggest that production of lactic acid is not the only cause of tumor acidity. *Proc. Natl. Acad. Sci. U.S.A.* **90**, 1127–1131 (1993). doi: 10.1073/pnas.90.3.1127; pmid: 8430084
54. G. Helmlinger, A. Sckell, M. Dellian, N. S. Forbes, R. K. Jain, Acid production in glycolysis-impaired tumors provides new insights into tumor metabolism. *Clin. Cancer Res.* **8**, 1284–1291 (2002). pmid: 11948144
55. F. Bonnay *et al.*, Oxidative Metabolism Drives Immortalization of Neural Stem Cells during Tumorigenesis. *Cell* **182**, 1490–1507.e19 (2020). doi: 10.1016/j.cell.2020.07.039; pmid: 32916131
56. H. Chen, A. Chomyn, D. C. Chan, Disruption of fusion results in mitochondrial heterogeneity and dysfunction. *J. Biol. Chem.* **280**, 26185–26192 (2005). doi: 10.1074/jbc.M503062200; pmid: 15899901
57. M. Yu *et al.*, Mitochondrial fusion exploits a therapeutic vulnerability of pancreatic cancer. *JCI Insight* **4**, e126915 (2019). doi: 10.1172/jci.insight.126915; pmid: 31335325
58. J. Hagenbuchner, A. V. Kuznetsov, P. Obexer, M. J. Ausserlechner, BIRC5/Survivin enhances aerobic glycolysis and drug resistance by altered regulation of the mitochondrial fusion/fission machinery. *Oncogene* **32**, 4748–4757 (2013). doi: 10.1038/onc.2012.500; pmid: 23146905
59. S. Vyas, E. Zaganjor, M. C. Haigis, Mitochondria and Cancer. *Cell* **166**, 555–566 (2016). doi: 10.1016/j.cell.2016.07.002; pmid: 27471965
60. M. Momcilovic *et al.*, In vivo imaging of mitochondrial membrane potential in non-small-cell lung cancer. *Nature* **575**, 380–384 (2019). doi: 10.1038/s41586-019-1715-0; pmid: 31666695
61. A. Viale *et al.*, Oncogene ablation-resistant pancreatic cancer cells depend on mitochondrial function. *Nature* **514**, 628–632 (2014). doi: 10.1038/nature13611; pmid: 25119024
62. R. Masoud *et al.*, Targeting Mitochondrial Complex I Overcomes Chemoresistance in High OXPHOS Pancreatic Cancer. *Cell Rep. Med.* **1**, 100143 (2020). doi: 10.1016/j.xcrm.2020.100143; pmid: 33294863
63. J. Schmoellerl *et al.*, EVI1 drives leukemogenesis through aberrant ERG activation. *Blood* **141**, 453–466 (2023). doi: 10.1182/blood.2022016592; pmid: 36095844

ACKNOWLEDGMENTS

We thank all members of the Palm and Zuber laboratories for experimental advice and helpful discussions. We thank F. Sanchez-Rivera for gifting cell lines; A. Winkelkotte for help with Seahorse experiments; M. Schneider and D. Helm at the DKFZ Proteomics Core Facility for quantitative proteomics; F. Blum, T. Rubner, and the DKFZ flow cytometry facility; the DKFZ light microscopy facility; M. Fellner for cloning CRISPR libraries; A. Sommer and the VBCF-NGS team for deep sequencing services; the IMP BioOptics flow cytometry team; the IMP/IMBA Comparative Medicine Facility for mouse colony maintenance; R. Heinen and the IMP/IMBA Molecular Biology Service for continuous support; T. Koecher and the VBCF Metabolomics Facility for helpful discussions; and B. Pacheco-Fiallos for help with illustrations. **Funding:** Research at the IMP is generously supported by Boehringer Ingelheim and the Austrian Research Promotion Agency (Headquarter grant FFG-852936). Vienna BioCenter Core Facilities (VBCF) are supported by the Austrian Federal Ministry of Education, Science and Research and the city of Vienna. The German Research Foundation (DFG) provided funding to S.G. and W.P. (PA 3679/3-1) and to M.T.S. and A.S. (FOR-2314 and SPP-2306). **Author contributions:** S.G. and R.K. contributed equally and will put their name first on the citation in their CVs; W.P. and J.Z. jointly conceived the project and designed the research together with S.G. and R.K; S.G. and R.K. conducted all experiments with help from M.T.S., L.W., and J.H.; F.A. provided bioinformatics support; S.G., R.K., W.P., and J.Z. analyzed and interpreted original data; M.T.S. and A.S. provided input on experimental designs; W.P., J.Z., S.G., and R.K. cowrote the manuscript with input from all authors; W.P. and J.Z. jointly supervised this work. **Competing interests:** J.Z. is a founder, shareholder, and scientific adviser of Quantro Therapeutics GmbH and a shareholder and scientific adviser of Mirimus Inc. J.Z. and the Zuber laboratory receive research support and funding from Boehringer Ingelheim. Other authors declare no competing interests. **Data and materials availability:** All data are available in the manuscript or the supplementary materials. All unique and stable reagents generated in this study are available from the lead contacts on reasonable request with a completed materials transfer agreement. **License information:** Copyright © 2025 the authors, some rights reserved; exclusive licensee American Association for the Advancement of Science. No claim to original US government works. https://www.science.org/about/science-licenses-journal-article-reuse

SUPPLEMENTARY MATERIALS

science.org/doi/10.1126/science.adp7603
Materials and Methods; Figs. S1 to S13; Table S1; References (*64*–*76*);
MDAR Reproducibility Checklist; Data S1 to S6

Submitted 10 April 2024; resubmitted 23 April 2025; accepted 30 July 2025

10.1126/science.adp7603

Science
JOURNALS AAAS



Publish your research in the *Science* family of journals

The *Science* family of journals (*Science, Science Advances, Science Immunology, Science Robotics, Science Signaling*, and *Science Translational Medicine)* are among the most highly-regarded journals in the world for quality and selectivity. Our peer-reviewed journals are committed to publishing cutting-edge research, incisive scientific commentary, and insights on what's important to the scientific world at the highest standards.

Submit your research today!

Learn more at **Science.org/journals**

RESEARCH ARTICLE SUMMARY

CANCER

MTAP deficiency confers resistance to cytosolic nucleic acid sensing and STING agonists

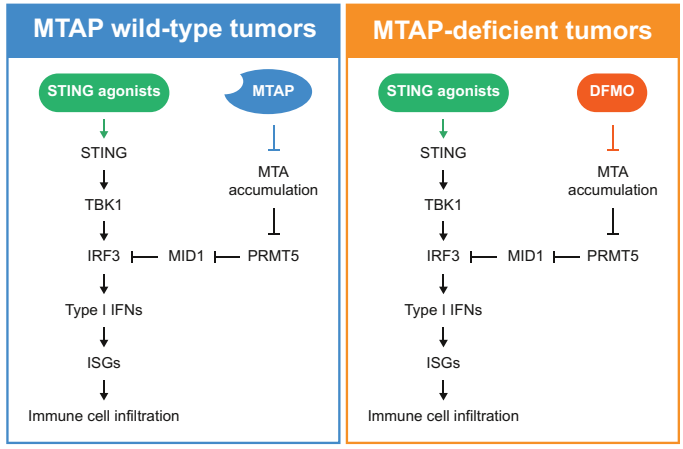
Jung-Mao Hsu*†, Chunxiao Liu†, Weiya Xia, Chung-Yu Chen, Wei-Chung Cheng, Junwei Hou, Mien-Chie Hung*

Full article and list of author affiliations: https://doi.org/10.1126/science.adl4089

INTRODUCTION: Cytosolic nucleic acid–sensing pathways have emerged as promising therapeutic targets to enhance the efficacy of immune checkpoint blockade, especially in immunologically "cold" tumors. Activation of these pathways stimulates type I interferon (IFN-I) signaling and the expression of interferon-stimulated genes (ISGs), promoting immune cell recruitment and potentially converting cold tumors into immune-active, "hot" tumors. Stimulator of interferon genes (STING) agonists, which activate this innate immune pathway, have shown potent antitumor activity in preclinical models. However, clinical trials have not replicated these effects in patients, highlighting a translational gap and the need to better understand the regulatory mechanisms and resistance factors influencing STING pathway activation in human cancers.

RATIONALE: Chromosome 9p21.3, which is frequently homozygously deleted in multiple cancer types, includes the *methylthioadenosine phosphorylase* (*MTAP*) gene and nearby loci such as cyclin dependent kinase inhibitor 2A (CDKN2A), CDKN2B, and, in some cases, IFN-I gene clusters. Although co-deletion of the IFN cluster has been linked to the immune-cold phenotype associated with 9p21.3 loss, our findings show that MTAP deletion independently impairs cytosolic nucleic acid sensing. Analysis of The Cancer Genome Atlas (TCGA), excluding cases with homozygous IFN cluster deletions, revealed a positive correlation between MTAP and IFN-I expression. We also identified MTAP loss as a common feature in human tumors that is largely absent in standard mouse models. Collectively, these observations led us to hypothesize that MTAP deficiency intrinsically suppresses nucleic acid sensing and contributes to STING agonist resistance.

RESULTS: Using multiple isogenic cell line models, we found that MTAP deletion suppresses IFNβ and downstream ISG induction by down-regulation of interferon regulatory factor 3 (IRF3), a key transcription factor in nucleic acid sensing. Mechanistically, MTAP loss results in the accumulation of its substrate, methylthioadenosine (MTA), which inhibits the methyltransferase protein arginine methyltransferase 5 (PRMT5). In MTAP-intact cells, PRMT5 inhibition or knockdown similarly reduced IRF3 expression and impaired nucleic acid sensing, establishing PRMT5 as a positive IRF3 regulator. MTA is also secreted and can suppress PRMT5 activity and IRF3 in neighboring MTAP-proficient cells, contributing to a paracrine-immunosuppressive environment. We further identified the E3 ubiquitin ligase Midline-1 (MID1), which targets IRF3 for degradation, as being up-regulated in MTAP-deficient, PRMT5-inhibited, or PRMT5-depleted cells. PRMT5 represses MID1 by depositing the repressive histone mark symmetric dimethylation at arginine 3 of histone H4 (H4R3me2s) at its promoter; MTAP deficiency abrogates this regulation, leading to increased MID1 and IRF3 destabilization. Treatment with the US Food and Drug Administration–approved ornithine decarboxylase inhibitor DL-α-difluoromethylornithine (DFMO) reduced MTA, restored PRMT5 activity, suppressed MID1, and rescued IRF3 levels and nucleic acid sensing in MTAP-deficient cells. In syngeneic mouse tumor models, MTAP-deficient tumors were resistant to STING agonists. However, combination therapy with STING agonists and DFMO overcame this resistance, leading to robust antitumor responses and increased immune infiltration.



MTAP-dependent regulation of the STING pathway and therapeutic strategy with STING agonists. In MTAP-deficient tumors, MTA accumulation inhibits PRMT5, impairing STING agonist–induced immune cell infiltration through IRF3 down-regulation. DFMO treatment may alleviate this suppression. By contrast, MTAP-intact tumors maintain intact STING activation, supporting a robust immune response. These findings support a MTAP-guided approach to STING agonist–based therapies and highlight DFMO as a potential sensitizing agent.

CONCLUSION: This study identifies MTAP deficiency as a key suppressor of cytosolic nucleic acid sensing and as a determinant of STING agonist resistance in human tumors. MTAP status may thus serve as a biomarker for patient stratification, and targeting polyamine metabolism may improve the clinical efficacy of STING-based immunotherapies. Mechanism-informed combination strategies may help to bridge the translational gap in innate immune activation therapies. □

*Corresponding author. Email: mhung@mail.cmu.edu.tw (M.-C.H.); hsujm@mail.cmu.edu.tw (J.-M.H.) †These authors contributed equally to this work. **Cite this article as J.-M. Hsu *et al.*, *Science* 390, eadl4089 (2025). DOI: 10.1126/science.adl4089**

CANCER

MTAP deficiency confers resistance to cytosolic nucleic acid sensing and STING agonists

Jung-Mao Hsu[1,2]*†, Chunxiao Liu[3,4]†, Weiya Xia[2,4,5], Chung-Yu Chen[2,5], Wei-Chung Cheng[2,6], Junwei Hou[7], Mien-Chie Hung[1,2,4,5,8]*

Cytosolic nucleic acid–sensing pathways are potential targets for cancer immunotherapy. Although stimulator of interferon genes (STING) agonists have shown substantial antitumor effects in animal models, their clinical efficacy in human tumors remains unclear. Deletion of methylthioadenosine phosphorylase (MTAP) is a common genomic alteration in human tumors but is rare in preclinical syngeneic mouse models. We found that homozygous *MTAP* deletion in human tumors creates a tumor microenvironment that obstructs cytosolic nucleic acid–sensing pathways by down-regulating interferon regulatory factor 3 (IRF3), leading to resistance to STING agonists. Targeting polyamine biosynthesis reverses IRF3 down-regulation, restoring sensitivity to STING agonists in MTAP-deficient tumors. Our findings suggest that MTAP genetic status may inform patient responses to STING agonist therapy and offer an alternative strategy for boosting antitumor immune responses using STING agonists in *MTAP*-deleted tumors.

Immune-desert tumors, also known as "cold" tumors, are characterized by a tumor microenvironment with limited infiltration of immune cells, particularly $CD8^+$ T cells. Such tumors are generally less responsive to immunotherapy because of their inability to elicit a robust immune response against cancer cells. To address this clinical challenge, cytosolic nucleic acid–sensing pathways have emerged as promising targets for cancer immunotherapy (*1*, *2*). Activation of these pathways triggers the production of type I interferon (IFN-I) and downstream interferon-stimulated genes (ISGs), which subsequently increases the recruitment and activation of immune cells within the tumor microenvironment. This mechanism has the potential to transform "cold" tumors into "hot" tumors, which have a higher degree of immune cell infiltration and should be more amenable to immunotherapy (*1*, *2*).

Despite the impressive antitumor activity demonstrated by multiple stimulator of interferon genes (STING) agonists in preclinical animal models, their clinical efficacy in human tumors remains to be determined, with clinical trials thus far reporting no obvious benefit (*1*, *2*). The translational gap between animal and human studies poses a substantial obstacle to the development of STING agonists. To address this challenge, a deeper understanding of the regulation of cytosolic nucleic acid–sensing pathways and the underlying mechanisms of STING agonist resistance in human tumors is imperative.

Here, we investigated the impact of human tumor-associated genetic alterations on the efficacy of STING agonists. Methylthioadenosine phosphorylase (MTAP) is genetically deleted in multiple human cancers and provides a highly attractive therapeutic target that has so far eluded all efforts. We reveal an unexpected inhibitory effect of homozygous *MTAP* deletion on cytosolic nucleic acid–sensing pathways, resulting in resistance to STING agonists. Moreover, our results demonstrate that targeting polyamine metabolism represents an attractive approach to overcoming this inhibitory pathway and has the potential to enhance the efficacy of STING agonists.

Results

MTAP deficiency inhibits cytosolic nucleic acid–sensing pathways

To explore the impact of human tumor-associated genetic alterations on the therapeutic efficacy of STING agonists, we applied the TIMER algorithm (*3*), a method for evaluating the correlation between gene expression and immune infiltration levels, to The Cancer Genome Atlas (TCGA) cohort. We observed that the expression of *MTAP*, a gene residing on the short arm of human chromosome 9 (9p21.3), was positively correlated with tumor infiltration of antigen-presenting cells, namely, dendritic cells (DCs) and macrophages, as well as $CD8^+$ T cells, across various cancer types (fig. S1A). Moreover, there was a positive Spearman correlation between *MTAP* expression and IFN-I expression in multiple cancer types in the TCGA cohort (fig. S1B). These results are in line with published reports demonstrating that homozygous deletions of loci on chromosome 9p21.3 are associated with "cold" tumor-immune phenotypes (*4*).

The chromosomal region 9p21.3 is a frequent target of homozygous deletions occurring in ~13% of all cancers (*4*, *5*) (fig. S1, C and D). Although these deletions vary in size, most bear a gene cluster containing three tumor suppressors: *cyclin dependent kinase inhibitor 2A* (*CDKN2A*), *CDKN2B*, and *MTAP*. About 400 kb upstream from the *CDKN2A*/*CDKN2B*/*MTAP* cluster is another gene cluster encoding 16 IFN-Is, which is co-deleted with the *CDKN2A*/*CDKN2B*/*MTAP* cluster in about one-third of cancers bearing chromosome 9p21.3 homozygous deletion (*4*, *5*) (fig. S1, C and D). Therefore, some reports attribute the "cold" tumor-immune phenotype of cancers with chromosome 9p21.3 homozygous deletions to the co-deletion of the IFN gene cluster (*5*, *6*). However, we observed that depletion of MTAP, but not CDKN2A or CDKN2B, inhibited IFNβ induction by poly(dA:dT), a synthetic analog of B-DNA. In addition, *MTAP* knockdown inhibited IFNβ induction by the synthetic double-stranded RNA analog poly(I:C), or by the native STING agonist 2′,3′-cyclic GMP-AMP (2′,3′-cGAMP) (fig. S1, E and F). Moreover, after excluding samples carrying a homozygous deletion of the IFN gene cluster from the entire TCGA cohort, MTAP expression remained positively correlated with the expression of IFN-Is (fig. S1G). These data led us to hypothesize that homozygous *MTAP* deletion directly inhibits cytosolic nucleic acid–sensing immune responses, potentially obstructing the therapeutic efficacy of STING agonists.

Homozygous deletion of *MTAP* occurs frequently in various human cancers (Fig. 1A). To further validate the inhibitory effects of MTAP deficiency on cytosolic nucleic acid–sensing immune responses, we generated isogenic cell line pairs from multiple cancer types that vary only in MTAP expression either by knocking out endogenous *MTAP* in *MTAP*-intact cells or by reintroducing exogenous MTAP into cells harboring intrinsic homozygous *MTAP* deletion. Subsequently, the cell line pairs were compared to assess the influence of MTAP deficiency on the induction of IFNβ and downstream ISGs, namely *MX1* and *ISG15*, in response to poly(dA:dT) and poly(I:C) stimulation. Consistent with fig. S1F, *MTAP* deletion attenuated cytosolic nucleic acid–sensing pathways across multiple human cancers (Fig. 1, B to M).

MTAP deficiency down-regulates IRF3 expression

To determine the mechanism responsible for MTAP deficiency–mediated inhibition of cytosolic nucleic acid–sensing pathways, we

[1]Graduate Institute of Biomedical Sciences, China Medical University, Taichung, Taiwan. [2]Cancer Biology and Precision Therapeutics Center, China Medical University, Taichung, Taiwan. [3]Institute of Precision Medicine, The First Affiliated Hospital, Sun Yat-sen University, Guangzhou, Guangdong, China. [4]Department of Molecular and Cellular Oncology, The University of Texas MD Anderson Cancer Center, Houston, TX, USA. [5]Center for Molecular Medicine, China Medical University, Taichung, Taiwan. [6]Ph.D. Program for Cancer Molecular Biology and Drug Discovery, China Medical University, Taichung, Taiwan. [7]Department of Otolaryngology Head and Neck Surgery and National Clinical Research Center for Geriatric Disorders, Xiangya Hospital, Central South University; Otolaryngology Major Disease Research Key Laboratory of Hunan Province, Changsha, Hunan, China. [8]Department of Biotechnology, Asia University, Taichung, Taiwan. ***Corresponding author. Email: mhung@mail.cmu.edu.tw (M.-C.H.); hsujm@mail.cmu.edu.tw (J.-M.H.)** †These authors contributed equally to this work.

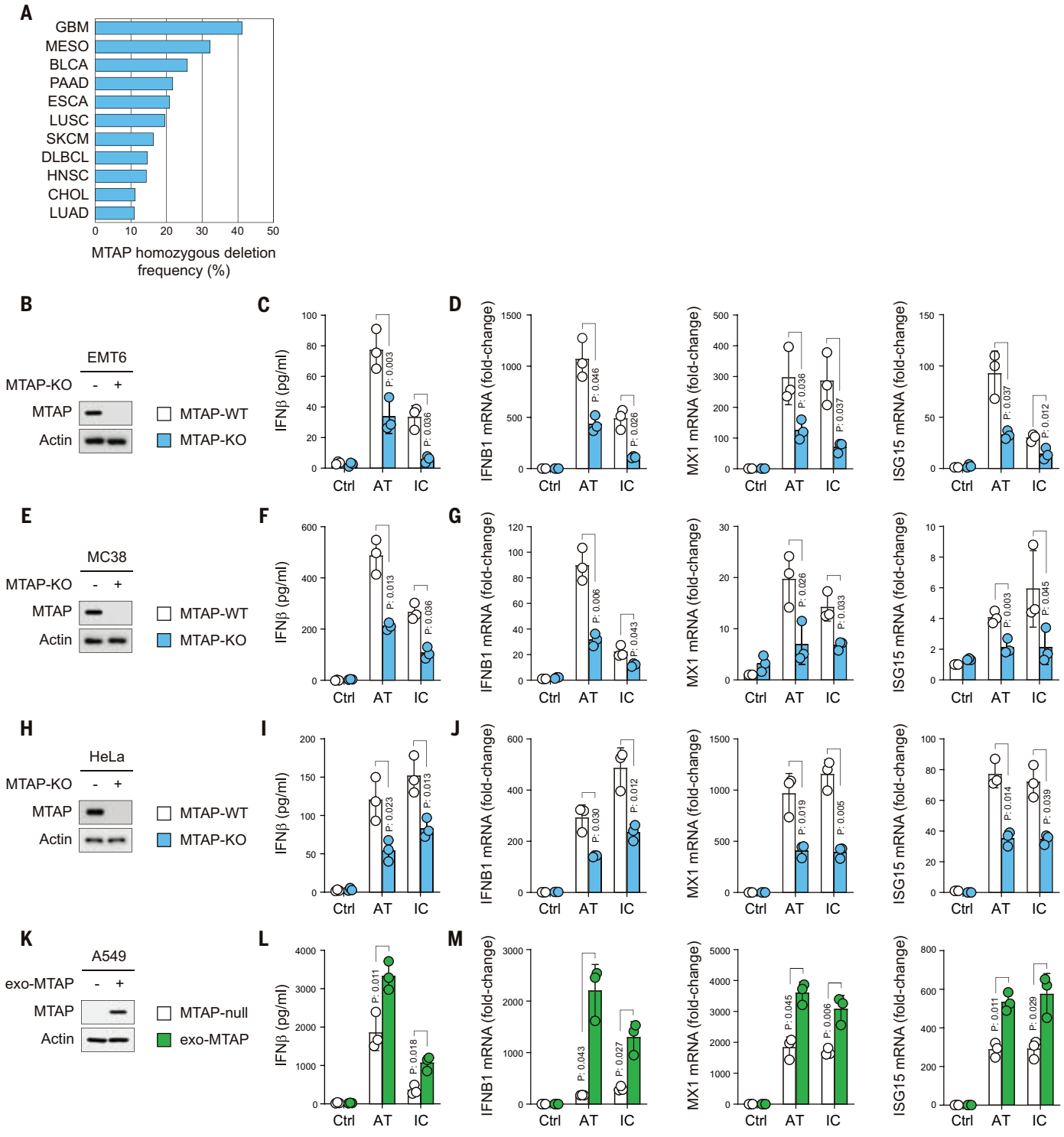


Fig. 1. MTAP deficiency suppresses cytosolic nucleic acid–sensing pathways. (**A**) Frequency of homozygous *MTAP* deletion in selected human cancers from the TCGA cohort. Only cancer types with a *MTAP* deletion frequency >10% are presented. BLCA, bladder urothelial carcinoma; CHOL, cholangiocarcinoma; DLBCL, diffuse large B-cell lymphoma; ESCA, esophageal carcinoma; GBM, glioblastoma multiforme; HNSC, head and neck squamous cell carcinoma; LUAD, lung adenocarcinoma; LUSC, lung squamous cell carcinoma; MESO, mesothelioma; PAAD, pancreatic adenocarcinoma; SKCM, skin cutaneous melanoma. (**B** to **J**) The influence of *MTAP* knockout on poly(dA:dT) (AT)– and poly(I:C) (IC)–mediated induction of IFNβ and ISGs in MTAP-expressing cells. Endogenous MTAP expression in MTAP-WT cells, EMT6 [(B) to (D)], MC38 [(E) to (G)], and HeLa [(H) to (J)], was knocked out (MTAP-KO) using the CRISPR/Cas9 system to generate the MTAP-WT and MTAP-KO isogenic pairs. The isogenic cell pairs were stimulated with AT or IC and subjected to ELISA for IFNβ protein induction [(C), (F), amd (I)] and to RT-qPCR for *IFNB1*, *MX1*, and *ISG15* gene induction [(D), (G), and (J)]. (**K** to **M**) The effect of exogenous MTAP on AT- and IC-mediated induction of IFNβ and ISGs in MTAP-deleted cells. The MTAP-WT and MTAP-KO isogenic cell pair was generated by reintroducing exogenous MTAP (exo-MTAP) into A549 cells, which harbor intrinsic homozygous *MTAP* deletion (MTAP-null) (K). The isogenic cell pair was stimulated with AT or IC, and subjected to ELISA quantification for IFNβ protein induction (L) and RT-qPCR for *IFNB1*, *MX1*, and *ISG15* gene induction (M). In (C), (D), (F), (G), (I), (J), (L), and (M), data are shown as the mean ± SD of three independent experiments.

compared cell line pairs with or without MTAP expression. We assessed the differential expression of key molecules involved in cytosolic nucleic acid–sensing and downstream signaling transduction, including nucleic acid sensors [cyclic GMP-AMP synthase (cGAS), retinoic acid–inducible gene I (RIG-I), and melanoma differentiation–associated protein 5 (MDA5), adaptors [STING and mitochondrial antiviral signaling (MAVS)], and effectors [TANK binding kinase 1 (TBK1) and interferon regulatory factor 3 (IRF3)]. The results showed that MTAP positively regulates IRF3 expression (Fig. 2, A and B). Consistent with our observations in isogenic cell line pairs, IRF3 expression levels positively correlated with MTAP abundance in cancer cell lines (Fig. 2C) and clinical tumor specimens (Fig. 2, D and E) with physiologically high or low MTAP expression. IRF3 is an essential transcriptional regulator of IFN-I production and IFN-mediated innate immune responses (*7*, *8*). The lack of IRF3 impairs IFN-I expression induced by cytosolic nucleic acid–sensing pathways (*9*). To determine whether IRF3 down-regulation suppresses cytosolic nucleic acid–sensing signaling in MTAP-deficient cells, we reintroduced exogenous IRF3 into *MTAP*-knockout (MTAP-KO) cells. IRF3 restoration substantially compromised the inhibitory effects of MTAP loss on cytosolic nucleic acid–sensing pathways (Fig. 2, F to J). Collectively, these findings suggest that MTAP deficiency inhibits cytosolic nucleic acid–sensing signaling through IRF3 down-regulation.

MTA-sensitive PRMT positively regulates IRF3 expression

Next, we sought to determine how MTAP deficiency leads to IRF3 down-regulation. MTAP is the rate-limiting enzyme in the methionine salvage pathway, regenerating methionine from the polyamine biosynthesis by-product 5′-methylthioadenosine (MTA) and thereby maintaining methionine levels in vivo (fig. S2). MTAP deficiency results in a global alteration of intracellular metabolites, among which MTA displays the greatest increase in *MTAP*-deleted cells (*10*, *11*). MTA is structurally similar to S-adenosyl methionine, the methyl donor substrate for methylation. Thus, accumulated MTA is considered a competitive inhibitor of methyltransferase activity. Previous studies in MTAP-deficient cells demonstrated that accumulated MTA selectively inhibits protein arginine methyltransferase 5 (PRMT5) (*11*–*13*). PRMT5 is a key type II arginine methyltransferase that regulates numerous biological pathways in mammalian cells through the symmetric dimethylation of arginine residues on histones and nonhistone proteins. Consistent with these findings, we observed reduced PRMT5 activity in MTAP-deficient cells. This was indicated by decreased levels of cellular symmetric arginine dimethylation (sdme-RG) and reduced symmetric dimethylation at arginine 3 of histone H4 (H4R3me2s) in our MTAP-KO isogenic cancer cell line compared with its *MTAP*-expressing wild-type (MTAP-WT) counterpart (fig. S3, A and B). Moreover, we observed that suppressed IRF3 expression was concurrent with reduced PRMT5 activity (fig. S3, A and B). Further, PRMT5 expression positively correlated with tumor infiltration of antigen-presenting cells, including DCs and macrophages, as well as $CD8^+$ T cells, in the TCGA cohort (fig. S4). On the basis of these observations, we hypothesized that reduced PRMT5 activity is responsible for IRF3 down-regulation in MTAP-deficient cells. We validated this hypothesis by demonstrating that PRMT5 inhibition in MTAP-WT cancer cells through PRMT5-specific methyltransferase inhibitors (Fig. 3A and fig. S3C) or small hairpin (sh)RNA–mediated knockdown (Fig. 3B and fig. S3E) was sufficient to suppress IRF3 expression and inhibit IFNβ and ISG induction by poly(dA:dT) and poly(I:C) (Fig. 3, C to F). Together, these results suggest that accumulated MTA in *MTAP*-deleted cancers induces a hypomorphic PRMT5 state that inhibits IRF3 expression and cytosolic nucleic acid–sensing pathways.

Paracrine effects broaden MTAP deficiency–mediated inhibition of cytosolic nucleic acid–sensing pathways

Cytosolic nucleic acid–sensing pathways in cancers and the tumor microenvironment contribute to triggering and bridging innate and adaptive immune responses against tumors (*14*–*16*). We already demonstrated that PRMT5 inhibition leads to IRF3 down-regulation in MTAP-intact cancer cells (Fig. 3, A and B). We also found that in MTAP-intact immune cells, IRF3 expression and cytosolic nucleic acid–sensing signaling are positively regulated by PRMT5 (Fig. 3, G to J, and fig. S3, D and F). Thus, PRMT5, an MTA-sensitive PRMT, is likely a general positive regulator of IRF3 expression. Published reports indicate that MTA is cell membrane permeable through both nonspecific nucleoside transport and passive diffusion (*17*, *18*). *MTAP* deletion in tumor cells results in an accumulation of MTA in both intracellular and extracellular environments (*19*). Tumor-derived MTA metabolites suppress $CD8^+$ T cell functions and promote the immunosuppressive alternative activation (M2) of macrophages in a paracrine manner (*20*, *21*). Together, these findings raised the possibility that MTAP-deficient tumors inhibit IRF3 expression and cytosolic nucleic acid–sensing pathways in neighboring MTAP-intact cells through paracrine effects. To test this hypothesis, we compared $CD45^+$ cells isolated from EMT6 mammary tumor xenografts established in immunocompetent mice. $CD45^+$ cells from MTAP-KO EMT6 tumors exhibited lower PRMT5 methyltransferase activity and IRF3 expression than those from MTAP-WT EMT6 tumors (fig. S5, A to C). Additionally, conditioned medium from in vitro cultures of MTAP-KO, but not from MTAP-WT, suppressed PRMT5 activity and IRF3 expression in MTAP-expressing cancer and immune cells (fig. S5, D and E). These findings suggest a paracrine inhibitory effect of MTAP-deficient tumors on IRF3 expression in neighboring MTAP-expressing cells. As *MTAP* deletion induces MTA accumulation together with global metabolite alteration (*10*, *11*), we investigated whether MTA is the main agent modulating IRF3 expression in MTAP-expressing cells. Our results showed that MTA treatment alone is sufficient to inhibit PRMT5 activity and IRF3 expression, as well as poly(dA:dT)– and poly(I:C)–stimulated induction of IFNβ and ISGs in MTAP-expressing cancer and immune cells (figs. S3G and S5, F to L). Collectively, these results suggest that accumulated MTA secreted from *MTAP*-deleted cancer cells generates an immunosuppressive tumor microenvironment that attenuates cytosolic nucleic acid–sensing immune responses.

MTAP deficiency down-regulates IRF3 expression through MID1 induction

To investigate the mechanisms underlying the specific down-regulation of IRF3 in MTAP-deficient cells, we performed RNA sequencing (RNA-seq) followed by differential gene expression (DGE) analysis. This approach allowed us to compare WT cells with those subjected to *MTAP* knockout, *PRMT5* knockdown, or PRMT5 inhibition (data S1 to S5). Across all three DGE analyses, we did not observe any significant and consistent alterations in the expression of *IRF3* (IRF3) or other key molecules of the cytosolic nucleic acid–sensing pathways, including *DDX58* (RIG-I), *IFIH1* (MDA5), *MAVS* (MAVS), *CGAS* (cGAS), *STING1* (STING), and *TBK1* (TBK1) (Fig. 4, A to C). These findings suggest that transcriptional regulation is unlikely to be the primary mechanism underlying the down-regulation of IRF3 in MTAP-deficient cells.

Consistently, all three DGE analyses revealed that *MID1* (Midline-1, MID1), a known E3 ligase of IRF3 (*22*), is up-regulated in cells with *MTAP* knockout, *PRMT5* knockdown, or PRMT5 inhibition (Fig. 4, A to C). We validated these findings using quantitative reverse transcription polymerase chain reaction (RT-qPCR) and Western blotting (Fig. 4, D to G), which prompted us to explore the role of the proteasome in IRF3 down-regulation in MTAP-deficient cells. Treatment of MTAP-WT and MTAP-KO cells with the proteasome inhibitor MG132 restored IRF3 protein levels in MTAP-KO cells, suggesting the involvement of the ubiquitin-proteasome system (Fig. 4H). Further, knockdown of MID1 in MTAP-KO cancer cells restored IRF3 protein expression to levels comparable to those in MTAP-WT cells (Fig. 4I). Conversely, ectopic expression of MID1 alone caused IRF3 down-regulation in MTAP-WT cancer cells (Fig. 4J). We also observed elevated MID1 levels

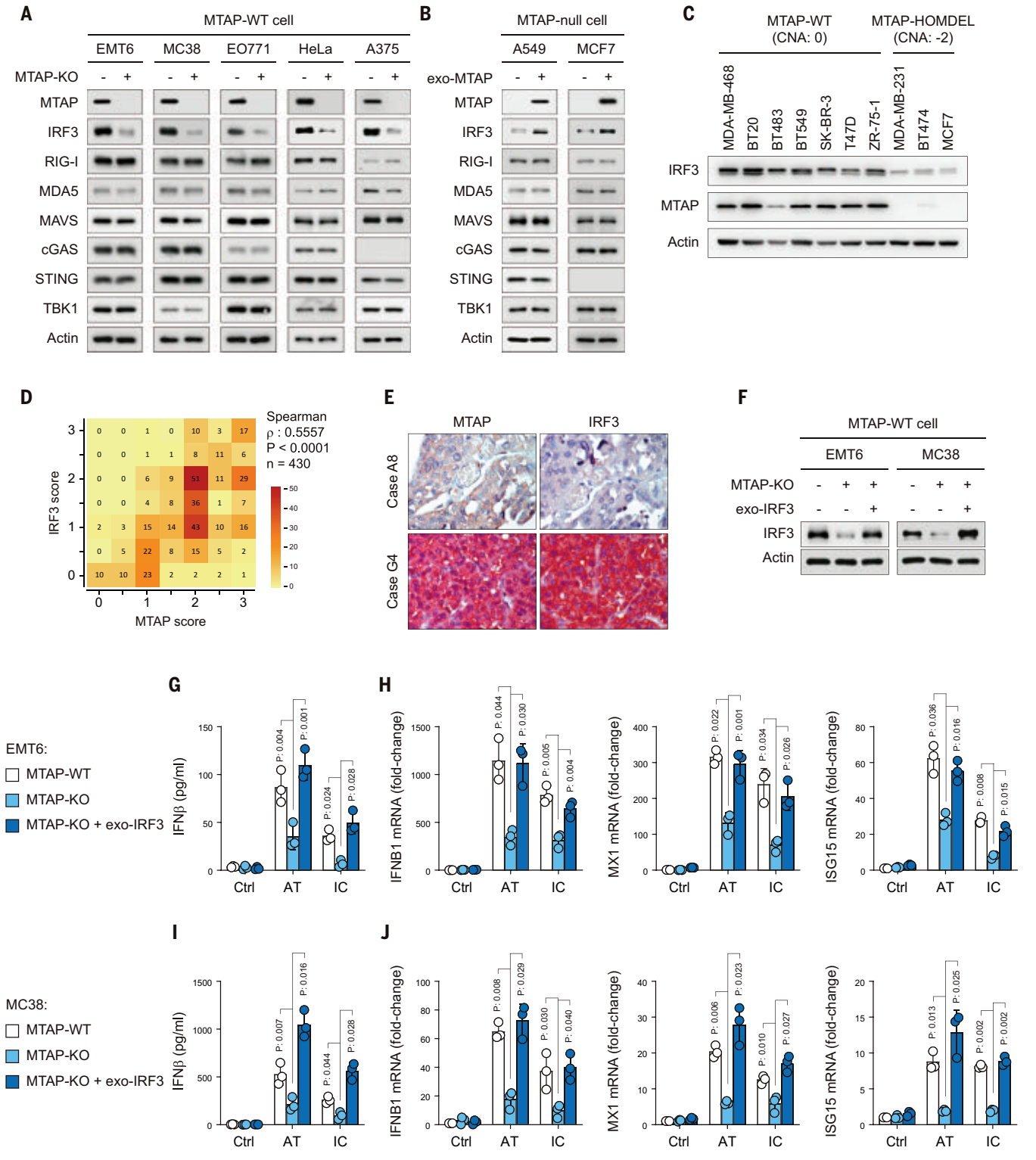


Fig. 2. MTAP loss inhibits the cytosolic nucleic acid–sensing pathway through IRF3 down-regulation. (**A**) Comparison of the expression levels of key molecules of cytosolic nucleic acid–sensing pathways before and after MTAP-KO in MTAP-WT cells. (**B**) Comparison of the expression levels of key molecules of cytosolic nucleic acid–sensing pathways before and after exo-MTAP expression in cells bearing intrinsic homozygous *MTAP* deletion (MTAP-null). (**C**) Comparison of IRF3 expression between breast cancer cell lines with homozygous *MTAP* deletions (CNA: −2) and those with a normal diploid number (CNA: 0). (**D**) Spearman correlation analysis between MTAP and IRF3 protein expression in human tumor samples ($n = 430$). Human tumor tissue microarray sections were stained with anti-MTAP and anti-IRF3 antibodies by IHC, scored, and then subjected to correlation analysis. The number in each cell indicates the case number of each group. (**E**) Representative images of IHC staining for MTAP and IRF3 in the tissue microarray. Cases A8 and G4 are double-negative and double-positive staining, respectively. (**F** to **J**) The influence of MTAP-KO and exo-IRF3 on AT- and IC-mediated induction of IFNβ and ISG in MTAP-expressing EMT6 and MC38 cells. EMT6 and MC38 cells treated with MTAP-KO and exo-IRF3 as indicated (F) were stimulated with AT and IC, and then subjected to ELISA quantification for IFNβ protein induction [(G) and (I)] and RT-qPCR for *IFNB1*, *MX1*, and *ISG15* gene induction [(H) and (J)]. In (G) to (J), data are shown as mean ± SD of three independent experiments.

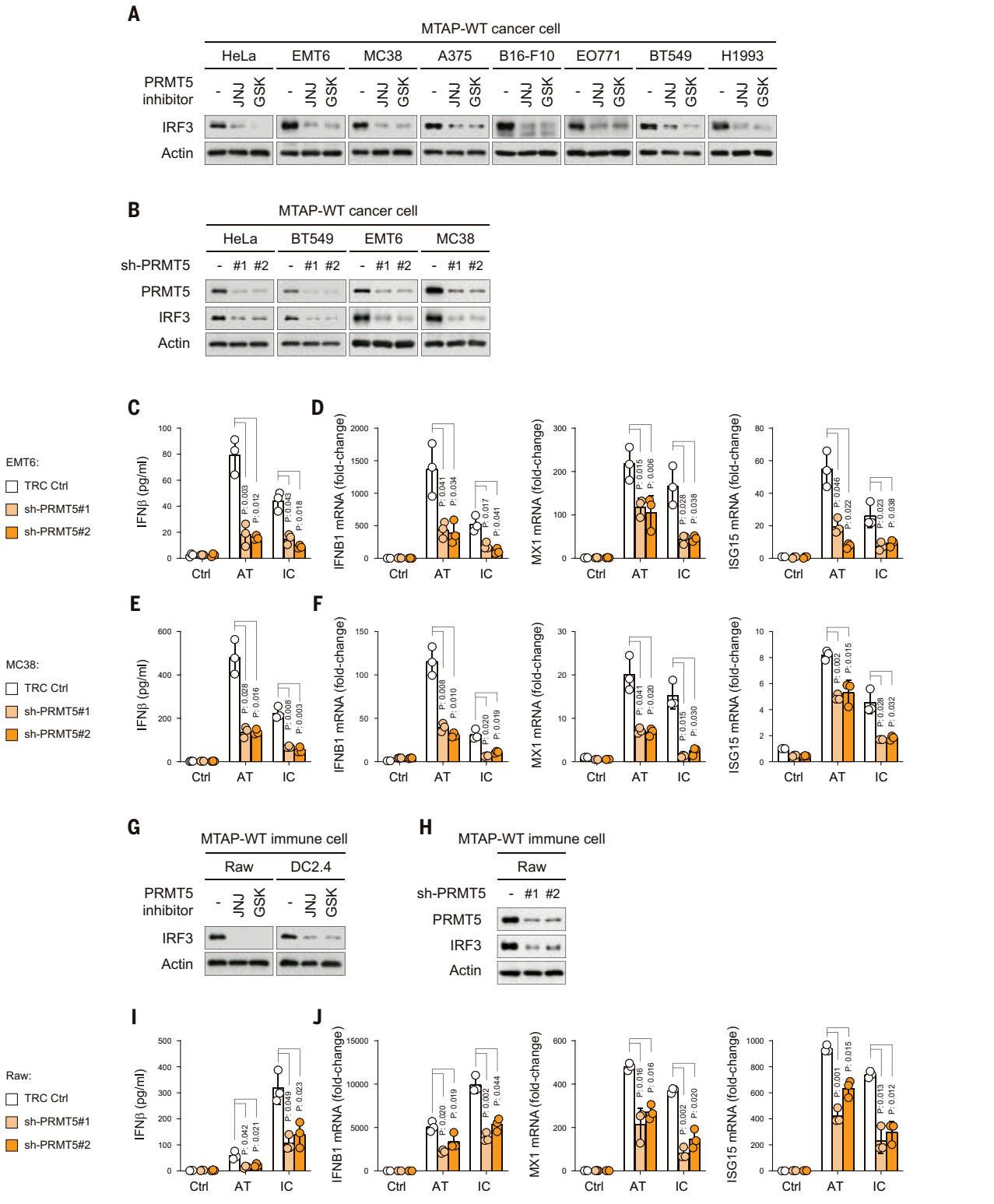


Fig. 3. PRMT5 positively regulates IRF3 expression. (**A**) Western blot of IRF3 after treatment of MTAP-WT cancer cells with the PRMT5 arginine methyltransferase inhibitors GSK3326595 (GSK) and JNJ64619178 (JNJ). (**B**) Influence of PRMT5 knockdown on IRF3 expression in MTAP-WT cancer cells. MTAP-WT cancer cells were treated with two PRMT5 shRNAs (sh-PRMT5) and analyzed by Western blot for IRF3. (**C** to **F**) The influence of PRMT5 knockdown on AT- and IC-mediated induction of IFNβ and ISGs in MTAP-WT cancer cells. MTAP-WT cancer cells with PRMT5 knockdown were stimulated with AT and IC, and then subjected to ELISA quantification for IFNβ induction [(C) and (E)] and RT-qPCR for *IFNB1*, *MX1*, and *ISG15* gene induction [(D) and (F)]. (**G**) Western blot of IRF3 after treatment of MTAP-WT immune cells with PRMT5 arginine methyltransferase inhibitors GSK and JNJ. Raw, Raw 264.7. (**H**) The influence of PRMT5 knockdown on IRF3 protein expression in MTAP-WT immune cells (Raw 264.7). Raw 264.7 cells were treated with two PRMT5 shRNAs (sh-PRMT5) and analyzed by Western blot for IRF3. (**I** and **J**) The influence of PRMT5 knockdown on AT- and IC-mediated induction of IFNβ and ISGs in MTAP-WT immune cells (Raw 264.7). Raw 264.7 cells with *PRMT5* knockdown were stimulated with AT and IC, and then subjected to ELISA quantification for IFNβ induction (I) and RT-qPCR for *IFNB1*, *MX1*, and *ISG15* gene induction (J). In (C), (D), (E), (F), (I), and (J), data are shown as mean ± SD of three independent experiments.

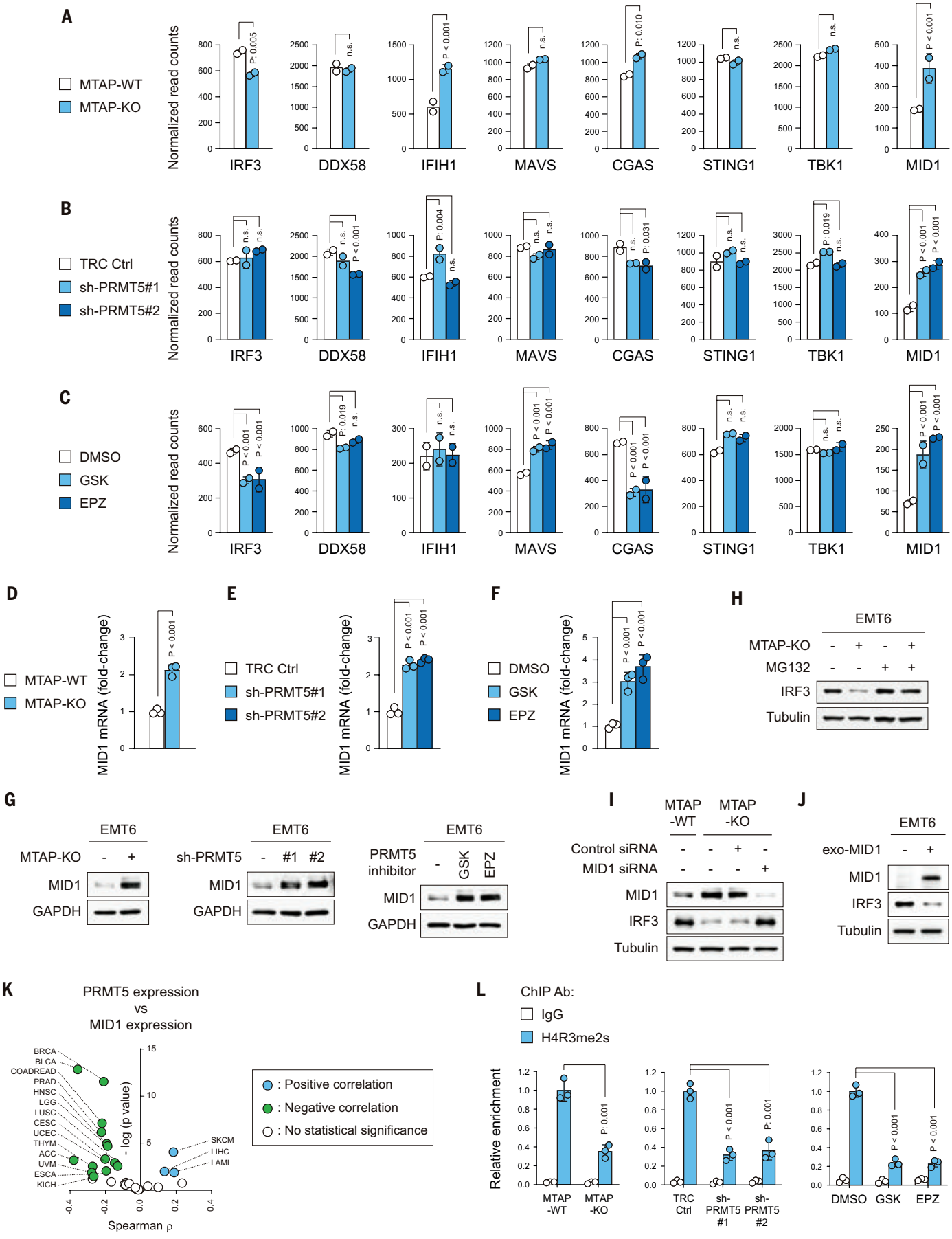

A
MTAP-WT
MTAP-KO
Normalized read counts
IRF3
DDX58
IFIH1
MAVS
CGAS
STING1
TBK1
MID1
B
TRC Ctrl
sh-PRMT5#1
sh-PRMT5#2
C
DMSO
GSK
EPZ
D
MID1 mRNA (fold-change)
E
F
H
EMT6
MTAP-KO
MG132
IRF3
Tubulin
G
sh-PRMT5
PRMT5 inhibitor
MID1
GAPDH
I
MTAP -WT
MTAP -KO
Control siRNA
MID1 siRNA
J
exo-MID1
K
PRMT5 expression vs MID1 expression
- log (p value)
Spearman ρ
: Positive correlation
: Negative correlation
: No statistical significance
L
ChIP Ab:
IgG
H4R3me2s
Relative enrichment

Fig. 4. MTAP deficiency down-regulates IRF3 expression by inhibiting PRMT5-dependent transcriptional repression of MID1. (**A** to **C**) RNA-seq comparison of differential expression of *IRF3* (IRF3), *DDX58* (RIG-I), *IFIH1* (MDA5), *MAVS* (MAVS), *CGAS* (cGAS), *STING1* (STING), *TBK1* (TBK1), and *MID1* (Midline-1, MID1) in MTAP-WT and MTAP-KO cells (A) in cells subjected to PRMT5 knockdown (B) or treated with PRMT5 inhibitors GSK3326595 (GSK) and EPZ015666 (EPZ) (C). (**D** to **F**) RT-qPCR comparison of *MID1* gene expression in MTAP-WT and MTAP-KO cells (D) in cells subjected to PRMT5 knockdown (E) or treated with PRMT5 inhibitors (F). (**G**) Western blot comparison of MID1 protein expression in MTAP-WT and MTAP-KO cells in cells subjected to PRMT5 knockdown or treated with PRMT5 inhibitors. (**H**) Western blot analysis of the effect of the proteasome inhibitor MG132 on IRF3 expression in MTAP-KO cells. (**I**) Western blot analysis of the effect of MID1 knockdown on IRF3 expression in MTAP-KO cells. (**J**) Western blot analysis of the effect of exogenous MID1 on IRF3 expression in MTAP-WT cells. (**K**) Spearman correlation between PRMT5 and MID1 expression in each cancer type within the TCGA cohort. The Spearman correlation coefficient (ρ) of each cancer type is plotted against the −log (*P* value) of the same cancer type, with each dot representing the result of an individual cancer type. Blue dots indicate positive correlation with statistical significance ($P \leq 0.05$), green dots indicate negative correlation with statistical significance ($P \leq 0.05$), and white dots indicate no statistical significance. ACC, adrenocortical carcinoma; BRCA, breast invasive carcinoma; CESC, cervical and endocervical cancer; COADREAD, colorectal adenocarcinoma; KICH, kidney chromophobe; LAML, acute myeloid leukemia; LGG, brain lower grade glioma; LIHC, liver hepatocellular carcinoma; PRAD, prostate adenocarcinoma; THYM, thymoma; UCEC, uterine corpus endometrial carcinoma; UVM, uveal melanoma. (**L**) ChIP–RT-qPCR comparison of H4R3me2s enrichment on the promoter region of the *MID1* gene in MTAP-WT and MTAP-KO cells, in cells subjected to PRMT5 knockdown, or treated with PRMT5 inhibitors. In (A) to (C), data are shown as mean ± SD of two independent experiments. In (D) to (F) and (L), data are shown as mean ± SD of two independent experiments.

in $CD45^+$ cells from EMT6 (MTAP-KO) xenografts and in MTAP-WT cells treated with conditioned medium derived from MTAP-KO cells (fig. S5, C and E). Collectively, these findings indicate that elevated MID1 levels drive IRF3 down-regulation in MTAP-KO cells.

Our data demonstrate that MTAP deficiency leads to reduced PRMT5 activity and elevated MID1 expression. In MTAP-WT cells, both pharmacological inhibition and genetic knockdown of PRMT5 resulted in elevated MID1 expression at the mRNA and protein levels. Analysis of the TCGA cohort further showed a negative correlation between PRMT5 and MID1 expression across multiple cancer types (Fig. 4K). Next, we investigated whether MID1 expression is directly regulated by PRMT5. PRMT5 suppresses gene expression by introducing symmetric dimethylation in the promoter regions of target genes, primarily at H4R3me2s and arginine 8 of histone H3 (H3R8me2). Chromatin immunoprecipitation (ChIP) analysis revealed enrichment of the H4R3me2s mark at the MID1 promoter, which was reduced after *MTAP* knockout, *PRMT5* knockdown, or PRMT5 inhibition (Fig. 4L). These findings suggest that MID1 is directly regulated by PRMT5-dependent H4R3me2s and that MTAP deficiency down-regulates IRF3 expression by inhibiting PRMT5-dependent transcriptional repression of MID1.

DFMO compromises the inhibition of MTAP deficiency on cytosolic nucleic acid–sensing pathways

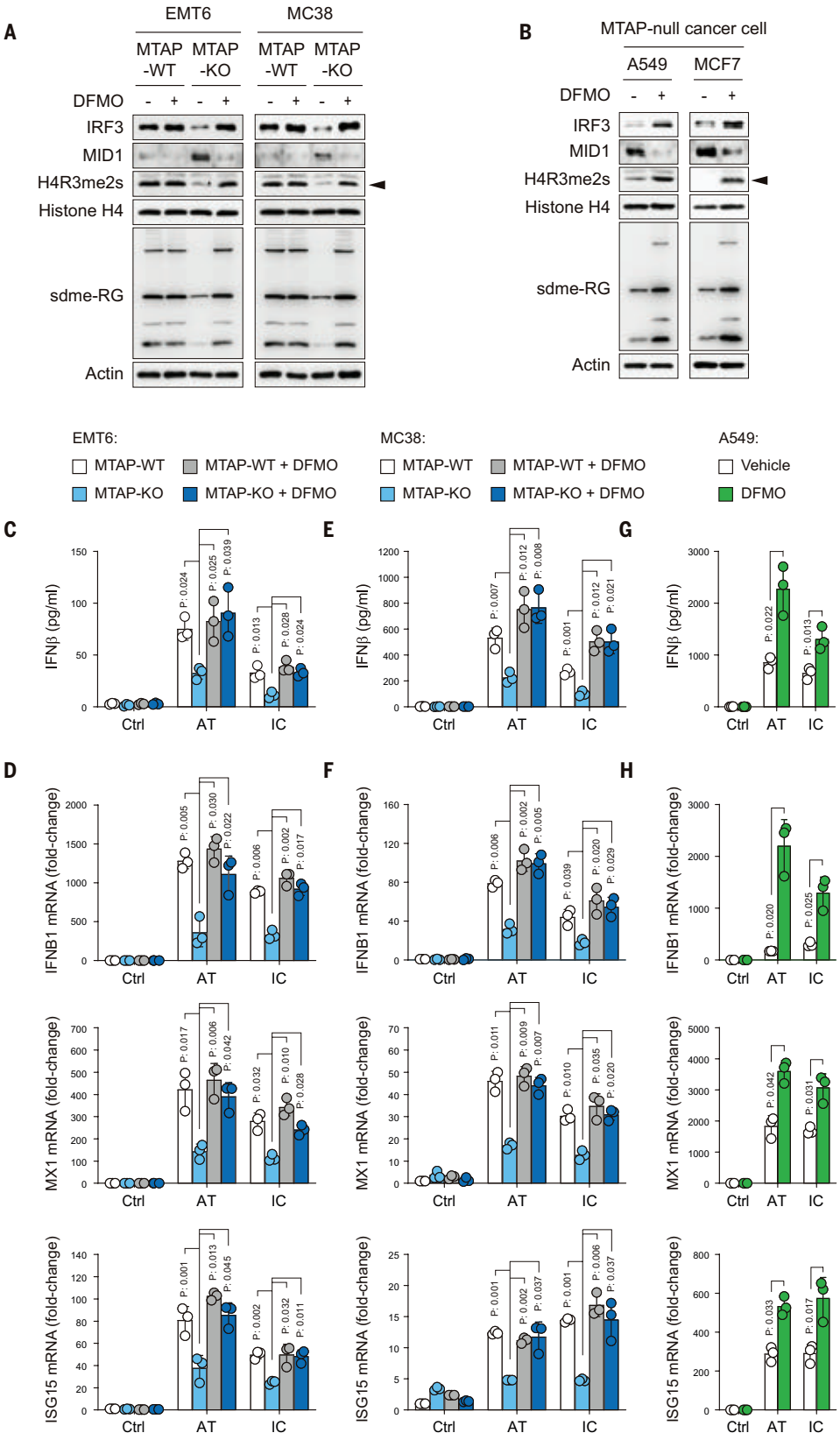
Intracellular MTA levels are regulated positively by polyamine biosynthesis and negatively by MTAP (fig. S2) (*23*–*26*). This correlation suggests that inhibiting polyamine biosynthesis may restore IRF3 expression and compromise the inhibitory effects of MTAP loss on cytosolic nucleic acid–sensing immune responses. Multiple inhibitors target the polyamine metabolic enzymes in cancer prevention and treatment (*25*). Among them, DL-α-difluoromethylornithine (DFMO), an irreversible inhibitor of ornithine decarboxylase (ODC) (fig. S2), is the only agent approved by the UF Food and Drug Administration (FDA) for clinical use (*25*, *27*). Inhibition of ODC by DFMO attenuates MTA accumulation (*28*). We found that DFMO treatment restored PRMT5 activity and inhibited MTA accumulation and MID1 expression in MTAP-KO cells, thereby recovering IRF3 expression to a level comparable to that of MTAP-WT cells (Fig. 5A and fig. S6). DFMO exerted similar modulatory effects in cells bearing intrinsic homozygous *MTAP* deletion (Fig. 5B). Moreover, DFMO compromised the inhibitory effects of MTAP deficiency on poly(dA:dT)– and poly(I:C)–mediated induction of IFNβ and ISGs (Fig. 5, C to H). Collectively, these results suggest that targeting polyamine metabolism with DFMO may recover reduced cytosolic nucleic acid–sensing signaling in MTAP-deficient cells.

DFMO overcomes STING agonist resistance in MTAP-deficient cancers

The low response rate of human tumors to STING agonists in clinical trials represents a major obstacle to their development as cancer immunotherapies (*1*, *2*). Because homozygous *MTAP* deletion inhibits cytosolic nucleic acid–sensing signaling, we explored the therapeutic efficacy of STING agonists on MTAP-deficient human tumors. We previously showed that MTAP deficiency reduces IFNβ induction by 2′,3′-cGAMP, a native agonist of human STING (fig. S1F). Natural cyclic dinucleotides such as 2′,3′-cGAMP, are electronegative, hydrophilic, and highly susceptible to enzymatic degradation by phosphodiesterases within the host cell or in systemic circulation (*29*, *30*). Therefore, they have poor cell membrane permeability and low metabolic stability in tumor tissues, resulting in narrow therapeutic windows. To overcome these application barriers, numerous classes of synthetic cyclic dinucleotides, such as MIW815 (ADU-S100) and E7766, and non-nucleotide small-molecule STING agonists, such as MSA2, are being developed (*29*, *30*). MIW815 (ADU-S100) mimics 2′,3′-cGAMP and shows improved stability, lipophilicity, and antitumor control in animal models by inducing substantially higher levels of IFN-Is than endogenous 2′,3′-cGAMP (*31*). E7766, a macrocycle-bridged STING agonist derivative of MIW815, has a high degree of chemical and metabolic stability because of the macrocycle's conformational rigidity. It exhibits pan-genotypic activity across seven human STING genotypes, as well as potent antitumor activities in murine tumor models, without serious adverse effects (*32*). Both MIW815 and E7766 were designed to be administered by intratumoral injection. Conversely, orally administered MSA2 preferentially targets tumor tissue because the acidified tumor microenvironment facilitates its cellular entry and retention. This unique characteristic of MSA2 resolves the delivery flaw of conventional STING agonists (*33*). We used these three STING agonists to investigate the impact of MTAP deficiency and DFMO treatment on the therapeutic efficacy of STING agonists. The results showed that MTAP deficiency suppressed STING agonist–mediated induction of IFNβ and ISGs, and this inhibitory effect was compromised by DFMO (Fig. 6, A to F, and fig. S7).

Most murine cancer cell line–derived syngeneic mouse models that have been commonly used to assay STING agonists have WT *MTAP* alleles (fig. S8), suggesting that these models may not reveal the potential impact of MTAP deficiency on STING agonist therapy. Using our isogenic cell pairs, we analyzed the impact of MTAP deficiency on STING agonist–induced antitumor effects and systemic immune responses in bilateral syngeneic mouse tumor models. In the EMT6 breast cancer model, MTAP-WT or MTAP-KO tumors were established on both flanks of syngeneic mice. The left flank tumor was treated intratumorally with MIW815, and the right flank tumor remained untreated (*31*, *34*) (fig. S9A). Our data were consistent with published reports demonstrating that MIW815 monotherapy suppresses the growth of MTAP-WT tumors and prolongs the survival of tumor-bearing mice (*31*, *34*) (Fig. 6, G to I, and fig. S9, B and C). Although MIW815 was injected only into the left flank tumor, we observed tumor regression in both flanks, indicating the potential of this STING agonist to elicit systemic antitumor immune responses. In contrast to MTAP-WT tumors, MTAP-KO tumors showed no significant response to MIW815 monotherapy (Fig. 6, G to I, red line, and fig. S9, B and C). However, combining MIW815 with 2% (w/v) DFMO (Fig. 6, G to I, orange line) could effectively kill MTAP-KO

Fig. 5. DFMO restores IRF3 expression and cytosolic nucleic acid sensing in MTAP-deficient cells. (**A**) Western blot comparison of the effects of DFMO on IRF3 expression, MID1 expression, H4R3me2s, and cellular sdme-RG in MTAP-WT and MTAP-KO cells. (**B**) Western blot analysis of the effects of DFMO on IRF3 expression, MID1 expression, histone H4R3me2s, and cellular sdme-RG in cells with intrinsic homozygous *MTAP* deletion (MTAP-null). (**C** to **F**) Comparison of the influence of DFMO on AT- and IC-mediated induction of IFNβ and ISGs in MTAP-WT and MTAP-KO cells. DFMO-treated MTAP-WT and MTAP-KO isogenic cell pairs were stimulated with AT and IC and then subjected to ELISA quantification for IFNβ protein induction [(C) and (E)] and RT-qPCR for *IFNB1*, *MX1*, and *ISG15* gene induction [(D) and (F)]. (**G** and **H**) The effects of DFMO on AT- and IC-mediated induction of IFNβ and ISGs in cells bearing intrinsic homozygous *MTAP* deletion. A549 cells with or without DFMO treatment were stimulated with AT and IC and then subjected to ELISA quantification for IFNβ protein induction (G) and RT-qPCR for *IFNB1*, *MX1*, and *ISG15* gene induction (H). In (C) to (H), data are shown as mean ± SD of three independent experiments.



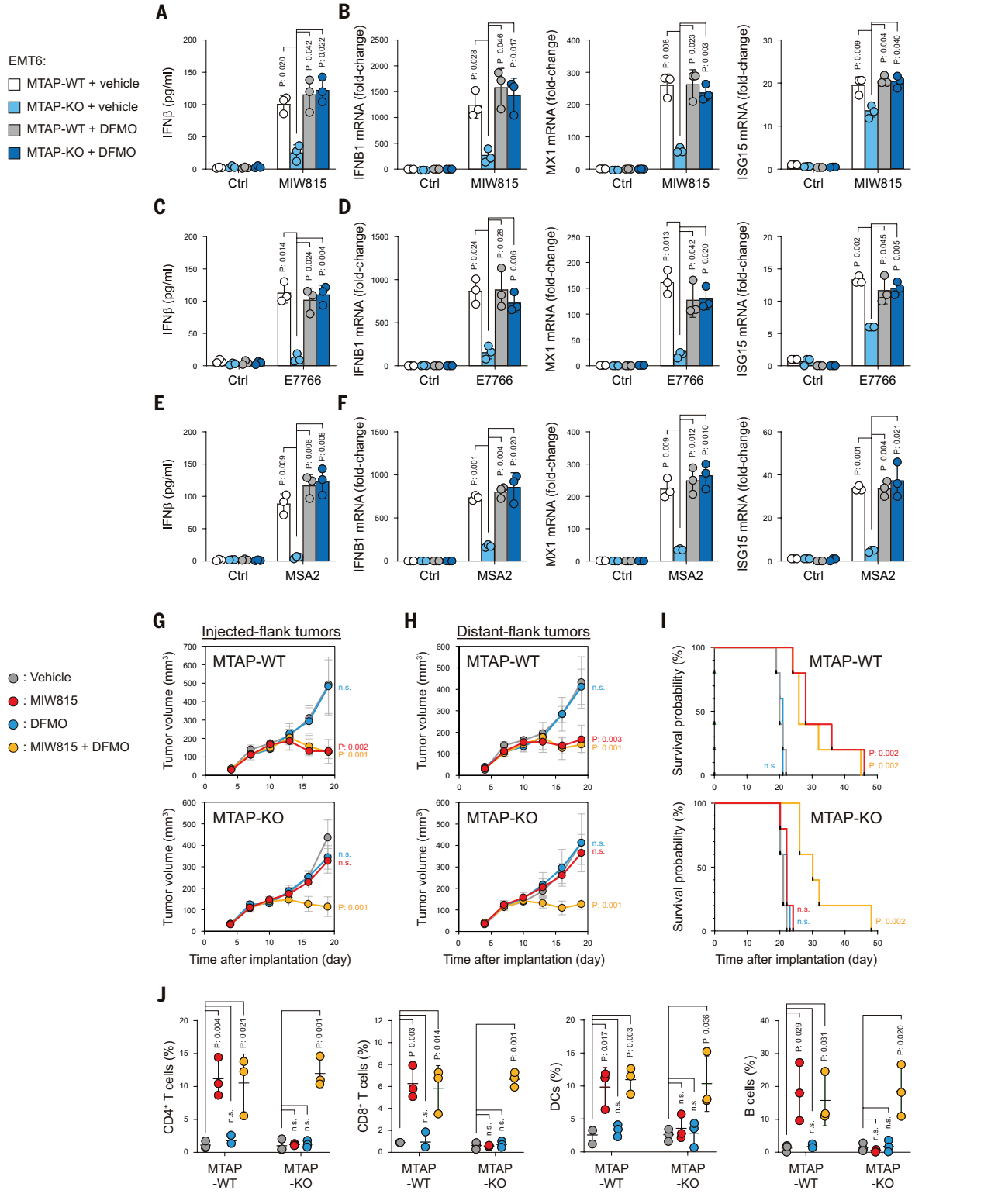


Fig. 6. DFMO sensitizes MTAP-deficient cancers to STING agonists. (**A** to **F**) Comparison of the influence of DFMO on STING agonist–mediated induction of IFNβ and ISGs in EMT6 MTAP-WT and MTAP-KO cells. EMT6 MTAP-WT and MTAP-KO isogenic cell pairs were treated with DFMO and then stimulated with STING agonists MIW815 [(A) and (B)], E7766 [(C) and (D)], or MSA2 [(E) and (F)]. Cells were then subjected to ELISA quantification for IFNβ protein induction [(A), (C), and (E)] and RT-qPCR for *IFNB1*, *MX1*, and *ISG15* gene induction [(B), (D), and (F)]. (**G** and **H**) Average tumor growth kinetics of MTAP-WT or MTAP-KO tumors implanted in the injected flank (G) and distant flank (H) of mice over the treatment period. Student's *t* tests were performed to assess differences between the vehicle-treated group and other treatment groups. (**I**) Overall survival of mice inoculated with MTAP-WT or MTAP-KO tumors over the treatment period. Log-rank (Mantel-Cox) tests were performed to compare survival differences between the vehicle-treated group and other treatment groups. (**J**) Relative proportions of $CD4^+$ T cells, $CD8^+$ T cells, DCs, and B cells within left-flank tumors of each treatment group. In (A) to (F), data are shown as mean ± SD of three independent experiments. In (G) to (I), $n = 5$ mice per group; in (J), $n = 3$ mice per group.

tumors, demonstrating significantly greater efficacy than monotherapy. These results suggest that DFMO sensitizes MTAP-KO tumors to MIW815.

To further understand the biological mechanisms driving treatment response, we characterized the immune composition within tumors from each treatment group by mass cytometry analysis (Fig. 6J and fig. S10). Consistent with published reports (*31*, *34*), MIW815 monotherapy enhanced immune cell infiltration into the MTAP-WT tumor microenvironment (Fig. 6J and fig. S10C). By comparison, MIW815 monotherapy was not as effective at recruiting immune cells into MTAP-KO tumors. However, combining MIW815 with DMFO restored their responsiveness to the STING agonist and enhanced immune cell infiltration (Fig. 6J and fig. S10C). Together, these results suggest that combining DFMO with a STING agonist can overcome resistance to STING agonists in MTAP-deficient tumors.

To broaden the applicability of our mechanism across tumor models, we investigated the therapeutic efficacy of MIW815 combined with 0.5% (w/v) DFMO in the MC38 colon carcinoma model established in C57BL/6 WT and C57BL/6 Irf3$^{-/-}$ mice (fig. S11A). Consistent with our findings in the EMT6 breast cancer model (Fig. 6, G and H), MTAP deficiency impaired the therapeutic efficacy of STING agonist monotherapy, whereas DFMO enhanced the sensitivity to STING agonists in the C57BL/6 WT MC38 colorectal cancer model (fig. S11, B, D, and E). These findings collectively highlight the potential broad applicability of our proposed mechanism across different tumor models. In C57BL/6 Irf3$^{-/-}$ mice (fig. S11, C, F, and G), MTAP-WT and MTAP-KO tumors responded differently to STING agonist monotherapy, and DFMO continued to sensitize MTAP-KO tumors to STING agonists, reflecting the trend observed in C57BL/6 WT mice. This observation may be attributed to the fact that whereas IRF3 deficiency impairs STING activation in the tumor microenvironment, MC38 xenografts retain IRF3 expression and act as a source of IFN-I production during STING agonist treatment. Our results align with previous reports suggesting that the cGAS-STING pathway in both cancers and the tumor microenvironment contributes to the activation of antitumor immune responses by STING agonists (*14*–*16*).

MTAP deficiency and STING promoter methylation contribute to STING agonist resistance in different patient populations

We have demonstrated that homozygous *MTAP* deletion underlies resistance to STING agonist treatment. In addition to genetic deletion, epigenetic silencing of the *MTAP* gene through promoter hypermethylation has emerged as an alternative mechanism causing the loss of MTAP expression in tumor cells (*35*–*37*). Promoter hypermethylation has also been shown to epigenetically silence *STING* expression in human tumors, thereby hampering STING signaling and reducing the efficacy of STING agonists. Demethylation using clinically available DNA methylation inhibitors reinstates *STING* expression, potentially improving the response to STING agonist therapy (*38*–*40*). We therefore systematically investigated the combined effects of these two genetic and epigenetic alterations on the resistance of human tumors to STING agonists using the DriverDB cancer omics database (*41*) (fig. S12). In the DNA hypermethylation analysis performed by the MethylMix algorithm, we observed that *STING* was hypermethylated in 11 of the 24 cancer types examined, whereas *MTAP* displayed high levels of methylation only in sarcomas, with no observed hypermethylation in *TBK1* and *IRF3* (fig. S12A). By contrast, copy number analysis revealed that only *MTAP*, but not *STING*, *TBK1*, or *IRF3*, was significantly deleted across various cancer types (fig. S12B). These findings suggest that the expression of *MTAP* and *STING* genes is primarily inactivated by distinct mechanisms in human tumors.

We combined the sample populations with hypermethylation and homozygous deletion for each gene, referring to this combined group as the inactivation population (fig. S12C). Subsequently, we examined the proportion of tumors carrying MTAP inactivation, STING inactivation, or both within individual cancer types (fig. S12D) as well as across the entire TCGA cohort (fig. S12E). We found that nine of 33 cancer types contained >50% of samples with MTAP inactivation, STING inactivation, or both (fig. S12D). In the entire TCGA cohort, ~11 and 27% of tumors carried MTAP inactivation and STING inactivation, respectively, whereas only ~2% had both MTAP and STING inactivation co-occurring (fig. S12E). These findings suggest that MTAP and STING deficiencies contribute to STING agonist resistance in two largely separate patient populations.

Discussion

Our findings in preclinical models indicate that homozygous *MTAP* deletion contributes to STING agonist resistance through IRF3 down-regulation. This represents a previously underrecognized difference between human tumors and preclinical syngeneic mouse models that may help to address challenges encountered with STING agonists in human clinical trials. Moreover, the genetic status of *MTAP* may serve as a biomarker to guide patient selection for STING agonist therapy (fig. S13). We found that DFMO, an FDA-approved inhibitor of polyamine biosynthesis, counteracts IRF3 down-regulation and restores the responsiveness of MTAP-deficient tumors to STING agonists. Thus, targeting polyamine metabolism may offer an alternative approach to enhancing antitumor immune responses in *MTAP*-deleted tumors, potentially bridging the existing translational gap of STING agonists. Collectively, these findings warrant further validation in human clinical trials to confirm their therapeutic potential and translational relevance.

Polyamines are highly positively charged molecules. This characteristic enables them to bind to negatively charged molecules such as DNA, RNA, proteins, and phospholipids, thereby stabilizing and modifying their structures and functions (*25*, *42*, *43*). Polyamines play crucial roles in various biochemical and physiological processes, including DNA and RNA stabilization, gene regulation, cell cycle progression, ionic balance, antioxidant defense, and the regulation of apoptosis. These processes are essential for maintaining cellular homeostasis, growth, and adaptation to stress (*25*, *42*, *43*). ODC, a rate-limiting enzyme in polyamine synthesis, is aberrantly expressed in cancer cells, driven by multiple oncogenic pathways. Moreover, dysregulation of the polyamine biosynthesis pathway plays a critical role in tumor transformation and progression (*25*, *42*, *43*). Considering these factors, DFMO, an irreversible inhibitor of ODC, has been extensively evaluated in clinical trials over several decades for its potential as a cancer therapeutic. Recently, it was approved for the oral treatment of neuroblastoma (*27*). Previously, it was approved for the treatment of sleeping sickness caused by *Trypanosoma brucei* subsp. *gambiense* through intravenous injection and for the management of hirsutism through topical application (*25*). The extensive clinical trial history of DFMO provides valuable safety data regarding its administration. Overall, the most common adverse effects associated with this ODC inhibitor are generally manageable and reversible, with serious adverse events being relatively rare (*44*). Its favorable safety profile thus supports the feasibility of combining DFMO with STING agonists to improve their therapeutic efficacy.

In addition to the resistance mechanism that we have described, *STING* gene silencing through promoter hypermethylation has recently been identified as another mechanism of resistance to STING agonists. This resistance could potentially be overcome using clinically available DNA methylation inhibitors (*38*–*40*). Through a comprehensive multiomic analysis, we have demonstrated that the inactivation of the *MTAP* and *STING* genes primarily occurs through distinct mechanisms in human tumors. This observation underscores the importance of developing mechanism-based therapeutic strategies to combat STING agonist resistance arising from diverse mechanisms. STING agonist resistance resulting from homozygous *MTAP* deletion or *STING* promoter hypermethylation could be effectively countered using DFMO or DNA methylation inhibitors, respectively. Furthermore, inactivation

of MTAP and STING contributes to STING agonist resistance in two largely distinct patient populations, collectively constituting ~40% of the total cancer population (fig. S12E). This proportion underscores the critical need for patient stratification in STING agonist therapy.

Materials and methods

Cell culture and treatments

EMT6, MC38, HeLa, A549, EO771, A375, MCF7, B16-F10, GL-261, Hepa 1-6, HY-19636, and BT549 cells were maintained in Dulbecco's modified Eagle's medium (DMEM) with high glucose plus 10% fetal bovine serum (Cytiva). Raw264.7, DC2.4, P3X63Ag8.653, 4T1, CT26, and NCI-H1993 cells were grown in RPMI 1640 plus 10% fetal bovine serum (Cytiva). All cell lines were characterized as mycoplasma negative and validated by STR DNA fingerprinting. To inhibit PRMT5 arginine methyltransferase activity by selective inhibitors or 5′-methylthioadenosine (MTA), cells were treated with GSK3326595/EPZ015938 (Selleckchem, S8664, 1 μM), JNJ64619178 (Selleckchem, S8624, 0.1 μM), GSK3235025/EPZ015666 (Selleckchem, S7748, 10 μM) or MTA (Sigma, D5011, 200 μM) for 5 days. To inhibit proteasome, cells were treated with MG132 (Selleckchem, S2619, 0.5 μM) for 24 hours. To inhibit polyamine synthesis by DFMO, cells were treated with DFMO (Selleckchem, S4582, 25μM) for 5 days, with daily replacement with fresh DFMO. To activate the cytosolic nucleic acid–sensing pathways, cells were directly treated with MIW815 (ChemieTek, CT-ADUS100, 100 μg/ml), E7766 (MCE, HY-111999A, 100 μg/ml), or MSA2 (Selleckchem, S9681, 30 μg/ml), or were stimulated with poly(dA:dT) (InvivoGen, tlrl-patn, 0.1 μg/ml), poly(I:C) (InvivoGen, tlrl-pic, 0.05 μg/ml), or 2′3′-cGAMP (InvivoGen, tlrl-nacga23, 1 μg/ml) delivered by Lipofectamine 2000. To detect IFNβ induction, the conditioned medium after 24-hour stimulation was collected and subjected to an enzyme-linked immunosorbent assay (ELISA). To detect IFNB1, MX1, and ISG15 gene induction, cells were harvested after a 12-hour stimulation and subjected to RT-qPCR assays.

Plasmids and generation of stable cells

Lentiviral-based plasmids for IRF3, MTAP, and MID1 overexpression were obtained from the RNA technology platform and gene manipulation core of Academia Sinica or from GeneCopoeia. Lentiviral based shRNA plasmids used to knock down PRMT5, MTAP, and CDKN2B were purchased from Sigma and the RNA technology platform and gene manipulation core of Academia Sinica, Taiwan. CRISPR/Cas9 knockout plasmids and homology-directed repair (HDR) plasmids for MTAP knockout and CDKN2A knockout were purchased from Santa Cruz Biotechnology. The target sequences of shRNAs and single-guide RNAs (sgRNAs) are listed in table S1. For lentivirus packaging and transduction, the lentiviral plasmids mentioned above and the packaging vectors psPAX2 and pMD2G were co-transfected into human embryonic kidney (HEK) 293T cells, and viral particles were harvested 72 hours after transfection. Cells were infected with viruses by spinoculation at 800*g* for 30 min. Two days after transduction, cells were selected using puromycin for 7 days. For CRISPR gene knockout, CRISPR/Cas9 knockout plasmids and the paired HDR plasmids were co-transfected into cells by using Lipofectamine 2000 (Invitrogen). Two days after transduction, cells were selected by puromycin for 7 days.

RT-qPCR assays

Total RNA was extracted from cells by using TRIzol (Invitrogen) and processed directly into complementary DNA by reverse transcription using the SuperScript III kit (Invitrogen) according to the manufacturer's instructions. RT-qPCR assays were performed in triplicate with 2× Universal SYBR Green Fast qPCR Mix (ABclonal, RK21203) in the StepOnePlus system (Applied Biosystems). The primer sequences are listed in table S2. The mRNA levels of target genes were normalized to that of GAPDH in the same samples and expressed as the fold difference compared with that of control. Data were presented as the mean ± SD of three independent experiments, and statistical significance was determined using two-tailed paired Student's *t* tests. *P* values < 0.05 were considered significant.

ChIP

Chromatin was prepared from EMT6 cells using an Active Motif ChIP kit (Active Motif, 53086), and a ChIP-grade anti-histone H4 (Arg3) symmetric dimethylation antibody (Millipore, 17-10250) was used for the ChIP process. DNA extracted from 10 μl of preimmunoprecipitated samples served as the input control. RT-qPCR analyses of the immunoprecipitated DNA samples were conducted as described above, using the primer pair listed in table S2 and normalizing to the input. The condition with the highest enrichment was assigned a value of 1, with all other conditions normalized accordingly. Data are presented as the mean ± SD from three independent experiments, and statistical significance was assessed using two-tailed paired Student's *t* tests. *P* values < 0.05 were considered significant.

ELISA

Quantification of IFNβ levels released in the medium was conducted by using ELISA kits (PBL Assay Science, 41410 and 42400) according to the manufacturer's instructions. Data are presented as the mean ± SD of three independent experiments, and statistical significance was determined using two-tailed paired Student's *t* tests. *P* values < 0.05 were considered significant.

Protein extraction and Western blot analysis

Whole-cell extracts were prepared by lysing the cells in a lysis buffer containing 50 mM Tris-HCl (pH 7.6), 150 mM NaCl, 1% NP-40, 1% sodium deoxycholate, 0.1% sodium dodecyl sulfate (SDS), and 1× protease inhibitor (Roche) freshly added before lysis. To perform immunoblotting, cell lysates were subjected to SDS-PAGE, transferred onto polyvinylidene fluoride membranes (Bio-Rad), and then analyzed by Western blot using the indicated antibodies. Detailed information on the antibodies is provided in table S3. Image capture and analysis were performed using the iBright Western Blot Imaging Systems (Invitrogen). The images presented are representative of three independent experiments. The original images of key Western blot data are presented in fig. S14.

Immunohistochemical staining of human tumor tissue microarrays

Human tissue microarrays were purchased from TissueArray.Com LLC (MC6163). Immunohistochemial (IHC) staining of MTAP and IRF3 were performed by incubation of the tissue specimens with antibodies against MTAP (Abcam, ab126770, 1:600 dilution) or IRF3 (Abcam, ab68481, 1:500 dilution), followed by a biotin-conjugated secondary antibody and an avidin-biotin-peroxidase complex. Visualization of the slides was performed using amino-ethyl carbazole chromogen. The intensity of staining was ranked by two pathologists into four groups, high (score: 3), medium (score: 2), low (score: 1), and negative (score: 0), according to histological scores. The results of 430 tumor tissue specimens were subjected to Spearman rank correlation coefficient analysis to examine the correlation between MTAP and IRF3 expression. *P* values < 0.05 were considered statistically significant.

Animal studies

The systematic antitumor effects of DFMO and MIW815 were analyzed using the EMT6 breast tumor model and the MC38 colorectal cancer model. In the EMT6 model, tumors derived from MTAP-WT or MTAP-KO EMT6 cells were established by injecting 5×10^5 cells into the mammary fat pads on both flanks of BALB/c mice. Tumor diameter was measured by caliper, and tumor volume (in cubic millimeters) was calculated using the formula [(major axis in mm) × (minor axis in mm)^2 × 0.5]. When tumors reached ~200 mm^3 in volume (day 7), tumor-bearing mice from both cell lines were randomly assigned to four groups ($n = 5$ per group) receiving MIW815 (ChemieTek), DFMO (Sigma), or both. DFMO was administered orally at a concentration of 2% (w/v) in drinking water for 10 consecutive days. MIW815 (25 μg per treatment)

was given intratumorally into the left-flank tumor on days 10, 13, and 16. In the MC38 model, MTAP-WT or MTAP-KO MC38 tumors were established by injecting 5×10^5 cells into both flanks of C57BL/6 (n = 8 per group) or C57BL/6 Irf3$^{-/-}$ ($n = 5$ per group) mice. When tumors reached ~200 mm^3 in volume (day 12), tumor-bearing mice were randomly grouped and treated with MIW815, DFMO, or both. DFMO was administered orally at a concentration of 0.5% (w/v) in drinking water for 12 consecutive days. MIW815 (25 μg per treatment) was given intratumorally into the left-flank tumor on days 15, 18, and 21. At the experimental end point, the mice were sacrificed using CO_2 exposure followed by cervical dislocation, and their tumors were excised for subsequent analysis. All animal-based research was conducted according to the guidelines and requirements set forth by the Public Health Service Policy on Humane Care and Use of Laboratory Animals, the US Department of Health and Human Services' *Guide for the Care and Use of Laboratory Animals*, the Animal Welfare Act, and the MD Anderson Institutional Animal Care and Use Committee.

Isolation of CD45$^+$ cell population from tumors

To isolate CD45$^+$ tumor-infiltrating leukocytes from mouse tumors, tumors were excised and dissociated using a gentleMACS Dissociator (Miltenyi Biotec). Subsequently, CD45$^+$ cells were purified using CD45 (TIL) MicroBeads (Miltenyi Biotec, 130-110-618). The purity of the isolated cells was assessed by flow cytometry with a CD45 antibody (Miltenyi Biotec, 130-110-797).

Quantification of MTA

An aliquot of 100 μl of cell lysate and 200 μl of ice-cold methanol was placed in an Eppendorf centrifuge tube. After vortexing for 5 min and centrifuging at 14,000 rpm for 10 min, the supernatant was transferred to a new Eppendorf tube. This extraction procedure was performed twice, and all supernatants were pooled and dried using a speed vacuum concentrator (CentriVap Concentrator, Labconco, Kansas City, MO, USA). Finally, the extract was reconstituted in 50 μl of deionized water and analyzed by ultra-high-performance liquid chromatography–tandem mass spectrometry (UHPLC-MS/MS). The UHPLC separation was performed using an Ultimate 3000 UHPLC system (Thermo Scientific, San Jose, CA, USA). The chromatographic separation was carried out on a Waters ACQUITY UPLC C18 column (2.1 × 100 mm, 1.7 μm, Waters, Milford, MA, USA). The solvents used were deionized water containing 0.2% formic acid (solvent A) and acetonitrile containing 0.1% formic acid (solvent B). The UHPLC gradient was as follows: from 0 to 1 min, 5% B; from 1 to 2.5 min, increasing from 5% B to 100% B; from 2.5 to 6 min, maintaining at 100% B; from 6 to 6.5 min, decreasing from 100% B to 5% B; and from 6.5 to 10 min, maintaining at 5% B. MS/MS detection was performed on a Thermo Scientific Q-Exactive Plus high-resolution mass spectrometer with a heated electrospray ionization source. The mass spectrometer operated in positive ion mode with a spray voltage of 4.0 kV. Selected reaction monitoring scan mode was used with an ion transition from m/z 298.09 (precursor ion) to m/z 136.06 (product ion) for the quantification of MTA.

Quantification of polyamine

A 100-μl aliquot of cell lysate and 50 μl of ice-cold 10% perchloric acid was placed in an Eppendorf centrifuge tube and incubated in an ice bath for 10 min. After centrifugation for 10 min at 14,000 rpm, the supernatant was transferred to a new Eppendorf tube, and 100 μl of saturated sodium carbonate solution was added, followed by the addition of 200 μl of dansyl chloride (5 mg/ml in acetone). The mixture was then derivatized in the dark at 70°C for 10 min. After this, 200 μl of proline (0.1 g/ml) was added to remove excess dansyl chloride. The dansyl-derivatized polyamines were extracted using 200 μl of ethyl acetate, and the extract was dried using a speed vacuum concentrator. The analyte was then reconstituted in 50 μl of acetonitrile and analyzed by UHPLC-MS/MS. The UHPLC-MS/MS setup used for analyzing the dansyl-derivatized polyamines was identical to that used for MTA analysis. The solvent used for the separation of polyamines was a 10 mM ammonium formate solution containing 0.1% formic acid (solvent A) and acetonitrile (solvent B). The chromatographic gradient was as follows: from 0 to 0.5 min, 50% B; from 0.5 to 2.5 min, increasing from 50% B to 100% B; from 2.5 to 6.5 min, maintaining at 100% B; from 6.5 to 7 min, decreasing from 100% B to 50% B; and from 7 to 10 min, maintaining at 50% B. In selected reaction monitoring scan mode, the following ion transitions were used to quantify the polyamines: m/z 555.20 to m/z 170.09 for putrescine, m/z 845.31 to m/z 360.17 for spermidine, and m/z 1135.42 to m/z 360.17 for spermine.

ODC-PEPC-MDH-linked assay

ODC activity in cell lysates was measured using a method modified from that of Smithson *et al.* (*45*). The assay buffer (66 mM Tris, 25 mM NaCl, 8 mM $MgSO_4$, 0.01% Triton X-100, pH 8.05) was freshly prepared before use. Cell lysates were prepared in lysis buffer [assay buffer supplemented with 5.7 mM dithiothreitol (DTT)], quantified using the Bradford assay, and adjusted to a concentration of 1 mg/ml. The assay was performed in a 96-well plate by adding 120 μl of Pointe Scientific Liquid-Stable CO_2 Reagents (Thermo Fisher Scientific, 22666300) and 40 μl of cell lysates per well. The plate was preincubated at 37°C for 10 min to allow temperature equilibration. The reaction was initiated by adding 80 μl of substrate mix (assay buffer containing 5 mM L-ornithine, 100 μM pyridoxal-5′-phosphate, and 5.7 mM DTT). The plate was then immediately sealed with an ELISA plate sealer, and the decrease in absorbance at 405 nm was monitored every minute for 60 min at 37°C. Blank wells in which lysates were replaced with assay buffer were included as negative controls. Absorbance at 405 nm was plotted over time for each well. The slope of the linear portion of the curve (ΔA405/min) was calculated, and background activity from blank wells was subtracted from all sample values. ODC activity was then determined using the following formula: ODC activity (pmol CO_2/h/mg protein) = 6000 × [ΔA405/min × reaction volume (ml)]/[$\varepsilon \times d \times$ protein amount (mg)], where ε is the extinction coefficient of thio-NADH at 405 nm (11.9 mM^{-1} cm^{-1}), and d is the pathlength of the solution in the well (typically 0.63 cm for 240 μl in a 96-well plate).

RNA-seq analysis

Samples were collected independently in duplicates, and the RNA-seq procedure was conducted by the Taiwan Genomics Industry Alliance (TGIA). Sequencing libraries were generated from 1 μg of total RNA using the RNA HyperPrep kit with RiboErase (Kapa Biosystems, Pleasanton, CA, USA) and sequenced on the NovaSeq 6000 instrument (Illumina, San Diego, CA, USA). All RNA sample preparation procedures adhered to Illumina's official protocol. The Agilent SureSelect Strand-Specific RNA Library Preparation Kit was used for library construction, followed by size selection using AMPure XP beads (Beckman Coulter, USA). Base calling was performed using Illumina's bcl2fastq program v2.20. The de-multiplexed sequencing data were processed with Trimmomatic (version 0.36) to remove any adapters and poor-quality sequences using a sliding-window approach. Resulting read pairs were aligned with the HISAT2 aligner against the mouse reference genome (GRCm38.p6) to obtain read counts and fragments per kilobase per million data for genes and transcripts. The expression analysis settings were as follows: gene-level fold change < -2 or > 2, gene-level P value < 0.05, with the ANOVA method using the Ebayes approach. The sequencing data are available through the Sequence Read Archive under BioProject accession number PRJNA1204203.

Database acquisition and analysis

For figs. S1A and S4, the Spearman correlation between immune infiltration levels and the expression of gene of interest, calculated by the TIMER algorithm, was acquired from the TIMER2.0 database (http://timer.cistrome.org/). For Fig. 1A and fig. S1D, the homozygous deletion

frequency of the gene of interest within the TCGA cohort was obtained from the cBioPortal for Cancer Genomics database (http://www.cbioportal.org). In the portal, gene copy number levels were determined using the Genomic Identification of Significant Targets in Cancer (GISTIC) or RAE algorithms, in which a level of –2 denoted a homozygous deletion.

To analyze the Spearman correlation between MTAP and IFN-I expression in each cancer type of the entire TCGA cohort, as shown in fig. S1B, the gene expression data (RNA Seq V2 RSEM) of individual genes were downloaded from the cBioPortal for Cancer Genomics database, and their correlation was analyzed using GraphPad Prism. To examine the gene expression correlation between MTAP and IFN-I expression within a tumor cohort after excluding those with homozygous deletions of the IFN gene cluster, as shown in fig. S1G, we acquired copy number variation (CNV) data from cBioPortal. We then identified and excluded samples carrying IFNA1 CNV (–2), IFNB1 CNV (–2), or both from the TCGA cohort. The remaining cohort was subsequently subjected to Spearman correlation analysis between MTAP and IFN-I expression.

For fig. S12, the dysfunctional events associated with STING, TBK1, IRF3, and MTAP in the TCGA dataset were retrieved from the DriverDB cancer omics database (*41*). Copy number alterations (CNAs) were determined using the GISTIC algorithm (*46*). Homozygous deletion events were stringently characterized by a GISTIC score of –2. Additionally, the methylation status of these genes, including both hypermethylation and hypomethylation, was evaluated using the MethylMix algorithm (*47*). Inactive events in the genes were defined as the presence of homozygous deletion, hypermethylation, or both.

Tumor cell profile analysis by cytometry by time of flight

To characterize the tumor-infiltrating lymphocyte profile, tumors were excised and digested into single cells using a gentleMACS Dissociator and a mouse Tumor Dissociation Kit (Miltenyi Biotec). Tumor-infiltrating lymphocytes were enriched on a Ficoll gradient (Sigma-Aldrich), incubated with Cell-ID Cisplatin-195Pt (Fluidigm) at room temperature for 5 min, washed, and then incubated with a mixture of metal-labeled antibodies (table S4) at room temperature for 30 min. A sample of labeled cells was analyzed using the cytometry by time of flight 2 instrument (Fluidigm) at the MD Anderson Flow Cytometry and Cellular Imaging Core facility. Cytometry by time of flight data were analyzed by viSNE in Cytobank (Beckman Coulter Life Sciences).

Statistical analysis

Unless otherwise specified, the data presented in bar graphs represent the mean ± SD of three independent experiments. The experimental data were analyzed using GraphPad Prism, and Student's t test was used. For all statistical analyses, P values ≤ 0.05 were considered statistically significant, whereas "n.s." denotes results that were not statistically significant.

REFERENCES AND NOTES

1. K. M. Garland, T. L. Sheehy, J. T. Wilson, Chemical and biomolecular strategies for STING pathway activation in cancer immunotherapy. *Chem. Rev.* **122**, 5977–6039 (2022). doi: 10.1021/acs.chemrev.1c00750; pmid: 35107989
2. E. N. Chin, A. Sulpizio, L. L. Lairson, Targeting STING to promote antitumor immunity. *Trends Cell Biol.* **33**, 189–203 (2023). doi: 10.1016/j.tcb.2022.06.010; pmid: 35931610
3. T. Li *et al.*, TIMER: A web server for comprehensive analysis of tumor-infiltrating immune cells. *Cancer Res.* **77**, e108–e110 (2017). doi: 10.1158/0008-5472.CAN-17-0307; pmid: 29092952
4. G. Han *et al.*, 9p21 loss confers a cold tumor immune microenvironment and primary resistance to immune checkpoint therapy. *Nat. Commun.* **12**, 5606 (2021). doi: 10.1038/s41467-021-25894-9; pmid: 34556668
5. F. M. Barriga *et al.*, MACHETE identifies interferon-encompassing chromosome 9p21.3 deletions as mediators of immune evasion and metastasis. *Nat. Cancer* **3**, 1367–1385 (2022). doi: 10.1038/s43018-022-00443-5; pmid: 36344707
6. M. Grard *et al.*, Homozygous co-deletion of type I interferons and CDKN2A genes in thoracic cancers: Potential consequences for therapy. *Front. Oncol.* **11**, 695770 (2021). doi: 10.3389/fonc.2021.695770; pmid: 34249754
7. T. M. Petro, IFN regulatory factor 3 in health and disease. *J. Immunol.* **205**, 1981–1989 (2020). doi: 10.4049/jimmunol.2000462; pmid: 33020188
8. C. A. Jefferies, Regulating IRFs in IFN driven disease. *Front. Immunol.* **10**, 325 (2019). doi: 10.3389/fimmu.2019.00325; pmid: 30984161
9. H. Yanai *et al.*, Revisiting the role of IRF3 in inflammation and immunity by conditional and specifically targeted gene ablation in mice. *Proc. Natl. Acad. Sci. U.S.A.* **115**, 5253–5258 (2018). doi: 10.1073/pnas.1803936115; pmid: 29712834
10. S. M. Sanderson, P. G. Mikhael, V. Ramesh, Z. Dai, J. W. Locasale, Nutrient availability shapes methionine metabolism in p16/*MTAP*-deleted cells. *Sci. Adv.* **5**, eaav7769 (2019). doi: 10.1126/sciadv.aav7769; pmid: 31249865
11. K. Marjon *et al.*, MTAP deletions in cancer create vulnerability to targeting of the MAT2A/PRMT5/RIOK1 axis. *Cell Rep.* **15**, 574–587 (2016). doi: 10.1016/j.celrep.2016.03.043; pmid: 27068473
12. G. V. Kryukov *et al.*, MTAP deletion confers enhanced dependency on the PRMT5 arginine methyltransferase in cancer cells. *Science* **351**, 1214–1218 (2016). doi: 10.1126/science.aad5214; pmid: 26912360
13. K. J. Mavrakis *et al.*, Disordered methionine metabolism in MTAP/CDKN2A-deleted cancers leads to dependence on PRMT5. *Science* **351**, 1208–1213 (2016). doi: 10.1126/science.aad5944; pmid: 26912361
14. J. Kwon, S. F. Bakhoum, The cytosolic DNA-sensing cGAS-STING pathway in cancer. *Cancer Discov.* **10**, 26–39 (2020). doi: 10.1158/2159-8290.CD-19-0761; pmid: 31852718
15. Y. Gan *et al.*, The cGAS/STING pathway: A novel target for cancer therapy. *Front. Immunol.* **12**, 795401 (2022). doi: 10.3389/fimmu.2021.795401; pmid: 35046953
16. N. Samson, A. Ablasser, The cGAS-STING pathway and cancer. *Nat. Cancer* **3**, 1452–1463 (2022). doi: 10.1038/s43018-022-00468-w; pmid: 36510011
17. J. D. Stoeckler, S. Y. Li, Influx of 5′-deoxy-5′-methylthioadenosine into HL-60 human leukemia cells and erythrocytes. *J. Biol. Chem.* **262**, 9542–9546 (1987). doi: 10.1016/S0021-9258(18)47967-7; pmid: 3474231
18. M. Cartenì-Farina, F. della Ragione, G. Cacciapuoti, M. Porcelli, V. Zappia, Transport and metabolism of 5′-methylthioadenosine in human erythrocytes. *Biochim. Biophys. Acta* **727**, 221–229 (1983). doi: 10.1016/0005-2736(83)90407-8; pmid: 6838867
19. G. Kirovski *et al.*, Down-regulation of methylthioadenosine phosphorylase (MTAP) induces progression of hepatocellular carcinoma via accumulation of 5′-deoxy-5′-methylthioadenosine (MTA). *Am. J. Pathol.* **178**, 1145–1152 (2011). doi: 10.1016/j.ajpath.2010.11.059; pmid: 21356366
20. F. C. Henrich *et al.*, Suppressive effects of tumor cell-derived 5′-deoxy-5′-methylthioadenosine on human T cells. *OncoImmunology* **5**, e1184802 (2016). doi: 10.1080/2162402X.2016.1184802; pmid: 27622058
21. L. J. Hansen *et al.*, MTAP loss correlates with an immunosuppressive profile in GBM and its substrate MTA stimulates alternative macrophage polarization. *Sci. Rep.* **12**, 4183 (2022). doi: 10.1038/s41598-022-07697-0; pmid: 35264604
22. X. Chen *et al.*, Ubiquitin E3 ligase MID1 inhibits the innate immune response by ubiquitinating IRF3. *Immunology* **163**, 278–292 (2021). doi: 10.1111/imm.13315; pmid: 33513265
23. Y. Li, Y. Wang, P. Wu, 5′-Methylthioadenosine and Cancer: Old molecules, new understanding. *J. Cancer* **10**, 927–936 (2019). doi: 10.7150/jca.27160; pmid: 30854099
24. S. M. Sanderson, X. Gao, Z. Dai, J. W. Locasale, Methionine metabolism in health and cancer: A nexus of diet and precision medicine. *Nat. Rev. Cancer* **19**, 625–637 (2019). doi: 10.1038/s41568-019-0187-8; pmid: 31515518
25. R. A. Casero Jr., T. Murray Stewart, A. E. Pegg, Polyamine metabolism and cancer: Treatments, challenges and opportunities. *Nat. Rev. Cancer* **18**, 681–695 (2018). doi: 10.1038/s41568-018-0050-3; pmid: 30181570
26. R. A. Casero Jr., L. J. Marton, Targeting polyamine metabolism and function in cancer and other hyperproliferative diseases. *Nat. Rev. Drug Discov.* **6**, 373–390 (2007). doi: 10.1038/nrd2243; pmid: 17464296
27. E. S. Duke *et al.*, US Food and Drug Administration approval summary: Eflornithine for high-risk neuroblastoma after prior multiagent, multimodality therapy. *J. Clin. Oncol.* **42**, 3047–3057 (2024). doi: 10.1200/JCO.24.00546; pmid: 38917371
28. K. Kee *et al.*, Metabolic and antiproliferative consequences of activated polyamine catabolism in LNCaP prostate carcinoma cells. *J. Biol. Chem.* **279**, 27050–27058 (2004). doi: 10.1074/jbc.M403323200; pmid: 15096507
29. C. Ding, Z. Song, A. Shen, T. Chen, A. Zhang, Small molecules targeting the innate immune cGAS–STING–TBK1 signaling pathway. *Acta Pharm. Sin. B* **10**, 2272–2298 (2020). doi: 10.1016/j.apsb.2020.03.001; pmid: 33354501
30. A. Amouzegar, M. Chelvanambi, J. N. Filderman, W. J. Storkus, J. J. Luke, STING agonists as cancer therapeutics. *Cancers* **13**, 2695 (2021). doi: 10.3390/cancers13112695; pmid: 34070756
31. L. Corrales *et al.*, Direct activation of STING in the tumor microenvironment leads to potent and systemic tumor regression and immunity. *Cell Rep.* **11**, 1018–1030 (2015). doi: 10.1016/j.celrep.2015.04.031; pmid: 25959818
32. D. S. Kim *et al.*, E7766, a macrocycle-bridged stimulator of interferon genes (STING) agonist with potent pan-genotypic activity. *ChemMedChem* **16**, 1741–1743 (2021). doi: 10.1002/cmdc.202100068; pmid: 33522135

33. B. S. Pan *et al.*, An orally available non-nucleotide STING agonist with antitumor activity. *Science* **369**, eaba6098 (2020). doi: 10.1126/science.aba6098; pmid: 32820094
34. K. E. Sivick *et al.*, Magnitude of therapeutic STING activation determines $CD8^+$ T cell-mediated anti-tumor immunity. *Cell Rep.* **25**, 3074–3085.e5 (2018). doi: 10.1016/j.celrep.2018.11.047; pmid: 30540940
35. M. Ishii *et al.*, Methylthioadenosine phosphorylase gene is silenced by promoter hypermethylation in human lymphoma cell line DHL-9: Another mechanism of enzyme deficiency. *Int. J. Oncol.* **26**, 985–991 (2005). doi: 10.3892/ijo.26.4.985; pmid: 15753993
36. C. Hellerbrand *et al.*, Promoter-hypermethylation is causing functional relevant downregulation of methylthioadenosine phosphorylase (MTAP) expression in hepatocellular carcinoma. *Carcinogenesis* **27**, 64–72 (2006). doi: 10.1093/carcin/bgi201; pmid: 16081515
37. W. J. Woollard *et al.*, Independent loss of methylthioadenosine phosphorylase (MTAP) in primary cutaneous T-cell lymphoma. *J. Invest. Dermatol.* **136**, 1238–1246 (2016). doi: 10.1016/j.jid.2016.01.028; pmid: 26872600
38. R. Falahat *et al.*, Epigenetic reprogramming of tumor cell-intrinsic STING function sculpts antigenicity and T cell recognition of melanoma. *Proc. Natl. Acad. Sci. U.S.A.* **118**, e2013598118 (2021). doi: 10.1073/pnas.2013598118; pmid: 33827917
39. J. T. Low *et al.*, Epigenetic STING silencing is developmentally conserved in gliomas and can be rescued by methyltransferase inhibition. *Cancer Cell* **40**, 439–440 (2022). doi: 10.1016/j.ccell.2022.04.009; pmid: 35487217
40. R. Falahat *et al.*, Epigenetic state determines the in vivo efficacy of STING agonist therapy. *Nat. Commun.* **14**, 1573 (2023). doi: 10.1038/s41467-023-37217-1; pmid: 36949064
41. S. H. Liu *et al.*, DriverDBv3: A multi-omics database for cancer driver gene research. *Nucleic Acids Res.* **48**, D863–D870 (2020). pmid: 31701128
42. T. R. Murray-Stewart, P. M. Woster, R. A. Casero Jr., Targeting polyamine metabolism for cancer therapy and prevention. *Biochem. J.* **473**, 2937–2953 (2016). doi: 10.1042/BCJ20160383; pmid: 27679855
43. J. Li, Y. Meng, X. Wu, Y. Sun, Polyamines and related signaling pathways in cancer. *Cancer Cell Int.* **20**, 539 (2020). doi: 10.1186/s12935-020-01545-9; pmid: 33292222
44. F. L. Meyskens Jr., E. W. Gerner, Development of difluoromethylornithine (DFMO) as a chemoprevention agent. *Clin. Cancer Res.* **5**, 945–951 (1999). pmid: 10353725
45. D. C. Smithson, A. A. Shelat, J. Baldwin, M. A. Phillips, R. K. Guy, Optimization of a non-radioactive high-throughput assay for decarboxylase enzymes. *Assay Drug Dev. Technol.* **8**, 175–185 (2010). doi: 10.1089/adt.2009.0249; pmid: 20085486
46. R. Beroukhim *et al.*, Assessing the significance of chromosomal aberrations in cancer: Methodology and application to glioma. *Proc. Natl. Acad. Sci. U.S.A.* **104**, 20007–20012 (2007). doi: 10.1073/pnas.0710052104; pmid: 18077431
47. O. Gevaert, R. Tibshirani, S. K. Plevritis, Pancancer analysis of DNA methylation-driven genes using MethylMix. *Genome Biol.* **16**, 17 (2015). doi: 10.1186/s13059-014-0579-8; pmid: 25631659

ACKNOWLEDGMENTS

Funding: This work was supported by the National Science and Technology Council of Taiwan (NSTC grant 113-2639-B-039-001-ASP and T-Star Center NSTC grant 114-2634-F-039-001 to M.-C.H. and MOST grants 109-2314-B-039-006-MY2 and 111-2320-B-039-045-MY3 to J.-M.H.); the Ministry of Health and Welfare of Taiwan (grants MOHW114-TDU-B-222-144016 and MOHW114-TDU-B-222-000020 to M.-C.H.); a China Medical University YingTsai Young Scholar Award (CMU108-YTY-02 to J.-M.H.); "Cancer Biology and Precision Therapeutics Center, China Medical University" from The Featured Areas Research Center Program within the framework of the Higher Education Sprout Project by the Ministry of Education of Taiwan; and the National Nature Science Foundation of China (grants 32400748 and 82472897 to C.L. and grants 82173107 and 82372703 to J.H.). **Author contributions:** Conceptualization: J.-M.H.; Investigation: J.-M.H., C.L., W.X., W.-C.C., C.-Y.C., J.H.; Funding acquisition: J.-M.H., M.-C.H.; Supervision: J.-M.H., M.-C.H.; Writing – original draft: J.-M.H., M.-C.H.; Writing – review & editing: All authors. **Competing interests:** M.-C.H. and J.-M.H. are listed as inventors on patent application TWI836429B, submitted by China Medical University, which covers a method for predicting cancer patient susceptibility to STING agonists by detecting MTAP expression. **Data and materials availability:** All data are available in the main text or the supplementary materials. The sequencing data are available through the Sequence Read Archive under BioProject accession number PRJNA1204203. All reagents used for this study will be shared upon request with other researchers in academia. **License information:** Copyright © 2025 the authors, some rights reserved; exclusive licensee American Association for the Advancement of Science. No claim to original US government works. https://www.science.org/about/science-licenses-journal-article-reuse

SUPPLEMENTARY MATERIALS

science.org/doi/10.1126/science.adl4089
Figs. S1 to S14; Tables S1 to S4; Data S1 to S5; MDAR Reproducibility Checklist

Submitted 17 October 2023; resubmitted 31 December 2024; accepted 10 July 2025

10.1126/science.adl4089

RESEARCH ARTICLE SUMMARY

YEAST GENETICS

A genome-to-proteome map reveals how natural variants drive proteome diversity and shape fitness

Christopher M. Jakobson†, Johannes Hartl†, Pauline Trébulle, Michael Mülleder, Daniel F. Jarosz*‡, Markus Ralser*‡

Full article and list of author affiliations: https://doi.org/10.1126/science.adu3198

INTRODUCTION: Understanding the genotype-phenotype relationship remains one of the central challenges in genetics, with implications that range from evolution to health and disease. Although genome-wide association studies have identified many links between DNA and phenotype, the molecular underpinnings of these connections often remain elusive. Consequently, even in intensively studied genes and pathways, many natural genetic variants have uncertain effects.

RATIONALE: Proteins are the primary functional product of the genome, so connecting genetic changes to their consequences for both the proteome and cell physiology can shed light on this problem. Focusing on the meiotic progeny of a yeast strain isolated from a vineyard and another from an immunocompromised patient, we sought to chart a natural, nucleotide-resolution genome-to-proteome map. To do this, we exploited the combination of fast and precise mass spectrometry proteomics and super-resolution genetic mapping to uncover more than 6400 genotype-protein associations, including more than 1600 effects on protein levels assigned to individual polymorphisms.

RESULTS: Even the modest natural genetic variation between the two parental yeast isolates caused broad and functionally coherent proteomic changes. The aggregated effects of multiple variants in core signaling networks, such as the Ras–cAMP-dependent protein kinase (PKA) pathway, underscored the power of polygenic adaptation to drive rapid divergence. Moreover, protein levels in the progeny often transgressed beyond those of the parents, revealing how latent genome variation creates proteome diversity through meiosis. Thus, these natural proteomes reflect a complex interplay of directional and stabilizing selection.

We detected potent trans-regulatory effects that often originated in metabolism and other factors not conventionally associated with gene regulation, providing mechanistic insights into the long-standing observation that trans-regulatory variation is distributed throughout the genome. Coding variants played a predominant role in trans effects, likely owing to their dual capacity to influence protein abundance and function. Furthermore, single-nucleotide resolution allowed us to pinpoint trans-acting coding variants both within and outside of the core functional domains of proteins.

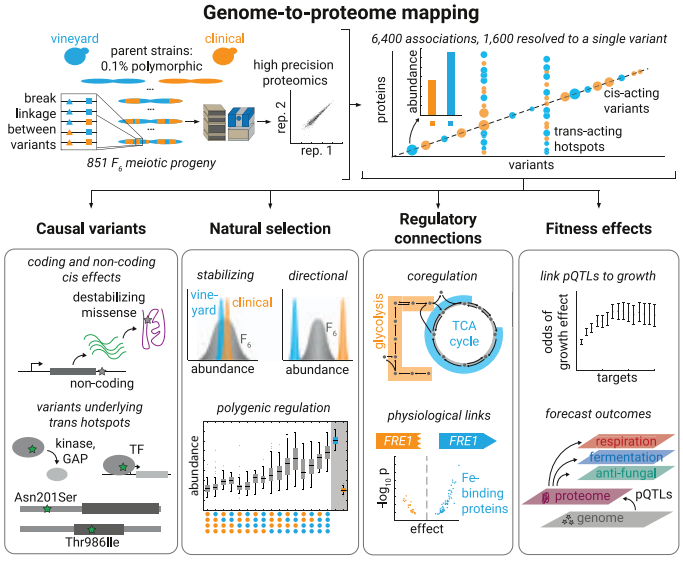
In more than 90% of cases, the genotype-protein connections that we identified revealed coherent regulatory relationships not evident from genetic and physical interaction databases. Moreover, variants with complex genetic background effect in the parental strains showed strong regulatory effects in their progeny, highlighting the power of our approach to identify functional variation.

The genome-to-proteome map that we charted in one standard condition persisted across environments and forecasted the effectsof genetic variation under diverse perturbations. Proteomic profiling thus reflects a latent molecular space that is broadly predictive of consequences for the organism, even if those effects only emerge later under newfound stress.

CONCLUSION: Our findings illustrate that high-resolution mapping of the molecular connections from the genome to the proteome to complex traits is a powerful framework to understand the mechanisms underlying adaptation and to forecast the functional consequences of genetic variants. □

*Corresponding author. Email: jarosz@stanford.edu (D.F.J.); markus.ralser@charite.de (M.R.) †These authors contributed equally to this work. ‡These authors contributed equally to this work. **Cite this article as C. M. Jakobson *et al.*, *Science* 390, eadu3198 (2025). DOI: 10.1126/science.adu3198**

A nucleotide-resolution genome-to-proteome map. We charted connections from the genome to protein levels in 851 meiotic progeny of two wild yeast strains. The resulting atlas pinpointed cis- and trans-acting causal variants, revealed widespread signatures of selection, identified previously unknown regulatory connections, and forecasted the phenotypic impact of natural genetic variation across environments. TF, transcription factor; GAP, GTPase activating protein; TCA, tricarboxylic acid; pQTLs, protein quantitative trait loci.



YEAST GENETICS

A genome-to-proteome map reveals how natural variants drive proteome diversity and shape fitness

Christopher M. Jakobson[1]†, Johannes Hartl[2,3]†, Pauline Trébulle[4], Michael Mülleder[5], Daniel F. Jarosz[1,6]*‡, Markus Ralser[2,3,7]*‡

Understanding how genetic variation translates into complex phenotypes remains a fundamental challenge. In this work, we address this by mapping genome-to-proteome relationships in 800 progeny of a cross between two yeast strains adapted to distinct environments. Despite the modest genetic distance between the parents, we observed notable proteomic diversity and mapped more than 6400 genotype-protein associations, with more than 1600 linked to individual genetic variants. Proteomic adaptation emerged from a conserved network of cis- and trans-regulatory variants, often originating from proteins not traditionally linked to gene regulation. This atlas allowed us to forecast organismal fitness effects across diverse conditions. By connecting genomic and proteomic landscapes at unprecedented resolution, our study provides a framework for predicting the phenotypic outcomes of natural genetic variation.

Genetic variation plays a central role in health and disease, yet three decades into the genomic era, we are unable to predict the phenotypic effects of most mutations (*1*). The problem is even more acute for rare variants, which are often presumed to be deleterious but cannot be characterized by population genetics (*2*). These challenges arise because we lack systems-level understanding of how the effects of DNA mutations propagate to other molecular layers and ultimately affect cellular physiology.

Many large-scale efforts to associate genetic variation with molecular phenotypes have focused on mRNA levels (*3*) or splicing (*4*). Yet, the proteome predominantly exerts function, and pioneering experiments have established the possibility of mapping variants to protein levels directly (*5*–*7*). However, in humans, two barriers limit the explanatory power of these datasets: A pragmatic focus on the plasma proteome provides only an indirect representation of regulation in cells, and human populations harbor a large excess of rare polymorphisms. Consequently, genetic associations explain little of the variation in plasma protein levels [e.g., 2.7% (*8*)].

By contrast, a direct link between genetic variation and the proteome can be made in single-celled organisms. The model eukaryote used in this work, *Saccharomyces cerevisiae*, combines small genome size with the ability to control meiosis and mating in the laboratory. Crosses between strains of this budding yeast have linked genetic variants to changes in mRNA and protein expression at genome-wide scale (*5*, *9*–*12*) and have been used to investigate the regulation of model transcripts and proteins (*13*–*16*). Yet, the number of proteins or strains examined in these studies has often been small (~100 progeny) (*12*, *17*, *18*), and even large collections of wild isolates cannot resolve linked genomic regions to individual causal polymorphisms (*19*, *20*).

This barrier can be overcome by intercrossing the progeny of two closely related strains, which results in a panel in which linkage between neighboring variants has been broken and genetic associations can be mapped to individual variants (*21*). In this work, we combine high-throughput proteomics (*22*) with nucleotide-resolution genetic mapping in a library of 851 segregants (*21*) to comprehensively chart a natural genotype-to-protein map. This molecular atlas comprises thousands of variant-protein associations, many revealed solely at the protein level. Proteins exhibited widespread transgression, highlighting substantial latent potential of the genome to create proteomic diversity. Natural selection pervasively remodeled the proteomes of the two closely related parental strains, revealing general molecular principles underlying causality. Integration with a complementary genotype-to-phenotype map revealed that variants controlling protein levels in the absence of stress drive resistance to diverse perturbations. These results suggest that genotype-to-protein maps are conserved across environments and can forecast the molecular and phenotypic consequences of genetic variation.

Results

Mass spectrometry–based proteomics to probe molecular adaptation

Two chief obstacles to understanding the mechanistic influence of the genome on the proteome are the excess of rare polymorphisms in natural populations and the difficulty of precisely measuring protein levels in cells at sufficient scale. In this work, we addressed these challenges using 851 F_6 isolates from a population of haploid yeast derived from mating two parents—one from the mucosa of an immunocompromised patient treated in Italy (YJM975; henceforth YJM) (*23*) and the other from a California vineyard (RM11; RM) (*24*) (Fig. 1A). Despite substantial phenotypic diversification, they harbor few polymorphisms (~0.1% divergence; comparable to that between two unrelated humans) in very-low-linkage disequilibrium, which enables high-resolution genetic mapping (*21*).

To measure protein levels in these strains, we took advantage of ultrahigh-pressure, high-flow chromatography; scanning SWATH acquisition (*22*); and deep neural network data processing strategies (*25*). To benchmark proteome diversity, we also included 22 diverse isolates from the Saccharomyces Genome Resequencing Project (SGRP) (*26*) (data S1 and S2). We obtained a proteome dataset of very high quantitative precision: coefficient of variation (CV) 15.6 to 19.9% for biological replicates of RM and YJM, with negligible batch effects (Fig. 1B and fig. S1, A and B).

Standing and latent variation in the proteome

Despite modest genetic distance (~12,000 variants) and similar proliferation in standard laboratory conditions (fig. S1C), the parental proteomes were highly diverged: 826 of 1225 proteins differed in intensity (67.4%; $n = 36$ to 39; Benjamini-Hochberg–corrected q value < 0.05; 190 with fold-change > 1.5; 66 with fold-change > 2) (Fig. 1C). Up- and down-regulated subsets were functionally coherent: The clinical isolate (YJM) had higher levels of amino acid and purine biosynthesis and gluconeogenesis proteins, whereas the vineyard isolate (RM) had higher levels of proteins associated with oxidative phosphorylation and the tricarboxylic acid (TCA) cycle (data S3).

Protein abundance spanned a large range in the progeny, and many protein levels transgressed beyond their abundances in the parents (Fig. 1D). Despite this, our approach yielded high broad-sense heritability (median 76.2%), which depended only modestly on whether a

[1]Department of Chemical and Systems Biology, Stanford University School of Medicine, Stanford, CA, USA. [2]Berlin Institute of Health (BIH) at Charité – Universitätsmedizin Berlin, Berlin, Germany. [3]Department of Biochemistry, Charité – Universitätsmedizin Berlin, Berlin, Germany. [4]Centre for Human Genetics, Nuffield Department of Medicine, University of Oxford, Oxford, UK. [5]Core Facility High-Throughput Mass Spectrometry, Charité – Universitätsmedizin Berlin, Berlin, Germany. [6]Department of Developmental Biology, Stanford University School of Medicine, Stanford, CA, USA. [7]Max Planck Institute for Molecular Genetics, Berlin, Germany. ***Corresponding author. Email: jarosz@stanford.edu (D.F.J.); markus.ralser@charite.de (M.R.)** †These authors contributed equally to this work. ‡These authors contributed equally to this work.

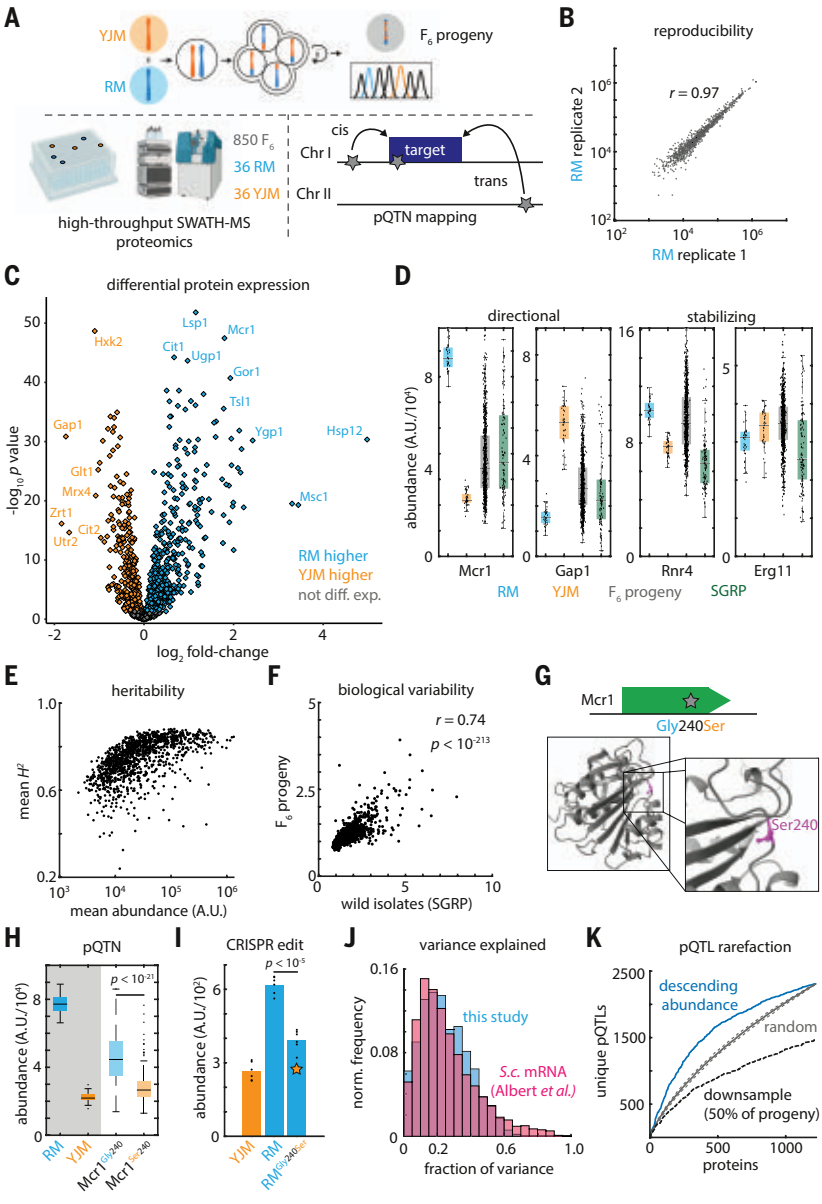


Fig. 1. A variant-resolution genome-to-proteome map. (**A**) Schematic of the mass spectrometry–based proteomics and genetic mapping approach. Chr, chromosome; MS, mass spectrometry. (**B**) Representative reproducibility across biological replicates of the vineyard (RM) isolate. Pearson's *r* as indicated; *P* value by *t* statistic. (**C**) Volcano plot illustrating $\log_2$ fold-change in protein abundance (abscissa) and Benjamini-Hochberg–corrected *t* test *P* value (ordinate) between the vineyard (RM) and clinical (YJM) parents. $n = 36$ to 39 replicates. (**D**) Estimated abundance of Mcr1 and Gap1 and Rnr4 and Erg11 in RM parent (blue), YJM parent (orange), F_6 progeny (gray), and SGRP wild strains (green). Boxes show median and upper and lower quartiles; whiskers show 1.5 times the interquartile range. A.U., arbitrary units. (**E**) Mean broad-sense heritability of protein abundance (ordinate) as a function of estimated absolute protein abundance (abscissa) for all proteins measured in at least 80% of samples. (**F**) Normalized CV among the SGRP wild strains as compared with the mean CV in the parental isolates (ordinate) as a function of normalized CV among F_6 progeny (abscissa). Pearson's *r* as indicated; *P* value by *t* statistic. (**G**) Schematic and predicted AlphaFold2 protein structure of a cis-acting missense variant in Mcr1. (**H**) Genetic mapping of a cis-acting SNP controlling the abundance of Mcr1. (**I**) CRISPR reconstruction and mass spectrometry to validate the effect of the $Mcr1^{Gly240Ser}$ variant. $n = 6$; *P* value by two-sided *t* test. (**J**) Histogram of the fraction of total variance explained by the global (cis- and trans-acting) model in this study (blue) and in a highly powered eQTL mapping study in budding yeast (pink) (*11*). (**K**) Rarefaction plot of distinct trans-acting pQTL associations discovered, ordered by decreasing estimated protein abundance (blue) and in 100 random orders (gray). Also shown (black dashed) is the same statistic for downsampled real data using only 50% of the F_6 progeny.

protein was high or low abundance (Fig. 1E) and was limited primarily by technical variability (fig. S1D). All told, 710 proteins exhibited a distribution among the F_6 progeny not expected by chance. In total, 286 proteins had greater variability in the offspring, indicating stabilizing selection in the parents, whereas the distribution was narrower than expected for another 424 proteins ($q < 0.01$), which suggests that directional selection was at play (fig. S1, E to H) (*27*).

The most variable proteins in the progeny were highly variable across wild isolates spanning genetic diversity in this species (*26*) [correlation coefficient (r) = 0.74; $P < 10^{-213}$] (Fig. 1F). Thus, proteomic diversification released by meiosis in our experiment was broadly representative of natural variation, perhaps reflecting conserved regulatory networks in *S. cerevisiae* and a shared latent capacity for diversification.

A nucleotide-resolution proteogenomic map in a model eukaryote

We next performed genetic mapping (*21*) to associate variants with protein abundance (Fig. 1A), identifying 6476 variant-protein associations [protein quantitative trait loci (pQTLs)] controlling 923 proteins [~10% false discovery rate (FDR)] (data S4). Of these, 1650 (25.5%) were fine-mapped to a single polymorphism [protein quantitative trait nucleotide (pQTN)]—a level of resolution seldom achievable directly from statistical mapping. In the case of mitochondrial NADH-cytochrome *b5* reductase Mcr1 (*28*), for example, a coding single-nucleotide polymorphism (SNP) ($Mcr1^{Gly240Ser}$) was associated with reduced levels in cis (Fig. 1, G and H). Genome editing and proteome analysis confirmed that this polymorphism was alone sufficient to decrease Mcr1 levels by nearly 40% (Fig. 1I).

Our model explained a median of 30.4% of broad-sense heritability, and, owing to the high heritability of protein abundance, we explained 22.8% of the overall variance [comparable to maps of mRNA abundance in yeast (*11*)] (Fig. 1J). We were well-powered to detect associations of modest effect (~95% sensitivity for effects of 0.1 SD; ~63% for 0.025 SD) (fig. S1I); thus, missing heritability likely arises from numerous additional pQTLs of small-effect, epistatic interactions (*29*) or nongenetic influences (fig. S1J).

The rate at which we discovered additional trans pQTLs declined as we considered additional proteins (Fig. 1K and fig. S1K), and downsampling our data to 50% of the progeny yielded just 3498 associations (54% of the complete atlas). The 1200 proteins that we quantified were enriched for highly abundant and essential proteins and constituted the majority of the cell's total proteomic mass. At least 1000 were subject to genetic control (differential expression or regulation by a pQTL), even in these closely related isolates. Thus, we capture the molecular genetic basis of both standing and latent variation for a large fraction of the proteome.

Testing the impact of causal variants across the species

We next examined the penetrance of cis-pQTLs across the transcriptomes and proteomes of natural yeast isolates (*19*, *30*) (Fig. 2A). Across these diverse backgrounds, both Odc2 and Rdl1 transcript and protein levels, for example, were affected by the cis-acting variants that we identified (Fig. 2B). Of 67 associations that we tested,

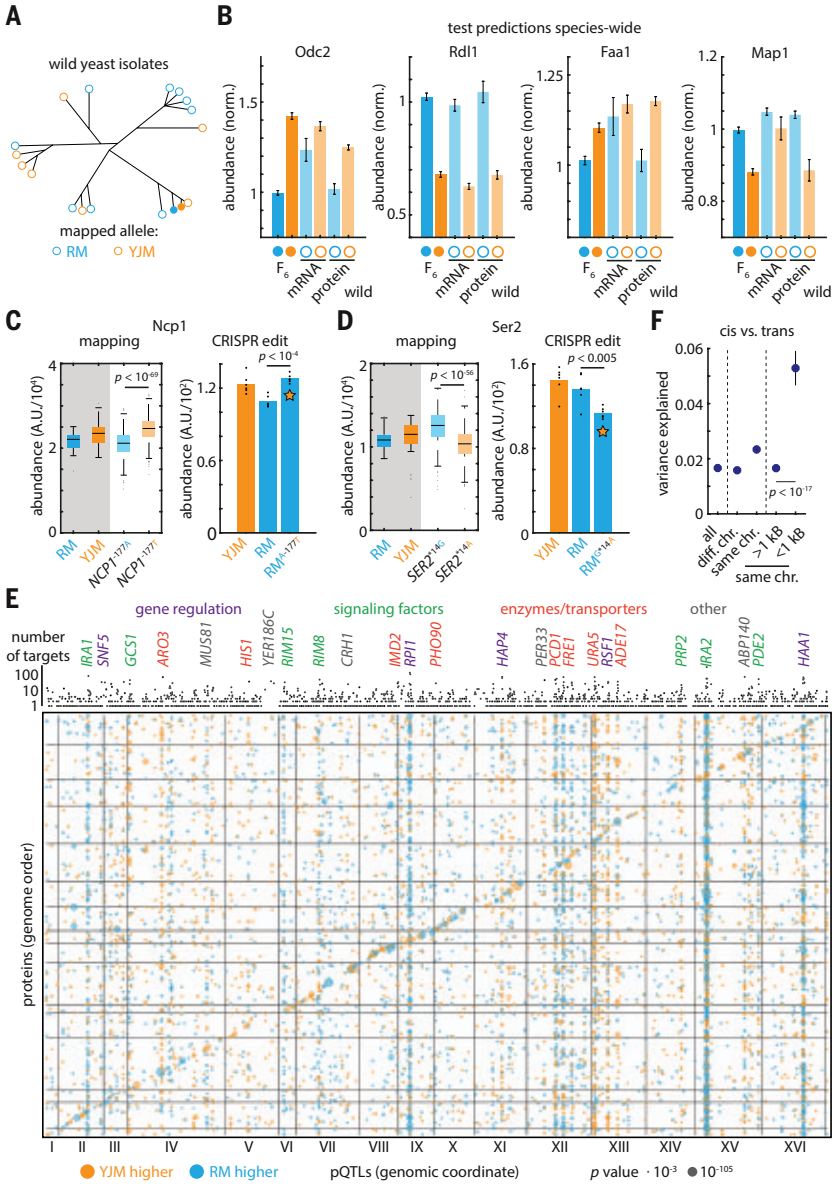


Fig. 2. Variant-to-molecule atlas reveals protein-level regulation. (**A**) Schematic of statistical replication strategy. (**B**) (Left) Genetic mapping of cis-acting effects on Odc2 and Rdl1 protein abundance and replication of this signal in the orthogonal 1002 Yeast Genomes (*19*) transcriptomes and proteomes. (Right) As in the left, but for Faa1 and Map1; these signals were evident only at the proteomic level in the replication data. Data shown are medians ± SEMs. (**C**) (Left) Genetic mapping of cis-acting effect on Ncp1 protein abundance. (Right) CRISPR reconstruction and mass spectrometry to test the effect of the $NCP1^{A\text{-}177T}$ variant. $n = 6$; P value by two-sided t test. (**D**) As in (C), but for the $SER2^{G*14A}$ variant. (**E**) Bubble plot indicating the genomic position of all pQTLs. pQTL positions and encoding genes are arranged in genome order. Orange dots indicate that clinical (YJM) allele increases protein level, and blue dots indicate that vineyard (RM) allele increases level. Dots are sized by genetic mapping P value. Indicated above is the number of target proteins controlled by each locus (aggregated by gene); highlighted are trans hotspots color coded by gene function, as indicated. (**F**) Variance explained by pQTLs with the indicated distance to the encoding gene for the target protein. P values by Student's t test; dots indicate means, and bars indicate standard errors.

46 were replicated in this independent experiment ($P < 10^{-3}$) (fig. S2A), including several instances (e.g., Faa1 and Map1) in which cis-regulatory effects were observed in the proteome but not in the transcriptome (Fig. 2B). Thus, the pQTLs that we charted were evident species-wide, and proteomics captured both mRNA regulation that propagated to protein levels and effects that emerged primarily in the proteome (*31*).

mRNA- and protein-level gene regulation

We next compared our protein mapping data with allele-specific mRNA expression (ASE) analysis of the F_0 hybrid of the parental strains, a proxy for transcriptional cis regulation (fig. S2B) (*32*). Only 30 of 127 proteins with a cis-pQTL had a significant mRNA allelic imbalance (data S5), which indicates that some cis effects arose more strongly in protein rather than mRNA levels. To examine this property further, we selected two regulatory cis-pQTNs—one upstream of *NCP1*, encoding a P450 reductase, and one in the 3′ untranslated region of *SER2*, which encodes phosphoserine phosphatase. The *NCP1* variant significantly affected protein level but not mRNA ASE [perhaps owing to its impact on an adjacent small noncanonical open reading frame (ORF) (*33*)], whereas the *SER2* variant affected both mRNA and protein levels (fig. S2B). We then reconstructed these variants (*34*) and measured mRNA and protein levels. In both cases, exchange of the variant recapitulated the effects: The $NCP1^{A\text{-}177T}$ polymorphism up-regulated Ncp1 protein ($P < 10^{-4}$) but not mRNA levels ($P = 0.30$), whereas $SER2^{G*14A}$ down-regulated both *SER2* mRNA and protein levels ($P < 0.04$; $P < 0.005$) (Fig. 2, C and D, and fig. S2C). Thus, precision proteomics can detect pQTL effects that arise through changes in the transcriptome and others that are not evident in mRNA levels.

Noncanonical regulators underlying trans-acting hotspots

Our atlas reflected considerable complexity in protein expression regulation: The median protein was controlled by five loci, and 22.6% of proteins were controlled by more than 10 pQTLs (fig. S2D). A total of 98% of associations involved trans-acting loci (>1 kb away), whereas the remainder were nearby and likely acted in cis. Much of the trans regulation was due to a small number of hotspots (*9*, *10*): The 100 most pleiotropic trans-pQTL genes (out of ~2000) accounted for 44% of associations.

The transcription factor *PHO2*, for instance, controlled seven adenine biosynthetic enzymes (fig. S2E). Yet, as noted previously (*10*), many regulatory hotspots did not harbor DNA binding proteins or regulatory factors. We found that many of these associations were in fact driven by metabolic enzymes or membrane transporters (Fig. 2E): The uracil transporter *FUR4* controlled the uracil biosynthetic pathway, and the inosine monophosphate dehydrogenase *IMD2*, involved in guanosine 5′-triphosphate (GTP) synthesis, controlled the abundance of several metabolic enzymes (fig. S2E). Overall, although individual cis-acting variants were of larger effect (5.29% variance explained versus 1.66% for trans effects; $P < 10^{-17}$) (Fig. 2F), the cumulative effect of trans regulation was much larger (10.9% of variance explained in trans versus 0.74% in cis across all proteins; $P < 10^{-263}$) (fig. S2F). This comprehensive atlas positioned us to investigate how natural genetic variation drives proteomic adaptation through multiple loci throughout the genome.

Regulatory adaptation underlying diverged proteomes

The prominent hotspots at *IRA1*, *IRA2*, and *PDE2* (Fig. 3A) controlled the abundance of up to 300 proteins, with coherent subsets up- and down-regulated by each allele. Mcr1 abundance, for example, ranged

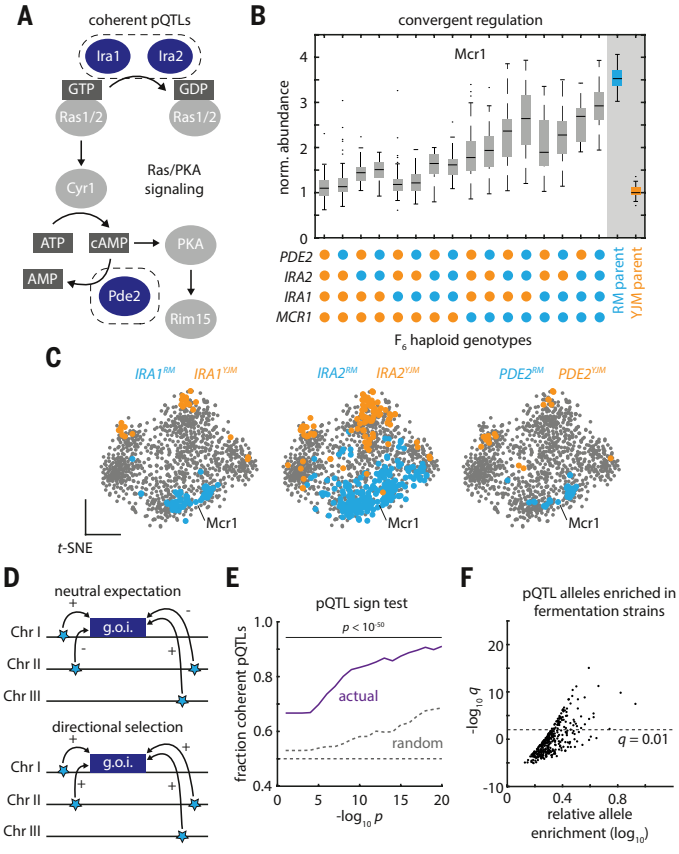


Fig. 3. Polygenic adaptation reflecting natural selection on protein abundance. (**A**) Schematic of Ras-PKA signaling highlighting the Ira1, Ira2, and Pde2 proteins, which harbored trans-acting hotspots. (**B**) Mcr1 protein levels as a function of F_6 progeny genotypes at the *PDE2*, *IRA2*, *IRA1*, and *MCR1* loci, as indicated. Boxes show median and upper and lower quartiles; whiskers show 1.5 times the interquartile range. (**C**) Clustering (*t*-SNE embeddings) of proteins based on their covariation among the F_6 progeny; highlighted are proteins up-regulated by the vineyard (blue) and clinical (orange) alleles of *IRA1*, *IRA2*, and *PDE2*, as indicated. (**D**) Schematic illustrating the principle of the pQTL sign test. (**E**) Mean fraction of coherent trans-pQTLs across all mapped associations (ordinate) as a function of trans-pQTL *P* values (abscissa). Actual mapping data are shown in purple; random expectation across all trans-pQTLs, regardless of protein target, is shown in gray; *P* values by binomial test. (**F**) Scatter plot illustrating pQTL alleles most strongly enriched in the fermentation-associated niche, showing the relative enrichment of the minor allele (abscissa) and the Bonferroni-corrected Fisher's exact test *q* value (ordinate).

nearly threefold depending on the genotype at the hotspot loci and a cis-acting SNP at the *MCR1* locus (Fig. 3B). To visualize these concerted effects, we generated a *t*-distributed stochastic neighbor embedding (*t*-SNE) of the correlations in protein abundance. Proteins that were up-regulated in the clinical or vineyard parent formed pronounced clusters, and similar sets of proteins were regulated by each Ras–cAMP-dependent protein kinase (PKA) hotspot (Fig. 3C). Consistent with these variants controlling downstream transcriptional activation (table S1), our genetic mapping results agreed well with the transcriptomic effects of *IRA1*, *IRA2*, and *PDE2* deletions (fig. S3A) (*35*). This key signaling axis has previously been implicated in global gene expression evolution within and between yeast species (*36*).

Many pQTL variants were common in natural yeast populations: 52% occurred at a frequency of greater than 10%, which we considered high frequency (*19*) (fig. S3B). Strains bearing the $IRA1^{RM}/IRA2^{RM}$ allele combination, for instance, were isolated from several similar ecological niches (*19*), which led us to investigate the proteomic consequences of the Ras-PKA hotspots across these backgrounds (*30*). Our atlas accurately forecasted the effects of these genotypes: Protein levels in strains with $IRA1^{RM}/IRA2^{RM}$ and $IRA1^{YJM}/IRA2^{YJM}$ alleles agreed well with our predictions (fig. S3C). Thus, these trans-regulatory effects were highly penetrant across other genetic backgrounds, despite wild strains harboring hundreds of thousands of other variants.

Directional selection on protein levels

The convergence of these hotspots suggested that selection might have driven polygenic adaptation through these variants, with one set of niches favoring higher expression of the RM–up-regulated module and another the YJM–up-regulated module. We formalized this hypothesis in a variation on Orr's sign test (*37*), in which we calculated the fraction of pQTLs controlling a protein that acted in the same direction and compared this statistic with the extent of coherence expected by chance (Fig. 3D). The effects of pQTLs were highly coherent ($P < 10^{-250}$ for pQTL-pQTL pairs with $P < 10^{-10}$), and this coherence was pronounced across a range of pQTL *P* value thresholds (Fig. 3E). The trends that we observed were driven by both RM-higher and YJM-higher coherent pQTL-pQTL pairs (fig. S3D), and the test was robust to the choice of proteins considered (fig. S3E). These data indicate that the RM and YJM parental backgrounds have undergone directional selection on the expression of many proteins, driven by multiple variants controlling the same regulatory modules.

We next tested whether selection had enriched these alleles in particular ecological niches (*19*). The *IRA2* pQTL allele was enriched among strains from fermentative environments ($q < 10^{-6}$) (fig. S3F), and many other pQTL alleles showed evidence of enrichment: 73 were enriched among fermentation strains, as were 24 alleles among human-associated isolates ($q < 10^{-2}$) (Fig. 3F and fig. S3G). Alleles of *RSF2* (respiration factor 2; $q < 10^{-10}$) and *PSE1* (protein secretion enhancer 1; $q < 10^{-9}$), for example, were enriched in the fermentation and human-associated niches, respectively (fig. S3, H and I). Altogether, evidence of stabilizing and directional selection, together with niche-specific enrichments, suggest that many proteins and pQTLs that we investigated are ecologically relevant.

Coding variation driving protein abundance in cis and trans

Protein abundance can be controlled by coding (protein-altering, nonsynonymous) or noncoding (regulatory, and also potentially synonymous) variants in cis or in trans (Fig. 4A). Both often affected levels in cis: Just under half of the cis-acting pQTNs that we identified altered protein-coding sequences, and coding and noncoding variants had similar effect sizes (Fig. 4B). The impact of missense variants in cis was consistent with a destabilization-driven mechanism: All seven cis-acting missense pQTNs predicted by FoldX (*38*) to destabilize their encoded proteins by more than 1 kcal/mol decreased protein abundance (Fig. 4C). Protein-altering trans-pQTNs, however, exerted much larger effects on their targets compared with noncoding trans-acting variants (Fig. 4D). $Ira2^{Asn201Ser}$, for instance, was identified in our map to strongly affect the abundance of Mcr1 (Fig. 4E). To confirm that this variant was causally responsible, we introduced the variant in the vineyard strain and observed a pronounced decrease in Mcr1 levels ($P < 0.001$) (Fig. 4F).

This led us to speculate that coding trans pQTNs—which perturb the protein products of the genes in which they arise—might help us understand the biochemical features of causal variants. We first used the BLOSUM62 metric (*39*) to assess conservation of missense trans pQTNs as compared with all other segregating missense variants. Unexpectedly, missense pQTNs scored as biochemically less disruptive compared with the control variants ($P < 10^{-9}$) (Fig. 4G), which suggests that knowledge of the reference and alternate amino acid residues alone was insufficient to predict functional outcomes. With this in mind,

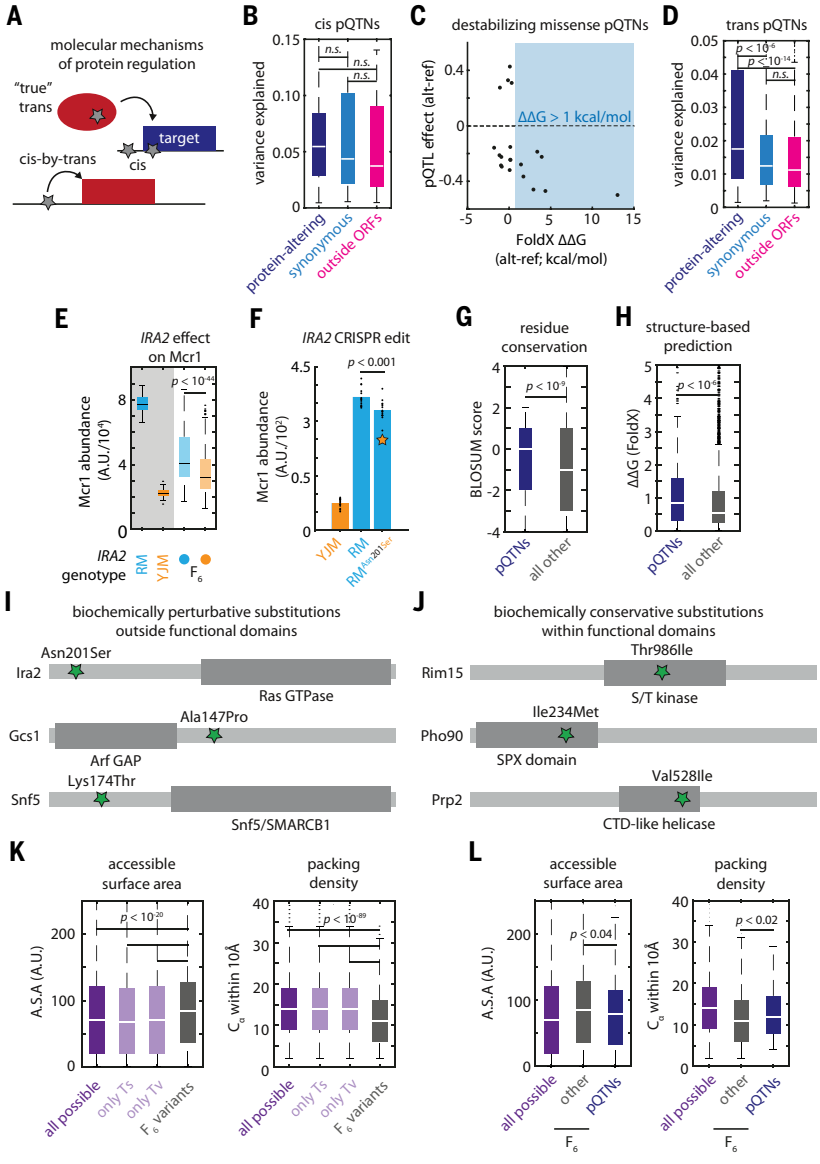


Fig. 4. Biochemical constraints revealed by proteomic mapping. (**A**) Schematic illustrating possible molecular mechanisms of cis and trans regulation. (**B**) Effect size of protein-altering, synonymous, and regulatory cis-pQTNs, as indicated. Boxes show median and upper and lower quartiles; whiskers show 1.5 times the interquartile range. (**C**) pQTL effect on protein levels (alternative versus reference allele; ordinate) as a function of predicted variant effect from FoldX (abscissa). (**D**) Effect size of protein-altering, synonymous, and regulatory trans-pQTNs, as indicated. Boxes show median and upper and lower quartiles; whiskers show 1.5 times the interquartile range. *P* values by two-sided *t* test. (**E**) Predicted effect from genetic mapping of the *IRA2*^{Asn201Ser} missense variant on Mcr1 levels. *P* value by *F* test. (**F**) CRISPR reconstruction and mass spectrometry to validate the effect of the *IRA2*^{Asn201Ser} variant on Mcr1 levels. $n = 15$; *P* value by two-sided *t* test. (**G** and **H**) BLOSUM62 (G) and FoldX scores (H) for missense trans-pQTNs (blue) as compared with all other segregating missense variants (gray). Boxes show median and upper and lower quartiles; whiskers show 1.5 times the interquartile range. *P* values by Mann-Whitney *U* test. (**I** and **J**) Illustrative conservative pQTN substitutions (I) and perturbative pQTN substitutions (J) with functional domains of the mutated proteins indicated. (**K**) Solvent-accessible surface area and number of C_α within 10 Å for all possible missense SNPs (purple; also shown are subsets resulting from transitions and transversions) and all missense variants segregating in the F_6 mapping panel (gray). (**L**) As in (K) for all possible missense SNPs (purple), missense pQTNs identified in this study (blue), and all other missense variants segregating in the F_6 mapping panel (gray). *P* values by Mann-Whitney *U* test.

we used FoldX predictions—which incorporate protein structures—to score pQTNs and control variants (*38*). In this case, trans pQTNs were more disruptive to predicted protein stability than other segregating missense SNPs (median ΔΔG ~ 0.83 versus 0.54 kcal/mol; $P < 10^{-6}$) (Fig. 4H).

This suggested that local structural context was important. Consistent with this idea, biochemically perturbative missense trans-pQTNs often occurred outside the core functional domains of proteins: Ira2^{Asn201Ser} (356 targets) lay outside of the Rho guanosine triphosphatase (GTPase) domain; Gcs1^{Ala147Pro} (50 targets) outside of the ArfGAP catalytic domain; and Snf5^{Lys174Thr} (37 targets) in a disordered region outside of the conserved SNF5/SMARCB1 domain (Fig. 4I). The opposite was true for more biochemically conservative substitutions: Rim15^{Thr986Ile} (36 targets) lay in the kinase domain; Pho90^{Ile234Met} (31 targets) in the SPX domain; and Prp2^{Val528Ile} (24 targets) in the helicase domain (Fig. 4J). We also noted that Ura5^{Gly73Val}, which controlled 79 targets, lay in the core phosphoribosyltransferase domain—this may account for its strong and widespread effects. Thus, trans-regulatory effects depended on the local protein environment, emerging both from modest biochemical perturbations to core functional domains and more severe alterations outside of these regions.

We hypothesized that two parameters might capture local protein structure: (i) a residue's solvent-accessible surface area and (ii) the number of other alpha-carbon atoms within 10 Å (packing density) (*40*). Exploiting AlphaFold2-predicted backbone structures (*41*), we calculated these statistics for every residue in the proteome. We first compared missense variants in our cross with all possible missense SNPs that could arise. The variants present in the progeny were 20% more solvent exposed and had a 21% lower local packing density ($P < 10^{-20}$, $P < 10^{-90}$; invariant to transitions versus transversions) (Fig. 4K and fig. S4A). Nevertheless, among the fixed variants, both metrics distinguished missense pQTNs from other segregating missense variants: pQTNs were 6% more buried and occurred in 9% more densely packed regions ($P < 0.04$; $P < 0.02$) (Fig. 4L). These enrichments arose despite the wide range of biochemical contexts in which the variants occurred. Collectively, these data illustrate how nucleotide-resolution genotype-to-molecule maps can reveal both predictable and unexpected biochemical mechanisms changing protein abundance and, in turn, explain the prevalence of natural variants.

Protein covariation reveals foundational proteome architecture

Precise deletion and knockdown experiments yield rich information on functional connectivity (*42*–*44*) but remain challenging in nonmodel organisms and for essential genes. Protein covariation analysis is a powerful alternative strategy (*45*). We therefore calculated the correlations in protein abundance across our mapping cohort, noting many signals that reflected known metabolic functionality. For instance, levels of the glycolytic hexokinase Hxk2 were strongly anticorrelated with its paralog Hxk1 and the hexokinase Glk1 (fig. S5A). Both Hxk1 and Glk1 are repressed by Hxk2 under low glucose concentrations (*46*), and Hxk1 and Glk1 levels were tightly correlated, as was Emi2, a paralog

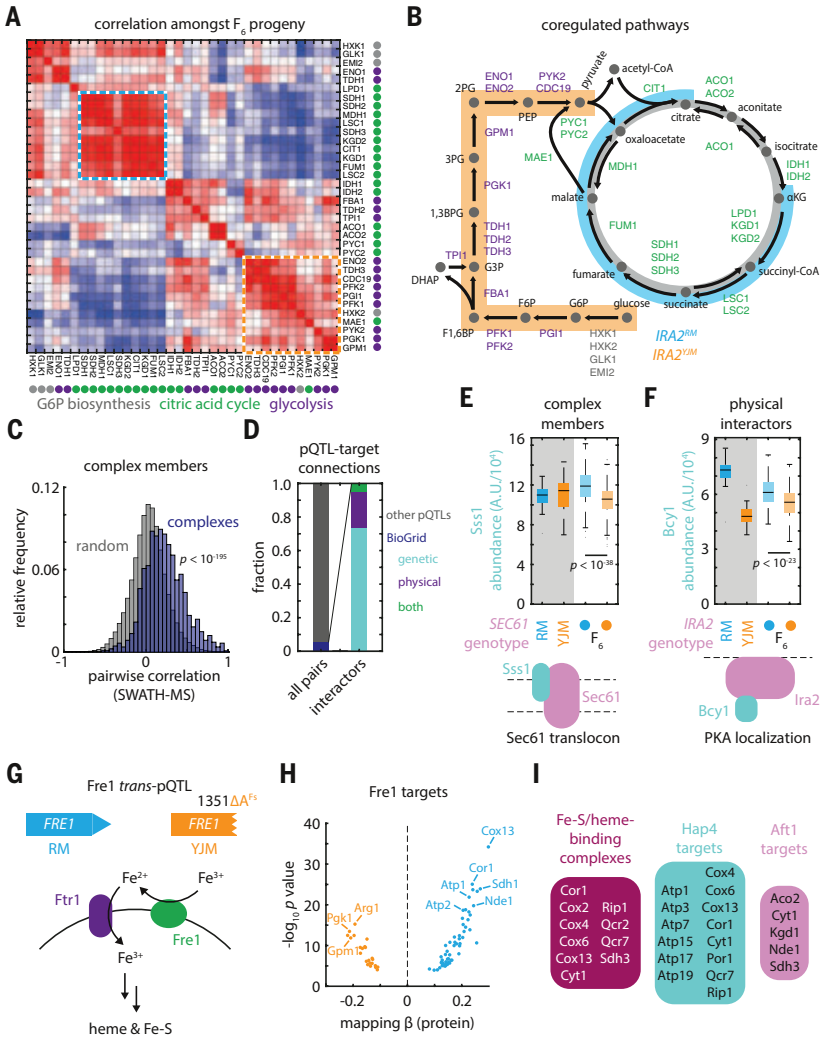


Fig. 5. pQTLs reveal molecular and functional connectivity. (**A**) Heatmap of pairwise protein abundance correlations in F_6 progeny among enzymes of glycolysis (purple) and citric acid cycle (green). (**B**) Schematic of metabolites and enzymes from (A), with metabolites highlighted in blue and orange if an enzyme catalyzing a reaction involving that metabolite is up-regulated by the *IRA2*^{RM} or *IRA2*^{YJM} allele, respectively. (**C**) Pairwise protein abundance correlations between complex members (blue) as compared with all possible pairs of measured proteins (gray). *P* value by Mann-Whitney *U* test. (**D**) Cumulative frequencies of pQTL-target connections reflecting BioGRID interactions (blue) and all other pQTL-target pairs (gray) (left) and, among BioGRID interactions, those annotated as genetic (blue), physical (purple), or both genetic and physical (green) (right). (**E**) Sss1 abundance in vineyard and clinical parents and in F_6 progeny with *SEC61* genotypes, as indicated. (**F**) Bcy1 abundance in vineyard and clinical parents and in F_6 progeny with *IRA2* genotypes, as indicated. (**G**) Schematic of the role of Fre1 in iron reduction and uptake at the plasma membrane (*88*). (**H**) Volcano plot illustrating predicted effects on abundance from genetic mapping (abscissa) and forward selection *F* test *P* value (ordinate) for the *FRE1* trans-pQTL. (**I**) Downstream *FRE1* pQTL targets that bind iron or heme or that are targets of Hap4 or Aft1, as indicated.

of Glk1 (*47*). These relationships reflected the broad tradeoff between fermentation and respiration, and these regulons formed pronounced covarying clusters (Fig. 5A) that were coherently controlled by the *IRA2* alleles described above (Fig. 5B). This covariation structure was much more evident among the progeny than in biological replicates of the parents (fig. S5B).

We then investigated whether covariation in the progeny was representative of covariation in a species-wide survey (*30*) and within ~5000 viable gene deletion strains (*44*). The architecture of covariation was conserved, with correlation coefficients agreeing well between these independent experiments [$r = 0.56$ for F_6 progeny versus 1002 Yeast Genomes (*19*); 0.52 for F_6 progeny versus precise deletions]. Thus, the modest genetic divergence harbored by our mapping panel drives proteome diversity mirroring that caused by a much broader range of genetic variation.

Systems biology of variant-protein associations

To probe the physical and genetic connections embedded in our data, we assessed whether members of the same macromolecular complex (*48*) covaried in their abundance. The mean correlation between complex members was 0.224, as compared with 0.038 for all protein-protein pairs ($P < 10^{-195}$) (Fig. 5C). These data resolved the fine details of complexes and metabolic pathways: The F1 core structural subunits of the mitochondrial adenosine 5′-triphosphate (ATP) synthase were highly correlated (fig. S5C), and enzymes with functional overlaps or that physically associate (e.g., Idh1/Idh2, Kgd1/Kgd2) covaried tightly (fig. S5D). The STRING database coexpression metric, which aggregates mRNA and protein data (*49*), was also significantly correlated with protein covariation in our measurements ($P < 10^{-250}$) (fig. S5E), as was the genetic interaction similarity score from the Cell Map ($P < 10^{-191}$) (*50*) (fig. S5F), which measures functional relatedness based on genetic epistasis analysis.

Reasoning that covariation can be caused by physical or genetic interactions between proteins, we searched our atlas for connections between complex subunits [ComplexEBI (*51*)] and genetic or protein-protein interactors [BioGRID (*52*)] (Fig. 5D). Only one trans-pQTL connected two complex members: Sss1 and Sec61 participate in the conserved Sec61-SecYEG translocon, and Sss1 plays a key role in the stability of Sec61 (Fig. 5E) (*53*). A further 354 (~5.6%) trans-pQTL–target pairs connected known interactors (Fig. 5D). Of these, 74.0% were genetic interactors, 20.9% physical, and 5.1% both genetic and physical (consistent with the overall proportions of genetic and physical interactions; binomial $P = 0.42$, $P = 0.92$). *IRA2*, for instance, controlled the abundance of the PKA regulatory subunit Bcy1; these proteins physically interact in the Ras-PKA signaling complex (Fig. 5F) (*54*). *PDE2* controlled an array of its genetic interactors, including Cox6, Cox12, Cyt1, Qcr2, and Qcr7, all of which are involved in respiration—a process tightly linked to Pde2-mediated cAMP signaling (*55*). Thus, trans-pQTL relationships reflect known functional associations between proteins and describe a rich regulatory network not captured by documented physical and genetic interactions.

Functionalizing the proteome reveals cryptic natural regulatory activity

A surprising example of these physiological networks arose at *FRE1*, which encodes a ferric reductase important in iron and copper uptake and metabolism (Fig. 5G) (*56*). This hotspot, attributable to a frameshift in *FRE1* in the clinical strain background, controlled 79 proteins (56 up-regulated by the vineyard allele and 23 by the clinical allele) (Fig. 5H). Only two regulated genes exhibited genetic interactions with *FRE1*, and none of the proteins were physical interactors. Yet, many of the targets and associated complexes contain heme or iron-sulfur clusters (e.g., Cor1, Cox2/4/6/13, Cyt1, Qcr2/7, Rip1, and Sdh3) or were otherwise involved in respiration (e.g., Atp1/2/3/5/7/15/17/19, Cit1, Fum1, Kgd1/2, Mdh1, and Sdh1/3) (Fig. 5I). Iron metabolism and mitochondrial function are intimately linked (*57*).

The down-regulated set of proteins was highly enriched ($P < 10^{-19}$) (*58*) for targets of the heme activator proteins (Hap) 2/3/4/5 transcription factor complex, which responds to intracellular heme levels (*59*, *60*). Conversely, proteins up-regulated in the *FRE1* loss-of-function background were enriched for targets of Nhp6 ($P < 10^{-4}$), which acts with Aft1 (activator of ferrous transport) to up-regulate iron transport (*61*). Thus, impaired heme and iron-sulfur cluster synthesis—due to loss of Fre1 activity—led to widespread down-regulation of enzyme components that depend on iron and an up-regulation of compensatory transport machinery. The effects of this natural allele were reminiscent of coherent functional responses induced by deletions of the *GAL* genes (*62*). Their ubiquity in our atlas suggests that nature exploits these underappreciated regulatory relationships—some may even be mediated directly by cofactors or metabolites.

Prioritizing causal variants at drug-resistance loci

Variants that affect molecular phenotypes are thought to be more likely to underlie organismal traits, and a promising application of variant-to-molecule maps is prioritizing causal variants underlying genetic associations (*8*). To assess this heuristic, we analyzed a complementary high-resolution genotype-to-phenotype map (*32*) across an array of carbon sources, antifungal drugs, mutagens, and toxic metals (data S6). We noted that the RM allele of a regulatory variant, *ERG11*^{T122014C}, was predicted to up-regulate Erg11 protein, the mechanistic target of azole antifungals in *S. cerevisiae* (*63*), and to reduce sensitivity to azoles. Yet phenotypic mapping also implicated a missense variant, Erg11^{Lys433Asn}, as important for fluconazole sensitivity (Fig. 6A and fig. S6A). Upon reconstruction in the sensitive background, mass spectrometry confirmed that the upstream regulatory variant controlled protein level, as predicted (Fig. 6B). The neighboring missense variant did not affect abundance—instead likely affecting protein folding or catalysis. Both variants, however, reduced azole sensitivity in an additive fashion ($P < 0.05$) (Fig. 6C). This example and others (*21*, *34*, *64*) emphasize that the architecture of a causal locus can be complex and that noncoding variation cannot be neglected in drug resistance (*65*).

Integrated proteogenomic mapping also resolved the fitness effect of the noncoding cis-pQTN *NCP1*$^{A\text{-}177T}$ (Fig. 6D). Ncp1 associates with Erg11, and phenotypic mapping suggested that a causal locus for fluconazole sensitivity was present near *NCP1*, but we failed to implicate a QTN (Fig. 6E). Yet, when we reconstructed the putative causal variant and subjected the gene-edited strain to azole treatment, the higher-expressing *NCP1*$^{-177T}$ allele decreased azole sensitivity ($P < 10^{-4}$) (Fig. 6F). The *NCP1* variant did not affect growth in the absence of the drug (fig. S6B) nor significantly increase Erg11 levels (fig. S6C), which indicates that the effect on azole sensitivity was related to Ncp1 abundance. These case studies illustrate how proteogenomic mapping can inform detailed hypotheses regarding the function of natural variants.

Molecular mapping pinpoints a hidden causal variant

Trans-regulatory variants are often thought to have widespread effects on phenotype by altering the expression of many downstream targets (*15*). Yet, despite the large number of proteins regulated by the *IRA2* hotspot, QTN mapping revealed few variant-phenotype associations at the locus (Fig. 6, G and H). To understand this discrepancy, we first confirmed that the trans-pQTL hotspot reflected a change in Ira2 and not a linked variant. Comparing our mapping results with an *IRA2* deletion allele (*44*) strongly suggested that the hotspot was attributable to loss of Ira2 function: The consequences of the YJM allele of *IRA2* were highly concordant with the deletion ($r = -0.81$; $P < 10^{-80}$) (fig. S6D). Much weaker correlations were observed with deletions of the neighboring *ATG19* and *REX4* genes ($r = -0.08$ and $r = 0.30$). We next tested whether the Ira2^{Asn201Ser} polymorphism (fig. S6E) was alone responsible for the predicted effects. Reconstructing the variant had widespread effects that agreed with our mapping results: Nearly all of the proteomic effects in the clinical strain (YJM) background (94%; $P < 10^{-19}$) and the majority in the vineyard

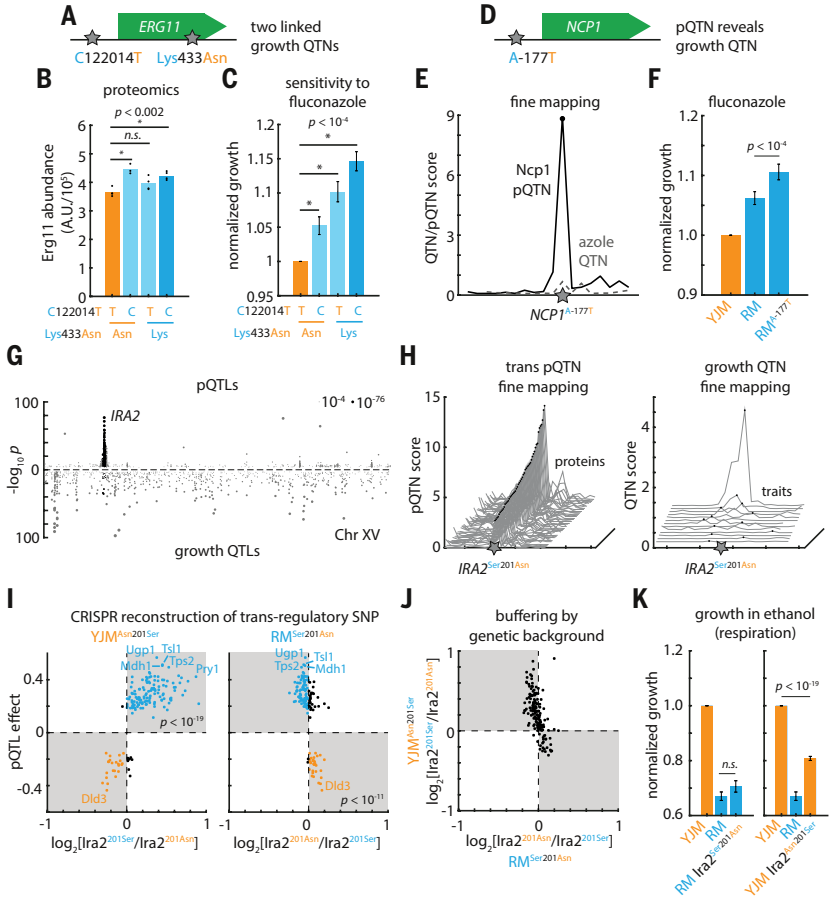


Fig. 6. Cryptic fitness effects embedded in the variant-to-protein map. (**A**) Schematic of *ERG11*^{T1220124C} and Erg11^{Asn433Lys} variants. (**B**) Mass spectrometry of Erg11 protein levels in clinical (YJM) WT and CRISPR-edited YJM *ERG11*^{T1220124C}, YJM Erg11^{Asn433Lys}, and YJM *ERG11*^{T1220124C} Erg11^{Asn433Lys} mutant strains. $n = 4$; *P* values by Student's *t* test. (**C**) Growth of clinical (YJM) WT and CRISPR-edited YJM *ERG11*^{T1220124C}, YJM Erg11^{Asn433Lys}, and YJM *ERG11*^{T1220124C} Erg11^{Asn433Lys} mutant strains in fluconazole. $n = 96$; *P* values by Student's *t* test. (**D**) Schematic of *NCP1*$^{A\text{-}177T}$ variant. (**E**) Fine-mapping of Ncp1 cis-pQTN as compared with fine-mapping of the azole-sensitivity QTL in the vicinity of *NCP1*. (**F**) Growth of clinical (YJM), vineyard (RM), and CRISPR-edited RM *NCP1*$^{A\text{-}177T}$ mutant strains in fluconazole. $n = 96$; *P* value by Student's *t* test. (**G**) Miami plot of pQTLs (top) and growth QTLs (bottom) on chromosome XV. *IRA2* pQTLs and QTLs are highlighted in black. (**H**) pQTN fine-mapping scores for the top 50 *IRA2*-target associations (left) and QTN fine-mapping scores for *IRA2* growth QTL associations (right). (**I**) Predicted *IRA2* pQTN effects from genetic mapping (this study; ordinate) as compared with measured effects of CRISPR-edited YJM Ira2^{Asn210Ser} (left) and RM Ira2^{Ser201Asn} mutants (right). Mass spectrometry–estimated abundances normalized to WT in each case. (**J**) Measured effects of CRISPR-edited YJM Ira2^{Asn210Ser} (ordinate) and RM Ira2^{Ser201Asn} (abscissa) mutants. (**K**) Growth of clinical (YJM), vineyard (RM), and CRISPR-edited RM Ira2^{Ser201Asn} mutant (left) and YJM Ira2^{Asn210Ser} mutant (right) in ethanol. $n = 96$; *P* values by Student's *t* test.

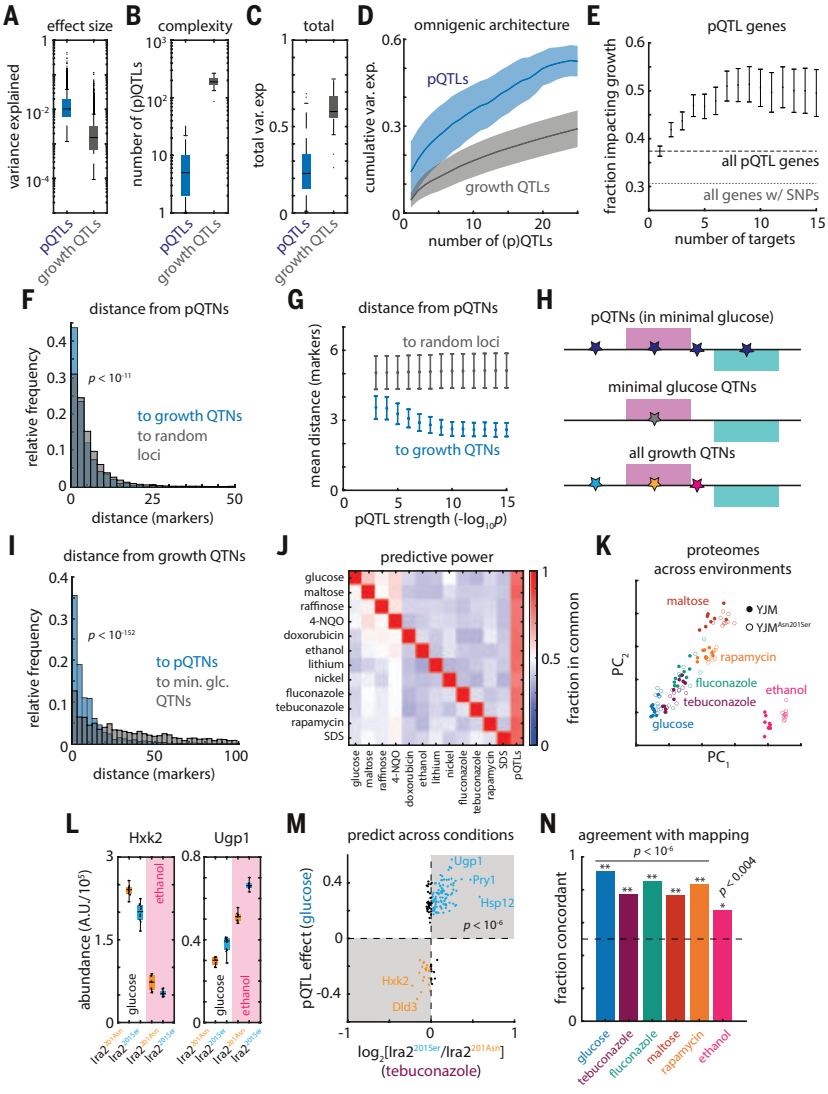


Fig. 7. Proteomes identify causal variants underlying quantitative traits. (**A** to **C**) Effect size (variance explained) (A), total number of (p)QTLs (B), and total variance explained for pQTLs (blue) and growth QTLs (gray) (C). (**D**) Cumulative variance explained by pQTLs (blue) and growth QTLs (gray) as a function of the number of (p)QTLs considered. (**E**) Fraction of pQTL genes having at least one associated growth QTN (ordinate) as a function of number of targets (abscissa). Also shown are this statistic for all pQTL genes (dashed black line) and all genes with polymorphisms in our panel (gray dashed line). Shown are means ± SEMs. (**F**) Relative frequency histogram of the distance from pQTNs to the nearest phenotypic QTN (blue) and (gray) randomly selected sets of markers of the same size. *P* value by Kolmogorov–Smirnov test between real and permuted data. (**G**) As in (F), as a function of pQTN strength (maximum − $\log_{10} P$; abscissa). (**H**) Schematic of pQTNs (blue), growth QTNs in minimal glucose medium (no stress; gray), and stress-responsive growth QTNs (various colors). (**I**) As in (F), but illustrating the distance from stress-responsive growth QTNs to (blue) the nearest pQTN and (gray) growth QTNs discovered in minimal glucose (no stress). *P* value by Kolmogorov–Smirnov test. (**J**) Heatmap of the relative fraction of QTLs in common between environments (ordinate) and environments and pQTLs (abscissa), as indicated. See also fig. S7. (**K**) PCA of YJM975 WT and Ira2^{Asn201Ser} CRISPR-edited strains in glucose, tebuconazole, fluconazole, rapamycin, maltose, and ethanol, as indicated. (**L**) Abundance of Hxk2 (left) and Ugp1 (right) in YJM975 WT and Ira2^{Asn201Ser} CRISPR-edited strains as indicated in glucose (white) or ethanol (pink). (**M**) Predicted *IRA2* pQTN effects from genetic mapping (this study; ordinate) as compared with measured effects of CRISPR-edited YJM Ira2^{Asn210Ser} in tebuconazole. Mass spectrometry–estimated abundances normalized to WT. (**N**) Fraction of protein abundance effects of YJM Ira2^{Asn210Ser} that agree with pQTL mapping in conditions as indicated. *P* values by Fisher's exact test; dashed line indicates one-half.

(RM) background (78%; $P < 10^{-11}$) agreed with our predictions (Fig. 6I). Thus, Ira2^{Asn201Ser} is a true pleiotropic trans-pQTN.

Although highly sensitive, our mapping approaches [like most, with a handful of exceptions (*29*)] assume a linear model of phenotype. We therefore entertained the possibility that although the regulatory effects of the Ira2^{Asn201Ser} variant were as predicted, its phenotypic consequences were modified by genetic background. Its quantitative consequences were much more pronounced in the YJM background than in its RM counterpart, despite widespread directional concordance (Fig. 6J). Growing genome-edited strains on various carbon sources revealed notable fitness effects that were both strain- and condition-specific: The vineyard allele was highly deleterious to growth on ethanol, whereas the clinical variant had a minimal fitness effect (Fig. 6K). Conversely, the clinical variant modestly affected fermentative growth, whereas the vineyard variant had no significant effect (fig. S6F). These asymmetric phenotypes were likely obscured in statistical mapping owing to the segregation of suppressing alleles responsible for the strong background effect. Thus, molecular mapping can unmask hidden fitness effects of highly pleiotropic regulatory hotspots and forecast their impact under conditions where these effects emerge.

Forecasting variant effects from molecular phenotypes

In concordance with an omnigenic model in which several core genes contribute to phenotypes (*66*), stress-response traits were more complex than protein levels, and stress-response QTLs exhibited smaller median effect sizes ($P < 10^{-16}$) (Fig. 7A). Even though we identified fewer pQTLs per protein than QTLs per growth trait (Fig. 7B), these loci nonetheless explained a substantial fraction of the total variance (22.8% versus 58.7% median total variance explained) (Fig. 7C). Thus, on a per-(p) QTL basis, the cumulative variance explained was substantially higher for protein abundance as compared with growth traits [$P < 10^{-21}$ for the first 10 (p)QTLs] (Fig. 7D). Moreover, consistent with a preferential role for trans-hotspots in affecting phenotype, stronger pQTL genes had more targets (fig. S7A) and were more likely to affect growth (Fig. 7E).

The proteomic measurements that determined our variant-to-protein map were made in the absence of stress: The cis-regulatory variant at *ERG11* (Fig. 6A) was identified as a pQTN in media without azoles but potently regulated azole sensitivity, and the proteomic impact of the *IRA2* hotspot was readily apparent in minimal glucose medium, even though its fitness consequences emerged in respiratory conditions. Moreover, stress-response QTLs were highly condition-specific: We saw little decline in the identification of QTLs as we considered additional environments (fig. S7B). These observations suggested that a latent proteomic layer could forecast phenotypic outcomes.

Overall, our genome-to-proteome map contained rich information on causality: pQTNs were much closer to stress-response QTNs than expected by chance ($P < 10^{-11}$) (Fig. 7F), with stronger pQTNs progressively more so (Fig. 7G and fig. S7C). Moreover, the effect sizes of pQTNs and stress-response QTNs were correlated ($r = 0.29$; $P < 10^{-16}$) (fig. S7D). We therefore hypothesized

that growth phenotypes reflected the combined effects of underlying variants controlling protein levels (Fig. 7H). Across all the environments that we surveyed, pQTNs discovered in minimal glucose medium were much more predictive of causality under stress ($P < 10^{-152}$) compared with growth QTNs from the minimal glucose condition (Fig. 7I). Thus, pQTL mapping is a rich source of causal variants that are candidates to influence growth under stress. Because QTL mapping in minimal glucose medium likely identified essentially all major contributors to growth under this condition, pQTL mapping holds greater latent information on a fundamentally broader set of candidate loci.

Rapamycin and tebuconazole resistance, for instance, shared few large-effect QTLs in common (e.g., *HPF1*) and were predominantly driven by distinct loci (e.g., at *RICTOR/AVO3* and *ERG11*): Of the 663 causal loci identified in rapamycin, only 268 (40%) coincided with one of the 635 causal loci underlying tebuconazole resistance (fig. S7E). By contrast, pQTLs had much greater overlap, with 489 tebuconazole-resistance loci (77%) and 534 rapamycin-resistance loci (81%) coinciding with a pQTL. This was true in general: Across diverse environments we tested, an average of 78% of stress-resistance QTLs colocalized with a pQTL, in contrast to an average of only 48% of QTLs coinciding between stress conditions (Fig. 7J).

This suggested that molecular effects of genetic diversity preexisted in unstressed cells and emerged into cellular phenotypes under stress. To directly test whether pQTL effects persisted across environments, we measured proteomes of YJM975 wild-type (WT) and Ira2^{Asn201Ser} CRISPR-edited strains in glucose, tebuconazole, fluconazole, rapamycin, maltose, and ethanol. Principal components analysis (PCA) revealed clustering both by environment and strain identity (Fig. 7K) as stress caused pronounced proteomic changes in the WT strain: A total of 711 to 1544 were proteins differentially expressed, depending on the condition (representing 23 to 50% of proteins we detected) (fig. S7, F and G). Yet, despite this widespread remodeling, the effects of the *IRA2* variant on protein levels as detected in the standard growth condition were preserved, both in proteins up- and down-regulated relative to the mapping environment (Fig. 7L). We calculated the concordance of these changes with pQTL mapping across all conditions (Fig. 7M) and found that our genotype-protein map remained broadly predictive of proteomic outcomes ($P < 10^{-7}$; $P < 0.008$) (Fig. 7N). Thus, molecular mapping likely holds powerful promise in forecasting the functional consequences of mutations, even if the maps are charted before pathologies emerge.

Discussion

Because proteins link the DNA blueprint to physiology, mapping the effects of natural variants on the proteome is a promising bridge from genotype to phenotype. Yet attributing causality remains challenging. In this work, we integrate super-resolution genetic mapping with quantitative, high-precision proteomics to overcome these barriers and systematically connect natural genetic variation to proteomic diversity, in many cases with nucleotide resolution.

Although we do not quantify all proteins, we capture the most abundant fraction (which is enriched for essential genes and network hubs) particularly well, and our dataset spans a large fraction of the proteome on a molar basis (*44*). Additional functional relationships will likely be identified by mapping posttranslational modifications (*17*) and protein-protein interactions (*67*), and other molecular layers, such as metabolite levels and the position and role of proteins in metabolic networks (*68*), may further disentangle effects on protein stability versus activity.

We nonetheless achieved explanatory power comparable to the most complete genome-to-mRNA maps (*11*), with the advantage of resolution that often implicates single nucleotides rather than chromosomal regions. Our results suggest that limited concordance between eQTLs and pQTLs reported in prior studies might have been in part the consequence of limited statistical power (*31*, *69*). Nonetheless, the molecular effects of many regulatory mechanisms, including translation efficiency, protein stability, and turnover, do not manifest in the transcriptome. Consequently, many cis-pQTLs were evident only at the proteome level.

The functional divergence of the parental proteomes was driven by a large fraction of the variation between their genomes. Many of these alleles were common in wild populations, which suggests that such variants provide a rich vein of proteomic diversity. A sign test revealed that directional selection had reshaped the proteomes of the parents despite their relatively recent evolutionary divergence. Moreover, proteins expressed similarly in the parents often transgressed to produce more extreme levels in the offspring—a common property of mRNA abundance and organismal phenotypes (*9*, *10*, *70*) but more rarely reported for proteins (*36*). The meiotic reassortment of natural genetic diversity thus diversifies the proteome yet further by releasing cryptic variation. The frequency of transgression and niche-specific enrichments of pQTL alleles together suggest that the levels of many proteins affect fitness and are subject to selection. These and many prior observations (*71*) call into question the baseline assumption that most segregating genetic variation is functionally neutral and instead suggest that, from the proteomic perspective (*72*), many variants likely reflect an intricate interplay between stabilizing and directional selective pressures.

The resolution of our atlas provides a molecular view into the basis of trans regulation. Whereas cis-acting effects were balanced between coding and noncoding variants, coding variation had a privileged role in trans regulation of protein levels. This may be because coding variants can alter both protein function and abundance, whereas noncoding variants primarily affect the latter. Given that few genes are haploinsufficient, tolerance of small changes in the amount of a gene product may be a general property. Moreover, changes in transcript level are often buffered in the proteome (*30*).

The functional genetic architecture of budding yeast is more deeply characterized than that of perhaps any other organism. Yet, 94% of the pQTLs that we identified reflected physiological regulatory connections not captured by physical or genetic interactions. Inbred crossing thus represents a powerful strategy to dissect functional networks, particularly in organisms where systematic genetic modification remains intractable.

Previous efforts have noted that haplotypes driving trans-regulatory change often do not harbor a transcription factor or other canonical regulatory protein (*10*). Our data indicate that these effects often arise from the profound self-regulatory structure of metabolism: Many trans-regulatory variants that we discovered alter metabolic enzymes or transporters. The widespread dependence of important enzyme classes, including oxidoreductases and transferases, on iron and other cofactors highlight the far-reaching potential of this mechanism (*73*). Moreover, the full scope of metabolite-protein interactions is only beginning to be characterized (*74*), and these newfound functional connections may represent a previously unexplored class of targets for therapeutically modulating physiological regulation.

Beyond pinpointing causal variants underlying cellular traits, charting the genetic architecture of the proteome uncovered previously hidden relationships between genotype and phenotype. Proteomics revealed the potent functional impact of the Ira2^{Asn201Ser} variant, which was masked even in well-powered genotype-to-phenotype mapping. The regulatory effect of the polymorphism was buffered across all of its targets in the RM parent, implicating either a tightly linked suppressor variant, an epigenetic suppressor, or multiple suppressor alleles throughout the genome. Compensation mechanisms with these characteristics are not unusual, and in other genetic backgrounds, the same variant exhibits strong epistasis within the *IRA2* gene (*75*). Notably, cryptic effects like these do not manifest as "missing heritability" (*76*) but rather "hidden causality" because they are suppressed in most progeny. Our findings suggest that genotype-to-protein maps show the way to discover the largely uncharted impact of cryptic genetic variants.

Our findings establish that such maps also reveal a molecular foundation on which to predict the phenotypic effects of genetic variation. Many variants controlling resistance to stress were initially phenotypically silent, but their effects on the proteome were already evident and allowed us to identify variants that affected fitness in new environments. Thus, data from a single tissue or from serum likely hold molecular regulatory information to support inferences across contexts, and latent proteome diversity can likely forecast emerging phenotypic differences under stress. Integrating these data may overcome the difficulty of predicting phenotype across conditions using genomic data alone and allow us to nominate variants that are likely to cause disease even before pathologies develop.

Materials and methods

Materials availability

All strains and plasmids used in this study are available on request to D.F.J. (jarosz@stanford.edu). The F_6 haploid mapping panel is also available from the National Collection of Yeast Cultures (NCYC).

Data and code availability

All mass spectrometry proteomics data have been deposited to the ProteomeXchange Consortium through the PRIDE (*77*) partner repository with the dataset identifier PXD062635. All computer code and data required to reproduce our findings can be found on Zenodo (*78*). Custom genetic mapping and protein structure analysis code is also available on GitHub (https://github.com/cjakobson/pqtl-mapping). Analyses and plots for the figures can be reproduced by cloning the *pqtl-mapping* repository, downloading the contents of the *pqtl-mapping-dependencies* folder, and running *plotting_master_script.m* (see Zenodo repository).

Yeast strains and segregant library

S. cerevisiae strains for genetic mapping were generated and genotyped previously (*21*). Briefly, ~1000 F_6 progeny from a cross between RM11 and YJM975 were arrayed from single-colony isolates and subjected to whole-genome sequencing. To avoid confounding effects of segregating auxotrophic markers in our proteomics experiments, we selected ~850 strains from the original panel that were auxotrophic only for uracil (leucine auxotrophy also segregates). In addition to these progeny, we included at least three biological replicates of the RM11 (YDJ6649) and YJM975 (YDJ6635) haploid parental isolates in each 96-well plate of our measurement campaign. These haploid strains are auxotrophic only for uracil to match the F_6 segregant progeny. Also included were representative haploid wild isolates (22 strains in up to $n = 6$ replicates) from throughout the world, as cataloged in the SGRP collection (*26*). Strains were randomly allocated to plates and positions. The plate layouts and strain identifiers for the proteomics campaign can be found in data S1. A table of other yeast strains used in this study can be found in table S2.

1002 Yeast Genomes (*19*) isolates were sorted into eight broad ecotypes (baking, dairy, fermentation, human-associated, plant, soil, waste, and other) based on their isolation annotations. For example, fermentation-associated isolates included strains from wine conserved in amphora, fermenting grape must, and spontaneous grape fermentation (as well as those annotated simply as "wine"); and human-associated isolates included strains from clinical sputum, abscess on epididymis, and infected nail (as well as those annotated simply as "human").

Media and culture conditions

Unless otherwise noted, yeast were propagated in minimal glucose medium with uracil (20 g/liter glucose; 6.7 g/liter yeast nitrogen base; 20 mg/liter uracil; 20 g/liter agar as needed for solid medium). Samples for growth phenotyping were pregrown for 24 to 48 hours at 30°C on minimal glucose agar with uracil on Singer PlusPlates before replica pinning to growth conditions as indicated using a Singer ROTOR.

For proteomics, samples were spotted from 12 × 96-well cryo stocks to Singer PlusPlates with 40 ml agar minimal medium using a Singer ROTOR and grown for 48 hours at 30°C. Cells were then transferred with the Singer ROTOR to 96-well plates with 200 µl minimal medium and incubated for 16 hours. Then, 160 µl of each well of this preculture was transferred to 2 ml wells in a 96-deep-well plate with 1440 µl minimal medium and with one 2 mm borosilicate bead per well. Plates were sealed with a Breathe Easier sealing membrane (Sigma Aldrich) and incubated on four shakers (Heidolph Titramax 1000, 750 rpm, 30°C, 8 hours). All plates from all batches were grown together in the same incubator using the same batch of growth medium. After incubation, 1.4 ml were transferred to fresh 96-deep-well plates, and harvested by centrifugation (5 min, 4000*g*). The supernatant was discarded, plates sealed with adhesive aluminum foils, and the pellets stored frozen until further processing (−80°C). Subsequently, in each well, 1600 µl sterilized water was added to the ~200 µl culture remaining in original incubation plates, plates were quickly vortexed, and the optical density at 600 nm (OD_{600}) was determined using a multiwell plate reader (SparkStacker, Tecan). For proteomes of reconstructed strains, samples were prepared in a similar fashion, containing strains YDJ6635, YDJ8281, YDJ8436, and YDJ8437 (set 1); YDJ6635, YDJ6649, YDJ8524, YDJ8525, and YDJ8526 (set 2); and YDJ6635, YDJ6649, YDJ8527, YDJ8528, YDJ8529, and YDJ8578 (set 3).

For proteomes of YJM975 and YJM975 *IRA2*$^{A>G}$ challenged with rapamycin (2000 nM), fluconazole (100 µg/ml), tebuconazole (10 µg/ml), strains were initially prepared as above, and after 16 hour of preculturing on minimal medium, 160 µl cell suspension was transferred to 96-deep-well plates with 1440 µl minimal medium containing respective drugs, and were then again incubated and processed as described above. As a control, growth on minimal medium with glucose and without drug was included. For growth on maltose, the same protocol was applied, but the 16-hour preculture was prepared in minimal medium with 2% maltose, and 320 µl were transferred to 1280 µl minimal medium with 2% maltose. For growth on ethanol, colonies obtained as described above from agar minimal glucose medium were used to inoculate 15 ml glass round bottom tubes containing 3.5 ml minimal medium with 2% ethanol at a OD_{600} of 0.15 to 0.2, incubated at 30°C for 48 hours of shaking at 300 rpm (1-cm radius) on a neoLabLine DOS-10L orbital shaker, were transferred to deep-well plates, and were harvested and processed as described for all other samples.

Proteomics sample preparation

Frozen pellets were thawed on ice. Segregant samples were processed in three batches with 4 × 96-well plates each, whereas reconstruction strains were prepared in 96-well plates in their respective sampling batches. In all cases, the plates constituting a batch were grown, harvested, and processed for proteomics together. To each well/plate, glass beads (acid washed, 100) were dispensed using a prefilled custom-made plate releasing ~100 mg beads per well, followed by centrifugation (0.5 min, 4°C, 1000*g*). Then, 200 µl of freshly prepared 7 M urea with 0.1 M ammonium bicarbonate (ABC) was added to each well. Plates were sealed using Cap Mats and cells were lysed by bead milling with a Genogrinder (MiniG, SPEX) for 5 min at 1500 rpm, followed by quick centrifugation (1 min, 4°C, 3000*g*). Samples were then processed as previously described (*30*) on a Biomek i7 pipetting robot. To this end, 20 µl 5 mM dithiothreitol (DTT) was added to each well, mixed, and shortly centrifuged and incubated for 1 hour at 30°C. Sample was left at room temperature for 15 min, and 20 µl 5 mM IAA was added, mixed, and briefly centrifuged, and incubated for 30 min in the dark at room temperature. Reduced and alkylated samples were then diluted with 1000 µl 0.1 M ABC, mixed and centrifuged briefly, and 500 µl diluted lysate was transferred to a plate containing 2 µg trypsin/LysC per well, and incubated for 17 hours at 37°C. The digest was stopped by addition of 25 µl 20% formic acid and purified using solid-phase extraction in 96-well format. Plates were conditioned

with 200 µl methanol (centrifuged at 50*g*), washed twice 200 µl with 50% acetonitrile/water (centrifuged at 150*g*), equilibrated twice with 0.1% formic acid in water (centrifuged at 150*g*, 250*g*). 500 µl per well was loaded (centrifuged at 250*g*) and washed four times with 200 µl 0.1% formic acid in water (centrifuged at 250*g*), followed by another centrifugation step at 250*g*. Peptides were eluted in three steps with 110 µl each, 50% acetonitrile/water, and dried to completeness in a vacuum concentrator. Samples were then redissolved in 40 µl 0.1% formic acid, and ready for analysis.

Liquid chromatography–mass spectrometry

For proteomics, samples were injected in randomized order within acquisition batches, and after 10 samples, a quality control sample consisting of a pool of all samples was injected. Digested peptides were separated on a high-flow chromatographic gradient and recorded by mass spectrometry using scanning SWATH (*22*) on an Agilent Infinity II HPLC combined with a SCIEX 6600 TripleTOF platform. Five micrograms of sample were injected onto a reverse phase HPLC column (Luna Omega 1.6 µm C18 100A, 30 × 2.1 mm, Phenomenex) and resolved by gradient elution at column temperature of 30°C with 0.1% formic acid in water (Solvent A) and 0.1% formic acid in acetonitrile (Solvent B). All solvents were of LC-MS grade. The gradient separation was at a flow rate of 0. 8 ml/min flow with the steps 0 min (1% B), 0.1 min (5% B), 2.65 min (32% B), 3 min (40% B), followed by wash steps with 1.2 ml/min flow at 3.5 min (80% B) to 3.7 min (80% B), and column equilibration with 1 ml/min flow from 3.8 min (1% B) to 4.8 min (1% B). For mass spectrometry analysis, the scanning SWATH precursor isolation window was 10 m/z, the bin size was set to 20% of the window size, the cycle time was 0.41 s, the precursor range was set to 400 to 900 m/z, the fragment range to 100 to 1500 m/z as previously described in Messner *et al*. (*22*). A Sciex IonDrive TurboV source was used with ion source gas 1 (nebulizer gas), ion source gas 2 (heater gas) and curtain gas set to 50 psi, 40 psi, and 35 psi, respectively. The source temperature and ion spray voltage were set to 450°C and 5500 V, respectively.

For validation of reconstructed strains from set 3, proteome samples were analyzed on a ZenoTOF 7600 system mass spectrometer (SCIEX), coupled to a 1290 Infinity II LC (Agilent). Before MS analysis, peptides were chromatographically separated on a Phenomenex Luna Omega column (1.6 µm C18 100A, 30 × 2.1 mm) heated to 50°C, using a flow rate of 0.5 ml/min where mobile phase A and B are 0.1% formic acid in water and 0.1% formic acid in acetonitrile, respectively. The gradient program was as follows: 1% to 36% B in 5 min, increase to 80% B at 0.8 ml over 0.5 min, which was maintained for 0.2 min and followed by equilibration with starting conditions for 2 min. For data independent acquisition Zeno SWATH MS/MS acquisition scheme was used with 80 variable size windows and 13 ms accumulation time. Ion source parameters were set to: Ion source gas 1 and 2 were set as 60 and 65 psi, respectively; curtain gas 55, CAD gas 7 and source temperature at 600°C; Spray voltage was set at 4000 V.

For proteomes of YJM975 and YJM975 *IRA2*$^{A>G}$ across different environments, samples were analyzed on a Bruker timsTOF HT mass spectrometer coupled to a 1290 Infinity II LC system (Agilent). Samples were injected in randomized order between strains, but in a block design between conditions. Before MS detection, 2 µg peptides were chromatographically separated on a Phenomenex Luna Omega column (1.6 µm C18 100A, 30 × 2.1 mm) heated to 50°C, using a flow rate of 0.5 ml/min where mobile phase A and B were 0.1% formic acid in water and 0.1% formic acid in acetonitrile, respectively. The LC gradient was run as follows: 3% to 36% B in 5 min, increase to 80% B at 0.85 ml over 0.5 min, which was maintained for 0.20 min followed by equilibration with starting conditions for 2 min while the flow was also reduced to starting conditions. diaPASEF MS acquisition was chosen, the electrospray source (Bruker VIP-HESI, Bruker Daltonics) was operated at 3000 V of capillary voltage, 10.0 liter/min of drying gas, and 240°C drying temperature. The diaPASEF windows scheme was as followed: We sampled an ion mobility range from $1/K_0 = 0.7$ to 1.30 V·s/cm^2 using ramp and accumulation times of 72.0 ms. The collision energy was lowered as a function of increasing ion mobility from 59 eV at $1/K_0 = 1.6$ V·s/cm^2 to 20 eV at $1/K_0 = 0.6$ V·s/cm^2. For all experiments, TIMS elution voltages were calibrated linearly to obtain the reduced ion mobility coefficients ($1/K_0$) using three Agilent ESI-Low Tuning Mix ions (m/z, $1/K_0$: 622.0289, 0.9848 V·s/cm^2; 922.0097, 1.1895 V·s/cm^2; and 1221.9906, 1.3820 V·s/cm^2).

CRISPR genome editing

Genome editing was conducted as previously described (*34*). Briefly, yeast transformed with appropriate CRISPEY gene editing plasmids were induced for editing in galactose, quenched on YPD, and single colonies lacking the editing plasmid were isolated by selection on 5-FOA. Candidate edited strains were genotyped by polymerase chain reaction (PCR) amplification of the relevant locus followed by Sanger sequencing.

Reverse-transcription quantitative PCR

Cells were grown in biological triplicate to OD_{600} ~ 1 and harvested by centrifugation. Total RNA was extracted using a Qiagen RNEasy kit according to the manufacturer's directions and reverse transcribed using an Agilent AffinityScript reverse transcription kit according to the manufacturer's directions using random hexamers. Primer pairs for *SER2*, *NCP1*, and *PFK1* are described in table S2. Amplification was performed using a BioRad CFX Connect and an NEB Luna qPCR kit according to the manufacturer's directions. Relative mRNA levels were estimated from two technical replicates per biological replicate based on the C_q of the target transcript relative to *PFK1*, which was used for normalization across samples.

Proteome quantification and data processing

Mass spectrometry data were processed using an experimentally derived gas-phase fractionation spectral library using the DIA-NN software (*25*) (version 1.8) with MS1 mass accuracy of 1.2×10^{-5}, MS2 mass accuracy of 2×10^{-5}, and a scan window radius of 6. Blanks and poorly growing samples (Z-scored $OD_{600} < -2.5$) were excluded, as were non-proteotypic precursors and entries with either Global.Q.Value, Global.PG.Q.Value, Q.Value, or PG.Q.Value > 0.01. Precursors were filtered to those occurring in >80% of samples and those with CV > 0.3 in quality control injections were excluded. To account for plate effects, the plate-wise median for each precursor was adjusted to the grand median across all samples. Protein groups were quantified using maxLFQ (*79*) in the DIA-NN R package (*25*); a total of 1225 proteins were identified across 1042 samples. Proteomic differences were similarly distributed between high- and low-abundance proteins; with the exception of the lowest abundance fraction, their higher variance may be due in part to technical variability. After batch correction, we obtained proteomes with a median technical CV on proteins of ~11.0% (from repeated injection of a control consisting of a pool of all processed samples). The proteomes contained few missing values, allowing stringent filtering: Peptides shared across at least 80% of samples quantified 1225 proteins, with an average of just 2.3% missing values (data S2). The quantified proteins accounted for ~70% of the proteome on a molar basis, and the estimated protein quantities correlated well with absolute protein levels reported previously (*80*) (fig. S8A). Proteomics acquired for validation experiments (sets 1 to 3) and of strains cultivated in different environments was processed in similar fashion, but with default preprocessing settings in DIA-NN (version 1.8) and using the specific genes matrix as a direct output of estimated protein abundances.

Simulations and power calculations

We estimated the sensitivity of our pQTL mapping approach using in silico simulated protein abundance traits. Briefly, we generated

simulated protein abundance vectors and performed pQTL mapping across a range of key parameters, including the number of F_6 progeny used and the number of underlying pQTLs per protein. Summary results of these simulations can be found in fig. S8B. On the basis of these data, we conducted our mapping experiment with the greatest possible number of F_6 haploid isolates that were auxotrophic only for uracil, to maximize our sensitivity to pQTLs of modest effect.

We were well-powered to detect allele-specific expression of mRNAs for which we mapped cis-pQTLs (117 of 127 had a tag SNP in the associated ORF; median depth 183 read counts). Previous analyses suggest that, for read depths of 100 and 1000 counts, we were powered to detect true major allele frequencies of 0.7 and 0.58, respectively, at $q < 0.01$ (*32*).

Heritability estimates

We estimated broad-sense protein abundance heritability—that is, the fraction of variance attributable to strain identity—separately based on biological replicates of each haploid parent control (RM11 and YJM975), following Bloom *et al.* (*29*). We used a linear mixed effect model that accounted for the harvest optical density (OD_{600}) of each control sample (abundance ~ 1 + OD_{600}). These estimates accorded well between the parental controls (fig. S8C) and were not sensitive to median normalization.

Genetic mapping

Genetic mapping was conducted essentially as in (*21*), using protein abundance as the quantitative trait. Protein abundance estimates from DIA-NN and maxLFQ were normalized to mean 0 and SD 1, and we appended to the haploid genotype matrix a "pseudogenotype" representing the harvest OD_{600} of each sample. This proved important for a subset of proteins, as found previously (*11*, *44*) (fig. S8D). Thanks to preprocessing before protein abundance estimation with maxLFQ, we observed little effect of batch on the protein abundance traits used for mapping. Across all measured protein groups in the F_6 progeny, no proteins exhibited significant batch-to-batch variation (*t* test; Bonferroni-corrected $q < 10^{-3}$).

Owing to the polygenic nature of the protein abundance traits, the uniform segregation of alleles in our mapping panel, and the relatively modest overall variation in protein abundance, Z-scoring yielded minimally skewed distributions for the majority of proteins: 1151 of 1214 proteins exhibited absolute trait skewness less than 1, and 1101 exhibited kurtosis less than 2 (fig. S8, E and F).

After coarse mapping of pQTLs by stepwise selection, fine mapping of pQTNs was performed by analysis of variance (ANOVA), as described previously (*21*). FDR was estimated per-protein by 100 permutations of real abundance data; the empirical *P* value cutoffs were set to achieve ~10% FDR. This procedure was conducted for the entire genotype matrix in the so-called global mapping. In parallel, we conducted local mapping that only considered loci within 10 markers of the ORF encoding the protein in question. Empirically, we found that cis-acting pQTL effects accorded well between the global and local approaches (fig. S8G); the analyses in the paper are based on the global analysis. The genetic inflation factor λ_{median} in the global analysis was less than 1.1 for 1078 of 1214 proteins that we measured (fig. S8, H and I).

In concordance with widespread transgression, we identified at least one pQTL for 233 of the 399 proteins that were not differentially expressed between the parents (mean 2.63 pQTLs per protein) (fig. S8J). Accordingly, the true biological variability released in the cross (CV among the F_6 progeny normalized to parental CV) was highly predictive of the number of pQTLs discovered for a protein ($r = 0.60$; $P < 10^{-117}$) (fig. S8K).

Transcription factor enrichment analyses

Examining the proteins up-regulated in the parental isolates, transcription factor target analyses (*58*) indicated that the YJM–up-regulated gene set was highly enriched for targets of the Sfp1, Stb3, Dot6, Tod6, and Gcn4 transcription factors, whereas the YJM–down-regulated module was likely regulated by Sut1, Msn2/4, Hap3/5, and Gis1 (table S1). Yet, there were no trans-regulatory hotspots at the genes encoding these factors. We therefore scrutinized our genotype-to-protein map further to identify other possible origins of these proteomic changes. We found that three of the most pleiotropic trans-acting loci in our experiment (*IRA1*, *IRA2*, and *PDE2*) were centered at genes in the Ras-PKA pathway (*55*, *81*, *82*), a signaling pathway conserved from yeast to humans (*83*). The Ras-PKA network integrates nutritional signals to control metabolism and proliferation and is associated with adaptation to fermentation (*84*) as well as virulence in pathogenic yeasts (*85*). Two well-characterized targets of the Ras-PKA signaling pathway [via the kinase Rim15 (*86*)] are the Gis1 and Msn2/4 transcription factors, consistent with our transcription factor target analyses.

Mutation simulations and protein structure analysis

Simulations of all possible missense variants were conducted on the basis of the S288C reference genome R64. Briefly, we generated in silico all possible single-nucleotide changes to all S288C ORFs and categorized these as missense or synonymous and as transitions or transversions. Allele frequencies for extant variants were determined with reference to the 1002 Yeast Genomes (*19*) genotype matrix.

Predicted protein structures of all *S. cerevisiae* S288C ORFs were retrieved from https://alphafold.ebi.ac.uk/download#proteomes-section. Each ORF was analyzed with DSSP (*87*) as well as using custom code to calculate the number of neighboring alpha-carbons. Based on these analyses, we annotated each possible missense SNP generated above with these structural parameters.

Phenotypic mapping

Phenotype data for ~15,000 F_6 diploid isolates from the RM11 × YM975 cross grown in various environmental conditions were released previously as part of our study of the effects of Hsp90 on the genotype-to-phenotype map (*32*). In this work, we reanalyzed the control dataset (without Hsp90 inhibition) from that study to identify QTLs and QTNs for growth under stress. Genetic mapping was conducted essentially as described above and previously (*21*). Across 12 environments, we mapped 9321 QTLs and resolved 2519 QTNs to a single causal variant (FDR ~10%; see Materials and methods), which explains a median of 64% of the phenotypic variance at the final experimental time point (data S6).

REFERENCES AND NOTES

1. M. J. Landrum *et al.*, ClinVar: Public archive of relationships among sequence variation and human phenotype. *Nucleic Acids Res.* **42**, D980–D985 (2014). doi: 10.1093/nar/gkt1113; pmid: 24234437
2. S. Gudmundsson *et al.*, Variant interpretation using population databases: Lessons from gnomAD. *Hum. Mutat.* **43**, 1012–1030 (2022). doi: 10.1002/humu.24309; pmid: 34859531
3. GTEx Consortium, Genetic effects on gene expression across human tissues. *Nature* **550**, 204–213 (2017). doi: 10.1038/nature24277; pmid: 29022597
4. N. Wagner *et al.*, Aberrant splicing prediction across human tissues. *Nat. Genet.* **55**, 861–870 (2023). doi: 10.1038/s41588-023-01373-3; pmid: 37142848
5. E. J. Foss *et al.*, Genetic basis of proteome variation in yeast. *Nat. Genet.* **39**, 1369–1375 (2007). doi: 10.1038/ng.2007.22; pmid: 17952072
6. C. Damerval, A. Maurice, J. M. Josse, D. de Vienne, Quantitative trait loci underlying gene product variation: A novel perspective for analyzing regulation of genome expression. *Genetics* **137**, 289–301 (1994). doi: 10.1093/genetics/137.1.289; pmid: 7914503
7. K. Suhre, M. I. McCarthy, J. M. Schwenk, Genetics meets proteomics: Perspectives for large population-based studies. *Nat. Rev. Genet.* **22**, 19–37 (2021). doi: 10.1038/s41576-020-0268-2; pmid: 32860016
8. M. Pietzner *et al.*, Mapping the proteo-genomic convergence of human diseases. *Science* **374**, eabj1541 (2021). doi: 10.1126/science.abj1541; pmid: 34648354
9. R. B. Brem, G. Yvert, R. Clinton, L. Kruglyak, Genetic dissection of transcriptional regulation in budding yeast. *Science* **296**, 752–755 (2002). doi: 10.1126/science.1069516; pmid: 11923494

10. G. Yvert *et al.*, *Trans*-acting regulatory variation in *Saccharomyces cerevisiae* and the role of transcription factors. *Nat. Genet.* **35**, 57–64 (2003). doi: 10.1038/ng1222; pmid: 12897782
11. F. W. Albert, J. S. Bloom, J. Siegel, L. Day, L. Kruglyak, Genetics of *trans*-regulatory variation in gene expression. *eLife* **7**, e35471 (2018). doi: 10.7554/eLife.35471; pmid: 30014850
12. P. Picotti *et al.*, A complete mass-spectrometric map of the yeast proteome applied to quantitative trait analysis. *Nature* **494**, 266–270 (2013). doi: 10.1038/nature11835; pmid: 23334424
13. F. W. Albert, S. Treusch, A. H. Shockley, J. S. Bloom, L. Kruglyak, Genetics of single-cell protein abundance variation in large yeast populations. *Nature* **506**, 494–497 (2014). doi: 10.1038/nature12904; pmid: 24402228
14. L. Parts *et al.*, Heritability and genetic basis of protein level variation in an outbred population. *Genome Res.* **24**, 1363–1370 (2014). doi: 10.1101/gr.170506.113; pmid: 24823668
15. P. Vande Zande, M. S. Hill, P. J. Wittkopp, Pleiotropic effects of trans-regulatory mutations on fitness and gene expression. *Science* **377**, 105–109 (2022). doi: 10.1126/science.abj7185; pmid: 35771906
16. E. E. Schadt *et al.*, Genetics of gene expression surveyed in maize, mouse and man. *Nature* **422**, 297–302 (2003). doi: 10.1038/nature01434; pmid: 12646919
17. J. Grossbach *et al.*, The impact of genomic variation on protein phosphorylation states and regulatory networks. *Mol. Syst. Biol.* **18**, e10712 (2022). doi: 10.15252/msb.202110712; pmid: 35574625
18. O. T. Schubert, J. S. Bloom, M. J. Sadhu, L. Kruglyak, Genome-wide base editor screen identifies regulators of protein abundance in yeast. *eLife* **11**, e79525 (2022). doi: 10.7554/eLife.79525; pmid: 36326816
19. J. Peter *et al.*, Genome evolution across 1,011 *Saccharomyces cerevisiae* isolates. *Nature* **556**, 339–344 (2018). doi: 10.1038/s41586-018-0030-5; pmid: 29643504
20. É. Caudal *et al.*, Pan-transcriptome reveals a large accessory genome contribution to gene expression variation in yeast. *Nat. Genet.* **56**, 1278–1287 (2024). doi: 10.1038/s41588-024-01769-9; pmid: 38778243
21. R. She, D. F. Jarosz, Mapping Causal Variants with Single-Nucleotide Resolution Reveals Biochemical Drivers of Phenotypic Change. *Cell* **172**, 478–490.e15 (2018). doi: 10.1016/j.cell.2017.12.015; pmid: 29373829
22. C. B. Messner *et al.*, Ultra-fast proteomics with Scanning SWATH. *Nat. Biotechnol.* **39**, 846–854 (2021). doi: 10.1038/s41587-021-00860-4; pmid: 33767396
23. M. J. McCullough, K. V. Clemons, C. Farina, J. H. McCusker, D. A. Stevens, Epidemiological investigation of vaginal *Saccharomyces cerevisiae* isolates by a genotypic method. *J. Clin. Microbiol.* **36**, 557–562 (1998). doi: 10.1128/JCM.36.2.557-562.1998; pmid: 9466776
24. T. Török, R. K. Mortimer, P. Romano, G. Suzzi, M. Polsinelli, Quest for wine yeasts—An old story revisited. *J. Ind. Microbiol.* **17**, 303–313 (1996). doi: 10.1007/BF01574705
25. V. Demichev, C. B. Messner, S. I. Vernardis, K. S. Lilley, M. Ralser, DIA-NN: Neural networks and interference correction enable deep proteome coverage in high throughput. *Nat. Methods* **17**, 41–44 (2020). doi: 10.1038/s41592-019-0638-x; pmid: 31768060
26. G. Liti *et al.*, Population genomics of domestic and wild yeasts. *Nature* **458**, 337–341 (2009). doi: 10.1038/nature07743; pmid: 19212322
27. H. B. Fraser, Detecting selection with a genetic cross. *Proc. Natl. Acad. Sci. U.S.A.* **117**, 22323–22330 (2020). doi: 10.1073/pnas.2014277117; pmid: 32848059
28. K. Hahne, V. Haucke, L. Ramage, G. Schatz, Incomplete arrest in the outer membrane sorts NADH-cytochrome b_5 reductase to two different submitochondrial compartments. *Cell* **79**, 829–839 (1994). doi: 10.1016/0092-8674(94)90072-8; pmid: 8001120
29. J. S. Bloom, I. M. Ehrenreich, W. T. Loo, T.-L. V. Lite, L. Kruglyak, Finding the sources of missing heritability in a yeast cross. *Nature* **494**, 234–237 (2013). doi: 10.1038/nature11867; pmid: 23376951
30. J. Muenzner *et al.*, Natural proteome diversity links aneuploidy tolerance to protein turnover. *Nature* **630**, 149–157 (2024). doi: 10.1038/s41586-024-07442-9; pmid: 38778096
31. E. M. Teyssonnière *et al.*, Species-wide quantitative transcriptomes and proteomes reveal distinct genetic control of gene expression variation in yeast. *Proc. Natl. Acad. Sci. U.S.A.* **121**, e2319211121 (2024). doi: 10.1073/pnas.2319211121; pmid: 38696467
32. C. M. Jakobson, J. Aguilar-Rodríguez, D. F. Jarosz, Hsp90 shapes adaptation by controlling the fitness consequences of regulatory variation. bioRxiv 2023.10.30.564848 [Preprint] (2023). doi: 10.1101/2023.10.30.564848
33. A. Wacholder *et al.*, A vast evolutionarily transient translatome contributes to phenotype and fitness. *Cell Syst.* **14**, 363–381.e8 (2023). doi: 10.1016/j.cels.2023.04.002; pmid: 37164009
34. E. Sharon *et al.*, Functional Genetic Variants Revealed by Massively Parallel Precise Genome Editing. *Cell* **175**, 544–557.e16 (2018). doi: 10.1016/j.cell.2018.08.057; pmid: 30245013
35. P. Kemmeren *et al.*, Large-scale genetic perturbations reveal regulatory networks and an abundance of gene-specific repressors. *Cell* **157**, 740–752 (2014). doi: 10.1016/j.cell.2014.02.054; pmid: 24766815
36. M. Weith *et al.*, Genetic effects on molecular network states explain complex traits. *Mol. Syst. Biol.* **19**, e11493 (2023). doi: 10.15252/msb.202211493; pmid: 37485750
37. H. A. Orr, Testing natural selection vs. genetic drift in phenotypic evolution using quantitative trait locus data. *Genetics* **149**, 2099–2104 (1998). doi: 10.1093/genetics/149.4.2099; pmid: 9691061
38. J. Schymkowitz *et al.*, The FoldX web server: An online force field. *Nucleic Acids Res.* **33**, W382–W388 (2005). doi: 10.1093/nar/gki387; pmid: 15980494
39. S. Henikoff, J. G. Henikoff, Amino acid substitution matrices from protein blocks. *Proc. Natl. Acad. Sci. U.S.A.* **89**, 10915–10919 (1992). doi: 10.1073/pnas.89.22.10915; pmid: 1438297
40. J. Echave, S. J. Spielman, C. O. Wilke, Causes of evolutionary rate variation among protein sites. *Nat. Rev. Genet.* **17**, 109–121 (2016). doi: 10.1038/nrg.2015.18; pmid: 26781812
41. J. Jumper *et al.*, Highly accurate protein structure prediction with AlphaFold. *Nature* **596**, 583–589 (2021). doi: 10.1038/s41586-021-03819-2; pmid: 34265844
42. M. Costanzo *et al.*, The genetic landscape of a cell. *Science* **327**, 425–431 (2010). doi: 10.1126/science.1180823; pmid: 20093466
43. G. Giaever *et al.*, Functional profiling of the *Saccharomyces cerevisiae* genome. *Nature* **418**, 387–391 (2002). doi: 10.1038/nature00935; pmid: 12140549
44. C. B. Messner *et al.*, The proteomic landscape of genome-wide genetic perturbations. *Cell* **186**, 2018–2034.e21 (2023). doi: 10.1016/j.cell.2023.03.026; pmid: 37080200
45. G. Kustatscher *et al.*, Co-regulation map of the human proteome enables identification of protein functions. *Nat. Biotechnol.* **37**, 1361–1371 (2019). doi: 10.1038/s41587-019-0298-5; pmid: 31690884
46. A. Rodríguez, T. de la Cera, P. Herrero, F. Moreno, The hexokinase 2 protein regulates the expression of the GLK1, HXK1 and HXK2 genes of Saccharomyces cerevisiae. *Biochem. J.* **355**, 625–631 (2001). doi: 10.1042/bj3550625; pmid: 11311123
47. M. Umekawa, K. Hamada, N. Isono, S. Karita, The Emi2 Protein of *Saccharomyces cerevisiae* is a Hexokinase Expressed under Glucose Limitation. *J. Appl. Glycosci.* **67**, 103–109 (2020). doi: 10.5458/jag.jag.JAG-2020_0007; pmid: 34354536
48. B. H. M. Meldal *et al.*, Complex Portal 2022: New curation frontiers. *Nucleic Acids Res.* **50**, D578–D586 (2022). doi: 10.1093/nar/gkab991; pmid: 34718729
49. D. Szklarczyk *et al.*, The STRING database in 2023: Protein–protein association networks and functional enrichment analyses for any sequenced genome of interest. *Nucleic Acids Res.* **51**, D638–D646 (2023). doi: 10.1093/nar/gkac1000; pmid: 36370105
50. M. Costanzo *et al.*, A global genetic interaction network maps a wiring diagram of cellular function. *Science* **353**, aaf1420 (2016). doi: 10.1126/science.aaf1420; pmid: 27708008
51. B. H. M. Meldal *et al.*, Complex Portal 2018: Extended content and enhanced visualization tools for macromolecular complexes. *Nucleic Acids Res.* **47**, D550–D558 (2019). doi: 10.1093/nar/gky1001; pmid: 30357405
52. R. Oughtred *et al.*, The BioGRID database: A comprehensive biomedical resource of curated protein, genetic, and chemical interactions. *Protein Sci.* **30**, 187–200 (2021). doi: 10.1002/pro.3978; pmid: 33070389
53. Y. Esnault, D. Feldheim, M. O. Blondel, R. Schekman, F. Képès, *SSS1* encodes a stabilizing component of the Sec61 subcomplex of the yeast protein translocation apparatus. *J. Biol. Chem.* **269**, 27478–27485 (1994). doi: 10.1016/S0021-9258(18)47010-X; pmid: 7961662
54. F. Galello, S. Moreno, S. Rossi, Interacting proteins of protein kinase A regulatory subunit in *Saccharomyces cerevisiae*. *J. Proteomics* **109**, 261–275 (2014). doi: 10.1016/j.jprot.2014.07.008; pmid: 25065647
55. P. Sass, J. Field, J. Nikawa, T. Toda, M. Wigler, Cloning and characterization of the high-affinity cAMP phosphodiesterase of Saccharomyces cerevisiae. *Proc. Natl. Acad. Sci. U.S.A.* **83**, 9303–9307 (1986). doi: 10.1073/pnas.83.24.9303; pmid: 3025832
56. A. Dancis, R. D. Klausner, A. G. Hinnebusch, J. G. Barriocanal, Genetic evidence that ferric reductase is required for iron uptake in *Saccharomyces cerevisiae*. *Mol. Cell. Biol.* **10**, 2294–2301 (1990). doi: 10.1128/mcb.10.5.2294-2301.1990; pmid: 2183029
57. J. Vowinckel *et al.*, The metabolic growth limitations of petite cells lacking the mitochondrial genome. *Nat. Metab.* **3**, 1521–1535 (2021). doi: 10.1038/s42255-021-00477-6; pmid: 34799698
58. F. Zambelli, G. Pesole, G. Pavesi, Pscan: Finding over-represented transcription factor binding site motifs in sequences from co-regulated or co-expressed genes. *Nucleic Acids Res.* **37**, W247–W252 (2009). doi: 10.1093/nar/gkp464; pmid: 19487240
59. J. R. Mattoon, E. Caravajal, D. Guthrie, Effects of *hap* mutations on heme and cytochrome formation in yeast. *Curr. Genet.* **17**, 179–183 (1990). doi: 10.1007/BF00312865; pmid: 2182199
60. D. S. McNabb, I. Pinto, Assembly of the Hap2p/Hap3p/Hap4p/Hap5p-DNA complex in *Saccharomyces cerevisiae*. *Eukaryot. Cell* **4**, 1829–1839 (2005). doi: 10.1128/EC.4.11.1829-1839.2005; pmid: 16278450
61. G. S. Fragiadakis, D. Tzamarias, D. Alexandraki, Nhp6 facilitates Aft1 binding and Ssn6 recruitment, both essential for *FRE2* transcriptional activation. *EMBO J.* **23**, 333–342 (2004). doi: 10.1038/sj.emboj.7600043; pmid: 14739928
62. T. Ideker *et al.*, Integrated genomic and proteomic analyses of a systematically perturbed metabolic network. *Science* **292**, 929–934 (2001). doi: 10.1126/science.292.5518.929; pmid: 11340206
63. F. Karst, F. Lacroute, Ergosterol biosynthesis in *Saccharomyces cerevisiae*. *Mol. Gen. Genet.* **154**, 269–277 (1977). doi: 10.1007/BF00571282; pmid: 200835

64. C. M. Jakobson, R. She, D. F. Jarosz, Pervasive function and evidence for selection across standing genetic variation in *S. cerevisiae*. *Nat. Commun.* **10**, 1222 (2019). doi: 10.1038/s41467-019-09166-1; pmid: 30874558
65. A. S. Jellen-Ritter, W. V. Kern, Enhanced expression of the multidrug efflux pumps AcrAB and AcrEF associated with insertion element transposition in *Escherichia coli* mutants Selected with a fluoroquinolone. *Antimicrob. Agents Chemother.* **45**, 1467–1472 (2001). doi: 10.1128/AAC.45.5.1467-1472.2001; pmid: 11302812
66. E. A. Boyle, Y. I. Li, J. K. Pritchard, An Expanded View of Complex Traits: From Polygenic to Omnigenic. *Cell* **169**, 1177–1186 (2017). doi: 10.1016/j.cell.2017.05.038; pmid: 28622505
67. S. Besse *et al.*, Genetic landscape of an *in vivo* protein interactome. bioRxiv 2023.12.14.571726 [Preprint] (2023). doi: 10.1101/2023.12.14.571726
68. O. Lemke *et al.*, The role of metabolism in shaping enzyme structures over 400 million years. *Nature* **644**, 280–289 (2025). doi: 10.1038/s41586-025-09205-6
69. F. W. Albert, L. Kruglyak, The role of regulatory variation in complex traits and disease. *Nat. Rev. Genet.* **16**, 197–212 (2015). doi: 10.1038/nrg3891; pmid: 25707927
70. L. H. Rieseberg, M. A. Archer, R. K. Wayne, Transgressive segregation, adaptation and speciation. *Heredity* **83**, 363–372 (1999). doi: 10.1038/sj.hdy.6886170; pmid: 10583537
71. A. D. Kern, M. W. Hahn, The Neutral Theory in Light of Natural Selection. *Mol. Biol. Evol.* **35**, 1366–1371 (2018). doi: 10.1093/molbev/msy092; pmid: 29722831
72. A. L. Cope, J. G. Schraiber, M. Pennell, Macroevolutionary divergence of gene expression driven by selection on protein abundance. *Science* **387**, 1063–1068 (2025). doi: 10.1126/science.ads2658; pmid: 40048509
73. J. D. Fischer, G. L. Holliday, S. A. Rahman, J. M. Thornton, The structures and physicochemical properties of organic cofactors in biocatalysis. *J. Mol. Biol.* **403**, 803–824 (2010). doi: 10.1016/j.jmb.2010.09.018; pmid: 20850456
74. I. Piazza *et al.*, A map of protein-metabolite interactions reveals principles of chemical communication. *Cell* **172**, 358–372.e23 (2018). doi: 10.1016/j.cell.2017.12.006; pmid: 29307493
75. S. Lutz, K. Van Dyke, M. A. Feraru, F. W. Albert, Multiple epistatic DNA variants in a single gene affect gene expression in *trans*. *Genetics* **220**, iyab208 (2022). doi: 10.1093/genetics/iyab208; pmid: 34791209
76. T. A. Manolio *et al.*, Finding the missing heritability of complex diseases. *Nature* **461**, 747–753 (2009). doi: 10.1038/nature08494; pmid: 19812666
77. Y. Perez-Riverol *et al.*, The PRIDE database at 20 years: 2025 update. *Nucleic Acids Res.* **53**, D543–D553 (2025). doi: 10.1093/nar/gkae1011; pmid: 39494541
78. C. M. Jakobson, J. Hartl, P. Trébulle, M. Mülleder, D. Jarosz, M. Ralser, pQTL-mapping-rev1, version revision1, Zenodo (2025). doi: 10.5281/zenodo.14933903
79. J. Cox *et al.*, Accurate proteome-wide label-free quantification by delayed normalization and maximal peptide ratio extraction, termed MaxLFQ. *Mol. Cell. Proteomics* **13**, 2513–2526 (2014). doi: 10.1074/mcp.M113.031591; pmid: 24942700
80. Q. Huang, D. Szklarczyk, M. Wang, M. Simonovic, C. von Mering, PaxDb 5.0: Curated Protein Quantification Data Suggests Adaptive Proteome Changes in Yeasts. *Mol. Cell. Proteomics* **22**, 100640 (2023). doi: 10.1016/j.mcpro.2023.100640; pmid: 37659604
81. K. Tanaka, K. Matsumoto, A. Toh-E, *IRA1*, an inhibitory regulator of the *RAS*-cyclic AMP pathway in *Saccharomyces cerevisiae*. *Mol. Cell. Biol.* **9**, 757–768 (1989). doi: 10.1128/mcb.9.2.757-768.1989; pmid: 2540426
82. K. Tanaka, B. K. Lin, D. R. Wood, F. Tamanoi, IRA2, an upstream negative regulator of RAS in yeast, is a RAS GTPase-activating protein. *Proc. Natl. Acad. Sci. U.S.A.* **88**, 468–472 (1991). doi: 10.1073/pnas.88.2.468; pmid: 1988946
83. C. A. D'Souza, J. Heitman, Conserved cAMP signaling cascades regulate fungal development and virulence. *FEMS Microbiol. Rev.* **25**, 349–364 (2001). doi: 10.1111/j.1574-6976.2001.tb00582.x; pmid: 11348689
84. J. Molinet *et al.*, Wild Patagonian yeast improve the evolutionary potential of novel interspecific hybrid strains for lager brewing. *PLOS Genet.* **20**, e1011154 (2024). doi: 10.1371/journal.pgen.1011154; pmid: 38900713
85. D. A. Hogan, P. Sundstrom, The Ras/cAMP/PKA signaling pathway and virulence in *Candida albicans*. *Future Microbiol.* **4**, 1263–1270 (2009). doi: 10.2217/fmb.09.106; pmid: 19995187
86. I. Pedruzzi, N. Bürckert, P. Egger, C. De Virgilio, *Saccharomyces cerevisiae* Ras/cAMP pathway controls post-diauxic shift element-dependent transcription through the zinc finger protein Gis1. *EMBO J.* **19**, 2569–2579 (2000). doi: 10.1093/emboj/19.11.2569; pmid: 10835355
87. R. P. Joosten *et al.*, A series of PDB related databases for everyday needs. *Nucleic Acids Res.* **39**, D411–D419 (2011). doi: 10.1093/nar/gkq1105; pmid: 21071423
88. L. Ramos-Alonso, A. M. Romero, M. T. Martínez-Pastor, S. Puig, Iron Regulatory Mechanisms in *Saccharomyces cerevisiae*. *Front. Microbiol.* **11**, 582830 (2020). doi: 10.3389/fmicb.2020.582830; pmid: 33013818

ACKNOWLEDGMENTS

We thank F. Amari, K. Textoris-Taube, A. Lehmann, C. Kilian, and D. Ludwig (Charite – Universitätsmedizin Berlin) for technical assistance with proteomics sample preparation and measurements. We thank the members of the Jarosz and Ralser laboratories for helpful discussions. **Funding:** This study was supported by the National Institutes of Health (DP2-GM119140, RF1-AG057334, R01-AG06341801, and R01-HG012366 to D.F.J. and F32-GM125162 to C.M.J.); the National Science Foundation (NSF-MCB116762 to D.F.J.); a Searle Scholar Award (14-SSP-210 to D.F.J.); a Kimmel Scholar Award (SKF-15-154 to D.F.J.); a Vallee Scholar Award (to D.F.J.); and a Discovery Innovation Award from Stanford University (to D.F.J.). D.F.J. is also a Science and Engineering Fellow of the David and Lucile Packard Foundation. This study was also supported by Swiss National Science Foundation Postdoc Mobility fellowship 191052 (to J.H.); the European Research Council (ERC) under grant agreement ERC-SyG-2020 951475 (to M.R.); the Ministry of Education and Research (BMBF), as part of the National Research Node "Mass spectrometry in Systems Medicine" (MSCoresys), under grant agreement 031L0220 (to M.R.); and the Deutsche Forschungsgemeinschaft (DFG, German Research Foundation) under Germany's Excellence Strategy – EXC 3118/1 – project no. 533770413 (to M.R.) and no. 492697668 (to M.M.). P.T. is supported by funding from the European Union's Horizon 2020 research and innovation program under the Marie Skłodowska-Curie grant agreement no. 101026830. Some of the computing for this project was performed on the Sherlock cluster. We thank Stanford University and the Stanford Research Computing Center for providing computational resources and support that contributed to these research results. **Author contributions:** Conceptualization: C.M.J., J.H., D.F.J., M.R.; Formal analysis: C.M.J., J.H., P.T.; Funding acquisition: J.H., D.J.F., M.R.; Investigation: C.M.J., J.H.; Methodology: C.M.J., J.H., M.M.; Software: C.M.J.; Supervision: D.F.J., M.R.; Visualization: C.M.J., J.H.; Writing – original draft: C.M.J., J.H.; Writing – review & editing: C.M.J., J.H., D.F.J., M.R. **Competing interests:** M.R. is founder and shareholder of Eliptica Limited. The other authors declare that they have no competing interests. **Data and materials availability:** All mass spectrometry proteomics data have been deposited to PRIDE with the dataset identifier PXD062635. All data and code required to reproduce the mapping results and figures can be found on Zenodo (*78*). All strains and plasmids used in this study are available on request to D.F.J. (jarosz@stanford.edu). The F_6 haploid mapping panel is also available from NCYC. **License information:** Copyright © 2025 the authors, some rights reserved; exclusive licensee American Association for the Advancement of Science. No claim to original US government works. https://www.science.org/about/science-licenses-journal-article-reuse. This research was funded in whole or in part by the Swiss National Science Foundation (Postdoc Mobility fellowship 191052), a cOAlition S organization, and by the European Research Council (ERC) (ERC-SyG-2020 951475); as required, the author will make the Author Accepted Manuscript (AAM) version available under a CC BY public copyright license.

SUPPLEMENTARY MATERIALS

science.org/doi/10.1126/science.adu3198
Figs. S1 to S8; Tables S1 and S2; References (*89*–*91*); MDAR Reproducibility Checklist; Data S1 to S6

Submitted 3 November 2024; accepted 11 July 2025

10.1126/science.adu3198

RESEARCH ARTICLE SUMMARY

TRANSPOSON

Mechanism of DNA targeting by human LINE-1

Wenxing Jin*†, Cong Yu†, Yan Zhang†, Changchang Cao, Tianfan Xia, Ge Song, Zhaokui Cai, Yuanchao Xue, Bing Zhu, Rui-Ming Xu*

Full article and list of author affiliations: https://doi.org/10.1126/science.adu3433

INTRODUCTION: Retrotransposons copy and insert their coding sequences into new genomic locations via RNA intermediates, posing risks to genome integrity. In humans, the only autonomously active retrotransposon is the long interspersed nuclear element–1 (LINE-1), which invades the genome through target-primed reverse transcription (TPRT). This process is catalyzed by the LINE-1–encoded open reading frame 2 protein (ORF2p), which has endonuclease (EN) and reverse transcriptase (RT) activities. In this study, we investigated the molecular mechanisms governing LINE-1 genome targeting and TPRT execution by ORF2p.

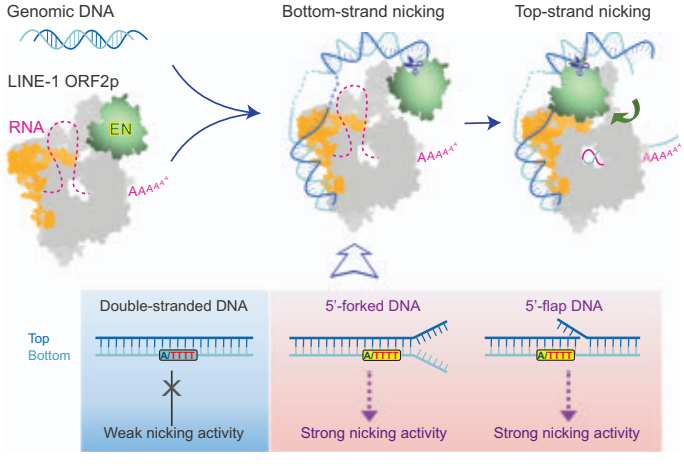
RATIONALE: We produced human ORF2p in eukaryotic cells and purified a complex of ORF2p with endogenous nucleic acids. The structure and the composition of the complex were analyzed by cryo–electron microscopy (cryo-EM), deoxyribonuclease and ribonuclease digestions, and DNA and RNA sequencing (RNA-seq). Furthermore, we conducted in vitro EN activity assays to investigate the features of DNA substrates preferred by ORF2p for efficient cleavage.

RESULTS: Purification of LINE-1 ORF2p from either insect or human cells revealed tight binding between the protein and endogenous nucleic acids. Cryo-EM analysis identified two distinct pieces of copurified nucleic acids: an A-form RNA/DNA hybrid positioned in the RT active site pocket and a B-form double-stranded DNA (dsDNA) with a single-stranded tail bound to the ORF2p's exterior surface, primarily through sequence-independent charge interactions. Structure comparison of the ORF2p and other non–long terminal repeat retrotransposon complexes revealed a generally similar DNA binding path, but ORF2p notably differed from others in lacking determinants for sequence-specific DNA binding and having a flexibly tethered EN domain located distant from the dsDNA binding region. Consistent with the biochemical and structural characterizations, sequencing of copurified DNA revealed prominent enrichment of repetitive satellite DNA elements. RNA-seq data indicated that ORF2p could bind and reverse transcribe a wide range of cellular RNAs.

Inspired by the structural finding of the binding of unwound DNA to ORF2p and the knowledge that LINE-1 integration occurred primarily during DNA replication, we investigated whether replication-intermediate DNA structures influence the EN activity of ORF2p. In vitro nuclease activity assays showed great stimulation of ORF2p activity toward DNA substrates having a fork or flap structure approximately 6 to 10 base pairs away in the 5′ direction of the strand carrying the TTTTT/AA consensus ORF2p cleavage motif. Cleavage of the opposite strand predominantly occurred between TA, TC, and TG dinucleotides 8 to 12 nucleotides (nts) away. As a result, nicking on both DNA strands by ORF2p resulted in a staggered flanking offset of 8 to 12 nts, which accounted for the generation of target site duplication from LINE-1 integration.

CONCLUSION: Our discovery of ORF2p's binding mode to genomic DNA and its preferential nicking of forked and 5′-flap DNA, together with the ubiquitous presence of short nicking motifs, provides a clearer understanding of the TPRT process of LINE-1, in which ORF2p encounters DNA promiscuously and makes a productive cut only when its binding region coincides with the presence of suitably structured DNA, such as that generated during DNA replication. Stable binding of ORF2p to the dsDNA allows nicking of both strands of downstream DNA by the flexibly tethered EN domain in a stepwise manner. □

*Corresponding authors. Email: jinwenxing@ibp.ac.cn (W.J.); rmxu@ibp.ac.cn (R.-M.X.)
†These authors contributed equally to this work. **Cite this article as W. Jin *et al.*, *Science* 390, eadu3433 (2025). DOI: 10.1126/science.adu3433**



DNA binding mode and target preference of LINE-1 ORF2p. (Top, left to right) Depiction of a model of DNA targeting—bottom- and top-strand nicking by ORF2p during the TPRT process of LINE-1. The contour of the ORF2p structure is shown, with the DNA binding region colored in orange, the EN domain in green, and the rest of the structure in gray. The dashed magenta line followed by a stretch of "A's" illustrates the RNA template with an adenine-rich 3′ tail, and the curved green arrow in the far-right panel indicates the movement of the EN domain for nicking distinct DNA strands. (Bottom) Panels show the preference of DNA substrates by ORF2p observed in in vitro nuclease assays.

TRANSPOSON

Mechanism of DNA targeting by human LINE-1

Wenxing Jin[1]*†, Cong Yu[1]‡†, Yan Zhang[1]†, Changchang Cao[1], Tianfan Xia[1,2], Ge Song[1], Zhaokui Cai[1], Yuanchao Xue[1,2], Bing Zhu[1,2,3], Rui-Ming Xu[1,2,4]*

Long interspersed nuclear element–1 (LINE-1 or L1), the only autonomously active retrotransposon in humans today, constitutes a large proportion of the genome and continues to evolve the genome and impact fundamental biological processes. L1 retrotransposition critically depends on its endonuclease and reverse transcriptase subunit open reading frame 2 protein (ORF2p), which targets genomic loci and nicks DNA using an evolutionarily distinct yet not fully understood mechanism. Our structural and biochemical analyses revealed that ORF2p is a structure-dependent endonuclease. It binds a double-stranded DNA region upstream of the nicking site and recognizes a downstream forked or flap structure for efficient DNA nicking. This discovery suggests that L1 mobilization piggybacks on chromosomal processes with noncanonical DNA structure intermediates.

More than one-third of our genome is made up of retrotransposons, which are DNA elements capable of jumping from one genomic locus to another via an RNA intermediate (*1*). These mobile DNA elements impact many aspects of genome biology and physiopathological processes, including genome evolution, embryonic development, and aging (*2*, *3*). In humans, two major types of retrotransposons, a long terminal repeat (LTR) and a non-LTR type, can be distinguished. LTR retrotransposons, also known as endogenous retroviruses (ERVs), contain direct sequence repeats flanking the sequence that are akin to retroviral sequences (*4*, *5*); non-LTR retrotransposons lack the terminal sequence repeats and use a process called target-primed reverse transcription (TPRT) for mobilization (*6*, *7*). The only retrotransposon still capable of autonomous retrotransposition in humans today is the long interspersed nuclear element–1 (LINE-1 or L1) (*8*), which is an ancient non-LTR retrotransposon comprising ~17% of the human genome (*9*). At present, the vast majority of L1s have lost transposition ability, and an estimated ~100 copies are still active (*10*, *11*).

The RNA polymerase II–transcribed L1 mRNA encodes two open reading frames—open reading frame 1 (ORF1) and ORF2—in the sense direction and is polyadenylated at the 3′ end (*2*). ORF1 protein (ORF1p) is an RNA chaperone involved in the assembly of active L1 ribonucleoprotein (RNP) complexes, and ORF2p is a multifunctional protein containing an endonuclease (EN) and a reverse transcriptase (RT) domain. Although both are required for retrotransposition of L1, ORF1p is not needed for mobilization of certain short interspersed elements (SINEs), such as *Alu* (*12*). In the TPRT model, the EN domain of ORF2p makes a first nick on the DNA strand, designated the bottom strand, bearing the consensus sequence of 5′-TTTT/AA-3′ (*13*). The 3′ end of the nicked strand then primes the synthesis of cDNA by ORF2p through pairing with the 3′ A-rich sequence of the mRNA template (*14*, *15*). Subsequent steps include synthesizing the second strand of DNA and joining the free ends of the newly synthesized L1 cDNA to genomic DNA (*3*). Molecular details of these later steps are poorly understood, although it is believed that cellular DNA repair pathways are involved (*16*–*18*).

An unresolved fundamental mechanistic question is what ORF2p's biochemical property might determine as its preference for genomic regions to integrate. Knowledge from the better-characterized eukaryotic non-LTR transposable element, R2 from *Bombyx mori* (R2Bm), shows its specific integration into the 28*S* ribosomal DNA (rDNA) locus through recognition of a sequence motif upstream of the integration site by the R2Bm protein, which is homologous to human L1 ORF2p (*19*). In the more distantly related group II introns, both the intronic RNA and the RT (maturase) coordinate to recognize the DNA target sites (*20*–*22*). By contrast, genome-wide profiling of L1 insertion revealed no apparent preference for genomic locations or chromatin features in human cells (*23*, *24*). Yet, functional and genomic analyses have implicated connections between the L1 retrotransposition and cellular DNA replication processes (*23*–*26*). However, an understanding at the molecular level is lacking.

In this study, we reconstructed a cryo–electron microscopy (cryo-EM) model in which a split-end endogenous double-stranded DNA (dsDNA) is bound to the exterior surface of ORF2p and an RNA/DNA hybrid is located in the RT active site channel. We observed conformational changes of key RT active site residues upon the binding of deoxynucleotide triphosphate (dNTP) and metal ions. The derived structure model depicts an evolutionary link between the TPRT mechanisms of human L1, insect R2, and group II introns (*27*–*29*). We also discovered that ORF2p is a structure-dependent endonuclease. This finding provides a mechanistic basis for the predominant S phase integration of L1 (*23*–*26*).

Purification and cryo-EM reconstruction of ORF2p complexes

Full-length ORF2p was produced both in insect High Five (Hi5) and human embryonic kidney 293F (HEK293F) cells. The N-terminal FLAG-tagged and C-terminal Strep-tagged ORF2p was purified through sequential steps of streptavidin affinity, cation-exchange, and size-exclusion chromatography. Regardless of the expression host, the last step of the purification procedure, conducted at 1 M NaCl, eluted two peaks of highly purified ORF2p, yet persistent presence of nucleic acids (NAs) was evident (Fig. 1, A and B). Denaturing urea polyacrylamide gel electrophoresis (PAGE) analysis revealed that the predominant species of copurifying NA was DNA, judging from the outcome of ribonuclease (RNase) and deoxyribonuclease (DNase) digestions (Fig. 1C and fig. S1A). Consistently, the DNase-treated sample eluted from the sizing column later than the untreated sample (peak 2), whereas the RNase-treated sample behaved nearly the same way as the untreated sample (Fig. 1D).

The nuclease-treated samples were prone to aggregation and precipitation under conditions suitable for cryo-EM studies. Therefore, the peak 2 sample from insect cells was used for single-particle cryo-EM analysis without nuclease treatment. Two datasets yielded a 3.60-Å map, which encompasses all ORF2p domains, and a 3.3-Å map, in which the EN domain was disordered (Fig. 1, E and F, and figs. S1 and S2). In both maps, in addition to the protein density, two conspicuous pieces of extra densities were attributable to NA (Fig. 1, E and F). The A-form duplex bound inside the RT active site channel of ORF2p can clearly be identified as the RNA/cDNA hybrid. The B-form double-stranded NA (dsNA) density with a single-stranded extension bound to the outer surface of ORF2p was DNA from host cells, according to our earlier analysis (Fig. 1, C and D). The assignment of DNA matches the structure model determined by Ghanim *et al.* (*30*) but differs from an earlier L1 RNP model in which an A-form dsRNA segment was fitted

[1]State Key Laboratory of Epigenetic Regulation and Intervention, Institute of Biophysics, Chinese Academy of Sciences, Beijing, China. [2]School of Life Sciences, University of Chinese Academy of Sciences, Beijing, China. [3]New Cornerstone Science Laboratory, Institute of Biophysics, Chinese Academy of Sciences, Beijing, China. [4]Key Laboratory of Systems Health Science of Zhejiang Province, School of Life Science, Hangzhou Institute for Advanced Study, University of Chinese Academy of Sciences, Hangzhou, Zhejiang, China. ***Corresponding authors. Email: jinwenxing@ibp.ac.cn (W.J.); rmxu@ibp.ac.cn (R.-M.X.)** ‡Present address: MRC Laboratory of Molecular Biology, Cambridge, UK. †These authors contributed equally to this work.

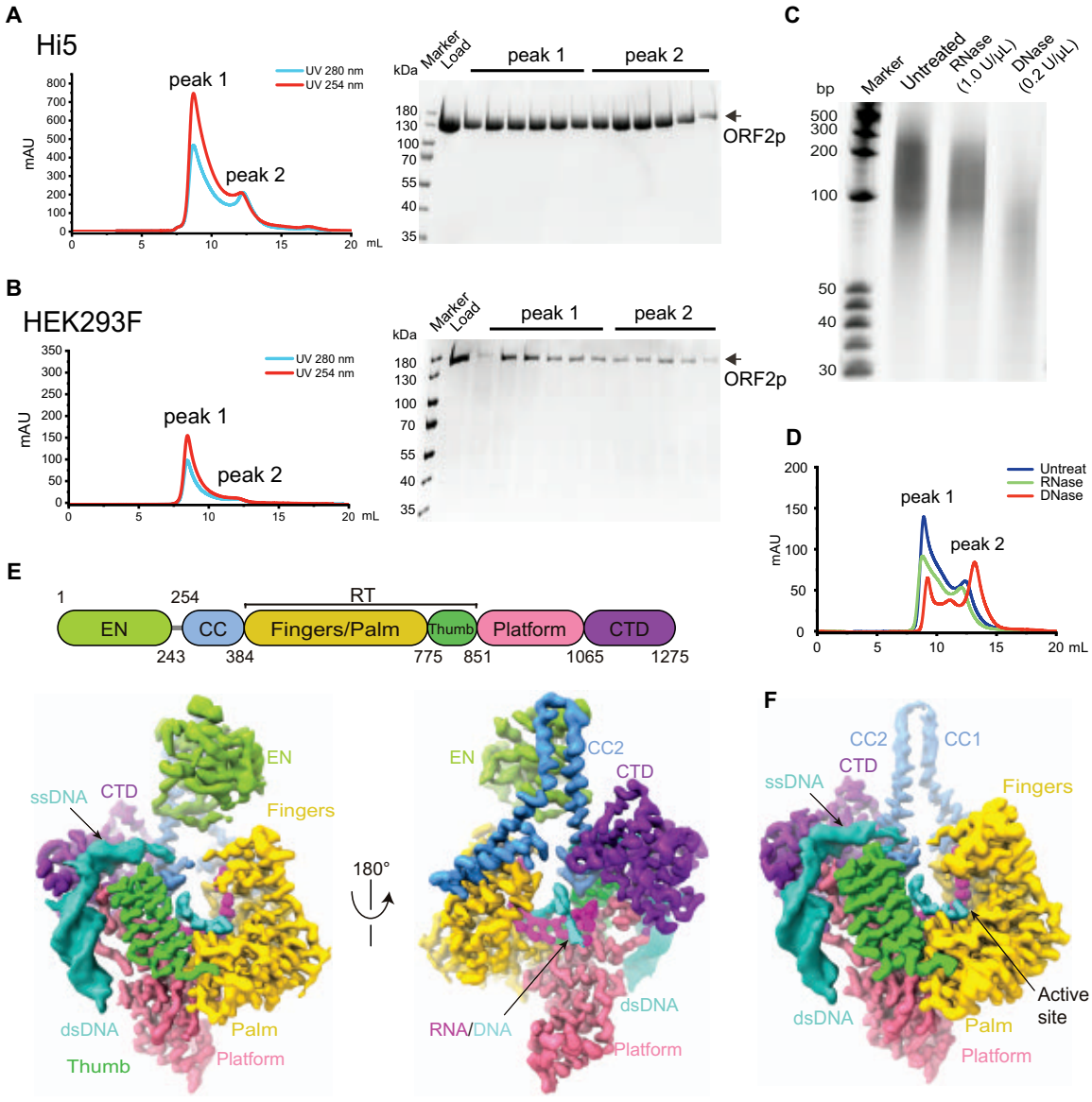


Fig. 1. ORF2p sample preparation and cryo-EM 3D reconstruction. (**A**) (Left) Sizing column elution profile of ORF2p produced in Hi5 cells. Ultraviolet (UV) absorptions at 280 and 254 nm are plotted in cyan and red curves, respectively. (Right) Coomassie-stained SDS-PAGE analysis of eluted fractions shown in the left panel. mAU, milli-absorbance units. (**B**) Left and right panels show the same analyses as in (A), with the ORF2p sample produced in HEK293F cells. (**C**) Urea PAGE gel analysis showing copurified nucleic acids in peak 2 fractions in (A). DNase or RNase treatment of the Hi5 cell–produced ORF2p was conducted between the strep-affinity and heparin column steps. Lanes from left to right: DNA marker in base pairs, untreated sample, RNase-treated sample, and DNase-treated sample, respectively. (**D**) UV 280-nm sizing column elution profile of the samples shown in (C). The blue, green, and red lines represent those of untreated sample, RNase-treated sample, and DNase-treated sample, respectively. (**E**) Front (bottom left) and back (bottom right) views of the 3.6-Å cryo-EM density map of ORF2p with copurified endogenous nucleic acids. Protein density regions are colored according to the coloring scheme of the protein domains shown at the top. Putative DNA densities are colored cyan, and the density for RNA is colored magenta. (**F**) Front view of the 3.3-Å density map from a separately prepared cryo-EM sample.

into the nearly identical B-form density (*31*, *32*) (fig. S3, A and B). A series of analyses below further corroborated our assignment.

We first asked whether partial digestion of ORF2p with DNase or RNase would selectively affect the exterior NA density. Cryo-EM samples prepared from digestion with 0.1 to 0.2 U/μl of DNase showed mildly to highly aggregated particles, while those treated with 0.6 to 1.0 U/μl of RNase had no obvious changes (fig. S4, A and B). One cryo-EM dataset from a sample treated with 0.1 U/μl of DNase and another dataset from 0.6 U/μl of RNase treatment were collected (fig. S4C). The same procedure and standard of data processing were applied, and the two sets of particles—after two-dimensional (2D) classifications—were merged for 3D classifications. This procedure yielded two major classes of well-formed particles: The larger class (Class 1) showed an intact dsNA density, whereas the density was missing in Class 2 particles (fig. S4C). The substantially higher percentage of ORF2p particles with the RNase-resistant dsNA density, compared with those treated with DNase, supports the assignment of DNA to the extra NA density (fig. S4C).

Sequencing of copurified DNA in peak 2 samples from both HEK293F (Fig. 2A) and Hi5 (fig. S5A) cells showed the presence of diverse genomic DNA elements, notably satellite and repeat sequences (*33*, *34*) (Fig. 2, A and B). Of the identified DNA peak regions [peak plus

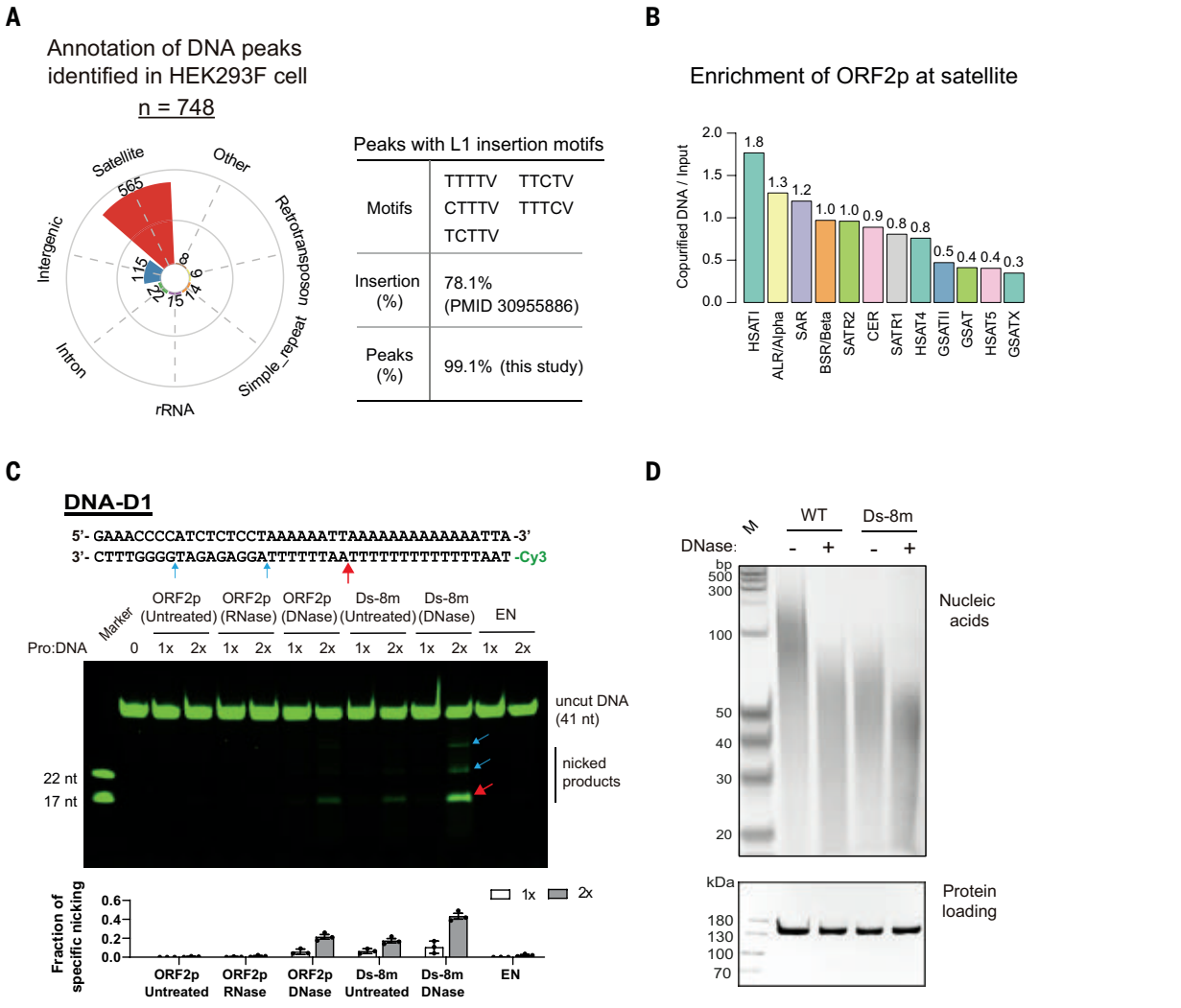


Fig. 2. Identification of DNA bound to ORF2p. (**A**) High-throughput sequencing results of copurified DNA. (Left) Circular bar plot showing distribution of DNA peaks in samples prepared from HEK293F cells. DNA peaks were identified with the MACS2 program. DNA extracted from the total lysate before protein purification was set as the input control, and the threshold was set with the option of '-q 1e-3''. (Right) The L1 insertion motifs identified by Flasch *et al*. (*23*) were found in 741 of the DNA peaks. (**B**) Bar plots showing the ratios between the percentage of sequence reads mapped onto the indicated satellite repeats in the peak 2 sample and the percentage in the input sample before purification. (**C**) (Top) DNA substrate used for the ORF2p nicking assay. (Middle) Denaturing urea PAGE analysis showing DNA nicking activities of ORF2p samples with and without pretreatment of DNase and RNase; 0.8 pmol of DNA, 1× and 2× amount of ORF2p, a putative dsNA binding defective mutant (ds-8m: K842, K858, K876, K880, R945, K946, K1063, and N1066 all changed to Ala), and the EN domain alone were used in the reactions. Red and blue arrows indicate the major and minor cleavage products, respectively. Single-letter abbreviations for the amino acid residues are as follows: A, Ala; D, Asp; F, Phe; I, Ile; K, Lys; N, Asn; Q, Gln; R, Arg; S, Ser; and W, Trp. (Bottom) Bar plots showing the nicking efficiency—defined by the ratio of the densiometric intensity of the nicked products and that of the entire lane—of the above reactions. Error bars represent SEM derived from three repeats. (**D**) (Top) Urea PAGE gel analysis of DNA copurified with wild type (WT) or the ds-8m mutant of ORF2p, performed as shown in Fig. 1C. (Bottom) SDS-PAGE analysis of ORF2p shown as a loading control.

50 base pairs (bps) at end], 99.1% contain short DNA sequence motifs frequently associated with L1 insertions in human cell lines (*23*) (Fig. 2A). Lastly, we reasoned that ORF2p-bound endogenous DNA may interfere with ORF2p's binding to DNA substrates, thus affecting the DNA nicking activity in vitro. We tested this hypothesis by a nuclease activity assay using the peak 2 sample directly or ORF2p samples with an extra step of DNase or RNase digestion before the last two steps of purification. A 41-bp dsDNA (DNA-1) with Cy3 fused to the 5′ end of the strand bearing two tandem EN cleavage motifs was used as a substrate. The results showed that the DNase-treated ORF2p cut DNA much more efficiently than the untreated or RNase-treated ORF2p did (Fig. 2C). This enhancement of ORF2p nuclease activity was due to reduction of DNA binding by DNase treatment, because ds-8m—an ORF2p mutant substituting eight positively charged amino acids to alanines at the putative dsDNA binding region—bound much less NA and showed an elevated level of EN activity even without DNase treatment (Fig. 2, C and D). DNase treatment of ds-8m further reduced the amount of bound NA and boosted its nuclease activity.

Sequencing of copurified RNA identified a host of cellular transcripts enriched through the purification process of HEK293F cell–expressed ORF2p (fig. S5B). Collectively, the markedly enriched RNAs tended to be those of highly expressed host genes (fig. S5C). For comparison, the codon-optimized ORF2p mRNA was enriched approximately fivefold, whereas two Alu RNAs were enriched shy of threefold (fig. S5B). This finding suggests that ORF2p can bind a wide range of cellular RNAs when L1 is overexpressed, such as in certain diseases.

Overall structure and the RT active site

A complete model encompassing all functional domains and a model lacking the EN domain of ORF2p were built from the 3.6-Å and 3.3-Å maps, respectively (Fig. 3, A and B; fig. S6; and table S1). Overall, the full-length model agrees well with the AlphaFold2-predicted model [root-mean-squared deviation (RMSD) 1.85Å; fig. S6J] or previously determined cryo-EM structures, which aligned with the full-length ORF2p with RMSDs of 1.51 Å (PDB ID: 9HDO), 1.43 Å (PDB ID: 8UW3), and 1.48 Å (PDB ID: 8C8J) (*30*, *31*, *35*). The EN domain appeared to be mobile, as evidenced by its relatively lower regional resolution (5 to 6.5 Å) (fig. S1F). Excluding the EN domain, the two ORF2p models are nearly identical (RMSD 0.51 Å). Subsequently, we will use the two models interchangeably in describing the structure, unless explicitly specified otherwise.

Except for the EN domain, all parts of ORF2p fold into a compact structure centered around the RT catalytic core, which is composed of the evolutionarily conserved fingers, palm, and thumb subdomains spatially arranged as those in the catalytic subunit of HIV-1 RT (*36*). The platform and the C-terminal domains (CTDs) pack against the thumb subdomain, and the towering coiled-coil (CC) domain bridges the fingers and thumb subdomains above the RT active site channel, where an RNA/cDNA hybrid is bound (Fig. 3, A and B). A total of 10 base-paired and 2 unpaired 5′ RNA bases and 10 completely paired DNA bases were modeled (Fig. 3C). The catalytic active site is located next to the 3′ end of cDNA, and the structure is highly conserved among distinct RTs (fig. S7). In particular, Asp702 and Asp703 of the FADD motif contact the last nucleotide at the 3′ end of cDNA (Fig. 3C).

Compared with the crystal structure of the ORF2p core domain, our structure does not have a dNTP and a divalent metal ion bound in the RT active site (*35*). To probe dynamic changes of active site residues during the RT reaction, we determined a cryo-EM structure of ORF2p bound to dNTP and $MnCl_2$ at 3.0 Å (fig. S8, A to E). Mn^{2+} competed for the Mg^{2+} binding site, and its density allowed easier visualization by cryo-EM (*37*, *38*). The cryo-EM map showed extra densities for a dNTP and a Mn^{2+} ion next to the 3′ end of cDNA (Fig. 3C), and the entire RT active site structure agrees well with the crystal structure (*35*) (fig. S8F). Asp600 coordinates the binding of the Mn^{2+} ion, together with Asp702 and Asp703 of the FADD motif, and occupies a key position to facilitate the covalent incorporation of dNTP to the 3′ end of the cDNA (Fig. 3D). Lys519 and Arg531 become ordered upon the binding of dNTP and interact with the phosphate groups of dNTP together with Lys737. The sugar moiety of dNTP rests against Ala604, Phe605, and Gln659 (Fig. 3, C and D). The functional consequences of these observations are supported by mutagenesis results (*8*, *39*) (fig. S7C).

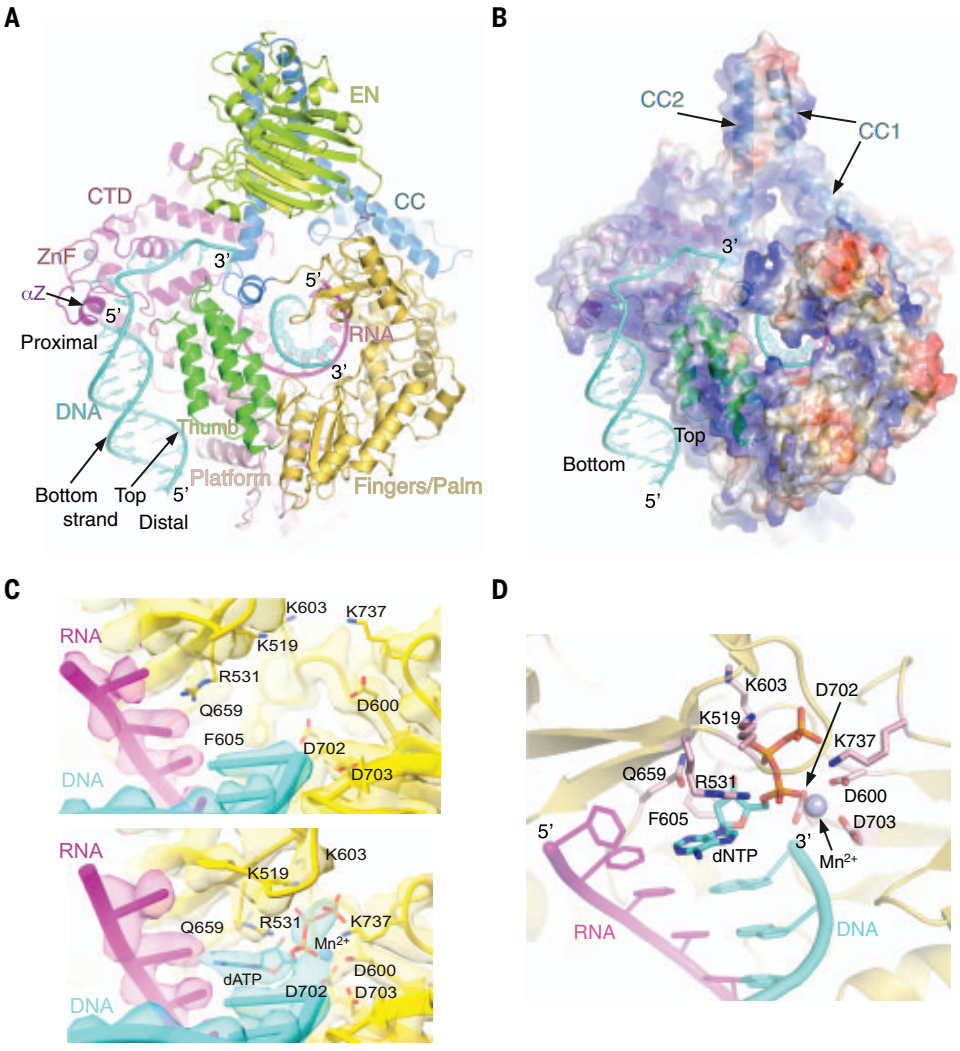


Fig. 3. Overall structure of the ORF2p complex. (**A**) Cartoon representation of the 3.6-Å structure in which all domains of ORF2p are ordered. Protein domains are colored as in Fig. 1E and labeled, DNA is colored cyan, and RNA is colored magenta. The structure is shown in the front view as in Fig. 1E. (**B**) Front view of the 3.3-Å structure in which the endonuclease (EN) domain is disordered. The protein is shown in a surface representation colored according to electrostatic potential distribution (blue, positive; white, neutral; red, negative). The semitransparent surface is superimposed with the cartoon model of the structure colored as in (A). The coiled-coil domain helices 1 and 2 (CC1 and CC2) are labeled. (**C**) The RT catalytic active site without dNTP bound (top) and with dNTP bound (bottom). Relevant ORF2p residues are shown in a stick model. (**D**) A close view of configuration of the ORF2p RT active site in the presence of dNTP and a manganese ion.

DNA binding mode

A 12-bp dsDNA is modeled into the helical portion of the density adjacent to an extensive positively charged surface region along the border between the platform and the CTD domains (Fig. 3, A and B). The double-stranded portion is interrupted by the insertion of a protruded α helix, termed α_Z here, located N-terminal to the CCHC (Cys1130, 1134, and 1147, and His1142) zinc finger (ZnF) in the CTD of ORF2p (Fig. 4A). The functionally important ZnF stabilizes α_Z for interaction with DNA (*8*). The top strand of DNA has an 8-nucleotide (nt) single-stranded 3′-extension, which runs toward the center of ORF2p along a cleft formed between the CTD and thumb domains (Fig. 4A). Additional weak densities beyond the distal end of the dsDNA were visible but could not be reliably modeled, suggesting a heterogeneous conformation there.

Numerous positively charged residues are located within bonding distances to

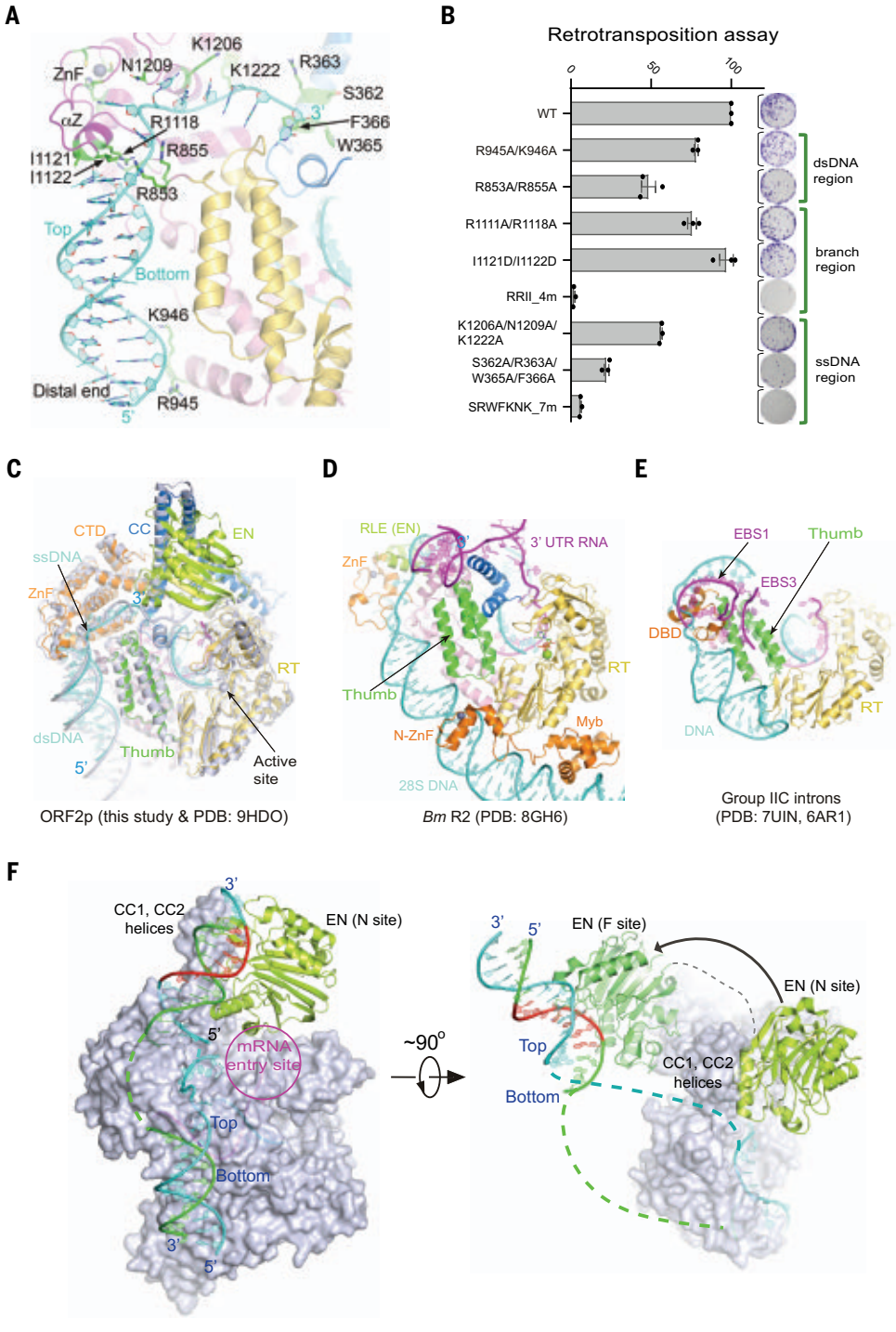


Fig. 4. DNA binding mode of ORF2p. (**A**) Close view of ORF2p-DNA interactions. Involved ORF2p residues are shown as sticks and labeled. (**B**) Cellular retrotransposition assay in HeLa cells. (Right) Images of G418 (Gibco)–resistant HeLa cell colonies from transfection of pBS-L1PA1 plasmids carrying WT or mutant ORF2 constructs in a six-well plate. (Left) Quantification of colony formation in transfections shown to the right. RRII_4m indicates the R1111A/R1118A/I1121D/I1122D quadruple mutation, and SRWFKNK indicates the heptad mutant combining the triple and tetra mutations shown immediately above it. The mean colony numbers in cells transfected with the WT construct are set at 100%, and error bars represent SEM derived from three repeats. (**C** to **E**) Side-by-side comparison of the ORF2p, which is shown as a superposition of structures from this study and that of PDB ID 9HDO, R2Bm (PDB ID 8GH6), and group IIC intron complex structures, placed in the same viewing direction by aligning the RT domains. The latter was prepared from PDB ID 7UIN with the coordinates of DNA, maturase, and the EBS1/3 RNA fragments; and the coordinates for the superimposed RNA/DNA hybrid were obtained from PDB ID 6AR1 by aligning the structures of two maturases. DBD, DNA binding domain; EBS, exon binding site; UTR, untranslated region. (**F**) (Left) Superposition of the EN-DNA cocrystal structure (PDB ID 7N8S) by aligning the EN domain structure with that in the full-length ORF2p structure. The EN location is designated the "N" site. Hypothetical joining of DNA strands between superimposed structures is indicated with dashed lines (green, bottom strand; cyan, top strand). The red-colored DNA region indicates the TTTTT/AA EN nicking motif. The pink circle denotes the mRNA entry region of the ORF2p RT active site channel. (Right) An alternative location of the EN domain (F site, colored lime) obtained by rotating around the CC domain helices, indicated by the curved arrow. The gray dashed line indicates the covalent link between the EN domain and the rest of ORF2p. Hypothetical joining of DNA strands between the modeled EN-DNA complex and that in the cryo-EM structure is indicated by green and cyan dashed lines. An EN domain in position N is shown for reference.

the backbone of the dsDNA but without any apparent base contacts. Selective DNA backbone contacts include charged residues Arg945 and Lys946 near the distal end of dsDNA and Arg853 and Arg855 next to the proximal end (Fig. 4A). An R945A K946A (R945/K946→A/A) double mutation resulted in a noticeable but insignificant reduction of L1 retrotransposition activity, whereas the R853A/R855A double mutation showed a more appreciable effect (Fig. 4B). At the proximal end, the protruded α_Z of ORF2p caps the dsDNA and splits the two strands. In particular, Ile1121 and Ile1122 make hydrophobic and van der Waals interactions with the last paired bases of the DNA duplex, whereas Arg1118 also from α_Z and Arg1111 from a neighboring loop contact the backbone near the 5′-end of the bottom strand. Each of the I1121D/I1122D and R1111A/R1118A double mutants appeared to have small effects on the L1 activity, but a combination of both was detrimental (Fig. 4B).

The single-stranded DNA (ssDNA) portion of the top strand occupies the cleft between the CTD and the thumb subdomain and spans the N-terminal end of α_Z in the CTD and the C-terminal region of the CC domain (Fig. 4A). The bottom of the ssDNA binding cleft is positively charged, and the ssDNA is bound with the backbone against the bottom of the cleft and the nucleotide bases facing outward. Several CTD residues located at the rim of the cleft, including Lys1206, Asn1209, and Lys1222—and a handful of residues at the C-terminal end of the CC2 helix, including Ser362, Arg363, Trp365

and Phe366—are in position to interact with ssDNA. Changing all three CTD residues, all four CC2 residues or both sets of residues to alanines showed obvious defects in L1 retrotransposition (Fig. 4B).

Comparison of DNA binding modes

ORF2p binds DNA in a manner highly similar to that of a recently determined structure (Fig. 4C) (*30*). Comparing the DNA binding mode of ORF2p with that of R2Bm and the group IIC intron maturase revealed interesting similarities and differences (*27*–*30*, *40*). DNA targets are spatially positioned with respect to the proteins in an evolutionarily related manner (Fig. 4, C to E). There are three noticeable differences: First, the dsDNA bound to the maturase of group IIC intron is not in a canonical B form owing to extensive interactions with the co-bound RNA, which was mostly omitted in the figure for viewing clarity (*29*). Second, the dsDNA bound to R2Bm and the IIC maturase are tilted toward the thumb domain by ~40° compared with that in the ORF2p structure because ORF2p has a more extensive dsDNA-interacting interface on its platform domain (Fig. 4A). Third, different DNA targeting mechanisms are used by the three RTs. Recognition of 28*S* rDNA by R2Bm is achieved through the binding of the ZnF and Myb modules to specific sequences upstream of the cleavage site (*27*, *28*). Group IIC intron recognizes DNA through interaction between the maturase's DNA binding domain and the forked and single-stranded regions of DNA, as well as base pairings between the intronic RNA and DNA (*29*) (Fig. 4E). In the ORF2p complex, only sequence-independent interactions between the DNA backbone and ORF2p were observed. This observation provided the structural basis for the observed lack of sequence preferences in L1 integration (*23*, *24*).

Additionally, an α helix in the ZnF module of both ORF2p and R2Bm unwinds a DNA region upstream of the nicking site. In the group IIC intron, a pair of short helices play the same role in the absence of a ZnF module. In all three proteins, the ZnF and its counterpart play a conserved role of directing the binding of the 3′-end ssDNA tail (Fig. 4, C to E). By contrast, the group IIC intron maturase does not contain an EN domain, and the DNA-nicking restriction-like EN (RLE) domain of R2Bm is located at the C-terminal end of the protein and is rigidly tethered to the ZnF, placing the RLE in an active position for nicking DNA (*27*, *28*). In L1 ORF2p, the EN domain is located at the N terminus and is flexibly placed against the CC domain helices in one structure and disordered in others. The observed EN domain position, designated position "N" here for its location near the mRNA entry site, is not in an enzymatically active conformation for nicking the bottom strand because it is not near DNA and sits on top of the mRNA entry side of the RT active site channel (Fig. 4, C and F). At the start of TPRT, the 5′ portion of the mRNA lining up outside of the channel can easily bump into the EN domain. We superimposed the cocrystal structure of the ORF2p EN domain with DNA onto the EN domain (site N) in the structure of full-length ORF2p (*41*). Notably, the 5′ end of the strand ready to be nicked by EN is placed near the 3′ end of the top strand ssDNA in the current structure. Two hypothetical continuous DNA strands in the superimposed structure can be depicted (Fig. 4F). In this model, however, the top strand is lined up with the EN domain for nicking.

For the nicking of the bottom strand of DNA to initiate TPRT, we prefer an alternative model in which the EN domain swings around the long CC domain helices and points the opposite end of DNA toward the core domains of ORF2p (Fig. 4F). We call this alternative position of the EN domain position "F" for its location far away from the mRNA entry site. This assumption is not unfounded because we did observe weak, diffuse densities next to the CC helices in 2D classifications of images that gave rise to a disordered EN domain (fig. S2A). Additionally, dynamic positioning of the EN domain with respect to the RT core domains were observed in other cryo-EM and modeling studies (*30*, *35*, *42*). Placing the EN-DNA cocrystal structure at position F allows the construction of a model in which EN nicks the bottom strand. In this scenario, upon the nicking and the release of the EN domain, the 3′-end of the bottom strand has sufficient freedom to access the RT active site to prime the RT reaction.

ORF2p is a structure-dependent endonuclease

Observation of the unwound dsDNA bound to ORF2p led us to explore whether the structure of DNA had an impact on ORF2p's DNA nicking activity. Using the DNase-treated ORF2p sample for the EN activity assay, we found that a forked structure located 5′ to the DNA cleavage motif (Y5) significantly enhanced ORF2p's cleavage efficiency, whereas only a basal level of cleavage activity was observed for a perfectly paired DNA (Fig. 5A). No such enhancement was observed when the fork was located 3′ to the cleavage motif (Y3), demonstrating a clear preference for the directionality of the DNA forks. For an efficient and specific cut of the DNA strand, we showed that a distance of 6 to 10 bp between the branch point and the DNA cleavage site—and a cleavage motif with a minimum of four consecutive thymines preceding an adenine—was needed (fig. S9, A and B).

On the opposite (top) strand, which lacks a run of thymines, the ORF2p cut occurred specifically in TA or TC dinucleotides 8 to 12 bp away from the major cleavage site on the bottom strand, regardless of the orientation of the DNA forks (Fig. 5A). As expected, the cleavage efficiency was also higher when the fork was located 5′ to the cleaved strand. In addition to the TA and TC junctions, cleavage between a TG dinucleotide was also observed (fig. S10A).

Considering the link between L1 retrotransposition and DNA replication (*23*–*26*), we also tested the ability of ORF2p to cleave 5′-flap DNA, which is a major intermediate in the lagging strand replication. A 5′-TTTTTT/AA-3′ ORF2p cleavage motif was placed on the parental (bottom) or the newly synthesized (top) strand 8 nt away from either side of the flap (Fig. 5B). We found that, when the cleavage motif was located on the parental strand, ORF2p preferentially cleaved the site positioned to the left of the flap; and the preferential cleavage site was swapped when the cleavage motif was placed on the Okazaki fragment (Fig. 5B). Cleavage results on the opposite strand are shown in fig. S10B.

Discussion

In this study, we uncovered important aspects of the L1 TPRT mechanism, including the manner by which ORF2p engages DNA, the interplay between DNA binding and the EN activity during TPRT, and the impact of DNA structure on the EN activity. We first determined the structures of ORF2p bound to copurified endogenous DNA. This finding firmly established the DNA binding mode of ORF2p during TPRT, together with the structure of the in vitro reconstituted complex (*30*). The structural information also allowed deeper insights into the TPRT mechanism of L1. For instance, the stably positioned EN domain that we and others observed, termed site N, appeared to be unsuited for making the initial cut on the strand bearing the ORF2p cleavage motif for two reasons. First, the EN domain is situated immediately above the mRNA entry channel of the RT active center, so it is likely to clash with the bound mRNA being reverse transcribed. Second, according to the EN domain-DNA cocrystal structure, the orientation of the EN domain is incompatible with the cleavage of the first strand of DNA (*41*) (Fig. 4F). Instead, the observed EN domain posture resembles one that is ready for making a cut on the second strand. On the basis of the DNA binding manner of the RLE domain of R2Bm and its functional similarity with the EN domain of L1 (*27*, *28*), and also on the basis of cryo-EM and molecular dynamics simulation results showing that the EN domain can adopt various conformations (*30*, *35*, *42*), we hypothesize that the EN domain may rotate around the CC domain helices, possibly under the influence of bound mRNA, to a location further from the mRNA entry channel, termed site F, where the EN active site aligns with the DNA scissile bond for the first nick (Fig. 4F).

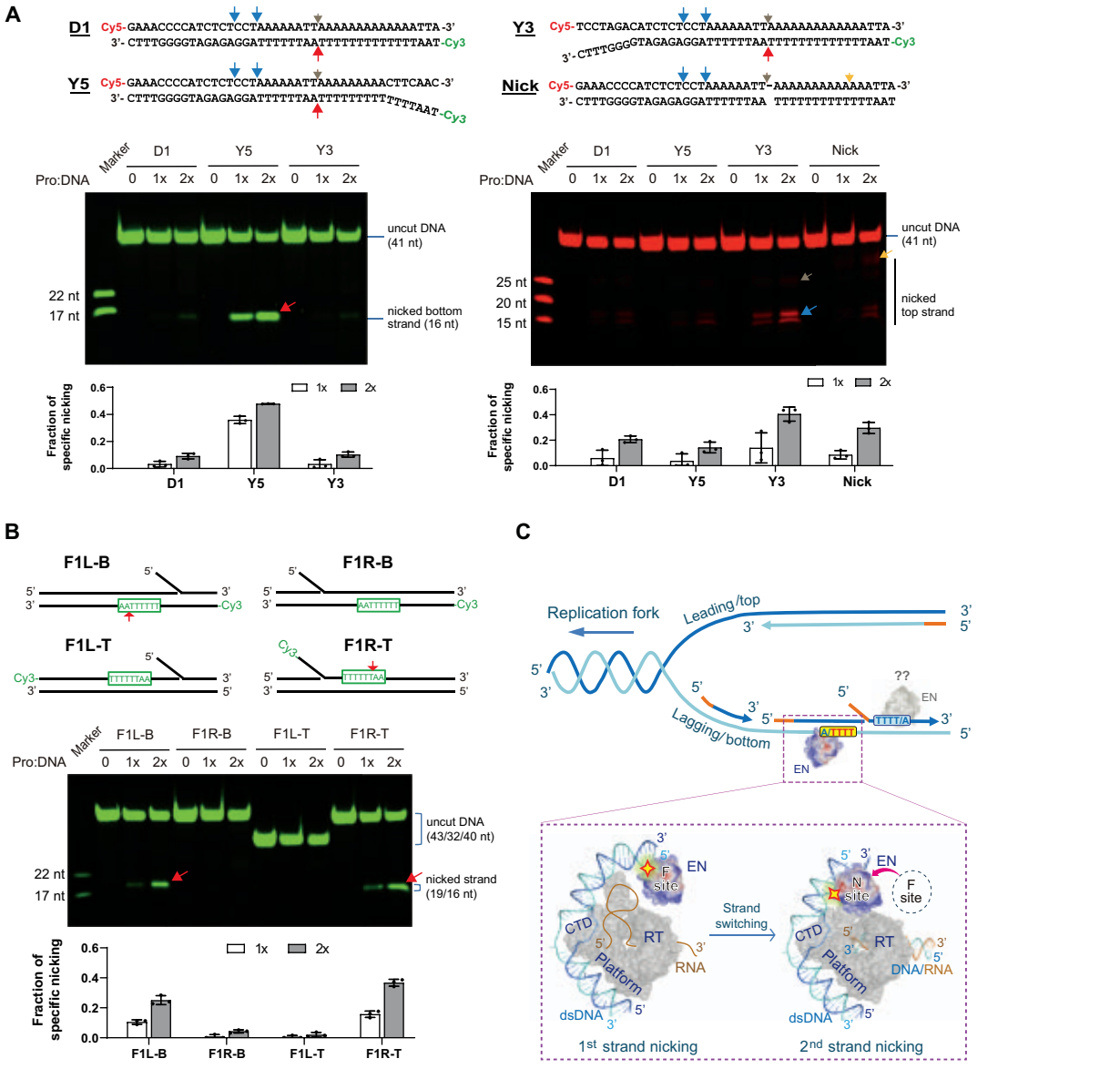


Fig. 5. ORF2p is a structure-selective endonuclease. (**A**) (Top) Sequences and structures of four DNA substrates used for assaying the DNA nicking activity of ORF2p. For D1, Y5, and Y3, the 5′-end of the bottom strand carrying the ORF2p nicking motif (TTTTTT/AA) is fused with a Cy3, and the 5′-end of the opposite strand is fused with a Cy5. The "Nick" DNA mimics a pre-nick substrate where the linkage between T and A in the nicking motif is not joined and there is no Cy3 fused. The colored arrows indicate the nick positions revealed below. (Middle) Denaturing urea PAGE analysis of ORF2p cleavage reactions, performed with DNase-treated ORF2p as described in Fig. 2C. The left panel shows the cleavage of the bottom strand of the indicated DNAs. The red arrow indicates the position of the Cy3-fused cleavage product. The right panel shows the cleavage of the top strand detected by Cy5. The colored arrows point to cleavage products nicked at the positions indicated by the same color arrows shown above the DNA sequences at the top. (Bottom) Bar plots showing the nicking efficiency of the reactions shown above. Error bars represent SEM derived from three repeats. (**B**) The top four panels show schematics of 5′ flap DNAs used for the ORF2p nicking assay. The ORF2p cleavage motif is placed at the locations indicated by the green boxes. (Middle) Representative gel of a denaturing urea PAGE analysis of ORF2p (with DNase treatment) cleavage reactions. (Bottom) Bar plots showing quantitation of the ORF2p cleavage activities in reactions as shown above. Error bars represent SEM derived from three repeats. (**C**) Spring-loaded model of L1 retrotransposition. First, ORF2p targets EN cleavage sites located near 5′-flaps in the parental (bottom) strand during lagging strand synthesis. The EN cleavage site on the top strand is an equally good substrate of ORF2p in vitro, but the reason for its being suppressed in vivo is unknown (indicated with question marks). Possible subsequent steps are depicted in the inset: As shown in Fig. 4F, the observed EN domain position (site N) near the template RNA entry channel is a preferential conformation in the absence of mRNA. The presence of mRNA triggers it to rotate out to a far site (site F). The two EN positions have opposite DNA binding directionality. The first DNA strand cleavage occurs when EN is in site F, where the EN domain orientation matches the direction of the cleavage motif on DNA. The exit of mRNA from the RT active site makes room for the EN to return to site N, where the EN domain aligns with the direction of the cleavage motif on the second strand.

We also discovered that ORF2p preferentially nicked forked or flap DNA, and this preference is highly sensitive to the direction of the ORF2p cleavage motif with respect to the fork or flap structure. A single-stranded extension upstream of the cleavage site also enhanced the efficiency of DNA nicking (*31*), although at a lower level compared with that of a 5′ forked DNA having an identical cleavage motif and a single-stranded region of the same length (fig. S10C). The 5′ forked structure may mimic the lagging strand template in front of the replication fork or the unwound DNA to be cut at the bottom strand (Fig. 4F). The F1L-B and F1R-T 5′-flap DNA also carry the same consensus

cleavage motif (fig. S10B), and they were cut with similar efficiencies. The preferential cut of F1L-B by ORF2p conforms to the cleavage preferences found through genomic analyses (Fig. 5B) (*23*, *24*, *26*). Efficient nick of the Okazaki-like fragment F1R-T was observed in vitro, but no preferential cleavage of these sites in cells has been reported. It is possible that they are protected by Okazaki fragment maturation factors, such as FEN1 (*43*).

Combined with the knowledge of predominant L1 retrotransposition in S phase and our discovery of ORF2p's property of preferential nicking of structured DNA, we have proposed a spring-loaded model of L1 retrotransposition, in which the EN domain conformational change, possibly through sensing the stage of reverse transcription, may play an important role in regulating the cleavage reaction on distinct strands of DNA (Fig. 5C). It should be pointed out that L1 retrotransposition also occurs in an EN-independent manner and in nondividing cells (*23*, *44*–*46*). Clearly, the molecular mechanisms active there require separate in-depth investigations.

Materials and methods

Plasmids and protein purification

Codon optimized human L1 ORF2p coding sequence was amplified from pBS-L1PA1-CH-mneo (Addgene #51288) (*47*) and cloned into pFastBac1 (Invitrogen). Flag and strep tags were engineered to fuse to the N- and C terminus of ORF2p, respectively. Expression of ORF2p (wild type or its ds-8m mutant) was achieved in insect Hi5 cells using the Bac-to-Bac baculovirus expression system (Invitrogen). For protein purification, cells from 1 liter culture were harvested at 48 hours post infection and resuspended in the lysis buffer containing 40 mM Tris (pH 8.0), 500 mM NaCl, 5% glycerol and 1/100 protease inhibitor cocktail (APExBIO). After extensive sonication, the protein was affinity purified by Strep-Tactin XT beads (IBA Life Science) and eluted in buffer A, which contains 20 mM HEPES (pH 7.0), 250 mM NaCl, 200 mM D-biotin, 1/100 protease inhibitor and 5% glycerol. The eluted sample was then loaded onto a heparin sepharose column. The eluted fractions highly enriched with ORF2p were pooled and concentrated before loading onto a Superdex 200 increase 10/60 XK column (GE Healthcare) in buffer D-1000 containing 20 mM HEPES (pH 7.0), 1 M NaCl and 1 mM DTT. Fractions from the monomeric ORF2p peak (peak 2) were pooled and the salt concentration was lowered to 500 mM NaCl by dialysis in buffer D-500. After concentration, the sample was either directly used for the preparation of cryo-EM frozen-hydrated grids or stored at −80°C for later use.

DNase or RNase treatment of ORF2p samples for cryo-EM use was performed at 37°C for 90 min at specified enzyme concentrations in the buffer D-400 plus 5 mM $CaCl_2$ and 10 mM $MgCl_2$. Enzymatically digested ORF2p samples to be used for biochemical assays were prepared by DNase or RNase treatment of the sample between the strep affinity and heparin column chromatography steps at 30°C for 90 min in buffer A plus 5 mM $CaCl_2$ and 10 mM $MgCl_2$.

Expression of ORF2p in the HEK293F cell, which does not express SV40 T-antigen, was carried out by transient transfection of plasmids constructed by inserting the same ORF2p cassette as in pFastBac1 into the pCAG vector. Cells from ~4 liter culture were harvested at 48 hours post transfection, and the protein was purified following the same procedure as that for ones from insect cells.

The EN domain of ORF2p (1-237 aa) was produced in the BLE21(DE3)-RIL strain of *Escherichia coli* as an N-terminal GST-fused protein using the pGEX-6P vector. Protein production was induced with 0.3 mM IPTG for 20 hours at 16°C. Harvested cells were lysed by sonication in the buffer with 40 mM Tris (pH 8.0), 500 mM NaCl, 5% glycerol and 1/100 protease inhibitor cocktail. The protein was first purified with the glutathione resins (GE Healthcare), followed by elution from the resins and cleavage of the GST tag by PreScission protease. The sample was then subjected to successive heparin sepharose column followed by Superdex 75 increase 10/60 XK column chromatography in buffer D-1000. Highly purified EN fractions were pooled, concentrated and stored at −80°C for use.

Cryo-EM sample preparation and data collection

To prepare L1 ORF2p samples for cryo-EM study, 3 μl of protein at a concentration of ~1 mg/ml was loaded onto glow-discharged 300 mesh R2/1 CryoMatrix/Amorphous alloy film grid (Zhenjiang Lehua Technology), which was blotted for 4 s at 12°C and 100% humidity. Then the grid was plunged into liquid ethane using an FEI Vitrobot Mark IV (Thermo Fisher Scientific). The dNTP/Mn^{2+} bound complexes were prepared by incubating the ORF2p protein with 1 mM dNTP and 1 mM $MnCl_2$ on ice for 30 min before sample vitrification. Data were collected on a Talos Arctica (Thermo Fisher Scientific) machine operated at 200 kV and equipped with a K2 direct electron detector and a BioQuantum energy filter with an energy slit of 20 eV (Gatan). Images were recorded using SerialEM (*48*) in super-resolution mode by beam-image shift data collection methods (*49*) at a magnification of ×130,000, resulting in a pixel size of 0.5 Å. The exposure time was 5.2 s, with a total exposure dose of 50 $e^-/Å^2$ fractionated in 32 frames. Data were collected with the defocus range from −1.5 to −2.2 μm.

Three full data sets were collected from native ORF2p samples. Dataset-1, which turns out to have the EN domain missing (L1 w/o EN), contains a total of 10,200 movie stacks; dataset-2 collected from ORF2p soaked with dNTP/Mn^{2+} (L1 dNTP/Mn^{2+}) includes 6273 movie stacks; and dataset-3, which has an intact ORF2p (L1-full), contains 5638 movie stacks. Additionally, two smaller data sets were collected from RNase or DNase treated ORF2p samples. These data were intended for analysis of nucleic acids bound to ORF2p, not for full structure determination. A total of 3579 and 1773 movie stacks were collected for the RNase and DNase treated samples, respectively.

Image processing

All datasets were processed using similar image preprocessing and particles picking methods. Movie frames were motion corrected (5 by 5 patch) with twofold binning and dose-weighted in cryoSPARC (*50*), resulting in a pixel size of 1.0 Å. Contrast transfer function (CTF) parameters were estimated with the patch-based method in cryoSPARC. Automatic particles picking was performed using cryoSPARC blob picker for the initial round of 2D classification, which generates templates for particle auto-picking of the whole dataset.

For dataset-1 (L1 w/o EN), a total of 13,427,426 particles were picked and extracted twofold binning using a 256-pixel box size. After several rounds of 2D classification, a total of 1,691,967 particles were selected for cryoSPARC ab initio reconstruction and heterogeneous refinement. One highly populated class containing 543,326 particles with clear secondary structural features was re-extracted using a 256-pixel box size without binning and subjected to non-uniform refinement, yielding a reconstruction of ORF2p at 3.9-Å resolution. To further improve the overall resolution, we enlarged the box size to 384 pixels and performed non-uniform refinement, the resolution was improved to 3.4 Å. After global CTF refinement and local refinement with a mask covering the protein complex, we obtained a 3.3-Å resolution cryo-EM map of ORF2p.

For dataset-2 (L1 dNTP/Mn^{2+}), a total of 8,656,725 particles were picked and extracted twofold binning using a 256-pixel box size. After several rounds of 2D classification, a total of 1,016,461 particles were selected for cryoSPARC ab initio reconstruction and heterogeneous refinement. One highly populated class containing 268,444 particles with clear secondary structural features was re-extracted using a 384-pixel box size without binning and subjected to non-uniform refinement, yielding a reconstruction of ORF2p at 3.09-Å resolution. After global CTF refinement and local refinement with a mask covering the protein complex, a 3-Å resolution cryo-EM map was obtained.

For dataset-3 (L1-full), a total of 6,728,585 particles were picked and extracted twofold binning using a 256-pixel box size. After several

rounds of 2D classification, a total of 433,458 particles were selected for cryoSPARC ab initio reconstruction and heterogeneous refinement. One highly populated class containing 155,336 particles with clear secondary structural features was re-extracted using a 384-pixel box size without binning and subjected to non-uniform refinement, yielding a reconstruction at 3.8-Å resolution. After global CTF refinement and local refinement with a mask covering the protein complex, we obtained a 3.6-Å resolution cryo-EM map.

The final cryo-EM maps above were post-processed in deepEMhancer (*51*) to improve interpretability. All resolutions were estimated according to the gold-standard Fourier shell correlation value of 0.143 criterion.

For datasets collected from RNase and DNase treated samples, 2,459,968 and 1,194,304 particles were respectively picked and extracted twofold binning using a 256-pixel box size. After several rounds of 2D classification, 215,867 and 219,652 particles were combined and re-extracted for 3D classification in RELION (*52*). The combined dataset was separated into four classes, including two junk classes and two well-resolved classes, Class 1 and Class 2. Class 1, consisting of 288,172 particles, showed presence of dsNAs. Of these, 155,636 particles originated from the RNase treated samples, while the remaining 132,536 particles came from the DNase treated samples. Class 2, consisting of 115,184 particles, showed no apparent bound dsNAs. Within this class, 41,915 particles were attributed to the RNase-treated samples, while 73,269 particles were from the DNase-treated samples.

Further 3D classification was performed separately on Class 1 and Class 2 to investigate the binding manner of nucleic acids. The four subclasses derived from Class 1 still exhibited the bound nucleic acids, with slight variations in length. In contrast, the four classes from Class 2 showed a consistent binding pattern, with no obvious nucleic acids bound.

Model building, refinement, and validation

Initial model building of L1 ORF2p was aided by the Alphafold2 predicted structure, which was docked into the cryo-EM map using UCSF Chimera (*53*). The model was further fitted into the density using iMODFIT plugin (*54*). An ideal dsDNA was generated in COOT (*55*) and modeled into the helical portion of the exterior density. The model of the ssDNA portion was manually built according to the corresponding density. An RNA/DNA hybrid was generated in COOT and docked into the cryo-EM map and further fitted using iMODFIT in Chimera. The EN domain was deleted in building the model into the cryo-EM map lacking the corresponding density. For the sample with dNTP/Mn^{2+}, a dATP and an Mn ion were modeled in COOT. All the models were adjusted manually using COOT and subjected to rounds of relaxation into the density using Rosetta, real-space refined using PHENIX (*56*). Secondary-structure and Ramachandran restraints were applied. Finally, the model was validated with MolProbity (*57*) and statistics for model refinement and validation are shown in table S1. Cryo-EM density map and structural model figures were prepared using Chimera, ChimeraX (*58*), COOT and PyMOL (Schrödinger).

Retrotransposition assay

Retrotransposition assays were performed in HeLa cells as described (*8*, *39*). ORF2p mutants were generated based on the plasmid of pBS-L1PA1-CH-mneo containing a complete human L1 coding sequence (ORF1p and ORF2p) and an intron disrupting a neomycin gene in the opposite direction. HeLa cells cultured in DMEM (Hyclone) supplemented with 10% FBS were plated in six-well plates for 24 hours, reaching a cell density of 8×10^4 cells/ml prior to transfection. Each transfection used 1.5 μg of plasmid to mix with 100 μl of Opti-MEM (Thermo Fisher), 3 μl of p3000 and 6 μl of Lipofectamine 3000 (Thermo Fisher). Transfection reagents were removed 12 hours later by changing to fresh culture medium. At 72 hours post transfection, the medium was replaced with DMEM plus 10% FBS and 800 μg/ml of G418 (Gibco). In the next 12 days, change to fresh medium with G418 took place every other day till the appearance of colonies. To count the G418 resistant colonies, cells were washed with PBS, fixed with 4% paraformaldehyde for 15 min on ice, and then stained with 0.1% crystal violet for 15 min at room temperature.

Sequencing of ORF2p bound DNA and RNA

Purified ORF2p-nucleic acid complexes from insect Hi5 or HEK293F cells were first digested with 0.1 mg/ml protease K plus 0.1% SDS at 50°C for 3 hours followed by phenol-chloroform extraction. Nucleic acids were then precipitated with 2.5× volume of ethanol, 300 mM NaOAc (pH 5.2) at −20°C and recovered by dissolving the precipitant in DEPC water. For DNA or RNA library preparation, the nucleic acids were treated with RNase A (Omega) or DNase 1 (Thermo Fisher) respectively, extracted by phenol chloroform and precipitated with 300 mM NaOAc (pH 5.2) and 2.5× volume of 100% ice-cold ethanol. DNA or RNA libraries were prepared using VAHTS library prep kit (ND610 or NR605) for Illumina sequencing (Novogene).

DNA-seq data analysis

Sequencing reads were first processed to remove adapters and low-quality sequences using Trim Galore (https://www.bioinformatics.babraham.ac.uk/projects/trim_galore/) with default parameters. The trimmed reads were then mapped to the reference genomes (hg38 for human HEK293F cell line data and tn1 (downloaded from https://cabbagelooper.org/) for cabbage looper Hi5 cell line data) using Bowtie2 (v2.3.4.4) (*59*). PCR duplicates were removed using SAMtools (v1.3.1) (*60*). Reads with a MAPQ score of 1 or >= 40 were retained using SAMtools (v1.3.1). To avoid potential interference by cDNA signal originating from the ORF2p activity, only non-exonal peaks were chosen for further identification. Peak identification was conducted using MACS2 (v2.1.1) (*61*) with the '-f BAMPE -g hs -q1e-3′ parameters. DNA extracted from the total lysate prior to protein purification was set as input control. Annotation was performed using the annotatePeaks.pl function in HOMER (*62*). Fragment length distributions for paired-end sequencing reads from both copurified and input DNA were calculated using the bamPEFragmentSize module from deepTools with the parameter '-n 100000'.

RNA-seq data analysis

After removing adapters and low-quality sequences as done in DNA-seq data analysis, rRNA was removed using BBMap (v38.90). Then filtered paired-end reads were aligned to the human reference genome (hg38) using STAR (v2.7.9a) (*63*) with default parameters. Read counts were calculated using featureCounts (*64*). RNA fold enrichments between ORF2p-bound RNA and input control RNA from total cell lysate were calculated using the R package edgeR (*65*). RNAs with read count >100 were kept for enrichment analysis. An RNA was considered enriched if the *P* value was <0.05 and fold enrichment was >2. The TPM (transcripts per million) values of each gene were generated using RSEM (v1.3.1) (*66*).

DNA cleavage assay

DNA strands bearing the ORF2p cleavage motif (termed bottom strand) were fused to a Cy3 fluorophore at their 5′ ends and annealed with partner strands (top strand) fused to a Cy5 fluorophore to form double-stranded or fork-shaped duplexes by first heating to 95°C and then cooling down to 4°C in a stepwise manner. The cleavage reactions were performed in a 10-μl reaction with 20 mM HEPES pH 7.5, 150 mM NaCl, 10 mM $MgCl_2$, 1 mM DTT, 0.8 pmol of DNA substrates, and 0.8/1.6 pmol (indicated as 1× / 2× in figures) of purified ORF2p (wild type or mutant, untreated or treated with DNase/RNase) or the EN protein. DNA substrates were first incubated with the protein on ice for 30 min, and the cleavage reaction was started by shifting the temperature to 37°C

for 30 min. The reaction mixture was then added with 2× TBE dye (Invitrogen) and loaded onto a 15% urea-PAGE gel for analysis. The gel was imaged using the ProteinSimple system, and the intensity of the target product and the uncut bands were quantified by ImageJ. The cleavage activity was obtained from dividing the intensity of the cleavage products by the total intensity of the entire lane and subtraction of the background value derived from the input lane. Three independent experiments were performed and average values were plotted. Error bars represent the standard error of the mean.

REFERENCES AND NOTES

1. J. D. Boeke, D. J. Garfinkel, C. A. Styles, G. R. Fink, Ty elements transpose through an RNA intermediate. *Cell* **40**, 491–500 (1985). doi: 10.1016/0092-8674(85)90197-7; pmid: 2982495
2. S. R. Richardson *et al.*, The Influence of LINE-1 and SINE Retrotransposons on Mammalian Genomes. *Microbiol. Spectr.* **3**, MDNA3-0061-2014 (2015). doi: 10.1128/microbiolspec.MDNA3-0061-2014; pmid: 26104698
3. C. Mendez-Dorantes, K. H. Burns, LINE-1 retrotransposition and its deregulation in cancers: Implications for therapeutic opportunities. *Genes Dev.* **37**, 948–967 (2023). doi: 10.1101/gad.351051.123; pmid: 38092519
4. N. Bannert, R. Kurth, The evolutionary dynamics of human endogenous retroviral families. *Annu. Rev. Genomics Hum. Genet.* **7**, 149–173 (2006). doi: 10.1146/annurev.genom.7.080505.115700; pmid: 16722807
5. C. R. Beck, J. L. Garcia-Perez, R. M. Badge, J. V. Moran, LINE-1 elements in structural variation and disease. *Annu. Rev. Genomics Hum. Genet.* **12**, 187–215 (2011). doi: 10.1146/annurev-genom-082509-141802; pmid: 21801021
6. D. D. Luan, M. H. Korman, J. L. Jakubczak, T. H. Eickbush, Reverse transcription of R2Bm RNA is primed by a nick at the chromosomal target site: A mechanism for non-LTR retrotransposition. *Cell* **72**, 595–605 (1993). doi: 10.1016/0092-8674(93)90078-5; pmid: 7679954
7. G. J. Cost, Q. Feng, A. Jacquier, J. D. Boeke, Human L1 element target-primed reverse transcription in vitro. *EMBO J.* **21**, 5899–5910 (2002). doi: 10.1093/emboj/cdf592; pmid: 12411507
8. J. V. Moran *et al.*, High frequency retrotransposition in cultured mammalian cells. *Cell* **87**, 917–927 (1996). doi: 10.1016/S0092-8674(00)81998-4; pmid: 8945518
9. International Human Genome Sequencing Consortium, Initial sequencing and analysis of the human genome. *Nature* **409**, 860–921 (2001). doi: 10.1038/35057062; pmid: 11237011
10. B. Brouha *et al.*, Hot L1s account for the bulk of retrotransposition in the human population. *Proc. Natl. Acad. Sci. U.S.A.* **100**, 5280–5285 (2003). doi: 10.1073/pnas.0831042100; pmid: 12682288
11. C. R. Beck *et al.*, LINE-1 retrotransposition activity in human genomes. *Cell* **141**, 1159–1170 (2010). doi: 10.1016/j.cell.2010.05.021; pmid: 20602998
12. M. Dewannieux, C. Esnault, T. Heidmann, LINE-mediated retrotransposition of marked Alu sequences. *Nat. Genet.* **35**, 41–48 (2003). doi: 10.1038/ng1223; pmid: 12897783
13. Q. Feng, J. V. Moran, H. H. Kazazian Jr., J. D. Boeke, Human L1 retrotransposon encodes a conserved endonuclease required for retrotransposition. *Cell* **87**, 905–916 (1996). doi: 10.1016/S0092-8674(00)81997-2; pmid: 8945517
14. D. A. Kulpa, J. V. Moran, Cis-preferential LINE-1 reverse transcriptase activity in ribonucleoprotein particles. *Nat. Struct. Mol. Biol.* **13**, 655–660 (2006). doi: 10.1038/nsmb1107; pmid: 16783376
15. C. Monot *et al.*, The specificity and flexibility of l1 reverse transcription priming at imperfect T-tracts. *PLOS Genet.* **9**, e1003499 (2013). doi: 10.1371/journal.pgen.1003499; pmid: 23675310
16. N. Gilbert, S. Lutz-Prigge, J. V. Moran, Genomic deletions created upon LINE-1 retrotransposition. *Cell* **110**, 315–325 (2002). doi: 10.1016/S0092-8674(02)00828-0; pmid: 12176319
17. D. E. Symer *et al.*, Human l1 retrotransposition is associated with genetic instability in vivo. *Cell* **110**, 327–338 (2002). doi: 10.1016/S0092-8674(02)00839-5; pmid: 12176320
18. N. Gilbert, S. Lutz, T. A. Morrish, J. V. Moran, Multiple fates of L1 retrotransposition intermediates in cultured human cells. *Mol. Cell. Biol.* **25**, 7780–7795 (2005). doi: 10.1128/MCB.25.17.7780-7795.2005; pmid: 16107723
19. T. H. Eickbush, D. G. Eickbush, Integration, Regulation, and Long-Term Stability of R2 Retrotransposons. *Microbiol. Spectr.* **3**, MDNA3-0011-2014 (2015). doi: 10.1128/microbiolspec.MDNA3-0011-2014; pmid: 26104703
20. G. Mohr, P. S. Perlman, A. M. Lambowitz, Evolutionary relationships among group II intron-encoded proteins and identification of a conserved domain that may be related to maturase function. *Nucleic Acids Res.* **21**, 4991–4997 (1993). doi: 10.1093/nar/21.22.4991; pmid: 8255751
21. J. V. Moran *et al.*, Splicing defective mutants of the COXI gene of yeast mitochondrial DNA: Initial definition of the maturase domain of the group II intron al2. *Nucleic Acids Res.* **22**, 2057–2064 (1994). doi: 10.1093/nar/22.11.2057; pmid: 8029012
22. A. M. Lambowitz, S. Zimmerly, Group II introns: Mobile ribozymes that invade DNA. *Cold Spring Harb. Perspect. Biol.* **3**, a003616 (2011). doi: 10.1101/cshperspect.a003616; pmid: 20463000
23. D. A. Flasch *et al.*, Genome-wide de novo L1 Retrotransposition Connects Endonuclease Activity with Replication. *Cell* **177**, 837–851.e28 (2019). doi: 10.1016/j.cell.2019.02.050; pmid: 30955886
24. T. Sultana *et al.*, The Landscape of L1 Retrotransposons in the Human Genome Is Shaped by Pre-insertion Sequence Biases and Post-insertion Selection. *Mol. Cell* **74**, 555–570.e7 (2019). doi: 10.1016/j.molcel.2019.02.036; pmid: 30956044
25. X. Shi, A. Seluanov, V. Gorbunova, Cell divisions are required for L1 retrotransposition. *Mol. Cell. Biol.* **27**, 1264–1270 (2007). doi: 10.1128/MCB.01888-06; pmid: 17145770
26. P. Mita *et al.*, LINE-1 protein localization and functional dynamics during the cell cycle. *eLife* **7**, e30058 (2018). doi: 10.7554/eLife.30058; pmid: 29309036
27. M. E. Wilkinson, C. J. Frangieh, R. K. Macrae, F. Zhang, Structure of the R2 non-LTR retrotransposon initiating target-primed reverse transcription. *Science* **380**, 301–308 (2023). doi: 10.1126/science.adg7883; pmid: 37023171
28. P. Deng *et al.*, Structural RNA components supervise the sequential DNA cleavage in R2 retrotransposon. *Cell* **186**, 2865–2879.e20 (2023). doi: 10.1016/j.cell.2023.05.032; pmid: 37301196
29. K. Chung *et al.*, Structures of a mobile intron retroelement poised to attack its structured DNA target. *Science* **378**, 627–634 (2022). doi: 10.1126/science.abq2844; pmid: 36356138
30. G. E. Ghanim, H. Hu, J. Boulanger, T. H. D. Nguyen, Structural mechanism of LINE-1 target-primed reverse transcription. *Science* **388**, eads8412 (2025). doi: 10.1126/science.ads8412; pmid: 40048554
31. A. Thawani, A. J. Florez Ariza, E. Nogales, K. Collins, Template and target-site recognition by human LINE-1 in retrotransposition. *Nature* **626**, 186–193 (2024). doi: 10.1038/s41586-023-06933-5; pmid: 38096901
32. X. J. Lu, DSSR-enabled innovative schematics of 3D nucleic acid structures with PyMOL. *Nucleic Acids Res.* **48**, e74 (2020). doi: 10.1093/nar/gkaa426; pmid: 32442277
33. N. Altemose *et al.*, Complete genomic and epigenetic maps of human centromeres. *Science* **376**, eabl4178 (2022). doi: 10.1126/science.abl4178; pmid: 35357911
34. M. G. Schueler, A. W. Higgins, M. K. Rudd, K. Gustashaw, H. F. Willard, Genomic and genetic definition of a functional human centromere. *Science* **294**, 109–115 (2001). doi: 10.1126/science.1065042; pmid: 11588252
35. E. T. Baldwin *et al.*, Structures, functions and adaptations of the human LINE-1 ORF2 protein. *Nature* **626**, 194–206 (2024). doi: 10.1038/s41586-023-06947-z; pmid: 38096902
36. L. A. Kohlstaedt, J. Wang, J. M. Friedman, P. A. Rice, T. A. Steitz, Crystal structure at 3.5 A resolution of HIV-1 reverse transcriptase complexed with an inhibitor. *Science* **256**, 1783–1790 (1992). doi: 10.1126/science.1377403; pmid: 1377403
37. E. C. Bolton, A. S. Mildvan, J. D. Boeke, Inhibition of reverse transcription in vivo by elevated manganese ion concentration. *Mol. Cell* **9**, 879–889 (2002). doi: 10.1016/S1097-2765(02)00495-1; pmid: 11983178
38. K. J. Fenstermacher, J. J. DeStefano, Mechanism of HIV reverse transcriptase inhibition by zinc: Formation of a highly stable enzyme-(primer-template) complex with profoundly diminished catalytic activity. *J. Biol. Chem.* **286**, 40433–40442 (2011). doi: 10.1074/jbc.M111.289850; pmid: 21953456
39. W. Wei, T. A. Morrish, R. S. Alisch, J. V. Moran, A transient assay reveals that cultured human cells can accommodate multiple LINE-1 retrotransposition events. *Anal. Biochem.* **284**, 435–438 (2000). doi: 10.1006/abio.2000.4675; pmid: 10964437
40. J. L. Stamos, A. M. Lentzsch, A. M. Lambowitz, Structure of a Thermostable Group II Intron Reverse Transcriptase with Template-Primer and Its Functional and Evolutionary Implications. *Mol. Cell* **68**, 926–939.e4 (2017). doi: 10.1016/j.molcel.2017.10.024; pmid: 29153391
41. I. Miller *et al.*, Structural dissection of sequence recognition and catalytic mechanism of human LINE-1 endonuclease. *Nucleic Acids Res.* **49**, 11350–11366 (2021). doi: 10.1093/nar/gkab826; pmid: 34554261
42. A. M. Kulakova, M. G. Khrenova, M. I. Zvereva, I. V. Polyakov, Domain Mobility in the ORF2p Complex Revealed by Molecular Dynamics Simulations and Big Data Analysis. *Int. J. Mol. Sci.* **26**, 73 (2024). doi: 10.3390/ijms26010073; pmid: 39795935
43. S. E. Tsutakawa *et al.*, Human flap endonuclease structures, DNA double-base flipping, and a unified understanding of the FEN1 superfamily. *Cell* **145**, 198–211 (2011). doi: 10.1016/j.cell.2011.03.004; pmid: 21496641
44. T. A. Morrish *et al.*, Endonuclease-independent LINE-1 retrotransposition at mammalian telomeres. *Nature* **446**, 208–212 (2007). doi: 10.1038/nature05560; pmid: 17344853
45. A. Macia *et al.*, Engineered LINE-1 retrotransposition in nondividing human neurons. *Genome Res.* **27**, 335–348 (2017). doi: 10.1101/gr.206805.116; pmid: 27965292
46. T. A. Morrish *et al.*, DNA repair mediated by endonuclease-independent LINE-1 retrotransposition. *Nat. Genet.* **31**, 159–165 (2002). doi: 10.1038/ng898; pmid: 12006980
47. B. J. Wagstaff, M. Barnerβoi, A. M.Roy-Engel, Evolutionary conservation of the functional modularity of primate and murine LINE-1 elements. *PLOS ONE* **6**, e19672 (2011). doi: 10.1371/journal.pone.0019672; pmid: 21572950

48. M. Schorb, I. Haberbosch, W. J. H. Hagen, Y. Schwab, D. N. Mastronarde, Software tools for automated transmission electron microscopy. *Nat. Methods* **16**, 471–477 (2019). doi: 10.1038/s41592-019-0396-9; pmid: 31086343
49. C. Wu, X. Huang, J. Cheng, D. Zhu, X. Zhang, High-quality, high-throughput cryo-electron microscopy data collection via beam tilt and astigmatism-free beam-image shift. *J. Struct. Biol.* **208**, 107396 (2019). doi: 10.1016/j.jsb.2019.09.013; pmid: 31562921
50. A. Punjani, J. L. Rubinstein, D. J. Fleet, M. A. Brubaker, cryoSPARC: Algorithms for rapid unsupervised cryo-EM structure determination. *Nat. Methods* **14**, 290–296 (2017). doi: 10.1038/nmeth.4169; pmid: 28165473
51. R. Sanchez-Garcia *et al.*, DeepEMhancer: A deep learning solution for cryo-EM volume post-processing. *Commun. Biol.* **4**, 874 (2021). doi: 10.1038/s42003-021-02399-1; pmid: 34267316
52. J. Zivanov *et al.*, New tools for automated high-resolution cryo-EM structure determination in RELION-3. *eLife* **7**, e42166 (2018). doi: 10.7554/eLife.42166; pmid: 30412051
53. E. F. Pettersen *et al.*, UCSF Chimera—A visualization system for exploratory research and analysis. *J. Comput. Chem.* **25**, 1605–1612 (2004). doi: 10.1002/jcc.20084; pmid: 15264254
54. J. R. Lopéz-Blanco, P. Chacón, iMODFIT: Efficient and robust flexible fitting based on vibrational analysis in internal coordinates. *J. Struct. Biol.* **184**, 261–270 (2013). doi: 10.1016/j.jsb.2013.08.010; pmid: 23999189
55. P. Emsley, B. Lohkamp, W. G. Scott, K. Cowtan, Features and development of Coot. *Acta Crystallogr. D* **66**, 486–501 (2010). doi: 10.1107/S0907444910007493; pmid: 20383002
56. P. D. Adams *et al.*, PHENIX: A comprehensive Python-based system for macromolecular structure solution. *Acta Crystallogr. D* **66**, 213–221 (2010). doi: 10.1107/S0907444909052925; pmid: 20124702
57. V. B. Chen *et al.*, MolProbity: All-atom structure validation for macromolecular crystallography. *Acta Crystallogr. D* **66**, 12–21 (2010). doi: 10.1107/S0907444909042073; pmid: 20057044
58. T. D. Goddard *et al.*, UCSF ChimeraX: Meeting modern challenges in visualization and analysis. *Protein Sci.* **27**, 14–25 (2018). doi: 10.1002/pro.3235; pmid: 28710774
59. B. Langmead, S. L. Salzberg, Fast gapped-read alignment with Bowtie 2. *Nat. Methods* **9**, 357–359 (2012). doi: 10.1038/nmeth.1923; pmid: 22388286
60. H. Li *et al.*, The Sequence Alignment/Map format and SAMtools. *Bioinformatics* **25**, 2078–2079 (2009). doi: 10.1093/bioinformatics/btp352; pmid: 19505943
61. Y. Zhang *et al.*, Model-based analysis of ChIP-Seq (MACS). *Genome Biol.* **9**, R137 (2008). doi: 10.1186/gb-2008-9-9-r137; pmid: 18798982
62. S. Heinz *et al.*, Simple combinations of lineage-determining transcription factors prime cis-regulatory elements required for macrophage and B cell identities. *Mol. Cell* **38**, 576–589 (2010). doi: 10.1016/j.molcel.2010.05.004; pmid: 20513432
63. A. Dobin *et al.*, STAR: Ultrafast universal RNA-seq aligner. *Bioinformatics* **29**, 15–21 (2013). doi: 10.1093/bioinformatics/bts635; pmid: 23104886
64. Y. Liao, G. K. Smyth, W. Shi, featureCounts: An efficient general purpose program for assigning sequence reads to genomic features. *Bioinformatics* **30**, 923–930 (2014). doi: 10.1093/bioinformatics/btt656; pmid: 24227677
65. M. D. Robinson, D. J. McCarthy, G. K. Smyth, edgeR: A Bioconductor package for differential expression analysis of digital gene expression data. *Bioinformatics* **26**, 139–140 (2010). doi: 10.1093/bioinformatics/btp616; pmid: 19910308
66. B. Li, C. N. Dewey, RSEM: Accurate transcript quantification from RNA-Seq data with or without a reference genome. *BMC Bioinformatics* **12**, 323 (2011). doi: 10.1186/1471-2105-12-323; pmid: 21816040

ACKNOWLEDGMENTS

We thank B. Zhu, X. Huang, and staff members at the Center for Biological Imaging (CBI) of Institute of Biophysics (IBP), Chinese Academy of Sciences (CAS), for support in cryo-EM data collection, and F. Liu at IBP for help with figure preparation. We also thank X.-D. Fu at West Lake University and Z. Zhang at Columbia University Medical Cancer for helpful discussions. **Funding:** This work was supported by National Natural Science Foundation of China grant 32330021 (R.-M.X.), National Key Research and Development Program of China grant 2023YFA0913401 (W.J.), CAS Strategic Priority Research Program grants XDB1000000 (W.J.) and XDB37010100 (R.-M.X.), and CAS Basic Research Program Based on Major Scientific Infrastructures grant JZHKYPT-2021-05 (R.-M.X.). **Author contributions:** Conceptualization: W.J., R.-M.X.; Funding acquisition: W.J., R.-M.X.; Investigation: W.J., C.Y., Y.Z., C.C., T.X., G.S., Z.C.; Methodology: W.J., C.Y., Y.Z., C.C., Y.X., B.Z., R.-M.X.; Project administration: W.J., R.-M.X.; Supervision: R.-M.X., Y.X., B.Z.; Visualization: W.J., C.Y., Y.Z.; Writing – original draft: W.J., C.Y., Y.Z., R.-M.X.; Writing – review & editing: All authors. **Competing interests:** The authors declare that they have no competing interests. **Data and materials availability:** Atomic models and EM maps have been deposited in the Protein Data Bank and the Electron Microscopy Data Bank, respectively. The accession codes are as follows: PDB 9K6G and EMD-62126 for the 3.3-Å structure of nucleic acids–bound L1 ORF2p (without EN); PDB 9K6H and EMD-62127 for the 3.0-Å structure of ORF2p with DNA and RNA/cDNA hybrid bound to dNTP and Mn^{2+}; PDB 9K6I and EMD-62128 for the 3.6-Å structure of full-length ORF2p with nucleic acids. Raw data of DNA and RNA sequencing generated in this study have been deposited in the National Genomics Data Center, China National Center for Bioinformation/Beijing Institute of Genomics, CAS (GSA:CRA020140 for cabbage looper samples and GSA-human: HRA009125 for human samples), accessible at https://ngdc.cncb.ac.cn. **License information:** Copyright © 2025 the authors, some rights reserved; exclusive licensee American Association for the Advancement of Science. No claim to original US government works. https://www.science.org/about/science-licenses-journal-article-reuse

SUPPLEMENTARY MATERIALS

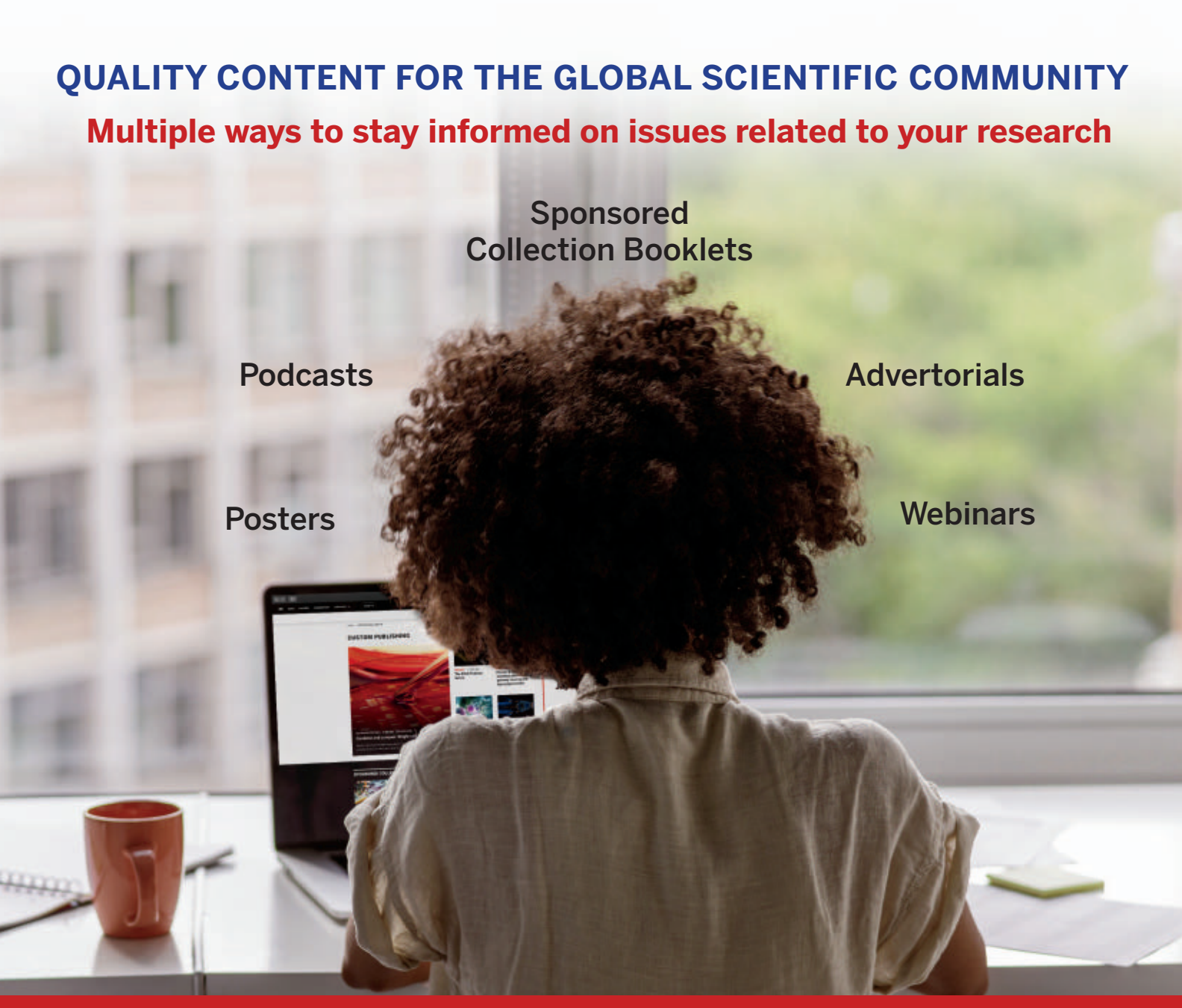
science.org/doi/10.1126/science.adu3433
Figs. S1 to S10; Tables S1 and S2; MDAR Reproducibility Checklist

Submitted 3 November 2024; accepted 3 July 2025

10.1126/science.adu3433

QUALITY CONTENT FOR THE GLOBAL SCIENTIFIC COMMUNITY

Multiple ways to stay informed on issues related to your research



Science
AAAS

Scan the code and start exploring the latest advances in science and technology innovation!

Science.org/custom-publishing

Brought to you by the *Science*/AAAS Custom Publishing Office.

Posters **Podcasts** **Sponsored Collection Booklets** **Advertorials** **Webinars**

RESEARCH ARTICLE SUMMARY

IMMUNOLOGY

T cell cholesterol transport links intestinal immune responses to dietary lipid absorption

Yajing Gao†, John P. Kennelly†, Xu Xiao, Emily Whang, Alessandra Ferrari, Alexander H. Bedard, Julia J. Mack, Alexander Nguyen, Sonal Srikanth, Thomas Weston, Lauren F. Uchiyama, Whitaker Cohn, Danielle H. Cho, Min Sub Lee, Julian Whitelegge, Yousang Gwack, Stephen G. Young, Steven J. Bensinger, Peter Tontonoz*

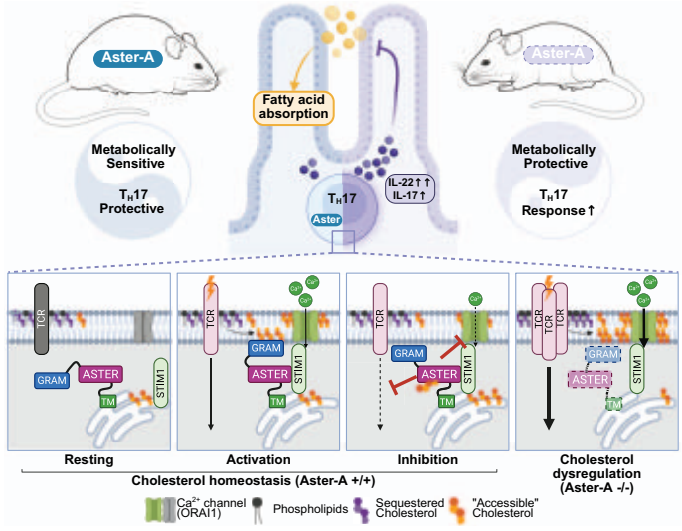
Full article and list of author affiliations: https://doi.org/10.1126/science.adt4169

INTRODUCTION: Impaired lipid flux can lead to cellular and tissue dysfunction in human diseases, yet the pathways that maintain membrane lipid homeostasis remain incompletely defined. Immune cells, which must adapt to evolving threats and distinct microenvironments, may be especially reliant on their ability to reorganize membranes for optimal function. The initiation and resolution of immune responses also likely require timely recalibration of the cellular lipid repertoire. Whether and how immune cell membrane homeostasis affects organ function and systemic metabolism are incompletely understood.

RATIONALE: Cholesterol is an indispensable lipid component of the mammalian plasma membrane (PM). We previously characterized the Aster family of nonvesicular lipid transporters, which transfer cholesterol from the PM to the endoplasmic reticulum. Despite established links between cholesterol abundance and immune signaling, it is unknown how immune cells fine-tune membrane cholesterol.

RESULTS: We traced fatty acid uptake in the small intestine of mice and found that specific deletion of Aster-A in T cells reduced fatty acid absorption and conferred resistance to diet-induced obesity. Loss of Aster-A increased a gene expression signature associated with T helper 17 (T_H17) cells among small intestine resident T cells. We found that Aster-A was highly expressed in T_H17 cells and was indispensable for maintaining appropriate PM cholesterol levels in this cell type. Using specific cholesterol probes, we determined that T cell receptor (TCR) activation transiently increased the accessible PM cholesterol pool, which recruited Aster-A to restrain excess PM cholesterol accumulation. In the absence of Aster-A, excess PM cholesterol was funneled into a distinct cellular lipid pool, the sphingomyelin-sequestered pool, leading to increased TCR nanoclustering. Consequently, Aster-A–deficient T_H17 cells exhibited elevated TCR signaling and effector cytokine [interleukin-17 (IL-17) and IL-22] production. Proximity labeling in T cells revealed an interaction between Aster-A and stromal interaction molecule 1 (STIM1), a core component mediating Ca^{2+} entry after TCR activation. We found that accessible PM cholesterol was required for TCR-induced Ca^{2+} influx and that Aster-A dampened this process. Aster-A thus restrained both the early signals directly triggered by the TCR and the later signaling events that depend on Ca^{2+} influx.

Single-cell transcriptomics and immune profiling further pinpointed increased IL-22 levels in T_H17 cells from the small intestines of T cell–specific Aster-A–deficient mice. Acute administration of IL-22 before feeding was sufficient to suppress intestinal fatty acid uptake. Conversely, blocking IL-22 with neutralizing antibodies, genetic ablation of *Il22* from T cells, or antibiotic depletion of microbial signals that maintain gut T_H17 cells each restored dietary fat absorption or diet-induced weight gain.



Nonvesicular cholesterol transport links intestinal T cell immunity to lipid absorption. T cell activation induces PM accumulation of accessible cholesterol and recruits Aster-A, which extracts cholesterol and transfers it to the endoplasmic reticulum to dampen TCR nanoclustering. Aster-A–STIM1 association at the PM further restrains Ca^{2+} influx during TCR activation (indicated by a lightning bolt). Aster-A guards against excessive intestinal T_H17 responses, thereby coordinating dietary lipid flux and systemic metabolism. GRAM, GRAM domain of Aster-A; ORAI1, calcium release-activated calcium modulator 1; TM, transmembrane domain of Aster-A. [Figure created with BioRender.com]

CONCLUSION: Our work identifies a rapid, on-demand regulator of immune membrane homeostasis. Aster-A responds to TCR activation–induced PM remodeling and subsequently removes excess membrane cholesterol to restrain TCR signaling cascades. We propose that membrane lipid remodeling may serve to promote microenvironmental adaptation by controlling tissue T cell reactivity. Dysregulation and accumulation of T cell PM cholesterol therefore has the potential to lead to aberrant gut T_H17 effector function, alters immune-epithelial communication, and modulates intestinal and systemic nutrient metabolism. □

*Corresponding author. Email: ptontonoz@mednet.ucla.edu †These authors contributed equally to this work. Cite this article as Y. Gao *et al.*, *Science* 390, eadt4169 (2025). DOI: 10.1126/science.adt4169

IMMUNOLOGY

T cell cholesterol transport links intestinal immune responses to dietary lipid absorption

Yajing Gao[1,2]†, John P. Kennelly[1,2]†, Xu Xiao[1,2]‡, Emily Whang[1,2,3], Alessandra Ferrari[1,2]§, Alexander H. Bedard[1,2], Julia J. Mack[4,5], Alexander Nguyen[1,2,6], Sonal Srikanth[7], Thomas Weston[8]¶, Lauren F. Uchiyama[1,2,5], Whitaker Cohn[9], Danielle H. Cho[1,2], Min Sub Lee[10,11], Julian Whitelegge[9], Yousang Gwack[6], Stephen G. Young[4,7], Steven J. Bensinger[10,11], Peter Tontonoz[1,2,5]*

The intrinsic pathways that control membrane organization in immune cells and their impact on cellular functions are poorly defined. We found that the nonvesicular cholesterol transporter Aster-A linked plasma membrane (PM) cholesterol availability in CD4 T cells to systemic metabolism. Aster-A was recruited to the PM during T cell receptor (TCR) activation, where it facilitated the removal of accessible cholesterol. Loss of Aster-A increased cholesterol accumulation in the PM, which enhanced TCR nanoclustering and signaling. Aster-A associated with stromal interaction molecule 1 (STIM1) and negatively regulated calcium (Ca^{2+}) flux. Aster-A deficiency promoted CD4 T cells to acquire a T helper 17 (T_H17) phenotype and stimulated interleukin-22 production, which reduced intestinal fat absorption and conferred resistance to diet-induced obesity. These findings delineate how immune cell membrane homeostasis links to systemic physiology.

The plasma membrane (PM) constitutes a major reservoir of unesterified cholesterol. The PM is thought to contain three cholesterol pools with distinct biochemical and biophysical properties (*1*): an essential pool required for membrane integrity and cell viability, a relatively inactive pool recognized by Ostreolysin A (OlyA) in which cholesterol is sequestered by sphingomyelin (SM) (*2*), and an active, or accessible, pool that can be readily mobilized and that can be detected by domain 4 of Anthrolysin O (ALOD4) (*3*, *4*).

Cellular and external cues, such as the uptake of lipoprotein-derived cholesterol, activation of SM degradation, and infection, regulate the size of the accessible cholesterol pool (*5*–*11*). Excess PM accessible cholesterol can move to the endoplasmic reticulum (ER) for esterification or be effluxed to extracellular lipoprotein acceptors (*6*, *12*–*15*). However, the functions of accessible cholesterol within the PM are poorly defined. The sole exception is hedgehog signaling in the primary cilium, where Patched-1 inactivation by Hedgehog ligands increases accessible cholesterol and potentiates the activation of Smoothened (*8*, *16*).

Nonvesicular sterol transport is recognized as being important for maintaining appropriate lipid distribution between cellular membrane compartments (*17*, *18*). The Aster proteins play an indispensable role in moving accessible cholesterol from the PM to the ER (*5*, *12*, *19*). Increased accessible PM cholesterol facilitates recruitment of the GRAM domain of Asters to the PM and the formation of PM-ER contact sites, through which the ASTER domain channels excess cholesterol to the ER (*12*, *19*). Aster proteins are required for the efficient internalization, storage, and utilization of diet- and lipoprotein-derived cholesterol in various metabolic and steroidogenic organs (*6*, *12*, *15*, *20*). Of particular interest, Aster-A is highly expressed in lymphoid organs (*12*), suggesting a yet-to-be-identified function for nonvesicular sterol transport in the immune system. How immune cell cholesterol homeostasis affects tissue-specific functions and systemic metabolism remains unexplored.

Studies involving chemical or indirect genetic approaches have reported that increasing PM cholesterol abundance can enhance T cell receptor (TCR) signaling (*21*–*25*). At the same time, cryo–electron microscopy (cryo-EM) structural studies have revealed that the resting αβTCR core contains two free cholesterol molecules that may serve to maintain the inactive state (*26*, *27*). Such studies imply that PM cholesterol availability must be tightly controlled during immune activation. However, it remains unknown whether T cells engage specific machinery to monitor and redistribute PM cholesterol. How membrane cholesterol dynamics are integrated with TCR signaling cascades has also not been defined.

Results

Dietary fatty acid absorption is decreased in mice that lack Aster-A in T lymphocytes

We generated Aster-A–deficient mice to analyze potential contributions of this cholesterol transporter to systemic metabolism. We observed that whole-body deletion of Aster-A impaired fatty acid uptake by the small intestine (SI). We gavaged Aster-A–deficient ($A^{-/-}$) or littermate control ($A^{+/+}$) mice with [^{3}H]triolein (18:1), a major fatty acid species in human and mouse diets, and measured the appearance of radioactivity in SI segments, plasma, and tissues (*28*, *29*). $A^{-/-}$ mice showed lower ^{3}H counts in the jejunum and lower total SI ^{3}H levels after 2 hours (Fig. 1A and fig. S1A) and a delay in the plasma ^{3}H appearance compared with $A^{+/+}$ controls (fig. S1B). In mice where Aster-A was deleted specifically in the liver, using $Albumin^{Cre}$ ($A^{\Delta Alb}$), or in the intestinal epithelium, using VillinCreERT ($A^{\Delta Vil}$) (fig. S1C), the intestinal uptake of [^{3}H]triolein was not altered (Fig. 1B-C), consistent with redundancy of Aster-A and -C in the liver and low Aster-A expression in SI epithelium (fig. S1D) (*6*, *15*). Thus, the decreased fatty acid absorption in $A^{-/-}$ mice was not due to intrinsic effects on enterohepatic tissues.

We sought to identify cell types with prominent Aster-A expression. In public mRNA expression datasets from humans and mice, secondary lymphoid organs (spleen and lymph nodes) exhibited abundant transcripts for Aster-A (*GRAMD1A*/*Gramd1a*) and low levels of transcripts for Aster-B and -C (*Gramd1b* and *Gramd1c*) (fig. S1, E and F). Examination of immune cell types in the ImmGen database (*30*) revealed high and specific expression of Aster-A in conventional T cells (fig. S1G). In mice where Aster-A was depleted in T cells specifically using $CD4^{Cre}$ (referred to as $A^{\Delta CD4}$ mice), *Gramd1a* transcripts in the $CD4^+$ and $CD8^+$ T cells were reduced by more than 100-fold and Aster-A protein levels were undetectable (fig. S2, A and B) compared with control mice that carried only floxed *Gramd1a* alleles (F/F). $A^{\Delta CD4}$ mice were born at Mendelian frequencies and exhibited normal development, suggesting no gross signs of early-onset immune disorders (fig. S2, C and D).

[1]Department of Pathology and Laboratory Medicine, University of California, Los Angeles, Los Angeles, CA, USA. [2]Department of Biological Chemistry, University of California, Los Angeles, Los Angeles, CA, USA. [3]Department of Pediatrics, Division of Gastroenterology, Hepatology, and Nutrition, David Geffen School of Medicine, University of California, Los Angeles, Los Angeles, CA, USA. [4]Department of Medicine, Division of Cardiology, David Geffen School of Medicine, University of California, Los Angeles, Los Angeles, CA, USA. [5]Molecular Biology Institute, University of California, Los Angeles, Los Angeles, CA, USA. [6]Vatche and Tamar Manoukian Division of Digestive Diseases, Department of Medicine David Geffen School of Medicine, University of California, Los Angeles, Los Angeles, CA, USA. [7]Department of Physiology, David Geffen School of Medicine, University of California, Los Angeles, Los Angeles, CA, USA. [8]Department of Human Genetics, David Geffen School of Medicine, University of California, Los Angeles, Los Angeles, CA, USA. [9]The Pasarow Mass Spectrometry Laboratory, University of California, Los Angeles, Los Angeles, CA, USA. [10]Department of Microbiology, Immunology and Molecular Genetics, University of California, Los Angeles, Los Angeles, CA, USA. [11]Department of Molecular and Medical Pharmacology, David Geffen School of Medicine, University of California, Los Angeles, Los Angeles, CA, USA.
***Corresponding author. Email: ptontonoz@mednet.ucla.edu** †These authors contributed equally to this work. ‡Present address: Saha Cardiovascular Research Center, Department of Physiology, University of Kentucky, Lexington, KY, USA. §Present address: Department of Nutritional Sciences and Toxicology, University of California, Berkeley, Berkeley, CA, USA. ¶Present address: Thermo Fisher Scientific, Hillsboro, OR, USA.

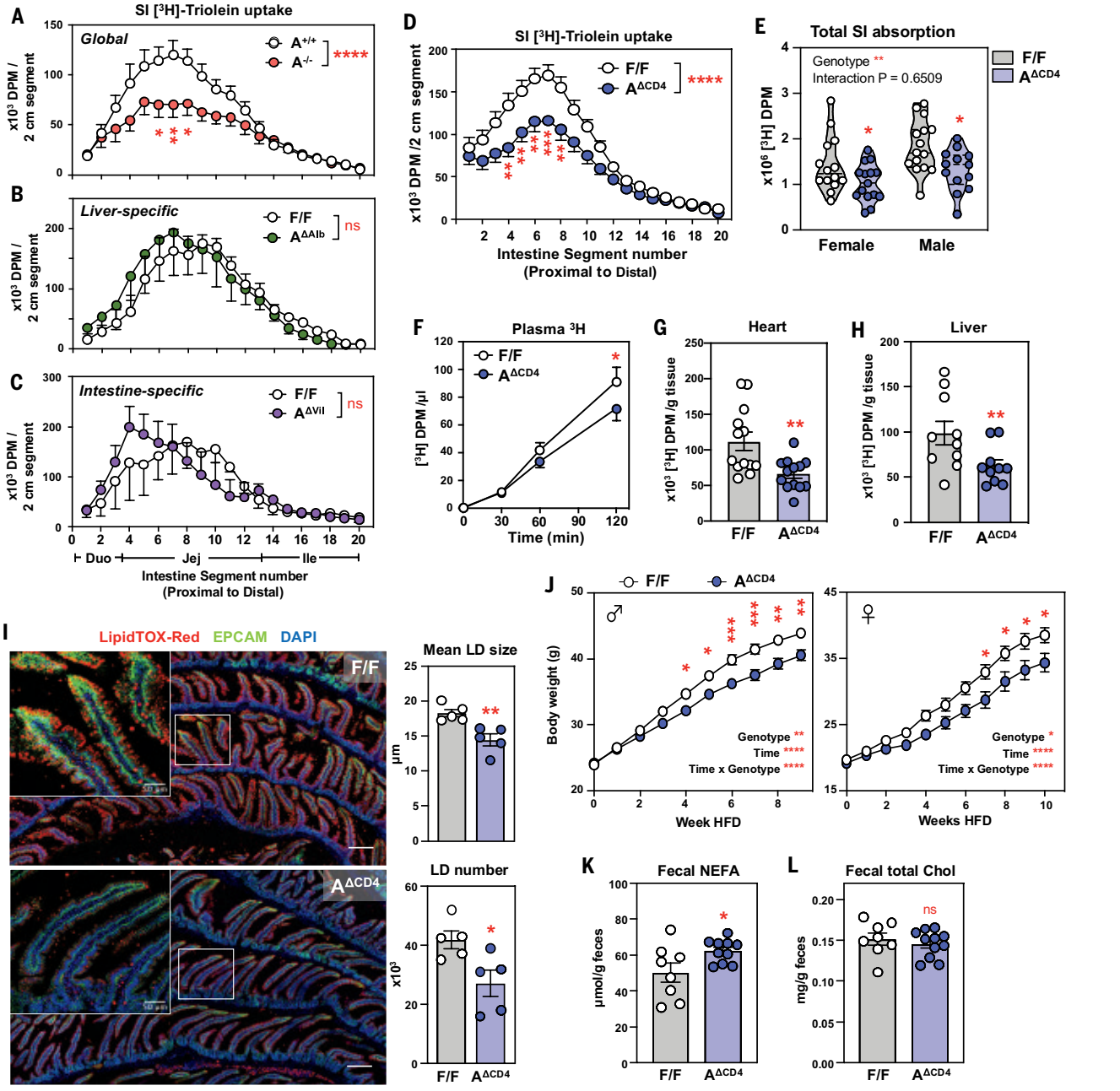


Fig. 1. Aster-A deficiency impairs fatty acid absorption in the SI and regulates diet-induced obesity. (**A**) Distribution of radioactivity in intestinal segments of Aster-A WT ($A^{+/+}$, $n = 13$) and global deficient ($A^{-/-}$, $n = 14$) littermate mice after an oral gavage of olive oil containing [^{3}H]triolein (18:1) for 2 hours. DPM, disintegrations per minute. (**B** and **C**) Distribution of radioactivity in intestinal segments of liver (hepatocyte)-specific [$A^{\Delta Alb}$ (B)] or intestinal epithelium–specific [$A^{\Delta Vil}$ (C)] Aster-A gene deletion (knockout) mice and their respective cre-negative floxed (F/F) littermate controls after an oral challenge of olive oil containing [^{3}H]triolein (18:1) for 2 hours ($n = 9$ and 6 mice per group for liver-specific knockout mice; $n = 4$ mice per group for intestinal epithelium–specific mice). (**D**) Distribution of radioactivity in intestinal segments of male and female F/F ($n = 29$) and littermate $A^{\Delta CD4}$ ($n = 28$) mice after an oral challenge of olive oil containing [^{3}H]triolein (18:1) for 2 hours. Data are pooled from at least three independent experiments. (**E**) Total radioactivity in SI from experiments in (D), separated by sex (female, $n = 14$ and 15 mice per group; male, $n = 15$ and 13 mice per group). (**F**) Kinetics of radioactivity in plasma of F/F ($n = 25$) and littermate $A^{\Delta CD4}$ mice ($n = 23$) after an oral challenge of olive oil containing [^{3}H]triolein (18:1). (**G** and **H**) Radioactivity in heart [(G), $n = 13$ mice per group) and liver [(H), $n = 10$ mice per group] from F/F and littermates $A^{\Delta CD4}$ after an oral challenge of olive oil containing [^{3}H]triolein (18:1) for 2 hours. Data are pooled from at least two independent experiments. (**I**) Confocal immunofluorescence imaging of neutral lipid accumulation (marked by LipidTOX-Red) in jejunum cross sections from F/F and littermate $A^{\Delta CD4}$ mice after an oral challenge of olive oil for 2 hours; scale bars are 200 µm. The insets show villi tips in higher magnification; scale bars are 50 µm. Shown on the right are the mean lipid droplet (LD) size and the total number of LDs per image. $n = 5$ mice per group pooled from two independent experiments. (**J**) Body weight of male (left) and female (right) F/F and littermate $A^{\Delta CD4}$ mice fed ad libitum with 60 kcal% HFD for 9 to 10 weeks (male, $n = 17$ and 16 mice per group; female, $n = 15$ mice per group). Data are pooled from at least three independent experiments. (**K** and **L**) Fecal nonesterified fatty acid (NEFA) (K) and total cholesterol (L) levels from F/F and littermate $A^{\Delta CD4}$ mice fed ad libitum with HFD for 10 days. $n = 8$ to 11 mice per group. Data are pooled from two independent experiments. For all panels, data are shown as mean ± SEM. For (A) to (D), (F), and (J), data points indicate mean values; for (E), (G) to (I), (K), and (L), data points indicate individual mice. The statistical analyses used are as follows: for (A) to (D), two-way analysis of variance (ANOVA) with Sidak's multiple comparison test; for (E), two-way ANOVA; for (F) and (G), repeated measure two-way ANOVA with Sidak's multiple comparison test; and for (G) to (I), (K), and (L), two-tailed unpaired Welch's *t* test. ns, not significant ($p > 0.05$); *$p < 0.05$; **$p < 0.01$; ***$p < 0.001$; ****$p < 0.0001$.

To examine whether T cell–intrinsic Aster-A affected fatty acid uptake by the SI, we gavaged $A^{\Delta CD4}$ or littermate F/F mice with [^{3}H]triolein. $A^{\Delta CD4}$ mice showed lower peak ^{3}H uptake in the duodenum and jejunum and reduced total intestinal ^{3}H absorption after 2 hours (Fig. 1D) in both males and females (Fig. 1E and fig. S3A). Moreover, the magnitude of the reduction was comparable to that observed in $A^{-/-}$ mice (Fig. 1A). $A^{\Delta CD4}$ mice also exhibited a reduced rate of ^{3}H appearance in plasma as well as lower ^{3}H uptake in heart and liver (Fig. 1, F to H). In line with the radiotracer data, an oral challenge of unlabeled olive oil (of which triolein is a major constituent) resulted in lower total plasma triglyceride levels in $A^{\Delta CD4}$ mice (fig. S3B). Thus, T cell–specific Aster-A deletion reduced the rate of fatty acid uptake into intestinal epithelium and subsequent entry into the systemic circulation.

We did not observe a difference in the SI length or in gastrointestinal transit times between F/F and $A^{\Delta CD4}$ mice fed a chow diet (fig. S3, C and D). Histopathology and EM studies revealed that jejunal villus and crypt morphology, villus length, and brush border morphology were indistinguishable in F/F and $A^{\Delta CD4}$ mice (fig. S3, E and F). No evidence of inflammation was observed in the lamina propria (LP) (fig. S3E). After olive oil gavage, villus tip enterocytes contained large unilocular lipid droplets in F/F mice compared with markedly smaller sized droplets in $A^{\Delta CD4}$ mice (fig. S3, E and F). We quantified the size and distribution of enterocyte lipid droplets by image analysis of large cross sections of jejunum stained with a neutral lipid probe. $A^{\Delta CD4}$ mice exhibited a shift in distribution to smaller droplet size and fewer numbers of lipid droplets (Fig. 1I and fig. S3G), accompanied by reduced expression of lipid droplet–associated gene expression in jejunal epithelium (fig. S3H). Furthermore, mice that harbored the $CD4^{Cre}$ allele but were heterozygous for the floxed Aster-A allele (CD4-Cre; $A^{F/+}$) showed no difference in [^{3}H]triolein uptake compared with $A^{F/+}$ littermates (fig. S4, A to C), thereby confirming that reduced fatty acid uptake in $A^{\Delta CD4}$ mice was linked to loss of Aster-A function in T cells and not to the presence of $CD4^{Cre}$ transgene. Furthermore, uptake of [^{14}C]cholesterol was comparable between F/F and $A^{\Delta CD4}$ mice (fig. S4, D and E). Thus, the impact of Aster-A in T cells on nutrient absorption was specific to fatty acid uptake and unrelated to any apparent SI pathology.

Resistance to diet-induced obesity in mice with Aster-A–deficient T lymphocytes

To understand the long-term metabolic impact of Aster-A loss in T cells, we challenged mice with a high-fat diet (HFD). Compared with F/F littermates, both female and male $A^{\Delta CD4}$ mice were resistant to HFD-induced weight gain (Fig. 1J). After 10 weeks of HFD, $A^{\Delta CD4}$ mice showed comparable body length to, but were phenotypically leaner than, F/F controls (fig. S5A). Tissue weights of liver, epididymal white adipose tissue, and inguinal white adipose tissue were lower in $A^{\Delta CD4}$ mice than in controls (fig. S5B). Analysis of body composition by magnetic resonance imaging (MRI) showed less fat mass in $A^{\Delta CD4}$ mice but no difference in lean mass (fig. S5, C and D). There were no body composition differences when mice were fed a normal chow diet (fig. S5E). Thus, T cell–specific loss of Aster-A conferred resistance to diet-induced obesity.

Loss of Aster-A in T cells blunted the inflammatory adipose tissue changes characteristic of obesity. Histological examination showed comparable fat cell size but reduced macrophage infiltration in epididymal white adipose tissue of HFD-fed $A^{\Delta CD4}$ mice (fig. S5F). Compared with F/F controls, $A^{\Delta CD4}$ mice were resistant to adipose resident macrophage ($F4/80^{hi}CD11b^{int}$) loss and showed less accumulation of inflammatory macrophages ($F4/80^{int}CD11b^{hi}$) (fig. S5, G and H). Furthermore, $A^{\Delta CD4}$ mice had reduced fat deposition in the liver (fig. S6A) and maintained better glucose tolerance and insulin sensitivity when fed HFD but not when fed a normal chow diet (fig. S6, B to E).

Lower adiposity in $A^{\Delta CD4}$ mice could not be attributed to differences in food intake, respiratory exchange ratio, or energy expenditure (fig. S7, A to C). However, with HFD feeding, $A^{\Delta CD4}$ mice showed increased fecal nonesterified fatty acids compared with controls (Fig. 1K), despite similar total fecal output and abundance of unabsorbed fecal cholesterol (Fig. 1L and fig. S7D). These results indicated overall reduced dietary fat absorption, in addition to altered uptake kinetics. Fecal triglyceride content and pancreatic lipase expression were similar between F/F and $A^{\Delta CD4}$ mice (fig. S7, E and F). We concluded that loss of Aster-A in T cells decreased intestinal fatty acid uptake, leading to resistance to obesity.

Loss of Aster-A in T cells enhances the T_H17 signature in the SI

Because loss of Aster-A in T cells affected SI fat absorption, we performed transcriptional profiling of $CD4^+$ and $CD8^+$ T cells from jejunal LP of mice that were acutely fed olive oil. Although few transcriptional changes related to T cell effector function were observed in the $CD8^+$ T cells (fig. S8A), genes that were up-regulated and enriched in $A^{\Delta CD4}$ $CD4^+$ T cells included *Il17a*, *Il17f*, and *Il22*, which encode the cytokines interleukin-17a (IL-17a), IL-17f, IL-22, respectively, and other genes previously associated with gut T helper 17 (T_H17) lineage and function (Fig. 2, A to C). We analyzed T cell lineage and cytokine producer frequencies in secondary lymphoid organs and SI-LP of normal chow–fed mice and found an increased frequency of IL-$17A^+$ and IL-22^+ CD4 T cells in mesenteric lymph nodes (mLNs) and SI-LP, respectively (fig. S8, B to E). By contrast, tissue residency markers and frequencies of other T cell lineages were largely unaltered (fig. S8F). Among T helper cell subtypes, Aster-A transcripts (*Gramd1a*) were prominently expressed in the T_H17 and regulatory T (T_{reg}) lineages in mice (Fig. 2D) and in T_H17 cells in humans (fig. S9, A and B). Aster-A protein levels were most abundant in T_H17 cells generated in vitro in the presence of IL-1β and IL-23 (fig. S9C), and they increased over the course of differentiation (fig. S9, D and E). The preferential expression of Aster-A in T_H17 cells corresponded with the predicted binding of transcription factors that enforce the T_H17 lineage, including JUN, STAT3, EGR2, and SMAD4, at the promotor region of *Gramd1a* (fig. S9F).

Aster-A modulates the accessible cholesterol pool in T_H17 cells

Aster proteins mobilize the accessible pool of cholesterol from the PM to the ER in several cell types (*6*, *12*, *15*, *20*). To determine whether Aster-A modulated PM cholesterol levels in T cells, we differentiated primary T_H17 cells from F/F or $A^{\Delta CD4}$ mice in defined serum-free media to limit extracellular cholesterol availability (fig. S10A) and monitored accessible cholesterol levels on the PM with the ALOD4 probe (*3*). $A^{\Delta CD4}$ T_H17 cells, but not naïve T cells, exhibited elevated accessible PM cholesterol compared with F/F controls (Fig. 2, E and F, and fig. S10B). Accessible cholesterol was distributed at "hot spots" on F/F T_H17 cells but was widely distributed on the PM of $A^{\Delta CD4}$ T_H17 cells, which resembled T cells forcibly loaded with exogenous cholesterol (Fig. 2G).

To test whether Aster-A contributed to membrane cholesterol homeostasis in the T_H17 lineage in vivo, we generated mixed bone marrow chimeric mice using F/F or $A^{\Delta CD4}$ donor and the congenic, wild-type (WT) $CD45.1^+$ competitor (Fig. 2H). This scheme allowed us to conduct an intrinsic comparison of the PM accessible cholesterol pool between Aster-A–sufficient and –deficient SI-LP CD4 T cells using a combination of ALOD4 and surface-marker staining (Fig. 2H). ALOD4 levels on $A^{\Delta CD4}$ RORγt^+ T_H17 cells were increased compared with that of the $CD45.1^+$ competitor (Fig. 2I). By contrast, no difference was observed between F/F T_H17 cells and the competitor or in RORγt^- non-T_H17 cells between any donor genotypes (Fig. 2I and fig. S10C). Thus, Aster-A regulated accessible cholesterol levels in SI T_H17 cells in a cell-intrinsic manner. Aster-A deficiency had no effect on RORγt^+ frequency in SI-LP T cells in the mixed bone marrow chimera setting (fig. S10D), consistent with our observations in steady-state mice (fig. S8E). Aster-A–mediated nonvesicular cholesterol transport was thus required to maintain PM cholesterol homeostasis in T_H17 cells in vitro and in vivo.

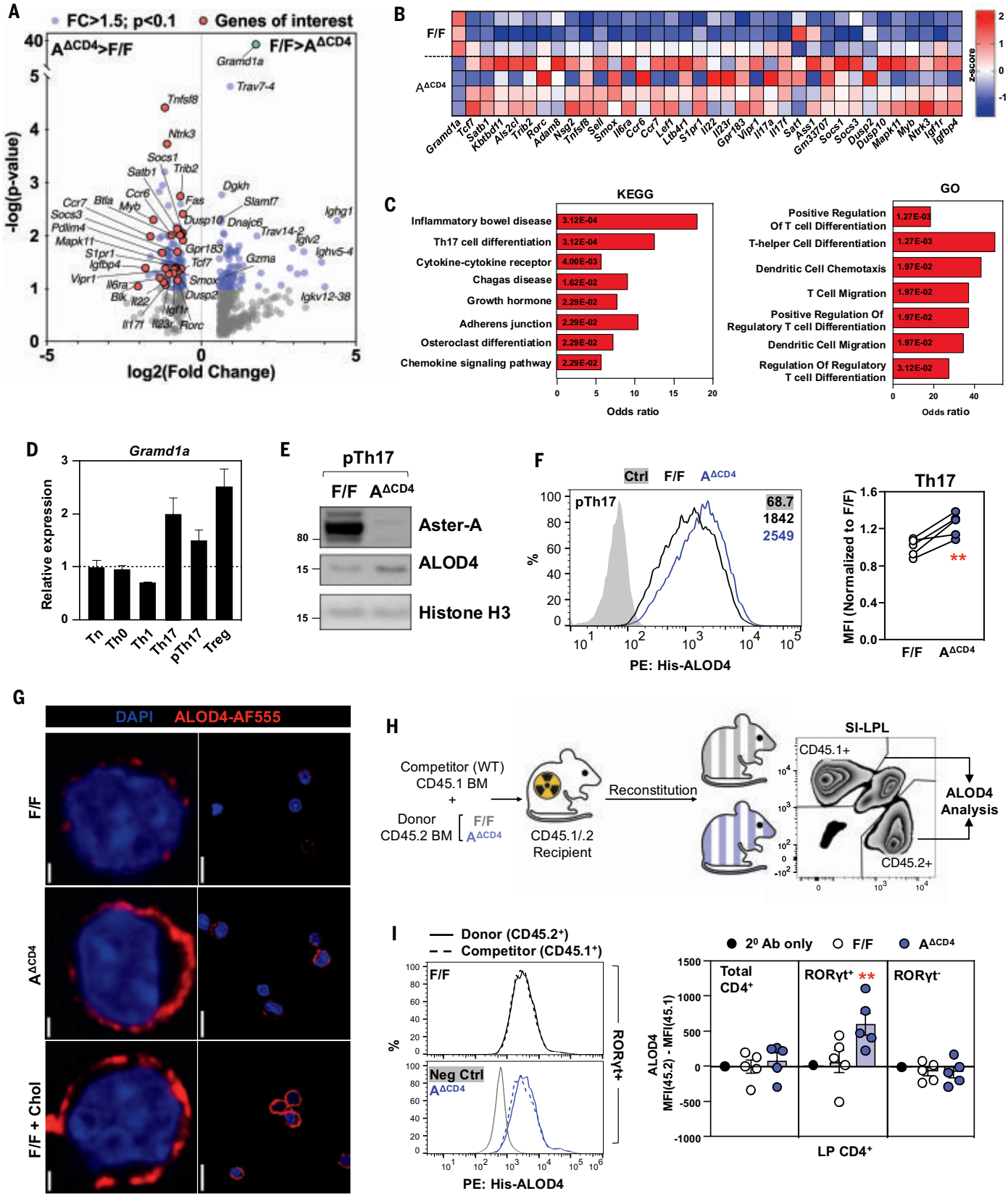


Fig. 2. Aster-A maintains the homeostasis of PM accessible cholesterol in T_H17 cells. (**A**) Volcano plot showing differentially expressed genes in $CD3^+CD4^+$ SI-LP T cells from F/F and littermate $A^{\Delta CD4}$ mice gavaged with olive oil for 2 hours. Blue dots indicate differentially expressed genes [fold change (FC) >1.5, $p < 0.1$]. Red dots indicate genes of interest. $n = 3$ or 4 biological replicates per group. (**B**) Heatmap of representative differentially expressed genes from (A). (**C**) Gene set enrichment analysis of all differentially expressed genes in LP $CD4^+$ T cells comparing $A^{\Delta CD4}$ with F/F. GO, Gene Ontology; KEGG, Kyoto Encyclopedia of Genes and Genomes. (**D**) mRNA expression of *Gramd1a* (Aster-A) in in vitro–differentiated T_H cell subtypes. T_H17 indicates IL-6 + TGFβ (transforming growth factor–β); pT_H17 indicates IL-6 + TGFβ + IL-1β + IL-23. Data are representative of at

least three independent experiments. (**E** and **F**) Western blot (E) and flow cytometry histogram (F) of ALOD4 in pT$_H$17 cells (gated on live cells) differentiated from F/F and A$^{\Delta CD4}$ naïve CD4$^+$ T cells. Mean fluorescence intensity (MFI) is shown in (F). $n = 5$ mice per genotype from three independent experiments. Secondary anti-His tag–phycoerythrin (PE) antibody alone, without His-ALOD4 staining, was used as a negative control. (**G**) Confocal immunofluorescence imaging of ALOD4 staining (red) of F/F and A$^{\Delta CD4}$ pT$_H$17 cells (IL-6 + TGFβ + IL-1β + IL-23) or loaded with 25 μM methyl-β-cyclodextrin–cholesterol for 1 hour (F/F + Chol). Scale bars are 1 μm (left panels) and 10 μm (right panels). 4′,6-Diamidino-2-phenylindole (DAPI; blue) staining indicates the nucleus. Data are representative of at least two independent experiments. (**H**) Schematic diagram of the competitive bone marrow reconstitution and ALOD4 staining assay. (**I**) Histogram (left) of accessible cholesterol levels (by ALOD4) in SI-LP RORγt$^+$ T cells and quantified difference of in total CD4$^+$, RORγt$^+$, or RORγt$^-$ T cells (right), comparing CD45.2$^+$ F/F or CD45.2$^+$ A$^{\Delta CD4}$ to the congenic competitor (WT CD45.1$^+$) in the same mice. $n = 5$ mice per group, representative of two independent experiments. The gating strategy is shown in fig. S21B. For (D) and (I), data are shown as mean ± SEM. For (F), data points and connecting lines indicate cells generated from littermate pairs; for (I), data points indicate individual recipient mice. The statistical analyses used are as follows: for (F), paired Student's *t* test; and for (I), two-way ANOVA with Tukey's multiple comparison test. $^{**}p < 0.01$. [(H) created with BioRender.com]

TCR activation generates accessible PM cholesterol and recruits Aster-A

To investigate the physiological signals that modulated accessible cholesterol, we examined PM dynamics in T$_H$17 cells after TCR activation by plate-bound anti-CD3 and anti-CD28. Control T$_H$17 cells maintained constant accessible cholesterol levels over 4 hours (Fig. 3A). Aster-A–deficient T$_H$17 cells exhibited elevated ALOD4 binding after activation, followed by a delayed rate of cholesterol removal (Fig. 3A). TCR-independent activation with phorbol 12-myristate 13-acetate (PMA) and ionomycin, by contrast, led to prolonged and unresolved accessible cholesterol accumulation in T$_H$17 cells of both genotypes (Fig. 3A). This finding indicated that T cell activation increased accessible PM cholesterol and that Aster-A was required for the normalization of PM cholesterol after TCR activation.

Aster proteins are recruited to the PM by accessible cholesterol (*5*, *6*, *10*, *12*, *19*). To test whether TCR activation was sufficient to recruit Aster-A to the PM, we expressed mCherry fused to the N-terminal GRAM domain of murine Aster-A in the EL-4 mouse T cell line. After synchronized TCR activation, the mCherry signal rapidly mobilized from perinuclear ER toward cell-surface TCRs (Fig. 3B and movie S1), indicating Aster-A recruitment to the PM. Ionomycin further provoked synchronized localization of the mCherry signal to the PM (Fig. 3B and movie S1).

To further resolve the kinetics, we used a dimerization-dependent fluorescent protein (ddFP) system composed of a high-sensitivity GRAM domain (B-GRAM-H) and a PM anchor fused to split fluorescent protein (*30*, *31*), allowing simultaneous detection of accessible cholesterol generation and GRAM recruitment to the PM (Fig. 3C). B-GRAM-H–ddFP was expressed in the EL-4 T cell line and the human Jurkat T cell line (fig. S11A), and ddFP dimerization was detected using flow cytometry. Jurkat cells, but not EL-4 cells, showed increased ddFP signal in response to PM cholesterol loading and thus were used for subsequent experiments (fig. S11B). When Jurkat cells were activated by TCR cross-linking, the ddFP signal increased by 3 min after activation (Fig. 3D) and remained elevated for up to 1 hour (Fig. 3E). Ionomycin treatment led to a larger increase in ddFP signal (Fig. 3F), tracking with a greater accumulation of the PM accessible cholesterol compared with TCR activation (Fig. 3A). These observations prompted us to explore whether a common mechanism altered PM cholesterol distribution during TCR-dependent and -independent activation.

Redistribution of cholesterol from the outer to inner leaflet of the PM, which enables sensing and transport by the Asters, can be triggered by altered transmembrane phospholipid asymmetry (*32*), such as phosphatidylserine (PS) scrambling. TCR-mediated activation triggers nonapoptotic, low-grade, and reversible PS flipping to the PM outer leaflet, in contrast to ionomycin, which generates persistent widespread PS scrambling (*33*–*35*). We confirmed these prior findings in primary T$_H$17 cells, Jurkat cells, and EL-4 cells using Annexin-V detection of outer leaflet PS (fig. S12A). We further tested whether TCR activation– or ionomycin-induced GRAM recruitment depends on TMEM16F, a major Ca^{2+}-dependent PS scramblase (*36*). 1PBC, a well-characterized TMEM16F inhibitor (*37*), eliminated the ionomycin-induced Annexin-V–high population, but the Annexin-V–low population induced by both TCR activation and ionomycin appeared to be TMEM16F independent (fig. S12, B and C). Accordingly, 1PBC largely abolished ionomycin-induced, but not TCR-induced, GRAM recruitment (fig. S12, D and F, and quantified in fig. S12, E and G). Thus, both TCR-dependent and -independent T cell activation generated accessible cholesterol and recruited Aster proteins to the PM, and TMEM16F-mediated PS scrambling contributed to this phenomenon upon ionomycin exposure.

Aster-A restrains TCR nanoclustering and dampens proximal TCR signaling

PM cholesterol composition has been proposed to modulate membrane TCR activity and avidity by affecting TCR nanoclustering (*22*, *38*). We tested whether loss of Aster-A affected the accessible and SM-sequestered cholesterol pools using ALOD4 and OlyA probes, respectively (*4*). A$^{\Delta CD4}$ T$_H$17 cells showed enhanced ALOD4 and OlyA binding to the PM compared with F/F T$_H$17 cells at steady state, and both pools expanded upon TCR activation (Fig. 3G). These data suggested that excess accessible PM cholesterol in Aster-A–deficient cells funneled into SM-sequestered domains.

We investigated whether the accumulation of accessible and SM-sequestered PM cholesterol in A$^{\Delta CD4}$ T$_H$17 cells altered TCR nanoclustering or signaling. Serial extraction of isolated T$_H$17 membranes by saponin and Brij97 allowed separation of nanoclustered complexes from monomeric TCR (*39*). Quantification of CD3ζ chain abundance in these fractions indicated that the loss of Aster-A increased the TCR nanocluster-to-monomer ratio (Fig. 4, A and B). Accordingly, after reactivation, A$^{\Delta CD4}$ T$_H$17 cells exhibited enhanced proximal TCR signaling, as well as increased phosphorylation of S6 and ERK, compared with control T$_H$17 cells (Fig. 4C and quantified in fig. S13A). Consequently, A$^{\Delta CD4}$ T$_H$17 cells showed increased frequency of IL-17A and IL-22 effector cytokine production and gene expression, reduced Foxp3 expression (Fig. 4, D and E), and a moderate increase in proliferation (fig. S13B). We conclude that Aster-A functions to restrain TCR nanoclustering and signaling in T$_H$17 cells by removing PM cholesterol.

To understand whether this pathway operated in vivo, we intraperitoneally administered CD3ε-specific antibody to mice (Fig. 4F), a challenge that elicits activation and expansion of mLN- and intestine-associated T$_H$17 cells (fig. S13C) (*40*). After anti-CD3ε injection, ALOD4 staining of F/F mLN T cells showed unchanged accessible cholesterol levels at 8 hours and a moderate increase at 24 hours (Fig. 4G). By contrast, accessible PM cholesterol accumulated substantially in A$^{\Delta CD4}$ mLN T cells 8 to 24 hours after injection (Fig. 4G). Furthermore, anti-CD3ε treatment markedly expanded RORγt$^+$ CD4 T cells in the mLNs of A$^{\Delta CD4}$ mice at 24 hours, consistent with our finding that Aster-A dampens T$_H$17 reactivation (Fig. 4H). These data demonstrated that TCR activation led to increased PM accessible cholesterol and that Aster-A is required for its timely removal to limit T$_H$17 activation and expansion.

Spatial association of Aster-A with STIM1 in T cells

To gain further insight into mechanisms by which Aster-A modulates T cell function, we probed the Aster-A proximity interactome by harnessing TurboID fused to the N terminus of Aster-A (fig. S14A) (*41*). This fusion allowed identification of proteins proximal to Aster-A after

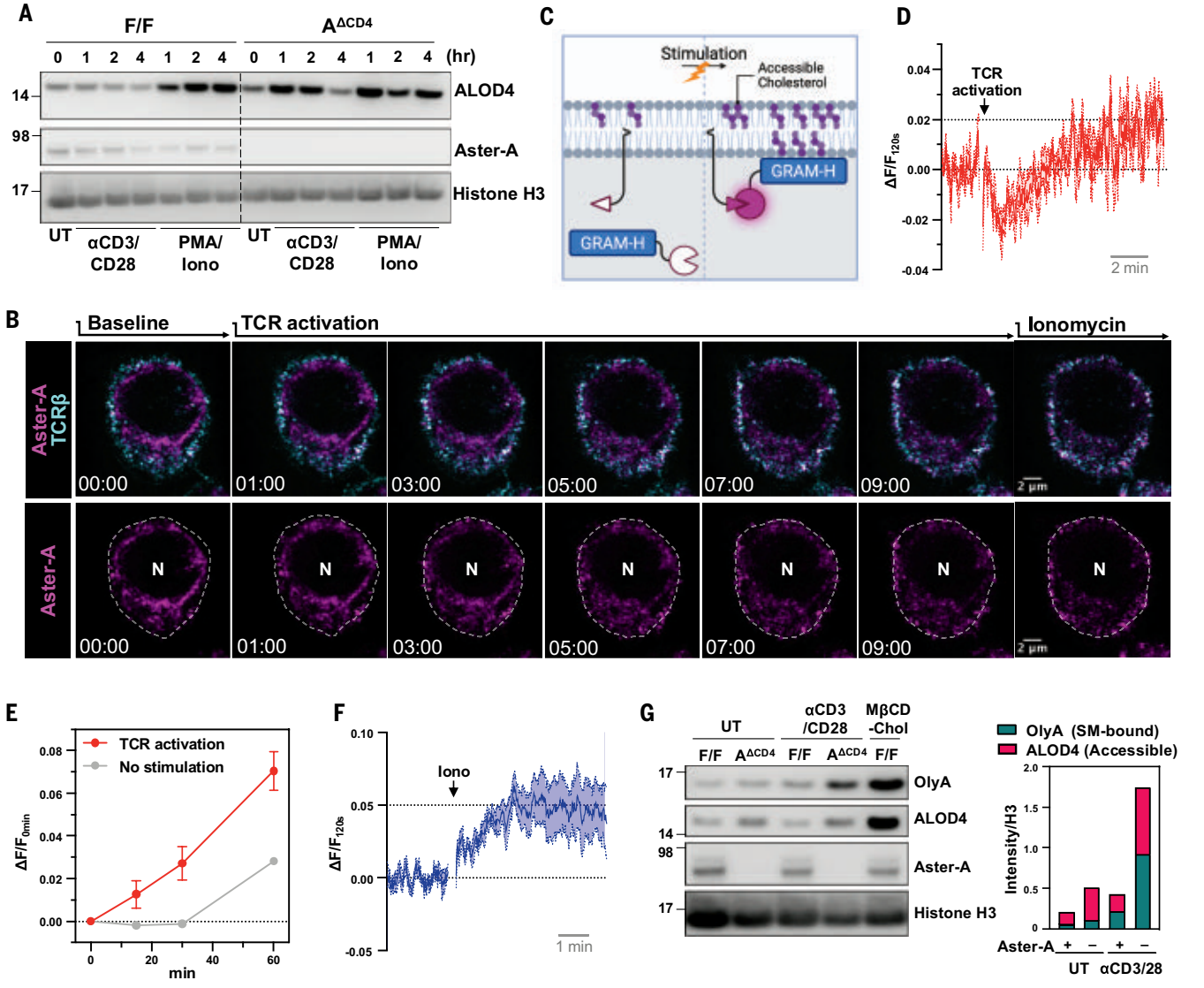


Fig. 3. TCR activation generates accessible cholesterol that rapidly recruits Aster-A to the PM. (**A**) Western blot analysis of PM ALOD4 staining (accessible cholesterol level) of in vitro–differentiated F/F and $A^{\Delta CD4}$ pT_H17 cells (IL-6 + TGFβ + IL-1β + IL-23) that were reactivated with plate-bound anti-CD3/CD28 antibody (1 μg/ml) for the indicated times. UT, untreated. (**B**) Live-cell confocal microscopy images showing the localization of mCherry–Aster-A in EL-4 cells unstimulated (Baseline), TCR cross-linked, or treated with 1 μM ionomycin. PM TCRβ was stained with anti-TCRβ–Alexa Fluor 647 antibodies. Scale bars are 2 μm. N, nucleus. (**C**) Schematic graph of PM recruitment–dependent B-GRAM-H ddFP dimerization. (**D**) Time course of ddFP fluorescence signal (normalized to the first 120 s of baseline signal) in response to TCR cross-linking. Shown is a trace of four independent recordings, with an average of 200 to 1000 cells per second per recording. (**E**) Kinetics of ddFP signal in a 60-min timescale. $n = 4$ independent recordings for TCR activation. (**F**) Time course of ddFP fluorescence signal (normalized to first 120 s of baseline signal) in response to 1 μM ionomycin. Shown is a trace of five independent recordings, with an average of 200 to 1000 cells per second per recording. (**G**) Western blot analysis of ALOD4 (accessible cholesterol level) and OlyA (SM-sequestered cholesterol level) staining of in vitro–differentiated F/F and $A^{\Delta CD4}$ T_H17 cells (IL-6 + TGFβ + IL-1β + IL-23) that were reactivated with plate-bound 1 μg/ml anti-CD3/CD28 antibody or loaded with 25 μM methyl-β-cyclodextrin–cholesterol (MβCD-Chol) for 1 hour. Data are representative of or pooled from at least two independent experiments. Data are shown as mean ± SEM. [(C) created with BioRender.com]

its recruitment to the PM by cholesterol loading or TCR activation (Fig. 5A). Excess PM cholesterol induced Aster-A self-biotinylation (Fig. 5B and fig. S14B), consistent with the reported oligomerization of Aster-A at PM-ER contact sites (*12*, *19*). Our screen revealed stromal interaction molecule 1 (STIM1)—a core component of the store-operated Ca^{2+} entry (SOCE) machinery and known PM-ER contact site protein (*42*–*46*)—to be in proximity to Aster-A. Aster-A association with STIM1 increased after both cholesterol loading (Fig. 5B and fig. S14B) and TCR activation (lane 3 in Fig. 5C). This association was enhanced by Ca^{2+} chelators that prolong STIM1 localization at PM-proximal ER (lane 4 in Fig. 5C) (*47*, *48*). Despite only pulling down a small fraction of endogenous or overexpressed STIM1 with Aster-A, their coimmunoprecipitation was nevertheless increased upon cholesterol loading (fig. S14, C and D). These data implied that Aster-A and STIM1 interacted transiently rather than forming a stable complex. By contrast, the intracellular TCR signaling components LCK and CD3ε did not show prominent interaction with Aster-A (Fig. 5C), suggesting that TCR nanoclustering in the setting of Aster-A deficiency was largely a result of preexisting PM cholesterol accumulation (Fig. 4A).

Previously identified residues that are required for Aster-B sensing and transfer of PM cholesterol are highly conserved in Aster-A (fig. S15A) (*19*, *49*). Homologous mutations in Aster-A resulted in corresponding

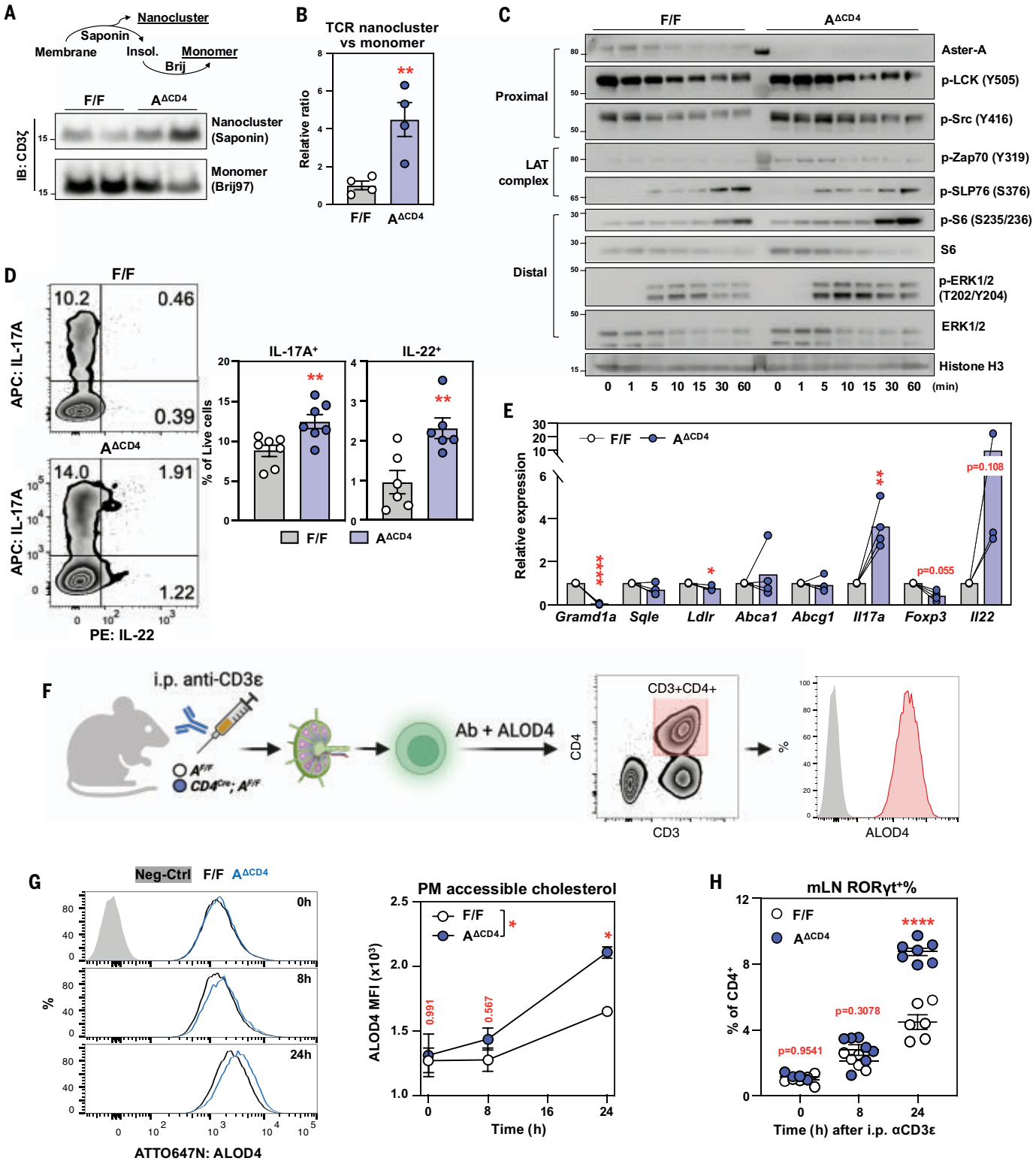


Fig. 4. Aster-A regulates TCR nanoclustering and effector responses of T_H17 cells through gating PM cholesterol level. (**A** and **B**) Western blot analysis of TCR (CD3ζ) clustering in in vitro–differentiated F/F and $A^{\Delta CD4}$ pT_H17 cells (IL-6 + TGFβ + IL-1β + IL-23). Shown are a representative blot (A) showing two biological replicates and a quantification (B) of Saponin-extracted (nanocluster) versus Brij97-extracted (monomer) CD3ζ intensity. $n = 4$ biological replicates from two independent experiments. (**C**) Western blot analysis of phosphorylation of LCK/Src, Zap70, SLP76, S6, and ERK1/2 after TCR activation. In vitro–differentiated pT_H17 cells were "rested" overnight without a differentiation cocktail or TCR stimulus and then reactivated with plate-bound anti-CD3 and anti-CD28 antibodies (1 μg/ml) for the indicated times. Histone H3 serves as overall input control. Data are representative of three independent experiments. (**D**) Frequency of in vitro–differentiated pT_H17 cells producing IL-17A or IL-22 (gated on live single cells). A representative flow plot is shown on the left, and quantifications are on the right. $n = 6$ or 7 mice per genotype from at least two independent experiments. (**E**) Gene expression from in vitro–differentiated pT_H17 cells. $n = 3$ or 4 biological replicates per genotype from three independent experiments. (**F**) Diagram of the experimental setup to probe PM

accessible cholesterol levels during T cell activation in vivo. i.p., intraperitoneal. (**G**) Shown on the left is a histogram of ALOD4 staining in mLN CD4 T cells ($CD45^+CD3^+CD4^+$) from F/F and $A^{\Delta CD4}$ mice that were intraperitoneally injected with anti-CD3ε (20 μg/mouse) for the indicated times or 20 μg isotype control antibody (0 hour time point). Shown on the right is the normalized mean fluorescence intensity (MFI) of ATTO647N-ALOD4. $n = 3$ or 4 mice per genotype per time point, representative of two independent experiments. (**H**) Frequency of $ROR\gamma t^+$ population in mLN $CD4^+$ T cells at the indicated time points after anti-CD3ε injection. $n = 4$ to 7 mice per group per time point, pooled from two independent experiments. For (B), (D), (G), and (H), data are shown as mean ± SEM. For (A) and (D), data points indicate cells generated from individual mice; for (E), data points and connecting lines indicate cells generated from paired biological replicates; for (G), data points indicate mean values; and for (H), data points indicate individual mice. The statistical analyses used are as follows: for (B) and (D), two-tailed Welsh's *t* test; for (E), multiple ratio paired *t* test; and for (G) and (H), two-way ANOVA with Sidak's multiple comparison test. $*p < 0.05$; $**p < 0.01$; $****p < 0.0001$. [(F) created with BioRender.com]

alterations in PM localization patterns in response to cholesterol loading (fig. S15B). Aster-A R186W, which contains a loss-of-function GRAM domain mutation (Arg^{186}→Trp) that diminishes cholesterol sensing capacity, failed to localize to the PM in response to cholesterol (fig. S15B). Coimmunoprecipitation of STIM1 with Aster-A R186W was reduced compared with WT Aster-A (fig. S14D). The observation that the abundant ER-resident protein calnexin did not coimmunoprecipitate with WT Aster-A suggested that recruitment of Aster-A and STIM1 to the PM was required for their association, despite the fact that they are both ER-anchored proteins (fig. S14C). To visualize the localization of Aster-A relative to STIM1, we reconstituted $A^{\Delta CD4}$ T_H17 cells with hemagglutinin (HA)–tagged Aster-A (Fig. 5D and fig. S14E). In resting T_H17 cells, both STIM1 and Aster-A localized primarily to perinuclear ER (row 1 in Fig. 5D). In response to synchronized TCR activation, WT Aster-A migrated to the PM and in proximity to the STIM1 "ring" or "cap" structure (row 2 in Fig. 5D). Aster-A R186W failed to translocate to the PM, but this did not adversely affect STIM1 localization (row 3 in Fig. 5D). Thus, when accessible cholesterol was available on the T cell PM, Aster-A increased its proximity to STIM1 owing to their colocalization at PM-ER contact sites.

Aster-A and accessible cholesterol regulate TCR-induced Ca^{2+} cascades

The coupling of STIM1 with the PM Ca^{2+} channel ORAI1 (calcium release–activated calcium modulator 1) is indispensable for SOCE and T_H17 effector function (*50*–*52*). The association of Aster-A and STIM1 suggested that Aster-A may regulate SOCE in T_H17 cells. Using flow-cytometry and imaging-based assays, we found that $A^{\Delta CD4}$ T_H17 cells showed increased TCR-dependent and ionophore-induced Ca^{2+} influx, without affecting STIM1 expression (Fig. 5E and fig. S16, A and B). By comparison, Aster-A deficiency did not affect SOCE in naïve T cells (fig. S16, B and C).

We asked whether cholesterol sensing or transport by Aster-A was required for the modulation of SOCE. In addition to Aster-A R186W, we generated and validated two additional homologous mutations: G184L (Gly^{184}→Leu), a gain-of-function GRAM domain mutation, which increased Aster-A localization to the PM; and 5P [I431P (Ile^{431}→Pro), S432P (Ser^{432}→Pro), N433P (Asn^{433}→Pro), Q434P (Gln^{434}→Pro), L435P (Leu^{435}→Pro)], a loss-of-function ASTER domain mutation that is unable to transport cholesterol. 5P was used as a reconstituted but nonfunctional control (fig. S15, A and B). Reconstitution of primary $A^{\Delta CD4}$ T_H17 cells with WT Aster-A or G184L decreased PM accessible cholesterol and Ca^{2+} flux (Fig. 5F and fig. S16, D and E). Conversely, reconstitution with loss-of-function mutations in the GRAM domain (R186W) or ASTER domain (5P) elevated PM accessible cholesterol and Ca^{2+} flux (Fig. 5F and fig. S16, D and E). Thus, regulation of Ca^{2+} flux required both recruitment of Aster-A to the PM and cholesterol transfer capacity. These data indicate that Aster-A negatively regulated TCR-induced SOCE in T_H17 cells.

Increasing PM cholesterol by treating T_H17 cells with methyl-β-cyclodextrin–cholesterol or low-density lipoprotein (LDL) promoted TCR-dependent SOCE, whereas removing PM cholesterol by 2-hydroxypropyl-β-cyclodextrin abolished it (fig. S16, F and G). To understand the specific role of the accessible cholesterol pool in STIM1-dependent Ca^{2+} flux, we incubated WT T_H17 cells with ALOD4 to sequester and immobilize accessible cholesterol on the outer leaflet of the PM. ALOD4 markedly dampened TCR-induced Ca^{2+} flux compared with treatment with the nonbinding mutant (*53*), whereas maximum flux induced by ionomycin was intact (Fig. 5H). Therefore, we propose a model in which accessible cholesterol generated by TCR activation supports SOCE, whereas the recruitment of Aster-A to the proximity of STIM1 curtails Ca^{2+} influx by modulating PM cholesterol composition.

Aster proteins are highly conserved in mammals (*12*). We generated an Aster-A–deficient Jurkat T cell clone by CRISPR-Cas9 and then reconstituted it with human Aster-A or an empty vector (fig. S16H). Stable expression of human Aster-A efficiently reduced both TCR- and ionomycin-triggered Ca^{2+} flux compared with empty vector–transduced cells (Fig. 5H), mirroring our observations for mouse T_H17 cells (Fig. 5E). These data revealed a functionally conserved accessible cholesterol–Aster-A/STIM1 axis that regulated Ca^{2+} responses in T cells.

IL-22 drives malabsorption in T cell Aster-A deficiency

We investigated the basis for dietary lipid malabsorption in $A^{\Delta CD4}$ mice. To explore factors in SI T_H17 cells that may affect absorption, we performed single-cell RNA sequencing (scRNA-seq) of SI-LP mononuclear cells. $CD90^+$ (based on *Thy1* expression, the gene that encodes CD90) clusters were subsequently extracted and further subclustered to reveal 23 distinct lymphocyte subpopulations, including conventional T cell subtypes, γδ T cells, innate lymphoid cells, and natural killer T cells (Fig. 6A and fig. S17A). Four prominent RORγt (*Rorc*)–expressing populations were identified, denoting T_H17 cells (cluster-8), $ROR\gamma t^+$ T_{reg} cells (cluster-7), γδT-17 cells (cluster-14), and type-3 innate lymphoid cells (ILC3, cluster-15) (Fig. 6B and fig. S17A). Examination of cluster-8 revealed that SI-LP T_H17 cells from $A^{\Delta CD4}$ mice expressed higher levels of *Il22*, with subtle changes in *Rorc* and *Il17a* expression (Fig. 6C and fig. S17B). The expression of other canonical cytokines produced by SI T_H17 cells, such as IL-17f, IL-21, and interferon-γ, were either below detection or comparable between genotypes (fig. S17B). Other markers associated with mucosal T_H17 effector or regulatory functions were not notably changed (fig. S17, C and D).

IL-22 is a mucosal T_H17-associated cytokine in mice that maintains gut homeostasis and mucosal defense by increasing the production of antimicrobial peptides and promoting epithelial regeneration (*54*, *55*). Consistent with our RNA-seq results (Figs. 2A and 6C), flow cytometry revealed increased $IL\text{-}22^+$ frequency among $A^{\Delta CD4}$ SI-LP CD4 T cells, which also often coexpressed IL-17A (Fig. 6D). We generated F/F and $A^{\Delta CD4}$ mice harboring an IL-22–GFP reporter allele (GFP, green fluorescent protein). $A^{\Delta CD4}$ SI-LP $CD4^+$ T cells were more frequently GFP^+ than SI-LP $CD4^+$ T cells of control mice (Fig. 6E), whereas the GFP^+ percentages of non-CD4 T cells and innate lymphocytes were comparable (fig. S18A). Induction of gut T_H17 cells and $IL\text{-}22^+$ populations in laboratory mice depends on the colonization of segmented filamentous bacteria (SFB) (*56*). Accordingly, increased IL-22 in $A^{\Delta CD4}$ mice was mainly attributed to TCR $V\beta14^+$ T cells, a major clonal response to SFB antigen (Fig. 6E) (*57*, *58*). Thus, loss of nonvesicular cholesterol transport in T_H17 cells led to increased IL-22–producing cells in SI-LP.

Chronic overexpression or loss of IL-22 alters nutrient metabolism (*59*–*63*). We assessed whether exogenous IL-22 could suppress the absorption of a bolus of triolein. A single administration of IL-22

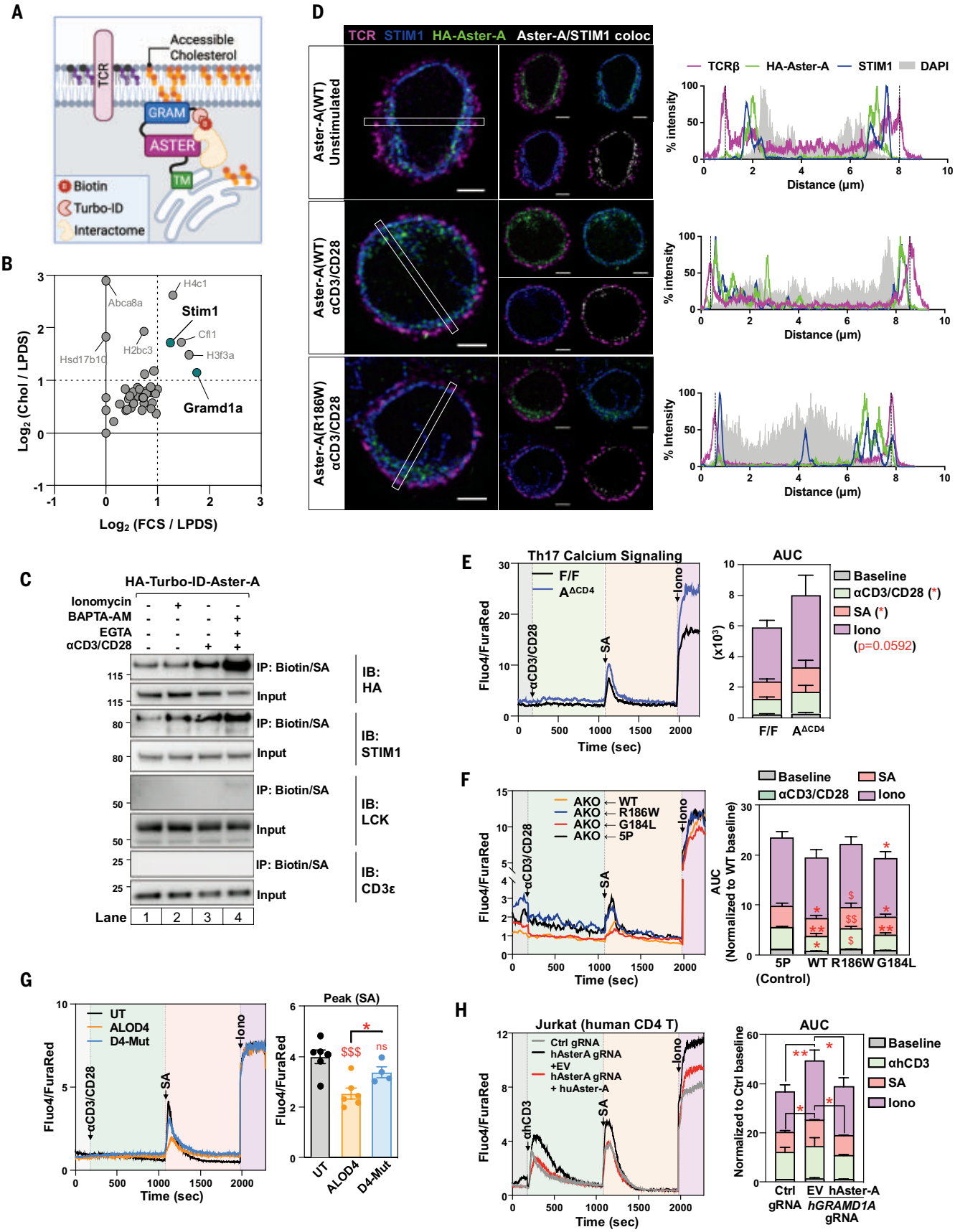


Fig. 5. Aster-A associates with STIM1 and modulates TCR-mediated Ca^{2+} signaling. (**A**) Schematic graph showing the proximal labeling strategy using N-terminal TurboID-fused Aster-A. (**B**) Results of semiquantitative proteomics showing differentially biotinylated proteins. EL-4 cells expressing TurboID–Aster-A were treated with 10%

lipoprotein-deficient serum (LPDS) media overnight, 10% fetal bovine serum (FCS) media overnight, or LPDS media and loaded with 100 μM methyl-β-cyclodextrin–cholesterol (Chol). (**C**) Western blot analysis of biotinylated proteins in TurboID–Aster-A EL-4 T cells stimulated with ionomycin (1 μM) or plate-bound anti-CD3/CD28 (5 μg/ml) in the presence or absence of BAPTA-AM (50 μM) and EGTA (10 mM) for 1 hour. SA, streptavidin. (**D**) Immunofluorescence analysis of cellular localization of HA–Aster-A, endogenous STIM1, and PM TCRβ in primary mouse T_H17 cells. $A^{\Delta CD4}$ T_H17 cells were reconstituted with HA-tagged WT or R186W Aster-A and were either unstimulated or stimulated with TCR cross-linking (soluble 5 μg/ml biotin–anti-CD3 and anti-CD28 followed by 10 μg/ml SA). Shown on the left are merged images of all three or two of the three channels, as well as HA–Aster-A/STIM1 colocalization (white). Shown on the right are the relative pixel intensities of TCRβ–Alexa Fluor 647, HA–Alexa Fluor 555, and STIM1–Alexa Fluor 488 from a cross section of the cell (white box). Scale bars are 2 μm. (**E**) Shown on the left are SOCE traces (median of the ratio of Ca^{2+} indicators Fluo-4 to FuraRed) from F/F and $A^{\Delta CD4}$ T_H17 cells that were restimulated with soluble biotin–anti-CD3 and anti-CD28 (5 μg/ml), followed by SA-mediated cross-linking (10 μg/ml) and ionomycin (1 μM). The trace is the average from $n = 3$ independent experiments. On the right, the area under curve (AUC) of each treatment is quantified. (**F**) Shown on the left is a representative SOCE trace from Aster-A–deficient ($A^{\Delta CD4}$) T_H17 cells reconstituted with 5P (ASTER domain loss of function, control), WT, R186W (GRAM domain loss of function), or G184L (GRAM domain gain of function) Aster-A. The trace is representative of three independent experiments. On the right, the AUC of each treatment is quantified. The * represents comparison to 5P mutant; the $ represents comparison to WT. $n = 5$ independent experiments. The gating strategy is shown in fig. S22. (**G**) Shown on the left is a representative SOCE trace from WT T_H17 cells restimulated as (E). Cells were treated with 20 μg/ml purified ALOD4 or the cholesterol nonbinding mutant (D4-Mut) 30 min before time 0. Shown on the right are quantifications of peak SOCE. $n = 4$ to 6 independent experiments. The $ represents comparison to the untreated condition. (**H**) Shown on the left is a representative SOCE trace from Ctrl guide RNA (gRNA) or Aster-A knockout (GRAMD1A gRNA) human Jurkat T cell clones reexpressed with empty vector (EV) or human Aster-A. On the right, the AUC of each treatment is quantified. $n = 3$ independent experiments. In (E) to (H), data are shown as mean ± SEM. For (G), data points indicate independent experimental replicates. The statistical analyses used are as follows: for (E), paired two-way ANOVA with Sidak's multiple comparison test; for (F) and (H), multiple paired one-way ANOVA with Tukey's multiple comparison test; and for (G), ordinary one-way ANOVA. ns, not significant ($p > 0.05$); *p or $$p$ < 0.05; **p or $$$p$ < 0.01; $$$$p$ < 0.001. [(A) created with BioRender.com]

for 1 hour before [^{3}H]triolein challenge markedly reduced radiolabel uptake across the length of the SI and its subsequent appearance in circulation (Fig. 6, F and G, and fig. S18B). To determine whether increased IL-22 production from $A^{\Delta CD4}$ T_H17 cells affected SI epithelial homeostasis, we assessed signaling and transcriptional components downstream of the IL-22 receptor. Jejunal epithelial scrapings from $A^{\Delta CD4}$ mice showed elevated STAT3 phosphorylation compared with scrapings from controls in both fasted and oil-fed states (Fig. 6H), confirming that IL-22 signals to jejunal epithelium, where most dietary fatty acids are absorbed. Furthermore, the distal ileum of $A^{\Delta CD4}$ mice showed elevated expression of IL-22–responsive antimicrobial peptides, regenerating islet-derived protein (Reg) 3β and Reg3γ (fig. S18C). Thus, the consequences of increased IL-22 production from $A^{\Delta CD4}$ T_H17 cells were evident throughout the length of the SI.

To directly test the hypothesis that elevated IL-22 contributed to lower fatty acid uptake in $A^{\Delta CD4}$ mice, we transiently blocked the effect of IL-22 with a neutralizing antibody (Fig. 6I). IL-22 neutralization effectively lowered *Reg3b* and *Reg3g* expression in $A^{\Delta CD4}$ mice compared with mice administered control isotype immunoglobulin G (IgG) (fig. S18C). Notably, blocking IL-22 also reversed the impairment of fatty acid absorption in $A^{\Delta CD4}$ mice (Fig. 6J). To further determine the contribution of T cell IL-22 to diet-induced obesity in $A^{\Delta CD4}$ mice, we generated $Il22^{F/F}A^{F/F}CD4^{Cre}$ and $Il22^{F/F}A^{F/F}$ mice (fig. S19A). $Il22^{F/F}A^{F/F}CD4^{Cre}$ and $Il22^{F/F}A^{F/F}$ mice showed no difference in weight gain when challenged with HFD (fig. S19B). SI [^{3}H]triolein uptake was also normalized between the two genotypes (fig. S19C), thus implicating the epistatic relationship between IL-22 and Aster-A in T cells. These data indicated that loss of Aster-A in T cells decreased fatty acid absorption and restrained diet-induced obesity via IL-22.

Gut-resident immune cells and IL-22 can influence the microbiota composition (*63*, *64*), which may independently affect responses to diet (*65*, *66*). However, F/F and $A^{\Delta CD4}$ mice fed HFD had similar fecal bacterial composition (fig. S20A). Depletion of gut bacteria and fungus with broad spectrum antibiotics effectively reduced *Il22* transcripts in SI and mLNs (fig. S20, B to D) and accordingly restored fatty acid uptake in $A^{\Delta CD4}$ mice (fig. S20, E and F). Furthermore, littermate F/F and $A^{\Delta CD4}$ mice that were individually housed or cohoused to either deviate or normalize microbiota showed similar differences in HFD-induced weigh gain and fat mass (fig. S20, G and H). Thus, the gut microbiota was required for IL-22 induction but itself did not directly contribute to impaired fatty acid uptake in $A^{\Delta CD4}$ mice. We conclude that the effect of T cell–specific loss of Aster-A changes fatty acid absorption through direct T cell–enterocyte communication mediated by IL-22.

Discussion

Aster proteins are recruited to PM-ER contact sites by accessible cholesterol and mobilize this pool to the ER (*12*). Here, we showed that the accessible PM cholesterol pool expands immediately after TCR activation, leading to Aster-A recruitment. Some of this additional accessible cholesterol, if not removed promptly, appeared to be funneled into the SM-sequestered domains (*21*, *22*), which supported TCR nanoclustering and reduced the threshold for activation. We posit that the heightened T_H17 effector function observed in vitro and in vivo in the absence of Aster-A arises from both the inability to rapidly remove accessible cholesterol generated by TCR activation and the increased abundance of TCR nanoclusters formed as a result of chronic accumulation of SM-cholesterol domains.

Excess ER free cholesterol is rapidly converted to cholesteryl esters by acyl-coenzyme A:cholesterol acyltransferases (ACATs) (*67*). Inhibition of ACAT1 causes PM cholesterol accumulation and potentiates TCR activity in cytotoxic T cells (*25*, *68*). Our results in T_H17 cells suggest that Asters most likely act upstream of ACATs in this regulatory axis. Loss of Aster-A alone does not seem to affect peripheral T cell composition, consistent with previous studies in which homeostatic T cell cholesterol content was perturbed by loss of SCAP/SREBP2, ACAT1, or SULT2B1B (*21*, *25*, *69*, *70*). Instead, PM cholesterol accumulates in Aster-A–deficient SI-LP T_H17 cells in a cell-autonomous manner. Dynamic expansion of the accessible cholesterol pool also occurred after T cell activation and was associated with the expansion of Aster-A–deficient $ROR\gamma t^+$ T_H17 cells in vivo. Thus, we propose that Aster-A is an indispensable guard of T_H17 membrane homeostasis.

It was unknown whether Asters cooperate with other classes of membrane contact-site proteins at the PM. We identified the proximity of Aster-A with STIM1 in activated T cells. The precise molecular details by which Aster-A affects STIM1 function in SOCE remain to be determined. Notably, two unbiased protein interaction and proximity maps also identified the association of Aster-A with STIM1 and TCR components (*71*, *72*). Prior microscopy studies in human epithelial and fibroblast cell lines suggested stable colocalization of STIM1 with GRAMD2A, but not GRAMD1A (encoding human Aster-A), at PM-ER contact sites (*73*). Given that we failed to coimmunoprecipitate a substantial quantity of STIM1 with Aster-A, we posit that their interaction is likely transient or indirect. Furthermore, murine T cells show only trace expression of *Gramd2*, suggesting that STIM1-containing PM-ER contact sites must be defined by a different set of proteins in T cells. Recruitment of the Aster GRAM domain to the PM requires dual recognition of accessible cholesterol and anionic phospholipids such as PS (*5*, *10*, *12*, *19*, *49*, *74*). Paradoxically, PS scrambling from the inner to outer leaflet appears to contribute to ionomycin-induced

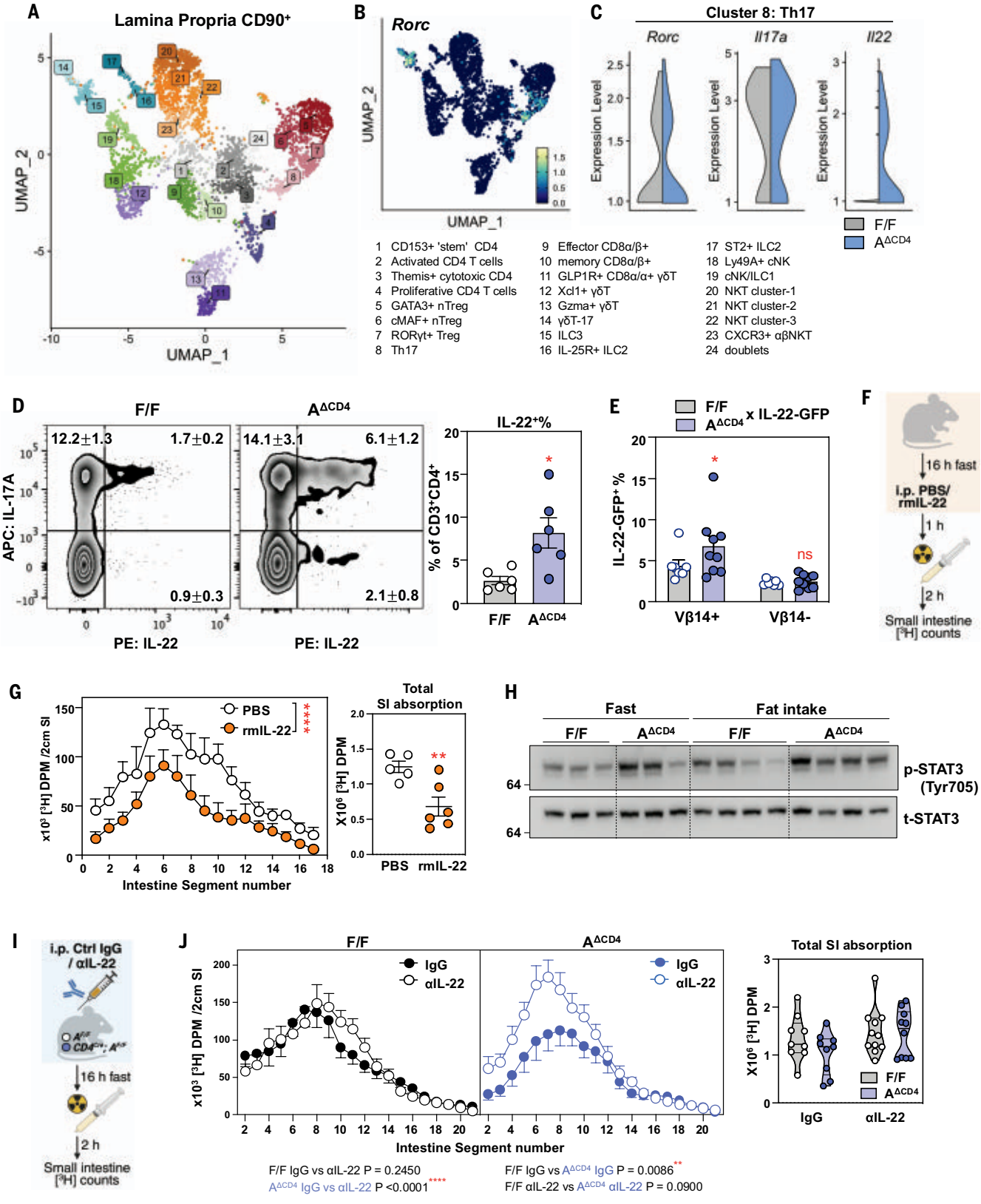


Fig. 6. Aster-A deficiency leads to IL-22–mediated inhibition of fatty acid absorption. (**A**) Uniform manifold approximation and projection (UMAP) analysis of scRNA-seq data from SI-LP CD90$^+$ (based on *Thy1* expression) cells from F/F and littermate A$^{\Delta CD4}$ mice. Cluster annotations are listed at the bottom right. $n = 1$ biological replicate pooled from three mice per group (total of 4239 cells in UMAP). (**B**) UMAP analysis of *Rorc* expression. (**C**) Violin plots of *Rorc*, *Il17a*, and *Il22* expression in cluster-8 (T_H17) cells from scRNA-seq analysis in (A) and (B). (**D**) Representative flow plots of IL-17A$^+$ and IL-22$^+$ SI-LP T cells (CD45$^+$CD3$^+$CD4$^+$) from F/F and littermate A$^{\Delta CD4}$ mice gavaged with olive oil for 2 hours. Quantified percentages are shown on the right. $n = 6$ mice per group, pooled from two independent experiments. The gating strategy is shown in fig. S24A. (**E**) Percentage of IL-22-GFP$^+$ in Vβ14$^+$ or Vβ14$^-$ SI-LP T cells (CD45$^+$ CD90$^+$CD3$^+$CD4$^+$) from Aster-A$^{F/F}$ *Il22*^{GFP}(F/F x IL-22–GFP) and littermates Aster-A$^{F/F}$ CD4^{Cre} *Il22*^{GFP} (A$^{\Delta CD4}$ x IL-22–GFP)

mice gavaged with olive oil for 2 hours. $n = 7$ to 9 mice per group, pooled from two independent experiments. The gating strategy is shown in fig. S24B. (**F**) Schematic diagram for the IL-22 treatment experiment in (G). (**G**) Shown on the left is the distribution of radioactivity in SI segments of C57/BL6J WT mice after an oral challenge of olive oil containing [^{3}H]triolein (18:1) for 2 hours. Mice were intraperitoneally injected with phosphate-buffered saline (PBS) or 1.5 μg IL-22 at 1 hour before triolein challenge. Shown on the right is the total radioactivity in the SI. $n = 5$ or 6 mice per group, representative of two independent experiments. (**H**) Western blot analysis of phospho-STAT3 (tyrosine 705) and total STAT3 (t-STAT3) in jejunal epithelial scrapings from F/F and littermate A$^{\Delta CD4}$ mice fasted for 16 hours (Fast) or gavaged with olive oil (Fat intake) for 2 hours. $n = 3$ or 4 mice per group, representative of two independent experiments. (**I**) Schematic diagram for the IL-22 neutralization experiment in (J). (**J**) Shown on the left is the distribution of radioactivity in SI segments of F/F and littermate A$^{\Delta CD4}$ mice after an oral challenge of olive oil containing [^{3}H]triolein (18:1) for 2 hours. Mice were treated with 250 μg anti–IL-22 (αIL-22) or control IgG antibody for 16 hours. Shown on the right is the total radioactivity in the SI. $n = 9$ to 11 mice per group, pooled from two independent experiments. For (D), (E), (G, right), and (J, right), data points indicate individual mice; for (G, left) and (J, left), data points indicate mean values. For (D), (E), (G), and (J), data are shown as mean ± SEM. For violin plots in (J), lines indicate median and quartiles. The statistical analyses used are as follows: for (D) and (G, right), two-tailed Welsh's *t* test; for (E), ordinary two-way ANOVA; and for (G, left) and (J), two-way ANOVA with Sidak's multiple comparison test. ns, not significant ($p > 0.05$); *$p < 0.05$; **$p < 0.01$; ****$p < 0.0001$. [(F) and (I) created with BioRender.com]

GRAM domain recruitment to the PM in T cells. The GRAM domain can bind anionic phospholipids other than PS, including phosphatidylinositol 4,5-bisphosphate [PI(4,5)P_2] and phosphatidic acid, which could serve as alternative PM localization signals in the absence of PS (*12*, *49*). STIM1 is known to reside in PI(4,5)P_2-rich domains (*46*, *75*, *76*), leading us to speculate that Aster-A could be recruited to STIM1 domains by these lipids. Reciprocal PS-PI(4,5)P_2 transport at the PM-ER contact sites has recently been found to fine-tune STIM1 clustering (*77*, *78*). Thus, additional mechanisms of PM phospholipid remodeling may act in conjunction or sequentially with Aster for regulation of TCR signaling and SOCE.

Excess LDL cholesterol can be incorporated into the membranes of immune cells and may promote immunopathology (*79*–*81*). In particular, enhanced T_H17-associated inflammation has been observed in various mouse models of hypercholesterolemia (*82*–*85*). Cholesterol internalized by LDL receptor-mediated endocytosis is liberated in the lysosome and then moves back to the PM, where it can be mobilized to the ER by Asters (*6*, *18*, *74*). Our results raise the intriguing question of whether Aster-A functions to curtail hypercholesterolemia-induced inflammatory T cell responses by resolving the PM accumulation of LDL-derived cholesterol. Further studies are required to fully understand potential anti-inflammatory roles of Asters in hypercholesterolemia and atherosclerosis.

Finally, our findings show that loss of membrane homeostasis in immune cells affects systemic lipid metabolism. Aster-A expression in T cells is required for appropriate fatty acid absorption and helps determine chronic metabolic responses to HFD. Although we specifically traced the uptake of labeled triolein, which is composed solely of 18:1 fatty acid, diet challenge and fecal analysis suggest a broad impairment of dietary fat absorption in A$^{\Delta CD4}$ mice. Importantly, increased IL-22 production mediates this T cell–intestinal cross-talk. In line with the well-established role of SFB in inducing IL-22$^+$ T_H17 cells (*56*, *58*, *86*), Aster-A deficiency led to major changes in IL-22 frequency in the SFB-associated clonal type. These observations imply that Aster-A tunes gut T_H17 reactivity to commensal bacteria under homeostatic conditions. Our results, along with recent studies demonstrating the metabolic protective role of SFB-elicited T_H17 cells (*62*), support the notion that mucosal lymphocytes exert important restraints on intestinal lipid handling.

Materials and methods

Mice

Aster-A$^{F/F}$ (exon 12-16 floxed) and Aster-A$^{-/-}$ (global knockout) mice were generated by C57BL/6 ES cell-based gene targeting as described previously (*5*, *6*). Aster-A$^{F/F}$ offsprings were backcrossed into C57BL/6N background and crossed with CD4^{Cre} (RRID:IMSR_JAX:022071) line to generate T-cell-specific knockout animals, with Albumin^{Cre} (RRID:IMSR_JAX:003574) line to generate liver-specific knockout animals, with Villin^{CreERT2} (RRID:IMSR_JAX:020282) line to generate tamoxifen-inducible, intestine epithelium-specific knockout animals. For tamoxifen-induced knockout, mice were injected intraperitoneally with 1 mg tamoxifen in 100 μl corn oil (both from Sigma Aldrich) per day for 5 days and used for experiments 5 days later. All studies involving cre-flox mice were performed in age- and sex-matched littermates. For studies involving wild-type (CD45.2) mice and congenic (CD45.1) mice, C57BL/6J mice (RRID:IMSR_JAX:000664) or CD45.1 congenic mice (RRID:IMSR_JAX:033076) were obtained from The Jackson Laboratories. CD45.1/.2 mice were generated by crossing WT C57BL/6J females with CD45.1 congenic males. IL-22^{GFP} mice (RRID:IMSR_JAX:035005) were purchased from Jax and crossed to CD4^{Cre}; Aster-A$^{F/F}$ (A$^{\Delta CD4}$) mice. *Il22*$^{hCD4.fl}$ (*Il22*$^{F/F}$) mice were originally generated by C. Zindl and C. Weaver (University of Alabama at Birmingham) (*87*) and were crossed to A$^{\Delta CD4}$ mice. Unless otherwise specified, 8-14 week old female and male mice were used for in vivo experiments and 6-10 week old female and male mice were used for in vitro experiments. All mice were housed in a temperature-controlled room (22°C with humidity approximately 50–65%) with a 12-hour light-dark cycle (06:00 to 18:00) under specific pathogen-free conditions. Unless otherwise specified in the experimental procedures below, mice were housed in ventilated cages containing nestlets as environmental enrichments, with a maximum of five adult mice per cage. Unless otherwise specified, mice were fed an irradiated chow diet (PicoLab Rodent Diet 20, 5053) and provided water ad libitum. Mice were euthanized by isoflurane overexposure, followed by secondary methods (cervical dislocation or organ harvest). All animal experiments were approved by the UCLA Institutional Animal Care and Research Advisory Committee (Animal protocol B-09-010, R-03-166, R-99-131).

Measurement of intestinal fatty acid absorption

For acute fatty acid uptake assay, mice were fasted for 16 hours and then intragastrically gavaged with 5 μCi [^{3}H]triolein (PerkinElmer) emulsified in 150 μl highly refined, low acidity olive oil (Sigma Aldrich). Blood was sampled using retro-orbital method at 0, 30, 60, 120 min time points. Two hours after gavage, mice were euthanized and small intestine was excised (between the base of the stomach and the cecal junction), flushed with at least 20 ml 0.5 mM sodium taurocholate in PBS, and cut it into 2 cm segments. Segments were incubated with 500 μl of 1N NaOH at 65°C overnight and then mixed with UltimaGold scintillation cocktail (PerkinElmer), and radioactive counts were collected using a Beckman LS6000 scintillation counter. Liver and heart were also harvested and rinsed extensively to remove blood and weighed. Liver medial lobe and heart were incubated with 1 ml and 500 μl of 1N NaOH, respectively, at 65°C overnight and ^{3}H was counted as above and normalized to tissue weight. Plasma was obtained from blood in K2-EDTA tubes followed by centrifugation at 2,000*g* for 15 min. Twenty microliters of plasma sample was mixed with 5 ml scintillation cocktail for counting.

Diet studies

Normal chow diet (PicoLab Rodent Diet 20, 5053) with 13.1 kcal% fat was purchased from LabDiet. The composition of major fatty acids (w/w) are as follows: 46.4% C18:2, 5.6% C18:3, 0.4% C20:4, 8.4% ω-3 fatty acids,

15.4% total saturated fatty acids, 20% total monounsaturated fatty acids. Rodent diet with 60 kcal% fat (high-fat diet) was purchased from Research Diet (D12492). The composition of major fatty acids (w/w) are as follows: 34.0% C18:1, 28.7% C18:2, 19.6% C16:0, 10.6% C18:0, 2.0% C18:3, 1.3% C16:1. Mice were co-housed with littermate of both genotypes, single-housed, or grouped by genotype as indicated in individual experimental conditions. Unless otherwise stated, mice were fed indicated diet and given water ad libitum when they reach 8-10 weeks of age or 23 g mean body weight for males, 19 g mean body weight for females. Body composition (fat and lean mass) was measured by magnetic resonance imaging (EchoMRI) at the beginning and end of each study. Body weight was measured weekly. Tissue weights were measured at euthanasia. Food intake measurement, metabolic chamber studies, and fecal 16S sequencing was performed in single-housed male mice.

Indirect calorimetry using metabolic cages

Four weeks after high fat diet feeding, respiratory exchange ratios and energy expenditure were measured by indirect calorimetry using the Oxymax Comprehensive Laboratory Animal Monitoring System (Columbus Instruments). Data were analyzed using CalR application (*88*).

Glucose and insulin tolerance assay (GTT/ITT)

Lean mass of mice was determined by MRI on the day prior to GTT/ITT. HFD-fed mice were fasted for 4 hours, followed by intraperitoneal injection of 1 mg per gram of lean mass for glucose, or 2.5 units per kg lean mass for insulin (Humulin) and blood glucose was measured by glucometer (Bayer) at the indicated times.

Mixed bone marrow transplant

CD45.1/CD45.2 recipient mice were irradiated using x-ray irradiator with two fractioned doses of 550 cGy with at least 4 hours interval. To harvest bone marrow, femurs and tibias were harvested from F/F, $A^{\Delta CD4}$, or competitor CD45.1 mice and removed of muscle tissues. Bone marrow single cell suspension was obtained by homogenizing bones using mortar and pestle. Unfractionated bone marrow cells from donor (CD45.2: F/F or $A^{\Delta CD4}$) and competitor mice (CD45.1) were mixed at 1:1 ratio and 8-10 million mixed bone marrow cells were intravenously injected through the tail vein into the recipients. Recipient mice were given 0.5 mg/ml Baytril (Enrofloxacin) in drinking water for 1-2 weeks prior to transplant and for 2 weeks after transplant to prevent opportunistic infection. Small intestinal lamina propria cells were harvested 8-10 weeks after transplant using the methods described below. Cells were stained with antibodies against CD45.1, CD45.2, CD3, CD4, ALOD4, and RORγt for flow cytometry analysis as described below. All antibody information is reported in table S1.

Acute IL-22 treatment and in vivo IL-22 neutralization experiments

In vivo IL-22 neutralization was performed by injecting 250 μg functional grade anti-human/mouse IL-22 (clone IL22JOP, ThermoFisher) intraperitoneally at the time of fasting (16 hours prior to [^{3}H]triolein gavage). Control mice were injected with 250 μg of isotype Rat IgG2a, κ (clone eBR2a). Acute IL-22 treatment was performed by intraperitoneal injection of 1.5 μg recombinant mouse IL-22 (Genscript) in DPBS. One hour later, mice were used for fatty acid absorption assay.

Depletion of microbiota by broad-spectrum antibiotics

Caging and food were sterilized by autoclaving/irradiation. Mice were given broad spectrum antibiotics (1 g/liter Ampicillin, 1 g/liter Neomycin, 1 g/liter Metronidazole, 0.5 g/liter Vancomycin, 1 g/liter Gentamycin, and 0.01 g/liter amphotericin B) in sterile drinking water for 2 weeks. Feces before and after antibiotics treatment were collected. Bacterial DNA was isolated from same quantity of feces using Quick-DNA Fecal/Soil Microbe Miniprep Kit (Zymo Research). Quantitative PCR of 16s rRNA was performed using primers in table S2.

Intraperitoneal anti-CD3ε antibody

Twenty micrograms of anti-mouse CD3ε (clone 145-2C11) or control polyclonal Armenian hamster IgG (both from BioXCell) was diluted in DPBS and injected peritoneally to mouse at indicated times prior to sacrifice. For ALOD4 staining, mesenteric lymph nodes were resected and processed to single cell suspension on ice in DPBS (Ca^{2+}, Mg^{2+}). Cells were stained with ALOD4 and live/dead stain for 1 hour at 4°C, followed by fixation and permeabilization (eBioscience FOXP3 Transcription Factor staining set), and antibody staining as described below.

Plasmids

Table S3 lists plasmids used and generated by this study. Full length mouse Aster-A coding sequence was cloned into: (i) 3xHA-TurboID pRetrox with TurboID (Addgene Plasmid #155203) located at N terminus of Aster-A GRAM domain with a GGGGS linker; (ii) MSCV-IRES-hCD2 (Addgene Plasmid no. 133061) vector with an N-terminal HA tag and GGGGS linker; (iii) an inframe N-terminal mCherry and 3x GGGGS linker, all by Gibson assembly (NEB). Aster-A functional mutations were identified from homologous amino acids between mouse Aster-A and human/mouse Aster-B (*19*, *49*) and cloned into MSCV-IRES-hCD2 vector by site-directed mutagenesis. C-terminal Myc-GGGGS-tagged mouse STIM1 was cloned from pcDNA3.1 mSTIM1 myc (Addgene Plasmid no. 17732) and inserted into pMSCV-Blast (Addgene Plasmid no. 75085) vector by Gibson assembly. Full-length human Aster-A was cloned from Jurkat cDNA and mCherry was tagged at N-terminal using methods above into a pMSCV-hygro (Addgene Plasmid no. 34565) vector. For CRISPR plasmids, guide RNA sequences (described below) were cloned into pSCAR_sgRNA_puro-mKate-lox2272 (Addgene Plasmid no. 162076) or pSCAR_sgRNA_hygro-tagBFP-lox5171 (Addgene Plasmid no. 162070) vectors using BsmBI sites.

Viral production and transduction

For retrovirus production for murine cells, 2.5 μg transfer plasmid and 0.63 μg pCL-ECO were co-transfected to 1×10^6 Platinum-E cell line in 6-well plate using OptiMEM and FugeneHD reagent for 6-8 hours. Media was replaced with appropriate culture media for the target cell, and virus supernatant was harvested at 48 and 72 hours post transfection. For retrovirus production for human cells, 2.5 μg transfer plasmid was transfected to Phoenix-AMPHO cell line and virus was harvested at 48 hours. For lentivirus production, 2.5 μg transfer vector, 1.875 μg psPAX2, 1.25 μg pMD2.G was co-transfected to Lenti-X cell line in a similar procedure as above. For integration deficient Cre lentivirus, 2.5 μg pLX-Cre-ppl-del, 1.875 μg psPAX2 D64V, 1.25 μg pMD2.G was co-transfected to Lenti-X cell line. For viral transduction of suspension cell lines, viral supernatant was harvested and cleaned through a 0.45 μm filter. Cells were spin infected in 12-well plates with 1-2 ml viral supernatant containing 8 μg/ml polybrene (for cell lines) or 10 μg/ml Protamine Sulfate (for primary T cells). Viral supernatant was replaced with normal growth medium 4-6 hours later and antibiotics selection was performed 48-72 hours post transduction. For some experiments, transduction was repeated 24 hours later to increase efficiency.

Cell lines, construction of stable overexpression cells, and CRISPR knockout cells

Platinum-E (RRID:CVCL_B488) retroviral packaging cell line was obtained from Cell Biolabs. Lenti-X 293T cell line (RRID:CVCL_4401) was obtained from Takara Bio. Phoenix-AMPHO (RRID:CVCL_H716), EL-4 (RRID:CVCL_0255), Jurkat (RRID:CVCL_0065) cell lines were obtained from the American Type Culture Collection.

To construct stable TurboID-expressing EL-4 lines, EL-4 cells were transduced with retrovirus containing pRetroX-3xHA-TurboID or pRetroX-3xHA-TurboID-GGGGS-mAster-A. Cells were selected with 10 μg/ml puromycin for 1 week and maintained in 0.3 μg/ml puromycin. To construct stable mCherry-tagged mAster-A expressing EL-4 line,

EL-4 cells were transduced with retrovirus containing pMSCV-mCherry-GGGGS-mAster-A, mCherry positive cells were FACS-sorted and used without further subcloning. To construct stable HA-tagged mAster-A expressing EL-4 line, EL-4 cells were transduced with retrovirus-containing pMSCV-HA-GGGGS-mAster-A (WT or R186W mutant)-IRES-hCD2, cells were FACS-sorted by surface hCD2 expression. STIM1 was further introduced by infecting HA-Aster-A cell lines with virus containing pMSCV-STIM1-Myc-His-Blast and cells were selected with 10 μg/ml Blasticidin for >1 week and maintained on 1 μg/ml Blasticidin. To construct PM-RA and B-GRAM-H (B-GRAM-H-ddFP) expressing cell lines, EL-4 or Jurkat cells were transduced with lentivirus containing pLJM1-PM-RA-BlastR and pLJM1-B-GRAM-H-NeoR. Cells were selected with 2 mg/ml G418 and 50 μg/ml Blasticidin for 1 week and maintained in 0.5 mg/ml G418 and 10 μg/ml Blasticidin. Protein expression in overexpression or reconstitution experiments was confirmed by Western blot.

To construct Aster-A knockout Jurkat human T cell lines, pSCAR-Cas9-GFP was introduced by lentiviral transduction and stable polyclonal Cas9-GFP expressing Jurkat cells were selected by FACS sorting. Cas9-GFP Jurkat cells were co-transduced with pSCAR_sgRNA1_puro-mKate-lox2272 or pSCAR_sgRNA2_hygro-tagBFP-lox5171 virus with two distinct gRNAs: gRNA1 targeting hAster-A exon 10 (5′-GTCTGTCAATAGCTCCTCAC-3′) and gRNA2 targeting exon 14 (5′-TCTCAATGAGCGACTTCACC-3′). The resultant deletion of exons in between will eliminate the majority of ASTER domain in addition to a frame shift. As control, Cas9-GFP Jurkat cells were transduced with the above sgRNA vector containing viruses where sgRNA1 (5′-GCACTACCAGAGCTAACTCA-3′) and sgRNA2 (5′-GTGCGAATACGCCACGCGAT-3′) do not target any human genome sequence. Cells were selected with 50 μg/ml Blasticidin, 10 μg/ml Puromycin, and 500 μg/ml Hygromycin for 1 week to allow deletion. Jurkat cells were single-cloned by FACS, and GRAMD1A knockout clones were selected by PCR and subsequently confirmed by the absence of hAster-A protein by Western blotting (anti-hAster-A, Bethyl labs). Control clone was selected to match growth rate, morphology, and cell size of the KO clone. Subsequently, Cas9-GFP, mKate, and tBFP was removed by transducing single clones with integrase deficient virus and isolated by GFP/mKate/tBFP-triple negative FACS sorting. hAster-A KO Jurkat clones were further reconstituted with HA-tagged hAster-A, or HA alone empty vector (EV) using amphotropic retrovirus and were selected by 500 μg/ml Hygromycin for 2 weeks.

Plasma and tissue lipid quantification

Plasma lipids were measured by colorimetric assay with L-Type TG M kit (Wako). Tissues were homogenized by dounce homogenizer in JP lysis buffer [10 mM Tris-HCl pH 7.4, 150 mM NaCl, 1 mM EDTA, Halt protease inhibitor cocktail (ThermoFisher)] and Folch method was used to extract lipids from materials containing 0.5-1 mg tissue protein (*89*). Protein content was measured by Bicinchoninic Acid Assay Protein Assay Kit (Pierce). Extracted lipids were dried under inert gas and resuspended in isopropanol and quantification was performed using the previously described kits. For cholesterol measurement in culture media, 1 ml of media was used for lipid isolation and quantification using Total Cholesterol E Kit (Wako).

Measurement of fecal NEFA and lipid species

Littermate mice were fed with high fat diet for 10 days and then single-housed with fresh cellulose bedding. Feces accumulated for 48 hours were collected, snap frozen, and pulverized using mortar and pestle. One hundred milligrams of fecal homogenate was used for lipid extraction with 19 volumes of 2:1 (v/v) chloroform:methanol using the Folch method. Solvent was removed by drying under nitrogen gas, resuspending in isopropanol, and measured using NEFA-Hr kit (Wako).

Thin layer chromatography was performed using lipid extraction from 25 mg fecal homogenates. Fecal lipids were extracted as described above, resuspended in chloroform, and dotted on a Silica Gel 60 TLC plate (Millipore Sigma). Samples are stacked using solvent 1 system ($CHCl_3$/MeOH = 2:1) and neutral lipid species were subsequently separated using solvent 2 system (Heptane/Isopropyl Ether/glacial Acetic Acid = 15:10:1). A mixed lipid standard (mouse liver lipid extract supplemented with 20 mM 18:1 fatty acid) was run along the samples to identify triglycerides and free fatty acids. Separated lipids were visualized by exposing to iodine vapor for 30 min.

Protein isolation from the intestinal epithelium

Intestines were harvested immediately following euthanasia and extensively flushed with PBS containing 1 mM dithiothreitol (DTT), Halt phosphatase and protease inhibitor cocktail. The proximal 1/6 of the intestine was designated as duodenum, middle 3/6 as jejunum, and last 2/6 as ileum. Indicated intestinal section was excised and longitudinally opened to expose the lumen. Epithelial scrapings were obtained by gently scraping the luminal tissue with two glass slides. To prevent protein degradation, scrapings were immediately snap frozen in liquid nitrogen. Scrapings were cut and weighed on dry ice, and approximately 100 mg sample was resuspended in 1 ml DS buffer [150 mM NaCl, 1.5 mM DTT, 50 mM Tris HCl pH 7.4, 1.25 mM EDTA, Halt phosphatase and protease inhibitor cocktails, 1 mM phenylmethylsulfonyl fluoride (PMSF)] and immediately homogenized on ice using motorized Dounce (850 rpm, 15 strokes). Homogenates were further sonicated (3 s × 3 at 50%) and lysates were cleared (2000*g*, 10 min, 4°C).

Total cell protein lysate

Cells were washed with PBS by centrifugation for at least 3 times, and pellet was lysed with RIPA buffer (containing protease and phosphatase inhibitor cocktails) on ice for 30 min. Lysate was cleared by centrifugation at 12,000 xg for 15 min. In some experiments, boiled 2X LDS sample buffer was directly added to cell pellets and DNA was sheared by sonication.

Western blot analysis

Protein content was determined by the Bicinchoninic Acid Assay Protein Assay Kit (Pierce) or Pierce 660 kit. An equal amount of protein was loaded into the NuPAGE 4-12% Bis-Tris gels (Invitrogen). Proteins were transferred to PVDF blotting membrane (Amersham Hybond). Membranes were blocked for 1 hour at room temperature with 5% non-fat milk in TBST buffer (TBS + 0.1% Tween 20) and incubated with primary antibodies listed in table S1 in 5% non-fat milk or 5% bovine serum albumin (BSA). IR800-, Cy3-, Cy5-, Horseradish peroxidase-conjugated anti-mouse, anti-rat and anti-rabbit IgG were used as secondary antibodies. The blot membrane was visualized using the Immobilon Forte Western HRP Substrate, SuperSignal West Femto Maximum Sensitivity Substrate, or directly imaged for fluorescent signal using ChemiDoc MP (BioRad).

RNA extraction and gene expression analyses

For tissue RNA isolation, approximately 50-100 mg frozen tissue was immediately homogenized in Trizol Reagent using preloaded 4 mm metal beads and Qiagen Tissue Lyzer. For RNA isolation from cells, cells pellets were lysed with 0.5-1 ml TriZol reagent for 5 min. Total RNA was extracted using the TRIzol method, quantified by NanoDrop (ThermoFisher) and reverse transcribed. cDNA was quantified by real-time PCR using iTaq Universal SYBR Green Supermix (Bio-Rad) on a QuantStudio 6 Flex 384-well qPCR system (Applied Biosystems). Gene expression levels were determined by using ΔΔCt method. Housekeeping gene *36b4* was used for normalization and every sample was analyzed in triplicate. Primers used for real-time PCR are listed in table S2.

Purification and fluorophore conjugation of ALOD4 and OlyA

pALOD4, pALOD4 non-binding mutant (G501A/T502A/T503A/L504A/Y505A/P506A) and pOlyA plasmids were obtained from AddGene or

gifted from the Radhakrishnan lab (table S3) and proteins were purified according to a previously published method (*4*). Briefly, plasmids encoding specified proteins were expressed in BL21 (DE3) pLysS *Escherichia coli* (Invitrogen). Cell pellets were lysed by sonication in lysis buffer containing 50 mM NaH_2PO_4, pH 7.0, 300 mM NaCl, 1 mg/ml lysozyme, 1 mM DTT, 2 mM PMSF and Halt protease inhibitor cocktail. The protein was bound to HisPur Ni-NTA Agarose resin (Thermo Scientific), washed twice with 50 mM imidazole, eluted with 300 mM imidazole, and subjected to size exclusion chromatography on Superdex 200. Fractions containing specified protein were concentrated to 1 mg/ml and stored at −80°C with glycerol until use. For ALOD4 labeling, ALOD4 was conjugated to Alexa Fluor 555-maleimide, Alexa Fluor-488-maleimide (ThermoFisher), or ATTO647N-maleimide (SigmaAldrich) followed by affinity purification using HisPur Ni-NTA Agarose resin and dialyzation. Labeling efficiency was determined using on Nanodrop (Thermo Fisher).

ALOD4 and OlyA staining

For confocal imaging, cells were plated on Shi-Fix coverslips or poly-D-lysine coated coverslips. Cells were washed with DPBS (Ca^{2+}, Mg^{2+}) with 0.2% BSA three times. The ALOD4 working solution (20 μg/ml in DPBS + 0.2% BSA) was passed through a 0.45 μm filter before addition to cells and incubating while rotating at 4 °C in the dark for 1-2 hours. Coverslips were washed three times with cold DPBS before being fixed with 3% paraformaldehyde (PFA) for 10-15 min at room temperature. After fixation, slides were washed with DPBS three times. For unconjugated ALOD4, cells were incubated with an anti-His antibody (27E8) overnight before incubation with fluorescently labeled secondary antibodies for 1 hour at room temperature. Cells were mounted on slides with ProLong Diamond Antifade Mountant with DAPI (Invitrogen). Images were acquired using an Inverted Leica TCS-SP8-SMD Confocal Microscope.

For flow cytometry of ALOD4 staining, cells were washed with cold DPBS (Ca^{2+}, Mg^{2+}) three times. Cells were incubated with ALOD4 working solution (20 μg/ml in DPBS) and Fixable Viability Dye eFluor450 (eBioscience) while rotating at 4°C in the dark for 1-2 hours. Cells were washed three times with DPBS containing 0.2% fatty acid-free BSA and fixed for 10-15 min with Fix/Perm buffer (BD) at 4°C before proceeding to the remaining flow cytometry staining procedure. For flow cytometry analysis of plasma membrane ALOD4 following anti-CD3ε mediated activation, plasma membrane accessible cholesterol density was estimated by normalizing ALOD4-ATTO647N signal to forward scatter (FSC) parameter to regress out the increased cell size and surface area using the following conversion formula:

$$\text{PM accessible cholesterol density} = \text{Intensity} < \text{ATTO647N} > / \left[4\pi(\text{Intensity} < \text{FSC} >)^2\right]$$

For Western blot analysis, cells were washed extensively with DPBS (Ca^{2+}, Mg^{2+}). Equal numbers of cells were incubated with ALOD4 and OlyA working solution (both 20 μg/ml) as above. Surface ALOD4/OlyA-bound cells were lysed with RIPA buffer before being probed with anti-His (27E8).

Histology

Whole mouse tissue was fixed in neutral formalin solution for at least 48 hours at room temperature, then rinsed extensively with water and preserved in 70% ethanol. Tissues were paraffin-embedded and cross-sectioned at 5 μm thickness. Hematoxylin and eosin (H&E) staining was performed by UCLA Translational Pathology Core Laboratory using routine procedures.

Immunofluorescence of the small intestine

Mice were fasted for 16 hours to synchronize metabolic status, then were intragastrically gavaged with 150 μl refined low acidity olive oil. Two hours later, mice were euthanized and cardiac perfused with 10 ml cold DPBS. Small intestine was excised between stomach to cecum and flushed with 10-15 ml cold DPBS to remove luminal content, followed by a slow luminal flush of 10 mL 4% paraformaldehyde to flash-fix the luminal epithelium. Small intestine was then longitudinally opened and rolled into a Swiss roll with luminal facing out, immobilized in tissue cassette and fixed overnight in 4% PFA on a 4°C rocker. Tissues were then dehydrated in 20% Sucrose in PBS for 24-48 hours on a 4°C rocker before embedding in OCT. Embedded tissue were sectioned at 18 μm thickness and attached to Superfrost Plus slides and further fixed with pre-chilled methanol in −20°C for 20 min, air-dried and rehydrated with PBST (PBS containing 0.05% Tween-20). Slides were incubated in blocking/permeabilization buffer [PBS + 0.3% Triton X-100 + 10% normal goat serum block (BioLegend)] for 1-2 hours at room temperature and stained overnight in blocking/permeabilization buffer containing anti-EPCAM-AlexaFluor 488 (G8.8). Slides were washed three to five times with PBST, stained with DAPI and lipidTOX-Red for 1 hour at room temperature, and mounted with Prolonged Diamond anti-fade mounting reagent (all from ThermoFisher). For confocal imaging of the Swiss roll for lipid droplet quantification, tile scan images were acquired on a Zeiss LSM900 confocal microscope using Plan-Apochromat 10x/0.45 M27 and 30 μm Z-stack to capture the full thickness of the tissue sections. Following acquisition, the tile scan images were processed using stitch feature and then displayed as a maximum intensity projection.

Quantification of lipid droplets

To quantify lipid droplet size and number from enterocytes in the intestine confocal images, stitched maximum intensity projection images were deconvoluted in ImageJ with the DeconvolutionLab2 plugin using a theoretical PSF generated with the PSFGenerator plugin. Processed images were then loaded into CellProfiler (*90*) for lipid droplet quantification using a customized pipeline. Briefly, EPCAM signal was used to delineate cell membranes and mask lumenal artifacts. LipidTOX-stained lipid droplets were identified using the *IdentifyPrimaryObjects* module and measurements extracted with the *MeasureSizeShape* module. Droplet measurements were inspected and analyzed in R.

Live-cell confocal imaging

First, 0.25×10^6 mCherry-Aster-A expressing EL-4 cells were resuspended in 500 μl warm Ringer's solution (155 mM NaCl, 4.5 mM KCl, 2 mM $CaCl_2$, 1 mM $MgCl_2$, 10 mM D-glucose, 5 mM HEPES) and plated onto poly-D-lysine coated 35 mm No. 1.5 Glass Coverslip culture dish (MatTek). Cells were then stained with AlexaFluor 647 anti-TCRβ (non-blocking clone H57-597, 2.5 μg) for 30 min on ice. Confocal live cell imaging was performed using the Leica Confocal SP8-STED/FLIM/FCS microscope equipped with an environmental control stage (5% CO_2, 37°C chamber and objective) and the 100x/1.40 objective. Live images (2048 × 2048 pixels per frame) were collected at 8000-Hz bidirectional scan speed with the resonance scanner using the following parameters: frame sequential mode, 15 s interval per acquisition, Pinhole = 1 Airy Unit (580 nm emission), pixel size = 102.8 pixels per micron with 5.84x digital zoom. mCherry channel was excited at 587 nm with 15% laser power and collected with a PMT gain of 1000V and a band pass of 595 to 640 nm. AlexaFluor647 channel was excited at 653 nm with 20% laser power and collected with a HyD gain of 200% and a band pass of 660 to 779 nm. Deconvolution was performed using the Leica LAS X Lightning Deconvolution module using the "adaptive" strategy. Bleach correction was performed using Histogram Matching Method (FIJI/ImageJ).

Dimerization-dependent fluorescent protein-fused GRAM domain recruitment assay

B-GRAM-H-ddFP expressing Jurkat cells were resuspended in Ringer's solution and warmed up to 37°C for 10-15 min. Live single cells were

gated based on forward and side scatter parameters. ddFP signals were recorded using mCherry channel (Ex-561 nm/ Filter-585/15) on a BD LSR Fortessa flow cytometer. For TCR stimulation, 5 μg/ml anti-human CD3 was added for 15 min and then 2 min of baseline signal was acquired before addition of 10 μg/ml streptavidin (crosslinking agent, BioLegend) and recording for another 5-10 min. Following first segment of acquisition, cells were returned to 37°C and were subsequently recorded at t = 15, 30, 60 min post activation (for 1 min each) to obtain kinetics over a longer time frame. For ionomycin stimulation, 1 μM ionomycin was directly added following the 2-min baseline recording. To pharmacologically inhibit phosphatidylserine scramblase TMEM16F, cells were pre-incubated with 10 μM 1PBC (Sigma Aldrich) for 30 min prior to recording. Kinetics platform in FlowJo v10 was used to plot time versus mCherry signal. Median with moving average was used to generate kinetics curve.

Electron microscopy

Ten-week-old F/F and $A^{\Delta CD4}$ female mice were fasted for 16 hours, then refed with refined low acidity olive oil for 2 hours. Small intestine were harvested, contents were flushed with PBS and a 0.5 cm ring shaped segment from proximal jejunum (measured at 8-10 cm from the end of stomach) was harvested and directly placed into EM fixative (2.5% glutaraldehyde, 2% paraformaldehyde, 2.1% sucrose 0.1 M sodium cacodylate) at 4°C overnight. The following day, the samples were washed 5 min, 5 times in cold 0.1 M sodium cacodylate and then postfixed with reduced osmium (2% OsO_4, 1.5% potassium ferricyanide, 0.1 M sodium cacodylate) for 1 hour. Next, samples were washed 5 times, 5 min each in cold H_2O then treated with 1% thiocarbohydrazide for 20 min at room temperature. Samples were then rinsed with H_2O for 5 times, 5 min each, and stained again with osmium (2%OsO_4 in H_2O) for 30 min. After another round of H_2O washes, the tissue was stained with 1% uranyl acetate (SPI Chem) at 4°C overnight. Tissues were dehydrated by incubating in a graded series of ethanol solutions (30%, 50%, 70%, 85%, 95%, 100%, 3 times each) for 8 min each. Then tissues were infiltrated with 33% (in acetone) EMbed 812 for 1 hour, 66% overnight, then 100% for 4 hours. Individual tissue pieces were then embedded in a flat mold and polymerized in a vacuum oven for 48 hours. Resin blocks were then trimmed and 500 nm sections were collected onto small silicon wafers using a Leica UC6 ultramicrotome and a Diatome diamond knife. For backscattered electron microscopy (BSEM): Wafers were mounted onto SEM stubs with double-sided carbon tape and imaged using a Zeiss Supra 40VP SEM equipped with a backscattered electron detector. Accelerating voltage was set to 13KeV and working distance at approximately 5 mm. BSEM was performed at the Electron Imaging Center for Nanomachines which is a part of the California NanoSystems Institute at UCLA.

Tissue processing and immune cell isolation

For isolation of immune cells from lymphoid tissues (spleen, lymph nodes, thymus), tissues were homogenized between two frosted slides. Single cell suspension was obtained by filtering using a 70 μm strainer. In some experiments, red blood cell removal was performed using Hybri-Max Red Blood Cell Lysing Buffer (Sigma Aldrich).

For isolation of immune cells from small intestine lamina propria, tissues were carefully removed of mesenteric fat and Peyer's patches. Then intestinal tissues were flushed of luminal contents, cut longitudinally open, and excised into 1-inch pieces. Cleaned tissues were extensively washed in cold HBSS buffer (HBSS + 25 mM HEPES) and then incubated in DTT buffer (HPSS + 25 mM HEPES + 3% fetal bovine serum + 1 mM DTT) for 10 min in an orbital shaker (200 rpm) at 37°C, extensively vortexed, and mucus in supernatant was removed through a 100 μm strainer. Epithelial layer was removed by two rounds of incubation with EDTA buffer (HBSS + 25 mM HEPES + 3% fetal bovine serum + 5 mM EDTA) for 10 min in an orbital shaker (200 rpm) at 37°C and followed by passing through 100 μm strainer. Remaining tissue was washed in HBSS, finely minced and digested (RPMI-1640, 0.5% fatty-acid free BSA, penicillin/streptomycin, glutamine, 1 mg/ml Collagenase D and 100 μg/ml DNase-I, 100 μg/ml Dispase II) for 35-55 min in an orbital shaker (150 rpm) at 37°C. Tissues were then vigorously vortexed and RPMI-1640 media containing 10% FCS was added. The digested tissue was filtered using 40 μm strainer. Cells were pelleted and loaded on 40%/80% Percoll gradient centrifugation (1,000*g*, 20 min at room temperature with no deceleration). Lamina propria mononuclear cells were collected from the interphase and washed with cold culture media or FACS buffer. For ALOD4 staining of ex vivo lamina propria cells, tissues were isolated and digested in 0.5% fatty-acid free BSA (Sigma) containing buffer in replacement of FCS.

For isolating adipose stromal-vascular fraction (SVF), mice were perfused with 10 ml cold PBS and adipose tissues were excised and weighed. Tissues were minced into 1 mm cubes and incubated in digestion buffer (HBSS + 10 mM HEPES + 10 mg/ml Collagenase D + 2% FCS + 10 mM $CaCl_2$, 4 ml/g tissue) for 40 min with orbital shaking (100 rpm) at 37°C. Digested tissue was vortexed for 2 min, pushed through 70 μm strainer and pelleted (500*g*, 10 min). Supernatant containing mature fat cells were discarded and pellet containing SVF cells was washed again with cold culture media or FACS buffer.

Flow cytometry staining and analysis

Antibodies used for flow cytometry analysis are listed in table S1. For the surface flow cytometry analysis, cell suspensions were resuspended in FACS buffer (DPBS, 2% FCS or 0.5% BSA, 2 mM EDTA), blocked with Fc block (anti-CD16/CD32), and subsequently stained with fluorophore conjugated antibodies. In some experiments, biotin-conjugated surface antibodies were used and subsequently stained with secondary streptavidin-PerCP-Cy5.5 (Biolegend). For non-conjugated ALOD4, a secondary PE anti-His Tag antibody (J095G46) was used and sample stained with secondary antibody but not ALOD4 was used as negative control. DAPI or LIVE/DEAD Fixable dyes were used to exclude dead cells. For intracellular cytokine staining, cells were cultured in 50 ng/ml PMA (Sigma-Aldrich), 1 μM ionomycin (Sigma-Aldrich) in the presence of 5 μg/ml brefeldin A (BioLegend) for 4-6 hours and then were stained with Live/Dead Fixable dye according to manufacturer's protocol. Cells were fixed and permeabilized using the Cytofix/Cytoperm kit (BD) and stained with antibodies diluted in permeabilization buffer. For intracellular transcription factor staining, cells were stained with Live/Dead Fixable dye and then fix, permeabilized according to FOXP3 fix/perm buffer set (eBioscience) protocol. Samples were acquired on a BD Verse or LSR-II flow cytometer. Data were analyzed using FlowJo v10. Unless specifically indicated, cells are identified based on Forward and Side Scatter (FSC/SSC) and single cells are gated using FSC-A/H/W and SSC-A/H/W parameters. Experiment-specific flow gating strategies are shown in supplemental figures.

T cell isolation and differentiation

Naïve CD4 T cells were isolated from spleen and peripheral lymph nodes of 6-12 week old mice using naïve CD4 T cell isolation kit (Miltenyi or BioLegend). For "pathogenic" T_H17 (pT_H17) differentiation, naïve CD4 T cells were activated using plate-bound anti-CD3/CD28 (5 μg/ml) in X-VIVO15 media (LONZA) containing 25 ng/ml mIL-6 (Peprotech), 5 ng/ml hTGFβ1 (Miltenyi), 20 ng/ml mIL-1β (Peprotech), 20 ng/ml IL-23 (R&D Systems), 10 μg/ml anti-IFNγ, and 10 μg anti-IL-4 (both from Biolegend) for 4 days. For restimulation experiments, day-4 pT_H17 cells were removed from differentiation cocktail, washed and rested in fresh X-VIVO media overnight. T_H17 cells were restimulated using 1-2 μg/ml plate-bound anti-CD3/CD28. Differentiation of other T-cell subtypes was performed as follows: Th0: 20 unit/ml IL-2 (BioLegend); Th1: 20 unit/ml IL-2, 10 ng/ml IL-12 (Peprotech), 10 μg/ml anti-IL-4; Th2: 20 unit/ml IL-2, 5 ng/ml IL-4 (Peprotech), 10 μg/ml anti-IFNγ; non-pathogenic T_H17: 25 ng/ml mIL-6, 5 ng/ml hTGFβ1, 10 μg/ml anti-IFNγ, and 10 μg anti-IL-4; Th22: 25 ng/ml

mIL-6, 20 ng/ml mIL-1β, 20 ng/ml IL-23, 400 nM FICZ (Invivogen), 10 μg/ml anti-IFNγ, and 10 μg/ml anti-IL-4; Treg: 50 unit/ml IL-2, 5 ng/ml hTGFβ1, 10 μg/ml anti-IFNγ, and 10 μg/ml anti-IL-4.

Retroviral transduction of primary T_H17 cells

Naïve CD4 T cells were activated by plate-bound anti-CD3/CD28 (5 μg/ml) in differentiation X-VIVO15 media containing 25 ng/ml mIL-6, 5 ng/ml hTGFβ1, 20 ng/ml mIL-1β, 20 ng/ml IL-23, 10 μg/ml anti-IFNγ, and 10 μg/ml anti-IL-4 for 24 hours. Activated cells were then spin infected (2,500 rpm, 90 min, 32°C) with retroviral supernatant containing 20 units/ml IL-2 and 10 μg/ml protamine sulfate (Sigma-Aldrich), and incubated with viral supernatant for additional 4-6 hours. Then cells were returned to differentiation media. Spin-infection was repeated 24 hours later. Successfully transduced T cells were identified by their surface expression of human CD2, which does not cross-activate mouse TCR.

TCR nanocluster and monomer purification

Membrane fraction was purified from primary T_H17 cells using a modified serial lysis method (*39*). First, 5-10 × 10^6 T cells were extensively washed in cold PBS, incubated in hypotonic lysis buffer (10 mM HEPES, 42 mM KCl, 5 mM $MgCl_2$, protease inhibitor cocktail, 1 mM PMSF), and mechanically disrupted using tight-fitting glass Dounce homogenizer. Whole cells and nuclei were removed by centrifugation for 10 min at 150*g*. Membrane patch was purified by ultra-centrifugation at 100,000*g* for 30 min at 4°C and pellet was washed once more with hypotonic lysis buffer. To extract TCR nanocluster, membrane pellet was resuspended in serial lysis buffer (20 mM Tris-Cl pH 8, 2 mM EDTA, 137 mM NaCl, 10%v/v glycerol, protease inhibitor cocktail, 1 mM PMSF) containing 1% saponin and rotated end-to-end at 4°C for 15 min, followed by centrifugation at 14,000*g* for 15 min to obtain supernatant. The insoluble pellet was again resuspended in 1% saponin serial lysis buffer for a total of three rounds of extraction and supernatant was pooled. To extract TCR monomer, the insoluble pellet from previous step was further extracted for three rounds in serial lysis buffer containing 0.5% Brij97. Pooled extracts were reduced in LDS sample buffer and blotted with anti-CD3ζ.

Flow cytometry-based Ca^{2+} flux assay

Isolated naïve CD4 T cells were cultured in X-VIVO15 media overnight before performing the Ca^{2+} flux assay. Differentiated T_H17 cells were removed from differentiation cocktail, washed and "rested" overnight in fresh X-VIVO15 media without further stimulation or IL-2. For flow cytometry-based assay, T cells were labeled with 1 μM Fluo-4-AM and 1 μM FuraRed-AM mixed 1:1 with 20% Pluronic F-127 in DMSO (all from ThermoFisher) in X-VIVO15 media for 30 min at room temperature with gentle rotation, and then washed and resuspended in Ringer's solution. Labeled cells were warmed up to 37°C for 10-15 min to allow cleavage of AM ester and were kept in 37°C water bath during recording. Live single cells were gated based on forward and side scatter parameters. Fluo-4 (Ca^{2+} bound) and FuraRed (Ca^{2+} unbound) fluorescence were recorded on Ex-488nm/ Filter-530/30 and Ex-488nm/ Filter-695/40 channel on the following sequence: (i) 3 min of baseline acquisition; (ii) 15 min following the addition of 5 μg/ml of biotin-anti-CD3ε and biotin-anti-CD28 for mouse T cells, or 5 μg/ml of biotin-anti-hCD3 for Jurkat cells; (iii) 15 min following the addition of 10 μg/ml streptavidin, (iv) 5 min following addition of 1 μM Ionomycin (Sigma-Aldrich). Kinetics platform in FlowJo v10 was used to plot time versus median Fluo-4/FuraRed ratio and to calculate peak value and area under curve.

Single-cell ratiometric Ca^{2+} imaging

Single-cell Ca^{2+} flux assay for T cells was modified from a previous publication (*52*). Overnight rested T cells were loaded at 1 × 10^6 cells per ml with 1 μM Fura 2-AM for 30 minutes at 25°C, resuspended in loading medium, and attached to poly-L-lysine-coated coverslips for 15 min. For $[Ca^{2+}]_i$ measurements, cells were mounted in a RC-20 closed bath flow chamber (Warner Instrument Corp., Hamden, CT) and analyzed on an Olympus IX51 epifluorescence microscope with Slidebook (Intelligent Imaging Innovations, Inc.) imaging software. Fura-2 emission was detected at 510 nm with excitation at 340 and 380 nm, and the Fura-2 emission ratio (340/380) was acquired at every 5-s interval after subtraction of background. For each experiment, at least 100 individual cells were analyzed using OriginPro (Originlab).

Biotin affinity purification and sample preparation for proximity labeling

EL-4 lines stably transduced with pRetroX-3xHA-TurboID-Aster-A or pRetroX-3HA-TurboID (empty vector) were constructed as described above. Tight TRE promoter has a leakage expression in EL-4 cell line, which resulted in moderate expression of 3x-HA-TurboID-Aster-A and stable cell lines were therefore used without doxycycline induction.

TurboID or TurboID-Aster-A expressing EL-4 cells were cultured in 10% FCS complete culture media or starved with a cholesterol-depletion media containing 1% Lipoprotein-deficient serum, 5 μM Simvastatin, 50 μM Mevalonate for 18-24 hours. Depleted cells were either loaded with 100 μM MβCD-Cholesterol or maintained in fresh cholesterol-depletion media for 1 hour and 15 min. Cholesterol-rich samples were maintained in 10% FCS complete media for the same time. Then, 50 μM Biotin was added to the culture media for the last 30 min to facilitate labeling. Isolation of biotinylated proteins were performed based on a modified protocol (*41*). Cells were collected and washed extensively with cold PBS and incubated with lysis buffer (RIPA buffer containing 1X Halt protease and phosphatase inhibitor and 1 mM PMSF) with gentle agitation for 30 min on ice. Lysate were cleared by centrifugation at 12,000*g* for 15 min and protein concentration was determined by BCA assay. Equal quantities (900 μg) of cleared lysates in lysis buffer were incubated with 75 μl Streptavidin magnetic beads (Thermo Fisher Pierce) overnight at 4°C with gentle rotation. The beads were then washed at room temperature twice in lysis buffer for 5 min each, once with 1 ml 1 M KCl for 2 min, once with 1 ml 0.1 M Na_2CO_3 for ~10 s, once with 1 ml 2 M urea in 10 mM Tris-HCl (pH 8.0) for ~10 s, and again twice with 1 ml lysis buffer for 2 min.

In-solution tryptic digestion for mass spectrometry

The samples were heated at 95°C in elution buffer [12 mM sodium lauroyl sarcosine, 0.5% sodium deoxycholate, 50 mM triethylammonium bicarbonate (TEAB) containing tris(2-carboxyethyl)phosphine (10 mM) and chloroacetamide (40 mM)] for 20 min. The samples were then diluted 5-fold with 50 mM TEAB and digested with trypsin (1 μg) for 16 hours at 37°C. A 1:1 (volume/volume) ratio of ethyl acetate plus 1% trifluoroacetic acid (TFA) was added to the samples and samples were vortexed for 5 min. Samples were centrifuged at 16000*g* for 5 min at room temperature and the supernatant was discarded. The samples were desalted using a modified version of Rappsilber's protocol (*91*) in which the dried samples were reconstituted in acetonitrile/water/TFA (solvent A, 100 μl, 2/98/0.1, v/v/v) and then loaded onto a small portion of a C18-silica disk (3M, Maplewood, MN) placed in a 200 μl pipette tip. Prior to sample loading the C18 disk was prepared by sequential treatment with methanol (20 μl), acetonitrile/water/TFA (solvent B, 20 μl, 80/20/0.1, v/v/v) and finally with solvent A (20 μl). After loading the sample, the disc was washed with solvent A (20 μl, eluent discarded) and eluted with solvent B (40 μl). The collected eluent was dried in a centrifugal vacuum concentrator and reconstituted in 0.1% Formic Acid (10 μl) for LC-MS/MS analysis.

LC-MS/MS analysis

Aliquots of each sample (5 μl) were injected onto a reverse phase nanobore HPLC column (AcuTech Scientific, C18, 1.8μm particle size, 360 μm × 20 cm, 150 μm ID), equilibrated in solvent A (water/acetonitrile/FA, 98/2/0.1, v/v/v) and eluted (300 nl/minute) with an increasing

concentration of solvent B (acetonitrile/water/FA, 98/2/0.1, v/v/v: min/% F; 0/0, 5/3, 18/7, 74/12, 144/24, 153/27, 162/40, 164/80, 174/80, 176/0, 180/0) using an EASY-nLC II (Thermo Fisher Scientific). The effluent from the column was directed to a nanospray ionization source connected to a hybrid quadrupole-Orbitrap mass spectrometer (Q Exactive Plus, Thermo Fisher Scientific) acquiring mass spectra in a data-dependent mode alternating between a full scan (m/z 350-1700, automated gain control (AGC) target 3×10^6, 50 ms maximum injection time, FWHM resolution 70,000 at m/z 200) and up to 15 MS/MS scans (quadrupole isolation of charge states 2-7, isolation window 0.7 m/z) with previously optimized fragmentation conditions (normalized collision energy of 32, dynamic exclusion of 30 s, AGC target 1×10^5, 100 ms maximum injection time, FWHM resolution 35,000 at m/z 200).

Protein identification

For experimental mass spectrometry data acquisition and analysis workflow, the raw proteomic data were searched against a Uniprot database containing the complete mouse proteome using SEQUEST-HT (Version 2.4, Thermo Scientific), which provided measurements of relative abundance of the identified peptides. Decoy database searching was used to generate high confidence tryptic peptides (FDR <1%). Tryptic peptides containing amino acid sequences unique to individual proteins were used to identify and provide relative quantification between different proteins in each sample. We performed protein identification of all treatment conditions in both empty vector (TurboID only) and TurboID-Aster-A expressing cells. This approach enhanced confidence in identifying proximity associations. Potential non-specific associations were defined as proteins identified in substantial abundance in both control TurboID only and in experimental groups and were excluded from further analysis. The remaining protein abundance was compared between experimental conditions and ranked as shown in Fig. 5B and in data S3.

TurboID biotinylated protein IP and protein coimmunoprecipitation (co-IP)

Confirmation of MS results in cholesterol depletion/repletion conditions were performed as described above using 300-500 μg total protein. In TurboID labeling involving TCR activation, EL-4 cells are either cultured in 10% FCS complete media or pre-treated with DMSO or 50 μM BAPTA for 20 min at 37°C. Then cells were added to prewarmed culture plate precoated with 5 μg/ml anti-CD3/CD28 with or without 10 mM EGTA. The plate was centrifuged at 1,200 rpm for 1 min to facilitate cell attachment and TCR activation for 1 hour. For ionomycin treatment, 1 μM ionomycin was added to cells plated on non-coated culture plates for 1 hour. For all experiments, 50 μM biotin was added to the culture media for the last 30 min to facilitate labeling. Proteins were eluted by boiling beads in 30 μl 3X LDS loading buffer containing 2 mM free biotin and 20 mM DTT on a shaking thermo block (1,000 rpm) at 95°C for 10 min. For input control, 30 μg cleared lysate prior to beads incubation was diluted in 1X LDS loading buffer with 20 mM DTT.

Stable polyclonal EL-4 lines expressing HA empty vector, HA-mAster-A (WT), HA-mAster-A (R186W) or co-expression with Myc-mSTIM1 were constructed as above and treated in cholesterol replete or deplete conditions as described in the TurboID biotinylated protein IP section. After 1 hour treatment, cells were collected by centrifugation at 1,200 rpm, 5 min at 4°C and washed extensively with cold PBS. Cell pellets were then incubated with IP lysis buffer [20 mM Tris-HCl, 2 mM EDTA, 135 mM NaCl, 10% (vol/vol) glycerol, 0.5% Igepal CA-630, 2X Halt protease inhibitor cocktail, 2 mM PMSF, pH 7.5] for 30 min at 4°C with gentle rotation. Lysates are further sonicated with 20% amplitude, 3 cycles of 5 s on, 10 s off and insoluble fraction was removed by centrifugation at 12,000 xg for 15 min. Protein concentration was determined by BCA assay and 1 mg total protein was precleared with protein A/G PLUS beads (Santa Cruz Biotechnology) for 1 hour at 4°C. Cleared lysates were incubated with 10 μg mouse Anti-HA (16B2) overnight at 4°C with gentle rotation. Antibody bound proteins were precipitated with protein A/G PLUS beads (Santa Cruz Biotechnology) for 3-4 hours at 4°C while rotating. A/G beads were washed five times, 10 min each with 1x co-IP lysis buffer and proteins were eluted by incubating A/G beads in 20-40 μl 3X SDS sample buffer at 95°C for 10 min with 1,000 rpm shaking. Antibodies against HA Tag, STIM1, mouse Aster-A, or Myc Tag were used for immunoblotting.

Sample preparation and library construction for bulk mRNA sequencing

Small intestine lamina propria mononuclear cells were isolated using the method described above. One micromolar flavopiridol (RNA polymerase inhibitor) was included in all digestion steps to halt de novo transcription of stress-related genes as a result of tissue dissociation. Single cell suspension was FACS-gated on Single/Live cell/$CD45^+$/$CD90^+$/$CD3^+$ and sorted into $CD4^+$ and $CD8^+$ populations directly into 700 μl Trizol LS reagent. Sorting strategy is shown in fig. S21A. Total RNA was extracted using TRIzol and the miRNeasy Mini Kit with on-column DNase I digestion (Qiagen).

RNA library preparations and sequencing reactions were conducted at GENEWIZ, LLC. RNA samples were quantified using Qubit 2.0 Fluorometer (Life Technologies) and RNA integrity was checked using Agilent TapeStation 4200 (Agilent Technologies). RNA sequencing libraries were prepared using the NEBNext Ultra II RNA Library Prep Kit for Illumina using manufacturer's instructions. Briefly, poly-A mRNAs were initially enriched with Oligo dT beads. Enriched mRNAs were fragmented for 15 min at 94°C. First strand and second strand cDNA were subsequently synthesized. cDNA fragments were end repaired and adenylated at 3′ends, and universal adapters were ligated to cDNA fragments, followed by index addition and library enrichment by PCR with limited cycles. The sequencing library was validated on the Agilent TapeStation (Agilent Technologies) and quantified by using Qubit 4.0 Fluorometer (Invitrogen) as well as by quantitative PCR (KAPA Biosystems).

Bulk mRNA sequencing and analysis

The sequencing libraries were clustered on flowcells. After clustering, the flowcells were loaded on the Illumina HiSeq instrument (4000 or equivalent) according to manufacturer's instructions. The samples were sequenced using a 2x150bp Paired End configuration. Image analysis and base calling were conducted by the HiSeq Control Software (HCS). Raw sequence data (.bcl files) generated from Illumina HiSeq was converted into fastq files and de-multiplexed using Illumina's bcl2fastq 2.17 software. One mismatch was allowed for index sequence identification. Adapter and quality trimming of raw FASTQ files was performed using Trimmomatic. FastQC was used to perform quality control of the FASTQ files before and after trimming. Trimmed FASTQ files were aligned to GRCm38/mm10 using STAR package. HTSeq-count was used to extract gene counts and differential gene expression analysis was performed using DESeq2 package (doi:10.1186/s13059-014-0550-8) in R 4.1.1. Normalized gene expression of the individual samples is shown in data S1 and differentially expressed gene list is shown in data S2.

Single-cell RNA sequencing

Small intestine lamina propria mononuclear cells were isolated using the method described in the bulk mRNA sequencing section. Single Live $EPCAM^-$ $Ter119^-$ $CD31^-$ $CD45^+$ cells were sorted from 10- to 12-week-old female littermates on a BD Aria FACS sorter. Sorting strategy is shown in fig. S23. Then, 100,000 cells were sorted from each mouse ($n = 3$ /genotype) and pooled together before loading to a Chromium Single Cell Controller (10X Genomics). Libraries were prepared using a 10X Genomics 3′GEX Kits following the manufacturer's protocols. Libraries were then sequenced on an Illumina NovaSeq S2 using 2×50 bp paired end sequencing with a targeted depth of 50,000 read pairs per cell.

Raw reads were aligned to mouse mm10 genome using CellRanger (v7.2.0). Counts from ambient RNA was removed using CellBender [(v0.3.0); Github: broadinstitute/CellBender] and doublets were removed using scDblFinder [(v1.18.0); DOI: 10.18129/B9.bioc.scDblFinder]. Preprocessing was performed using Seurat [(v5.0.1); Github: satijalab/seurat] in R 4.3.1. Specifically, we filtered for cells with 500<nUMI <30000, 200<nGenes <10000 and percent.MT < 5%. Normalization was done using SCTransform with percent.MT regressed out. Initial data integration was done using the SelectIntegrationFeatures(), PrepSCTIntegration(), FindIntegrationAnchors () and IntegrateData() functions with RPCA method and 3000 variable features. Dimensional reduction was done using top 50 principal components (PCs) and subsequent Harmony integration. Visualization was performed using RunUMAP() function. Cell clustering was performed using the FindNeighbors() function (50 harmony embeddings, k = 35) and FindClusters() function with igraph and Leiden method (resolution = 0.6). To isolate lymphoid lineage for further analysis, we subset clusters expressing *Thy1* (CD90) from the original Seurat object. The same normalization and integration procedure was applied to lymphoid lineage clusters. To identify stable clusters, we performed bootstrapping of 80% of the cells 20 times, and tested stability of clusters from a wide range of parameters, including number of PCs used, k parameters in FindNeighbors() and resolution in FindClusters(). We decided to use 20 top PCs, k = 30 and resolution = 0.8 to maximizing cluster diversity while maintaining cluster stability. Cluster markers were identified using FindMarkers() function and manual annotation was performed using established cell markers. Cluster were manually annotated based on matching cluster markers (fig. S17A, list of markers is shown in data S4) with cell type ULI RNA-seq data in the Immgen database and previously published small intestine mononuclear cell single-cell RNA sequencing results (GSE124880).

Access and analysis of previously published gene expression and sequencing datasets

Tissue panel gene expression (fig. S1E) was analyzed in BioGPS repository from aggregated datasets GSE1133, GSE10246, GSE15998. Immune cell expression panel (fig. S1G) was obtained from ImmGen ULI RNA-seq data (GSE109125 and GSE127267). Human single cell meta-analysis (fig. S9, A and B) was performed using Swiss Portal for Immune Cell Analysis and scIBD database (*92*, *93*). ChIP-seq data (fig. S9F) was analyzed in Cistrome database using datasets GSM978770, GSM978769, GSM978772, GSM1126691, GSM2706520, GSM2387500. Sequencing tracks were visualized with Integrated Genome Viewer (2.16.2).

Statistical analysis

Data in all figures are representative of or pooled from at least two independent experiments or as indicated in the figure legends. Data are shown as Mean ± SEM. For experiments involving wildtype mice or mice of the same genotype, groups were assigned so that control and treatment groups have similar average body weight. In Cre-flox system or WT-KO genotypes, balanced numbers of littermate mice were used where possible and randomly assigned to experimental groups. Samples were processed in an order that alternated between WT/KO or control/treatment subjects. Formal blinding was not applied when performing the experiments or analyzing the data. Power calculations were not applied to predetermine sample size. Sample size was based on prior laboratory practice and literature reports on similar assays. Groups were compared using Prism software (v10.3.0). For statistics tests requiring normal distribution, datasets were first tested for normality and log normality using Kolmogorov-Smirnov test. If data distribution was not normal, it was first log-transformed, tested again using Kolmogorov-Smirnov for normality, before proceeding with the corresponding statistical tests. The statistical methods and correction used for each experiment are reported in the corresponding figure captions.

REFERENCES AND NOTES

1. A. Das, M. S. Brown, D. D. Anderson, J. L. Goldstein, A. Radhakrishnan, Three pools of plasma membrane cholesterol and their relation to cholesterol homeostasis. *eLife* **3**, e02882 (2014). doi: 10.7554/eLife.02882; pmid: 24920391
2. S. Endapally *et al.*, Molecular discrimination between two conformations of sphingomyelin in plasma membranes. *Cell* **176**, 1040–1053.e17 (2019). doi: 10.1016/j.cell.2018.12.042; pmid: 30712872
3. S. Endapally, R. E. Infante, A. Radhakrishnan, Monitoring and modulating intracellular cholesterol trafficking using ALOD4, a cholesterol-binding protein. *Methods Mol. Biol.* **1949**, 153–163 (2019). doi: 10.1007/978-1-4939-9136-5_12; pmid: 30790255
4. K. A. Johnson, A. Radhakrishnan, The use of anthrolysin O and ostreolysin A to study cholesterol in cell membranes. *Methods Enzymol.* **649**, 543–566 (2021). doi: 10.1016/bs.mie.2021.01.011; pmid: 33712199
5. A. Ferrari *et al.*, Aster proteins regulate the accessible cholesterol pool in the plasma membrane. *Mol. Cell. Biol.* **40**, e00255-e20 (2020). doi: 10.1128/MCB.00255-20; pmid: 32719109
6. X. Xiao *et al.*, Hepatic nonvesicular cholesterol transport is critical for systemic lipid homeostasis. *Nat. Metab.* **5**, 165–181 (2023). doi: 10.1038/s42255-022-00722-6; pmid: 36646756
7. Q. D. Zhou *et al.*, Interferon-mediated reprogramming of membrane cholesterol to evade bacterial toxins. *Nat. Immunol.* **21**, 746–755 (2020). doi: 10.1038/s41590-020-0695-4; pmid: 32514064
8. M. Kinnebrew *et al.*, Patched 1 reduces the accessibility of cholesterol in the outer leaflet of membranes. *eLife* **10**, e70504 (2021). doi: 10.7554/eLife.70504; pmid: 34698632
9. M. E. Abrams *et al.*, Oxysterols provide innate immunity to bacterial infection by mobilizing cell surface accessible cholesterol. *Nat. Microbiol.* **5**, 929–942 (2020). doi: 10.1038/s41564-020-0701-5; pmid: 32284563
10. M. N. Trinh *et al.*, Interplay between Asters/GRAMD1s and phosphatidylserine in intermembrane transport of LDL cholesterol. *Proc. Natl. Acad. Sci. U.S.A.* **119**, e2120411119 (2022). doi: 10.1073/pnas.2120411119; pmid: 34992143
11. M.-S. Lee, S. J. Bensinger, Reprogramming cholesterol metabolism in macrophages and its role in host defense against cholesterol-dependent cytolysins. *Cell. Mol. Immunol.* **19**, 327–336 (2022). doi: 10.1038/s41423-021-00827-0; pmid: 35017717
12. J. Sandhu *et al.*, Aster proteins facilitate nonvesicular plasma membrane to ER cholesterol transport in mammalian cells. *Cell* **175**, 514–529.e20 (2018). doi: 10.1016/j.cell.2018.08.033; pmid: 30220461
13. C. He *et al.*, Macrophages release plasma membrane-derived particles rich in accessible cholesterol. *Proc. Natl. Acad. Sci. U.S.A.* **115**, E8499–E8508 (2018). doi: 10.1073/pnas.1810724115; pmid: 30127022
14. X. Hu *et al.*, Release of cholesterol-rich particles from the macrophage plasma membrane during movement of filopodia and lamellipodia. *eLife* **8**, e50231 (2019). doi: 10.7554/eLife.50231; pmid: 31486771
15. A. Ferrari *et al.*, Aster-dependent nonvesicular transport facilitates dietary cholesterol uptake. *Science* **382**, eadf0966 (2023). doi: 10.1126/science.adf0966; pmid: 37943936
16. M. Kinnebrew *et al.*, Cholesterol accessibility at the ciliary membrane controls hedgehog signaling. *eLife* **8**, e50051 (2019). doi: 10.7554/eLife.50051; pmid: 31657721
17. E. Ikonen, V. M. Olkkonen, Intracellular cholesterol trafficking. *Cold Spring Harb. Perspect. Biol.* **15**, 041404 (2023). pmid: 37277190
18. J. P. Kennelly, P. Tontonoz, Cholesterol transport to the endoplasmic reticulum. *Cold Spring Harb. Perspect. Biol.* **15**, 041263 (2023). pmid: 35940908
19. T. Naito *et al.*, Movement of accessible plasma membrane cholesterol by the GRAMD1 lipid transfer protein complex. *eLife* **8**, e51401 (2019). doi: 10.7554/eLife.51401; pmid: 31724953
20. X. Xiao *et al.*, Aster-B-dependent estradiol synthesis protects female mice from diet-induced obesity. *J. Clin. Invest.* **134**, e173002 (2024). doi: 10.1172/JCI173002; pmid: 38175723
21. F. Wang, K. Beck-García, C. Zorzin, W. W. A. Schamel, M. M. Davis, Inhibition of T cell receptor signaling by cholesterol sulfate, a naturally occurring derivative of membrane cholesterol. *Nat. Immunol.* **17**, 844–850 (2016). doi: 10.1038/ni.3462; pmid: 27213689
22. E. Molnár *et al.*, Cholesterol and sphingomyelin drive ligand-independent T-cell antigen receptor nanoclustering. *J. Biol. Chem.* **287**, 42664–42674 (2012). doi: 10.1074/jbc.M112.386045; pmid: 23091059
23. M. Hose *et al.*, Cell-intrinsic ceramides determine T cell function during melanoma progression. *eLife* **11**, e83073 (2022). doi: 10.7554/eLife.83073; pmid: 36426850
24. J. Yuan *et al.*, Potentiating $CD8^+$ T cell antitumor activity by inhibiting PCSK9 to promote LDLR-mediated TCR recycling and signaling. *Protein Cell* **12**, 240–260 (2021). doi: 10.1007/s13238-021-00821-2; pmid: 33606190
25. W. Yang *et al.*, Potentiating the antitumour response of $CD8^+$ T cells by modulating cholesterol metabolism. *Nature* **531**, 651–655 (2016). doi: 10.1038/nature17412; pmid: 26982734
26. W. W. A. Schamel, B. Alarcon, T. Höfer, S. Minguet, The allostery model of TCR regulation. *J. Immunol.* **198**, 47–52 (2017). doi: 10.4049/jimmunol.1601661; pmid: 27994168
27. Y. Chen *et al.*, Cholesterol inhibits TCR signaling by directly restricting TCR-CD3 core tunnel motility. *Mol. Cell* **82**, 1278–1287.e5 (2022). doi: 10.1016/j.molcel.2022.02.017; pmid: 35271814

28. B. Wang *et al.*, Intestinal phospholipid remodeling is required for dietary-lipid uptake and survival on a high-fat diet. *Cell Metab.* **23**, 492–504 (2016). doi: 10.1016/j.cmet.2016.01.001; pmid: 26833026
29. J. P. Kennelly *et al.*, Intestinal de novo phosphatidylcholine synthesis is required for dietary lipid absorption and metabolic homeostasis. *J. Lipid Res.* **59**, 1695–1708 (2018). doi: 10.1194/jlr.M087056; pmid: 30007917
30. D. H. Z. Koh *et al.*, Visualization of accessible cholesterol using a GRAM domain-based biosensor. *Nat. Commun.* **14**, 6773 (2023). doi: 10.1038/s41467-023-42498-7; pmid: 37880244
31. T. Naito, M. Na, D. H. Z. Koh, Y. Saheki, "Using GRAM domain–based biosensors to monitor accessible cholesterol distribution in live cells" in *Intracellular Lipid Transport: Methods and Protocols*, *Methods in Molecular Biology*, vol. 2888, G. Drin, Ed. (Springer, 2025), pp. 67–82.doi: 10.1007/978-1-0716-4318-1_6
32. M. Doktorova *et al.*, Cell membranes sustain phospholipid imbalance via cholesterol asymmetry. *Cell* **188**, 2586–2602.e24 (2025). doi: 10.1016/j.cell.2025.02.034; pmid: 40179882
33. D. Sputay *et al.*, Immune cell activation produces locally scrambled foci of plasma membrane lipids. *Faraday Discuss.* **259**, 45–59 (2025). doi: 10.1039/D4FD00205A; pmid: 40351229
34. K. Fischer *et al.*, Antigen recognition induces phosphatidylserine exposure on the cell surface of human $CD8^+$ T cells. *Blood* **108**, 4094–4101 (2006). doi: 10.1182/blood-2006-03-011742; pmid: 16912227
35. Y. Hu *et al.*, Scramblase TMEM16F terminates T cell receptor signaling to restrict T cell exhaustion. *J. Exp. Med.* **213**, 2759–2772 (2016). doi: 10.1084/jem.20160612; pmid: 27810927
36. J. Suzuki, M. Umeda, P. J. Sims, S. Nagata, Calcium-dependent phospholipid scrambling by TMEM16F. *Nature* **468**, 834–838 (2010). doi: 10.1038/nature09583; pmid: 21107324
37. S. Feng *et al.*, Identification of a drug binding pocket in TMEM16F calcium-activated ion channel and lipid scramblase. *Nat. Commun.* **14**, 4874 (2023). doi: 10.1038/s41467-023-40410-x; pmid: 37573365
38. S. Pathan-Chhatbar *et al.*, Direct regulation of the T cell antigen receptor's activity by cholesterol. *Front. Cell Dev. Biol.* **8**, 615996 (2021). doi: 10.3389/fcell.2020.615996; pmid: 33490080
39. M. Swamy, W. W. A. Schamel, Purification of the T cell antigen receptor and analysis by blue-native PAGE. *Methods Mol. Biol.* **514**, 135–150 (2009). doi: 10.1007/978-1-60327-527-9_10; pmid: 19048218
40. E. Esplugues *et al.*, Control of T_H17 cells occurs in the small intestine. *Nature* **475**, 514–518 (2011). doi: 10.1038/nature10228; pmid: 21765430
41. K. F. Cho *et al.*, Proximity labeling in mammalian cells with TurboID and split-TurboID. *Nat. Protoc.* **15**, 3971–3999 (2020). doi: 10.1038/s41596-020-0399-0; pmid: 33139955
42. T. Balla, G. Gulyas, Y. J. Kim, J. Pemberton, Phosphoinositides and calcium signaling. A marriage arranged in ER-PM contact sites. *Curr. Opin. Physiol.* **17**, 149–157 (2020). doi: 10.1016/j.cophys.2020.08.007; pmid: 32944676
43. Y.-J. Chen, C. G. Quintanilla, J. Liou, Recent insights into mammalian ER-PM junctions. *Curr. Opin. Cell Biol.* **57**, 99–105 (2019). doi: 10.1016/j.ceb.2018.12.011; pmid: 30739879
44. W. Y. Chung, A. Jha, M. Ahuja, S. Muallem, Ca^{2+} influx at the ER/PM junctions. *Cell Calcium* **63**, 29–32 (2017). doi: 10.1016/j.ceca.2017.02.009; pmid: 28262262
45. P. G. Hogan, R. S. Lewis, A. Rao, Molecular basis of calcium signaling in lymphocytes: STIM and ORAI. *Annu. Rev. Immunol.* **28**, 491–533 (2010). doi: 10.1146/annurev.immunol.021908.132550; pmid: 20307213
46. Y. Saheki, P. De Camilli, Endoplasmic reticulum-plasma membrane contact sites. *Annu. Rev. Biochem.* **86**, 659–684 (2017). doi: 10.1146/annurev-biochem-061516-044932; pmid: 28301744
47. V. A. Barr *et al.*, Dynamic movement of the calcium sensor STIM1 and the calcium channel Orai1 in activated T-cells: Puncta and distal caps. *Mol. Biol. Cell* **19**, 2802–2817 (2008). doi: 10.1091/mbc.e08-02-0146; pmid: 18448669
48. W.-W. Shen, M. Frieden, N. Demaurex, Local cytosolic Ca^{2+} elevations are required for stromal interaction molecule 1 (STIM1) de-oligomerization and termination of store-operated Ca^{2+} entry. *J. Biol. Chem.* **286**, 36448–36459 (2011). doi: 10.1074/jbc.M111.269415; pmid: 21880734
49. B. Ercan, T. Naito, D. H. Z. Koh, D. Dharmawan, Y. Saheki, Molecular basis of accessible plasma membrane cholesterol recognition by the GRAM domain of GRAMD1b. *EMBO J.* **40**, e106524 (2021). doi: 10.15252/embj.2020106524; pmid: 33604931
50. U. Kaufmann *et al.*, Calcium signaling controls pathogenic Th17 cell-mediated inflammation by regulating mitochondrial function. *Cell Metab.* **29**, 1104–1118.e6 (2019). doi: 10.1016/j.cmet.2019.01.019; pmid: 30773462
51. S. Kahlfuss *et al.*, STIM1-mediated calcium influx controls antifungal immunity and the metabolic function of non-pathogenic Th17 cells. *EMBO Mol. Med.* **12**, e11592 (2020). doi: 10.15252/emmm.201911592; pmid: 32609955
52. B. Wu, J. S. Woo, Z. Sun, S. Srikanth, Y. Gwack, Ca^{2+} signaling augmented by ORAI1 trafficking regulates the pathogenic state of effector T cells. *J. Immunol.* **208**, 1329–1340 (2022). doi: 10.4049/jimmunol.2100871; pmid: 35217583
53. A. Gay, D. Rye, A. Radhakrishnan, Switch-like responses of two cholesterol sensors do not require protein oligomerization in membranes. *Biophys. J.* **108**, 1459–1469 (2015). doi: 10.1016/j.bpj.2015.02.008; pmid: 25809258
54. M. Keir, Y. Yi, T. Lu, N. Ghilardi, The role of IL-22 in intestinal health and disease. *J. Exp. Med.* **217**, e20192195 (2020). doi: 10.1084/jem.20192195; pmid: 32997932
55. R. Basu *et al.*, Th22 cells are an important source of IL-22 for host protection against enteropathogenic bacteria. *Immunity* **37**, 1061–1075 (2012). doi: 10.1016/j.immuni.2012.08.024; pmid: 23200827
56. I. I. Ivanov *et al.*, Induction of intestinal Th17 cells by segmented filamentous bacteria. *Cell* **139**, 485–498 (2009). doi: 10.1016/j.cell.2009.09.033; pmid: 19836068
57. Y. Yang *et al.*, Focused specificity of intestinal TH17 cells towards commensal bacterial antigens. *Nature* **510**, 152–156 (2014). doi: 10.1038/nature13279; pmid: 24739972
58. Y. Goto *et al.*, Segmented filamentous bacteria antigens presented by intestinal dendritic cells drive mucosal Th17 cell differentiation. *Immunity* **40**, 594–607 (2014). doi: 10.1016/j.immuni.2014.03.005; pmid: 24684957
59. J. Talbot *et al.*, Feeding-dependent VIP neuron-ILC3 circuit regulates the intestinal barrier. *Nature* **579**, 575–580 (2020). doi: 10.1038/s41586-020-2039-9; pmid: 32050257
60. K. Mao *et al.*, Innate and adaptive lymphocytes sequentially shape the gut microbiota and lipid metabolism. *Nature* **554**, 255–259 (2018). doi: 10.1038/nature25437; pmid: 29364878
61. Z. A. Sullivan *et al.*, γδ T cells regulate the intestinal response to nutrient sensing. *Science* **371**, eaba8310 (2021). doi: 10.1126/science.aba8310; pmid: 33737460
62. Y. Kawano *et al.*, Microbiota imbalance induced by dietary sugar disrupts immune-mediated protection from metabolic syndrome. *Cell* **185**, 3501–3519.e20 (2022). doi: 10.1016/j.cell.2022.08.005; pmid: 36041436
63. X. Wang *et al.*, Interleukin-22 alleviates metabolic disorders and restores mucosal immunity in diabetes. *Nature* **514**, 237–241 (2014). doi: 10.1038/nature13564; pmid: 25119041
64. L. A. Zenewicz *et al.*, IL-22 deficiency alters colonic microbiota to be transmissible and colitogenic. *J. Immunol.* **190**, 5306–5312 (2013). doi: 10.4049/jimmunol.1300016; pmid: 23585682
65. Y. Wang *et al.*, The intestinal microbiota regulates body composition through NFIL3 and the circadian clock. *Science* **357**, 912–916 (2017). doi: 10.1126/science.aan0677; pmid: 28860383
66. F. Bäckhed, J. K. Manchester, C. F. Semenkovich, J. I. Gordon, Mechanisms underlying the resistance to diet-induced obesity in germ-free mice. *Proc. Natl. Acad. Sci. U.S.A.* **104**, 979–984 (2007). doi: 10.1073/pnas.0605374104; pmid: 17210919
67. T. Y. Chang, C. C. Y. Chang, D. Cheng, Acyl-coenzyme A:cholesterol acyltransferase. *Annu. Rev. Biochem.* **66**, 613–638 (1997). doi: 10.1146/annurev.biochem.66.1.613; pmid: 9242919
68. N. M. Schmidt *et al.*, Targeting human Acyl-CoA:cholesterol acyltransferase as a dual viral and T cell metabolic checkpoint. *Nat. Commun.* **12**, 2814 (2021). doi: 10.1038/s41467-021-22967-7; pmid: 33990561
69. K. T. Kennewick, S. J. Bensinger, Decoding the crosstalk between mevalonate metabolism and T cell function. *Immunol. Rev.* **317**, 71–94 (2023). doi: 10.1111/imr.13200; pmid: 36999733
70. Y. Kidani *et al.*, Sterol regulatory element-binding proteins are essential for the metabolic programming of effector T cells and adaptive immunity. *Nat. Immunol.* **14**, 489–499 (2013). doi: 10.1038/ni.2570; pmid: 23563690
71. E. L. Huttlin *et al.*, Dual proteome-scale networks reveal cell-specific remodeling of the human interactome. *Cell* **184**, 3022–3040.e28 (2021). doi: 10.1016/j.cell.2021.04.011; pmid: 33961781
72. C. D. Go *et al.*, A proximity-dependent biotinylation map of a human cell. *Nature* **595**, 120–124 (2021). doi: 10.1038/s41586-021-03592-2; pmid: 34079125
73. M. Besprozvannaya *et al.*, GRAM domain proteins specialize functionally distinct ER-PM contact sites in human cells. *eLife* **7**, e31019 (2018). doi: 10.7554/eLife.31019; pmid: 29469807
74. M. N. Trinh *et al.*, Last step in the path of LDL cholesterol from lysosome to plasma membrane to ER is governed by phosphatidylserine. *Proc. Natl. Acad. Sci. U.S.A.* **117**, 18521–18529 (2020). doi: 10.1073/pnas.2010682117; pmid: 32690708
75. W. M. Henne, J. Liou, S. D. Emr, Molecular mechanisms of inter-organelle ER-PM contact sites. *Curr. Opin. Cell Biol.* **35**, 123–130 (2015). doi: 10.1016/j.ceb.2015.05.001; pmid: 26025028
76. X. Cao *et al.*, The ER/PM microdomain, $PI(4,5)P_2$ and the regulation of STIM1–Orai1 channel function. *Cell Calcium* **58**, 342–348 (2015). doi: 10.1016/j.ceca.2015.03.003; pmid: 25843208
77. W. Y. Chung *et al.*, PtdSer as a signaling lipid determined by privileged localization of ORP5 and ORP8 at ER/PM junctional foci to determine PM and ER PtdSer/PI(4)P ratio and cell function. *Proc. Natl. Acad. Sci. U.S.A.* **120**, e2301410120 (2023). doi: 10.1073/pnas.2301410120; pmid: 37607230
78. G. Gulyas *et al.*, LIPID transfer proteins regulate store-operated calcium entry via control of plasma membrane phosphoinositides. *Cell Calcium* **106**, 102631 (2022). doi: 10.1016/j.ceca.2022.102631; pmid: 35853265
79. M. Reina-Campos *et al.*, Metabolic programs of T cell tissue residency empower tumour immunity. *Nature* **621**, 179–187 (2023). doi: 10.1038/s41586-023-06483-w; pmid: 37648857
80. A. H. Pollock *et al.*, Prolonged intake of dietary lipids alters membrane structure and T cell responses in $LDLr^{-/-}$ mice. *J. Immunol.* **196**, 3993–4002 (2016). doi: 10.4049/jimmunol.1501261; pmid: 27183636

81. R. K. W. Mailer, A. Gisterå, K. A. Polyzos, D. F. J. Ketelhuth, G. K. Hansson, Hypercholesterolemia enhances T cell receptor signaling and increases the regulatory T cell population. *Sci. Rep.* **7**, 15655 (2017). doi: 10.1038/s41598-017-15546-8; pmid: 29142309
82. Q. Gao *et al.*, A critical function of Th17 proinflammatory cells in the development of atherosclerotic plaque in mice. *J. Immunol.* **185**, 5820–5827 (2010). doi: 10.4049/jimmunol.1000116; pmid: 20952673
83. Y. U. Kim, P. Kee, D. Danila, B.-B. Teng, A critical role of PCSK9 in mediating IL-17-producing T cell responses in hyperlipidemia. *Immune Netw.* **19**, e41 (2019). doi: 10.4110/in.2019.19.e41; pmid: 31921471
84. Y. Wang *et al.*, Interleukin-17-producing $CD4^+$ T cells promote inflammatory response and foster disease progression in hyperlipidemic patients and atherosclerotic mice. *Front. Cardiovasc. Med.* **8**, 667768 (2021). doi: 10.3389/fcvm.2021.667768; pmid: 33981738
85. R. Saigusa, H. Winkels, K. Ley, T cell subsets and functions in atherosclerosis. *Nat. Rev. Cardiol.* **17**, 387–401 (2020). doi: 10.1038/s41569-020-0352-5; pmid: 32203286
86. S. Omenetti *et al.*, The intestine harbors functionally distinct homeostatic tissue-resident and inflammatory Th17 cells. *Immunity* **51**, 77–89.e6 (2019). doi: 10.1016/j.immuni.2019.05.004; pmid: 31229354
87. C. L. Zindl *et al.*, A nonredundant role for T cell-derived interleukin 22 in antibacterial defense of colonic crypts. *Immunity* **55**, 494–511.e11 (2022). doi: 10.1016/j.immuni.2022.02.003; pmid: 35263568
88. A. I. Mina *et al.*, CalR: A web-based analysis tool for indirect calorimetry experiments. *Cell Metab.* **28**, 656–666.e1 (2018). doi: 10.1016/j.cmet.2018.06.019; pmid: 30017358
89. J. Folch, M. Lees, G. H. Sloane Stanley, A simple method for the isolation and purification of total lipides from animal tissues. *J. Biol. Chem.* **226**, 497–509 (1957). doi: 10.1016/S0021-9258(18)64849-5; pmid: 13428781
90. D. R. Stirling *et al.*, CellProfiler 4: Improvements in speed, utility and usability. *BMC Bioinformatics* **22**, 433 (2021). doi: 10.1186/s12859-021-04344-9; pmid: 34507520
91. J. Rappsilber, M. Mann, Y. Ishihama, Protocol for micro-purification, enrichment, pre-fractionation and storage of peptides for proteomics using StageTips. *Nat. Protoc.* **2**, 1896–1906 (2007). doi: 10.1038/nprot.2007.261; pmid: 17703201
92. H. Nie *et al.*, Single-cell meta-analysis of inflammatory bowel disease with scIBD. *Nat. Comput. Sci.* **3**, 522–531 (2023). doi: 10.1038/s43588-023-00464-9; pmid: 38177426
93. M. Andreatta, F. P. A. David, C. Iseli, N. Guex, S. J. Carmona, SPICA: Swiss portal for immune cell analysis. *Nucleic Acids Res.* **50**, D1109–D1114 (2022). doi: 10.1093/nar/gkab1055; pmid: 34747477
94. Y. Gao, P. Tontonoz, W. Cohn, J. Whitelegge, T cell cholesterol transport links intestinal immune responses to dietary lipid absorption. Dryad (2025); https://doi.org/10.5061/dryad.w9ghx3g31.

ACKNOWLEDGMENTS

We thank all members of the Tontonoz, Tarling-Vallim, Mack, Young, and Bensinger labs at University of California, Los Angeles (UCLA) for advice and discussions and for sharing reagents and resources. pALOD4 and pOlyA were a gift from A. Radhakrishnan (UT Southwestern Medical Center), and the *Il22*$^{hCD4.fl}$ strain was a kind gift from C. L. Zindl, S. N. Harbour, and C. T. Weaver (University of Alabama at Birmingham). We thank the CNSI Microscopy Core, Broad Stem Cell Core Facilities, Flow Cytometry Core, Translational Pathology Core Laboratory, UCLA Microbiome Core, and Technology Center for Genomics and Bioinformatics at UCLA for their service and experimental suggestions. We also thank L. Qi for assisting with scRNA-seq analysis and C. I. Corrales for supporting the generation of TurboID–expressing cell lines. **Funding:** This work was supported by National Institutes of Health (NIH) grants R01 DK126779 and R01 HL175773 (P.T.); Transatlantic Network of Excellence, Leducq Foundation, 19CDV04 (P.T., S.G.Y.); NIH grant P01 HL146358 (P.T., S.G.Y., S.J.B.); NIH grant R35 HL139725 (S.G.Y.); Damon Runyon Foundation/The Mark Foundation Postdoctoral Fellowship DRG-2424-21, NIH grant K99 DK138289, and, in part, by the UCLA Jonsson Comprehensive Cancer Center's Office of Cancer Training and Education (Y.Ga.); NIH–National Center for Advancing Translational Sciences grant UL1TR001881 (Y.Ga., P.T.); American Heart Association Postdoctoral Fellowship 903306 (J.P.K.); American Heart Association Postdoctoral Fellowship 18POST34030388 and UCSD-UCLA Diabetes Research Center P30 (DK063491) (X.X.); CDI NIH K12 Junior Faculty Career Development Grant (1K12HD111040), Today's and Tomorrow's Children Fund Bridge Grant, and UCLA David Geffen School of Medicine Office of Physician Scientist Career Development Bridge Grant (E.W.); University of California, San Diego (UCSD)–UCLA Diabetes Research Center P30 (DK063491) (E.W., P.T.); American Diabetes Association Postdoctoral fellowship 1-19-PDF-043-RA and Ermenegildo Zegna Founder's Scholarship 2017 (A.F.); NIH grants T32 DK007180 and K08DK136706 (A.H.N.); NIH grant F30 DK134050 and UCLA-Caltech Medical Scientist Training Program T32 GM008042 (L.F.U.); and NIH grants R01AI146615 (Y.Gw.) and R01AI146352 (S.S.). **Author contributions:** Conceptualization: Y.Ga., J.P.K., P.T.; Methodology: Y.Ga., J.P.K., X.X., A.H.B., S.S., T.W., A.N., W.C.; Investigation: Y.Ga., J.P.K., X.X., E.W., A.F., J.J.M., S.S., D.H.C., T.W., L.F.U.; Visualization: Y.Ga., J.P.K., X.X., A.H.B., T.W., J.J.M., S.S.; Funding acquisition: Y.Ga., P.T.; Project administration: Y.Ga., P.T.; Supervision: P.T., S.G.Y., J.J.M., S.J.B., S.S., Y.Gw., J.W.; Resources: A.N., M.S.L., S.J.B.; Writing – original draft: Y.Ga., P.T.; Writing – review & editing: Y.Ga., J.P.K., X.X., P.T. **Competing interests:** All authors declare that they have no competing interests. **Data and materials availability:** All data needed to evaluate the conclusions in the paper are available in the manuscript or the supplementary materials. Sequencing data generated in this study have been deposited to the Gene Expression Omnibus (GEO) under accession nos. GSE277067 (bulk CD4 RNA-seq) and GSE277138 (scRNA-seq). Proteomics mass spectrometry data generated in this study have been deposited to Dryad (*94*). The biological materials that were used are readily available from the authors or from standard commercial sources. Aster-$A^{F/F}$ mice are available from P.T. under a material agreement with UCLA. **License information:** Copyright © 2025 the authors, some rights reserved; exclusive licensee American Association for the Advancement of Science. No claim to original US government works. https://www.science.org/about/science-licenses-journal-article-reuse

SUPPLEMENTARY MATERIALS

science.org/doi/10.1126/science.adt4169
Figs. S1 to S39; Tables S1 to S3; MDAR Reproducibility Checklist; Data S1 to S4; Movie S1
Submitted 26 September 2024; accepted 1 August 2025
10.1126/science.adt4169



AAAS.ORG/COMMUNITY







AAAS' Member Community is a one-stop destination for scientists and STEM enthusiasts alike. It's "Where Science Gets Social": a community where facts matter, ideas are big and there's always a reason to come hang out, share, discuss and explore.

Member COMMUNITY
AAAS

AMERICAN ASSOCIATION FOR THE ADVANCEMENT OF SCIENCE

RESEARCH ARTICLE SUMMARY

AGING

A cGAS-mediated mechanism in naked mole-rats potentiates DNA repair and delays aging

Yu Chen†, Zhixi Chen†, Hao Wang, Zhen Cui, Kai-Le Li, Zhiwei Song, Lingjiang Chen, Xiaoxiang Sun, Xiaoyu Xu, Yixue Zhang, Li Tan, Jian Yuan, Rong Tan, Min-Hua Luo, Fang-Lin Sun, Haipeng Liu, Ying Jiang*, Zhiyong Mao*

Full article and list of author affiliations: https://doi.org/10.1126/science.adp5056

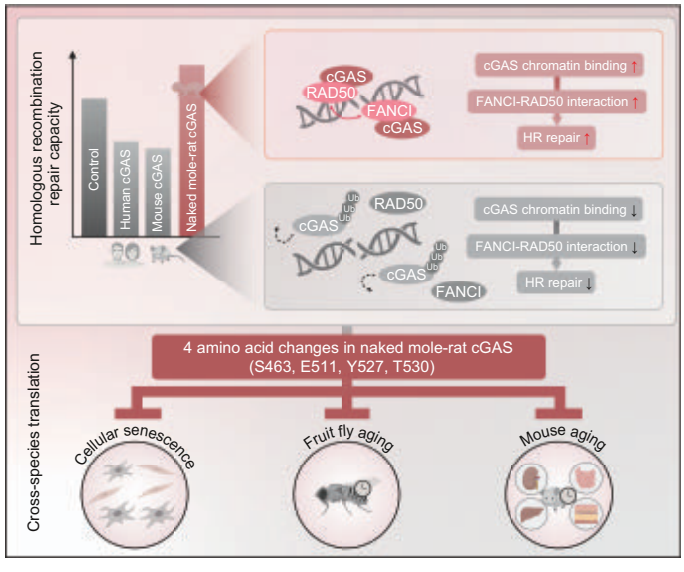
INTRODUCTION: The naked mole-rat (*Heterocephalus glaber*) is an extraordinarily long-lived rodent with a maximum life span of ~37 years. Although its exceptional longevity is thought to result from a combination of adaptations affecting diverse biological processes, the molecular mechanisms protecting the naked mole-rat from genomic instability—a primary hallmark of aging—remain unclear.

RATIONALE: DNA repair constitutes a crucial mechanism for stabilizing the genome. Earlier studies have demonstrated that the DNA sensor cyclic guanosine monophosphate–adenosine monophosphate synthase (cGAS) participates in regulating DNA double-strand break repair by suppressing the homologous recombination (HR) pathway, thereby promoting genomic instability. Although enhanced function of DNA repair proteins contributes to the evolution of longevity, it remains unexplored whether evolution has selected for the attenuation of negative regulators such as cGAS.

RESULTS: In a panel of assays, we found that naked mole-rat cGAS, in contrast to human and mouse cGAS, enhanced HR repair efficiency. This functional reversal is mediated by the substitution of four specific amino acid residues within the C-terminal domain of the cGAS protein. Mechanistically, this amino acid alteration enabled naked mole-rat cGAS to prolong its retention on chromatin in the wake of DNA damage by modulating its ubiquitination status, thereby altering its interaction with the segregase P97. The prolonged presence of naked mole-rat cGAS on chromatin facilitated the formation of a complex between the canonical HR factor RAD50 and FANCI, a factor primarily associated with the Fanconi anemia pathway. We further demonstrated that FANCI promoted the chromatin recruitment of RAD50, thereby potentiating HR repair. Consequently, naked mole-rat cGAS attenuated stress-induced cellular senescence, mitigated organ degeneration, and extended life span in fruit flies. Critically, reverting these four amino acid residues abolished these protective effects. Furthermore, adeno-associated virus–mediated delivery of naked mole-rat cGAS to aged mice reduced frailty, attenuated hair graying, lowered circulating levels of immunoglobulin G and interleukin-6, and decreased cellular senescence markers in multiple tissues. Once again, these beneficial effects were dependent on the four specific amino acids.

CONCLUSION: Using comparative molecular biology, our work reveals that the negative regulatory function of cGAS in HR repair is reversed in the longest-lived rodent, the naked mole-rat, by an alteration of four specific amino acid residues. This alteration confers naked mole-rat cGAS with a greater capacity to stabilize the genome, counteract cellular senescence and organ aging, and promote extended life span and health span. □

*Corresponding author. Email: ying_jiang@tongji.edu.cn (Y.J.); zhiyong_mao@tongji.edu.cn (Z.M.) †These authors contributed equally to this work. **Cite this article as Y. Chen *et al.*, *Science* 390, eadp5056 (2025). DOI: 10.1126/science.adp5056**



Divergent cGAS function in naked mole-rats. The cGAS-mediated suppression of homologous recombination repair is reversed in the longest-lived rodent, the naked mole-rat. Four amino acid changes maintain its cGAS at a low level of ubiquitination after DNA damage, conferring prolonged chromatin binding (E, Glu; S, Ser; T, Thr; Y, Tyr). This facilitates FANCI and RAD50 interaction, enhancing HR repair. These molecular changes contribute to reduced cellular senescence, delayed organ aging, and life-span extension. [Figure created with BioRender.com]

AGING

A cGAS-mediated mechanism in naked mole-rats potentiates DNA repair and delays aging

Yu Chen[1]†, Zhixi Chen[1]†, Hao Wang[1], Zhen Cui[1], Kai-Le Li[1], Zhiwei Song[1], Lingjiang Chen[1], Xiaoxiang Sun[1], Xiaoyu Xu[1], Yixue Zhang[1], Li Tan[2], Jian Yuan[3], Rong Tan[4], Min-Hua Luo[5], Fang-Lin Sun[1], Haipeng Liu[3], Ying Jiang[1]*, Zhiyong Mao[1]*

Efficient DNA repair might make possible the longevity of naked mole-rats. However, whether they have distinctive mechanisms to optimize functions of DNA repair suppressors is unclear. We find that naked mole-rat cyclic guanosine monophosphate–adenosine monophosphate synthase (cGAS) lacks the suppressive function of human or mouse homologs in homologous recombination repair through the alteration of four amino acids during evolution. The changes enable cGAS to retain chromatin longer upon DNA damage by weakening TRIM41-mediated ubiquitination and interaction with the segregase P97. Prolonged chromatin binding of cGAS enhanced the interaction between repair factors FANCI and RAD50 to facilitate RAD50 recruitment to damage sites, thereby potentiating homologous recombination repair. Moreover, the four amino acids mediate the function of cGAS in antagonizing cellular and tissue aging and extending life span. Manipulating cGAS might therefore constitute a mechanism for life-span extension.

The naked mole-rat (*Heterocephalus glaber*) is an extraordinarily long-lived rodent with an ~37-year maximum life span (*1*)—around an order of magnitude greater than that of comparably sized relatives. Naked mole-rats have transcriptomes and protein coding sequences that are more similar to those of humans than those of mice (*2*). This establishes these animals as models for scrutinizing the molecular mechanisms behind successful aging. Genome stabilization is important in the evolution of longevity across various species (*3*–*5*). However, current understanding of the adaptations at the molecular level in DNA repair, which help maintain genomic stability in response to endogenous or exogenous DNA damage, remains limited in naked mole-rats.

DNA double-strand breaks (DSBs) are the most deleterious type of DNA damage, and their accumulation is associated with aging (*6*–*9*). Homologous recombination (HR) repair is one of the DSB repair pathways; it is a complicated process involving several major steps (*10*), whose defects are associated with premature aging in both mice and humans (*7*, *11*–*13*). The Fanconi anemia (FA) pathway, responsible for repairing DNA interstrand cross-links, is closely related to the HR pathway (*14*, *15*). FANCI, one of the core regulators of interstrand cross-link repair, also functions in the response to replication stress independently of its role in the FA pathway (*16*, *17*). Thus, FA factors may function in other types of DNA repair as well.

[1]Shanghai Key Laboratory of Maternal Fetal Medicine, Clinical and Translational Research Center of Shanghai First Maternity and Infant Hospital, Frontier Science Center for Stem Cell Research, School of Life Sciences and Technology, Tongji University, Shanghai, China. [2]Key Laboratory of Medical Epigenetics and Metabolism, Institutes of Biomedical Sciences, Fudan University, Shanghai, China. [3]School of Medicine, Tongji University, Shanghai, China. [4]Department of Oncology, Xiangya Cancer Center, Xiangya Hospital, Central South University, Changsha, China. [5]State Key Laboratory of Virology, Wuhan Institute of Virology, Chinese Academy of Sciences, Wuhan, China. ***Corresponding author. Email: ying_jiang@tongji.edu.cn (Y.J.); zhiyong_mao@tongji.edu.cn (Z.M.)** †These authors contributed equally to this work.

As the primary cytosolic DNA sensor, cyclic guanosine monophosphate–adenosine monophosphate (GMP-AMP) synthase (cGAS) senses cytosolic DNA of exogenous or endogenous origin to catalyze the synthesis of cyclic GMP-AMP (cGAMP). This, in turn, triggers stimulator of interferon genes (STING)–mediated innate immune responses (*18*, *19*). cGAS is also localized in the nucleus to suppress HR repair, potentially promoting tumorigenesis in both human and mouse cells (*20*, *21*), which might shorten life span. Several positive regulators in DNA repair, such as sirtuin 6 (*SIRT6*) and breast cancer gene 1 (*BRCA1*), are positively selected during the evolution of longevity (*22*, *23*), but it is yet to be determined whether cGAS inhibits HR in naked mole-rats as it does in humans or mice.

Naked mole-rat cGAS promotes HR repair to stabilize the genome

cGAS was cloned from a naked mole-rat fibroblast line (*24*). We confirmed that it had the canonical innate immunity regulatory function (fig. S1A), while its catalytic activity was decreased compared with human and mouse cGAS (fig. S1, B and C). Naked mole-rat cGAS was recruited to a microirradiation-induced DNA damage site in both naked mole-rat fibroblasts and human U-2 OS cells (Fig. 1, A and B), indicating that it may function in the DNA damage response. Overexpression of human or mouse cGAS inhibited HR repair, as measured with a green fluorescent protein (GFP)–based HR reporter (*25*) (fig. S1, D and E). In contrast, naked mole-rat cGAS overexpression enhanced HR in a dose-dependent manner (Fig. 1C and fig. S1, D and E). CRISPR-Cas9–mediated depletion of cGAS in naked mole-rat cells suppressed HR repair, and its restoration rescued the decline of HR (Fig. 1D and fig. S1, F and G), further indicating that naked mole-rat cGAS exerted an opposite function in HR repair compared with human or mouse cGAS. Overexpression of a catalytically inactive naked mole-rat cGAS mutant (E257A/D259A or D351A) also stimulated HR (fig. S1, H and I), highlighting that the enhancement of HR by naked mole-rat cGAS is independent of its enzymatic activity. Because HR only occurs in S and G2 phases of the cell cycle, when sister chromatids are available, we also confirmed that the modulation of cell cycle distribution is not the mechanism by which naked mole-rat cGAS promotes HR (fig. S1J).

Consistent with the enhanced HR repair efficiency, immunostaining experiments revealed that naked mole-rat cGAS overexpression accelerated recruitment of RAD51, the critical recombinase involved in HR repair (Fig. 1, E and F), resulting in faster clearance of the DSB marker, γH2AX foci (fig. S1, K to M). Comet assays confirmed that naked mole-rat cGAS enhanced genomic stability (Fig. 1, G and H), whereas its loss destabilized the genome (Fig. 1, I and J).

Four amino acids underlie the HR promotion effect of naked mole-rat cGAS

To further elucidate the molecular basis behind the naked mole-rat cGAS–specific regulation of HR, we investigated which domains in naked mole-rat cGAS were responsible for its stimulatory effect on HR efficiency. Chimeric cGAS genes were generated by fusing naked mole-rat and human N and C termini. Chimeric cGAS with naked mole-rat N terminus and human C terminus lost HR stimulation effect, whereas human N terminus and naked mole-rat C terminus retained it (Fig. 2, A and B, and fig. S2A). We subsequently divided the C-terminal domain into three subdomains and created chimeric cGAS genes by replacing the three subdomains of naked mole-rat cGAS with the corresponding subdomains of human cGAS (Fig. 2C). Repair efficiency analysis indicated that naked mole-rat C3 domain (444–554) potentiated HR repair (Fig. 2D and fig. S2B).

A sequence comparison of the C3 domains identified 16 amino acid (aa) residues specific to the naked mole-rat cGAS sequence (fig. S2C). These residues may contribute to differences in cGAS-mediated regulation of HR. We therefore created the 16-aa replacements in

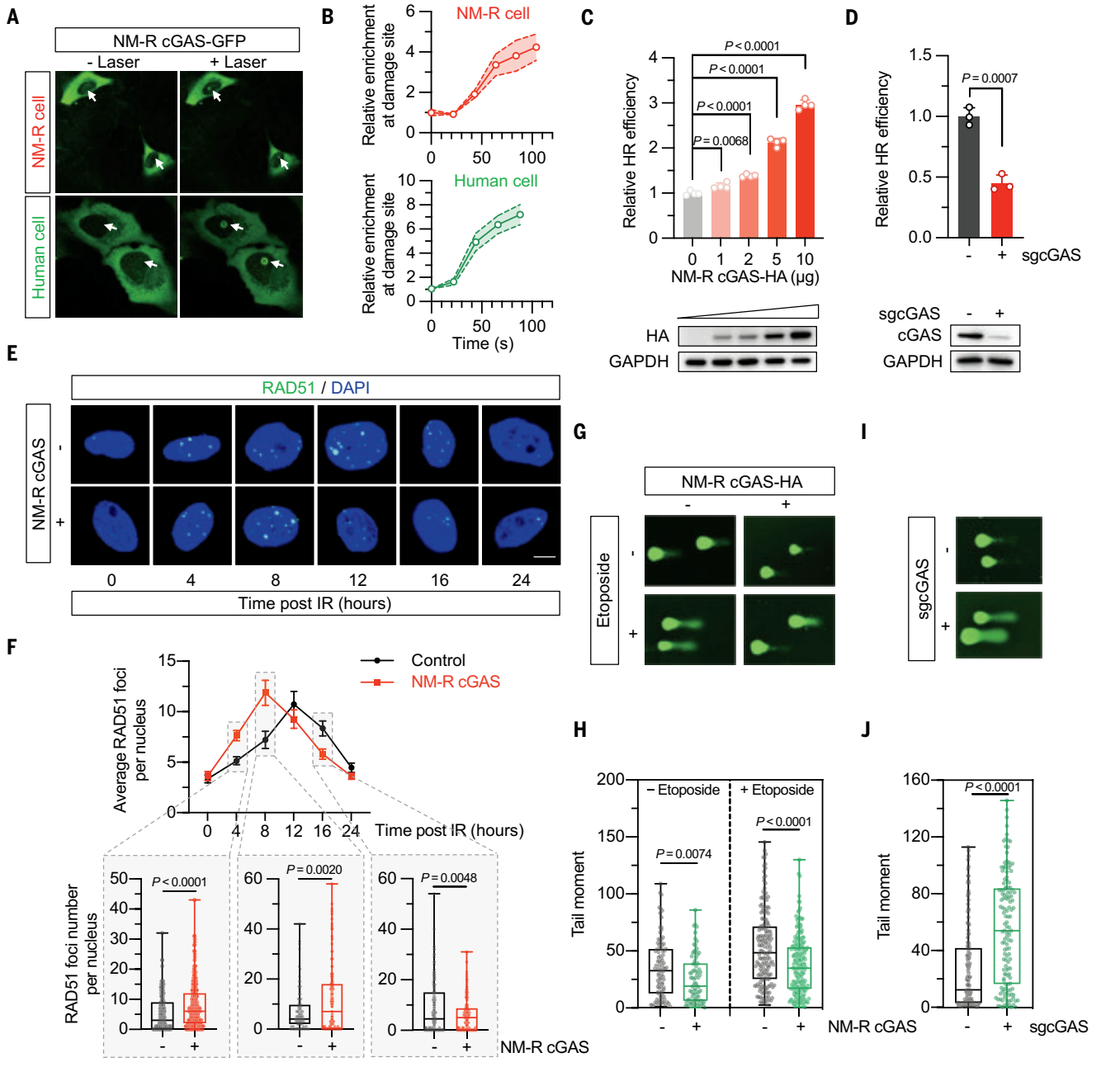


Fig. 1. Naked mole-rat cGAS promotes HR repair to stabilize the genome. (**A** and **B**) Recruitment of GFP-tagged naked mole-rat (abbreviated as "NM-R" in figures and figure captions) cGAS to DNA damage sites in human and NM-R cells. Representative images of cGAS recruitment in Large T immortalized NM-R skin fibroblasts (NSFs) and U-2 OS cells are shown in (A); arrows indicate the positions where cells were irradiated. The quantifications of fluorescence intensity are shown in (B), the area within error bands (SEM) is color-filled. (**C**) Relative HR repair efficiency in NSFs. Cells were transfected with increasing amounts of vectors encoding NM-R cGAS-HA together with I-SceI–linearized HR reporters and plasmids encoding DsRed. The expression of cGAS-HA was confirmed by Western blot. (**D**) Relative HR repair efficiency in a pool of NSFs transfected with Cas9 and single guide RNA targeting cGAS. The expression of cGAS was confirmed by Western blot. For (C) and (D), the error bars indicate SD, and Student's *t* test was used for significance determination between two groups. (**E** and **F**) Analysis of RAD51 recruitment in NSFs with or without NM-R cGAS overexpression. NSFs were irradiated with x-ray at a dosage of 8 Gy and then harvested for immunostaining at the indicated time points after irradiation (scale bar: 5 μm). Error bars indicate SEM. (**G** and **H**) Genomic stability analysis with comet assay in NSFs overexpressing NM-R cGAS. Cells were treated with or without 50 μM etoposide for 2 hours before being harvested. (**I** and **J**) Genomic stability analysis with comet assay in NSFs with cGAS depletion. Mann-Whitney *U* test was used for significance determination between two groups.

both naked mole-rat and human cGAS and analyzed the effects of these mutants on HR repair. Changing the 16 aa residues in naked mole-rat cGAS abolished its HR repair stimulatory effect, whereas altering the 16-aa residues in human cGAS led to the abrogation of HR repair inhibition (fig. S2, D and E), indicating the critical role of the 16-aa residues.

We further identified four mutations, S463D, E511K, Y527L, and T530K, that at least partially abolished HR stimulation (Fig. 2E and fig. S2F). Introduction of the four amino acid substitutions into naked mole-rat cGAS (S463D+E511K+Y527L+T530K) significantly diminished its stimulatory effect on HR repair, whereas the corresponding 4-aa mutations in human cGAS (D431S+K479E+L495Y+K498T)

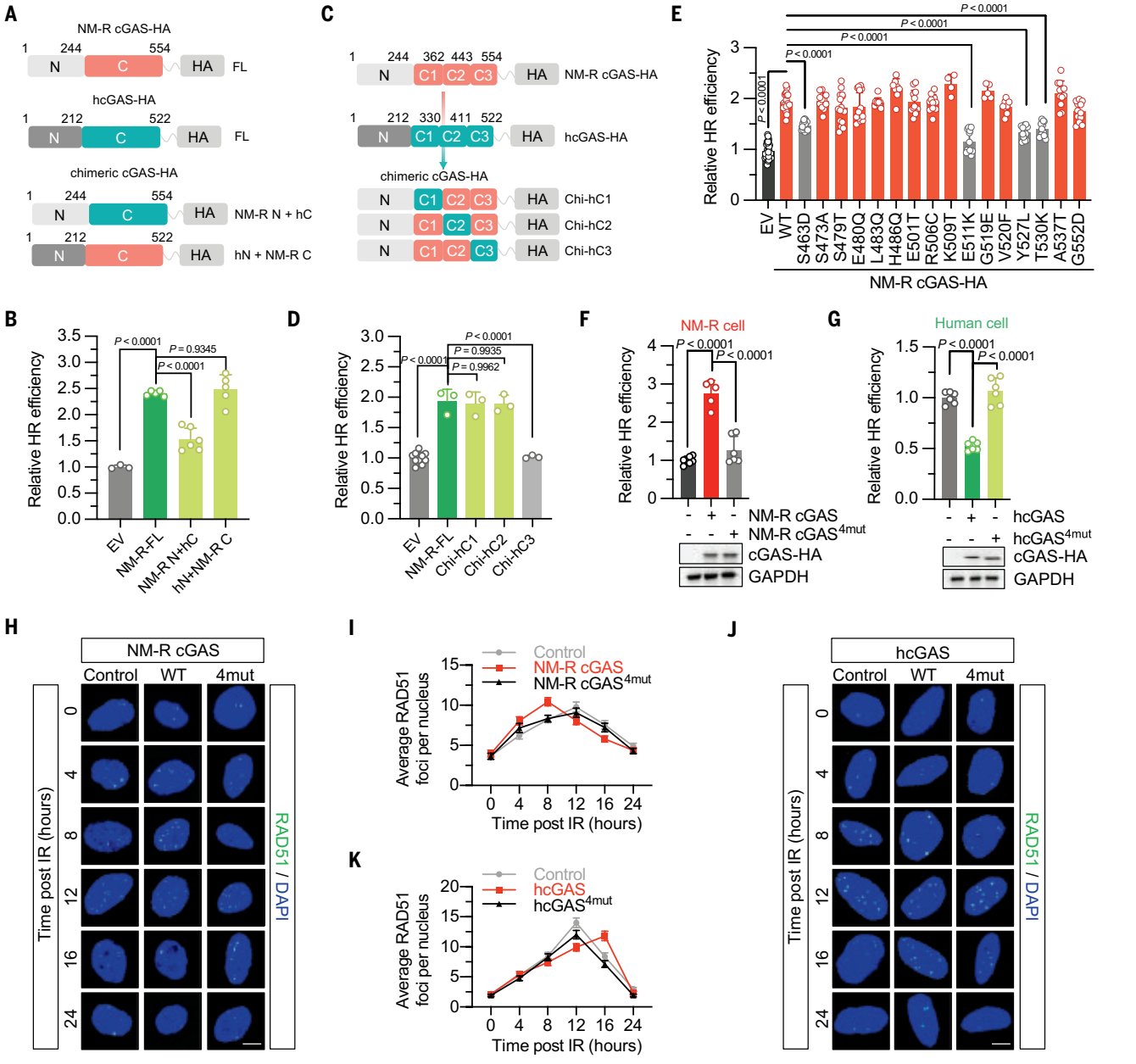


Fig. 2. Four amino acids mediate the role of naked mole-rat cGAS in potentiating HR. (**A**) Schematic representation of the HA-tagged full-length (FL) NM-R and human cGAS and the chimeric NM-R-human cGAS. (**B**) Analysis of overexpressing chimeric NM-R cGAS on HR efficiency in NSFs. (**C**) Schematic representation of the NM-R cGAS with C-terminal subdomains substituted according to the sequence of human cGAS. (**D**) The effect of NM-R cGAS with the corresponding human C-terminal subdomains substituted on HR efficiency in NSFs. One-way analysis of variance (ANOVA) with Tukey's multiple comparison test was performed for (B) and (D). (**E**) The effect of the 16 single amino acid mutations on the relative HR repair efficiency. Single-letter abbreviations for the amino acid residues are as follows: A, Ala; C, Cys; D, Asp; E, Glu; F, Phe; G, Gly; H, His; I, Ile; K, Lys; L, Leu; M, Met; N, Asn; P, Pro; Q, Gln; R, Arg; S, Ser; T, Thr; V, Val; W, Trp; and Y, Tyr. Amino acid substitution was introduced into the NM-R cGAS corresponding to the human cGAS sequence, respectively. Vectors encoding cGAS or its mutants were cotransfected with linearized HR reporter and the vectors encoding DsRed to NSFs. FACS was performed at 48 hours after transfection. One-way ANOVA with Dunnett's T3 multiple comparison test was performed. (**F**) The effect of overexpressing WT or the 4-aa–substituted NM-R cGAS on the relative HR repair efficiency in NSFs. The expression of cGAS was confirmed by Western blot. (**G**) The effect of overexpressing WT or the 4-aa–substituted human cGAS on the relative HR repair efficiency in human skin fibroblasts, HCA2-hTERT. One-way ANOVA with Dunnett's multiple comparison test was performed for (F) and (G). (**H** to **K**) Immunofluorescence analysis of the RAD51 foci kinetics in NSFs or HCA2-hTERT overexpressing NM-R [(H) and (I)] or human [(J) and (K)] cGAS WT or 4mut, respectively (scale bars: 10 μm). Cells were irradiated with x-ray at a dosage of 8 Gy and harvested at indicated time points. The error bars indicate SD in (B) and (D) to (G) and indicate SEM values in (I) and (K).

abolished its HR inhibitory effect (Fig. 2, F and G). Consistently, the naked mole-rat cGAS 4-aa mutant lost its stimulatory effect on recruiting RAD51 (Fig. 2, H and I, and fig. S3, A and B), whereas the human cGAS 4-aa mutant reversed the inhibitory effect on RAD51 recruitment (Fig. 2, J and K, and fig. S3, C and D). The role of the four residues in regulating RAD51 recruitment is conserved in mice (fig. S3, E to H). Mutations in either naked mole-rat or human cGAS did not affect their canonical DNA sensing function (fig. S3, I and J), indicating that the effect of the four substitutions on DNA repair is uncoupled from its canonical innate immunity function. Phylogenetic analysis of cGAS protein sequences across three major rodent clades revealed that the 4-aa changes evolved gradually within the naked

mole-rat–related clade but are not observed in other rodents or long-lived mammalian species outside Rodentia. Two exceptions include the gray squirrel (*Sciurus carolinensis*) and the blind mole-rat (*Spalax galili*), which have Y503 and T606, corresponding to naked mole-rat cGAS Y527 and T530, respectively (fig. S3K).

Prolonged chromatin binding of naked mole-rat cGAS is mediated by four amino acid changes

Given that cGAS is enriched at DNA damage sites when DSBs occur, we compared retention of naked mole-rat and human cGAS on chromatin after DNA damage. We extracted chromatin from human embryonic kidney 293FT (HEK-293FT) cells after 8 grays (Gy) of x-ray irradiation. Both naked mole-rat and human cGAS were enriched on chromatin, and naked mole-rat cGAS exhibited a stronger chromatin binding compared with human cGAS at 30 min after DNA damage (Fig. 3A). The 4-aa mutations in naked mole-rat cGAS accelerated its dissociation from chromatin, whereas human cGAS 4-aa mutant was retained on chromatin with a higher level than wild-type (WT) human cGAS at 30 min after DNA damage (Fig. 3A).

The segregation of DNA repair factors from chromatin often requires the protein segregase P97, which extracts substrates with K48-linked ubiquitins from DSB sites (*26*, *27*). We compared the ubiquitination of naked mole-rat and human cGAS in HEK-293FT cells after DNA damage. Ubiquitination of human cGAS, but not naked mole-rat cGAS, increased after ionizing radiation (IR), and 4-aa mutations caused this difference (Fig. 3B). Consequently, the interaction between naked mole-rat cGAS and P97 decreased at 15 min after irradiation, whereas the interaction between human cGAS and P97 increased (Fig. 3C). Consistent with this observation, the 4-aa mutations in naked mole-rat cGAS led to a stronger cGAS-P97 interaction at 15 min after irradiation,

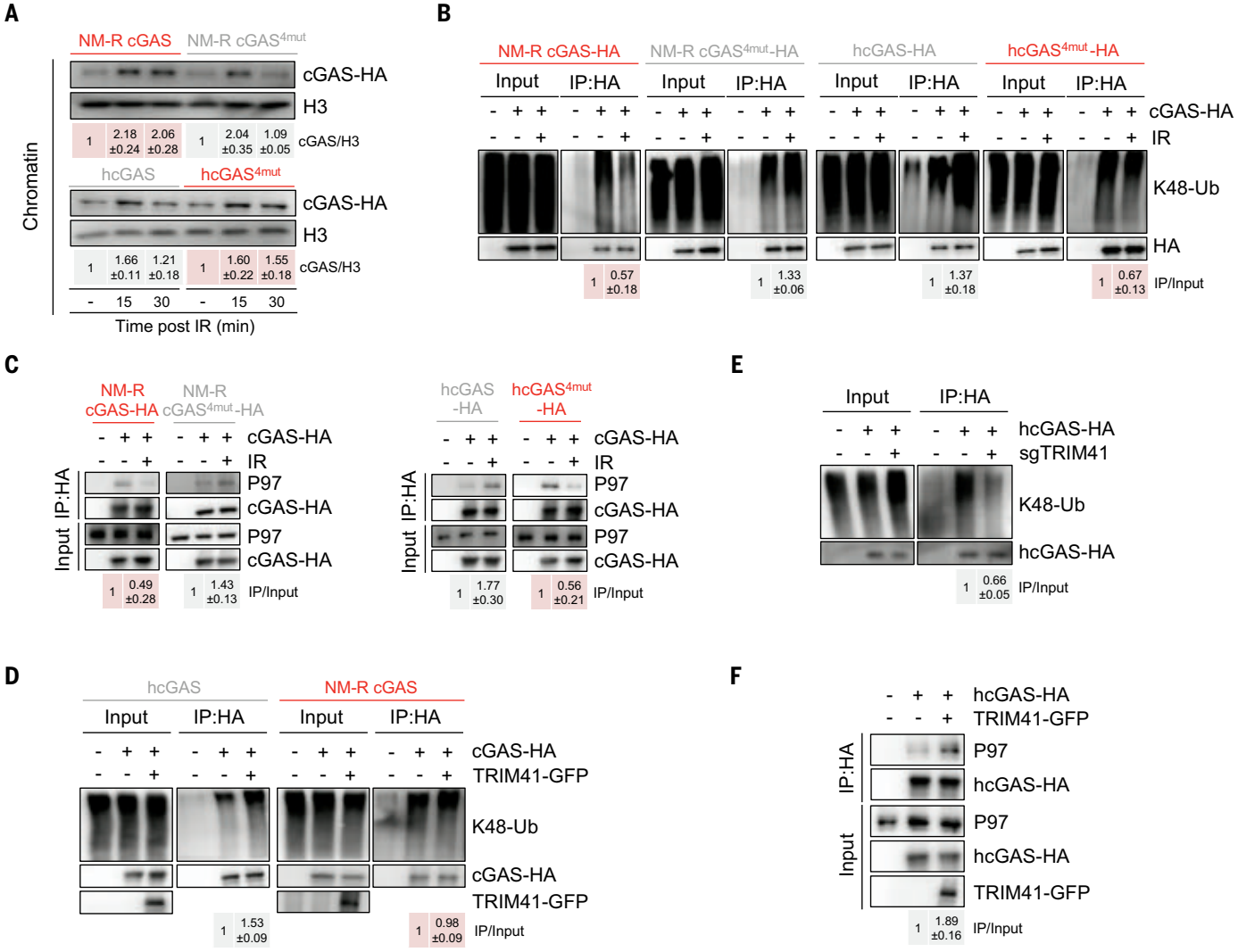


Fig. 3. Naked mole-rat cGAS retains chromatin binding longer after DNA damage. (**A**) Analysis of the amount of chromatin-bound WT or 4mut human/NM-R cGAS after the occurrence of DNA damage in HEK-293FT cells. Cells transfected with cGAS or its mutant were treated with x-ray at a dosage of 8 Gy the next day. The gray scales of chromatin-bound cGAS-HA relative to H3 are shown. (**B**) Analysis of the K48-linked ubiquitination level of WT or 4mut human/NM-R cGAS after DNA damage occurs in HEK-293FT cells. Cells were harvested at 15 min after irradiation. (**C**) Analysis of the interaction between P97 and WT or 4mut human/NM-R cGAS in HEK-293FT cells at 15 min after irradiation. (**D**) The effect of human TRIM41 overexpression on the K48-linked ubiquitination of human/NM-R cGAS in HEK-293FT cells. (**E**) The effect of TRIM41 depletion on the K48-linked ubiquitination of human cGAS in HeLa cells. Cells were harvested at 15 min after irradiation. (**F**) Analysis of the interaction between P97 and human cGAS upon human TRIM41 overexpression in HEK-293FT cells. All experiments were independently repeated three times. Quantification results represent the mean ± SD from all the replicates and are shown in all panels of the figure.

whereas the increase in human cGAS-P97 association was abrogated by the 4-aa mutations (naked mole-rat cGAS, 0.49 ± 0.28; naked mole-rat cGAS^{4mut}, 1.43 ± 0.13; hcGAS, 1.77 ± 0.30; hcGAS^{4mut}, 0.56 ± 0.21) (Fig. 3C). Experiments on chromatin retention, ubiquitination, and P97 interaction using mouse cGAS and its 4-aa mutant yielded consistent results (fig. S4).

DNA damage enhances the interaction between human cGAS and an E3 ubiquitin ligase TRIM41 (*28*). We therefore tested the effect of TRIM41 on the ubiquitination of human and naked mole-rat cGAS. Coimmunoprecipitation (co-IP) analysis revealed that TRIM41 overexpression enhanced human cGAS ubiquitination by ~1.53-fold but had no obvious effect on the ubiquitination of naked mole-rat cGAS (Fig. 3D). Moreover, depletion of TRIM41 in human cells decreased cGAS ubiquitination, and TRIM41 overexpression promoted the interaction between human cGAS and P97 (Fig. 3, E and F).

Naked mole-rat cGAS facilitates FANCI-mediated RAD50 recruitment to boost HR repair

Because naked mole-rat cGAS was bound longer on chromatin after DNA damage than human cGAS, we sought to determine whether naked mole-rat cGAS might act as a platform for recruiting DNA repair factors. We used co-IP assays followed by mass spectrometry on samples from irradiated naked mole-rat skin fibroblasts and identified the potential DNA repair factors as the targets of naked mole-rat cGAS in promoting HR. These included FANCI, RAD50, and PARP1 (Fig. 4A and table S1). Human cGAS inhibits HR repair by impeding the formation of the PARP1-Timeless complex (*20*). However, co-IP experiments revealed that in naked mole-rat cells, the PARP1-Timeless interaction was undetectable (fig. S5, A and B), and DNA damage stimuli failed to enhance the interactions between naked mole-rat cGAS and PAR or PARP1 (fig. S5, C and D), which were observed in human cells. Thus, it is unlikely that naked mole-rat cGAS regulates HR repair through altering the PARP1-Timeless interaction.

Therefore, we conducted further investigations to determine whether there is an interaction between naked mole-rat FANCI or RAD50 and cGAS. Co-IP experiments using ectopically expressed proteins revealed that GFP-tagged naked mole-rat cGAS interacted with hemagglutinin (HA)–tagged naked mole-rat FANCI (Fig. 4B). Endogenous co-IP was done in human fibroblasts, as commercial antibodies against both naked mole-rat proteins were unavailable for the immunoprecipitation assay, and the result validated the cGAS-FANCI interaction (Fig. 4C). Additionally, the association between naked mole-rat RAD50 and cGAS was confirmed through both exogenous and endogenous co-IP (Fig. 4, D and E). RAD50 is a well-characterized DSB repair factor, but FANCI mainly repairs interstrand cross-linked DNA lesions (*14*). Microirradiation experiments showed that naked mole-rat FANCI was recruited to laser-induced DSBs (Fig. 4F). Tagged overexpressed naked mole-rat FANCI and RAD50 interacted with each other, and IR enhanced their interaction by ~1.84-fold (Fig. 4, G and H). Additionally, in vitro co-IP assay confirmed their interaction (fig. S6A). These data led us to test whether FANCI and RAD50 cooperate to regulate DSB repair and whether naked mole-rat cGAS promotes HR through enhancing their interaction.

We confirmed the FANCI-RAD50 interaction in human cells (fig. S6B), indicating that the potential regulation of the complex is evolutionarily conserved. Using co-IP assay, we found that both the regions 701–750 aa and 851–900 aa in FANCI were critical to its interaction with RAD50; and the 1–98 aa region in RAD50 mediated its interaction with FANCI (fig. S6, C to H). Deleting the interaction regions (FANCI Δ851–900, RAD50 Δ2–98) diminished FANCI-RAD50 interaction (fig. S7, A and B). While co-overexpression of WT FANCI and RAD50 cooperatively enhanced HR repair, this effect was lost when the interaction-deficient mutants were coexpressed (Fig. 4, I and J, and fig. S7, C and D). Thus, the formation of FANCI-RAD50 complex may promote HR repair.

Naked mole-rat cGAS enhanced the interaction between FANCI and RAD50, but human cGAS exerted the opposite effect (Fig. 4K and fig. S7E). Replacement of 16 aa and 4 aa reduced naked mole-rat cGAS–mediated FANCI-RAD50 interaction, whereas overexpressing human or mouse cGAS mutants promoted FANCI-RAD50 interaction (Fig. 4, L and M, and fig. S7, F to H). Proximity ligation assays (PLAs) confirmed that naked mole-rat cGAS enhanced the FANCI-RAD50 interaction, whereas human cGAS disrupted it. This functional divergence was mediated by the four critical amino acid residues (Fig. 4, N and O).

Given the direct FANCI-RAD50 interaction (fig. S6A), prolonged chromatin association of naked mole-rat cGAS might increase their chance of encountering each other, thereby enhancing FANCI-RAD50 interaction to promote HR repair. Conversely, transient chromatin binding of human cGAS may remove FANCI and RAD50 from chromatin. Thus, human cGAS might act as a competitive binding factor, impairing FANCI-RAD50 association. Indeed, the suppressive effect of human cGAS on FANCI-RAD50 interaction was abolished when cells were treated with CB-5083, a P97 inhibitor, indicating that cGAS chromatin binding is critical to its impact on FANCI-RAD50 interaction (Fig. 4P). The human cGAS 4-aa mutant–mediated enhancement of human FANCI-RAD50 interaction did not result in a stimulation in HR repair efficiency (Fig. 2G). We found that it still retained its suppressive effect on the Timeless-PARP1 interaction (fig. S7I). This latter negative regulation on HR by the human cGAS 4-aa mutant might somehow compromise its positive function through targeting the FANCI-RAD50 complex.

The binding of RAD50 to DNA is one of the earliest events in DNA damage response and is vital for DNA repair through HR. Chromatin fractionation experiments revealed that naked mole-rat FANCI facilitated the loading of RAD50 onto chromatin after DNA damage (Fig. 4Q). Additionally, overexpression of naked mole-rat cGAS promoted the recruitment of RAD50 to chromatin (Fig. 4R). Notably, depleting FANCI abolished this stimulatory effect (Fig. 4S), indicating that FANCI is required for naked mole-rat cGAS–mediated RAD50 recruitment. To further verify that naked mole-rat cGAS promoted HR by targeting FANCI and RAD50, we performed RAD51 immunofluorescence staining in irradiated naked mole-rat cells. Overexpression of naked mole-rat cGAS accelerated the recruitment of RAD51 in the control cells, whereas it failed to promote RAD51 recruitment in cells with FANCI or RAD50 depleted (Fig. 4, T and U, and fig. S7J).

Four–amino acid substitution modulates cellular senescence, tissue aging, and life span

Although impaired DNA repair accelerates aging, whether boosting DNA repair counteracts aging remains unclear. We investigated the effects of naked mole-rat and human cGAS and their 4-aa mutants on stress-induced premature cellular senescence (SIPS). To exclude any interference from the canonical DNA sensing function on cellular senescence (*29*, *30*), we generated vectors expressing enzymatically inactive cGAS (naked mole-rat: cGAS$^{E257A/D259A}$, cGAS$^{4mut,E257A/D259A}$; human: cGAS$^{E225A/D227A}$, cGAS$^{4mut,E225A/D227A}$; mouse: cGAS$^{E211A/D213A}$, cGAS$^{4mut,E211A/D213A}$; with all enzymatic mutations abbreviated as "E/D" thereafter). Overexpressing naked mole-rat cGAS$^{E/D}$ in naked mole-rat cells significantly suppressed SIPS as assessed through β-galactosidase staining and the expression of p21, a marker of cellular senescence. However, the introduction of the 4-aa mutations in naked mole-rat cGAS abrogated these suppressive effects (Fig. 5, A to C). In contrast, in human skin fibroblast HCA2-hTERT cells overexpressing human or mouse cGAS$^{E/D}$, irradiation induced a higher percentage of senescent cells and a higher expression of p21 compared with the control cells, and the 4-aa mutations reversed these effects (Fig. 5, D to F, and fig. S8, A to C). These findings demonstrate contrasting roles of cGAS and the functional significance of the 4-aa mutations in modulating cellular senescence. We also assessed the role of human versus naked mole-rat cGAS in tumorigenesis using both soft agar assay and in vivo xenograft models. Human cGAS promoted oncogenic transformation, and this could be prevented by the four

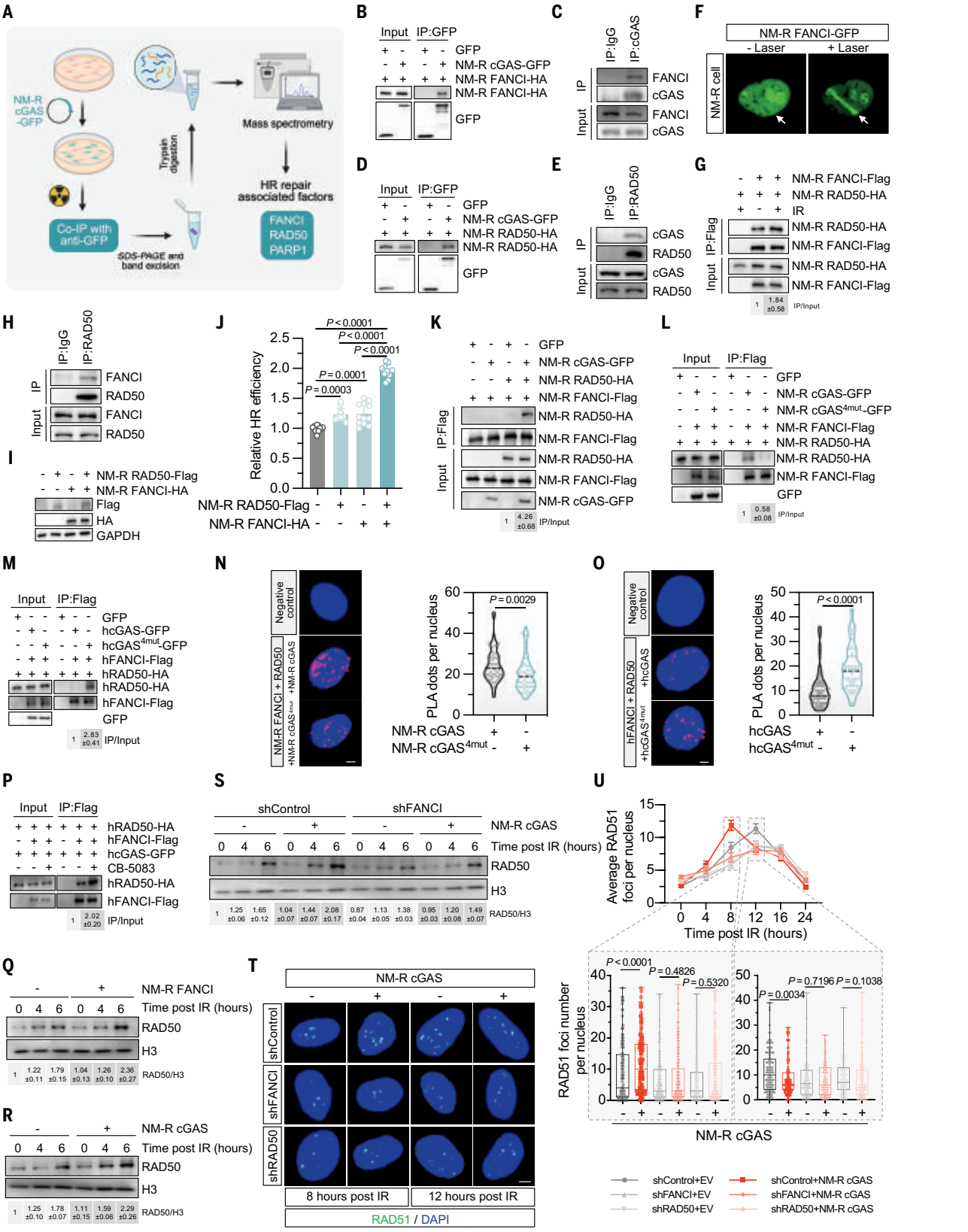


Fig. 4. Naked mole-rat cGAS enhances FANCI-RAD50 interaction to promote RAD50 recruitment. (**A**) Experimental design for identifying candidate HR repair–associated factors interacting with NM-R cGAS. NSFs transfected with GFP-tagged NM-R cGAS were collected 15 min after exposure to 8 Gy of x-ray for co-IP and subsequent mass spectrometry. [Figure panel created with BioRender.com] (**B** and **C**) Co-IP validation of the protein interaction between cGAS and FANCI. NM-R cGAS and FANCI were ectopically expressed in NSFs in (B), and the endogenous interaction was analyzed in HCA2-hTERT cells in (C). (**D** and **E**) Co-IP validation of the protein interaction between NM-R cGAS and RAD50. cGAS and RAD50 were ectopically expressed in NSFs in (D), and their endogenous interaction was analyzed in NSFs in (E). (**F**) Recruitment of GFP-tagged NM-R

FANCI to laser microirradiation–induced DNA damage site in NSFs. Arrows indicate the position where the cell was irradiated. (**G**) Co-IP analysis of the interaction between NM-R FANCI and RAD50 in NSFs. Cells were treated with or without x-ray at a dosage of 8 Gy. Fifteen minutes later, cells were harvested for co-IP. (**H**) Endogenous interaction between NM-R FANCI and RAD50 in NSFs. (**I** and **J**) The effect of NM-R FANCI and/or NM-R RAD50 overexpression on the relative HR repair efficiency in NSFs. Empty vector was cotransfected to make the total amount of transfected plasmids equal. The protein expression was confirmed by Western blot in (I), and the relative repair efficiency is shown in (J). The error bars indicate SD. (**K**) Analysis of the effect of overexpressing NM-R cGAS on NM-R FANCI-RAD50 interaction in HEK-293FT cells. (**L**) The effect of 4-aa mutant of NM-R cGAS on NM-R FANCI-RAD50 interaction in HEK-293FT cells. (**M**) The effect of 4-aa mutant of human cGAS on human FANCI-RAD50 interaction in HEK-293FT cells. (**N** and **O**) The effect of overexpressing NM-R (N) and human (O) cGAS or their mutants on FANCI-RAD50 interaction by PLA assay in HeLa cells (scale bars: 5 μm). (**P**) The effect of P97 inhibitor CB-5083 treatment on the human cGAS–mediated disruption of FANCI-RAD50 interaction in HEK-293FT cells. Cells were treated with CB-5083 at a concentration of 10 μM for 4 hours. (**Q**) RAD50 chromatin recruitment upon NM-R FANCI overexpression. (**R**) RAD50 chromatin recruitment upon NM-R cGAS overexpression. (**S**) The effect of NM-R cGAS overexpression on RAD50 chromatin recruitment in cells with or without FANCI depleted. For (Q) to (S), HEK-293FT cells were treated with or without x-ray at a dosage of 8 Gy and harvested at 4 and 6 hours after irradiation. (**T** and **U**) Analysis of RAD51 recruitment in NSFs with FANCI or RAD50 depletion. NSFs were exposed to x-ray at a dosage of 8 Gy and harvested at indicated time points. Mann-Whitney *U* test was used for significance determination (scale bar: 5 μm).

naked mole-rat–mimicking substitutions. Conversely, naked mole-rat cGAS suppressed tumorigenesis, and this was abolished by the 4-aa changes (fig. S8, D to K).

Proficient DNA repair may contribute to longevity during evolution. Given the prolonged chromatin retention of naked mole-rat cGAS, which could potentially act as a platform for recruiting DNA repair factors, we investigated its potential role as a promoter of longevity in other model organisms. We chose *Drosophila* as a model organism because it lacks the canonical DNA sensor cGAS (*31*, *32*). We created transgenic *Drosophila* lines that expressed naked mole-rat cGAS$^{E/D}$, human cGAS$^{E/D}$, or their 4-aa mutants. Guts from young and aged *Drosophila* were dissected for RNA sequencing (RNA-seq). Principal components analysis (PCA) indicated that the aged naked mole-rat cGAS$^{E/D}$ and human cGAS$^{4mut,E/D}$ group were dissimilar to other aged groups but located closer to the young groups. These data suggested that overexpression of naked mole-rat cGAS$^{E/D}$ alters the transcriptome, and the 4-aa mutations are required for the effect (fig. S8L). The AgingClock gene set comprises 33 genes showing decreased expression with age in both *Drosophila* and mice (*33*). Using this gene set for gene set enrichment analysis (GSEA) to score a sorted list of genes, we observed increased expression of AgingClock genes in the aged naked mole-rat cGAS$^{E/D}$ group versus naked mole-rat cGAS$^{4mut,E/D}$ group, and decreased expression of AgingClock genes in the aged human cGAS$^{E/D}$ group versus the human cGAS$^{4mut,E/D}$ group (Fig. 5G). We also determined young genes and old genes (abundant in young and aged *Drosophila*, respectively) by analyzing our young and aged control *Drosophila* data. Compared with the 4-aa mutants, overexpressing naked mole-rat cGAS$^{E/D}$ exhibited significant up-regulation of young genes and down-regulation of old genes in the gut of aged *Drosophila* (fig. S8M). Similar results were also found in the human cGAS$^{4mut,E/D}$ versus human cGAS$^{E/D}$ group (fig. S8N). Aged *Drosophila* are prone to infection (*34*). By analyzing age-related differentially expressed genes (DEGs) within each genotype and performing Gene Ontology (GO) term enrichment, we found that naked mole-rat cGAS$^{4mut,E/D}$ and human cGAS$^{E/D}$ overexpression caused increased expression of immune response genes, and this was not observed in naked mole-rat cGAS$^{E/D}$ and human cGAS$^{4mut,E/D}$ groups (fig. S8, O and P).

We performed a detailed analysis of gut function in aged *Drosophila*. Previous studies have reported that aged *Drosophila* typically exhibit increased gut cell proliferation and intestinal stem cell (ISC) activity (*35*–*37*). Immunostaining with anti–phosphorylated histone 3 (pH3) revealed that overexpression of naked mole-rat cGAS$^{E/D}$ significantly reduced intestinal cell proliferation in aged *Drosophila*, whereas the introduction of the 4-aa mutations abrogated this protective effect (Fig. 5, H and I). In contrast, overexpression of human cGAS$^{E/D}$ increased intestinal cell proliferation, and the introduction of the 4-aa mutations in human cGAS reversed this phenotype (Fig. 5, H and I). ISCs were further analyzed by immunostaining for Delta, a ligand for the Notch receptor (*38*), and similar results were obtained (Fig. 5, J and K). Additionally, a Smurf assay was done to assess gut permeability by tracking the penetration of edible blue dye. Naked mole-rat cGAS$^{E/D}$ reduced age-related gut permeability, whereas human cGAS$^{E/D}$ increased it. The four mutations were again critical for regulating gut permeability (fig. S8Q). Moreover, we conducted feeding infection experiments with *Enterococcus faecalis* and *Serratia marcescens*. *Drosophila* overexpressing naked mole-rat cGAS$^{E/D}$ lived longer than the control group, whereas overexpression of human cGAS$^{E/D}$ shortened survival time. The 4-aa mutations were crucial in regulating pathogen resistance (fig. S8, R and S).

We further used a climbing assay to evaluate their motor coordination (*39*, *40*). Naked mole-rat cGAS$^{E/D}$ overexpression improved climbing performance in aged *Drosophila*, whereas human cGAS$^{E/D}$ overexpression impaired it; both effects were reversed by the 4-aa mutations (fig. S9, A and B). Additionally, overexpression of naked mole-rat cGAS$^{E/D}$ also mitigated age-related decrease in egg-laying, whereas naked mole-rat cGAS$^{4mut,E/D}$ did not. Similarly, the hcGAS$^{4mut,E/D}$ group showed delayed reproductive decline compared with the hcGAS$^{E/D}$ group (fig. S9C).

Life-span analysis indicated that naked mole-rat cGAS$^{E/D}$ extended the mean and maximum life span in *Drosophila*, and the 4-aa mutations abrogated the increase. In contrast, human cGAS$^{E/D}$ shortened both the mean and maximum life span, and the 4-aa mutations rescued the decline in life span (Fig. 5, L and M, and fig. S9D). This effect remained consistent under various environmental temperatures (fig. S9, E to H).

We injected adeno-associated viruses (AAVs) carrying naked mole-rat cGAS$^{E/D}$, naked mole-rat cGAS$^{4mut,E/D}$, or the control vector into the tail vein of 17-month-old mice (Fig. 5N). The mouse frailty index (*41*) was used to evaluate health status at 2 months after injection. Mice injected with naked mole-rat cGAS$^{E/D}$ exhibited a more variable but significantly lower frailty index score compared with control mice, whereas naked mole-rat cGAS$^{4mut,E/D}$ injection had no such improvement (Fig. 5O). Macroscopic examination revealed that mice injected with naked mole-rat cGAS$^{E/D}$ displayed less severe skin lesions and milder hair graying compared with control mice. However, the effects were absent in mice injected with naked mole-rat cGAS$^{4mut,E/D}$ (Fig. 5, P and Q, and fig. S10A). Aging is associated with increased levels of immunoglobulin G (IgG) (*42*, *43*) and interleukin-6 (IL-6) (*44*) in plasma. We found that the naked mole-rat cGAS$^{E/D}$ group exhibited significantly lower amounts of IgG and IL-6 in the blood compared with both the 4-aa mutant and control groups (Fig. 5, R and S). Moreover, naked mole-rat cGAS$^{E/D}$ significantly reduced senescent cell accumulation in livers; however, 4-aa mutation abolished this effect (Fig. 5, T and U). Further examination of γH2AX levels confirmed that fewer DSBs accumulated in the livers of the naked mole-rat cGAS$^{E/D}$ group in comparison to the other two groups (Fig. 5, V and W). The senescence counteraction effect was also observed in the kidney and intestine (fig. S10, B to E). The naked mole-rat cGAS$^{E/D}$ group showed reduced blood creatinine levels (fig. S10F), indicating improved renal function. Collectively, our data reveal the functional significance of the 4-aa mutations in naked mole-rat cGAS for modulating tissue aging in mice.

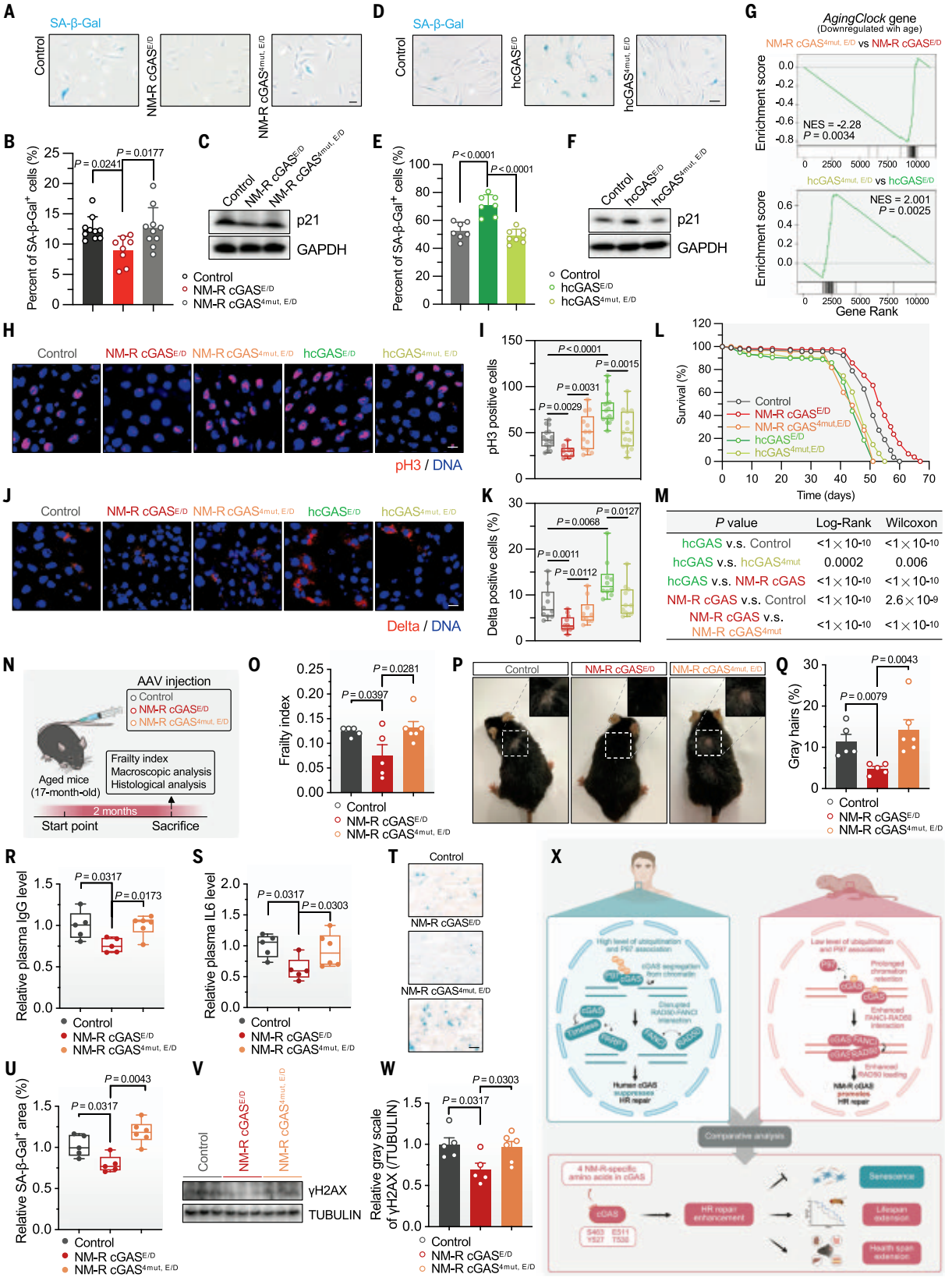


Fig. 5. Four amino acids confer a stronger capacity on naked mole-rat cGAS to suppress SIPS, counteract aging, and extend life span. (**A** to **C**) SA-β-gal staining [(A) and (B)] and p21 protein level analysis (C) of NSFs overexpressing catalytically inactive NM-R cGAS and NM-R cGAS 4-aa mutant. E/D stands for E257A/D259A in NM-R. Cells were treated with 8 Gy x-ray to induce SIPS (scale bar: 100 μm). (**D** to **F**) SA-β-gal staining [(D) and (E)] and p21 protein level analysis (F) of hcGAS–depleted HCA2-hTERT cells overexpressing catalytically inactive hcGAS and hcGAS 4-aa mutant. E/D stands for E225A/D227A in human. Cells were treated with 6 Gy x-ray to induce SIPS (scale bar: 200 μm). One-way ANOVA with Tukey's multiple comparison was used for (B) and (E). (**G**) GSEA plots showing the expression of AgingClock genes in the *Drosophila* gut. NES,

normalized enrichment score. (**H** to **K**) pH3 [(H) and (I)] and Delta [(J) and (K)] staining of the aged *Drosophila* gut (scale bars: 10 μm). (**L** and **M**) Life-span analysis in transgenic *Drosophila* expressing enzymatically inactive human/NM-R cGAS or human/NM-R cGAS 4-aa mutant at 29°C (L). Both log-rank and Gehan-Breslow-Wilcoxon test were used for significance determination (M). (**N**) Experimental design of the AAV injection experiment. [Figure panel created using illustrations from the NIAID NIH BioArt source under a public domain license] (**O**) Frailty index scores of AAV-injected mice. (**P** and **Q**) Hair and skin condition of AAV-injected mice. Representative images are shown in (P), and ratios of gray hairs were analyzed in (Q) (100 hairs counted for each mouse). (**R** and **S**) ELISA analysis of the plasma IgG (R) and IL-6 (S) level. (**T** and **U**) SA-β-gal staining in the livers of AAV-injected mice (T) (scale bar: 50 μm). Quantifications are shown in (U). (**V** and **W**) Western blot analysis of γH2AX levels in mouse livers. Mann-Whitney *U* test was used. (**X**) In human cells, the ubiquitination of cGAS increases upon DNA damage, leading to enhanced P97-mediated chromatin dissociation, and subsequently disrupts FANCI-RAD50 interaction. Human cGAS also diminishes the PARP1-Timeless interaction after DNA damage. Collectively, human cGAS delays RAD51 recruitment to inhibit HR repair. In NM-R cells, no PARP1-Timeless interaction has been observed. Moreover, the four amino acid changes in cGAS lead to a retained chromatin binding through affecting its ubiquitination and interaction with P97 and further enable a stronger FANCI-RAD50 association and RAD50 chromatin binding, eventually promoting RAD51 recruitment to potentiate HR. Differences in four amino acid residues between NM-R and human cGAS reduce the inhibitory effect of NM-R cGAS on HR repair. This adaptation enhances its ability to counteract cellular senescence, extend life span in *Drosophila*, and mitigate tissue aging in mice. [Figure panel created with BioRender.com]

Discussion

The exceptional longevity observed in naked mole-rats is attributed to a combination of various adaptations that affect different biological processes (*45*), including intercellular communication (*46*), cell cycle arrest (*47*), stress response (*48*), epigenetic regulation (*24*), and proteostasis (*49*), many of which are closely associated with the hallmarks of aging. Nevertheless, the molecular mechanisms responsible for safeguarding naked mole-rats from genomic instability remain so far unknown. DSB repair capacity negatively correlates with cancer incidence and age (*9*, *22*, *50*–*53*). A study of 18 rodents with different maximum life spans demonstrated that DSB repair efficiency correlates with maximum life spans, and the longevity gene *Sirt6* is probably positively selected during evolution (*22*). The work indicates that the enzymatic activity of SIRT6 cloned from the long-lived beaver is stronger than that of the short-lived mouse (*22*). The critical HR factor *BRCA1* is positively selected in naked mole-rats (*23*). However, whether the negative regulators involved in DSB repair are also under positive selection has received little attention. The DNA sensor cGAS negatively regulates HR repair in humans (*20*) and mice (fig. S1C). Our present work reveals the opposite function of naked mole-rat cGAS in HR, suggesting that the *CGAS* gene in the longest-lived rodent is also under positive selection.

RAD50 has traditionally been recognized as a critical component of the MRN complex (MRE11-RAD50-NBS1), where it plays a role in holding the broken DNA ends and sister chromatids together to facilitate HR (*54*). On the other hand, FANCI, an essential factor in the FA pathway, primarily functions in recruiting downstream factors during cross-link repair (*14*). We observed that the interaction between naked mole-rat FANCI and RAD50 was enhanced in a stress-dependent manner. Furthermore, naked mole-rat and human cGAS exerted opposite effects on the formation of the FANCI-RAD50 complex. Naked mole-rat cells exhibit slower growth rates compared with those of mouse or human cells (*55*). As a result, DSBs might persist for longer periods in naked mole-rat cells without being repaired, eventually leading to sterile inflammation and the onset of aging. The specific regulation of the FANCI-RAD50 interaction, which can be further enhanced in the presence of cGAS, might be particularly important to HR-directed repair in naked mole-rats.

We demonstrated that decreased interaction between naked mole-rat cGAS and P97 allowed cGAS to stay bound to chromatin for a longer period. Notably, in addition to FANCI and RAD50, the prolonged retention of naked mole-rat cGAS on chromatin might serve as a scaffold that also facilitates the recruitment and assembly of other downstream repair machineries. Moreover, the optimization of cGAS function in naked mole-rats is probably not the only mechanism for up-regulating DSB repair, as we also observed distinct mechanisms, such as the loss of the PARP1-Timeless interaction (fig. S5, A and B).

Our work provides a molecular basis for how DNA repair is activated to contribute to the exceptional longevity during evolution in naked mole-rats (Fig. 5X). We identified four amino acid residues in the naked mole-rat cGAS that allow the enhancement of HR-directed repair. These findings support the notion that efficient DNA repair decelerates the aging process and raise the possibility that targeting cGAS to enhance DNA repair could provide an intervention strategy for promoting longevity.

Materials and methods

Cell culture and transfection

Human HCA2-hTERT [generated using HCA2 (RRID: CVCL_E2UW)] (*56*), U-2 OS (RRID: CVCL_0042), HEK-293FT (RRID: CVCL_6911), HeLa (RRID: CVCL_0030), and all the derived cell lines were cultured in Dulbecco's modified Eagle's medium (DMEM, Corning, Cat. #10-013-CVR) supplemented with 10% fetal bovine serum (Gibco, Cat. #10270-106), 1% nonessential amino acids (Gibco, Cat. #11140-050), and 1% penicillin-streptomycin (Gibco, Cat. #15140-122). Cells were maintained at 37°C in a 5% CO_2 humidified incubator. All naked mole-rat skin fibroblasts (NSFs) (*24*) were cultured in DMEM supplemented with 15% fetal bovine serum, 1% nonessential amino acids, and 1% penicillin-streptomycin. NSFs were maintained at 32°C in a 5% CO_2 and 3% O_2 humidified incubator. All cells were tested free of mycoplasma contamination with PCR periodically. HCA2-hTERT, NSF, and all the derived cell lines were transfected on a Lonza 4D electroporation machine with the DT-130 program. HeLa cell line with *TRIM41* depletion was generated in our prior work (*28*) and was transfected using a Lonza 4D electroporation machine with the CN-114 program. U-2 OS cells were transfected with Lipofectamine 2000 reagents. HEK-293FT cells were transfected with polyethylenimine (PEI)–mediated method.

Mice

Mice were housed in a specific-pathogen-free environment and subjected to a 12-hour light/dark cycle, with free access to water and food. Naked mole-rat cGAS and its mutant were introduced into 17-month-old male C57BL/6 mice (Shanghai Model Organisms Center, Inc., Cat. #SM-001) via AAV-mediated gene delivery, with AAVs packaged by Taitool Bioscience (Shanghai, China). Simple randomization was used to allocate mice to control and treatment groups. Two months after injection, the mice were assessed using a previously reported frailty index (*41*). Macroscopic analysis was conducted to evaluate hair and skin condition using established methods (*57*, *58*). The mice were then sacrificed for tissue dissection. The animal studies were approved by the Biological Research Ethics Committee of Tongji University (reference number: TJLAC-020-002).

Plasmid construction

Total RNA was extracted from NSF cells and HCA2-hTERT cells using an RNASimple Total RNA Kit (Tiangen, Cat. #DP419) and was subsequently reverse transcribed into cDNA with TransScript One-Step gDNA Removal and cDNA Synthesis SuperMix (Trans, Cat. #AT311-02). The cDNA was used as the template for amplifying the open reading frames of *CGAS*, *FANCI*, *RAD50*, and *TIMELESS* then inserted into the expression vector containing the HA/Flag/GFP tag. The truncated mutants of cGAS were created on the basis of the full-length expression vector, using ClonExpress Ultra One Step Cloning Kit (Vazyme, Cat. #C115). The

vectors encoding cGAS with point mutations were generated by the site-specific mutagenesis method (Transgen, Cat. #FM111-02). All plasmids used in this study have been confirmed by Sanger sequencing.

Antibodies and reagents

The antibodies used in this study were as follows: anti-cGAS (Abclonal, Cat. #A8335, RRID: AB_2770305), anti-p97 (Abclonal, Cat. #A2795, RRID: AB_2764635), anti-K48-linkage specific polyubiquitin (Cell Signaling Technology, Cat. #8081, RRID: AB_10859893), anti-histone H3 (Cell Signaling Technology, Cat. #4499, RRID: AB_10544537), anti-γH2AX (S139) (Cell Signaling Technology, Cat. #9718, RRID: AB_2118009), anti-PARP1 (Abclonal, Cat. #A0942, RRID: AB_2757470), anti-PAR (Trevigen, Cat. #4335-MC-100, RRID: AB_2572318), anti-RAD51 (Abcam, Cat. #ab176458, RRID: AB_2665405), anti-RAD50 (Abclonal, Cat. #A3078, RRID: AB_2764881), anti-FANCI (Abcam, Cat. #ab74332, RRID: AB_1280969), anti-p21 (Abcam, Cat. #ab109199, RRID: AB_10861551), anti-Ser10-pH3 (Abcam, Cat. #ab5176, RRID: AB_304763), anti-Delta (DSHB, Cat. #C594.9B, RRID: AB_528194), anti-HA (Cell Signaling Technology, Cat. #3724, RRID: AB_1549585), anti-GFP (Abcam, Cat. #ab290, RRID: AB_303395), anti-Flag (Abclonal, Cat. #AE005, RRID: AB_2770401), anti-GAPDH (Proteintech, Cat. #60004, RRID: AB_2919223), anti-β-tubulin (Bioworld, Cat. #AP0064, RRID: AB_2797447), goat anti-Rabbit IgG (H+L) DyLight 488 (Thermo Fisher, Cat. #35552, RRID: AB_2552862), Cy3 AffiniPure goat anti-Mouse IgG (H+L) (Jackson, Cat. #115-165-003, RRID: AB_2338680) and Cy3 AffiniPure goat anti-Rabbit IgG (H+L) (Jackson, Cat. #111-165-003, RRID: AB_2338000). Antibody-conjugated beads used for co-IP assay were GFP-TRAP (ChromoTek, Cat. #gta-20), anti-HA magnetic beads (Bimake, Cat. #B26201) and anti-Flag magnetic beads (Bimake, Cat. #B26101). Etoposide (Cat. #S1225) was purchased from Selleckchem, P97 inhibitor CB-5083 (Cat. #B6032) was purchased from APExBIO.

Immunofluorescence

Cells were cultured on coverslips in 12-well plates and treated with x-ray the following day. They were then harvested for immunofluorescence analysis at the indicated time points. Initially, the cells were rinsed three times with phosphate-buffered saline (PBS) and fixed with 4% paraformaldehyde for 15 min at room temperature. For RAD51 staining, cells were treated with cytoskeleton buffer (100 mM NaCl, 10 mM PIPES, 1 mM EGTA, 3 mM $MgCl_2$, 300 mM sucrose and 0.5% Triton X-100) at 4°C for 10 min, followed by three rinses before fixation. After fixation, the cells were rinsed again three times with PBS and permeabilized using 0.25% Triton X-100 for 10 min at room temperature. Next, the cells were rinsed three additional times with PBS and blocked with 2% bovine serum albumin (BSA) for 1 hour at room temperature. Following this, the cells were incubated overnight at 4°C with the primary antibody. The next day, the cells were rinsed three times with PBS and incubated with the secondary antibody for 1 hour at room temperature. Afterward, the cells were rinsed three more times, and the coverslips were mounted in a mounting medium containing 4′,6-diamidino-2-phenylindole (DAPI). Finally, images were acquired using a Nikon laser scanning confocal microscope.

Coimmunoprecipitation

Cells transfected with the indicated plasmids were treated with x-ray or drugs according to the information provided in the figure legends before being harvested. The cells were washed with precooled PBS and then lysed in RIPA buffer [50 mM Tris-Cl (pH 7.4), 150 mM NaCl, 1% sodium deoxycholate, 0.1% SDS, 1 mM EDTA, 1% Triton X-100 and protease inhibitor] for 30 min on ice. Subsequently, the lysates were sonicated at 10% duty for 3 min in an ice water bath. The cell debris was removed by centrifugation at 13,500 rpm for 15 min at 4°C. A small aliquot of the supernatant was used as input, and the remaining lysate was precleared with IgG and Protein A/G beads before immunoprecipitation with the indicated antibodies. Alternatively, the lysate was directly used for immunoprecipitation with antibody-conjugated beads on a rotator at 4°C. For in vitro coimmunoprecipitation assay, purified proteins were mixed in the in vitro reaction buffer (150 mM NaCl, 25 mM Tris-Cl, 1% NP-40 and protease inhibitor) before the antibody was added and then rotated at 4°C overnight. On the next day, Protein A/G beads were added into the mixture if no antibody-conjugated beads were used for IP, and the mixture was incubated on the rotator for 2 hours at 4°C. Then the beads were washed five times with RIPA buffer and subsequently boiled for 10 min at 100°C for SDS-PAGE (polyacrylamide gel electrophoresis) and Western blot analysis.

Mass spectrometry

To investigate the candidate targets of naked mole-rat cGAS, NSF cells were transfected with GFP-tagged naked mole-rat cGAS. The transfected cells were then treated with 8 Gy x-ray and harvested 15 min after irradiation. The cells were lysed as described above and immunoprecipitated using GFP-trap. All precipitated samples were subjected to mass spectrometry analysis. For the mass spectrometry analysis, the samples were digested, and liquid chromatography–mass spectrometry (LC-MS) analysis was performed using a nanoflow EASYnLC 1200 system (Thermo Fisher Scientific, Odense, Denmark) coupled to an Orbitrap Fusion Lumos mass spectrometer (Thermo Fisher Scientific, Bremen, Germany). For protein identification, the results were processed using the UniProt *H. glaber* protein database (UP000006813, download in 20191227) and the Protein Discoverer (version 1.4.0.288, thermo Fisher Scientific) with Mascot (version 2.7.0, Matrix Science).

Chromatin isolation

The cells were washed with PBS once. Then, 200 μl of solution A [10 mM HEPES (pH 7.9), 10 mM KCl, 1.5 mM $MgCl_2$, 0.34 M sucrose, 1 mM dithiothreitol (DTT), 10% glycerol, and protease inhibitor] was used to lyse the cells for 10 min on ice. After the lysis step, cytoplasmic proteins were separated by centrifugation at 1300*g* for 4 min at 4°C. The resulting nuclear pellet was washed once with solution A and then lysed in 200 μl of solution B (3 mM EDTA, 0.2 mM EGTA, 1 mM DTT, and protease inhibitor) for 30 min on ice. After the second lysis step, the samples were centrifugated at 1700*g* for 4 min, and the pellet obtained was washed once with solution B and then centrifuged at 10,000*g* for 1 min. Finally, the protein pellet was sonicated for 15 s in solution A, and micrococcal nuclease (NEB, Cat. #M0247) was added for digestion at 37°C for 30 min. The reaction was halted by adding 1 mM EGTA. The proteins were then boiled for 10 min before performing Western blot analysis.

Duolink proximity ligation assay (PLA)

A Duolink PLA was performed using the Sigma PLA kit (Cat. #DUO92101). Briefly, cells were cultured on coverslips in 12-well plates. After fixation and permeabilization, the cells on the slides were incubated with 20 μl of Duolink blocking solution at 37°C for 1 hour. The primary antibody, diluted in Duolink antibody diluent, was added and incubated overnight at 4°C. Subsequently, the cells were washed twice with 1× wash buffer A at room temperature before being incubated with the probe mixture at 37°C for 1 hour. The slides were washed with 1× wash buffer A and then incubated with ligase in 1× ligation buffer at 37°C for 30 min. The slides were subsequently washed twice with 1× wash buffer A before being incubated in the 1× amplification buffer (containing polymerase) at 37°C for 100 min. Finally, the slides were washed twice with 1× wash buffer B and once with 0.01× wash buffer B. The slides were mounted with the Duolink in situ mounting medium with DAPI.

HR repair efficiency measurement

The repair efficiency measurement was performed as previously reported (*50*, *59*). Briefly, for HR efficiency analysis in human cells, 3×10^5 HCA2-hTERT-H15C cells, which were stably integrated with the HR reporter, were transfected with 2 μg of empty vectors or vectors encoding indicated genes, 2 μg of I-SceI–encoding plasmids, together

with 5 ng of DsRed encoding plasmids for transfection efficiency control. For HR efficiency analysis in naked mole-rat cells, 3×10^5 NSF cells were transfected with 2 μg of empty vectors or vectors encoding indicated genes, 100 ng of I-SceI–linearized HR reporters, and 30 ng of DsRed encoding plasmids. Transfected cells were collected at 48 hours after transfection for fluorescence-activated cell sorting (FACS) analysis on a FACSverse (BD Biosciences). The raw FACS data were analyzed by FlowJo (Ashland). The ratio of GFP^+ cells (%) to $DsRed^+$ cells (%) was calculated and normalized such that the control group mean equaled 1. Normalized ratios are the reported HR efficiency.

Cell cycle analysis

For cell cycle distribution analysis, cells transfected with the indicated plasmids were collected and washed with precooled PBS. Subsequently, the cells were fixed overnight with 70% ethanol at –20°C. The next day, the cells were centrifuged at 1000 rpm for 7 min and washed twice with PBS. Cells were then treated with 100 mg/ml RNase A for 30 min at room temperature. Cells were centrifuged at 1000 rpm, and 20 μg/ml propidium iodide (PI) was used for resuspending the pellet. The PI-stained samples were analyzed on a FACSverse (BD Biosciences). The raw data were further analyzed using the FlowJo software.

Comet assay

Cells with cGAS overexpression or depletion were treated with or without etoposide (50 μM) for 2 hours (the control group was treated with the solvent, dimethyl sulfoxide). After the treatment, the cells were collected and washed with PBS. Subsequently, they were diluted with PBS to a concentration of 3×10^5 cells/ml. The cells were mixed with low-melting agarose at the ratio of 1:9 and tiled onto the Comet-slide. The following procedures for lysis, unwinding, electrophoresis, and staining were performed according to the manufacturer's instructions (Trevigen, Cat. #4250-050-K). The comet was analyzed with CaspLab software.

Laser microirradiation

The microirradiation was used to analyze the recruitment of indicated factors to DNA damage site as previously reported (*20*). GFP-tagged gene expression vectors were transfected into indicated cells. The cells were kept in a heated chamber and pre-sensitized with 100 μM of 8-methoxypsoralen before DNA damage was induced by microirradiation. Leica LAS AF software (LAS AF3.1.0) was used for image acquisition, and LAS X software was used for image analysis.

2′3′-cGAMP quantification

Herpes simplex virus 1 strain H129 (HSV-1 H129) was generated as previously described (*60*, *61*) with assistance from W. Zeng at Wuhan Institute of Virology, Chinese Academy of Sciences. Cells were infected at a multiplicity of infection (MOI) of 1 at 24 hours after seeding and harvested 8 hours after infection. For 2′3′-cGAMP quantification, cells were lysed with 50 μl M-PER Mammalian Protein Extraction Reagent (Thermo, Cat. #78503) per 1×10^6 cells on ice for 15 min. Lysates were centrifuged at 13,500 rpm for 15 min, and supernatants were analyzed using a 2′3′-cGAMP ELISA Kit (Cayman, Cat. #501700). Parallel samples harvested at 8 hours after infection were used for RNA extraction and quantitative real-time polymerase chain reaction (qRT-PCR) analysis of *IFNB* and *CXCL10* mRNA levels.

Quantitative RT-PCR

Cells were transfected with indicated plasmids or infected with HSV-1 then lysed for total RNA extraction. Total RNA was reverse transcribed into cDNA and used as the template for qRT-PCR with SYBR Green qPCR Mix (Roche, Cat. # 04913914001) on a ViiA 7 Real-Time PCR system (Applied Biosystems). The sequences of primers are as follows: *GAPDH*-F 5′-GACATCAAGAAGGTGGTGAA-3′; *GAPDH*-R 5′-TACCAGGAAATGAGCTTGAC-3′; *IFNB* (human)-F 5′-AGGACAGGATGAACTTTGAC-3′; *IFNB* (human)-R 5′-TGATAGACATTAGCCAGGAG-3′; *IFNB* (naked mole-rat)-F 5′-GAGATGCTCCAGAATATCTTGG-3′; *IFNB* (naked mole-rat)-R 5′-CCTGCAGGAGTGTCTTCAGA-3′. For analyzing knock down efficiency, the sequences of primers used are as follows: *FANCI* (naked mole-rat)-F 5′-TCTTCCATGAGCTGGTGCAG-3′; *FANCI* (naked mole-rat)-R 5′-GGGGGTCAGATGAGAACCAG-3′; *RAD50* (naked mole-rat)-F 5′-GAACAGGAAGCAGAAACTGC-3′; *RAD50* (naked mole-rat)-R 5′-CCTGTCTGAAGATCCTTCCA-3′.

Senescence-associated β-galactosidase (SA-β-gal) staining

To minimize the potential impact of cGAS enzymatic activity on senescence induction, we used an enzymatically inactive form of cGAS for β-gal staining assay. Human and naked mole-rat fibroblasts overexpressing either enzymatically inactive cGAS or its 4-aa mutant counterpart were subjected to irradiation and then cultured for 8 days before being harvested. The cells were fixed with 2% formaldehyde and 0.2% glutaraldehyde at room temperature for 5 min. After fixation, the cells were washed twice with PBS and stained overnight at 37°C with a staining solution composed of 1 mg/ml X-gal (in dimethylformamide), 40 mM citric acid/Na phosphate buffer, 5 mM potassium ferrocyanide, 5 mM potassium ferricyanide, 150 mM sodium chloride, and 2 mM magnesium chloride. The stained cells were imaged and blindly counted on an inverted microscope. For tissue staining, freshly dissected tissues from mice injected with AAVs were fixed in a fixative solution (0.5% glutaraldehyde, 1.25 mM EGTA, 2 mM $MgCl_2$ in citric acid/Na phosphate buffer) for 5 min. The tissues were then rinsed three times with 1× PBS and incubated in a staining solution (5 mM potassium ferricyanide, 5 mM potassium ferrocyanide, 2 mM $MgCl_2$, 1 mg/ml X-gal in citric acid/Na phosphate buffer) at 37°C. The tissues were embedded in OCT compound and immediately frozen at −80°C. Frozen sections were prepared, photographed, and analyzed using QuPath and ImageJ software.

Soft agar colony formation assay

The assay was performed as previously reported (*62*). Briefly, exponentially growing transformed human cells overexpressing cGAS or its mutant were resuspended in 2× DMEM and mixed with 0.7% upper agarose in a 1:1 ratio. Then, 1 ml of the mixture was added to a 35 mm culture dish that had previously been coated with 1 ml of a 1% lower agar-DMEM mixture. After solidification, the culture dish was maintained in a 37°C incubator with 5% CO_2 for 5 weeks. The colony numbers were scored in a blinded manner under a microscope.

Xenograft

Six-week-old immunocompromised female BALB/c nude mice (Shanghai Model Organisms Center, Inc., Cat. #SM-014) were used for xenograft experiments. A total of 3×10^6 transformed *CGAS* knockout human cells overexpressing cGAS or its mutants were resuspended in a PBS solution containing 20% Matrigel. The mixture was injected subcutaneously into the right flank of the mice. The mice were euthanized 2 months after injection, and the tumors were dissected and weighed. The maximum tumor diameter of 20 mm, approved by the Laboratory Animal Care Committee of Tongji University, was not exceeded.

Drosophila

The flies were reared on a cornmeal medium consisting of 1% agar, 5.9% brewer's yeast, 5.2% glucose, 2.6% brown sugar, and 5.9% cornmeal (w/v). The fly stocks were maintained at 25°C with a 12-hour dark/light cycle in incubators. The *actin-Gal4/Cyo, ubi-GFP* (TB00047) were obtained from the Tsinghua *Drosophila* Stock Center. For generation of the strains overexpressing cGAS, the coding sequence of cGAS or its mutants was cloned into the pNP vector, and the construct was subsequently inserted into the *attp40* locus. The following strains were generated by the Tsinghua *Drosophila* Stock Center: UAS-NM-R $cGAS^{E257A/D259A}$ overexpression, UAS-NM-R $cGAS^{4mut,E257A/D259A}$ overexpression, UAS-hcGAS$^{E225A/D227A}$ overexpression, and UAS-hcGAS$^{4mut,E225A/D227A}$ overexpression.

RNA-seq

Guts dissected from 20 *Drosophila* with the same genotype were pooled together as one biological repeat. Total RNA was isolated using the Trizol Reagent (Invitrogen Life Technologies), and 3 μg of RNA were used as input material for the RNA sample preparations. The sequencing library was then sequenced on NovaSeq 6000 platform (Illumina) at the Jiangbei New Area Biopharmaceutical Public Service Platform. For RNA-seq data processing, raw reads were processed with Trim_Galore (version 0.6.7) for adapter trimming and the removal of low-quality bases (Phred quality scores below 15). Reads were then aligned to the reference genome (GCF_000001215.4) using STAR (version 2.7.9a) (*63*). The resulting BAM files were used as input to count reads per gene with featureCounts (version 2.0.3) (*64*). Differential expression analysis was performed with DESeq2 (version 1.38.3), with thresholds set at $|\log_2 FC| > 1.5$ and $P_{adj} \leq 0.05$ (*65*). For PCA, variance stabilizing transformation (VST) (*66*) was applied to the DESeq2 output files to facilitate the comparison of *Drosophila* transcriptomes across different groups. PCA results, based on the first two principal components, were visualized with ggplot2 (version 3.4.1) (*67*). GSEA was performed using the prerank function in the GSEApy Python package (version 1.1.1) (*68*). Genes were preranked according to their $\log_2$FoldChange values derived from the DESeq2 analysis. The top 150 protein coding genes up-regulated in young and old *Drosophila* were identified as young genes and old genes, respectively. GO analysis was performed using the clusterProfiler R package (version 4.6.2) (*69*). All *P* values were adjusted for multiple testing corrections using the Benjamini-Hochberg method.

Immunostaining of the *Drosophila* gut

The guts were dissected from 40-day-old *Drosophila* maintained at 29°C and fixed in 4% formaldehyde for 30 min at room temperature. For pH3 staining, the guts were rinsed three times with PBT buffer (1× PBS containing 0.1% Triton X-100) and then blocked with a blocking buffer (5% BSA in PBT) for 1 hour. The samples were incubated overnight at 4°C with anti-Ser10-pH3 (Abcam, Cat. # ab5176, 1:200 dilution in blocking buffer). For Delta staining, the guts were rinsed twice with absolute ethanol for 10 min each, followed by rinses in 66, 50, and 33% ethanol-PBT solutions for 5 min each. The samples were then rinsed three times with PBT buffer, with each rinse lasting 10 min, before being incubated in blocking buffer for 1 hour. The guts were subsequently incubated overnight at 4°C with anti-Delta (DSHB, Cat. #C594.9B, 1:50 dilution in 5% BSA-PBT). The next day, the guts were washed three times with PBT and then incubated with either anti-mouse-Cy3 (Jackson, Cat. #115-165-003, 1:100 dilution in blocking buffer) or anti-rabbit-Cy3 (Jackson, Cat. #111-165-003, 1:100 dilution in blocking buffer) for 3 hours at room temperature. Finally, the guts were washed three times with PBT and mounted with DAPI-containing mounting buffer.

Smurf assay

The Smurf assay was conducted to investigate the intestinal barrier function in aged *Drosophila* of different genotypes. Forty-day-old *Drosophila* were fed a diet containing 5% nonabsorbable blue dye (FD&C Blue Dye No. 1) at 25°C. Six days after dye feeding, the *Drosophila* were anesthetized to examine dye leakage from the intestine into other tissues under a stereo microscope.

Pathogen infection

E. faecalis and *S. marcescens* were obtained from the R. Jiao at the Hoffmann Institute of Immunology, Guangzhou Medical University. Bacteria in the exponential growth phase were collected by centrifugation and resuspended in a 5% sucrose solution. A disc of filter paper was placed on the surface of the standard agar medium, and 200 μl of the bacteria suspension was pipetted onto the filter paper for infection. Forty-day-old *Drosophila* of various genotypes were fed with bacteria and maintained at 29°C. The bacterial solution was changed every 48 hours, and the survival of *Drosophila* was recorded.

Climbing assay

Forty-day-old *Drosophila* of various genotypes that had been maintained at 29°C were anesthetized with CO_2 and transferred to a new vial, where they were allowed to recover for 30 min. The vial was tapped gently to let the flies to settle at the bottom. The time taken for each individual to cross the 3 cm mark was recorded, and the climbing velocity of each fly was then calculated. In addition, the number of flies that crossed this distance within 2 min was counted.

Analysis of *Drosophila* reproductive capacity

Three female *Drosophila* at the indicated ages were paired with three 3-day-old male WT *Drosophila* in a vial at 29°C. To minimize paternal effects on fertility, the young male *Drosophila* were replaced with fresh ones every 3 days. The number of eggs laid was counted.

Enzyme-linked immunosorbent assay (ELISA)

Blood was collected from the heart of the anaesthetized AAV-injected mice. Plasma IgG levels were analyzed using a QuicKey Mouse Immunoglobulin G ELISA Kit (Elabscience, Cat. #E-TSEL-M0003). Plasma IL6 levels were assessed using a Mouse Interleukin 6 ELISA Kit (Elabscience, Cat. #E-EL-M0044). Plasma creatinine levels were measured using a Mouse Creatinine (Cr) ELISA Kit (mlbio, Cat. #ml037726). ELISA assays were conducted according to the manufacturer's instructions.

Life-span analysis in *Drosophila*

Actin-Gal4 flies were crossed with *Drosophila* strains carrying UAS-linked transgenes, and the resulting female flies from each genotype were collected immediately after eclosion. These flies were then transferred to vials, with each vial containing 20 flies of the respective genotype. The vials were maintained at 29°, 25°, or 19°C as indicated, and fresh medium was supplied to the flies every 3 to 4 days. Regular observations were made to record the number of deceased flies at specific intervals throughout the experiment.

Statistical analysis

The sample size for the experiments was determined on the basis of previous experience with similar studies and the generally accepted sample sizes used in related research. During data collection, the investigators were blinded whenever possible, including in the analysis of DNA repair–associated foci using immunofluorescence staining and SA-β-gal analysis. Data are expressed as the mean ± SD unless indicated otherwise. GraphPad Prism 8 software was applied for statistical analysis. Student's *t* test, Mann-Whitney *U* test, one-way ANOVA with multiple comparisons, log-rank test, and Gehan-Breslow-Wilcoxon test were used to determine significance level and are indicated in the figure legends. The precise *P* values are reported in the figures.

REFERENCES AND NOTES

1. B. P. Lee, M. Smith, R. Buffenstein, L. W. Harries, Negligible senescence in naked mole rats may be a consequence of well-maintained splicing regulation. *Geroscience* **42**, 633–651 (2020). doi: 10.1007/s11357-019-00150-7; pmid: 31927681
2. K. N. Lewis *et al.*, Unraveling the message: Insights into comparative genomics of the naked mole-rat. *Mamm. Genome* **27**, 259–278 (2016). doi: 10.1007/s00335-016-9648-5; pmid: 27364349
3. X. Zhou *et al.*, Beaver and naked mole rat genomes reveal common paths to longevity. *Cell Rep.* **32**, 107949 (2020). doi: 10.1016/j.celrep.2020.107949; pmid: 32726638
4. A. Tyshkovskiy *et al.*, Distinct longevity mechanisms across and within species and their association with aging. *Cell* **186**, 2929–2949.e20 (2023). doi: 10.1016/j.cell.2023.05.002; pmid: 37269831
5. S. R. R. Kolora *et al.*, Origins and evolution of extreme life span in Pacific Ocean rockfishes. *Science* **374**, 842–847 (2021). doi: 10.1126/science.abg5332; pmid: 34762458
6. R. R. White, J. Vijg, Do DNA double-strand breaks drive aging? *Mol. Cell* **63**, 729–738 (2016). doi: 10.1016/j.molcel.2016.08.004; pmid: 27588601
7. Y. Chen *et al.*, Fight to the bitter end: DNA repair and aging. *Ageing Res. Rev.* **64**, 101154 (2020). doi: 10.1016/j.arr.2020.101154; pmid: 32977059
8. Y. Chen *et al.*, Impaired end joining induces cardiac atrophy in a Hutchinson–Gilford progeria mouse model. *Proc. Natl. Acad. Sci. U.S.A.* **120**, e2309200120 (2023). doi: 10.1073/pnas.2309200120; pmid: 37967221

9. Y. Chen *et al.*, Androgen signaling stabilizes genomes to counteract senescence by promoting XRCC4 transcription. *EMBO Rep.* **24**, e56984 (2023). doi: 10.15252/embr.202356984; pmid: 37955230
10. W. D. Heyer, K. T. Ehmsen, J. Liu, Regulation of homologous recombination in eukaryotes. *Annu. Rev. Genet.* **44**, 113–139 (2010). doi: 10.1146/annurev-genet-051710-150955; pmid: 20690856
11. S. F. Shalabi *et al.*, Evidence for accelerated aging in mammary epithelia of women carrying germline *BRCA1* or *BRCA2* mutations. *Nat. Aging* **1**, 838–849 (2021). doi: 10.1038/s43587-021-00104-9; pmid: 35187501
12. L. Chen *et al.*, WRN, the protein deficient in Werner syndrome, plays a critical structural role in optimizing DNA repair. *Aging Cell* **2**, 191–199 (2003). doi: 10.1046/j.1474-9728.2003.00052.x; pmid: 12934712
13. S. Titus *et al.*, Impairment of BRCA1-related DNA double-strand break repair leads to ovarian aging in mice and humans. *Sci. Transl. Med.* **5**, 172ra21 (2013). doi: 10.1126/scitranslmed.3004925; pmid: 23408054
14. R. Ceccaldi, P. Sarangi, A. D. D'Andrea, The Fanconi anaemia pathway: New players and new functions. *Nat. Rev. Mol. Cell Biol.* **17**, 337–349 (2016). doi: 10.1038/nrm.2016.48; pmid: 27145721
15. J. Michl, J. Zimmer, M. Tarsounas, Interplay between Fanconi anemia and homologous recombination pathways in genome integrity. *EMBO J.* **35**, 909–923 (2016). doi: 10.15252/embj.201693860; pmid: 27037238
16. B. M. Sirbu *et al.*, Identification of proteins at active, stalled, and collapsed replication forks using isolation of proteins on nascent DNA (iPOND) coupled with mass spectrometry. *J. Biol. Chem.* **288**, 31458–31467 (2013). doi: 10.1074/jbc.M113.511337; pmid: 24047897
17. Y. H. Chen *et al.*, ATR-mediated phosphorylation of FANCI regulates dormant origin firing in response to replication stress. *Mol. Cell* **58**, 323–338 (2015). doi: 10.1016/j.molcel.2015.02.031; pmid: 25843623
18. L. Sun, J. Wu, F. Du, X. Chen, Z. J. Chen, Cyclic GMP-AMP synthase is a cytosolic DNA sensor that activates the type I interferon pathway. *Science* **339**, 786–791 (2013). doi: 10.1126/science.1232458; pmid: 23258413
19. J. Wu *et al.*, Cyclic GMP-AMP is an endogenous second messenger in innate immune signaling by cytosolic DNA. *Science* **339**, 826–830 (2013). doi: 10.1126/science.1229963; pmid: 23258412
20. H. Liu *et al.*, Nuclear cGAS suppresses DNA repair and promotes tumorigenesis. *Nature* **563**, 131–136 (2018). doi: 10.1038/s41586-018-0629-6; pmid: 30356214
21. H. Jiang *et al.*, Chromatin-bound cGAS is an inhibitor of DNA repair and hence accelerates genome destabilization and cell death. *EMBO J.* **38**, e102718 (2019). doi: 10.15252/embj.2019102718; pmid: 31544964
22. X. Tian *et al.*, SIRT6 is responsible for more efficient DNA double-strand break repair in long-lived species. *Cell* **177**, 622–638.e22 (2019). doi: 10.1016/j.cell.2019.03.043; pmid: 31002797
23. K. T. Davies, N. C. Bennett, G. Tsagkogeorga, S. J. Rossiter, C. G. Faulkes, Family wide molecular adaptations to underground life in African mole-rats revealed by phylogenomic analysis. *Mol. Biol. Evol.* **32**, 3089–3107 (2015). doi: 10.1093/molbev/msv175; pmid: 26318402
24. L. Tan *et al.*, Naked mole rat cells have a stable epigenome that resists iPSC reprogramming. *Stem Cell Reports* **9**, 1721–1734 (2017). doi: 10.1016/j.stemcr.2017.10.001; pmid: 29107597
25. Z. Mao, M. Bozzella, A. Seluanov, V. Gorbunova, Comparison of nonhomologous end joining and homologous recombination in human cells. *DNA Repair* **7**, 1765–1771 (2008). doi: 10.1016/j.dnarep.2008.06.018; pmid: 18675941
26. H. Meyer, C. C. Weihl, The VCP/p97 system at a glance: Connecting cellular function to disease pathogenesis. *J. Cell Sci.* **127**, 3877–3883 (2014). doi: 10.1242/jcs.093831; pmid: 25146396
27. M. Meerang *et al.*, The ubiquitin-selective segregase VCP/p97 orchestrates the response to DNA double-strand breaks. *Nat. Cell Biol.* **13**, 1376–1382 (2011). doi: 10.1038/ncb2367; pmid: 22020440
28. Z. Zhen *et al.*, Nuclear cGAS restricts L1 retrotransposition by promoting TRIM41-mediated ORF2p ubiquitination and degradation. *Nat. Commun.* **14**, 8217 (2023). doi: 10.1038/s41467-023-43001-y; pmid: 38086852
29. Z. Dou *et al.*, Cytoplasmic chromatin triggers inflammation in senescence and cancer. *Nature* **550**, 402–406 (2017). doi: 10.1038/nature24050; pmid: 28976970
30. D. Zhang *et al.*, A non-canonical cGAS-STING-PERK pathway facilitates the translational program critical for senescence and organ fibrosis. *Nat. Cell Biol.* **24**, 766–782 (2022). doi: 10.1038/s41556-022-00894-z; pmid: 35501370
31. A. Holleufer *et al.*, Two cGAS-like receptors induce antiviral immunity in *Drosophila*. *Nature* **597**, 114–118 (2021). doi: 10.1038/s41586-021-03800-z; pmid: 34261128
32. K. M. Slavik *et al.*, cGAS-like receptors sense RNA and control 3′2′-cGAMP signalling in *Drosophila*. *Nature* **597**, 109–113 (2021). doi: 10.1038/s41586-021-03743-5; pmid: 34261127
33. T. C. Lu *et al.*, Aging Fly Cell Atlas identifies exhaustive aging features at cellular resolution. *Science* **380**, eadg0934 (2023). doi: 10.1126/science.adg0934; pmid: 37319212
34. K. Garschall, T. Flatt, The interplay between immunity and aging in *Drosophila*. *F1000Res.* **7**, 160 (2018). doi: 10.12688/f1000research.13117.1; pmid: 29487742
35. B. Biteau, C. E. Hochmuth, H. Jasper, JNK activity in somatic stem cells causes loss of tissue homeostasis in the aging *Drosophila* gut. *Cell Stem Cell* **3**, 442–455 (2008). doi: 10.1016/j.stem.2008.07.024; pmid: 18940735
36. N. H. Choi, J. G. Kim, D. J. Yang, Y. S. Kim, M. A. Yoo, Age-related changes in Drosophila midgut are associated with PVF2, a PDGF/VEGF-like growth factor. *Aging Cell* **7**, 318–334 (2008). doi: 10.1111/j.1474-9726.2008.00380.x; pmid: 18284659
37. B. Biteau *et al.*, Lifespan extension by preserving proliferative homeostasis in *Drosophila*. *PLOS Genet.* **6**, e1001159 (2010). doi: 10.1371/journal.pgen.1001159; pmid: 20976250
38. B. Ohlstein, A. Spradling, Multipotent *Drosophila* intestinal stem cells specify daughter cell fates by differential notch signaling. *Science* **315**, 988–992 (2007). doi: 10.1126/science.1136606; pmid: 17303754
39. M. S. Grotewiel, I. Martin, P. Bhandari, E. Cook-Wiens, Functional senescence in *Drosophila melanogaster*. *Ageing Res. Rev.* **4**, 372–397 (2005). doi: 10.1016/j.arr.2005.04.001; pmid: 16024299
40. D. Rhodenizer, I. Martin, P. Bhandari, S. D. Pletcher, M. Grotewiel, Genetic and environmental factors impact age-related impairment of negative geotaxis in *Drosophila* by altering age-dependent climbing speed. *Exp. Gerontol.* **43**, 739–748 (2008). doi: 10.1016/j.exger.2008.04.011; pmid: 18515028
41. J. C. Whitehead *et al.*, A clinical frailty index in aging mice: Comparisons with frailty index data in humans. *J. Gerontol. A Biol. Sci. Med. Sci.* **69**, 621–632 (2014). doi: 10.1093/gerona/glt136; pmid: 24051346
42. S. Ma *et al.*, Spatial transcriptomic landscape unveils immunoglobin-associated senescence as a hallmark of aging. *Cell* **187**, 7025–7044.e34 (2024). doi: 10.1016/j.cell.2024.10.019; pmid: 39500323
43. L. Yu *et al.*, IgG is an aging factor that drives adipose tissue fibrosis and metabolic decline. *Cell Metab.* **36**, 793–807.e5 (2024). doi: 10.1016/j.cmet.2024.01.015; pmid: 38378001
44. M. Jergović *et al.*, IL-6 can singlehandedly drive many features of frailty in mice. *Geroscience* **43**, 539–549 (2021). doi: 10.1007/s11357-021-00343-z; pmid: 33629207
45. D. R. Valenzano, A. Aboobaker, A. Seluanov, V. Gorbunova, Non-canonical aging model systems and why we need them. *EMBO J.* **36**, 959–963 (2017). doi: 10.15252/embj.201796837; pmid: 28320740
46. X. Tian *et al.*, High-molecular-mass hyaluronan mediates the cancer resistance of the naked mole rat. *Nature* **499**, 346–349 (2013). doi: 10.1038/nature12234; pmid: 23783513
47. X. Tian *et al.*, *INK4* locus of the tumor-resistant rodent, the naked mole rat, expresses a functional p15/p16 hybrid isoform. *Proc. Natl. Acad. Sci. U.S.A.* **112**, 1053–1058 (2015). doi: 10.1073/pnas.1418203112; pmid: 25550505
48. K. N. Lewis *et al.*, Regulation of Nrf2 signaling and longevity in naturally long-lived rodents. *Proc. Natl. Acad. Sci. U.S.A.* **112**, 3722–3727 (2015). doi: 10.1073/pnas.1417566112; pmid: 25775529
49. J. Azpurua *et al.*, Naked mole-rat has increased translational fidelity compared with the mouse, as well as a unique 28S ribosomal RNA cleavage. *Proc. Natl. Acad. Sci. U.S.A.* **110**, 17350–17355 (2013). doi: 10.1073/pnas.1313473110; pmid: 24082110
50. Z. Li *et al.*, Impaired DNA double-strand break repair contributes to the age-associated rise of genomic instability in humans. *Cell Death Differ.* **23**, 1765–1777 (2016). doi: 10.1038/cdd.2016.65; pmid: 27391797
51. C. Garm *et al.*, Age and gender effects on DNA strand break repair in peripheral blood mononuclear cells. *Aging Cell* **12**, 58–66 (2013). doi: 10.1111/acel.12019; pmid: 23088435
52. R. Shakya *et al.*, BRCA1 tumor suppression depends on BRCT phosphoprotein binding, but not its E3 ligase activity. *Science* **334**, 525–528 (2011). doi: 10.1126/science.1209909; pmid: 22034435
53. Y. Chen *et al.*, Circadian factors CLOCK and BMAL1 promote nonhomologous end joining and antagonize cellular senescence. *Life Med.* **3**, lnae006 (2024). doi: 10.1093/lifemedi/lnae006; pmid: 39872667
54. K. P. Hopfner *et al.*, The Rad50 zinc-hook is a structure joining Mre11 complexes in DNA recombination and repair. *Nature* **418**, 562–566 (2002). doi: 10.1038/nature00922; pmid: 12152085
55. A. Seluanov *et al.*, Hypersensitivity to contact inhibition provides a clue to cancer resistance of naked mole-rat. *Proc. Natl. Acad. Sci. U.S.A.* **106**, 19352–19357 (2009). doi: 10.1073/pnas.0905252106; pmid: 19858485
56. V. Gorbunova, A. Seluanov, O. M. Pereira-Smith, Expression of human telomerase (hTERT) does not prevent stress-induced senescence in normal human fibroblasts but protects the cells from stress-induced apoptosis and necrosis. *J. Biol. Chem.* **277**, 38540–38549 (2002). doi: 10.1074/jbc.M202671200; pmid: 12140282
57. C. Schwartz *et al.*, Spontaneous atopic dermatitis in mice with a defective skin barrier is independent of ILC2 and mediated by IL-1β. *Allergy* **74**, 1920–1933 (2019). doi: 10.1111/all.13801; pmid: 30937919
58. M. Iida *et al.*, Hair graying with aging in mice carrying oncogenic RET. *Aging Cell* **19**, e13273 (2020). doi: 10.1111/acel.13273; pmid: 33159498
59. Y. Chen *et al.*, The SIRT6 activator MDL-800 improves genomic stability and pluripotency of old murine-derived iPS cells. *Aging Cell* **19**, e13185 (2020). doi: 10.1111/acel.13185; pmid: 33089974

60. W. B. Zeng *et al.*, Anterograde monosynaptic transneuronal tracers derived from herpes simplex virus 1 strain H129. *Mol. Neurodegener.* **12**, 38 (2017). doi: 10.1186/s13024-017-0179-7; pmid: 28499404
61. F. Xiong *et al.*, An HSV-1-H129 amplicon tracer system for rapid and efficient monosynaptic anterograde neural circuit tracing. *Nat. Commun.* **13**, 7645 (2022). doi: 10.1038/s41467-022-35355-6; pmid: 36496505
62. W. C. Hahn *et al.*, Creation of human tumour cells with defined genetic elements. *Nature* **400**, 464–468 (1999). doi: 10.1038/22780; pmid: 10440377
63. A. Dobin *et al.*, STAR: Ultrafast universal RNA-seq aligner. *Bioinformatics* **29**, 15–21 (2013). doi: 10.1093/bioinformatics/bts635; pmid: 23104886
64. Y. Liao, G. K. Smyth, W. Shi, featureCounts: An efficient general purpose program for assigning sequence reads to genomic features. *Bioinformatics* **30**, 923–930 (2014). doi: 10.1093/bioinformatics/btt656; pmid: 24227677
65. M. I. Love, W. Huber, S. Anders, Moderated estimation of fold change and dispersion for RNA-seq data with DESeq2. *Genome Biol.* **15**, 550 (2014). doi: 10.1186/s13059-014-0550-8; pmid: 25516281
66. S. Anders, W. Huber, Differential expression analysis for sequence count data. *Genome Biol.* **11**, R106 (2010). doi: 10.1186/gb-2010-11-10-r106; pmid: 20979621
67. H. Wickham, *Ggplot2: Elegant Graphics for Data Analysis* (Springer, 2009). doi: 10.1007/978-0-387-98141-3
68. Z. Fang, X. Liu, G. Peltz, GSEApy: A comprehensive package for performing gene set enrichment analysis in Python. *Bioinformatics* **39**, btac757 (2023). doi: 10.1093/bioinformatics/btac757; pmid: 36426870
69. T. Wu *et al.*, clusterProfiler 4.0: A universal enrichment tool for interpreting omics data. *Innovation (Camb.)* **2**, 100141 (2021). doi: 10.1016/j.xinn.2021.100141; pmid: 34557778
70. T. Chen *et al.*, The Genome Sequence Archive family: Toward explosive data growth and diverse data types. *Genomics Proteomics Bioinformatics* **19**, 578–583 (2021). doi: 10.1016/j.gpb.2021.08.001; pmid: 34400360

ACKNOWLEDGMENTS

The authors thank W. Zeng at Wuhan Institute of Virology, Chinese Academy of Sciences, for providing herpes simplex virus 1 (HSV-1) strain 129 (H129) and R. Jiao at Guangzhou Medical University for providing *E. faecalis* and *S. marcescens*. Illustrations in the summary figure, Fig. 4A, and the working model in Fig. 5X were created with BioRender.com. Figure 5N was generated using illustrations from the NIAID NIH BioArt source under a public domain license. **Funding:** This work was funded by National Natural Science Foundation of China (NSFC) grant 82225017 (Z.M.); National Key R&D Program of China grant 2022YFA1103700 (Z.M.); NSFC grants 32421002, 82361148131, and 32270750 (Z.M.); NSFC grants 32470796 and 32200595 (Y.C.), NSFC grants 32171288 and 32471341 (Y.J.); Shanghai Sailing Program 22YF1434300 (Y.C.); and Fundamental Research Funds for the Central Universities 22120240696, 22120250374 (Z.M.), and 22120240273 (Y.C.). **Author contributions:** Conceptualization: Z.M., Y.C.; Methodology: Y.C., Z.Ch., H.W., K.-L.L.; Investigation: Y.C., Z.Ch., H.W., Z.Cu., K.-L.L., Z.S., L.C., X.S., X.X., Y.Z., R.T.; Resources: L.T., M.-H.L.; Visualization: Y.C., Z.Ch., H.W., R.T.; Funding acquisition: Z.M., Y.C., Y.J.; Project administration: Z.M., Y.C., Y.J.; Supervision: Z.M., Y.C., Y.J.; Writing – original draft: Z.M., Y.C.; Writing – review & editing: Z.M., Y.C., Z.Ch., K.-L.L., H.W., J.Y., F.-L.S., H.L. **Competing interests:** The authors declare that they have no competing interests. **Data and materials availability:** All data are available in the main text or the supplementary materials. The RNA-seq data have been deposited at the Genome Sequence Archive (GSA) (70) at the China National Center for Bioinformation under accession number CRA027437. No new code was generated for this study. Further information and requests for materials may be directed to, and will be fulfilled by, the corresponding authors. **License information:** Copyright © 2025 the authors, some rights reserved; exclusive licensee American Association for the Advancement of Science. No claim to original US government works. https://www.science.org/about/science-licenses-journal-article-reuse

SUPPLEMENTARY MATERIALS

science.org/doi/10.1126/science.adp5056
Figs. S1 to S10; Table S1; MDAR Reproducibility Checklist

Submitted 13 May 2024; resubmitted 24 March 2025; accepted 12 August 2025
10.1126/science.adp5056

RESEARCH ARTICLE SUMMARY

MICROBIOME

Targeted protein evolution in the gut microbiome by diversity-generating retroelements

Benjamin R. Macadangdang*, Yanling Wang, Cora L. Woodward, Jessica I. Revilla, Bennett M. Shaw, Kayvan Sasaninia, Gillian E. Varnum, Sara K. Makanani, Chiara Berruto, Umesh Ahuja*, Jeff F. Miller*

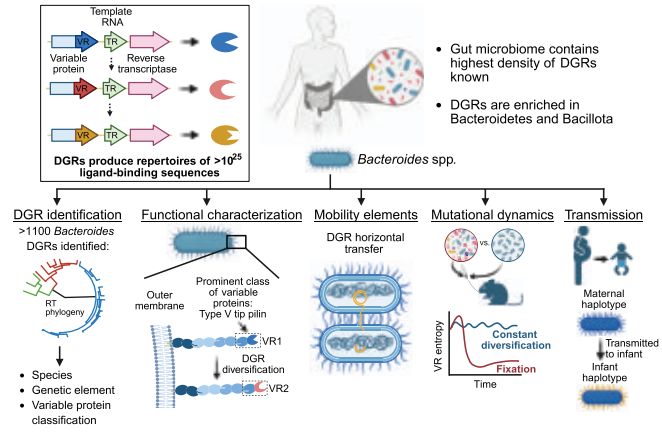
Full article and list of author affiliations: https://doi.org/10.1126/science.adv2111

INTRODUCTION: The gastrointestinal (GI) tract is home to trillions of microbes that form a dynamic and intricate ecosystem, deeply interconnected with human health and disease. Within this competitive environment, the ability to adapt to changing conditions is critical for colonization and persistence. Diversity-generating retroelements (DGRs) provide a distinctive mechanism that allows microbes to rapidly evolve in response to selective pressures. Through targeted, adenine-specific mutagenesis, they diversify sequences that encode ligand-binding domains to create vast repertoires of variable proteins with diverse functions. The human GI microbiome contains the greatest density of DGRs known in nature, with the majority found in Bacteroidetes and Bacillota genomes.

RATIONALE: Despite their abundance and ability to accelerate evolution, the distribution, dynamics, and functional roles of DGRs in host-associated microbial communities remain largely unexplored. To address this in the context of the gut microbiome, we focused on *Bacteroides* species, which are prominent gut commensals with established genetic tractability and well-documented relevance to host health. We systematically identified DGRs across human-derived isolates, classified the protein families they diversify, and examined their mechanisms of horizontal transfer. DGR activity was assessed in vitro and in vivo in gnotobiotic mice, and mutagenesis patterns were analyzed in the presence or absence of competing microbes. We also leveraged large-scale metagenomic datasets from mother-infant pairs to study the inheritance and behavior of DGRs after birth and during early microbiome development.

RESULTS: More than 1100 distinct DGRs were identified across 618 *Bacteroides* isolates representing 29 taxa that included the most abundant species found in humans. DGR-diversified proteins clustered into 35 distinct groups which defined three broad functional classes: (i) pilins and pilin-like proteins, (ii) cytoplasmic kinases, and (iii) viral receptor–binding proteins. Phylogenetic analyses also indicated that DGRs evolve as cohesive units and are horizontally transferred between strains. Given their potential roles in inter- and intraspecies interactions, we selected diversified pilin homologs for further characterization and discovered that a substantial subset likely function as adhesive subunits localized at the tips of type V pili, with DGR-directed mutagenesis targeting their ligand-binding motifs. Mating assays demonstrated that pilin-diversifying DGRs can horizontally transfer within and between species via integrative and conjugative elements (ICEs), and that ICE mobilization increases nearly 700-fold in the mucus layer of the lower GI tract.

Deep sequencing revealed that some *Bacteroides* DGRs are highly active, whereas others appear to be tightly regulated. In vitro and in monocolonized mice, DGR target proteins displayed random patterns of diversity. However, under competitive conditions in gnotobiotic mice, diversified pilin genes converged to express similar protein sequences despite being encoded by different DNA sequences, which is a hallmark of positive selection. Finally, analysis of metagenomic data from mother-infant pairs revealed that DGRs are transmitted across generations and are highly active in the infant gut, where they rapidly generate new protein variants.



Genome plasticity and protein evolution by *Bacteroides* diversity-generating retroelements. DGRs rapidly evolve ligand-binding proteins and are enriched in the human gut microbiome. We show that *Bacteroides* harbor a large and diverse assortment of DGRs, many of which diversify tip adhesins for type V pili and can be horizontally transferred between strains. When competing with other bacteria in the gut, and during transfer from mother to infant after birth, DGRs show evidence of positive selection. TR, template repeat; VR, variable repeat.

CONCLUSION: This study reveals that DGRs are widespread, dynamically regulated, and functionally consequential components of the gut microbiome. By enabling targeted hypervariability in proteins involved in adhesion, signaling, and other functions, DGRs are poised to contribute to microbial adaptability during ecological transitions and competitive interactions. Their transmission across generations and activation during periods of community instability highlight their potential for shaping early-life microbiome development. These findings provide a foundational framework for understanding targeted genome diversification in complex host-associated communities and point to new opportunities for engineering adaptive microbial systems to promote health. □

*Corresponding author: Email: bmacadangdang@mednet.ucla.edu (B.R.M.); uahuja@ucla.edu (U.A.); jfmiller@g.ucla.edu (J.F.M.) Cite this article as B. R. Macadangdang *et al.*, *Science* **390**, eadv2111 (2025). DOI: 10.1126/science.adv2111

MICROBIOME

Targeted protein evolution in the gut microbiome by diversity-generating retroelements

Benjamin R. Macadangdang[1,2]*, Yanling Wang[3], Cora L. Woodward[2], Jessica I. Revilla[4], Bennett M. Shaw[5], Kayvan Sasaninia[3], Gillian E. Varnum[3], Sara K. Makanani[3,6], Chiara Berruto[7], Umesh Ahuja[2]*, Jeff F. Miller[2,3,6]*

Diversity-generating retroelements (DGRs) accelerate evolution by rapidly diversifying variable proteins. The human gastrointestinal microbiota harbors the greatest density of DGRs known in nature, suggesting that they play adaptive roles in this environment. We identified >1100 distinct DGRs among human-associated *Bacteroides* species and discovered a subset that diversify adhesive components of type V pili and related proteins. We show that *Bacteroides* DGRs are horizontally transferred across species, display activity levels ranging from high to low, and preferentially alter the functional characteristics of ligand-binding residues on adhesive organelles. Specific variable protein sequences are enriched when *Bacteroides* strains compete with other commensal bacteria in gnotobiotic mice. Analysis of >2700 DGRs from diverse phyla in mother-infant pairs shows that *Bacteroides* DGRs are disproportionately transferred to vaginally delivered infants where they actively diversify. Our observations provide a foundation for understanding the potential roles of targeted genome plasticity in shaping host-associated microbial communities.

Natural selection acts on preexisting genetic variation to favor adaptive phenotypes. In bacteria, this variation primarily arises from mutations and horizontal gene transfer (*1*). Nonetheless, genomic integrity is vital for survival and reproductive success, prompting the evolution of mechanisms to channel mutagenesis to localized hotspots within genomes (*2*–*6*) and to limit horizontal transfer (*7*–*9*). Of the known systems that target mutagenesis, diversity-generating retroelements (DGRs) found in bacteria, archaea, and their viruses can generate some of the most extensive repertoires of DNA and protein sequence variants observed in nature (*10*, *11*). Through hypermutation of genes via a mechanism termed mutagenic retrohoming, a single DGR can produce up to 10^{30} distinct variable protein sequences (*12*). DGR target genes often encode ligand-binding proteins with mutations strategically confined to a discrete subset of codons within a variable repeat (VR) sequence that participates in ligand interactions (*13*). The remaining codons in VR, many of which encode structural scaffold residues, remain unmodified (*14*, *15*). This pattern of mutagenesis rapidly diversifies protein function without disrupting structure, leading to readily evolvable ligand-binding capabilities (*10*).

In addition to a diversified target gene that encodes a variable protein, a typical DGR includes a template repeat (TR), which is similar but not identical to VR, a promiscuous reverse transcriptase (RT), and one or more accessory genes (Fig. 1A). During mutagenic retrohoming, an RNA intermediate encoded by TR functions as a substrate for reverse transcription by the DGR RT, which selectively mismatches adenine residues. This results in random incorporation of any of the four nucleotides into a cDNA molecule at positions corresponding to TR adenines. Adenine-mutagenized cDNA is then integrated into VR, replacing the parental allele (*16*–*18*). Because TR is unaltered during this process, and all cis- and trans-acting factors required for mutagenic retrohoming remain intact, repeated rounds of VR diversification can occur indefinitely to optimize variable protein function.

The human gastrointestinal (GI) microbiome harbors a density of DGRs that exceeds that of any other ecosystem characterized to date (*19*), yet the dynamics and roles of accelerated protein evolution in this environment have never been systematically analyzed (*10*). Strains belonging to the Bacillota phylum and the Fibrobacteres, Chlorobi, and Bacteroidota (FCB) superphylum harbor the vast majority of human microbiome-associated DGRs (*19*). As constituents of the FCB group, *Bacteroides* spp. are prominent members of the GI microbiome, forming long-term associations with their human host (*20*). They impart health benefits such as secretion of anti-inflammatory molecules (*21*, *22*) and short-chain fatty acids (SCFAs) (*23*), but are also known to include pathobionts (*24*). Their amenability to in vitro cultivation and genetic manipulation positions them as a clinically pertinent model for exploring DGR dynamics and function in the context of their natural environment.

Single-nucleotide substitutions such as those produced by DGRs, as well as larger genomic variants such as insertions and deletions (indels) (*25*) or the acquisition of mobile genetic elements (MGEs) (*26*, *27*), can confer characteristics that have profound effects on bacterial phenotypes and fitness. Conventional metagenomic methods commonly lose variant information during assembly and may encounter challenges when categorizing mobile elements during binning (*28*–*38*). Thus, mechanisms underlying accelerated evolution, such as horizontally transferable, DGR-driven mutagenic retrohoming, often evade detection by conventional pipelines. Understanding the functions and phenotypes of complex microbial communities can best be accomplished in the context of extant genotypic variation. To that end, we explored how rapid, targeted evolution by DGRs contributes to *Bacteroides* diversity in the GI tract to gain a foundational understanding of how genome plasticity molds host-associated microbial communities.

Although first discovered in phage (*17*, *18*), here we focus on DGRs that diversify bacterial host proteins and show that they are prevalent in *Bacteroides*, with many targeting variable proteins homologous to type V pilins (*39*). We find that *Bacteroides* DGRs can be horizontally transferred between species and characterize their levels and patterns of mutagenesis. In the presence of competition with non-*Bacteroides* strains in mice, diversified VR regions converged to encode similar protein sequences and displayed other signs of positive selection. Finally, we show that Bacteroidota DGRs are preferentially passed between mothers and infants, where nearly 75% adopt a new, predominating VR haplotype by 1 year of age.

Results

DGRs are widespread and diverse in *Bacteroides* species

We analyzed a set of 1103 *Bacteroides* reference genomes encompassing 47 species from the NCBI RefSeq database (*40*) to determine the distribution of DGRs across taxa, understand their evolutionary relationships and modes of transmission, and identify functional motifs in the diversified proteins (fig. S1A). From this dataset, we found 1113 distinct DGRs distributed across 618 *Bacteroides* isolates (Fig. 1, B to D). These represented 29 of the 47 species in our dataset and encompassed 11 of the most abundant species in humans (table S4). A solitary DGR was found in 340 isolates (31%), and an additional 278 isolates (25%) contained multiple DGRs, with some genomes of *B. acidifaciens*, *B. xylanisolvens*, and

[1]Division of Neonatology and Developmental Biology, Department of Pediatrics, David Geffen School of Medicine at the University of California, Los Angeles, Los Angeles, CA, USA. [2]California NanoSystems Institute, Los Angeles, CA, USA. [3]Department of Microbiology, Immunology and Molecular Genetics, University of California, Los Angeles, Los Angeles, CA, USA. [4]Department of Molecular, Cell, and Developmental Biology, University of California, Los Angeles, Los Angeles, CA, USA. [5]David Geffen School of Medicine, University of California, Los Angeles, Los Angeles, CA, USA. [6]Molecular Biology Institute, University of California, Los Angeles, Los Angeles, CA, USA. [7]Division of Biology and Biological Engineering, California Institute of Technology, Pasadena, CA, USA. ***Corresponding author: Email: bmacadangdang@mednet.ucla.edu (B.R.M.); uahuja@ucla.edu (U.A.); jfmiller@g.ucla.edu (J.F.M.)**

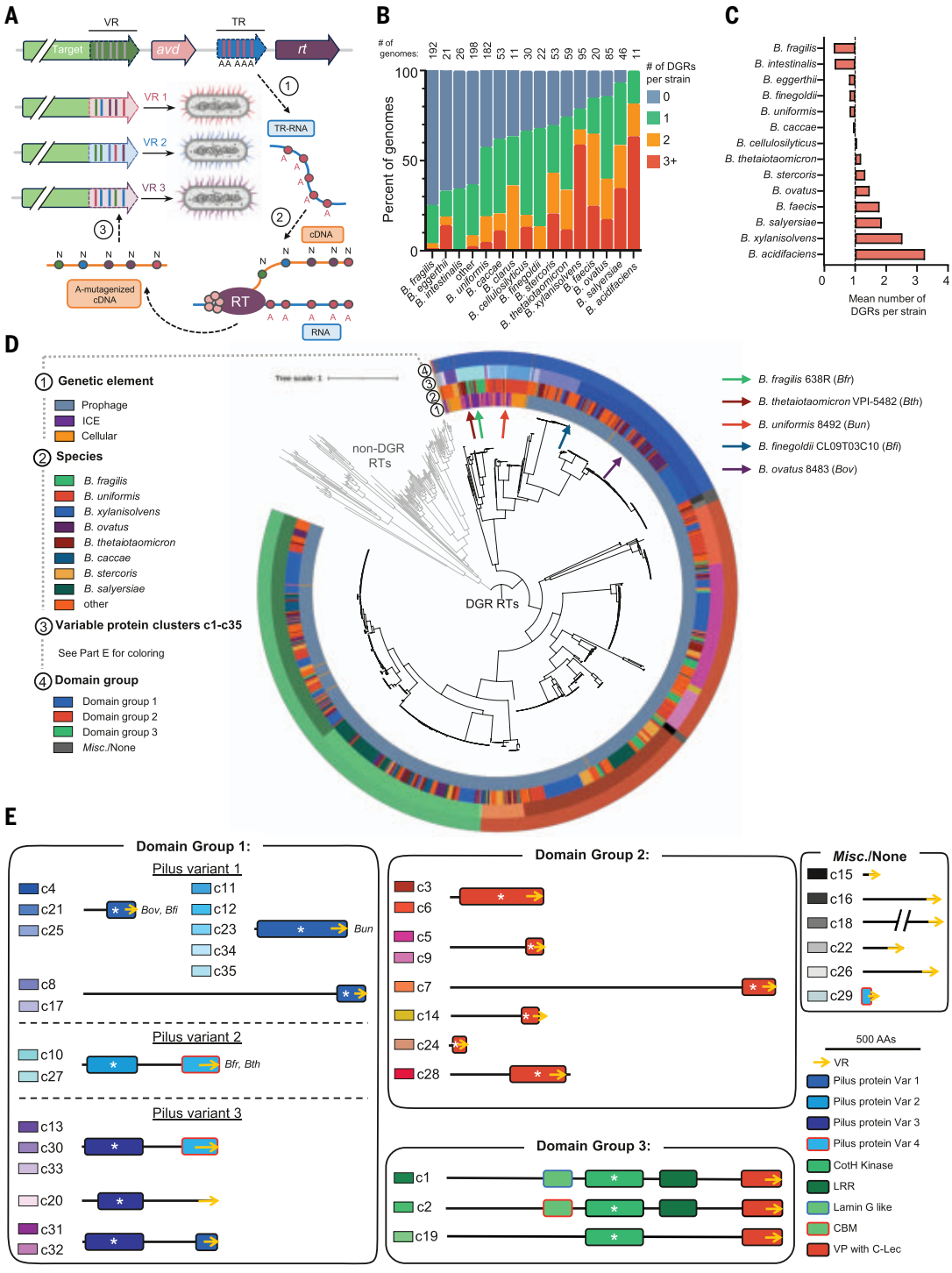


Fig. 1. DGRs are widely distributed in *Bacteroides*. (**A**) Schematic representation of the mechanism of DGR-mediated mutagenic retrohoming. A typical DGR locus is depicted on top. The target gene (green), which encodes a variable protein, contains a VR sequence which is the recipient of mutagenesis and typically ranges in size between 65 and 220 base pairs (bp) (mean 113 bp). An accessory protein, Avd (pink), helps guide the DGR-encoded RT (purple) to the TR-RNA template. Steps in mutagenic retrohoming include (1) production of TR-RNA; (2) error-prone cDNA synthesis with misincorporation at TR adenines; and (3) cDNA replacement of parental VR alleles (*10*,*16*,*17*,*116*). (**B**) The number of DGRs found within *Bacteroides* strains, grouped by species. (**C**) The mean number DGRs per strain grouped by species. The average number of DGRs in all strains (1.01) is set as the baseline. (**D**) Phylogeny of DGR RTs and non-DGR RTs in *Bacteroides* genomes. Rings depict the genomic location of the DGR (ring 1), species classification (ring 2), variable protein cluster (ring 3), and variable protein domain group (ring 4). Variable protein clusters (c1-c35) and domain groups are colored according to panel E (see materials and methods for clustering pipeline). The arrows indicate strains selected for further analysis. (**E**) Visual representation of each cluster, grouped by domain group. The most significant domain is denoted by the white asterisks. The color of each cluster corresponds to panel D, ring 3. LRR, leucine-rich repeats; CBM, carbohydrate-binding motif.

B. ovatus harboring up to five distinct elements (Fig. 1B and fig. S1B). DGRs were enriched in these and other species, whereas *B. fragilis* and *B. intestinalis* maintained fewer elements than average (Fig. 1C). These results show that DGRs are prevalent and abundant within *Bacteroides* spp. compared to most other bacterial taxa (*19*, *41*).

To investigate relationships among *Bacteroides* DGRs, we constructed a phylogenetic tree using DGR RT sequences and included non-DGR RTs from the same genomes for comparison (*42*) (Fig. 1D). Adjacent sequences were examined for MGEs such as prophages (*43*), integrative and conjugative elements (ICEs) (*44*), or plasmids (*10*, *19*). DGRs lacking such associations were classified as "cellular." To assess adaptive roles, variable proteins were clustered and compared to known protein domains (*45*). Clusters were further categorized into larger groups on the basis of shared domains with the greatest homology (Fig. 1E). For each DGR, information regarding mobility, species, variable protein clustering, and domain groups was overlayed in concentric rings surrounding a DGR RT phylogenetic tree (Fig. 1D). DGR RTs formed a monophyletic clade distinct from other classes of RTs, consistent with prior studies (*10*, *12*, *17*, *19*, *46*). Among the 1113 DGRs identified, the vast majority resided within predicted MGEs such as phage (91%) or ICE (4%), whereas the remaining 5% were chromosomally encoded (Fig. 1D, ring 1). Variable protein clustering (Fig. 1D, ring 3) and domain group relationships (Fig. 1D, ring 4) aligned with RT phylogeny, whereas species designations did not (Fig. 1D, ring 2), supporting the conclusion that *Bacteroides* DGRs evolve as cohesive units, encoding variable proteins that coevolve with their diversification machinery and are horizontally transferred between strains and species.

None of the *Bacteroides* variable proteins that we identified had previously been annotated; therefore, we used profile-based homology to infer their functions (*45*, *47*). VR sequences were uniformly located at the C termini of variable proteins and were predicted to adopt variant C-type lectin (C-Lec) folds as observed previously (*12*, *19*). Nearly all variable proteins (1092 out of 1113, 98.1%) contained structural domains with homology to one of three domain groups (Fig. 1E). Domain group 1 proteins have binding folds similar to those of type V pilins expressed by *Bacteroides*, *Porphyromonas*, and related species (PDB: 4EPS, 4QB7, and 5NF4) (*39*). This group contains a mixture of prophage-encoded (201 out of 287, 70%), ICE-encoded (13%), and cellular genome-encoded (17%) DGRs. Domain group 2 most closely matched a diversified *Thermus aquaticus* prophage-encoded protein (TaqVP, PDB: 5VF4) (*48*), and their exclusive association with prophage genomes suggests a role in phage tail fiber receptor binding. Domain group 3 contains large (>2000 amino acids), multidomain variable proteins with CotH kinase motifs (PDB: 5JDA) (*49*), adjacent to other functional domains such as a carbohydrate-binding motifs and leucine-rich repeats (Fig. 1E). Overall, *Bacteroides* DGR variable proteins display considerable modularity, whereby diversified C-terminal ligand-binding sequences are connected to motifs that are predicted to mediate pilus localization, association with phage tail fibers, signal transduction, or other functions.

Bacteroides DGRs encode pilus subunits and related variable proteins

On the basis of their conservation and widespread distribution, we reasoned that *Bacteroides* DGRs provide selective advantages to their hosts by accelerating evolution of variable proteins in the gut environment. To explore this notion, we focused on five related yet non-identical DGRs present in *B. fragilis 638R* (*Bfr*), *B. thetaiotaomicron VPI-5482* (*Bth*), *B. uniformis 8492* (*Bun*), *B. ovatus 8483* (*Bov*), and *B. finegoldii CL09T03C10* (*Bfi*) (Fig. 1D, arrows). Each of these DGRs diversifies variable proteins that share homology to adhesive pilins located at the tips of type V pili (domain group 1, Fig. 1E). Type V pili are modular, extracellular structures composed of anchor, stalk, and tip pilins (Fig. 2A), with numerous genes encoding homologs of each subunit type organized into operons spread throughout *Bacteroides* genomes (*39*). For example, *Bfr* contains 93 genes clustered into 22 operons that encode components of type V pili (fig. S2A). Although their roles in *Bacteroides* are still being defined, homologous pili in *Porphyromonas* spp. facilitate coaggregation and oral colonization (*50*, *51*).

The *Bfr*, *Bth*, and *Bun* variable protein genes (*bfrT*, *bthT*, and *bunT*) are positioned at the ends of operons predicted to encode anchor and stalk proteins, which link tip pilins to the bacterial cell surface (Fig. 2, A to C, and fig. S2B). The *Bov* and *Bfi* elements are located adjacent to prophage genes, but it is unclear whether they are carried by a phage (Fig. 1D and fig. S2B). All five *Bacteroides* DGRs encode an Avd-like protein (*52*), and *Bfr*, *Bth*, and *Bun* encode an additional accessory factor, Msl (MutS-like), with homology to the mismatch recognition domain of MutS (*12*) (Fig. 2, B to D). Each of the five TRs contains 30 to 45 adenines, providing the capacity to generate massively diverse repertoires of 10^{18} to 10^{27} potential VR DNA sequences, and 10^{14} to 10^{25} different polypeptides at the C termini of their cognate variable proteins.

We generated 3D structural predictions (pLDDT >90) for all five variable proteins and compared them to known atomic structures of *Bacteroides* pili (Fig. 2, B to E) (*39*, *53*). BfrT and BthT, which share 61% amino acid identity (AAI), display a hybrid pilin structure with three domains. Their N-terminal domains (NTDs) are homologous to that of BvuFim1C, a structurally characterized type V stalk pilin encoded by *P. vulgatus* (*39*) (Fig. 2B and tables S5 and S6). Their C-terminal domains (CTDs), which contain DGR-diversified residues, diverge from that of BvuFim1C and instead adopt a globular head structure similar to that of ligand-binding CTDs of tip pilins (Fig. 2B). Notably, both BfrT and BthT exhibited an additional third domain that connects stalk and tip domains together. The *Bun* DGR variable protein, BunT, adopts a canonical bipartite pilin structure, with N- and C-terminal domains that share high homology to BovFim1C (*39*) (Fig. 2C and table S5), a type V tip pilin encoded by *B. ovatus*. Whereas the globular head of BovFim1C is static, the BunT globular head displays diversifiable VR-encoded residues (Fig. 2C). The *Bov* and *Bfi* variable proteins, BovT and BfiT, are comparatively small, highly similar to each other (86.5% AAI), and fold into a structure that is homologous to the CTD globular head of BovFim1C (Fig. 2D), with N-terminal α helices replacing the pilin-like NTD (Fig. 2D and table S7). Despite low sequence identity, predicted structures of *Bacteroides* variable proteins showed strong structural alignment with DGR-diversified proteins from distant species (*14*, *15*), including a pronounced superimposition in the spatial locations of variable residues (Fig. 2E), providing evidence for the conservation of similar ligand-binding interactions (*13*).

Type V pilus biogenesis involves pilin translocation, lipidation, signal peptide cleavage, outer membrane targeting, and incorporation into a growing pilus (*39*, *54*, *55*) (Fig. 2A). BfrT, BthT, and BunT encode conserved N-terminal signal sequences, lipobox motifs, and protease-cleavable arginines required for pilus assembly (Fig. 2, B and C). To determine its cellular location, we expressed C-terminally tagged BfrT (*56*) and a lipidation-deficient mutant derivative (BfrT-C28A) (*55*) in *Bfr*. After induction and cell fractionation (fig. S3, A and B, and table S8), BfrT was readily detectable in membrane fractions in both preprocessed and mature forms, and in the periplasm as the mature form (Fig. 2F). Proteinase K treatment and immunofluorescence confirmed surface exposure of BfrT, whereas BfrT-C28A remained intracellular and protease resistant (Fig. 2F and fig. S3C). Mass spectroscopy of BfrT showed that cleavage occurred at R43 (fig. S3, D and E), as predicted. By contrast, tagged BovT and BfiT localized to the periplasm and were resistant to proteinase K (Fig. 2G). These observations identify two classes of variable proteins: *Bfr*, *Bth*, and *Bun* encode diversifiable type V pilus tip adhesins, whereas *Bov* and *Bfi* diversify periplasmic proteins related to tip pilins that may require additional factors for surface display or serve distinct, ligand-dependent roles.

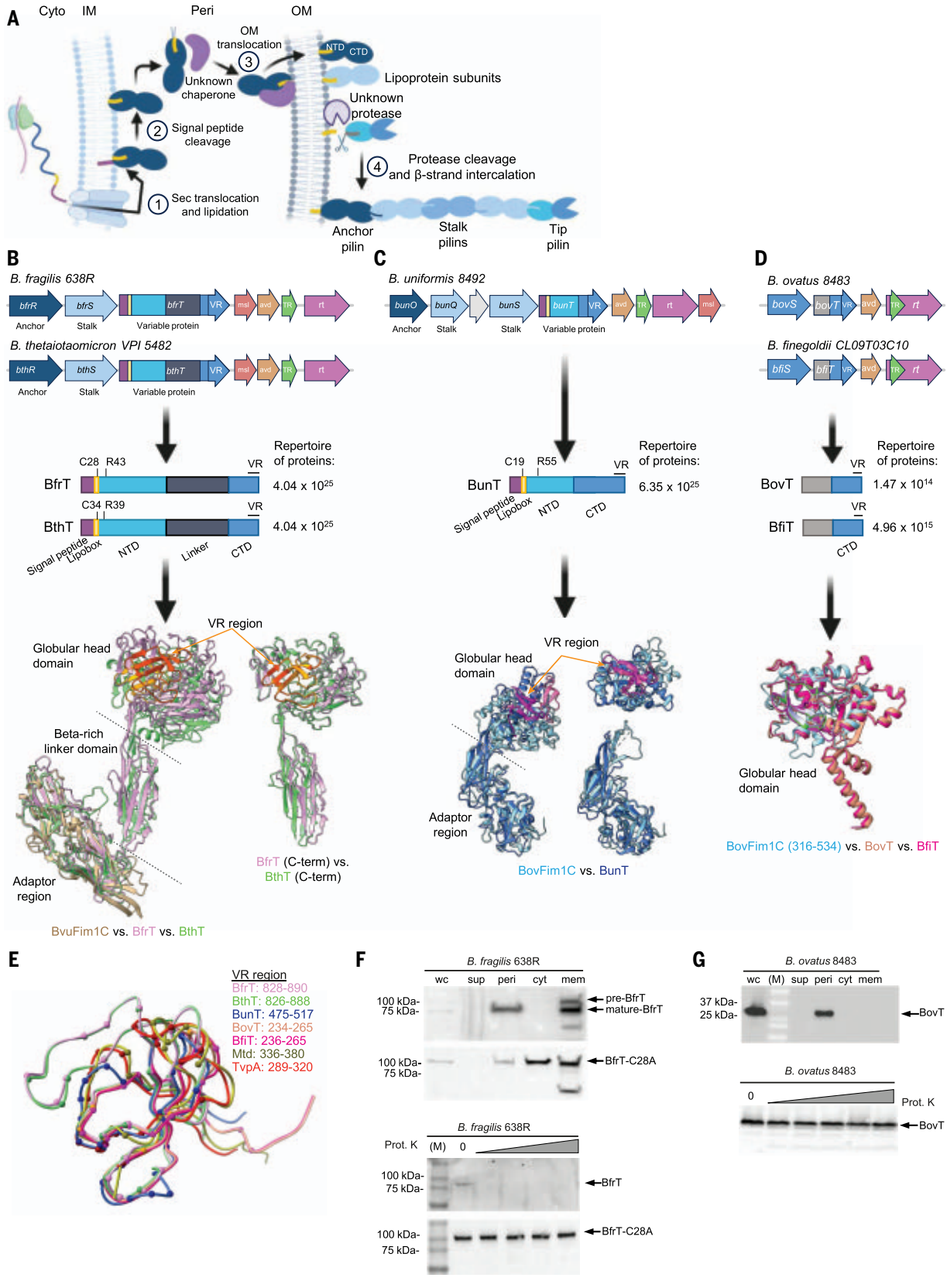


Fig. 2. *Bacteroides* DGRs diversify pilus tip adhesins and related proteins. (**A**) Cartoon representation of the steps in type V pilus assembly (*39*). (1) N-terminal signal peptide recognition and pilus subunit translocation across the inner membrane via the SecYEG translocon; (2) lipidation at a conserved cysteine residue within a lipobox motif and signal peptide cleavage; (3) translocation of the lipidated protein across the outer membrane via a lipoprotein (LPP) transporter;, and (4) incorporation into a growing pilus structure through protease-assisted cleavage, which simultaneously releases the protein from the membrane and creates an acceptor site for β-strand intercalation from an incoming subunit (*39*,*54*). CTD, C-terminal domain; Cyto, cytoplasm; IM, inner membrane; NTD, N-terminal domain; OM, outer membrane; Peri, periplasm. (**B** to **D**) DGR loci and

their upstream genes in *Bfr*, *Bth*, *Bun*, *Bov*, and *Bfi* isolates chosen for this study. Below each loci is a graphical representation of the variable proteins where each domain is colored and labeled with the predicted function. The number of variable proteins that can be generated through mutagenic retrohoming is specified to the right. The protein structures at the bottom are the superposition of the AlphaFold (*53*) structures of the variable proteins with known pilus protein structures. BvuFim1C [Protein Data Bank (PDB): 4QB7 (*39*)], BovFim1C [PDB: 4EPS (*39*)]. (**E**) Superposition of predicted VR-encoded structures for the five *Bacteroides* variable proteins in panels (B) to (D), with the VR-encoded structures of Mtd (gold) and TvpA (red) (*13*–*15*). The positions of variable residues, which are often superimposable in space, are shown as colored balls. (**F**) Immunoblot of BfrT and BfrT-C28A overexpressed in *Bfr* after cellular fractionation (top) or after intact whole cells were exposed to proteinase K (bottom). See materials and methods for fractionation protocol and fig. S3A for fractionation controls. (**G**) Immunoblot of BovT overexpressed in *Bov* after cellular fractionation (top) or after whole cells were exposed to proteinase K (bottom).

Horizontal transfer of *Bacteroides* DGRs

Horizontal transfer of DGRs that diversify phage tail fiber proteins has been well studied (*17*, *18*). By contrast, the mobility characteristics of DGRs that target bacterial proteins are relatively unexplored. To address this, we exploited the observation that the DGRs encoded by *Bfr* and *Bth* are flanked by mobility and transfer genes characteristic of ICEs (Fig. 3A and figs. S2B and S4A). Like phage, ICEs often confer selective advantages to their hosts by carrying cargo that encode colonization factors, metabolic capabilities, virulence determinants, antibiotic resistance (*57*–*64*), and, we hypothesize, DGRs.

We identified 41 DGRs residing within ICEs present in 10 distinct *Bacteroides* species, including the *Bfr*, *Bth*, *and Bun* elements in Fig. 2, B and C (table S4). Most target genes (38 out of 41) encode type V pilus adhesins from domain group 1 and are located directly downstream from anchor and stalk genes (fig. S4A). Of these 41 ICEs, 16 aligned closely with each other and shared conserved features including conjugation and DNA integration genes (*tra*, *int*), homologs of known transcriptional regulators (*merR*, *rteC*, *araC* family members) (*65*), and direct repeats resulting from site-specific chromosomal integration into a tRNA-Lys locus (Fig. 3A and fig. S4A). These DGRs also share similar TRs and RTs (tables S9 and S10), suggesting that they disseminated via horizontal transfer of an ancestral DGR-encoding ICE.

To measure ICE activity, we developed polymerase chain reaction (PCR) assays to differentiate integrated versus excised forms of the *Bfr* and *Bth* elements (Fig. 3A). When wild-type (WT) cells were grown in vitro, only the integrated form of the ICEs could be detected (Fig. 3B), consistent with the need for environmental cues to trigger mobility (*65*). We next identified ICE-associated regulatory loci (Fig. 3A) and created strains that ectopically express each regulatory factor (table S11). Overexpression of *araC2* induced ICE excision and circularization in *Bfr* and *Bth* (Fig. 3B). Overexpression of *merR* or *rteC*, however, eliminated both integrated forms and episomes, indicating the loss of ICEs through segregation (Fig. 3B and table S11). Excision of the *Bfr* ICE was dependent on the presence of an intact *int2* integrase gene (Fig. 3, A and B) but was unaffected by knocking out *int1*, *top1*, or *top2* (table S12). Finally, to determine whether inducing signals are provided in vivo, we colonized germ-free Swiss Webster mice with *Bfr* and measured relative levels of episome and chromosomal scar formation by quantitative PCR (qPCR). As shown in Fig. 3C, compared to *Bfr* plus empty vector cultured in vitro, we observed 17- and 27-fold increases in ICE activity in fecal pellets and cecal content, respectively, and a nearly 700-fold increase in colonic mucus, the natural habitat of *Bacteroides*.

Resident ICEs exclude integration by homologous mobile elements (*66*). To create recipient cells suitable for mating experiments, we overexpressed *merR* in *Bfr* and *Bth* to promote ICE excision and loss (Fig. 3B), creating ΔICE strains with vacant integration sites. Matings between isogenic WT donor and ΔICE recipients yielded transconjugants at frequencies of 10^{-5} to 10^{-7}, with *Bth* donors transferring more efficiently than *Bfr* donors (Fig. 3, D and E, and table S13). Deleting *bfrT* had no impact on transfer efficiency, indicating that the diversified tip adhesin is not required for conjugation. ICE transfer also occurred in gnotobiotic mice (fig. S4, B and C). Our results demonstrate that DGRs in *Bfr* and *Bth* are encoded within functional ICEs that undergo conjugative transfer in vitro and in vivo, providing an explanation for the phylogenetic distribution of DGRs in *Bacteroides* and a mechanism for the horizontal transfer of accelerated protein evolution between species.

Differential control and mechanistic conservation of mutagenic retrohoming

To characterize the real-time dynamics and mutational patterns of *Bacteroides* DGRs, we measured mutagenic retrohoming levels in vitro and in vivo and analyzed the diversified sequences. Strains carrying the DGRs shown in Fig. 2, B to D, were grown in vitro, then sampled over a 2-week period, and VRs were barcoded, amplified, and deep sequenced (Fig. 4A). We found that the *Bov* and *Bfi* elements exhibited markedly high levels of mutagenesis, with 13 or 40% of VRs diverging from the parental VR by day 14, respectively (Fig. 4B). This was unexpected and in contrast with other bacterial DGRs, which typically have low or absent activity in vitro, reflecting their apparent regulation (*10*, *19*). VR mutagenesis was abolished in strains harboring knockout mutations in *rt* (Δ*rt*) (Fig. 4C and fig. S5A) and restored by complementation with WT *rt* expressed at an ectopic location (fig. S5B). By contrast, DGRs from *Bfr*, *Bth*, and *Bun* showed a factor of 100 to 10,000 lower in vitro activity (Fig. 4B). To measure DGR activity in vivo, we monocolonized germ-free Swiss Webster mice with individual *Bacteroides* strains. Colonization levels in the GI tract were similar for each strain as measured by colony-forming units in fecal pellets (fig. S5C). *Bov* and *Bfi* DGRs retained high levels of activity within the murine GI tract, whereas mutagenesis levels observed with *Bfr*, *Bth*, and *Bun* remained low (Fig. 4B). Next, we used RNA sequencing (RNA-Seq) to probe relationships between mutagenic retrohoming and transcription of DGR-encoded genes. We observed significantly higher relative amounts of transcripts encoding *avd*, TR, and *rt* in high activity strains (*Bov* and *Bfi*, Fig. 4D) compared to those with low DGR activity (*Bfr*, *Bth*, *Bun*), suggesting that DGR mutagenesis is regulated, at least in part, at the transcriptional level. Thus, mutagenic retrohoming levels in our five *Bacteroides* strains fall into two categories. DGRs carried by *Bov* and *Bfi* are constitutively active, whereas those in *Bfr*, *Bth*, and *Bun* appear to be tightly regulated, as commonly observed in other systems (*19*, *67*).

Mutagenic retrohoming in *Bacteroides* demonstrated high specificity for misincorporation at TR adenines (Fig. 4E), a hallmark of DGR RTs observed across taxa (*16*, *18*, *67*). To identify positional effects, we exploited the constitutive activity of the *Bov* and *Bfi* DGRs to examine time-dependent levels of mutagenesis as a function of position within VR (Fig. 4F and fig. S5D). Mutations accumulated primarily in the central VR region, which is enriched for TR AAC motifs that allow random substitutions at one or both adenines (*10*, *12*). By contrast, VR positions at the 5′ and 3′ ends displayed minimal to no mutations despite the presence of TR adenines, consistent with boundary effects similar to those reported for the *Bordetella* phage BPP-1 DGR (*16*), including a crossover interval near the center of the 3′ boundary region where mutagenized cDNA integrates to replace parental VRs. Finally, we observed a median mutational density of about 50% of diversifiable VR positions (Fig. 4G and fig. S5F). A nearly identical mutational density was reported in *Bordetella* in vivo (*68*), and in vitro with cDNA synthesized by purified BPP-1 RT, Avd, and TR-RNA in the presence of deoxynucleotide triphosphates (dNTPs) (*69*, *70*). These observations highlight conservation of the mechanisms of adenine-specific

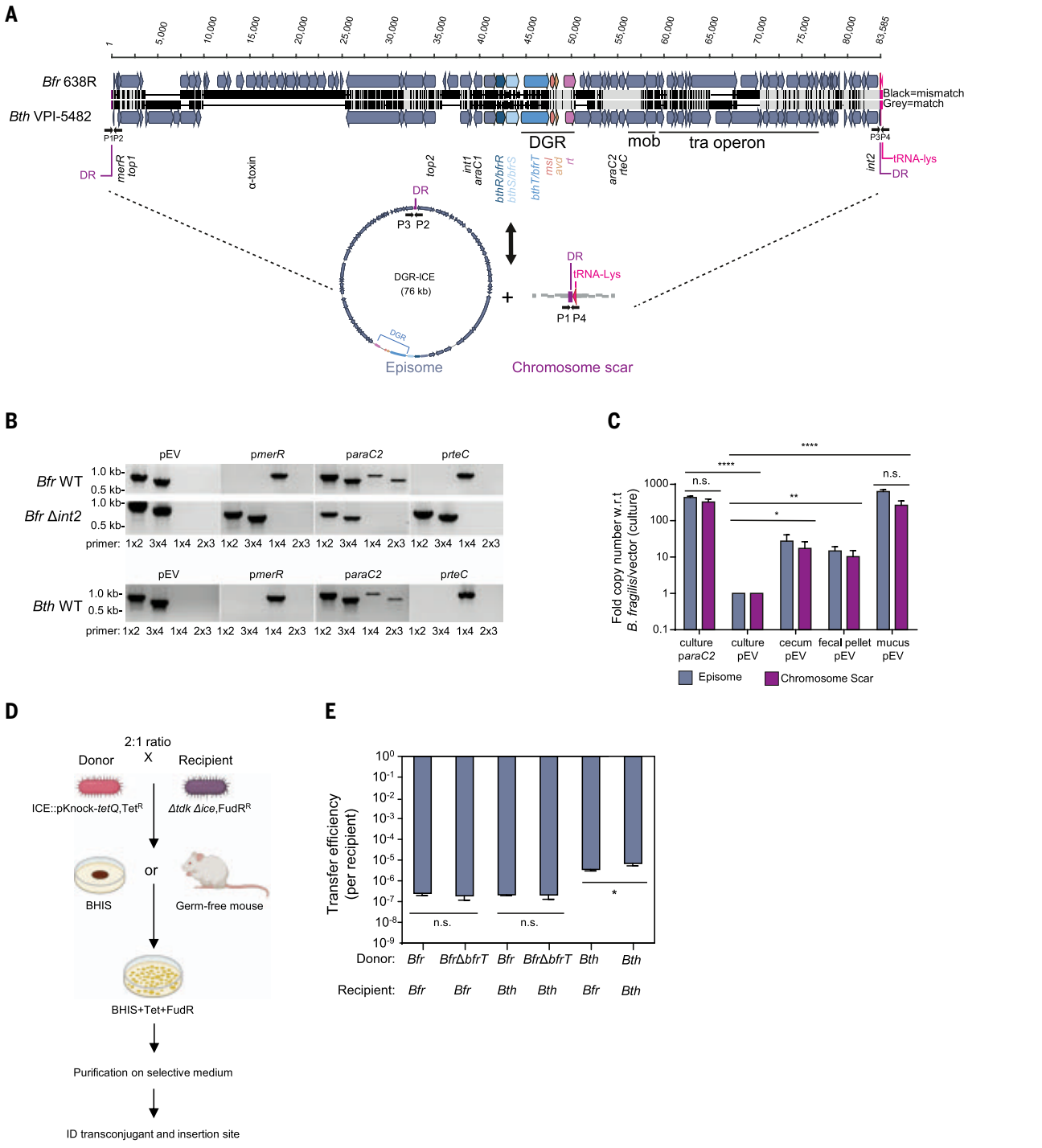


Fig. 3. *Bacteroides* DGRs are horizontally transferred between strains and species. (**A**) (Top) Synteny between *Bfr* and *Bth* ICEs. Important elements within each ICE, including the DGR loci, are labeled. (Bottom) Cartoon schematic of the *Bfr* ICE conversion between chromosomally integrated and episomal forms. Binding of primers P1 to P4 shown for integrated ICE, episomal ICE, and chromosomal scar. (**B**) PCR products from *Bfr* (top) and *Bth* (bottom) using primers to differentiate chromosomally integrated ICEs from excision products (episome and scar) following overexpression of designated ICE-encoded regulatory genes. pEV, empty vector. (**C**) Ratios of excised episomes or chromosomal scars to integrated ICEs, normalized to pEV-containing strains cultivated in vitro. Samples from cecum, fecal pellet, and mucus originate from monocolonized Swiss Webster (SW) mice ($n = 3$). (**D**) Experimental setup for ICE mating assays. (**E**) The transfer efficiency, defined as the number of transconjugant cells divided by the total number of recipient cells, of in vitro ICE mating assays. Statistical analysis: $^{*}P < 0.05$, $^{**}P < 0.01$, $^{****}P < 0.0001$; ns, not significant. analysis of variance (ANOVA) test with Holm-Sidak multiple comparison correction. Error bars, SD.

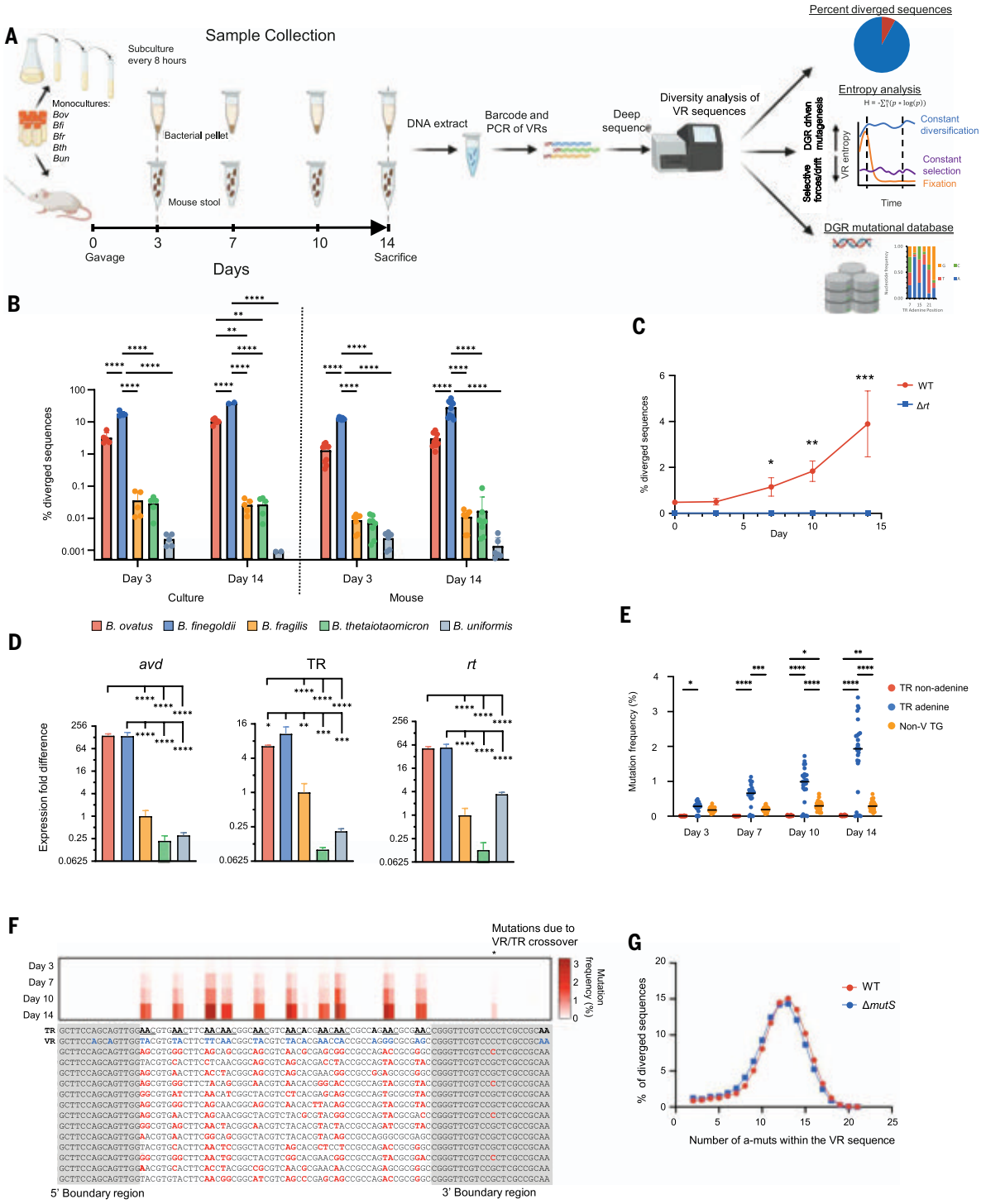


Fig. 4. *Bacteroides* DGRs are differentially active in vitro and in vivo. (**A**) Schematic of the experimental design. (**B**) Percentage of VRs that mutated from the parental VR sequence in cells grown in vitro or present in stool samples from monocolonized SW mice ($n = 5$ to 11). Error bars, SD. (**C**) Percentage of VR sequences that diverged from their cognate parental VRs in *Bov* WT and *Bov* Δ*rt* in stool samples from monocolonized SW mice ($n = 4$). Error bars, SD. (**D**) Expression of DGR encoded genes *avd*, TR, and *rt* measured by RNA-Seq and normalized to *gyrA*, from mid-log phase cells grown in vitro ($n = 4$). Error bars, SD of mean fold change. (**E**) Mutation frequencies of individual nucleotide positions within the *Bov* target gene over a 2-week period from a population of VRs extracted from stool samples of monocolonized mice ($n = 4$). (**F**) Nucleotide entropy at each position along the *Bov* VR for a population of VRs extracted from stool samples of monocolonized mice ($n = 4$). Below the graph are the parental TR and VR sequences followed by representative VR sequences at day 14. TR adenines are shown in bold, positions in VR corresponding to TR adenines are in blue, and positions in the mutated VR sequence that are different from the parental VR are shown in red. The gray boxes show the presumed 5′ and 3′ boundary regions where no adenine mutations are observed. (**G**) Distribution of the number of nucleotide substitutions per VR read in *Bov* WT versus *Bov* Δ*mutS* cells grown in vitro. Statistical analysis: $*P < 0.05$, $**P < 0.01$, $***P < 0.001$, $****P < 0.0001$. ANOVA test with Tukey multiple comparison correction [(B), (D), (G)] or Holm-Sidak multiple comparison correction (C).

mutagenesis and cDNA integration in distantly related DGRs and bacterial hosts.

Bacteroides DGRs preferentially create nonsynonymous substitutions that alter side-chain chemistry

The high levels of mutagenic retrohoming conferred by the *Bov* and *Bfi* DGRs allowed us to build the largest dataset of experimentally derived diversified VR sequences available to date. Notably, we were able to analyze mutational patterns from in vitro–grown cells without the influence of strong selective pressure. We found that 99.9% of the nearly 4.5 million DGR-directed amino acid changes were nonsynonymous substitutions (Fig. 5A and fig. S6, A to C). This strong bias reflects the bacterial genetic code and a high prevalence of TR AAY (AAC or AAT) (*15*) motifs, which account for 10 of the 12 variable codons between the 5′ and 3′ boundaries of the *Bov* VR (Fig. 4F). Across our *Bacteroides* dataset, AAY motifs (~10.5 per TR) outnumber single-adenine motifs (~5.1 per TR) (fig. S6, D and E; Mann-Whitney $P < 0.0001$), underscoring their significance. AAC motifs can generate 16 codons through adenine mutagenesis: 14 that encode distinct amino acids and two synonymous codons for serine, whereas a stop codon cannot be generated (Fig. 5B). The side chains of the 15 distinct amino acids produced by AAC mutagenesis encompass the entire range of available chemical properties, including polar uncharged, small hydrophobic, large hydrophobic, positive charge, negative charge, and no side chain (glycine) (Fig. 5B). Therefore, the predominance of TR AAY motifs leads to an expansive and chemically diverse list of amino acids at variable sites and an overwhelmingly high probability of producing nonsynonymous mutations due to adenine mutagenesis.

Closer examination revealed a nonrandom pattern of diversified residues that lead to altered chemical properties of side chains (fig. S6F). When adenine occupies the middle codon position, mutagenesis of the first base yields codons encoding distinct chemical side chains (Fig. 5B, arrow). Notably, we observed a nonrandom pattern in the nucleotide frequency at variable positions. Adenine was the most prevalent nucleotide at most of the variable positions in both *Bov* (Fig. 5, C and D) and *Bfi* (fig. S6, G and H), followed by guanine and thymine, whereas cytosine was rarely observed. When specifically focusing on VR positions corresponding to TR AAC motifs, an adenine was observed in the second position at very high frequencies that were often greater than 50%. Thus, the nucleotide frequency across variable positions in VR exhibits stochastic but nonuniform patterns, with a clear bias to incorporate adenines that result in frequent switching of amino acid side-chain chemistry.

Mechanistic models of mutagenic retrohoming predict the formation of heteroduplexes between mutagenized cDNAs and parental VR sequences with an unusually high density of mismatches (*10*, *68*, *70*). Taking advantage of the constitutive activity of the *Bov* DGR, we explored the impact of mismatch repair on the level and pattern of VR mutagenesis by knocking out *mutS*. *Bov*Δ*mutS* exhibited substantially higher levels of VR mutagenesis than WT, with up to 25 and 43% of VRs mutated by days 3 and 14, respectively, corresponding to an approximate 5- to 10-fold increase compared to the parent strain (Fig. 5E). Complementation with intact *mutS* restored mutagenic retrohoming to WT levels (fig. S6I). Intriguingly, analysis of nucleotide frequencies at mutated variable sites revealed an almost identical distribution (Fig. 4G) and pattern (Fig. 5, C and F) when diversified VRs were compared between *Bov* WT and *Bov*Δ*mutS*. These results support a mechanism in which MutS-mediated repair operates in an all-or-nothing manner, whereby VR heteroduplexes are either converted back to the parental sequence or fully escape mismatch repair.

DGR dynamics under competitive pressure

Estimating the percentage of VRs that have undergone mutagenic retrohoming provides an incomplete picture of the true extent of sequence diversity. For example, a population in which a majority of diverged VRs encode the same or a limited number of DNA or protein sequences would clearly be distinct from one in which most of the diverged sequences differed from each other. Thus, we calculated the Shannon entropy (*71*) of VRs that had undergone adenine mutagenesis under different conditions. Although this metric can be biased at small sample sizes (*72*), our large mutational dataset allows it to encompass the relative strengths of two opposing forces: (i) mutagenic retrohoming (fig. S6J), which increases VR entropy by randomizing sequences, and (ii) purifying selection, which reduces entropy by favoring beneficial variants (*19*).

We measured VR entropy in *Bov* populations grown in vitro or in germ-free mice colonized with or without altered Schaedler flora (ASF), an eight-member bacterial consortium that provides interspecies competition (*73*) (Fig. 5G). VR sequences derived from in vitro–grown cells displayed high levels of amino acid entropy at all timepoints (Fig. 5H), indicating that mutagenic retrohoming was primarily driving VR diversity. When *Bov* was introduced into germ-free mice, VR entropy displayed high values similar to those of in vitro samples, suggesting the absence of strong selective forces in monocolonized hosts. By contrast, co-colonization of *Bov* and ASF led to an appreciable decline in VR entropy by week 2, consistent with positive selection. Notably, samples from in vitro–grown or monoassociated *Bov* contained VRs that were almost entirely different from each other, whereas samples from mice co-colonized with ASF contained populations in which two to three distinct VRs constituted nearly 50% of all mutated sequences (Fig. 5I). Furthermore, in separately caged co-colonized mice, mutated populations of VRs had converged by day 14 to express similar amino acid sequences despite being encoded by different DNA sequences. As shown in Fig. 5J, this convergence involved substitutions of hydrophobic residues with polar ones, reshaping the VR-encoded surface to form a more open binding pocket, suggesting that these variant sequences have evolved to interact with a new, common ligand. Taken together, these observations suggest that microbial competition promotes decreased VR entropy through selection, shaping variant repertoires toward sequence convergence.

DGRs are active during the intergenerational handoff from mothers to infants

We hypothesized that dynamic changes that accompany the intergenerational handoff of gastrointestinal microbes from mothers to infants during birth could select for DGR-mediated adaptations that facilitate colonization and persistence in a new host. To explore the role of DGRs during this period, we performed an integrative analysis of retroelements present in metagenomic datasets of human fecal microbiomes from 144 longitudinally sampled mother-infant pairs (*74*–*76*), as well as from a dataset of 146 healthy adults (*77*) (fig. S7A). We identified 5106 different DGRs, of which 2740 were identified within mother-infant pairs, with 698 DGRs found only in infants and 1654 found only in mothers, and 388 DGRs that were apparently transmitted from mothers to infants during or after birth (Fig. 6A and table S14). Distinct DGRs were identified in all healthy adults and mothers, as well as in 134 out of 144 infants (93%). Of those infants without an identified DGR, sampling was only available up to 4 months of life, whereas all infants who were sampled at 1 year harbored DGRs. To gain a deeper understanding of these elements, we analyzed DGR phylogeny, variable protein domains, and predicted transfer vector, similar to our prior analysis with *Bacteroides* (Fig. 1) but expanded to include all phyla (Fig. 6B).

The majority of DGRs in our dataset were phage encoded or prophage encoded (93%). Of the 344 DGRs found in cellular genomes, plasmids, or ICEs, 214 (62%) were from Bacteroidota, and 106 (31%) were from Bacillota species. In Bacteroidota, these DGRs primarily diversify pilus subunits or other adhesive proteins, consistent with findings in Fig. 1D. By contrast, most Bacillota variable proteins classified as cellular, plasmid, or ICE-encoded have domains similar to those of phage receptor binding proteins, suggesting that this binding

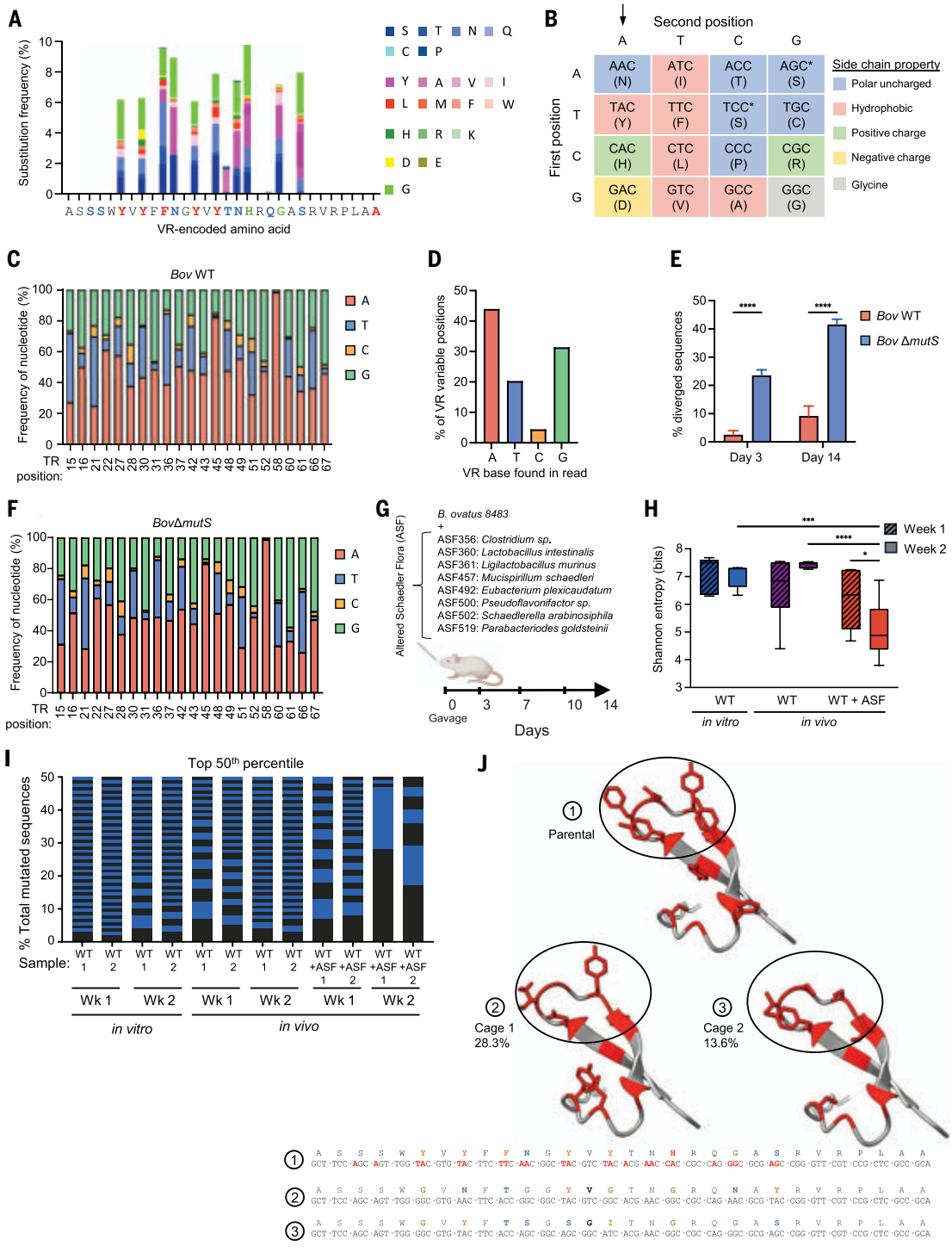


Fig. 5. *Bacteroides* DGRs are poised to alter amino acid side-chain chemistry and respond to competition in vivo. (**A**) Substitution frequency at *Bov* VR codons that correspond to TR adenines from cells grown in vitro. (**B**) Table showing codons that can be generated through mutagenic retrohoming of a TR AAC motif, colored by the chemical class of the amino acid side chain. (**C**) Nucleotide frequency at individual variable VR positions within diversified *Bov* VRs. The corresponding TR adenine position is listed below each bar. (**D**) Cumulative frequency of each of the four nucleotides at variable VR sites within diversified *Bov* VRs. (**E**) Percentage of VRs that mutated from the parental VR sequence in *Bov* WT and *Bov* Δ*mutS* cells grown in vitro. (**F**) Nucleotide frequency at individual variable VR positions within diversified *Bov* Δ*mutS* VRs. The corresponding TR adenine position is listed below each bar. (**G**) Co-colonization of germ-free mice with *Bov* with or without altered Schaedler flora (ASF), an eight-member bacterial community. (**H**) Shannon entropy of diversified VR sequences obtained from *Bov* cells grown in vitro or present in fecal samples of gnotobiotic mice ($n = 5$ to 11). $^{*}P < 0.05$, $^{**}P < 0.01$, $^{***}P < 0.001$; ANOVA with Tukey multiple comparison correction. (**I**) Graphical representation of *Bov* VR diversity from in vitro cultures and fecal samples of gnotobiotic mice, with alternating black and blue horizontal bars indicating the frequency of distinct VR sequences. (**J**) VR encoded predicted structures of the parental *Bov* VR and two of the most commonly observed VR sequences derived from fecal samples of separately caged gnotobiotic mice colonized with *Bov* plus ASF bacteria. The VR nucleotide and amino acid sequences are shown below and the frequency of the individual VR sequence within the diversified VR population is indicated. Single-letter abbreviations for the amino acid residues are as follows: A, Ala; C, Cys; D, Asp; E, Glu; F, Phe; G, Gly; H, His; I, Ile; K, Lys; L, Leu; M, Met; N, Asn; P, Pro; Q, Gln; R, Arg; S, Ser; T, Thr; V, Val; W, Trp; and Y, Tyr.

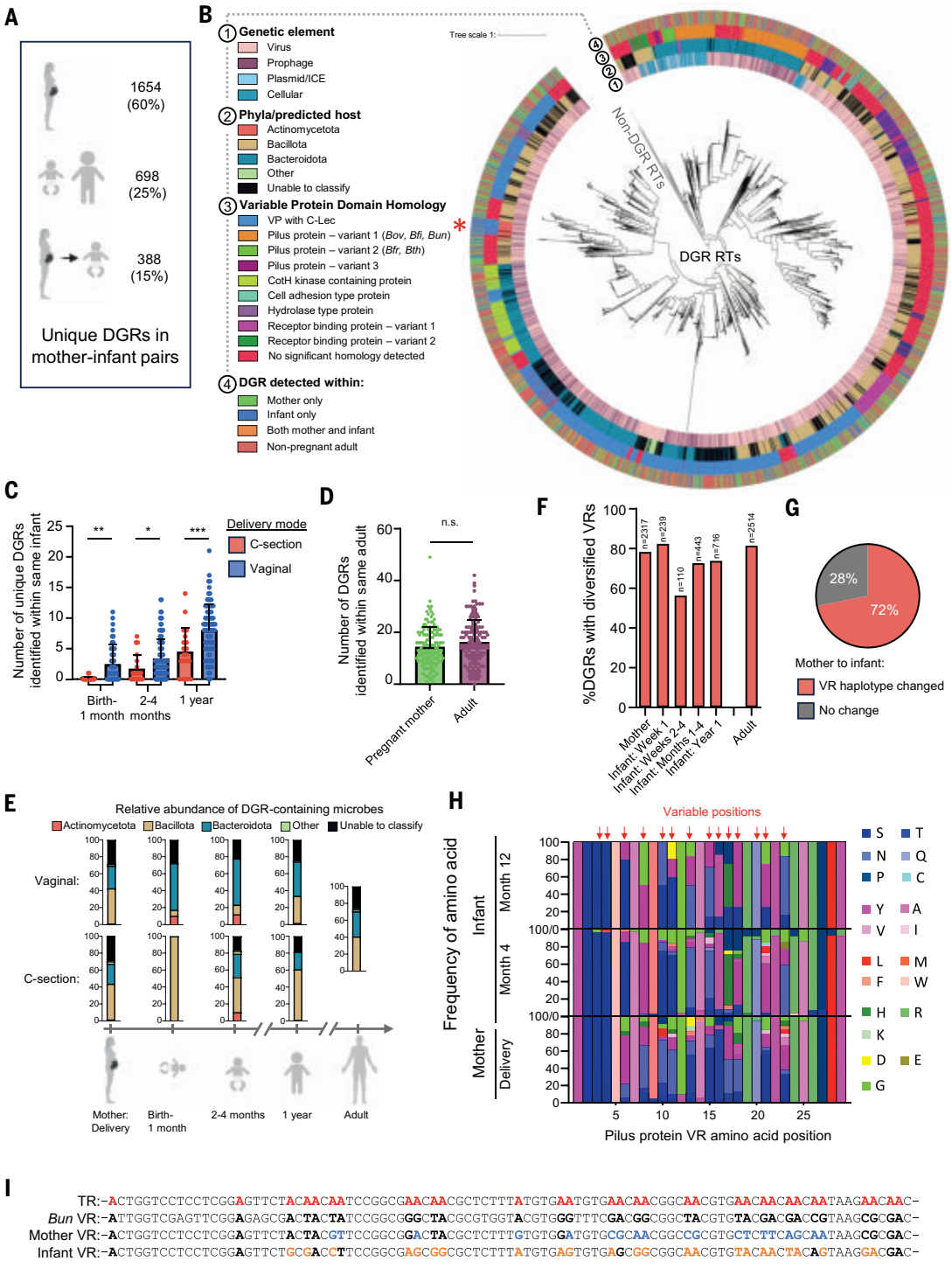


Fig. 6. DGRs undergo a burst of activity when transmitted from mother to infant. (**A**) Number of distinct DGRs found in mothers, in infants, or transmitted from mother to infant. (**B**) Phylogeny of DGR RTs found in metagenomes derived from mothers, infants, and healthy adults (*74*–*76*, *97*). Rings depict the genomic location of the DGR (ring 1), predicted host taxonomy to the phyla level (ring 2), variable protein homology (ring 3), and classification of the DGR host (ring 4). Red asterisk shows an area with Actinomycetota-harboring DGRs found primarily in infants. (**C**) Number of DGRs identified per infant, grouped by age and mode of delivery. $*P < 0.05$, $**P < 0.01$, $***P < 0.001$; ANOVA with Holm-Sidak multiple comparison correction. (**D**) Number of DGRs identified per adult. n.s.: not significant. (**E**) Taxonomic distribution of DGR-containing microbes, grouped by age and mode of delivery. (**F**) Percentagae of DGRs with mutations at VR positions that correspond to TR adenines, grouped by age. (**G**) Percentage of DGRs in which the predominant VR haplotype sequence changed between mother and infant ($n = 388$). (**H**) Frequency of VR encoded amino acids from a DGR that was transmitted from mother to infant. The target gene of this DGR is predicted to encode a type V pilus tip adhesin. (**I**) TR and VR sequences of *B. uniformis* 8492 (*Bun*) and the VRs from a similar DGR identified within a mother and her infant. Red, *Bun* TR adenines; bold, *Bun* VR nucleotides that correspond to TR adenines; blue, VR nucleotides that differ between *Bun* and the maternal VR sequence; orange, VR nucleotides that differ between the maternal and infant VR sequences.

module was co-opted to perform some other function. DGRs in this dataset were distributed throughout infants, mothers, and adults, except for a group of DGRs belonging to Actinomycetota (Fig. 6B, red star), which were enriched in infants, and to a lesser extent in mothers, but rarely found in nonpregnant adults.

Mode of delivery substantially affected DGR prevalence and abundance, with vaginally delivered infants harboring more DGRs at birth and throughout the first year of life than those born via C-section (Fig. 6C). At 1 year, infants had significantly fewer DGRs than mothers or healthy adults (Fig. 6, C and D; $P < 0.0001$, all comparisons of 1-year-olds versus adults), indicating ongoing DGR acquisition over time. Mode of delivery also correlated with the relative distribution of DGR-containing taxa and mirrors well-established vertical transmission patterns of bacterial strains at birth (*78*). Prior to delivery, there were no significant differences in the taxonomy of DGRs in mothers undergoing C-section compared to mothers delivering vaginally (Fig. 6E). After delivery, vaginally born infants, who have been shown to disproportionately acquire *Bacteroides* from their mother (*74*–*76*, *78*), had more DGRs from Bacteroidota, as expected. Infants born via C-section, however, acquired an initial set of DGRs that were almost exclusively encoded by Bacillota. By 1 year, DGR-associated taxa in both groups resembled adult profiles (Fig. 6E). No differences in DGR count or taxonomic distribution were observed on the basis of infant sex or feeding method (fig. S7, B to E). Together, these results demonstrate that vaginal delivery promotes early acquisition of a larger and more diverse set of DGRs that more closely resemble the phylogenetic distribution observed in adults.

To determine whether DGRs were active at any point within these samples, we aligned raw sequencing reads with identified VRs and searched for adenine-specific mutations. DGR activity in infants ranged from 56 to 80% during the first year of life and was comparable to maternal and adult levels (Fig. 6F). Next, we determined the consensus VR amino acid sequence at each timepoint and compared VR haplotypes between mothers and infants. Of 388 transmitted DGRs, 72% showed evidence of VR haplotype switching (Fig. 6G), suggesting selection for new variable proteins in infants. A representative example of a diversified type V pilin homolog that was present in a mother at birth, and subsequently detected in her infant's profile over the first year of life, is illustrated in Fig. 6H. Comparing VR sequences shows that a majority of variable codons underwent continued alterations that changed the chemical class of diversified residues at 4 months, stabilizing by 1 year.

DGRs transmitted from mothers to vaginally born infants were predominantly Bacteroidota (56%), rather than Bacillota (15%) (Fig. 6E), and they were more likely to diversify pilus proteins than the general population of DGRs (15% versus 10%, Chi-Square $P < 0.0001$). Notably, we identified DGRs in our dataset that were nearly identical to each of the *Bacteroides* elements depicted in Fig. 2, B to D. Although the *Bfr*, *Bth*, and *Bun* DGRs that we examined were quiescent under laboratory conditions (Fig. 4B), homologous elements were highly active in mothers and infants, showing clear evidence of adenine-templated VR mutagenesis (fig. S7, F and G, and table S15). For example, Fig. 6I shows TR and VR sequences from a *Bun* DGR homolog that diversifies a type V pilus tip adhesin, and the predominant VR haplotypes generated by a DGR that was transferred from mother to infant. As expected, elements homologous to the *Bov* and *Bfi* DGRs that were highly active in vitro and in germ-free mice were similarly active in humans.

These observations begin to characterize the abundance, distribution, and activities of DGRs in human infant and adult populations, highlighting their role in diversifying ligand-binding proteins, including pilus-associated adhesins. We show that DGRs are transmitted intergenerationally, with delivery mode profoundly influencing the relative abundance of DGR-containing microbes in the newborn gut, and maternal transmission is linked to the emergence of new, dominant VR haplotypes in infants, as would be expected for genotypic alterations that are subject to positive selection.

Discussion

Numerous studies have highlighted the impact of microbial genetic variation on human health and disease (*79*–*81*). This variation is driven by rapid adaptations that can quickly spread throughout microbial communities (*82*–*84*). DGRs play a distinctive role in variation and adaptation by creating hypermutable hotspots that produce unrivaled levels of protein diversity, through a mechanism that targets ligand-binding residues and is shared across vast phylogenetic distances. By characterizing the variable proteins, mutational dynamics, and modes of transmission of *Bacteroides* DGRs, we can build a foundation for understanding how genome plasticity shapes host-associated microbial communities.

Of more than 1100 distinct, DGR encoded variable proteins identified in human gut-associated *Bacteroides*, nearly 25% are predicted to diversify type V pilins (*39*, *54*). The genetic systems responsible for these structures display a high degree of modularity and redundancy, with gene number, location, and organization varying between species and strains (*39*, *54*). Fewer than half of the 16 multigene pilin operons in *Bfr* are expressed in vitro (fig. S2A), and many of these gene clusters are flanked by integrases, transposases, prophage loci, transfer genes, and other signs of mobility (*39*). Thus, differential expression and horizontal transfer may partly explain the modular complexity observed in *Bacteroides* genomes. For DGRs that target adhesive pilins in *Bfr*, *Bth*, and related taxa with homologous ICEs, we propose that two factors promote their dissemination and positive selection. The first involves properties of the conjugative elements, such as inducibility in mucus and the presence of stalk and anchor homologs that could help display diversified pilin tips. The second is the availability of new hosts with genetic backgrounds that are diverse and adapted to acquire horizontally transferred type V pilus genes. Adhesive pili are often observed to be essential determinants of microbe-host interactions involved in colonization, and microbe-microbe interactions that structure bacterial communities and facilitate biofilm formation (*50*, *51*). An understanding of the selective advantages conferred by type V pili will benefit from the construction of isogenic mutants that are completely devoid of surface pili or lack specific components, the availability of animal models that recapitulate adhesive interactions in the human GI tract, and the identification of ligands recognized by static as well as DGR-diversified tip adhesins. We expect these ligands to include peptides and carbohydrates such as mucins, cell-associated glycans, dietary fibers, and breast milk oligosaccharides (*10*, *13*).

Although the abundance of DGRs in nature attests to their selective advantages (*12*, *19*, *46*), how host cells balance the trade-off between accelerated evolution and loss of fitness remains unclear. One solution is to regulate mutagenic retrohoming. For example, bursts of mutagenesis during times of stress or environmental shifts interspersed with periods of quiescence could facilitate selection and fixation of adaptive traits (*19*). Considering this, it was not unexpected to observe minimal activity with the *Bfr*, *Bth*, and *Bun* DGRs in vitro or in gnotobiotic mice. Although it is possible that these DGRs are simply not active, we hypothesize that they are under tight regulation for several reasons: (i) They are intact and appear capable of encoding all cis- and trans-acting factors required for mutagenesis; (ii) we observe numerous close homologs of these DGRs that have disseminated between multiple *Bacteroides* species and strains (fig. S4A); (iii) diversification activity of nearly identical DGRs was readily detected in our mother-infant dataset (Fig. 6, H and I); and (iv) DGRs often show low levels of mutagenesis in the lab but have readily detectable activity in their natural environments (*10*, *19*). By contrast, the constitutively high levels of activity measured with the *Bov* and *Bfi* elements were unexpected but enabled us to examine DGR mutagenesis at a level of resolution that had not been previously attained. By creating a mutational database from the *Bov* and *Bfi* DGRs, we observed an overwhelming (>1000-fold) preference for introducing nonsynonymous substitutions in VR, a misincorporation bias that favors changes in the chemical

properties of side chains available for ligand binding, and a role for host-encoded MutS that supports an all-or-nothing model for repair of heteroduplex intermediates during mutagenic retrohoming. In germ-free mice, we measured a decrease in the Shannon entropy of *Bov* VR sequences that was dependent on the presence of competing microbes and resulted in the appearance of new predominant VR haplotypes, as expected for conditions that favor positive selective sweeps.

Hypervariable systems and assessments of purifying selection may provide a means for identifying genes and networks in microbial communities that confer contextually relevant fitness advantages. Accordingly, our working hypothesis is that DGRs that diversify bacterial proteins function, at least in part, to optimize colonization factors that promote engraftment and maintenance of host bacteria within the GI microbiota. If true, understanding DGRs and the variable proteins they diversify will not only have applications for understanding microbe-host interactions, but may also provide a means to engineer therapeutic microbial consortia capable of rapidly evolving colonization factors to promote efficient engraftment in new hosts. This could pave the way for future applications that harness the adaptive properties of DGRs to support health and reverse microbiome-associated diseases.

Limitations

There are two material limitations of our study that reflect broader challenges in efforts to understand diversity in human-associated microbial communities. The first involves the need to identify phenotypes from genotypic information, a transformative resource available on a massive scale that is rarely sufficient to provide causal links. DGRs were discovered on the basis of a phenotype, tropism switching by *Bordetella* phage, and the genetic basis was characterized with relative ease (*17*, *18*). By contrast, identifying the function of an uncharacterized gene, or the advantage of diversifying it, may require recapitulating natural environments that provide appropriate selective pressures, including signals for expression, receptors for ligand interactions, and many other context-dependent parameters. The "genotype to phenotype to mechanism" pathway can pose major challenges, but they are not necessarily insurmountable. In the case of DGRs and similar systems, for example, hypervariability can provide sensitive, real-time estimates of positive selection and the environmental conditions under which it occurs, leading to information that can be used to target hypothesis-driven discovery.

A second limitation involves the nature of metagenomic data available from existing large-scale efforts to characterize human microbiomes, which is primarily derived from short-read approaches that rarely reach sufficient depth to fully capture VR sequence variability and entropy. In addition, contigs assembled from short reads make it challenging to identify complete DGRs, resolve their genomic context, and determine their precise taxonomy, particularly for those encoded on MGEs. Thus, it is not yet possible to determine the rate at which DGR transfer by MGEs affects the developing infant microbiome. Future efforts that incorporate long-read sequencing of sufficient depth on well-curated longitudinally obtained mother-infant samples, along with Amplicon-Seq to deeply characterize diversified VRs, will be required to understand DGR dynamics after birth and to identify variable proteins subject to positive selection in developing infants.

Materials and methods

Bacterial strains, plasmids, primers, and growth conditions

Bacterial strains are described in table S1, plasmids are described in table S2, and primers are described in table S3. *E. coli* strains were grown aerobically at 37°C in Luria-Bertani medium (LB, BD Difco). *Bacteroides* strains were grown in Brain Heart Infusion (BHI, BD Difco) medium at 37°C, supplemented with vitamin K (5 μg/ml) and hemin (5 μg/ml), and incubated in an anaerobic chamber (Coy) under 5% H_2, 10% CO_2, 85% N_2. Antibiotics were added to the following final concentrations: carbenicillin (Cb), 100 μg/ml; gentamicin (Gm), 200 μg/ml; erythromycin (Erm), 5 or 25 μg/ml, tetracycline (Tet), 2 μg/ml, 5-fluoro-2′-deoxyuridine (FudR, 200 μg/ml), unless otherwise noted. Anhydrous tetracycline (aTC) was used at a concentration of 100 ng/ml. Backbone plasmids used in this study were pLGB13, pLGB36, and pNBU2_erm-TetR-P1T_DP-GH023 (*85*–*87*).

Mice

Germ-free Swiss Webster mice were purchased from Taconic Farms and bred in flexible film isolators. For gnotobiotic experiments, sterile litters of 8- to 10-week-old male and female mice were transferred into autoclaved microisolator cages where they were fed autoclaved chow diets ad libidtum and given autoclaved water supplemented with gentamicin 100 μg/ml. Altered Schaedler flora (ASF) live animal donor C57BL/6 mice were purchased from Taconic (ASF-DONOR-M/F) and fed an autoclaved chow diet ad libidtum and given autoclaved water. For monocolonization experiments, animals were orally gavaged with a 200 μl inoculum of an overnight culture of a given *Bacteroides* strain containing ~10^8 cells per gavage. For ASF experiments, approximately 1 g of fresh stool from an ASF donor mouse was vortexed into 1 ml of an overnight culture of *Bacteroides* immediately prior to oral gavage. For conjugation experiments, 100 μl of each donor and recipient strains were combined in a 1:1 ratio and orally gavaged to mice. Stool samples were collected on days 3, 7, 10, and 14. At least 3 ($n = 3$ to 11) mice were used for each experiment. All procedures were performed in accordance with an approved protocol following IUCAC guidelines at the University of California, Los Angeles and the IUCAC guidelines at the California Institute of Technology.

Plasmid generation.

Q5 high-fidelity DNA polymerase (New England Biolabs [NEB]) or Phusion high-fidelity DNA polymerase (NEB) were used for PCR cloning steps. To construct plasmids for deletion mutagenesis, a PCR fragment was generated that included 1 kb upstream and the first 12 codons of the targeted gene and a second fragment was generated to include the last 12 codons and 1 kb downstream of the targeted gene. The backbone plasmids pLGB36 (*Bfr* only) or pLGB13 (all others) were cut at the Bam HI (NEB) restriction site. PCR fragments were ligated together and into the backbone plasmid using NEBuilder HiFi assembly master mix (NEB). For overexpression mutants, the targeted gene was cloned into pNBU2_erm-TetR-P1T_DP-GH023 plasmid cut at Nco I and Sal I restriction sites using the NEBuilder HiFi assembly master mix. Plasmids were sequenced following cloning to ensure insertions were without mutations.

Conjugation and allelic exchange

Plasmids were transformed into *E. coli* S17-λpir and conjugated into *Bacteroides* strains as previously described (*85*). Briefly, *E. coli* S17-λpir donor cultures were grown in 25 ml of LB+Cb to an OD_{600} between 0.3 and 0.5. Recipient *Bacteroides* strains were grown in BHIS to an OD_{600} of 0.05 to 0.1. Both strains were mixed together in a 50 ml Falcon centrifuge tube and spun at 4000*g* for 10 min. Cell pellets were then resuspended in 100 μl of BHIS, plated on the center of a prewarmed BHIS plate, and incubated aerobically at 37°C for 14 to 16 hours. The mating spot was resuspended in BHIS and was diluted serially from 1:10 to 1:10,000. From each dilution, 100 μl was streaked onto BHIS+Gm+Erm selection plates and incubated at 37°C anaerobically. Colonies were picked after 2 days, restreaked on BHIS+Gm+Erm plates, and grown for two additional days. For overexpression mutants, stocks were made from an overnight culture of BHIS and integration was confirmed by PCR of attB sites using the appropriate primers in table S3. For allelic exchange protocols, isolates were grown in BHIS overnight, diluted to 1:1,000 or 1:10,000 in the morning, and plated on BHIS+aTC100 to induce the counterselection toxin. After 2 days, colonies were picked, and colony PCR screening was performed to determine which colonies contained the desired mutation and which colonies

reverted back to WT. Stocks were made of potential mutants. The mutation site including 1 kb upstream and downstream of the mutation, as well as the entire DGR locus, was amplified from chromosomal DNA and sequenced to ensure no undesired mutations were introduced.

Sample preparation and immunoblotting

For SDS–polyacrylamide gel electrophoresis (SDS-PAGE) sample preparation, *Bacteroides* strains were cultured in BHIS media and harvested as described previously (*88*). Proteins with ALFA-tags were detected using a monoclonal mouse antibody at a dilution of 1:5000 (anti-ALFA, NanoTag Biotechnologies, cat# N1583, RRID: AB_3075998). Immunodetection was carried out by chemifluorescence using horseradish peroxidase–labeled goat anti-mouse immunoglobulin G (IgG) and the ECL plus detection substrate (GE Healthcare). Chemifluorescent signals were visualized using a Typhoon scanner (GE Healthcare).

Cellular fractionation

Cellular fractionation was carried out as described (*89*) and is briefly summarized here. Overnight cultures ($n = 3$ each strain, biological repeats) of WT or mutant *Bacteroides* strains encoding inducible ALFA-tagged proteins were diluted 1:100 in a total volume of 1 L BHIS supplemented with 25 μg/ml Erm and incubated at 37°C until reaching OD 0.05 to 0.1. The target gene was then induced by addition of 100 ng/ml of aTC to the media and the culture was allowed to incubate for an additional 16 hours at room temperature (RT). The induced 1-liter culture was then pelleted by centrifugation at 10,000*g* and subsequently resuspended in 10 ml of spheroblast buffer (0.2 M Tris-HCl pH 8, 1 M sucrose, 1 mM EDTA, 1 mg/ml lysozyme) and incubated for 5 min at RT. A volume of 40 ml of ice-cold dH2O was then added to the suspension before placing on ice for 5 min to allow spheroblast formation. The suspension was then centrifuged at 200,000*g* for 45 min at 4°C. The resulting supernatant was collected as the periplasmic fraction and the pellet was resuspended in French press buffer (7.5 ml ice-cold 10 mM Tris-HCl pH 7.5, 5 mM EDTA, 0.2 mM DTT, 50 μl 1mg/ml DNase I). Cells were then ruptured in a French Press with two passes at 10^8 Pa. Unbroken cells in the lysate were removed by centrifugation at 10,000*g* for 10 min at 4°C. The lysate was then centrifuged at 280,000*g* for 4 hours at 4°C. The resulting supernatant was collected as the cytoplasmic fraction while the pellet contained crude membranes. Membrane fractions were diluted 1:1 with dH2O, centrifuged at ≥85,000*g* for 20 min at 4°C, washed 3x in 500 μl dH2O, and then stored at −20°C.

Proteinase K

Overnight cultures of *Bacteroides* strains ($n = 3$) carrying an inducible, ALFA-tagged variable protein (*Bfr* WT-ALFA, *Bfr* C28A-ALFA, or *Bov* WT-ALFA), were diluted 1:100 in a total volume of 10 ml BHIS supplemented with 25 μg/ml Erm and incubated at 37°C until reaching OD 0.1. Expression of the ALFA-tagged variable protein was then induced by addition of 10 ng/ml aTC. Induced cultures were incubated for 8 hours and then collected by centrifugation. Cells were resuspended at 2.5 OD/ml in a total volume of 5 ml phosphate-buffered saline (PBS) and 1 ml aliquots of the bacterial slurry were dispensed to 1.5-ml tubes and incubated for 1 hour at 37°C with one of the following Proteinase K quantities: 0 (control); 25 ng; 50 ng; 100 ng; 200 ng. Next, 10 μl phenylmethylsulfonyl fluoride (PMSF) was added to each tube and cells were collected by centrifugation at 10,000*g* and washed 2X with 1 ml PBS. Cells were resuspended in SDS sample dye with beta-mercaptoethanol, boiled for 10 min and analyzed by Western blot.

ALFA pulldown

ALFA-tagged *Bacteroides* variable proteins and their interacting protein partners were purified from an appropriate cellular fraction (periplasm for *Bov*, supernatant for *Bfr*) using the Anti-ALFA single-domain nanobody resin (ALFA SelectorST) according to manufacturer instructions. Briefly, 3 ml of the cellular fraction was diluted 1:1 with 2x binding buffer (50 mM Tris pH 7.5, 100 mM NaCl, 2 mM EDTA, 1% NP-40, 10% glycerol) supplemented with 10 μl/ml HALT protease (ThermoFisher). To this suspension, 200 μl of ALFA SelectorST was added and the mixture was incubated at 4°C with end-over-end rotation for 16 hours. The resin was collected by centrifugation and washed 2x with PBS containing 0.5% NP-40. The resin was then pelleted and resuspended in 200 μl of 1x Laemmli buffer (0.0625 M Tris pH 6.8, 2% sodium dodecyl sulfate, 10% glycerol, bromphenol blue) with 1% β-mercaptoethanol and then boiled for 5 min.

Mass spectroscopy

Immunoprecipitation eluates (ALFA pulldowns) or cellular fractions (fractionation controls) in 1x Laemmli buffer were diluted in equal volume of 100mM Tris-Cl pH 8.5 and reduced and alkylated by the sequential addition of 5 mM tris(2-carboxyethyl) phosphine and 10 mM iodoacetamide. This was followed by treatment with single-pot, solid-phase-enhanced sample preparation (SP3) protocol for protein clean-up (*90*). Following SP3, eluates were proteolytically digested with Lys-C and trypsin at 37°C overnight. The digested peptides were subjected to offline SP3-based peptide clean-up and subsequently analyzed by liquid chromatography–tandem mass spectrometry (LC-MS/MS). Briefly, peptides were separated by reversed-phase chromatography using 75-μm inner diameter fritted fused silica capillary column packed in-house to a length of 25 cm with bulk 1.9 mM ReproSil-Pur beads with 120 Å pores. The increasing gradient of acetonitrile was delivered by a Dionex Ultimate 3000 (Thermo Scientific) at a flow rate of 200 nl/min. MS/MS spectra were collected using data-dependent acquisition on an Orbitrap Fusion Lumos Tribrid mass spectrometer (Thermo Fisher Scientific) with an MS1 resolution (r) of 120,000 followed by sequential MS2 scans at a resolution (r) of 15,000. The data generated by LC-MS/MS were analyzed using the MaxQuant bioinformatic pipeline (*91*). The Andromeda integrated in MaxQuant was employed as the peptide search engine. Briefly, a maximum of two missed cleavages was allowed. The maximum false discovery rate for peptide and protein was specified as 0.01. Label-free quantification (LFQ) was enabled with LFQ minimum ratio count of 1. The parent and peptide ion search tolerances were set as 20 and 4.5 ppm respectively. The MaxQuant output files were subsequently processed for statistical analysis of differentially enriched proteins using Analytical R tools for mass spectrometry (artMS) (*92*).

Cellular fractionation controls

To assess the quality of protein enrichment from our cell fractionation protocol, we used mass spectrometry to identify all proteins in each fraction generated and then compared the change in abundance of each identified protein between each fraction (i.e., cytosol fraction compared to membrane fraction; cytosol fraction compared to periplasmic fraction; membrane fraction compared to periplasmic fraction). For each protein, the change in its abundance between fractions was graphed using the VolcaNoseR (*93*) web application. The $\log_2$ fold change of abundance was graphed over the x axis and the $-\log_{10}$ significance value of the change in abundance was graphed over the y axis. We then tracked specific proteins with previously reported subcellular localization data to evaluate the effectiveness of the fractionation protocol (table S8).

Detection of DGR-ICE integration, excision, and episome formation by PCR

Genomic DNA was prepared from cultured *Bfr* or *Bth* cells carrying overexpression constructs (pEV, p*araC2*, p*rteC*, p*merR*) using a DNeasy Blood and Tissue Kit (Qiagen). A 50-ng aliquot of DNA was used as template in a standard 50 μl PCR with primer sets that detect integrated DGR-ICE junction fragments or episomes and chromosomal scars resulting from ICE excision (Fig. 3A). To quantify ICE excision

in vivo, germ-free Swiss Webster mice ($n = 3$, biological repeats) were monocolonized by *Bfr* carrying the plasmid pFD340, which confers Erm resistance. Bacterial DNA was extracted from mouse feces and cecal content using the ZR fecal DNA miniprep kit (Zymo Research). DNA from *Bfr* cells in scraped colon mucus was prepared using DNeasy Blood and Tissue Kits (Qiagen) after pretreatment with *N*-acetyl-L-cysteine. Specifically, a freshly made NALC solution (50 ml 2.94% sodium citrate, 50 ml 4% sodium hydroxide, 500 mg *N*-acetyl-L-cysteine) was added to the mucus at 1:1 ratio (vol/vol), incubated at the room temperature for 1 hour with agitation until the sample attained desired fluidity. Quantitative PCR (qPCR) was performed on an iCycler iQ real-time PCR detection system (BioRad) with iQ SYBR Green Supermix (BioRad). Per each 30 µl qPCR, 30 ng DNA from various samples was used as template. Ct values for the episome and chromosomal scar were normalized to Ct values of the housekeeping gene, rpoD (BF638R_RS13245). Relative quantification of excised ICE in different samples was calculated by the ΔΔCt approach, using cultured *Bfr* with pFD340 as baseline. DNA extracted from in vitro–grown cultures of *Bfr* carrying p*araC2* was included as a positive control for high-level excision.

ICE transfer assays

To create ICEs and strains with compatible antibiotic markers, the Erm resistance cassette in pKnock-erm was first swapped with a *tetQ* marker, resulting pKnock-tetQ. The DGR-ICE from *Bfr* or *Bth* was tagged with the Tet resistance marker by inserting pKnock-tetQ downstream of *rt*. Mating experiments were designed to measure inter- and intraspecies ICE transfer. Briefly, three independent cultures of donor or recipient cells were grown to mid-log phase (OD_{600} 0.5), mixed at a 2:1 ratio, and spotted on sterile nitrocellulose membranes (0.45 µM, PALL Life Science). After incubation on nonselective BHIS plates for 16 to 24 hours, mating mixtures were washed off the filter into 2 ml of BHIS and plated onto selective BHIS medium with 2 µg/ml Tet and 200 µg/ml FudR. Putative transconjugants were purified and verified by PCR reactions with primer sets that are specific to the recipient or donor ICE. The transfer efficiency was calculated by dividing the number of genuine transconjugants by the number of recipients in each mating experiment. A similar transfer was also set up in gnotobiotic mice, except that both the tetQ-tagged donor and Δ*tdk*ΔICE recipient carry pFD340 to confer erythromycin resistance. Each mating pair was inoculated to four mice co-housed in one cage. Mouse feces were plated at days 1, 3, 5, 7, and 10 after inoculation.

Assays for mutagenic retrohoming

For in vitro assays, overnight cultures of *Bacteroides* strains were diluted to OD_{600} 0.01 in 3 ml of BHIS ($n = 3$, biological repeats). Every 8 hours, the OD_{600} was measured (OD_{600} between 0.5 and 0.8), and cultures were rediluted to OD_{600} 0.01 in 3 ml of fresh BHIS. Samples were collected by pelleting 1 OD_{600} of cells on days 3, 7, 10, and 14 for Amplicon-Seq. In vivo assays were conducted by collecting fecal pellets from monocolonized Swiss Webster mice on days 3, 7, 10, and 14 after gavage. Genomic DNA was extracted from pellets for Amplicon-Seq.

Amplicon-Seq of VR regions

Total DNA was extracted from bacterial cultures (PureLink Genomic DNA Mini Kit, Thermo Fisher) or stool (QIAamp Fast DNA Stool Mini Kit, Qiagen). Primers amplifying the VR region of each *Bacteroides* strain were designed with the forward primer containing a 20 bp random Unique Molecular Index (UMI) and an adapter, as described previously (*94*). Briefly, each forward primer was designed to anneal to the VR region at 62° to 64°C and was present in 1/10 the normal concentration. A second forward primer would anneal to the adapter of the first forward primer at a temperature of 68° to 70°C. The second forward primer and reverse primer contained partial Illumina adapter sequences. Cycling parameters included 1 cycle of 98°C for 3 min, 2 cycles of 98°C for 15 s, 62°C for 45 s, and 72°C for 30 s, followed by 38 cycles of 98°C for 15 s, 70°C for 45 s, followed by 72°C for 5 min. PCR products were purified using SPRI Select beads (Beckman Coulter) and sent for EZ Amplicon-Seq (Azenta Life Sciences).

Data processing of Amplicon-Seq reads

Raw reads were trimmed and contamination filtered with BBDuk using default parameters except a kmer length of 23 and mink length of 11. Data were then merged with BBMerge (*95*) using default parameters. Merged reads were then aligned to VR by creating a custom blastn (*96*) database created from the parental VR sequences of *Bfr*, *Bth*, *Bun*, *Bov*, and *Bfi* to allow for a large number of potential mismatches using the parameters for blastn word_size=8, reward=1, penalty=-1, evalue=1e-5, gapopen=6, gapextend=6, and perc_identity = 50. UMI and VR sequences were then extracted from the aligned read and compiled together. UMIs that contained mismatching sequences were discarded. Reads were then analyzed for the number of non-adenine mutations compared to parental strains and were observed to follow a bimodal distribution. The vast majority (>99.99%) of reads had fewer than 5% non-adenine mutations whereas the remaining reads consisted almost entirely of mutations, which represented spurious reads. Therefore, a threshold of >50% of non-adenine mutations was chosen to discard the spurious reads. The number of divergent reads was calculated by summing the number of reads with greater than 1 (i.e., 2 or more) adenine mutations compared to parental strain (to account for potential sequencing errors). When plotted on a log chart, a pseudocount of 1 mutated read was added to all samples.

Total RNA extraction, RNA-Seq library preparation, and Illumina sequencing

Bacteroides cultures were grown to mid-log phase (OD_{600} 0.3 to 0.5) and stationary phase (OD_{600} 0.7 to 1.0) in BHIS. Cells were flash-frozen in a dry ice-ethanol slurry, then pelleted by centrifugation at 16,000*g* for 1 min at 4°C. The bacterial pellets were stored at −80°C until RNA extraction. RNA was extracted using TRIzol reagent and the PureLink RNA Mini Kit following the manufacturer's instructions. Briefly, bacterial pellets were incubated with 1 ml of TRIzol for 5 min at room temperature, followed by the addition of 200 µl of chloroform. After 5 min at room temperature, the samples were centrifuged at 12,000*g* for 15 min at 4°C. The aqueous phase was transferred to a new tube, and an equal volume of 100% ethanol was added. This mixture was transferred to a spin cartridge and centrifuged at 12,000*g* for 15 s at room temperature.

RNA samples were treated with PureLink DNase I, according to the manufacturer's protocol. Following DNase treatment and four wash steps, RNA was eluted in 50 µl of RNase-free water by centrifugation at 12,000*g* for 1 min. Eluted RNA was transferred to RNase-free tubes and analyzed for quality by agarose gel electrophoresis. RNA integrity was assessed using the Bio-Rad ChemiDoc system, and RNA concentration was quantified with a NanoDrop One spectrophotometer (Thermo Fisher Scientific). Further RNA quality and concentration was validated on an Agilent 4200 TapeStation RNA ScreenTape, with all RIN scores above 8.0 and samples normalized to 250 ng starting mass. Library preparation was performed using Illumina's Stranded Total RNA Prep with Ribo-Zero Plus Microbiome, which targets depletion of microbiome rRNA prior to cDNA synthesis and library formation. Final libraries were validated using an Agilent 4200 TapeStation D1000 ScreenTape, with an average fragment size of 396 bp. Libraries were quantified using Invitrogen's Quant iT High Sensitivity dsDNA Kit and normalized during pooling. Samples were sequenced in 3 lanes of NovaSeq X Plus 10B PE 2x100.

Bacteroides dataset and mother-infant dataset acquisition

The NCBI Assembly database was searched for the term "Bacteroides" and filtered to include those assemblies within the RefSeq database

on 22 January 2021. Genome strain names were derived from the genome assembly reports. The list of strains and their corresponding RefSeq accession number that were included in this study is listed in table S16. For the mother-infant dataset, raw reads were downloaded from BioProject PRJNA475246 (*75*) or metagenomic assemblies (*74*, *76*, *97*) were downloaded as previously described (*98*). Raw reads had adapters trimmed and were quality filtered using BBDuk and merged using BBMerge (*95*). Merged reads were assembled into contigs using MegaHit (*28*) using parameters:–min-contig-len 500 -m 0.85–presets meta-sensitive. Contigs with length <2000 bp were then discarded and the resulting contigs were used for DGR identification. Taxonomic classification of contigs was performed by mmseqs2 using default parameters (*99*).

DGR identification from genomic and metagenomic datasets

A profile of previously identified DGR RT proteins (*12*, *100*) was built using HMMER (*47*). Predicted proteomes were derived from genomes and contigs using Prodigal (*101*) and the resulting predicted proteins were searched for hits using HMMscan. A 20-kb window on either side of RT hits was used as input to search for imperfect repeats using a custom BLAST script with parameters -word_size 8 -reward 1 -penalty -1 -gapopen 6 -gapextend 6 (*96*). The size of the window was chosen based on the size of previous windows used in other DGR identification pipelines (*12*, *19*, *100*) and through testing various window sizes in a subset of genomes. We found that window sizes larger than 20 kb would result in low specificity by identifying false positives through misassigning VR/TR pairs to the wrong RT when a genome encodes multiple DGRs while too small of a window would decrease the sensitivity of identifying large DGR loci that encode multiple accessory genes or variable proteins with large, multi-domain N-terminal extensions. Pairs were checked for one pair to be contained within a previously predicted open reading frame. Because there are many potential mismatches of reads to the VR sequence, traditional local aligners, such as Bowtie (*102*) or BWA (*103*) will trim or discard the read. To circumvent this challenge and determine DGR activity from metagenomic data, raw reads were mapped back to identified VRs by creating a custom BLAST database of the VR sequence using the same blastn parameters as above. Reads that fully or partially aligned were then checked for alignment to TR and the rest of the genome/contig by identifying if those reads had fewer mismatches than to VR. Any read that best aligned to the VR region was kept. Reads aligning to VR regions were then analyzed to determine whether mutations existed that corresponded to TR adenine positions. If adenine-specific mutations were found, the DGR was categorized as active. VR haplotypes were generated for each timepoint by generating the consensus VR sequence. The consensus sequence was compared between timepoints to determine if it differed.

Identification of non-DGR RTs

A previously built profile of all RTs in bacterial genomes (*42*) was modified to exclude the DGR RTs and rebuilt using HMMER. Proteomes from genomes or metagenomic contigs were searched for these RTs. The number of non-DGR RTs was reduced by random sampling and this subset was added to the identified DGR RTs for phylogenetic analysis.

Clustering of variable proteins

In order to cluster variable proteins, each primary amino acid sequence was used for an all-versus-all blastp (*96*) search. The result of the blastp was used as an edge weight for input into MCL clustering with inflation value of 2.0 (*104*). Within each cluster, a multiple sequence alignment was performed using MUSCLE (*105*). This alignment was input into HHpred (*45*) to search for functional domains within the proteins using the databases PDB_mmCIF70_17_Apr, Pfam-A_v35, and COG-KOG_v1.0. Functional domains with an e-value <1e-5 were considered hits. Domain groups were formed by grouping all variable proteins by the most significant domain hit.

Phylogenetic tree building

The RT phylogenetic tree was created by aligning each RT protein sequence, which was input into Fasttree2 using default parameters (*106*). Variable proteins were classified as pilus proteins if they shared a significant domain with the following PBDs: 4EPS (*39*), 4QB7 (*39*), 6JZJ (*54*), 5NF4 (*107*). Variable proteins were classified as TaqVP-like if they shared a significant domain with PDB: 5VF4 (*48*). Variable proteins were classified as phage receptor tail binding proteins if they shared a significant domain with PDB: 1YU0 (*15*).

DGR genomic assignments

Contigs containing DGRs were used as input for geNomad (*43*), which predicts regions of contigs to be viral or plasmid. Coordinates from those predictions were aligned to DGR coordinates. DGRs located on a contig predicted to be entirely viral were classified as virus. DGRs located within a viral region surrounded by bacterial genes were classified as prophage. A 100-kb window surrounding DGRs located within predicted plasmid regions was then used as input for ICEfinder (*44*) for ICE prediction. ICE synteny figures were generated using pyGenomeViz (*108*).

DGR gene transcription analysis.

Raw sequencing reads from RNA-seq experiments were quality filtered and trimmed with fastp v0.23.4 (*109*) with default parameters, then mapped to the reference genome of each respective species with bwa-mem2 (*110*) with default parameters. Mapping statistics were generated with bamtools (*111*) v2.5.1 and visualized with multiqc (*112*) v1.21. Reads in gene features were counted with featureCounts (*113*) function of the subread package at the fragment level (–countReadPairs) with fragments overlapping multiple features counted in both (-O). Total transcript counts were normalized to trimmed mean of M (TMM) values using NOISeq (*114*) with default parameters. Within each *Bacteroides* strain, DGR gene TMM values were normalized to *gyrA* gene TMM values. The ratio of DGR genes to *gyrA* was then compared across strains, setting *Bfr* ratios to 1 to generate relative ratios for each of the other strains.

VR mutagenesis and entropy analysis

VR mutagenesis frequency was calculated by taking the number of reads with >1 substitution from the canonical sequence divided by the total number of sequences. VR entropy was calculated using the formula:

$$Entropy = \; - \sum_{1}^{n} p * \log(p)$$

according to Shannon (*71*), where p is the frequency of a distinct VR sequence and n is the total number of distinct mutagenized VR sequences.

Statistical tests and metrics

Statistical comparisons were performed using the tests indicated in the figure legends. *P* values were generated using analysis of variance (ANOVA) or student's t test. Multiple comparison corrections were performed using Holm-Sidak method or Tukey's method, where appropriate. Statistical significance was defined at $\alpha = 0.05$.

Software and code availability

All software utilized for analysis in this study is listed in the Key Resources Table. Python code to identify DGRs from genomes will be made available at https://github.com/macadangdanglab/dgrdiscovery upon publication.

REFERENCES AND NOTES

1. K. Heilbron, M. Toll-Riera, M. Kojadinovic, R. C. MacLean, Fitness is strongly influenced by rare mutations of large effect in a microbial mutation accumulation experiment. *Genetics* **197**, 981–990 (2014). doi: 10.1534/genetics.114.163147; pmid: 24814466
2. D. Mazel, Integrons: Agents of bacterial evolution. *Nat. Rev. Microbiol.* **4**, 608–620 (2006). doi: 10.1038/nrmicro1462; pmid: 16845431
3. F. Müller, H. Tobler, Chromatin diminution in the parasitic nematodes ascaris suum and parascaris univalens. *Int. J. Parasitol.* **30**, 391–399 (2000). doi: 10.1016/S0020-7519(99)00199-X; pmid: 10731562
4. D. G. Schatz, P. C. Swanson, V(D)J recombination: Mechanisms of initiation. *Annu. Rev. Genet.* **45**, 167–202 (2011). doi: 10.1146/annurev-genet-110410-132552; pmid: 21854230
5. D. M. Fitzgerald, S. M. Rosenberg, What is mutation? A chapter in the series: How microbes "jeopardize" the modern synthesis. *PLOS Genet.* **15**, e1007995 (2019). doi: 10.1371/journal.pgen.1007995; pmid: 30933985
6. C. Shee, J. L. Gibson, M. C. Darrow, C. Gonzalez, S. M. Rosenberg, Impact of a stress-inducible switch to mutagenic repair of DNA breaks on mutation in Escherichia coli. *Proc. Natl. Acad. Sci. U.S.A.* **108**, 13659–13664 (2011). doi: 10.1073/pnas.1104681108; pmid: 21808005
7. F. Jiang, J. A. Doudna, CRISPR-Cas9 Structures and Mechanisms. *Annu. Rev. Biophys.* **46**, 505–529 (2017). pmid: 28375731
8. L. A. Marraffini, E. J. Sontheimer, CRISPR interference limits horizontal gene transfer in staphylococci by targeting DNA. *Science* **322**, 1843–1845 (2008). doi: 10.1126/science.1165771; pmid: 19095942
9. R. M. Wheatley, R. C. MacLean, CRISPR-Cas systems restrict horizontal gene transfer in Pseudomonas aeruginosa. *ISME J.* **15**, 1420–1433 (2021). doi: 10.1038/s41396-020-00860-3; pmid: 33349652
10. B. R. Macadangdang, S. K. Makanani, J. F. Miller, Accelerated Evolution by Diversity-Generating Retroelements. *Annu. Rev. Microbiol.* **76**, 389–411 (2022). doi: 10.1146/annurev-micro-030322-040423; pmid: 35650669
11. H. Doré *et al.*, Targeted hypermutation of putative antigen sensors in multicellular bacteria. *Proc. Natl. Acad. Sci. U.S.A.* **121**, e2316469121 (2024). doi: 10.1073/pnas.2316469121; pmid: 38354254
12. L. Wu *et al.*, Diversity-generating retroelements: Natural variation, classification and evolution inferred from a large-scale genomic survey. *Nucleic Acids Res.* **46**, 11–24 (2018). pmid: 29186518
13. J. L. Miller *et al.*, Selective ligand recognition by a diversity-generating retroelement variable protein. *PLOS Biol.* **6**, e131 (2008). doi: 10.1371/journal.pbio.0060131; pmid: 18532877
14. J. Le Coq, P. Ghosh, Conservation of the C-type lectin fold for massive sequence variation in a Treponema diversity-generating retroelement. *Proc. Natl. Acad. Sci. U.S.A.* **108**, 14649–14653 (2011). doi: 10.1073/pnas.1105613108; pmid: 21873231
15. S. A. McMahon *et al.*, The C-type lectin fold as an evolutionary solution for massive sequence variation. *Nat. Struct. Mol. Biol.* **12**, 886–892 (2005). doi: 10.1038/nsmb992; pmid: 16170324
16. H. Guo *et al.*, Diversity-generating retroelement homing regenerates target sequences for repeated rounds of codon rewriting and protein diversification. *Mol. Cell* **31**, 813–823 (2008). doi: 10.1016/j.molcel.2008.07.022; pmid: 18922465
17. S. Doulatov *et al.*, Tropism switching in Bordetella bacteriophage defines a family of diversity-generating retroelements. *Nature* **431**, 476–481 (2004). doi: 10.1038/nature02833; pmid: 15386016
18. M. Liu *et al.*, Reverse transcriptase-mediated tropism switching in Bordetella bacteriophage. *Science* **295**, 2091–2094 (2002). doi: 10.1126/science.1067467; pmid: 11896279
19. S. Roux *et al.*, Ecology and molecular targets of hypermutation in the global microbiome. *Nat. Commun.* **12**, 3076 (2021). doi: 10.1038/s41467-021-23402-7; pmid: 34031405
20. J. J. Faith *et al.*, The long-term stability of the human gut microbiota. *Science* **341**, 1237439 (2013). doi: 10.1126/science.1237439; pmid: 23828941
21. M. R. Charbonneau *et al.*, Sialylated Milk Oligosaccharides Promote Microbiota-Dependent Growth in Models of Infant Undernutrition. *Cell* **164**, 859–871 (2016). doi: 10.1016/j.cell.2016.01.024; pmid: 26898329
22. S. K. Mazmanian, J. L. Round, D. L. Kasper, A microbial symbiosis factor prevents intestinal inflammatory disease. *Nature* **453**, 620–625 (2008). doi: 10.1038/nature07008; pmid: 18509436
23. P. Portincasa *et al.*, Gut Microbiota and Short Chain Fatty Acids: Implications in Glucose Homeostasis. *Int. J. Mol. Sci.* **23**, 1105 (2022). doi: 10.3390/ijms23031105; pmid: 35163038
24. S. Jean, M. J. Wallace, G. Dantas, C. D. Burnham, Time for Some Group Therapy: Update on Identification, Antimicrobial Resistance, Taxonomy, and Clinical Significance of the Bacteroides fragilis Group. *J. Clin. Microbiol.* **60**, e0236120 (2022). doi: 10.1128/jcm.02361-20; pmid: 35700139
25. S. Schloissnig *et al.*, Genomic variation landscape of the human gut microbiome. *Nature* **493**, 45–50 (2013). doi: 10.1038/nature11711; pmid: 23222524
26. C. A. Liebert, R. M. Hall, A. O. Summers, Transposon Tn21, flagship of the floating genome. *Microbiol. Mol. Biol. Rev.* **63**, 507–522 (1999). doi: 10.1128/MMBR.63.3.507-522.1999; pmid: 10477306
27. L. S. Frost, R. Leplae, A. O. Summers, A. Toussaint, Mobile genetic elements: The agents of open source evolution. *Nat. Rev. Microbiol.* **3**, 722–732 (2005). doi: 10.1038/nrmicro1235; pmid: 16138100
28. D. Li, C.-M. Liu, R. Luo, K. Sadakane, T.-W. Lam, MEGAHIT: An ultra-fast single-node solution for large and complex metagenomics assembly via succinct de Bruijn graph. *Bioinformatics* **31**, 1674–1676 (2015). doi: 10.1093/bioinformatics/btv033; pmid: 25609793
29. A. Bankevich *et al.*, SPAdes: A new genome assembly algorithm and its applications to single-cell sequencing. *J. Comput. Biol.* **19**, 455–477 (2012). doi: 10.1089/cmb.2012.0021; pmid: 22506599
30. S. Nurk, D. Meleshko, A. Korobeynikov, P. A. Pevzner, metaSPAdes: A new versatile metagenomic assembler. *Genome Res.* **27**, 824–834 (2017). doi: 10.1101/gr.213959.116; pmid: 28298430
31. T. Namiki, T. Hachiya, H. Tanaka, Y. Sakakibara, MetaVelvet: An extension of Velvet assembler to de novo metagenome assembly from short sequence reads. *Nucleic Acids Res.* **40**, e155–e155 (2012). doi: 10.1093/nar/gks678; pmid: 22821567
32. Y. Peng, H. C. M. Leung, S. M. Yiu, F. Y. L. Chin, IDBA-UD: A de novo assembler for single-cell and metagenomic sequencing data with highly uneven depth. *Bioinformatics* **28**, 1420–1428 (2012). doi: 10.1093/bioinformatics/bts174; pmid: 22495754
33. T. J. Treangen *et al.*, MetAMOS: A modular and open source metagenomic assembly and analysis pipeline. *Genome Biol.* **14**, R2 (2013). doi: 10.1186/gb-2013-14-1-r2; pmid: 23320958
34. J. R. Kultima *et al.*, MOCAT2: A metagenomic assembly, annotation and profiling framework. *Bioinformatics* **32**, 2520–2523 (2016). doi: 10.1093/bioinformatics/btw183; pmid: 27153620
35. J. Alneberg *et al.*, Binning metagenomic contigs by coverage and composition. *Nat. Methods* **11**, 1144–1146 (2014). doi: 10.1038/nmeth.3103; pmid: 25218180
36. D. D. Kang, J. Froula, R. Egan, Z. Wang, MetaBAT, an efficient tool for accurately reconstructing single genomes from complex microbial communities. *PeerJ* **3**, e1165 (2015). doi: 10.7717/peerj.1165; pmid: 26336640
37. Y.-W. Wu, Y. Ye, A novel abundance-based algorithm for binning metagenomic sequences using l-tuples. *J. Comput. Biol.* **18**, 523–534 (2011). doi: 10.1089/cmb.2010.0245; pmid: 21385052
38. Y. Wang, H. C. M. Leung, S. M. Yiu, F. Y. L. Chin, MetaCluster 5.0: A two-round binning approach for metagenomic data for low-abundance species in a noisy sample. *Bioinformatics* **28**, i356–i362 (2012). doi: 10.1093/bioinformatics/bts397; pmid: 22962452
39. Q. Xu *et al.*, A Distinct Type of Pilus from the Human Microbiome. *Cell* **165**, 690–703 (2016). doi: 10.1016/j.cell.2016.03.016; pmid: 27062925
40. N. A. O'Leary *et al.*, Reference sequence (RefSeq) database at NCBI: Current status, taxonomic expansion, and functional annotation. *Nucleic Acids Res.* **44** (D1), D733–D745 (2016). doi: 10.1093/nar/gkv1189; pmid: 26553804
41. A. Vallota-Eastman *et al.*, Role of diversity-generating retroelements for regulatory pathway tuning in cyanobacteria. *BMC Genomics* **21**, 664 (2020). doi: 10.1186/s12864-020-07052-5; pmid: 32977771
42. F. Sharifi, Y. Ye, Identification and classification of reverse transcriptases in bacterial genomes and metagenomes. *Nucleic Acids Res.* **50**, e29–e29 (2022). doi: 10.1093/nar/gkab1207; pmid: 34904653
43. A. P. Camargo *et al.*, Identification of mobile genetic elements with geNomad. *Nat. Biotechnol.* **42**, 1303–1312 (2024). pmid: 37735266
44. M. Liu *et al.*, ICEberg 2.0: An updated database of bacterial integrative and conjugative elements. *Nucleic Acids Res.* **47**, D660–D665 (2019). doi: 10.1093/nar/gky1123; pmid: 30407568
45. J. Söding, A. Biegert, A. N. Lupas, The HHpred interactive server for protein homology detection and structure prediction. *Nucleic Acids Res.* **33**, W244–W248 (2005). doi: 10.1093/nar/gki408; pmid: 15980461
46. B. G. Paul *et al.*, Targeted diversity generation by intraterrestrial archaea and archaeal viruses. *Nat. Commun.* **6**, 6585 (2015). doi: 10.1038/ncomms7585; pmid: 25798780
47. S. R. Eddy, Accelerated Profile HMM Searches. *PLOS Comput. Biol.* **7**, e1002195 (2011). doi: 10.1371/journal.pcbi.1002195; pmid: 22039361
48. S. Handa, K. L. Shaw, P. Ghosh, Crystal structure of a Thermus aquaticus diversity-generating retroelement variable protein. *PLOS ONE* **14**, e0205618 (2019). doi: 10.1371/journal.pone.0205618; pmid: 30629599
49. K. B. Nguyen *et al.*, Phosphorylation of spore coat proteins by a family of atypical protein kinases. *Proc. Natl. Acad. Sci. U.S.A.* **113**, E3482–E3491 (2016). doi: 10.1073/pnas.1605917113; pmid: 27185916
50. J. L. Mark Welch, B. J. Rossetti, C. W. Rieken, F. E. Dewhirst, G. G. Borisy, Biogeography of a human oral microbiome at the micron scale. *Proc. Natl. Acad. Sci. U.S.A.* **113**, E791–E800 (2016). pmid: 26811460
51. J. L. Mark Welch, S. T. Ramírez-Puebla, G. G. Borisy, Oral Microbiome Geography: Micron-Scale Habitat and Niche. *Cell Host Microbe* **28**, 160–168 (2020). doi: 10.1016/j.chom.2020.07.009; pmid: 32791109
52. M. Alayyoubi *et al.*, Structure of the essential diversity-generating retroelement protein bAvd and its functionally important interaction with reverse transcriptase. *Structure* **21**, 266–276 (2013). doi: 10.1016/j.str.2012.11.016; pmid: 23273427

53. J. Jumper *et al.*, Highly accurate protein structure prediction with AlphaFold. *Nature* **596**, 583–589 (2021). doi: 10.1038/s41586-021-03819-2; pmid: 34265844
54. S. Shibata *et al.*, Structure of polymerized type V pilin reveals assembly mechanism involving protease-mediated strand exchange. *Nat. Microbiol.* **5**, 830–837 (2020). doi: 10.1038/s41564-020-0705-1; pmid: 32284566
55. M. K. Hospenthal, T. R. D. Costa, G. Waksman, A comprehensive guide to pilus biogenesis in Gram-negative bacteria. *Nat. Rev. Microbiol.* **15**, 365–379 (2017). doi: 10.1038/nrmicro.2017.40; pmid: 28496159
56. H. Götzke *et al.*, The ALFA-tag is a highly versatile tool for nanobody-based bioscience applications. *Nat. Commun.* **10**, 4403 (2019). doi: 10.1038/s41467-019-12301-7; pmid: 31562305
57. C. M. Johnson, A. D. Grossman, Integrative and Conjugative Elements (ICEs): What They Do and How They Work. *Annu. Rev. Genet.* **49**, 577–601 (2015). doi: 10.1146/annurev-genet-112414-055018; pmid: 26473380
58. M. G. Durrant, M. M. Li, B. A. Siranosian, S. B. Montgomery, A. S. Bhatt, A Bioinformatic Analysis of Integrative Mobile Genetic Elements Highlights Their Role in Bacterial Adaptation. *Cell Host Microbe* **27**, 140–153.e9 (2020). doi: 10.1016/j.chom.2019.10.022; pmid: 31862382
59. A. E. Franke, D. B. Clewell, Evidence for a chromosome-borne resistance transposon (Tn916) in Streptococcus faecalis that is capable of "conjugal" transfer in the absence of a conjugative plasmid. *J. Bacteriol.* **145**, 494–502 (1981). doi: 10.1128/jb.145.1.494-502.1981; pmid: 6257641
60. T. D. Mays, C. J. Smith, R. A. Welch, C. Delfini, F. L. Macrina, Novel antibiotic resistance transfer in Bacteroides. *Antimicrob. Agents Chemother.* **21**, 110–118 (1982). doi: 10.1128/AAC.21.1.110; pmid: 7081969
61. M. C. Roberts, A. L. Smith, Molecular characterization of "plasmid-free" antibiotic-resistant Haemophilus influenzae. *J. Bacteriol.* **144**, 476–479 (1980). doi: 10.1128/jb.144.1.476-479.1980; pmid: 6968310
62. N. B. Shoemaker, M. D. Smith, W. R. Guild, DNase-resistant transfer of chromosomal cat and tet insertions by filter mating in Pneumococcus. *Plasmid* **3**, 80–87 (1980). doi: 10.1016/S0147-619X(80)90036-0; pmid: 6278526
63. J. Botelho, H. Schulenburg, The Role of Integrative and Conjugative Elements in Antibiotic Resistance Evolution. *Trends Microbiol.* **29**, 8–18 (2021). doi: 10.1016/j.tim.2020.05.011; pmid: 32536522
64. D. D. Jaworski, D. B. Clewell, Evidence that coupling sequences play a frequency-determining role in conjugative transposition of Tn916 in Enterococcus faecalis. *J. Bacteriol.* **176**, 3328–3335 (1994). doi: 10.1128/jb.176.11.3328-3335.1994; pmid: 8195088
65. J. Park, A. A. Salyers, Characterization of the Bacteroides CTnDOT regulatory protein RteC. *J. Bacteriol.* **193**, 91–97 (2011). doi: 10.1128/JB.01015-10; pmid: 21037014
66. A. B. Russell *et al.*, A type VI secretion-related pathway in Bacteroidetes mediates interbacterial antagonism. *Cell Host Microbe* **16**, 227–236 (2014). doi: 10.1016/j.chom.2014.07.007; pmid: 25070807
67. D. Arambula *et al.*, Surface display of a massively variable lipoprotein by a Legionella diversity-generating retroelement. *Proc. Natl. Acad. Sci. U.S.A.* **110**, 8212–8217 (2013). doi: 10.1073/pnas.1301366110; pmid: 23633572
68. S. S. Naorem *et al.*, DGR mutagenic transposition occurs via hypermutagenic reverse transcription primed by nicked template RNA. *Proc. Natl. Acad. Sci. U.S.A.* **114**, E10187–E10195 (2017). doi: 10.1073/pnas.1715952114; pmid: 29109248
69. S. Handa, A. Reyna, T. Wiryaman, P. Ghosh, Determinants of adenine-mutagenesis in diversity-generating retroelements. *Nucleic Acids Res.* **49**, 1033–1045 (2021). doi: 10.1093/nar/gkaa1240; pmid: 33367793
70. S. Handa *et al.*, Template-assisted synthesis of adenine-mutagenized cDNA by a retroelement protein complex. *Nucleic Acids Res.* **46**, 9711–9725 (2018). doi: 10.1093/nar/gky620; pmid: 30007279
71. C. E. Shannon, A mathematical theory of communication. *Bell Syst. Tech. J.* **27**, 379–423 (1948). doi: 10.1002/j.1538-7305.1948.tb01338.x
72. M. K. Konopiński, Shannon diversity index: A call to replace the original Shannon's formula with unbiased estimator in the population genetics studies. *PeerJ* **8**, e9391 (2020). doi: 10.7717/peerj.9391; pmid: 32655992
73. M. Wymore Brand *et al.*, The Altered Schaedler Flora: Continued Applications of a Defined Murine Microbial Community. *ILAR J.* **56**, 169–178 (2015). doi: 10.1093/ilar/ilv012; pmid: 26323627
74. P. Ferretti *et al.*, Mother-to-Infant Microbial Transmission from Different Body Sites Shapes the Developing Infant Gut Microbiome. *Cell Host Microbe* **24**, 133–145.e5 (2018). doi: 10.1016/j.chom.2018.06.005; pmid: 30001516
75. M. Yassour *et al.*, Strain-Level Analysis of Mother-to-Child Bacterial Transmission during the First Few Months of Life. *Cell Host Microbe* **24**, 146–154.e4 (2018). doi: 10.1016/j.chom.2018.06.007; pmid: 30001517
76. F. Bäckhed *et al.*, Dynamics and Stabilization of the Human Gut Microbiome during the First Year of Life. *Cell Host Microbe* **17**, 690–703 (2015). doi: 10.1016/j.chom.2015.04.004; pmid: 25974306
77. J. Lloyd-Price *et al.*, Strains, functions and dynamics in the expanded Human Microbiome Project. *Nature* **550**, 61–66 (2017). doi: 10.1038/nature23889; pmid: 28953883
78. M. Yassour *et al.*, Natural history of the infant gut microbiome and impact of antibiotic treatment on bacterial strain diversity and stability. *Sci. Transl. Med.* **8**, 343ra81 (2016). doi: 10.1126/scitranslmed.aad0917; pmid: 27306663
79. M. Zepeda-Rivera *et al.*, A distinct Fusobacterium nucleatum clade dominates the colorectal cancer niche. *Nature* **628**, 424–432 (2024). doi: 10.1038/s41586-024-07182-w; pmid: 38509359
80. E. Yaffe, D. A. Relman, Tracking microbial evolution in the human gut using Hi-C reveals extensive horizontal gene transfer, persistence and adaptation. *Nat. Microbiol.* **5**, 343–353 (2020). doi: 10.1038/s41564-019-0625-0; pmid: 31873203
81. L. Zahavi *et al.*, Bacterial SNPs in the human gut microbiome associate with host BMI. *Nat. Med.* **29**, 2785–2792 (2023). doi: 10.1038/s41591-023-02599-8; pmid: 37919437
82. S. Zhao *et al.*, Adaptive Evolution within Gut Microbiomes of Healthy People. *Cell Host Microbe* **25**, 656–667.e8 (2019). doi: 10.1016/j.chom.2019.03.007; pmid: 31028005
83. N. R. Garud, B. H. Good, O. Hallatschek, K. S. Pollard, Evolutionary dynamics of bacteria in the gut microbiome within and across hosts. *PLOS Biol.* **17**, e3000102 (2019). doi: 10.1371/journal.pbio.3000102; pmid: 30673701
84. R. Wolff, N. R. Garud, Pervasive selective sweeps across human gut microbiomes. bioRxiv 2023.12.22.573162 [Preprint] (2023); https://doi.org/10.1101/2023.12.22.573162.
85. L. García-Bayona, L. E. Comstock, Streamlined Genetic Manipulation of Diverse *Bacteroides* and *Parabacteroides* Isolates from the Human Gut Microbiota. *mBio* **10**, e01762–e19 (2019). doi: 10.1128/mBio.01762-19; pmid: 31409684
86. T. Ito *et al.*, Genetic and Biochemical Analysis of Anaerobic Respiration in Bacteroides fragilis and Its Importance *In Vivo*. *mBio* **11**, e03238–e19 (2020). doi: 10.1128/mBio.03238-19; pmid: 32019804
87. B. Lim, M. Zimmermann, N. A. Barry, A. L. Goodman, Engineered Regulatory Systems Modulate Gene Expression of Human Commensals in the Gut, Engineered Regulatory Systems Modulate Gene Expression of Human Commensals in the Gut. *Cell* **169**, 547–558.e15 (2017). doi: 10.1016/j.cell.2017.03.045; pmid: 28431252
88. U. Ahuja *et al.*, Differential regulation of type III secretion and virulence genes in Bordetella pertussis and Bordetella bronchiseptica by a secreted anti-σ factor. *Proc. Natl. Acad. Sci. U.S.A.* **113**, 2341–2348 (2016). doi: 10.1073/pnas.1600320113; pmid: 26884180
89. M. Thein, G. Sauer, N. Paramasivam, I. Grin, D. Linke, Efficient subfractionation of gram-negative bacteria for proteomics studies. *J. Proteome Res.* **9**, 6135–6147 (2010). doi: 10.1021/pr1002438; pmid: 20932056
90. C. S. Hughes *et al.*, Single-pot, solid-phase-enhanced sample preparation for proteomics experiments. *Nat. Protoc.* **14**, 68–85 (2019). doi: 10.1038/s41596-018-0082-x; pmid: 30464214
91. J. Cox, M. Mann, MaxQuant enables high peptide identification rates, individualized p.p.b.-range mass accuracies and proteome-wide protein quantification. *Nat. Biotechnol.* **26**, 1367–1372 (2008). doi: 10.1038/nbt.1511; pmid: 19029910
92. D. Jimenez-Morales, A. R. Campos, J. V. Dollen, N. Krogan, D. Swaney, artMS: Analytical R tools for Mass Spectrometry. https://bioconductor.org/packages/release/bioc/html/artMS.html.
93. J. Goedhart, M. S. Luijsterburg, VolcaNoseR is a web app for creating, exploring, labeling and sharing volcano plots. *Sci. Rep.* **10**, 20560 (2020). doi: 10.1038/s41598-020-76603-3; pmid: 33239692
94. B. Fields, S. Moeskjaer, V. P. Friman, S. U. Andersen, J. P. W. Young, MAUI-seq: Metabarcoding using amplicons with unique molecular identifiers to improve error correction. *Mol. Ecol. Resour.* **21**, 703–720 (2021). doi: 10.1111/1755-0998.13294; pmid: 33171018
95. B. Bushnell, J. Rood, E. Singer, BBMerge - Accurate paired shotgun read merging via overlap. *PLOS ONE* **12**, e0185056 (2017). doi: 10.1371/journal.pone.0185056; pmid: 29073143
96. C. Camacho *et al.*, BLAST+: Architecture and applications. *BMC Bioinformatics* **10**, 421 (2009). doi: 10.1186/1471-2105-10-421; pmid: 20003500
97. C. Huttenhower *et al.*, Structure, function and diversity of the healthy human microbiome. *Nature* **486**, 207–214 (2012). doi: 10.1038/nature11234; pmid: 22699609
98. E. Pasolli *et al.*, Extensive Unexplored Human Microbiome Diversity Revealed by Over 150,000 Genomes from Metagenomes Spanning Age, Geography, and Lifestyle. *Cell* **176**, 649–662.e20 (2019). doi: 10.1016/j.cell.2019.01.001; pmid: 30661755
99. M. Steinegger, J. Söding, MMseqs2 enables sensitive protein sequence searching for the analysis of massive data sets. *Nat. Biotechnol.* **35**, 1026–1028 (2017). doi: 10.1038/nbt.3988; pmid: 29035372
100. B. G. Paul *et al.*, Retroelement-guided protein diversification abounds in vast lineages of Bacteria and Archaea. *Nat. Microbiol.* **2**, 17045–17045 (2017). doi: 10.1038/nmicrobiol.2017.45; pmid: 28368387
101. D. Hyatt *et al.*, Prodigal: Prokaryotic gene recognition and translation initiation site identification. *BMC Bioinformatics* **11**, 119 (2010). doi: 10.1186/1471-2105-11-119; pmid: 20211023
102. B. Langmead, S. L. Salzberg, Fast gapped-read alignment with Bowtie 2. *Nat. Methods* **9**, 357–359 (2012). doi: 10.1038/nmeth.1923; pmid: 22388286
103. H. Li, R. Durbin, Fast and accurate short read alignment with Burrows-Wheeler transform. *Bioinformatics* **25**, 1754–1760 (2009). doi: 10.1093/bioinformatics/btp324; pmid: 19451168

104. A. J. Enright, S. Van Dongen, C. A. Ouzounis, An efficient algorithm for large-scale detection of protein families. *Nucleic Acids Res.* **30**, 1575–1584 (2002). doi: 10.1093/nar/30.7.1575; pmid: 11917018
105. R. C. Edgar, MUSCLE: A multiple sequence alignment method with reduced time and space complexity. *BMC Bioinformatics* **5**, 113 (2004). doi: 10.1186/1471-2105-5-113; pmid: 15318951
106. M. N. Price, P. S. Dehal, A. P. Arkin, FastTree 2—Approximately maximum-likelihood trees for large alignments. *PLOS ONE* **5**, e9490 (2010). doi: 10.1371/journal.pone.0009490; pmid: 20224823
107. M. Hall, Y. Hasegawa, F. Yoshimura, K. Persson, Structural and functional characterization of shaft, anchor, and tip proteins of the Mfa1 fimbria from the periodontal pathogen Porphyromonas gingivalis. *Sci. Rep.* **8**, 1793 (2018). doi: 10.1038/s41598-018-20067-z; pmid: 29379120
108. Y. Shimoyama, pyGenomeViz: A genome visualization python package for comparative genomics. https://github.com/moshi4/pyGenomeViz.
109. S. Chen, Ultrafast one-pass FASTQ data preprocessing, quality control, and deduplication using fastp. *iMeta* **2**, e107 (2023). doi: 10.1002/imt2.107; pmid: 38868435
110. V. Md, S. Misra, H. Li, S. Aluru, Efficient Architecture-Aware Acceleration of BWA-MEM for Multicore Systems. *2019 IEEE Int. Parallel Distrib. Process. Symp. (IPDPS)* **00**, 314–324 (2019).
111. D. W. Barnett, E. K. Garrison, A. R. Quinlan, M. P. Strömberg, G. T. Marth, BamTools: A C++ API and toolkit for analyzing and managing BAM files. *Bioinformatics* **27**, 1691–1692 (2011). doi: 10.1093/bioinformatics/btr174; pmid: 21493652
112. P. Ewels, M. Magnusson, S. Lundin, M. Käller, MultiQC: Summarize analysis results for multiple tools and samples in a single report. *Bioinformatics* **32**, 3047–3048 (2016). doi: 10.1093/bioinformatics/btw354; pmid: 27312411
113. Y. Liao, G. K. Smyth, W. Shi, featureCounts: An efficient general purpose program for assigning sequence reads to genomic features. *Bioinformatics* **30**, 923–930 (2014). doi: 10.1093/bioinformatics/btt656; pmid: 24227677
114. S. Tarazona *et al.*, Data quality aware analysis of differential expression in RNA-seq with NOISeq R/Bioc package. *Nucleic Acids Res.* **43**, e140 (2015). doi: 10.1093/nar/gkv711; pmid: 26184878
115. B. R. Macadangdang *et al.*, Computer code for Targeted protein evolution in the gut microbiome by diversity-generating retroelements. DOI:10.5281/zenodo.15616919
116. Q. Liu *et al.*, Targeting surface protein SasX by active and passive vaccination to reduce Staphylococcus aureus colonization and infection. *Infect. Immun.* **83**, 2168–2174 (2015). doi: 10.1128/IAI.02951-14; pmid: 25776748

ACKNOWLEDGMENTS

We thank E. Hsiao and her laboratory members K. Yu and J. Paramo (UCLA), as well as S. Mazmanian (California Institute of Technology) for valuable advice and assistance with gnotobiotic mouse husbandry. We also thank E. Martens (University of Michigan) for providing several of the *Bacteroides* strains used in this study. We are indebted to S. Devkota (Cedars Sinai Medical Center), P. Ghosh (University of California, San Diego), and B. Paul (Marine Biological Laboratory, Woods Hole) for their insightful critiques of the manuscript. We acknowledge the use of resources at the UCLA Proteomics Laboratory for mass spectroscopy and the UCLA Neuroscience Genomics Core for RNA sequencing. The funders had no role in the design of the study; in the collection, analyses, or interpretation of data; in the writing of the manuscript; or in the decision to publish the results. Portions of all main figures (Figs. 1 to 6) and summary figure were produced in BioRender. **Funding:** National Institutes of Health (NIH) grant 1K08DK138316 (B.R.M.); NIH grant 5K12HD111040 (B.R.M.); NIH grant 5K12HD000850 (B.R.M.); NIH grant T32AI007323 (B.R.M.); JDS Family Foundation (J.F.M.); Kavli Endowment (J.F.M.). **Author contributions:** Conceptualization: B.R.M., Y.W., U.A., and J.F.M, with input from all authors. Methodology: B.R.M, Y.W., U.A., and J.F.M. Investigation: B.R.M., Y.W., C.W., J.I.R., K.S., G.E.V., C.B., S.K.M., and U.A. Software: B.R.M. and B.M.S. Writing – original draft: B.R.M. and J.F.M. Writing – review & editing: B.R.M., U.A., and J.F.M. Funding acquisition: B.R.M. and J.F.M. **Competing interests:** J.F.M. is a cofounder and chair of the scientific advisory board (SAB) of Pylum Biosciences, Inc., a member of the SAB of Notitia Biotechnologies, and an advisory board member of Seed Health, Inc. **Data and materials availability:** All data are available in the main text or supplementary materials and are free to access. Amplicon-Sequencing of DGRs is uploaded to the SRA database under the Bioproject PRJNA1186982. RNA-sequencing data are uploaded to the GEO database under the accession number GSE282133. Access |to the original code generated for this paper can be found at https://github.com/macadangdanglab/dgrdiscovery (*115*). All other software utilized in this manuscript is listed under the Materials and Methods section.

License information: Copyright © 2025 the authors, some rights reserved; exclusive licensee American Association for the Advancement of Science. No claim to original US government works. https://www.science.org/about/science-licenses-journal-article-reuse

SUPPLEMENTARY MATERIALS

science.org/doi/10.1126/science.adv2111
Figs. S1 to S7; Tables S1 to S16; MDAR Reproducibility Checklist

Submitted 13 December 2024; accepted 5 August 2025

10.1126/science.adv2111

ANIMAL BEHAVIOR

Total solar eclipse triggers dawn behavior in birds: Insights from acoustic recordings and community science

Liz A. Aguilar[1,2]*, Isaac Miller-Crews[1,2], Jeremy M. Dobris[1,3], Jo Anne Tracy[4], Paul Macklin[3], Shantanu Dixit[3], Ryan A. Jacobson[3], Rachel L. Evans[1], Evan L. McGuire[1], Daniel P. Beverly[1,5], Dustin G. Reichard[6]*, Kimberly A. Rosvall[1,2]*

On 8 April 2024, a total solar eclipse disrupted light-dark cycles for North American birds during the lead-up to spring reproduction. Compiling more than 10,000 community observations and artificial intelligence analyses of nearly 100,000 vocalizations, we found that bird behavior was substantially affected by these few minutes of unexpected afternoon darkness. More than half of wild bird species changed their biological rhythms, with many producing a dawn chorus in the aftermath of the eclipse. This natural experiment underscores the power of light in structuring animal behavior: Even when "night" lasts for just 4 minutes, robust behavioral changes ensue.

Humans have been captivated by total solar eclipses for millennia, and the 2024 "Great American Eclipse" on 8 April was no exception. April in North America is an interesting time for birds, many of which are preparing for their once-in-a-lifetime chance at reproduction. As tens of millions of people looked to the sky for their own once-in-a-lifetime experience, many wondered how wild birds would respond because birds use light to time important behaviors on a seasonal and daily basis (*1*, *2*). Because a total solar eclipse occurs in the same location once every three or four centuries (*3*), most free-living birds, like most people, have never seen day turn quickly to night, only to return again minutes later. Leveraging this natural experiment, we used autonomous recording units, machine learning, and community observations collected from Mexico to Canada to quantify how wild birds responded to this unexpected and sudden change in light.

Prior research lends some insight into this question, mainly through localized, anecdotal, or species-specific accounts (*4*, *5*). For example, during a 1932 eclipse, New England residents described "subdued" domestic poultry, cattle heading toward their barn, and frogs beginning their dusk chorus (*6*). In an observational study of zoo animals during the August 2017 eclipse, diurnal birds returned to evening roosts, whereas nocturnal species increased activity as totality approached (*7*). Also in 2017, this 2.5-min eclipse changed the vocalization rate for four bird species in Nebraska, and a soundscape analysis showed an increase in species richness during and after totality (*8*). Big data approaches are also using solar eclipses as natural experiments on the power of light. For example, Nilsson and colleagues used Doppler radar to monitor biotic airspace during the 2017 eclipse, noting decreased activity before totality and more idiosyncratic bursts of activity during totality (*9*). Concurrently with our study of the 2024 eclipse, Mann and colleagues sampled bird vocal activity at more than 300 locations (most in partial eclipse) and found that vocalizations were only affected in areas with at least 99% solar obscuration (*10*). Together, these findings emphasize that totality alters bird behavior, underscoring the need for new analyses of nonvocal behavior and species-specific effects.

Community science projects may resolve these uncertainties because they foster observations at a scale that is not otherwise possible. Such publicly collected data, also referred to as "citizen science" or "participatory science" (*11*), are accelerating discoveries in many fields (*12*–*16*), including ongoing projects on wild birds (*17*). For the 8 April 2024 solar eclipse, totality lasted for 2 to 4 min, with the Moon's shadow racing ~2500 km in a couple of hours (Fig. 1). To capitalize on the intense human interest surrounding this brief event, we created a smartphone app called "SolarBird," designed for users with zero bird-watching expertise. We publicized the app through local and national media, schools, and birding groups, gaining almost 11,000 observations. Users were asked to find a bird and observe it for 30 s, clicking up to 10 boxes to document its behavior (such as singing, flying, and eating) (fig. S1). We analyzed these data in relation to totality, and the app calculated the Sun's obscuration by means of GPS and time stamps [supplementary materials (SM), materials and methods].

To contextualize the app observations, we separately audio-recorded avian vocalizations before, during, and after totality on a localized scale. We were especially interested in sound because many birds use vocalizations to establish territories and attract mates (*18*, *19*), and the timing of the 8 April 2024 solar eclipse overlapped with the annual peak of these behaviors during the lead-up to breeding in the lower Midwest of the United States. Avian vocal output often peaks daily around dawn and dusk (*18*), when light levels change most dramatically, particularly near the spring equinox in temperate regions (the time and location of this eclipse). Using autonomous recording units, we quantified all birds vocalizing within microphone range (*20*) of 14 locations in southern Indiana (Fig. 1, inset). Autonomous recording units have previously facilitated key insights on vocal behavior and biodiversity (*21*), and coupled with machine learning (*22*), scientists can quantify vocalizations by species with limited human oversight (*23*). In particular, the artificial neural network BirdNET can identify more than 6000 bird species (*23*, *24*). Although this technology is relatively new (*25*), it is already mapping avian diversity with fewer person-hours than traditional point counts (*10*, *26*–*29*), accelerating scientific discovery at previously infeasible scales.

On the basis of prior evidence from solar eclipses (*4*–*9*) and the observation that light is often used to entrain biological rhythms (*1*, *2*, *30*), we hypothesized that the total solar eclipse would disrupt normal bird behavior. Specifically, we predicted that birds would exhibit dusk-like behaviors during totality, followed by reinitiation of morning behaviors, such as the dawn chorus, to coincide with the pseudo-dawn after totality.

Results and discussion

Observations by the public show marked effects on bird behavior

We filtered SolarBird data to focus on 6951 observations submitted by 1174 distinct users in the path of totality on April 8 (Fig. 1, black circles; data S1; and SM materials and methods). With user GPS and time stamps, we categorized observations as "before," "during," or "after" totality, the point when the Sun was 100% obscured. We used binomial generalized linear models to analyze bird behaviors during each period. Vocalizations (songs or calls) were the most common observation, with users reporting significantly higher rates during totality than in periods before or after (Fig. 2A and table S1). This pattern is consistent with the burst of vocalizations that some species exhibit around sunset.

[1]Department of Biology, Indiana University, Bloomington, IN, USA. [2]Center for the Integrative Study of Animal Behavior, Indiana University, Bloomington, IN, USA. [3]Luddy School of Informatics, Computing, and Engineering, Indiana University, Bloomington, IN, USA. [4]Office of Research, College of Arts and Sciences, Indiana University, Bloomington, IN, USA. [5]O'Neill School of Public and Environmental Affairs, Indiana University, Bloomington, IN, USA. [6]Department of Biological Sciences, Ohio Wesleyan University, Delaware, OH, USA.
***Corresponding author. Email: aguilare@iu.edu (L.A.A.); dgreicha@owu.edu (D.G.R.); krosvall@iu.edu (K.A.R.)**

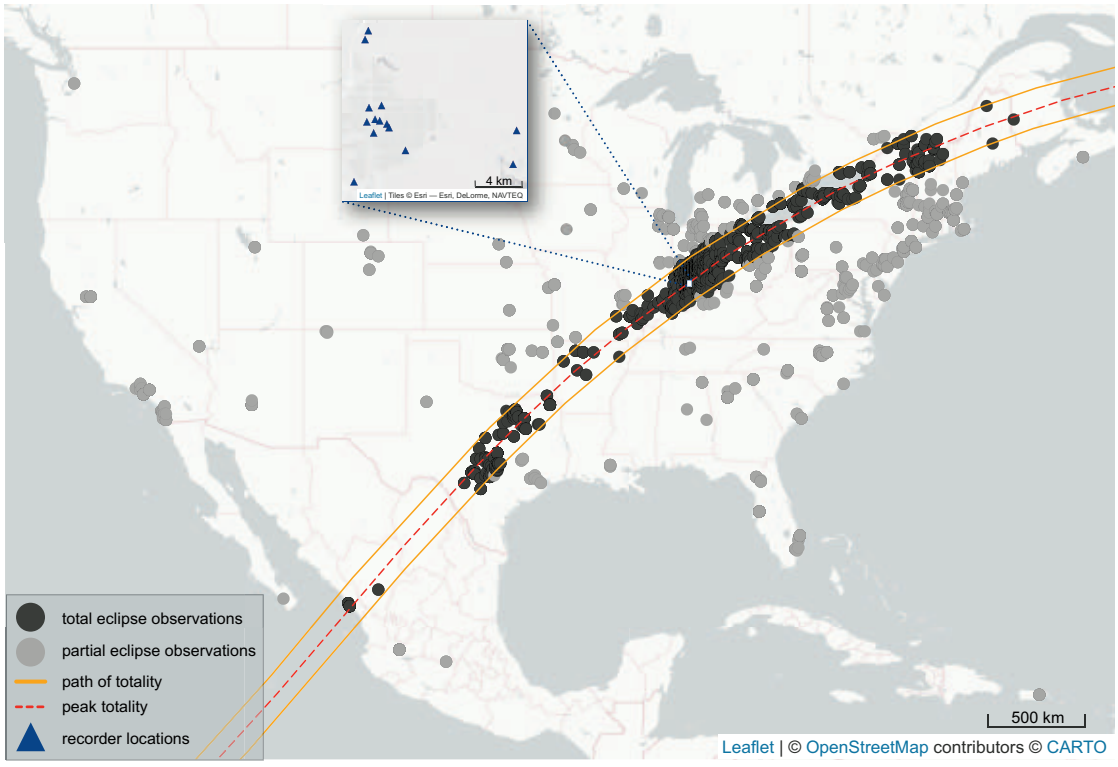


Fig. 1. Location of data collection. Circles indicate distinct SolarBird app observations submitted on 8 April 2024. Observations in the path of totality (100% obscuration; black) are the focus of our core analyses. Results from the path of partiality (5 to 99.9% obscuration; gray) are reported in fig. S2 and table S2. (Inset) Blue triangles (around Bloomington, Indiana) indicate locations for autonomous recording units.

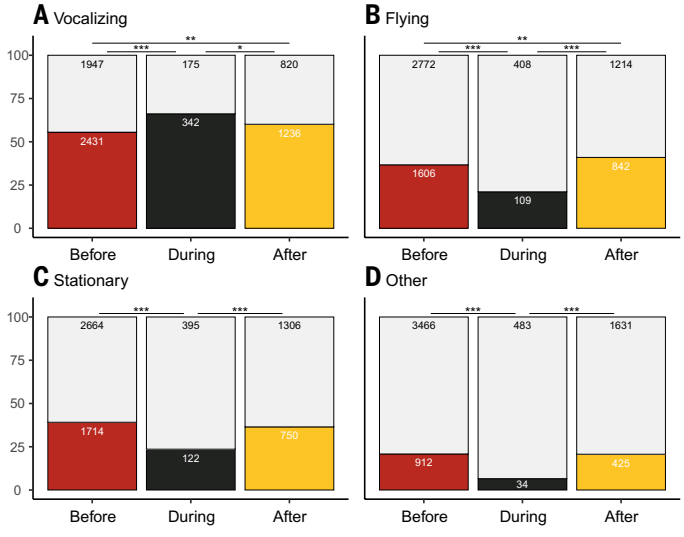


Fig. 2. Bird behaviors documented by SolarBird app users in the path of totality. Colored bars indicate observations submitted on 8 April before totality (Before; red), during totality (During; black), and after totality (After; yellow). (**A** and **B**) Reports of vocalizations and flying were significantly different between all three periods, whereas (**C** and **D**) reports of stationary and other were significantly lower only during totality. $*P < 0.05$, $**P < 0.01$, $***P < 0.001$. Exact P values are provided in table S1. Results outside the path of totality are reported in fig. S2 and table S2.

By contrast, observations of birds flying, remaining stationary, or other behaviors were documented at significantly lower rates during totality (Fig. 2, B, C, and D, and table S1). These totality-associated increases in vocalization and decreases in nonvocal behaviors may stem from observer bias; light levels during totality were low (11.3 ± 1.1 lux, mean ± SD) (fig. S4), and observers may have reported what they heard while viewing the Sun's corona. However, vocalizations and flying were both more commonly reported after versus before totality (Fig. 2, A and B, and table S1); this shift cannot be explained by differences in visibility. Instead, these results suggest that both behaviors increased after totality, which is consistent with a burst of activity after sunrise. Overall, these patterns were not found outside the path of totality (fig. S2 and table S2), where partial obscuration ranged from 5.8 to 99.9% (fig. S3).

AI shows that some species are especially sensitive to light

Our own recordings also documented marked changes in bird vocalizations. Across 14 locations near Bloomington, Indiana (39.16°N, 86.53°W), we detected 52 species on the afternoon of 8 April 2024 (threshold for inclusion: high confidence and more than 10 distinct detections across at least five recorders) (SM materials and methods and data S2). Totality began at approximately 15:05 Eastern Time (SM materials and methods) and lasted for about 4 min, and we focused on the 60 min before and after totality. After processing these 124 min with BirdNET (SM materials and methods), we detected 15,606 vocalizations from these 52 species (Fig. 3 and data S3). This total was 20 to 50% more than what we detected during the same afternoon 124 min on the day before (10,322) or after (13,008). For a subset of species, we validated these artificial intelligence (AI) detections with an expert birder (E.L.M.), who scored excerpts by ear using the event-recording software JWatcher v1.0. Human-scored counts and AI-derived counts from these same time periods were significantly correlated [generalized linear model (GLM): $t_{18} = 3.588$, $P = 0.002$, $d^2 = 0.419$] (fig. S7B). BirdNET detected fewer vocalizations than did the trained and consistent human (fig. S7), but BirdNET was a proportional reflection of human-scored vocalizations.

Responses to the eclipse were not uniform among species. Using a Bayesian approach trained on the afternoons of 6, 7, and 9 April (fig. S5

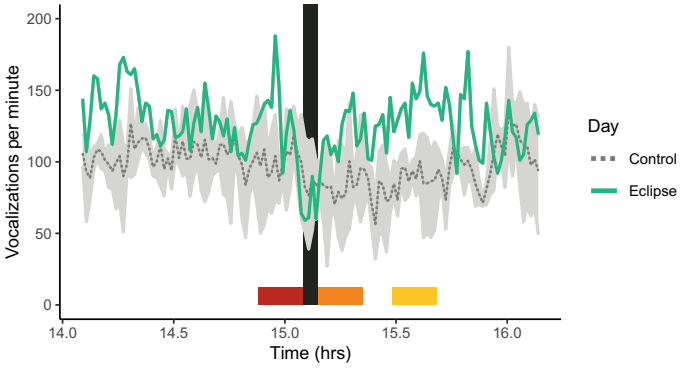


Fig. 3. Overview of vocalizations and analytical windows surrounding totality ± 1 hour. Total vocalizations were summed across 52 species for the eclipse afternoon (green) versus equivalent times on three "control" afternoons with no eclipse, with the dotted line indicating the average and the gray ribbon indicating the minimum and maximum on afternoons with no eclipse. Species-level data are the source for our formal analyses (Fig. 4), which focused on four scoring windows: 12 min just before totality (Before; red); 4 min during totality (Totality; black), 12 min just after totality (After; orange); and 12 min slightly later when a delayed dawn chorus might be expected (Later; yellow).

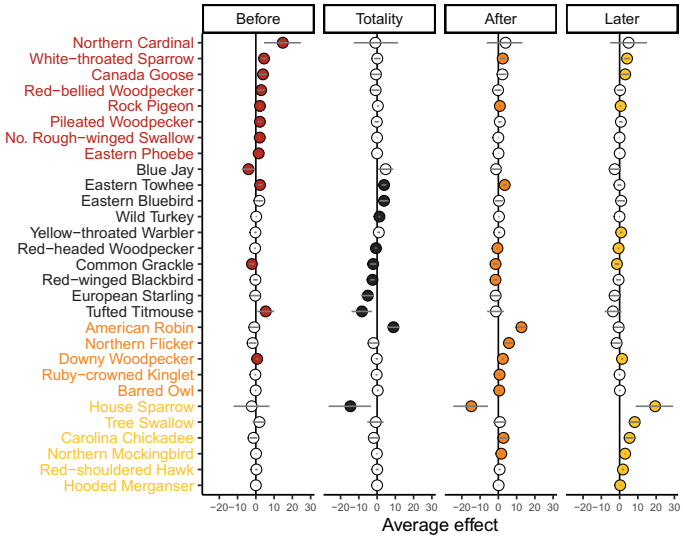


Fig. 4. Twenty-nine species responded to the eclipse. Species are sorted and colored according to the period in which they were most affected, including 12 min just before totality (Before; red), 4 min during totality (Totality; black), 12 min just after totality (After; orange), and 12 min slightly later when a delayed dawn chorus might be expected (Later; yellow). Further details on sampling periods are provided in Fig. 3 and SM materials and methods. Each point indicates an effect size (scaled per minute) with 95% confidence interval, colored if significant. All 52 species, including those not significantly affected, are shown in fig. S6.

and data S3), we found that 29 of 52 focal species were affected in at least one time period (Fig. 4). In the 12 min before the eclipse (hereafter "before"), when light levels were especially different from a normal day (SM materials and methods), we documented significant effects on 11 species, most of which (10 of 11) vocalized at higher rates than usual for that time of day.

During totality, 12 species were affected, with half decreasing and half increasing vocalization rate, relative to "control" afternoons with no eclipse. American robins (*Turdus migratorius*) displayed the strongest increase during the eclipse (nearly five times greater than in a typical afternoon). Considering that robins are the most abundant in our recordings and also ubiquitous across the United States, it is possible that the robins' vocal burst may partially account for the significant increase in vocalizations reported by app users.

The largest number of species ($n = 19$) significantly adjusted their vocalization rate after totality ended, either in the 12 min immediately after totality ("after") or the 12 min centered around 30 min after totality when a delayed dawn chorus might occur ("later"). Nearly all post-eclipse changes were significant increases relative to an afternoon with no eclipse, which is consistent with a pseudo-dawn chorus. Barred owls (*Strix varia*) produced four times as many calls on the eclipse afternoon compared with control afternoons, and American robins, which are notorious for their boisterous predawn chorus, vocalized at six times their normal rate just after totality.

Dawn chorus behavior is repeatable and predicts eclipse behavior

Next, we asked whether dawn and dusk behavior predicted behavior immediately before or during totality (akin to dusk) as well as immediately after totality or ~30 min later (akin to dawn). Using the two most recent dusks (6 and 7 April) and dawns (7 and 8 April), we used BirdNET to score 2-hour periods centered on the transition between civil twilight and sunrise or sunset. Using all the same parameters and thresholds as before, this yielded 47,932 more vocalizations (data S2 and S3). Vocalization rates (per min per species) were consistent across consecutive dawns and consecutive dusks, with similar onset and offset times each day (fig. S8). For example, American robins and barred owls vocalize most when it is still dark out, tapering by morning civil twilight and increasing again near evening civil twilight (fig. S5). Eastern towhees and European starlings exhibit a burst of vocalization in the morning around civil twilight and sunrise, respectively, but around sunset, only towhees increase their vocalization (fig. S5). Still other species vocalize continuously or off and on throughout a typical day, with no crepuscular peak (such as the house sparrow and northern cardinal) (fig. S5). These findings reinforce common knowledge among birders, that each species has a relatively stereotyped vocal response to naturally occurring changes in light.

We operationalized the dawn (or dusk) chorus as "present" if the species' per minute morning (or evening) peak showed a 100% increase relative to the afternoon (figs. S9 and S10) and used binomial regressions to assess whether dawn or dusk behavior predicted eclipse behavior (SM materials and methods). Because species with a robust chorus naturally display the greatest behavioral shift associated with everyday changes in light, we expected them to be overrepresented in those species affected by the eclipse. This prediction was not supported for dusk behavior, which was not predictive of eclipse behavior in the 12 min before (GLM: $z_{51} = 1.158$, $P = 0.25$) or 4 min during totality (GLM: $z_{51} = 0.951$, $P = 0.34$). However, species with a dawn chorus were more likely than expected by chance to exhibit a significant change in vocalization in the 12 min after totality (GLM: $z_{51} = 2.023$, $P = 0.04$) but not in the 12 min centered around 30 min after totality (GLM: $z_{51} = 0.458$, $P = 0.65$). In essence, even though the false night only lasted for 4 min, species that naturally produce a dawn chorus immediately began a new dawn chorus when the false night ended.

Implications

Changes in light surrounding dawn and dusk are thought to be the primary cue structuring circadian changes in behavior for most organisms (*30*). In this work, we show that when the light-dark cycle was altered by a total solar eclipse, entrained biological rhythms were disrupted for more than half of the observed wild bird species. This natural experiment—which essentially switched off the Sun for 4 min in the middle of an otherwise normal spring afternoon—is distinctive for several reasons. For one, light experiments often start from constant

light or constant dark (*30*, *31*) in laboratory environments that may not recapitulate natural behaviors or physiology (*32*). However, the total solar eclipse offers a large-scale manipulation that is both naturalistic and decoupled from time of day. Together, our AI- and app-derived data both underscore that the return of light is an especially salient cue, even when that switch occurs at an unexpected time (half a day early) and after an exceptionally short "night" (0.5% the length of the previous night). Eclipse-associated changes in light are also decoupled from other major environmental shifts that accompany ordinary midday changes in light (such as thunderclouds), although atmospheric pressure, temperature, and even plant photochemistry change surrounding a total solar eclipse (*33*) and may have played a role [but see (*10*)].

The reverse experiment—artificial light at night (ALAN)—affects everything from behavior to biodiversity, mediated through sometimes subtle changes in biological rhythms (*34*–*36*) and neurophysiology (*31*, *37*, *38*). With ALAN of just a few lux affecting ecosystems worldwide (*31*), we urgently need to understand why some organisms are more affected than others. Our results provide distinctive experimental evidence on these interspecific differences in light sensitivity (Fig. 4), including 23 species that were spread across different avian orders but were not significantly affected by the eclipse (fig. S6). Although it is possible that some species may have switched the nature of their vocalizations (for example, from mating to alarm calls), their otherwise behavioral insensitivity implies sensory mechanisms that maintain biological rhythms despite unusual changes in light.

Our study also highlights the underused ability of AI and community science to enrich one another. For example, publicly collected data can sometimes suffer from sampling bias (*12*), technology barriers (*15*), or quality control (*14*), yet our simple smartphone app was designed for users without specialized background or equipment. With their repeated observations, we learned that eclipse-related changes in vocalizations were accompanied by changes in movement (Fig. 2), and elements of our localized AI findings apply at a continental scale. In turn, our recordings provide species-level results (Fig. 4) that expand the public's observations (Fig. 2). Moving ahead through the Anthropocene, these technologies promise to lower the bar for active public engagement in science while deepening our understanding of the natural world.

REFERENCES AND NOTES

1. K. J. Gaston, J. P. Duffy, S. Gaston, J. Bennie, T. W. Davies, *Oecologia* **176**, 917–931 (2014).
2. T. D. Williams, *Physiological Adaptations for Breeding in Birds* (Princeton Univ. Press, 2012).
3. NASA, https://svs.gsfc.nasa.gov/5222.
4. G. W. Uetz *et al.*, *Ethology* **96**, 24–32 (1994).
5. M. L. Ferro, *Entomol. News* **129**, 348–359 (2020).
6. W. M. Wheeler, C. V. MacCoy, L. Griscom, G. M. Allen, H. J. Coolidge, *Proc. Am. Acad. Arts Sci.* **70**, 33–70 (1935).
7. A. Hartstone-Rose *et al.*, *Animals* **10**, 587 (2020).
8. E. M. B. Buckley *et al.*, *Ecol. Indic.* **95**, 353–369 (2018).
9. C. Nilsson, K. G. Horton, A. M. Dokter, B. M. Van Doren, A. Farnsworth, *Biol. Lett.* **14**, 20180485 (2018).
10. D. Mann *et al.*, *Sci. Rep.* **15**, 10113 (2025).
11. E. R. Ellwood *et al.*, *Trends Ecol. Evol.* **38**, 485–489 (2023).
12. J. R. B. Palmer *et al.*, *Nat. Commun.* **8**, 916 (2017).
13. G. N. Bratman *et al.*, *Sci. Adv.* **5**, eaax0903 (2019).
14. D. Fraisl *et al.*, *Nat. Rev. Methods Primers* **2**, 64 (2022).
15. J. K. Sheard *et al.*, *Philos. Trans. R. Soc. Lond. B Biol. Sci.* **379**, 20230106 (2024).
16. D. C. McKinley *et al.*, *Biol. Conserv.* **208**, 15–28 (2017).
17. B. L. Sullivan *et al.*, *Biol. Conserv.* **142**, 2282–2292 (2009).
18. C. A. Staicer, D. A. Spector, A. G. Horn, in *Ecology And Evolution Of Acoustic Communication In Birds*, D. E. Kroodsma, E. H. Miller, Eds. (Cornell Univ. Press, 1996), pp. 426–453.
19. C. K. Catchpole, P. J. B. Slater, *Bird Song: Biological Themes And Variations* (University Press, 1995).
20. D. J. Mennill, *Bioacoustics* **33**, 157–177 (2024).
21. S. Ross *et al.*, *Funct. Ecol.* **37**, 959–975 (2023).
22. D. Tuia *et al.*, *Nat. Commun.* **13**, 792 (2022).
23. S. Kahl, C. M. Wood, M. Eibl, H. Klinck, *Ecol. Inform.* **61**, 101236 (2021).
24. C. M. Wood, S. Kahl, *J. Ornithol.* **165**, 777–782 (2024).
25. C. Pérez-Granados, *Ibis* **165**, 1068–1075 (2023).
26. S. S. Sethi *et al.*, *Proc. Natl. Acad. Sci. U.S.A.* **121**, e2315933121 (2024).
27. Y. Lavner, R. Melamed, M. Bashan, Y. Vortman, *Ecol. Inform.* **80**, 102528 (2024).
28. B. Hack, C. A. Cansler, M. Z. Peery, C. M. Wood, *Condor* **126**, duad065 (2023).
29. L. Bielski, C. A. Cansler, K. McGinn, M. Z. Peery, C. M. Wood, *J. Field Ornithol.* **95**, art4 (2024).
30. R. G. Foster, S. Hughes, S. N. Peirson, *Biology* **9**, 180 (2020).
31. M. Grubisic *et al.*, *Sustainability* **11**, 6400 (2019).
32. R. M. Calisi, G. E. Bentley, *Horm. Behav.* **56**, 1–10 (2009).
33. D. P. Beverly *et al.*, *Sci. Rep.* **9**, 8839 (2019).
34. K. J. Gaston, T. W. Davies, S. L. Nedelec, L. A. Holt, in *Annual Review of Ecology, Evolution, and Systematics*, vol. 48, D. J. Futuyma, Ed. (2017), pp. 49–68.
35. U. Tuomainen, U. Candolin, *Biol. Rev. Camb. Philos. Soc.* **86**, 640–657 (2011).
36. K. J. Gaston, A. Sánchez de Miguel, *Annu. Rev. Environ. Resour.* **47**, 373–398 (2022).
37. G. C. Brainard, B. A. Richardson, L. J. Petterborg, R. J. Reiter, *Brain Res.* **233**, 75–81 (1982).
38. O. J. Marston *et al.*, *Mol. Brain* **1**, 19 (2008).
39. S. Dixit, R. Jacobson, MathCancer/Solarbird: Version 1.0.1: Integrating Zenodo (1.0.1). Zenodo (2025); https://doi.org/10.5281/zenodo.15750568.
40. I. Miller-Crews, imillercrews/Eclipse_bird: v1. Zenodo (2025); https://doi.org/10.5281/zenodo.15750579.

ACKNOWLEDGMENTS

We are grateful to M. Clapp and E. Derryberry for early advice, to T. Freeberg for additional recorders, to S. Marties for analytical support, to C. Pilachowski for the initial vision of SolarBird and early encouragement, to T. Mackin and IU Press for support with app distribution, to the reviewers for their feedback, and to all app users for sharing their eclipse experience with us (listed by name, with permission, in the supplementary text). **Funding:** This work was supported by NASA Indiana Space Grant Consortium F90002188.02.416 (to L.A.A. and K.A.R.); Ohio Wesleyan University (to D.G.R.); National Institutes of Health Common Themes in Reproductive Diversity Training Fellowship 2T32HD049336-16A1 (to I.M.-C.); National Science Foundation IOS-CAREER 1942192 (to K.A.R.), with REU support (to J.M.D.); National Science Foundation Graduate Research Fellowship (to L.A.A.); and United States Department of Agriculture–National Institute of Food and Agriculture 2023-67012-40083 (to D.P.B.). **Author contributions:** Conceptualization and funding acquisition: L.A.A., J.A.T., I.M.-C., D.G.R., K.A.R. App development: L.A.A., P.M., S.D., R.A.J., J.A.T. App validation and user interface design: S.D. AI validation and analyses: J.M.D., I.M.-C., K.A.R. Implementation in the field: R.L.E., E.L.M., D.G.R., D.P.B., K.A.R. Formal analysis and visualization: I.M.C., L.A.A., J.M.D., S.D., K.A.R. Writing – original: K.A.R., D.G.R., L.A.A. Writing – review & editing: All. **Competing interests:** The authors declare that they have no competing interests. **Data and materials availability:** All data are available in the main text and/or supplementary materials, with source code for SolarBird app development and scripts available on Zenodo and Github (*39*, *40*).

License information: Copyright © 2025 the authors, some rights reserved; exclusive licensee American Association for the Advancement of Science. No claim to original US government works. https://www.science.org/about/science-licenses-journal-article-reuse

SUPPLEMENTARY MATERIALS

science.org/doi/10.1126/science.adx3025
Materials and Methods; Supplementary Text; Figs. S1 to S11; Tables S1 to S3; References (*41*–*45*); MDAR Reproducibility Checklist; Data S1 to S3

Submitted 14 March 2025; accepted 19 August 2025

10.1126/science.adx3025

CELL BIOLOGY

Ubiquitin-mediated mitophagy regulates the inheritance of mitochondrial DNA mutations

Michele Frison[1,2], Brandon S. Lockey[1,2], Yu Nie[1,2], Zoe Golder[1,2], Eleni Theiaspra[1,2], Cameron D. Ryall[1,2], Camilla Lyons[1,2]†, Stephen P. Burr[1,2], Malwina Prater[1,2]‡, Lyuba V. Bozhilova[1,2]§, Angelos Glynos[1,2]‡, James B. Stewart[3], Nick S. Jones[4], Marcos R. Chiaratti[5], Patrick F. Chinnery[1,2]*

Mitochondrial synthesis of adenosine triphosphate is essential for eukaryotic life but is dependent on the cooperation of two genomes: nuclear and mitochondrial DNA (mtDNA). mtDNA mutates ~15 times as fast as the nuclear genome, challenging this symbiotic relationship. Mechanisms must have evolved to moderate the impact of mtDNA mutagenesis but are poorly understood. Here, we observed purifying selection of a mouse mtDNA mutation modulated by *Ubiquitin-specific peptidase 30* (*Usp30*) during the maternal-zygotic transition. In vitro, *Usp30* inhibition recapitulated these findings by increasing ubiquitin-mediated mitochondrial autophagy (mitophagy). We also found that high mutant burden, or heteroplasmy, impairs the ubiquitin-proteasome system, explaining how mutations can evade quality control to cause disease. Inhibiting USP30 unleashes latent mitophagy, reducing mutant mtDNA in high-heteroplasmy cells. These findings suggest a potential strategy to prevent mitochondrial disorders.

Mitochondria play a pivotal role in cell development, homeostasis, and death through their ability to integrate complex signals from the cell nucleus and environment (*1*). A critical mitochondrial function is the synthesis of adenosine triphosphate (ATP). ATP is a crucial energy source used in diverse cell processes including protein homeostasis and the maintenance of ionic gradients across membranes. Nearly all ATP is produced under aerobic conditions by oxidative phosphorylation. In mammals, this requires five multimeric enzyme complexes assembled from >90 protein subunits on the inner mitochondrial membrane. Thirteen essential subunits are encoded by the maternally inherited mitochondrial DNA (mtDNA), but most are synthesized in the cytoplasm from nuclear gene transcripts before being translocated into the organelle. Thus, the optimal generation of ATP depends on the cooperation of two distinct genomes that can only interact through their gene products. This complex arrangement is a consequence of the endosymbiotic origins of mitochondria ~2 billion years ago, but since that time, nuclear- and mtDNA-encoded genes have independently acquired many new mutations. Maintaining compatibility of genes from these two cellular compartments is fundamental for eukaryotic life, but the mechanisms responsible are poorly understood.

[1]Department of Clinical Neurosciences, School of Clinical Medicine, University of Cambridge, Cambridge Biomedical Campus, Cambridge, UK. [2]Medical Research Council Mitochondrial Biology Unit, University of Cambridge, Cambridge Biomedical Campus, Cambridge, UK. [3]Biosciences Institute, Faculty of Medical Sciences, Newcastle University, The Cookson Building, The Medical School, Framlington Place, Newcastle Upon Tyne, UK. [4]Department of Mathematics and Centre for the Mathematics of Precision Healthcare, Imperial College London, South Kensington, London, UK. [5]Department of Genetics and Evolution, Federal University of São Carlos, São Carlos, Brazil. *Corresponding author. Email: pfc25@cam.ac.uk †Present address: Epigenetics and Neurobiology Unit, European Molecular Biology Laboratory (EMBL) Rome, Monterotondo, Italy. ‡Present Address: Altos Labs Cambridge Institute, Cambridge, UK. §Present address: Nuffield Department of Women's and Reproductive Health, University of Oxford, Women's Centre, John Radcliffe Hospital, Oxford, UK.

Unlike the nuclear genome, each cell contains hundreds to thousands of copies of mtDNA that are continuously replicated independent of the cell cycle (so-called relaxed replication). This process exposes mtDNA to polymerase errors that contribute to a substitution rate ~10- to ~30-fold greater than that of the nuclear genome (*2*, *3*), making mtDNA mutations the most immediate threat to nuclear-mtDNA incompatibility. New mtDNA mutations only affect a proportion of the molecules within a cell (a state known as heteroplasmy), which enables functional complementation within an individual cell by wild-type mtDNA. Although heteroplasmy allows cells to tolerate new mtDNA alleles, it also means that severe mutations can spread throughout the population. To counteract this, a ~1000-fold reduction in cell mtDNA content has been observed in primordial germ cells (PGCs) of the developing female germ line of several vertebrate species, including humans (*4*). This creates a "genetic bottleneck," which accelerates the segregation of heteroplasmic alleles from low to high levels over just one or two generations, exposing deleterious mutations to selection at the organism level. However, milder mutations can escape this mechanism, eventually becoming the only mtDNA type (homoplasmy) in a cell, an individual, or different human populations. Although each mutation can be tolerated, mildly deleterious alleles accumulating down the maternal line would eventually cause "mutational meltdown" of the species (*5*). Cellular mechanisms must therefore have evolved to counteract this but are largely unknown.

There is emerging evidence across the animal kingdom of selection against deleterious heteroplasmic alleles during intergenerational maternal transmission (*4*), influenced by the nuclear genetic background (*6*). Genome-wide association studies implicate numerous loci (*7*, *8*), but the precise molecular basis has yet to be defined. Mitophagy, or the selective removal of mitochondria through the autophagy pathway, is the leading candidate mechanism (*9*, *10*), but there is limited evidence for this in vivo (*10*). Moreover, if there is an effective quality control (QC) mechanism, it is unclear how pathogenic mtDNA mutations ever reach levels that cause disease. Here, we found that selection during maternal transmission is modulated by ubiquitin-mediated mitophagy (UMM), which is inhibited by high levels of a pathogenic mtDNA mutation, allowing mutant alleles to be propagated from mother to offspring. Genetically or pharmacologically up-regulating endogenous UMM reduced the heteroplasmy levels of pathogenic mtDNA, implicating it as a therapeutic target.

USP30 loss enhances embryonic purifying selection

In humans, most inherited heteroplasmic pathogenic mtDNA mutations affect tRNA genes (*11*). To understand the inheritance mechanisms, we studied the mouse m.5024C>T $tRNA^{ala}$ (*mt-Ta*) mutation (*12*, *13*), which corresponds to a human disease–causing variant (*14*, *15*). Genetic ablation of *Bcl2l13* increases offspring heteroplasmy levels in m.5024C>T mice (*10*), implicating receptor-dependent autophagy in selection. Ubiquitin-specific peptidase 30 (USP30) is the mitochondria-resident deubiquitinase (DUB) (*16*), and its loss increases ubiquitination of mitochondrial proteins, triggering UMM (*17*–*19*). To determine whether mitochondrial QC was specifically involved, we crossed a constitutive *Usp30* knockout with a heteroplasmic m.5024C>T line and investigated transmission (Fig. 1A). Immunoblot analysis confirmed the complete absence of USP30 in our $Usp30^{-/-}$ mice, which did not affect the levels of other mitochondrial proteins or NADH–NAD^+ (reduced form of NAD^+–nicotinamide adenine dinucleotide) balance (fig. S1, A to D). Mice born of heterozygous parents had no detectable phenotype with a balanced Mendelian ratio (Fig. 1A; χ^2 test $P = 0.22$), showing the absence of USP30 did not affect fecundity.

Studying 52 mothers and 816 offspring, we failed to generate mice with >85% m.5024C>T (Fig. 1B and fig. S1E), consistent with previous reports (*12*, *20*), which suggested selection against high mutation loads during transmission, as observed in humans (*20*). The line of best fit comparing heteroplasmy levels in $Usp30^{+/-}$ mothers to those of their

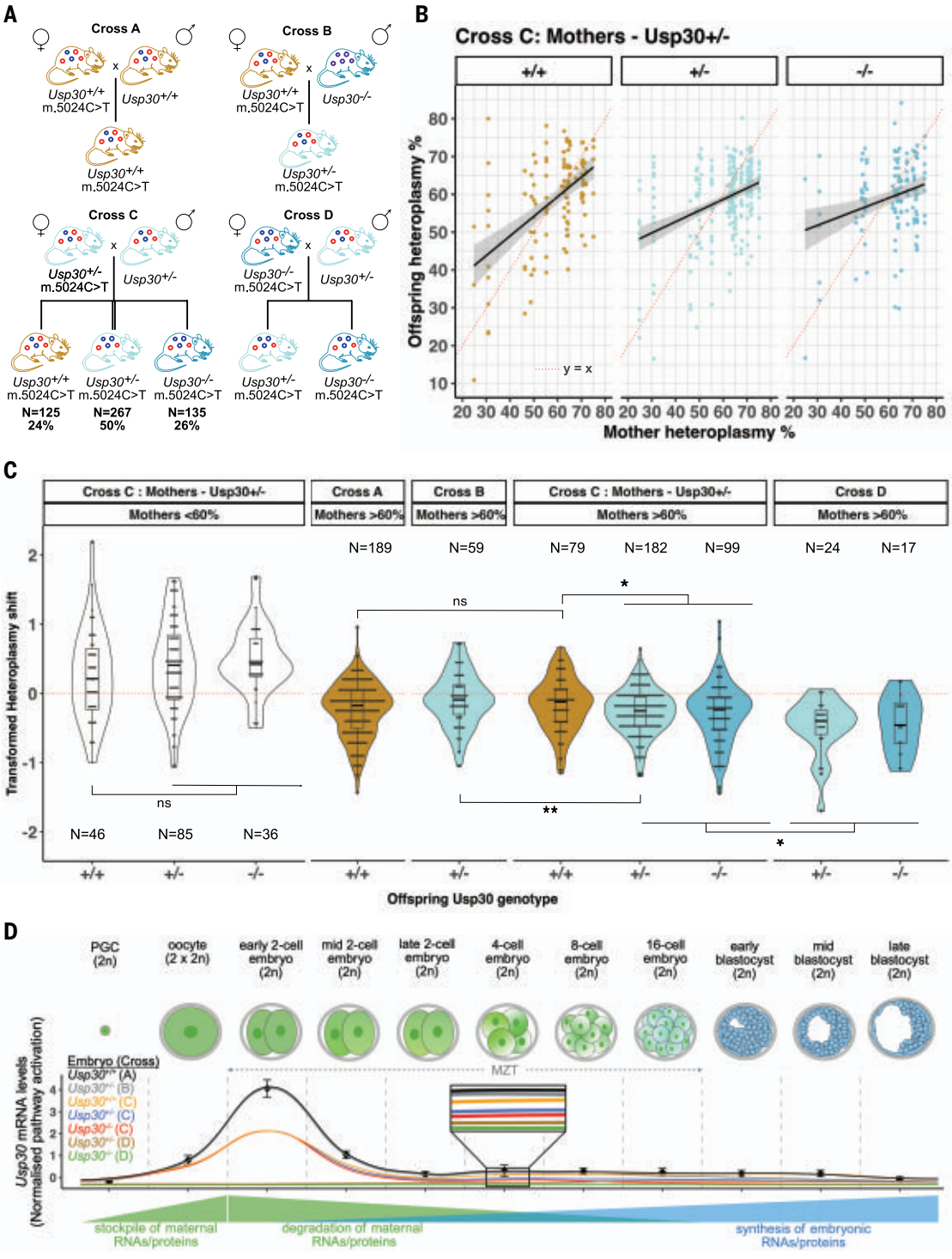


Fig. 1. *Usp30* ablation decreases m.5024C>T heteroplasmy during the embryonic MZT. (**A**) Four different crosses were used to quantify the effect of introducing a nuclear *Usp30* knockout allele, at different time points in germline development, on maternal transmission of mtDNA heteroplasmy. As shown in (D), PGCs and oocytes express both maternal alleles, whereas paternal alleles start expressing in the MZT. (**B**) Heteroplasmy in cross C mother-to-offspring pairs (26 $Usp30^{+/-}$ mothers and 527 offspring with the three *Usp30* genotypes) with linear regression trendlines. Dotted line corresponds to $y = x$ for reference. Shaded area, 95% CIs for the regression lines. (**C**) Mother-to-offspring heteroplasmy shift using the log-odds transformation (tHS) for mothers with <60% m.5024C>T and mothers with >60% m.5024C>T across the different generations corresponding to Fig. 1A. Animal numbers per condition: cross A, $N = 189$ animals from $N = 8$ mothers; cross B, $N = 59$ animals from $N = 5$ mothers; cross C, (from $N = 8$ mothers of heteroplasmy <60%: *Usp30*+/+, $N = 46$; +/−, $N = 85$; −/−, $N = 36$) (from $N = 19$ mothers of heteroplasmy >60%: +/+, $N = 79$; +/−, $N = 182$; −/−, $N = 99$); cross D, (from 4 mothers >60%: *Usp30*+/−, $N = 24$; −/−, $N = 17$). Mean mother heteroplasmies across >60% groups is 67.7 ± 1 and in <60% is 44.5 ± 1. $P < 0.01$ with a Welch's two-sample *t* test for the comparison of $Usp30^{+/-}$ cross B with cross C. Wilcoxon rank sum test was used for the other comparisons. NS, $P > 0.05$; $^*P < 0.05$. Bonferroni method was used for multiple test correction. (**D**) Diagram showing *Usp30* expression across developmental transmission, including the MZT, in cells of the germ line and the embryo, for the different Usp30 genotypes and crosses. Baseline expression is indicated in each cell phase with rhomboid dots as mean ± SEM and was extracted from public scRNA-seq data. The expression levels for the different *Usp30* genotypes and crosses are predicted from the public scRNA-seq data and the results of (C).

Usp30$^{+/+}$ offspring intersected the $y = x$ at ~60% mutant, consistent with the previously observed threshold for germline selection (*20*). Akaike information criterion–stepwise regression showed that the presence of at least one *Usp30* knockout allele modulated heteroplasmy inheritance in cross C offspring (Fig. 1B and fig. S1F). The heteroplasmy level in a pup depends on the level in the corresponding mother, the genetic bottleneck, and the effects of selection. It is therefore not possible to give a single figure to explain the impact of ablating Usp30 on pup heteroplasmy levels. However, for example, *Usp30*$^{+/-}$ mothers carrying ~75% mutant mtDNA transmitted an average of ~67% to *Usp30*$^{+/+}$ offspring but transmitted ~62% to *Usp30*$^{-/-}$ offspring (Fig. 1B). For mothers carrying two *Usp30* knockout alleles, the effect was doubled to ~10%. A comparison of the different genotypes by calculating the transformed heteroplasmy shift (tHS) between different mothers and their pups (*20*) confirmed that USP30 loss reduced the heteroplasmy of pups born to high-heteroplasmy mothers (Fig. 1C). There was no difference in the number of pups at weaning for any *Usp30* genotype, implying that the selection was not taking place at the whole organism level (fig. S1, G to J). Collectively, these findings suggest a reserve or latent capacity for mitochondrial QC at higher heteroplasmy levels that can be activated by suppressing USP30.

Scrutinizing the different crosses (Fig. 1, A and C) enabled us to pinpoint the developmental timing of the selection induced by USP30. The oocyte genome remains tetraploid ($2 \times 2n$) until ovulation when meiosis I is concluded, generating $2 \times n$ gametes that only become haploid on fertilization (Fig. 1D). Thus, maternal germ cells express the same alleles as the mother. After fertilization, oocyte proteins and RNAs are removed during the maternal-zygotic transition (MZT) and replaced by gene products from both parental genomes. The tHS of *Usp30*$^{+/-}$ offspring born to *Usp30*$^{+/+}$ >60% m.5024C>T mothers (cross B) was higher than the tHS of *Usp30*$^{+/-}$ offspring born of *Usp30*$^{+/-}$ mothers (cross C). Therefore, at least one maternal *Usp30* knockout allele must be present to decrease heteroplasmy, raising the possibility that USP30 is acting on maternal germ cells. A second knockout allele in the mothers doubled the tHS, showing maternal dose dependency. However, if this occurred in the female germ cells, then the same effect on tHS would also be apparent in *Usp30*$^{+/+}$ cross C offspring, born of *Usp30*$^{+/-}$ mothers. This was not the case, indicating that the mechanism must occur after fertilization but before the completion of the MZT (Fig. 1D). This is consistent with up-regulation of autophagy during this developmental period, which is required to metabolically sustain the preimplantation embryo (*21*) and remove oocyte proteins, RNAs, and paternal mtDNA (*22*). Analysis of public single-cell RNA sequencing (scRNA-seq) datasets supports this timing (Fig. 1D and fig. S2), with up-regulation of UMM pathways observed in the early embryo and *Usp30* expression peaking in the two-to-four–cell embryos. Thus, loss of *Usp30* mRNA of maternal origin coincides with an increase in expression of UMM pathways only in the MZT.

Heteroplasmy inhibits ubiquitin-mediated protein degradation, compromising UMM

To validate the latent capacity for mitochondrial QC at high heteroplasmy, we studied isogenic mouse embryonic fibroblasts (MEFs) using bafilomycin A1 (BafA1) and MG132 to measure the rate of degradation of ubiquitinated mitochondrial proteins through the lysosome and the proteasome. Comparing high-heteroplasmy (>60%) to low-heteroplasmy cells (<40%) revealed inhibition of mitochondrial ubiquitination in all three conditions (Fig. 2, A and B). Next, we determined whether m.5024C>T affects general autophagy. Immunoblotting showed no change in the bulk levels or flux of two autophagic markers, microtubule-associated protein 1 light chain 3 (LC3) A/B and sequestosome 1 (SQSTM1), at different BafA1 time points (6 and 24 hours) (Fig. 2E and fig. S3, A to D, F and G, and I to K). To determine the relative contribution of the ubiquitin-proteasome system (UPS) and autophagy to UMM, we measured autophagic flux and mitochondrial colocalization of punctae of SQSTM1, conjugated ubiquitin, WD-repeat PtdIns(3)P effector protein 2 (WIPI2), and ATG12 at steady state and with BafA1, at both time points (figs. S4 to S7). Although we did not observe a coherent change in autophagy for all markers (figs. S4, B and F; S6, B to D; and S7, B to D), we detected a decrease in the mitochondrial localization of SQSTM1 and ubiquitin punctae at high heteroplasmy (figs. S4, D and H, and S5, C and F). After both BafA1 time points, we did not observe a decrease in the amount of mitochondria covered by autophagic punctae (figs. S4, C and G; S6, E and F; and S7, E and F), unlike the effect seen on mitochondrial ubiquitination at 24 hours (Fig. 2, A and B, and fig. S5E). Lastly, we assayed the cell's ability to initiate autophagy by quantifying the WIPI2 and ATG12 punctae at differing heteroplasmy levels with metabolic stimulation (fig. S8). Again, we did not observe a coherent difference in autophagy activation between low- and high-heteroplasmy cells. Most notably, autophagosome formation was not impaired at high heteroplasmy, which corroborates our hypothesis that the m.5024C>T mutation selectively impairs mitophagy, rather than autophagy.

To explore the underlying mechanism, we analyzed differentially expressed genes (DEGs) in pathways linked to UMM in MEFs with different heteroplasmy levels (<40 vs >80%; Fig. 2C and fig. S9). Most DEGs were down-regulated at high heteroplasmy, including the ubiquitin-mediated proteolysis gene set (*23*), which was among the top hits in an unbiased single-cell transcriptome-wide analysis in m.5024C>T and m.5019C>T *mt-Ta* mice (*24*). We also found down-regulation of two proteasome subunit transcripts with no compensatory up-regulation. Bulk proteomics confirmed a decrease in components of the proteasome and the ubiquitin-mediated proteolysis pathway (Fig. 2D), without a clear effect on the autophagy or mitophagy pathways or any E3 ubiquitin ligases previously linked to mitophagy (fig. S10A). To validate the changes functionally in UPS gene expression, we assayed the rate of degradation of ubiquitinated proteins by the proteasome by comparing the accumulation of proteasome-sensitive ubiquitinated proteins (fig. S3E) in whole-cell lysates from low- and high-heteroplasmy cells (<40 vs >60%) (Fig. 2E). This showed a reduced rate of UPS-mediated degradation in high-heteroplasmy MEFs (Fig. 2F), confirming the lack of effect on the general autophagic flux or lysosome-dependent ubiquitin flux (fig. S3, I to M).

Impaired mitophagy at high heteroplasmy restores bioenergetic homeostasis

Under steady-state conditions, a decrease in the destruction of mitochondria should increase mitochondrial mass. We explored this using matrixQC, a tandem mitochondrial green fluorescent protein (mtGFP)–mCherry mitolysosomal flux reporter (*25*), to estimate the degradation rate of the mitochondrial matrix compartment (Fig. 3, A and B) and both 5-ethynyl-2′-deoxyuridine (EdU) and a DNA immunostain to quantify amount and replication rate of mtDNA (Fig. 3E). MtDNA nucleoids were increased in high-heteroplasmy cells, but the proportion that was replicating was the same as that in low-heteroplasmy MEFs (Fig. 3, G and H). Mitolysosomal flux was reduced by high levels of m.5024C>T heteroplasmy in glucose (Fig. 3D and fig. S11, A to C) and galactose (fig. S11, F and G), which renders MEFs dependent on oxidative phosphorylation, and after treatment with deferiprone (DFP), which induces mitophagy. We observed a decreased expression of *Bnip3l* (fig. S9B), which was probably causal for the decreased DFP-induced mitophagy at high heteroplasmy (*26*) but could not have been responsible for the defective mitolysosomal delivery in glucose, because high-heteroplasmy cells did not display defective recruitment of autophagosomes to mitochondria (figs. S4, C and G; S6, E and F; and S7, E and F). Upstream impairment of mitochondrial ubiquitination is thus responsible (Fig. 2, A and B, and fig. S5E). BNIP3L was not detected in our in vivo proteomics, and BNIP3, whose increase in expression is also required for DFP-induced mitophagy, was not down-regulated in mutant mice (fig. S10A).

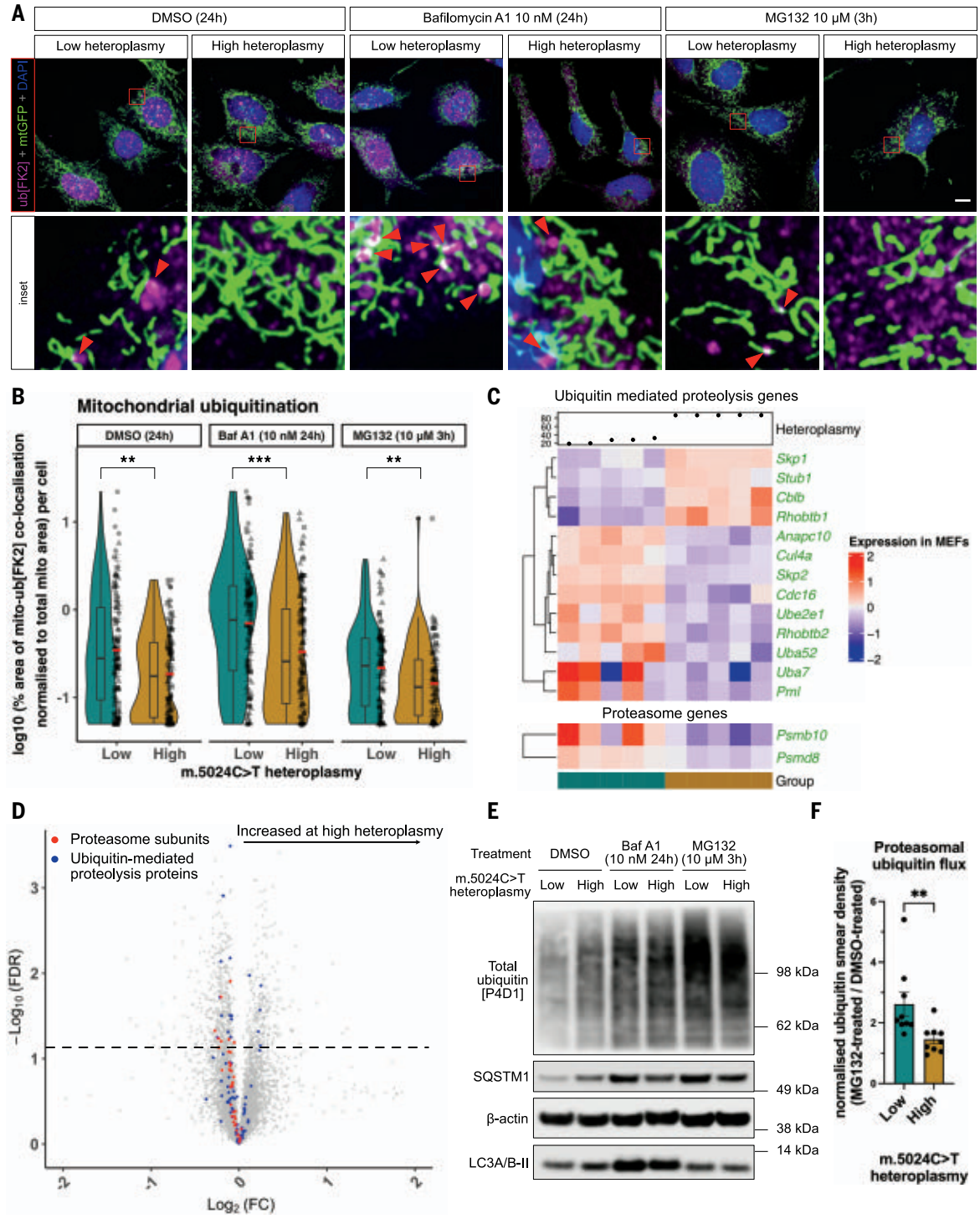


Fig. 2. Inhibition of the UPS impairs mitochondrial ubiquitination at high heteroplasmy levels. (**A**) Clonal MEFs with different m.5024C>T heteroplasmy levels were analyzed at steady state after treatment with the drug solvent dimethyl sulfoxide (DMSO), or after chemical interruption of the lysosomal flux with BafA1 or the proteasomal flux with MG132. Representative confocal images displaying colocalization between mitochondria (COX8A-targeted GFP) and conjugated ubiquitin (ub[FK2]). Red arrows indicate areas of colocalization. Scale bar, 10 µm. DAPI, 4′,6-diamidino-2-phenylindole. (**B**) Quantification of the extent of mitochondrial localization of conjugated ubiquitin, normalized to the total area of mitochondria per cell. $^{**}P < 0.01$ and $^{***}P < 0.001$ with Wilcoxon rank sum test. $N > 100$ cells per condition from at least three biological replicates. Data are shown as violin plots, boxplots, and beeswarm plots, with mean indicated in red. Dot shape indicates the biological repeat that each cell belongs to. (**C**) RNA-seq of 10 clonal MEF lines with differing heteroplasmy. DEGs extracted with DeSeq2 from the KEGG (Kyoto Encyclopedia of Genes and Genomes) pathways mmu04120 and mmu03050 are displayed. (**D**) Tandem mass tag (TMT) proteomics of high-heteroplasmy (>60%) m.5024C>T mouse brain cortex, highlighting the differential levels of proteins of the KEGG pathways mmu03050 and mmu04120. $N = 6$ animals (3 high-heteroplasmy m.5024C>T, 3 wild type). FC, fold change; FDR, false discovery rate. (**E**) Representative immunoblot from low- and high-heteroplasmy MEFs showing the levels of high-molecular-weight ubiquitin and the two main autophagy markers, at steady state and after blockage of the autophagic or proteasomal flux. β-actin was used as a loading control. (**F**) Quantification of the magnitude of increase in high-molecular-weight ubiquitinated proteins after inhibition of the proteasome in low and high m.5024>T MEFs. Mann-Whitney $P < 0.05$. $N = 9$ per condition (three biological replicates from three independent sets of clones). Errors bars, SEM. Heteroplasmy in immunoblot experiments: low, <40%; high, >60%.

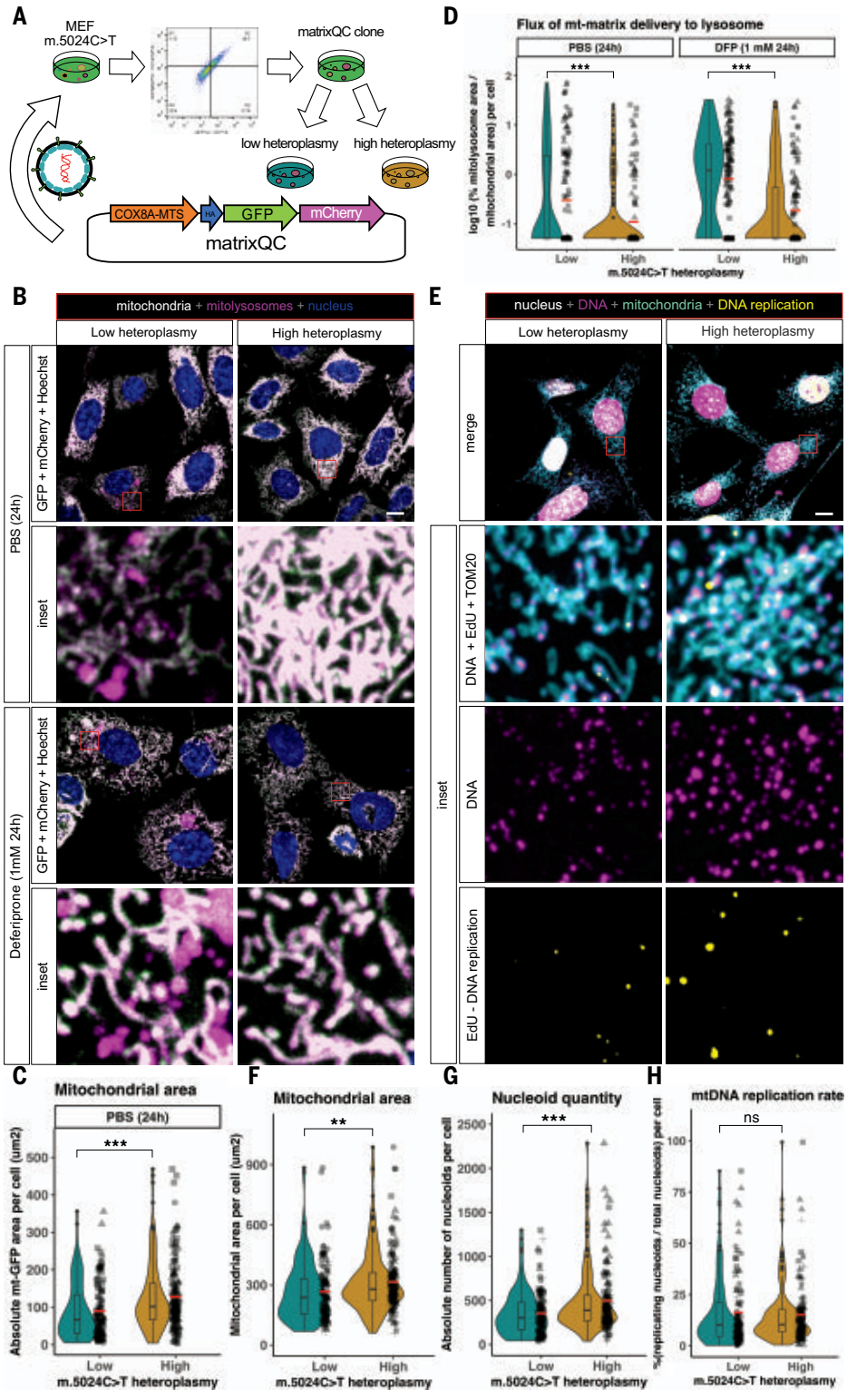


Fig. 3. m.5024C>T impairs mitophagy, leading to the accumulation of mitochondria and mtDNA. (**A**) MatrixQC is a GFP-mCherry reporter targeted to the mitochondrial matrix. GFP is quenched in acidic environments, whereas mCherry is not. Thus, $GFP^{-}mCherry^{+}$ signal identifies areas of the mitochondrial matrix that was delivered to the lysosome. Double positive signal localizes on the whole mitochondrial network. The matrixQC transgene was lentivirally transduced into a population of m.5024C>T MEF cells at a concentration that resulted in an average single insertion site. Cells were then subcloned two times to produce two populations of cells carrying the same lentiviral insertion site, but with varying heteroplasmy. HA, hemagglutinin. (**B** to **D**) These cells were then used for an imaging-based quantification (B) of the area of mitochondria per cell (C) and delivery of mitochondrial matrix material to the lysosome (D). $N > 100$ cells per condition from three independent experiments. PBS, phosphate-buffered saline (used as solvent for DFP). (**E** to **H**) Representative images (E) for the confocal imaging-based quantification of mitochondrial area (F), nucleoid abundance (G), and mtDNA replication (H) in low- and high-heteroplasmy cells. *P* values calculated from Wilcoxon rank sum test. $N > 120$ cells per condition from four independent experiments. Low heteroplasmy, <40%; high, >60%. Data are shown as violin plots, boxplots, and beeswarm plots, with mean indicated in red. Dot shape indicates the biological repeat that each cell belongs to. NS, $P > 0.05$; ***$P < 0.001$ from Wilcoxon rank sum test. Scale bar, 10 μm.

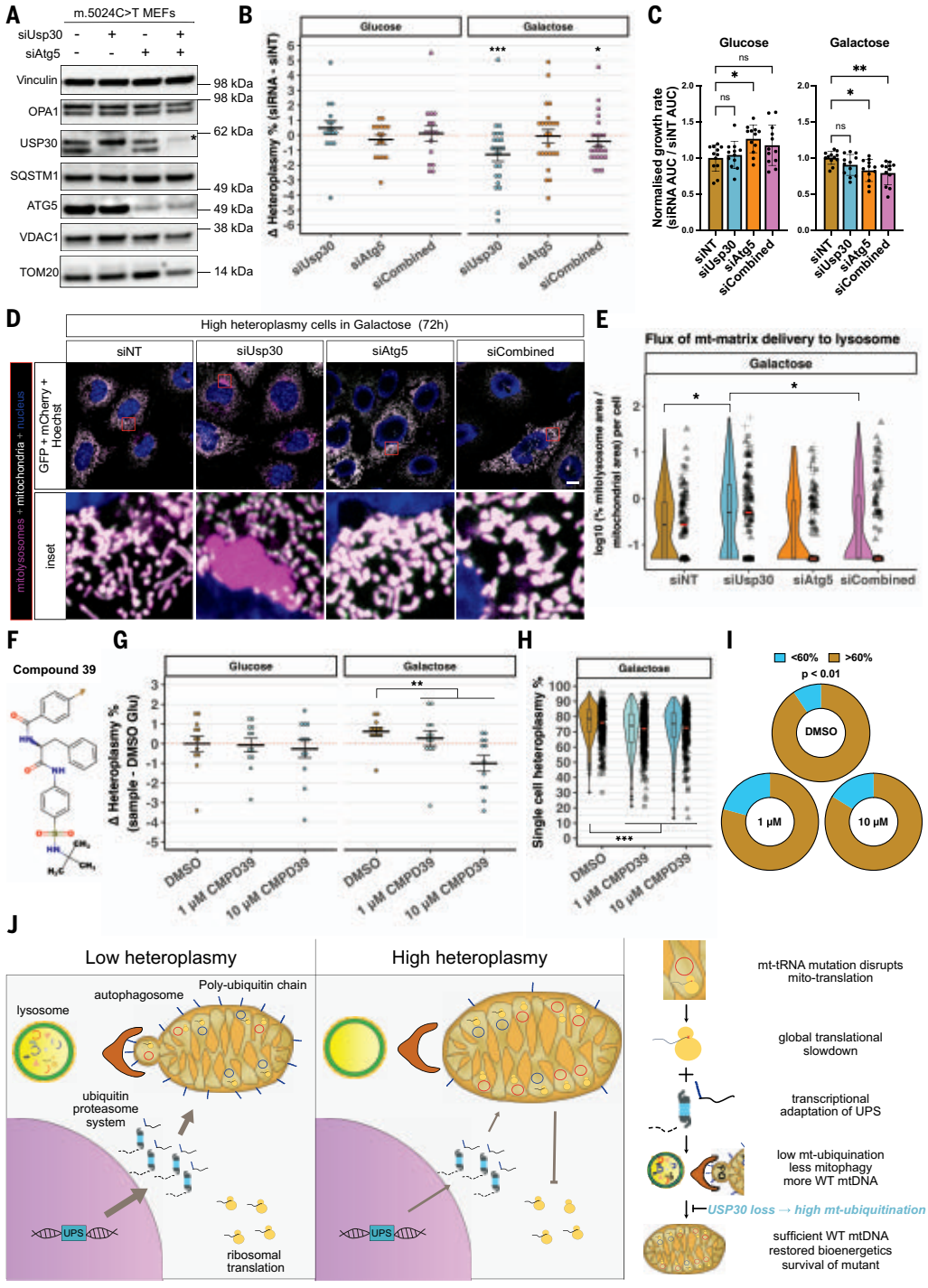


Fig. 4. USP30 loss or inhibition reduces heteroplasmy through mitophagy. (**A**) Representative immunoblot of siRNA knockdown of *Usp30* and *Atg5* in MEFs, 3 days after transfection. The asterisk (*) indicates an unspecific band. (**B**) Heteroplasmy difference (siRNA – siNT) in glucose or galactose media from three independent high-heteroplasmy clones after siRNA treatment, normalizing data from each clone at each time point to siNT. $N = 16$ to 24 per condition. *P* values were calculated against reference (siNT), separately for glucose and galactose. siNT, siNon-Targeting. (**C**) Normalized growth rates of siRNA-treated high-heteroplasmy MEFs in glucose or galactose over 3 days. *P* values were calculated through one-way analysis of variance from $N = 12$ per condition. AUC, area under the curve. (**D** and **E**) Confocal images of MEFs transduced with matrixQC indicating the effect of *Usp30* and *Atg5* knockdown on mitolysosomal delivery (D), with quantification in (E). $N > 100$ cells per conditions over four independent repeats. Scale bar, 10 μm. (**F**) Molecular structure of the USP30 inhibitor CMPD39. (**G**) Three independent high-heteroplasmy MEF clones were treated with vehicle (DMSO) or CMPD39 in glucose or galactose media for 4 days, and the heteroplasmy difference, to the mean of the untreated glucose condition group, was quantified. $N = 12$ per condition. (**H**) Single-cell heteroplasmy distributions from three different m.5024C>T clones treated with vehicle or CMPD39 in galactose media ($N > 250$ cells per condition from $N = 12$ independent experiments; Kolmogorov-Smirnov test $P < 0.001$). (**I**) Percentage of cells above or below 60% heteroplasmy in (H). $P < 0.05$ from mixed-effect model. $N = 11$ for DMSO and 1-μM CMPD39; $N = 9$ for 10-μM CMPD39 from three independent clones. All single-cell data are shown as violin plots, boxplots, and beeswarm plots, with mean indicated in red. Dot shape indicates the biological repeat that each cell belongs to. High heteroplasmy, >60%. *P* values were calculated through Wilcoxon rank sum test with Bonferroni correction (where appropriate), unless otherwise stated. *$P < 0.05$; **$P < 0.01$; ***$P < 0.001$. Error bars, mean ± SEM. (**J**) Schematic showing the cellular adaptations to high m.5024C>T heteroplasmy, the pathway leading to them, and the step of USP30 intervention. WT, wild type.

In vivo, we observed a general up-regulation of mitochondrial proteins, validated in MEFs (fig. S10, B to F), explaining the normal NADH–NAD^+ balance at high heteroplasmy (fig. S1, B to D). High-heteroplasmy MEF clones displayed an accumulation of mitochondria measured by mtGFP (Fig. 3C) and TOM20 (Fig. 3F), without increasing mitochondrial biogenesis (fig. S10G). Taken together, these findings indicate that the accumulation of mtDNA nucleoids and proteins induced by high heteroplasmy levels is likely due to decreased destruction, rather than increased synthesis. The m.5024C>T substitution disrupts mt-$tRNA^{ala}$ stability, affecting mitochondrial translation (*12*, *24*). Measuring the levels of ribosomal translation in whole-cell lysates showed that the defect was relayed outside of the organelle, slowing down cytosolic translation without affecting cytosolic ribosomal abundance (fig. S12, A to E), but not involving the integrated stress response (ISR) (fig. S12, F to H), as previously noted (*24*, *27*). Therefore, high levels of m.5024C>T heteroplasmy can induce a cellular adaptation that rewires cellular protein synthesis and degradation, resulting in slower organelle degradation and survival of the mutant (Fig. 4J).

Restoration of UMM decreases heteroplasmy

To provide further independent validation, we genetically silenced *Usp30* and the essential autophagy gene *Atg5* with short interfering RNA (siRNA) in high-heteroplasmy MEFs (Fig. 4A and fig. S13A). In high-glucose media, *siUsp30* did not affect bulk m.5024C>T heteroplasmy levels (Fig. 4B), despite appearing to selectively decrease its primary deubiquitination target, TOM20 (fig. S13B) (*19*), likely because under these conditions *siUsp30* did not induce additional mitophagy (fig. S13, C to F). However, after switching the nutrient media to galactose, *siUsp30* reduced heteroplasmy levels further (Fig. 4B and fig. S13G) and induced mitophagy (Fig. 4, D and E, and fig. S11, F and G). Combined treatment of *siUsp30* with *siPink1* did not increase mitophagy and did not decrease heteroplasmy (fig. S14), implying dependency on this pathway. Although a direct comparison of siUsp30 with the combined siRNAs found no significance, matrixQC analysis supported their involvement. Furthermore, the absence of an impact of *siUsp30* on cell growth rates (Fig. 4C) indicated that the mechanism was not dependent on cell proliferation or vegetative segregation and likely had no impact on cell fitness.

Finally, we explored whether posttranslational inactivation of USP30 was sufficient to modulate heteroplasmy. Compound 39 (CMPD39) (Fig. 4F) (*28*) reproduced the pattern observed with *siUsp30* (Fig. 4G and figs. S15, A to E, and S11, F and G) by increasing mitochondrial ubiquitination, but without triggering its lysosomal turnover in glucose media, which was activated in galactose (fig. S16). Single-cell analysis of heteroplasmy showed CMPD39 decreased mean heteroplasmy by 3 to 5% and decreased the number of cells with heteroplasmy >60% by 10% (Fig. 4, H and I), without any effect on cell fitness (fig. S15F). Therefore, enhancing UMM by blocking USP30 preferentially targets high-heteroplasmy cells (fig. 4G and S15G) forced to rely on oxidative phosphorylation.

Discussion

We show that mitochondrial ubiquitination modulates mtDNA heteroplasmy levels in vivo, shaping the inheritance of a heteroplasmic mtDNA mutation. This likely occurs at the subcellular level during early embryogenesis (MZT) when autophagy is up-regulated, providing a mechanism to ensure mtDNA-nuclear compatibility in the context of a rapidly mutating mitochondrial genome. A mechanism acting after fertilization has the added benefit of ensuring compatibility with both the maternal and recently introduced paternal nuclear alleles in combination. Our in vitro work corroborates this finding by showing that increasing mitochondrial ubiquitination reduces heteroplasmy levels by increasing organelle-specific UMM. We have not directly measured USP30 levels in the different crosses at the different germline stages, which would be technically very challenging. However, scRNA-seq data show the highest levels of *Usp30* expression in embryonic cells during the MZT, consistent with our conclusion that *Usp30*-mediated selection occurs at this developmental stage.

Our findings also provide a molecular mechanism for the "maintenance of wild-type" hypothesis, which predicts that heteroplasmic cells respond to a pathogenic allele by nonspecifically increasing the amount of mtDNA (*29*). In the short term, this maintains the absolute wild-type mtDNA levels and thus sustains oxidative phosphorylation. However, original in silico simulations presumed this mechanism worked through increased mitochondrial biogenesis (*29*), which was difficult to reconcile with mtDNA mutations known to compromise ATP synthesis. Our findings resolve this paradox. Rather than "turning on" new biosynthetic pathways, we show cells respond to mtDNA mutations by "turning off" cytosolic protein degradation. By suppressing the UPS, mitochondrial and mtDNA mass is increased through reduced mitophagy-mediated degradation, thus maintaining ATP synthesis. A mechanism that operates by switching off, not switching on, is likely to be both efficient and fail-safe but allows the transmission of mutant mtDNA in the germ line, explaining how de novo variants evade selection and cause disease.

It will be important to validate our findings in other mutant strains to confirm that our findings have wide relevance. The m.5024C>T models common human mutations in its inheritance pattern (*20*), such as the m.3243A>G. Impairment of mitophagy is observed in m.3243A>G fibroblasts (*30*) in mouse models of mitochondrial disease and affected tissues of patients (*31*). Furthermore, an age-dependent increase in copy number is observed in brains of patients with Parkinson's disease (*32*), a condition in which mitophagy contributes to pathogenesis (*33*). Nevertheless, analysis of other mutant models—e.g., the m.5019A>G (*24*), the MT-ATP6 (*34*), or the $PolgA^{D257A}$ "mutator" mouse—would determine whether our findings extend to mutations across the mitochondrial genome and are relevant for the age-related somatic accumulation of mtDNA mutations.

Our observations do not exclude the possibility that other mechanisms contribute to purifying selection at other developmental stages, including receptor-dependent autophagy (*10*). However, capitalizing on the latent capacity for enhanced UMM both in vitro and in vivo, we show USP30 is a potential target to reduce heteroplasmy. This has implications for treating and possibly preventing rare inherited mtDNA diseases, which affect ~1 in 8000 humans, particularly given the development of new small-molecule DUB inhibitors (*17*, *28*). Selection occurring during the MZT also raises the possibility of treating early embryos after in vitro fertilization to reduce the number of cells with a high mutation load before implantation. Finally, given emerging evidence that heteroplasmic mtDNA mutations accumulate in late-onset age diseases and cancer (*35*–*37*), therapeutical targeting of USP30 may have wider benefits in treating or preventing common disorders of aging.

REFERENCES AND NOTES

1. S. B. Vafai, V. K. Mootha, *Nature* **491**, 374–383 (2012).
2. W. M. Brown, M. George Jr., A. C. Wilson, *Proc. Natl. Acad. Sci. U.S.A.* **76**, 1967–1971 (1979).
3. R. Allio, S. Donega, N. Galtier, B. Nabholz, *Mol. Biol. Evol.* **34**, 2762–2772 (2017).
4. S. P. Burr, M. Pezet, P. F. Chinnery, *Dev. Growth Differ.* **60**, 21–32 (2018).
5. H. J. Muller, *Mutat. Res.* **1**, 2–9 (1964).
6. W. Wei *et al.*, *Science* **364**, eaau6520 (2019).
7. P. Nandakumar *et al.*, *Sci. Adv.* **7**, eabe7520 (2021).
8. R. Gupta *et al.*, *Nature* **620**, 839–848 (2023).
9. J. M. Palozzi *et al.*, *Cell Metab.* **34**, 1809–1823.e6 (2022).
10. L. S. Kremer *et al.*, *PLOS Genet.* **19**, e1010573 (2023).
11. G. S. Gorman *et al.*, *Ann. Neurol.* **77**, 753–759 (2015).
12. J. H. K. Kauppila *et al.*, *Cell Rep.* **16**, 2980–2990 (2016).
13. M.-L. Simard, A. Mourier, L. C. Greaves, R. W. Taylor, J. B. Stewart, *J. Pathol.* **245**, 311–323 (2018).
14. S. Finnilä, S. Tuisku, R. Herva, K. Majamaa, *J. Mol. Med.* **79**, 641–647 (2001).
15. R. McFarland *et al.*, *Neuromuscul. Disord.* **18**, 63–67 (2008).
16. D. Komander, M. J. Clague, S. Urbé, *Nat. Rev. Mol. Cell Biol.* **10**, 550–563 (2009).

17. T. Z. Fang *et al.*, *Nat. Commun.* **14**, 7295 (2023).
18. A. Sanchez-Martinez, A. Martinez, A. J. Whitworth, *PLOS Biol.* **21**, e3002244 (2023).
19. L. Phu *et al.*, *Mol. Cell* **77**, 1107–1123.e10 (2020).
20. H. Zhang *et al.*, *Sci. Adv.* **7**, eabi5657 (2021).
21. S. Tsukamoto *et al.*, *Science* **321**, 117–120 (2008).
22. R. Rojansky, M.-Y. Cha, D. C. Chan, *eLife* **5**, e17896 (2016).
23. M. Kanehisa, S. Goto, *Nucleic Acids Res.* **28**, 27–30 (2000).
24. S. P. Burr *et al.*, *Cell* **186**, 1212–1229.e21 (2023).
25. M. Long *et al.*, *EMBO J.* **41**, e109390 (2022).
26. G. F. G. Allen, R. Toth, J. James, I. G. Ganley, *EMBO Rep.* **14**, 1127–1135 (2013).
27. R. Filograna *et al.*, *Sci. Adv.* **5**, eaav9824 (2019).
28. E. V. Rusilowicz-Jones *et al.*, *Life Sci. Alliance* **5**, e202101287 (2021).
29. P. F. Chinnery, D. C. Samuels, *Am. J. Hum. Genet.* **64**, 1158–1165 (1999).
30. C.-Y. Chung *et al.*, *Autophagy* **21**, 881–896 (2024).
31. T. Mito *et al.*, *Cell Metab.* **34**, 197–208.e5 (2022).
32. C. Dölle *et al.*, *Nat. Commun.* **7**, 13548 (2016).
33. A. B. Malpartida, M. Williamson, D. P. Narendra, R. Wade-Martins, B. J. Ryan, *Trends Biochem. Sci.* **46**, 329–343 (2021).
34. P. Silva-Pinheiro *et al.*, *Nat. Biomed. Eng.* **7**, 692–703 (2023).
35. M. Kim, M. Mahmood, E. Reznik, P. A. Gammage, *Trends Cancer* **8**, 1046–1059 (2022).
36. C. Calabrese *et al.*, *PLOS Genet.* **18**, e1010068 (2022).
37. M. J. Keogh, P. F. Chinnery, *Biochim. Biophys. Acta* **1847**, 1401–1411 (2015).
38. M. Frison, Ubiquitin mediated mitophagy regulates the inheritance of mitochondrial DNA mutations, Zenodo (2025); https://zenodo.org/records/15878759.

ACKNOWLEDGMENTS

We thank G. Griffiths for providing the USP30 mice. We also acknowledge the help of K. Turner and Y. Kanse for the assistance on the management of the mouse colony. We thank the laboratories of A. Whitworth, J. Prudent, and R. Horvath for technical advice on imaging, ubiquitin, and translation, particularly L. Tilokani, L. C. Tabara, A. Zarate, and D. Hathazi. **Funding:** P.F.C. is currently funded by a Wellcome Discovery Award (226653/Z/22/Z), a Wellcome Collaborative Award (224486/Z/21/Z), the Medical Research Council Mitochondrial Biology Unit (MC_UU_00028/7), the Biological and Biotechnology Research Council (BB/Y003209/1), and the LifeArc Centre to Treat Mitochondrial Diseases (LAC-TreatMito). His research is supported by the NIHR Cambridge Biomedical Research Centre (BRC-1215-20014). The views expressed are those of the author(s) and not necessarily those of the NIHR or the Department of Health and Social Care. **Author contributions:** M.F. designed, carried out experiments, performed statistical analysis and generated the figures for all the data except for the following: B.S.L. performed all experiments with the USP30 inhibitor CMPD39, the generation of the Cellpose training models, and analysis of WIPI2/ATG12 immunofluorescence; Z.G. performed the NAD/H analysis, the proteomics sample preparation with A.G., and the PINK1 qPCR; Y.N. carried out the analysis of the proteomics data and generated the figures; S.P.B. carried out pyrosequencing of the F0 and, with A.G., generated of the heteroplasmic MEF clones without the matrixQC transgene; M.P. carried out the analysis and generated the figures for the RNA-seq (Fig. 2B); C.L. carried out the analysis and plotting of the other figures from the RNA-seq; C.D.R. carried out the analysis of germline gene expression from public scRNA-seq datasets; E.T. performed the imaging of matrixQC MEFs in galactose and with siRNA; L.V.B. advised on the in vivo experiment design and on the statistics. J.B.S. generated the m.5024C>T mouse colony and advised on the data. N.S.J. and M.R.C. assisted on the interpretation of the transmission data. M.F. and P.F.C. conceived the study and wrote the manuscript, with input from all authors. P.F.C supervised and oversaw the study. **Competing interests:** J.B.S. is a coinventor of the m.5024C>T mice and receives compensation for commercial use through Max Planck Innovation GmbH. **Data and materials availability:** All materials generated in this study are readily available from the authors. All data are available in the manuscript, in the supplementary materials, or at Zenodo (*38*). The m.5024C>T mouse line is available from J.B.S. under a material agreement with the Max Planck Institute for Biology of Aging. **License information:** Copyright © 2025 the authors, some rights reserved; exclusive licensee American Association for the Advancement of Science. No claim to original US government works. https://www.sciencemag.org/about/science-licenses-journal-article-reuse

SUPPLEMENTARY MATERIALS

science.org/doi/10.1126/science.adr5438
Materials and Methods; Figs. S1 to S16; References (*39*–*45*); MDAR Reproducibility Checklist

Submitted 5 July 2024; resubmitted 28 March 2025; accepted 17 July 2025

10.1126/science.adr5438

KIDNEY DISEASE

Reversible compromise of physiological resilience by accumulation of heteroplasmic mtDNA mutations

Huihui Huang[1], Yi Wang[2], Zsuzsanna K. Zsengeller[1], Joshua M. Gorham[3], Vamsidhara Vemireddy[4], Amanda J. Clark[1,5], Hui Pan[6], Jonathan M. Dreyfuss[6], Vasantha Jotwani[7], Michael G. Shlipak[7], Mark J. Sarnak[8], Chirag R. Parikh[9], Heather Thiessen-Philbrook[9], Ronit Katz[10], Sushrut S. Waikar[11], Nicole J. Lake[12], Monkol Lek[12], Wen Shi[13], Daniela Puiu[13], Yun Soo Hong[13], Jonathan G. Seidman[3], Dan E. Arking[13], Samir M. Parikh[1,4]*

Somatically acquired mitochondrial DNA (mtDNA) mutations accumulate with age, but the mechanisms and consequences of this accumulation are poorly understood. Here we show that transient injuries induce a burst of persistent mtDNA mutations that impair resilience to future injuries. mtDNA mutations suppressed energy-intensive nucleotide metabolism. Repletion of adenosine, but not other nucleotides, restored adenosine triphosphate generation, which required a nuclear-encoded purine biosynthetic enzyme, adenylate kinase 4 (AK4). Analysis of 369,912 UK Biobank participants revealed a graded association between mutation burden and chronic kidney disease severity as well as an independent increase in the risk of future acute kidney injury events ($P < 10^{-7}$). Heteroplasmic mtDNA mutations may therefore reflect the cumulative effect of acute injuries to metabolically active cells, impairing major functions in a fashion amenable to nuclear-controlled purine biosynthesis.

As the cell's powerhouse, individual mitochondria contain 2 to 10 copies of mitochondrial DNA (mtDNA), and each cell contains tens to thousands of mitochondria. This circular genome encodes 37 products that include core components of oxidative phosphorylation (OXPHOS), the final biochemical pathway for adenosine triphosphate (ATP) production, as well as ribosomal RNAs and transfer RNAs required for translation (*1*). Both inherited and acquired mtDNA mutations give rise to the state of mtDNA called heteroplasmy, in which two or more mtDNA alleles exist within the same cell. Heteroplasmic mtDNA mutations rise markedly after age 70 in humans, largely because of somatic changes (*2*). Emerging evidence shows that mtDNA mutations increase in frequency with age in mice, with the kidney having the highest mtDNA mutation frequency among major organs (*3*).

The theory of mtDNA mutations driving aging has, on one hand, been supported by a mouse genetic model of accelerated mtDNA mutations that exhibits accelerated multi-organ aging (*4*–*6*). However, the burden of mtDNA mutations in this genetic model exceeded normal mouse aging (*7*). The mechanisms by which an organ such as the kidney could accumulate mtDNA mutations and the consequences of this accumulation have not been studied.

In this study, we conducted a multi-omic interrogation of CRISPR-modified genetic models and analyses in a large human genomic dataset to investigate the relationships among mtDNA mutations, acute injuries, and chronic organ damage in the kidney. The results suggest a positive feedback loop in which acute injury induces mtDNA mutations that persist and impair energy metabolism and physiological resilience to future stressors in a fashion amenable to metabolic intervention; they also suggest that mtDNA heteroplasmy may be both a quantitative risk factor for susceptibility to acute kidney injury (AKI) and, independently, an indicator of chronic kidney disease (CKD) severity.

Results

Acute injury induces persistent mtDNA mutations that are associated with functional and structural tissue damage

We studied unrelated models of AKI progressing to CKD: ischemia-reperfusion injury (IRI) and crystalline damage after parenteral folic acid (FA) injection. We used 24 hours as the acute time point; chronic results were assessed 30 days after IRI and 14 days after FA injection (Fig. 1A). In both models, tubular injury and functional impairment—measured by serum creatinine (Scr) and blood urea nitrogen (BUN)—were evident at the acute time point; by the chronic time point, fibrosis had developed and was associated with increases in canonical markers fibronectin (*Fn*), collagen type 1 alpha 1 (*Col1α1*), and alpha-smooth muscle actin (*α-SMA*) (fig. S1).

Assessment of the mtDNA mutation hotspot displacement loop (D-loop) region (*1*) revealed lesions induced acutely by IRI or FA that persisted to the chronic time point; in contrast, no consistent changes were observed in mtDNA copy number in either injury model (fig. S2). Sequencing demonstrated that alternative alleles were distributed across the mtDNA genome, that the number of sites with alternative alleles increased approximately twofold acutely, and that this mutational burden persisted to the chronic time point (Fig. 1, B and C)—patterns corroborated by the fraction of alternative mtDNA alleles (Fig. 1D). Mutations spanned synonymous, nonsynonymous, and nonsense changes; and the burden of mutations at each time point was associated, respectively, with the extent of acute tissue injury and chronic fibrosis (Fig. 1, E to G). The FA model revealed similar results (Fig. 1, H to M). At either time point in either model, mutations were observed across the mtDNA genome with a distribution of alternative alleles not significantly different from random, consistent with spread beyond the D-loop hotspot (fig. S3).

We next studied kidney tissue obtained from individuals with varying levels of CKD undergoing nephrectomy, for example, for cancer treatment (table S1). A circular plot and heatmap of mtDNA mutations confirmed distribution of alternative alleles throughout the genome region (Fig. 1N and fig. S4, A to C). CKD kidneys exhibited mitochondrial impairment (Fig. 1O). Both the abundance of alternative mtDNA alleles and the fraction present in the coding region were linearly associated with the estimated glomerular filtration rate (eGFR), and there was no significant correlation between mtDNA copy number and eGFR (Fig. 1P and fig. S4, D and E). When we dichotomized the cohort by a common threshold for specialty care referral, mutational burden was higher in the more severe group (Fig. 1, Q and R).

[1]Division of Nephrology and Department of Medicine, Beth Israel Deaconess Medical Center and Harvard Medical School, Boston, MA, USA. [2]Department of Cardiology, Boston Children's Hospital and Harvard Medical School, Boston, MA, USA. [3]Department of Genetics, Harvard Medical School, Boston, MA, USA. [4]Division of Nephrology, Department of Internal Medicine, and Department of Pharmacology, University of Texas Southwestern, Dallas, TX, USA. [5]Division of Nephrology, Department of Pediatrics, University of Texas Southwestern and Children's Medical Center Dallas, Dallas, TX, USA. [6]Bioinformatics and Biostatistics Core, Joslin Diabetes Center, Harvard Medical School, Boston, MA, USA. [7]Kidney Health Research Collaborative, Department of Medicine, San Francisco Veterans Affairs Health Care System and University of California, San Francisco, San Francisco, CA, USA. [8]Division of Nephrology, Tufts Medical Center, Boston, MA, USA. [9]Division of Nephrology, Department of Medicine, Johns Hopkins University School of Medicine, Baltimore, MD, USA. [10]Department of Obstetrics and Gynecology, University of Washington, Seattle, WA, USA. [11]Section of Nephrology, Boston University Chobanian & Avedisian School of Medicine, Boston Medical Center, Boston, MA, USA. [12]Department of Genetics, Yale School of Medicine, New Haven, CT, USA. [13]McKusick-Nathans Institute, Department of Genetic Medicine, Johns Hopkins University School of Medicine, Baltimore, MD, USA. ***Corresponding author. Email: samir.parikh@utsouthwestern.edu**

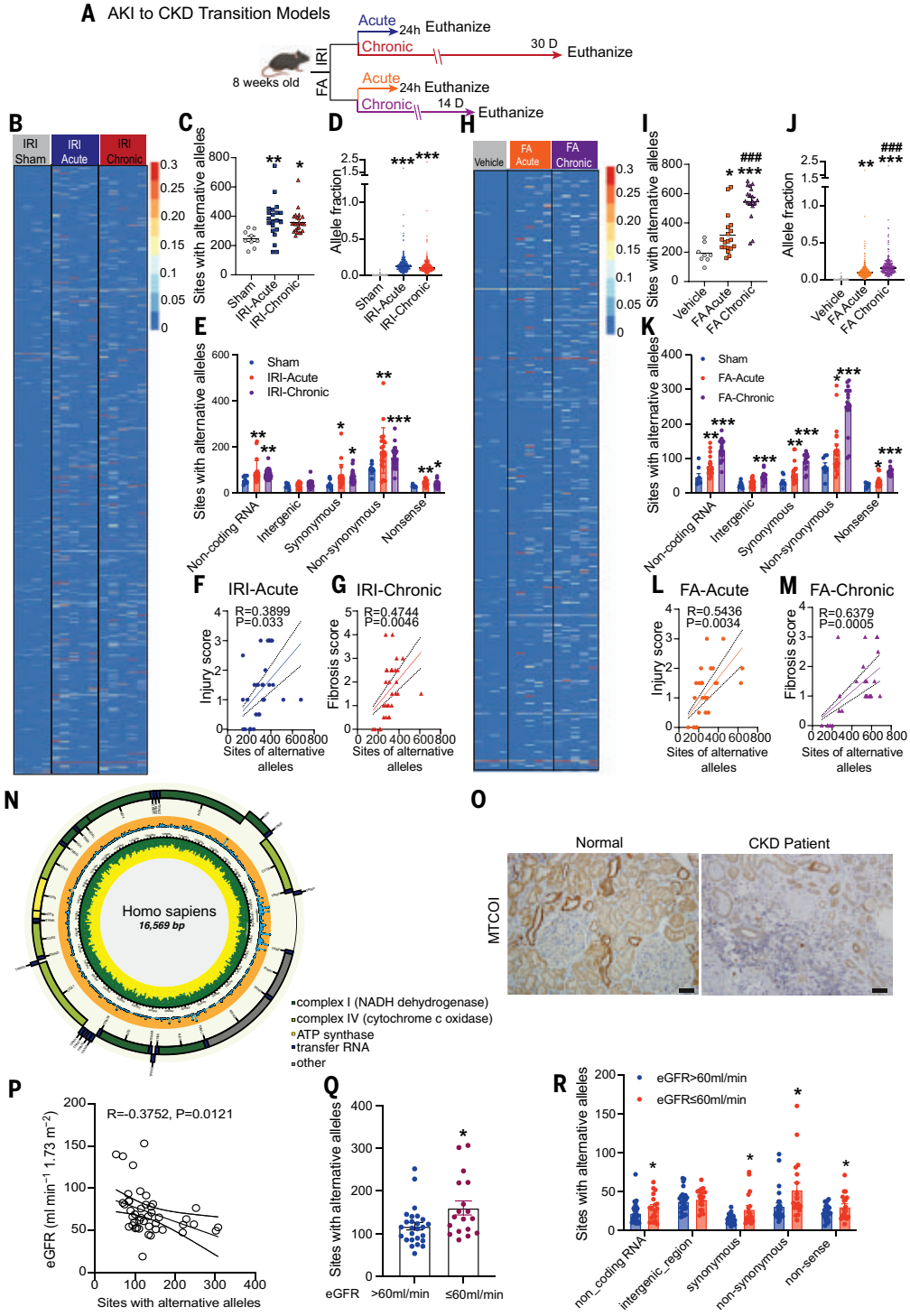


Fig. 1. Transient injury induces persistent mtDNA mutations in animals and across CKD stages in patients undergoing nephrectomy. (**A**) Schematic depicting time points for evaluation after kidney IRI or parenteral FA injection [250 mg/kg intraperitoneally (ip) × 1] to model AKI and CKD. (**B** to **G**) Characterization of acute and chronic mtDNA mutation burden after IRI: (B) mtDNA sequencing heatmap, row 1 is nucleotide position #1 in mtDNA genome, and color is indicative of alternative allele fraction at the position; (C) number of mtDNA sites with an alternative allele, where each symbol represents a single animal's kidney specimen; (D) fraction of variant alleles per 50 base pairs (bp) across the mtDNA genome; (E) classification of mutation type; (F) correlation of acute histological injury with acute mtDNA mutation burden; and (G) correlation of chronic histological fibrosis score with chronic mtDNA mutation burden. (**H** to **M**) Characterization of acute and chronic mtDNA mutation burden after FA, as in (B) to (G), respectively. $^{*}P < 0.05$, $^{**}P < 0.01$, $^{***}P < 0.001$, $^{****}P < 0.0001$ versus control. $^{\#\#\#}P < 0.001$ versus FA-Acute. (**N**) Circular plot showing genome-wide distribution of sites with alternative alleles among human kidney samples. (**O**) Representative immunohistochemistry comparing kidney expression of mitochondrially encoded cytochrome c oxidase subunit I (MTCOI) in control versus CKD human kidney. Scale bar, 100 μm. (**P**) Correlation of mtDNA mutation burden with eGFR in human kidneys ($n = 44$ patients). (**Q**) mtDNA mutation burden in CKD cohort above or below KDIGO (Kidney Disease: Improving Global Outcomes) stage 3, 60 ml min^{-1} 1.73 m^{-2}. (**R**) Annotation of mutation type in CKD cohort. $^{*}P < 0.05$, $^{**}P < 0.01$, $^{***}P < 0.001$, $^{****}P < 0.0001$ versus control.

Oxidative stress may drive acute injury and chronic impairment (*8*). To model this, we applied hydrogen peroxide (H_2O_2) for 30 min or 72 hours to renal tubular epithelial cells, representing acute and chronic exposure, respectively. After 30 min, four readouts of mtDNA damage were increased: (i) mitochondrial 8-oxo-2′-deoxyguanosine (8-OHdG) (*9*), (ii) D-loop lesions, (iii) number of sites with alternative alleles, and (iv) fraction of alternative alleles (fig. S5, A to F). mtDNA mutations represented a mixture of mutation types, reactive oxygen species (ROS) were elevated, and ATP generation was suppressed (fig. S5, G to I). Chronic exposure increased fibrosis markers (fig. S5J).

mtDNA mutations exacerbate energetic and physiological responses to transient stress in cells and mice

To examine sufficiency of somatic mtDNA mutation accumulation to impair cellular functions, we introduced a proofreading defect in the mitochondrial DNA polymerase, POLG (Fig. 2, A and B, and fig. S6A), that creates single nucleotide variants (SNVs) and larger deletions (*6*, *10*). Compared with isogenic control cells, $Polg^{D257A/-}$ cells (D257A, Asp^{257}→Ala) displayed a twofold increase in alternative mtDNA allele abundance and fraction, decreased mitochondrial respiration, increased glycolysis, and decreased expression of mitochondrially encoded respiratory chain subunits (Fig. 2, C to E, and fig. S6, B to D).

In agreement with prior $Polg^{D257A}$ work (*10*), ROS generation was not increased in $Polg^{D257A/-}$ cells (Fig. 2F). ATP generation, however, was reduced and further suppressed after transient H_2O_2 exposure (Fig. 2G). At baseline, $Polg^{D257A/-}$ cells displayed induction of fibrotic genes, which H_2O_2 exposure exacerbated further (Fig. 2H).

$Polg^{D257A}$ mice had normal kidney histology and function at baseline but more mtDNA lesions and mtDNA SNVs and decreased expression of OXPHOS complexes compared with $Polg^{+/+}$ mouse kidneys (fig. S7). After IRI, $Polg^{D257A}$ mice developed worse acute tissue injury and kidney function with more collagen deposition, scar formation, and fibrotic gene expression chronically compared with $Polg^{+/+}$ mice (Fig. 2, I to O). In the FA model, $Polg^{D257A}$ mice similarly developed worse outcomes at both time points (Fig. 2, P to V). These findings collectively indicate that increased acquired mtDNA mutation burden exacerbates energetic and physiological outcomes after transient stress.

mtDNA mutations suppress nucleotide biosynthesis, and adenosine restores metabolic functions through AK4

Metabolomics on IRI kidneys from $Polg^{D257A}$ and $Polg^{+/+}$ littermates unveiled both genotype- and injury-driven differences, including a decrease in many nucleotide intermediates and an increase in lipid species in $Polg^{D257A}$ kidneys (Fig. 3, A to D). The latter change was consistent with the decreased oxidative metabolism we observed in $Polg^{D257A/-}$ cells (fig. S6, B to D) and with published results in kidney injury (*11*, *12*). Several amino acids involved in purine biosynthesis—glutamate, glutamine, and glycine (*13*)—were decreased in IRI $Polg^{D257A}$ kidneys (Fig. 3D). Metabolomics of $Polg^{D257A/-}$ cells and isogenic controls reproduced the whole-kidney pattern of lipid accumulation and nucleotide metabolite depletion in $Polg^{D257A/-}$ cells (Fig. 3, E and F, and fig. S8A). Adenosine, adenosine monophosphate (AMP), and adenosine diphosphate (ADP) were all decreased in $Polg^{D257A/-}$ cells (fig. S8B).

To test whether ATP could be restored by nucleoside supplementation, we next applied adenosine, guanosine, cytidine, or thymidine to $Polg^{D257A/-}$ cells or controls. Only adenosine increased basal ATP generation (fig. S8, C to F). Adenosine also counteracted the deleterious effects of oxidative stress on ATP generation, mitochondrial membrane potential, mitochondrial respiration, and expression of fibrosis markers in $Polg^{D257A/-}$ cells without itself alleviating oxidative stress or affecting isogenic controls (Fig. 3, G and H, and fig. S8, G to O).

Like metabolomes, transcriptomes of IRI kidneys from $Polg^{D257A}$ and $Polg^{+/+}$ littermates were also highly correlated (correlation coefficient $r > 0.9$) within each experimental group and unveiled both genotype- and injury-driven differences (Fig. 3I and fig. S9, A and B). Adenylate kinase 4 (AK4) was decreased in $Polg^{D257A}$ kidneys compared with $Polg^{+/+}$ (Fig. 3, J and K, and fig. S9C). This enzyme facilitates phosphate group transfer between ATP and AMP (Fig. 3L) and localizes to mitochondria (*14*, *15*). Gene set enrichment and pathway analyses highlighted "ATP metabolic process" and decreased OXPHOS in $Polg^{D257A}$ compared with $Polg^{+/+}$ after injury (fig. S9, D and E) (*16*).

Adenosine can act through surface receptors or by cellular import (*17*). Three structurally distinct adenosine uptake inhibitors—cilostazol, dipyridamole, and *S*-(4-nitrobenzyl)-6-thioinosine (NBMPR)—each reduced adenosine-dependent ATP generation (fig. S10, A to D). In contrast, neither adenosine receptor 2A (ANR94) nor adenosine receptor 2B (MRS1754) inhibitors reduced adenosine-induced ATP generation in $Polg^{D257A/-}$ cells (fig. S10, E and F).

Excess or reduced AK4 exerted a bidirectional gene dose effect on ATP generation under oxidant stress (fig. S11, A to C). In the absence of oxidant stress, the AK inhibitor AP5A had no discernible effect on ATP generation on $Polg^{D257A/-}$ cells or controls (fig. S11, D and E). Either pharmacological inhibition or genetic reduction of AK4 attenuated the ability of adenosine to increase ATP generation in $Polg^{D257A/-}$ cells (Fig. 3, M and N, and fig. S11F). Together, these results show that AK4 is sufficient to increase ATP generation and required for adenosine-dependent ATP induction in cells bearing mtDNA mutations.

Adenosine restores resistance to injury in mtDNA-mutated animals through adenylate kinase

We next tested whether adenosine could restore injury resistance when mtDNA mutations were elevated. Histological injury and physiological impairment were more severe in $Polg^{D257A}$ mice than in littermate controls (Fig. 4A). Adenosine's protective effects were abrogated by concomitant AK inhibition (Fig. 4, B to D). Adenosine supplementation improved both scar formation and fibrotic gene expression, and concomitant AP5A once again abrogated these effects (Fig. 4, E and F).

Single-nucleus RNA sequencing (RNA-seq) of kidneys from control and $Polg^{D257A}$ mice showed that injury substantially reduced the proximal tubule population; in contrast, immune cell populations were low at baseline and rose only modestly after injury (Fig. 4, G and H, and fig. S12, A and B). Neither whole-blood cellular mtDNA nor $CD11b^+$ myeloid cells isolated from kidneys displayed an increase in mtDNA mutations after injury (fig. S12, C to H). Adenosine treatment upregulated genes involved with mitochondrial metabolism among proximal tubular epithelium cells (Fig. 4I), consistent with the metabolic actions of adenosine in $Polg^{D257A/-}$ cells in Fig. 3.

mtDNA mutation burden is independently associated with chronic disease severity and susceptibility to future acute kidney injury

Finally, we evaluated the relationships among mtDNA mutations, severity of CKD, and risk of AKI in the UK Biobank (Fig. 5A). Mutational burden was assessed by heteroplasmy count after applying a 5% variant allele frequency (VAF) cutoff and through analysis of evolutionary mitochondrial local constraint (MLC) to annotate functional consequences of mutations (*18*–*21*). Briefly, MLC assigns each variant a score ranging from 0, for a synonymous change, to 1, for a change predicted to be highly deleterious (table S2). A modified MLC score sum (mMSS) was calculated for each individual sample, inversely weighted by the homoplasmic frequency of the variant.

Heteroplasmy count was associated with lower eGFR (Fig. 5B). Converting heteroplasmy count to functional assessment through mMSS, we found that mMSS was even more significantly associated with lower eGFR [−0.71 ml min^{-1} 1.73 m^{-2} per SD of mMSS, 95% confidence interval (CI) −0.96 to −0.47, $P = 1.83 \times 10^{-8}$; Fig. 5C]. Including heteroplasmy count in the model with mMSS only moderately attenuated the effect (0.59 ml min^{-1} 1.73 m^{-2} per SD of mMSS, 95% CI −0.88 to −0.31, $P = 1.83 \times 10^{-8}$), suggesting a model in which heteroplasmy count increases with kidney function impairment and functionally damaging heteroplasmies may be linked to worsening kidney function.

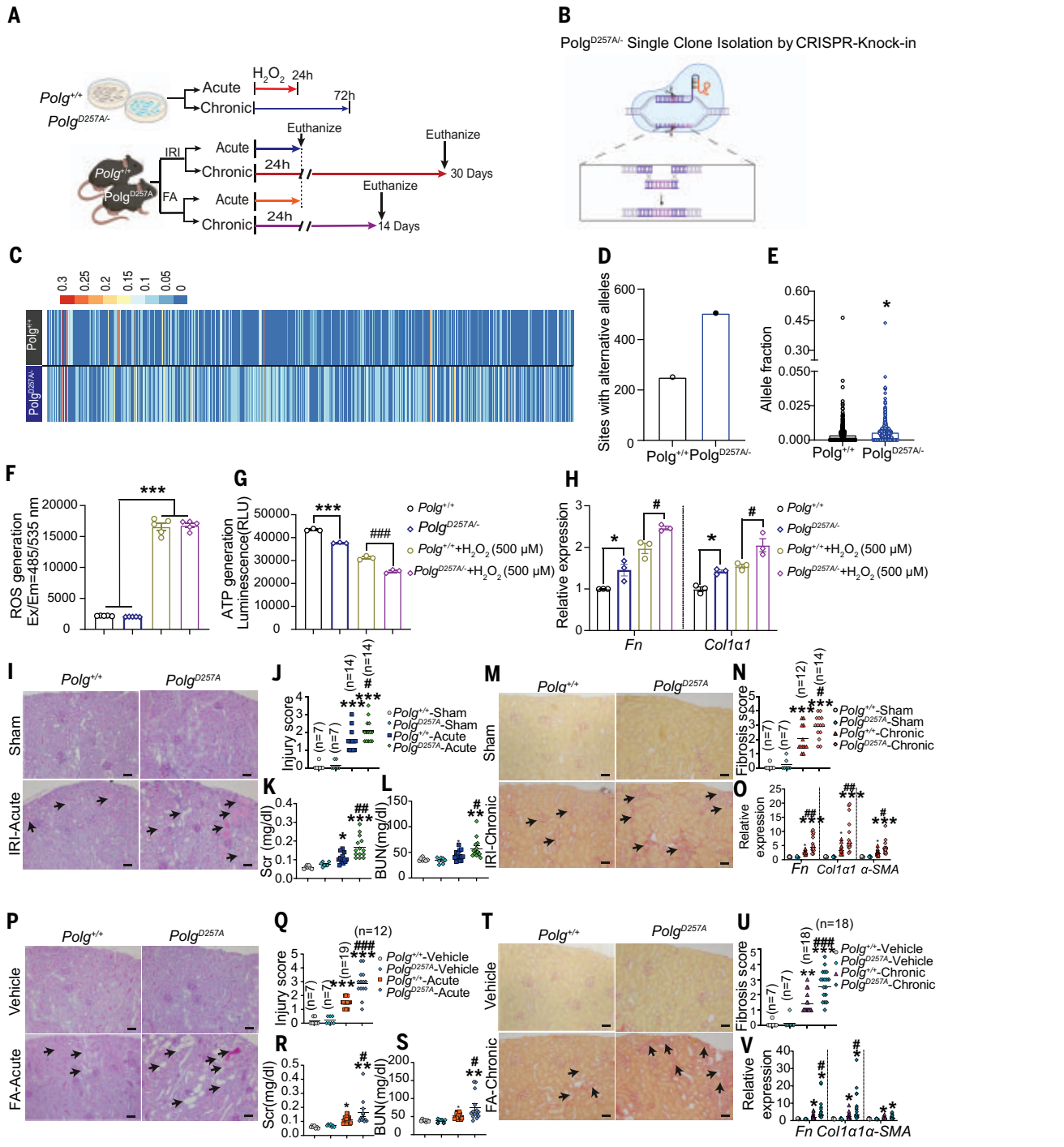


Fig. 2. mtDNA mutations exacerbate responses to transient stress in cells and mice. (**A**) Schematic depicting acute and chronic models of oxidative stress on cultured *Polg*$^{D257A/-}$ or *Polg*$^{+/+}$ isogenic renal tubular cells and time points for evaluation after either kidney IRI or parenteral FA injection (250 mg/kg ip × 1) in *Polg*^{D257A} mice versus littermate wild-type control *Polg*$^{+/+}$ mice. (**B**) Schematic to develop clonal *Polg*$^{D257A/-}$ cells. (**C** to **E**) Characterization of *Polg*$^{D257A/-}$ cells versus *Polg*$^{+/+}$ control cells at baseline: (C) mtDNA sequencing heatmap; (D) number of mtDNA sites with alternative alleles; and (E) fraction of variant alleles per 50 bp across the mtDNA genome. (**F** to **H**) Characterization of *Polg*$^{D257A/-}$ cells versus *Polg*$^{+/+}$ control cells treated with vehicle or H_2O_2 (500 μM for 24 hours): (F) ROS generation; (G) ATP generation; and (H) fibrosis marker expression. RLU, relative light units. (**I** to **L**) Acute outcomes after IRI: (I) periodic acid–Schiff (PAS)–stained representative photomicrographs of kidney cortex with arrows indicating dilated tubules (scale bar, 50 μm); (J) blinded quantification of histological tubular injury; (K) serum creatinine; and (L) blood urea nitrogen. (**M** to **O**) Chronic outcomes after IRI: (M) picrosirius red–stained representative photomicrographs of kidney cortex with arrows indicating areas of fibrosis (scale bar, 50 μm); (N) blinded quantification of histological fibrosis; and (O) polymerase chain reaction (PCR) of kidney cortex mRNA for fibrosis markers *Fn*, *Col1α1*, and *α-SMA*. (**P** to **S**) Acute outcomes after FA injection, as in (I) to (L), respectively. (**T** to **V**) Chronic outcomes after FA injection, as in (M) to (O), respectively. *$P < 0.05$, **$P < 0.01$, ***$P < 0.001$ versus control. #$P <$ 0.05, ##$P < 0.01$, ###$P < 0.001$ versus *Polg*$^{+/+}$-Acute or *Polg*$^{+/+}$-Chronic, as indicated.

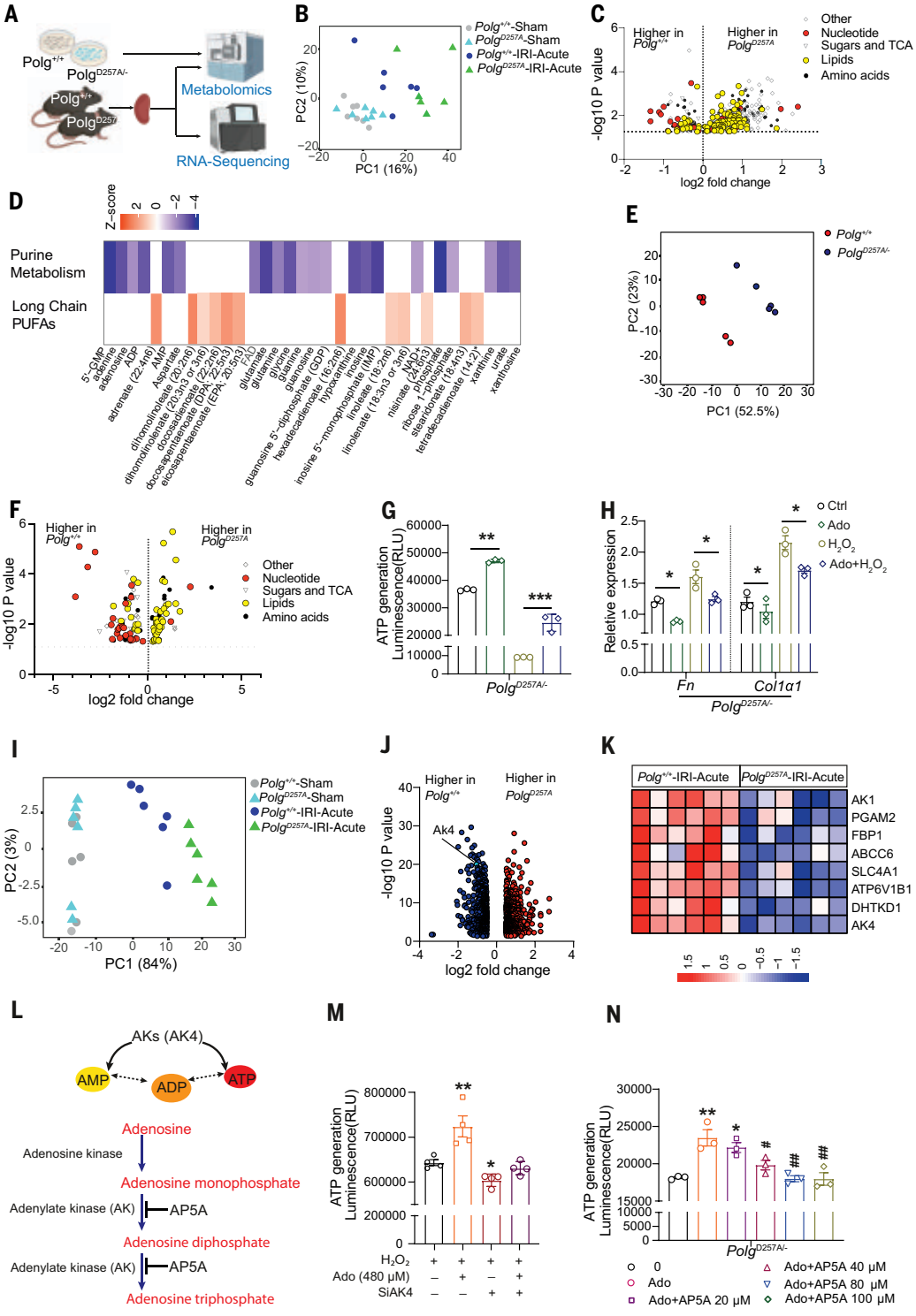


Fig. 3. Adenosine restores ATP generation in mtDNA mutation–induced nucleotide biosynthesis suppression cells through AK4. (**A**) Schematic depicting metabolomics and RNA-seq analysis of *Polg*^{D257A} kidneys versus *Polg*$^{+/+}$ controls, and metabolomics analysis of *Polg*$^{D257A/-}$ cells versus isogenic controls. (**B**) Principal components analysis and (**C**) volcano plot of kidney metabolomes after acute IRI in *Polg*^{D257A} kidneys versus *Polg*$^{+/+}$ controls. TCA, tricarboxylic acid. (**D**) Representative functional classification heatmap of metabolites confirming reduction of purine metabolites and accumulation of fatty acids after IRI in *Polg*^{D257A} kidneys versus *Polg*$^{+/+}$ controls. (**E**) Principal components analysis and (**F**) volcano plot of kidney metabolomes after acute IRI in *Polg*^{D257A} cells versus isogenic *Polg*$^{+/+}$ controls. (**G**) ATP generation at 24 hours in control, adenosine (480 μM), and/or H_2O_2 (100 or 500 μM) treatment conditions in *Polg*$^{D257A/-}$ cells. (**H**) PCR for fibrosis markers *Fn* and *Col1α1* at 72 hours in the indicated condition in *Polg*$^{D257A/-}$ cells. *$P < 0.05$, **$P < 0.01$, ***$P < 0.001$ versus control. (**I** to **K**) RNA-seq and analysis of *Polg*^{D257A} kidneys versus *Polg*$^{+/+}$ controls: (I) principal components analysis and (J) volcano plot of acute IRI transcripts; and (K) heatmap of components of "ATP metabolic process" gene set. (**L**) Schematic of reactions catalyzed by AKs and actions of the AK inhibitor compound AP5A. (**M**) ATP generation in *Polg*$^{D257A/-}$ cells treated with or without adenosine (Ado) (480 μM) and/or AK4 siRNA under H_2O_2 conditions (500 μM for 24 hours). (**N**) ATP generation in *Polg*$^{D257A/-}$ cells 24 hours after adenosine (480 μM) and increasing concentrations of AK inhibitor AP5A. *$P < 0.05$, **$P < 0.01$, ***$P < 0.001$ versus control. ###$P < 0.001$ versus second condition from left in (M) and (N). #$P < 0.05$, ##$P < 0.01$ versus Ado condition in (N).

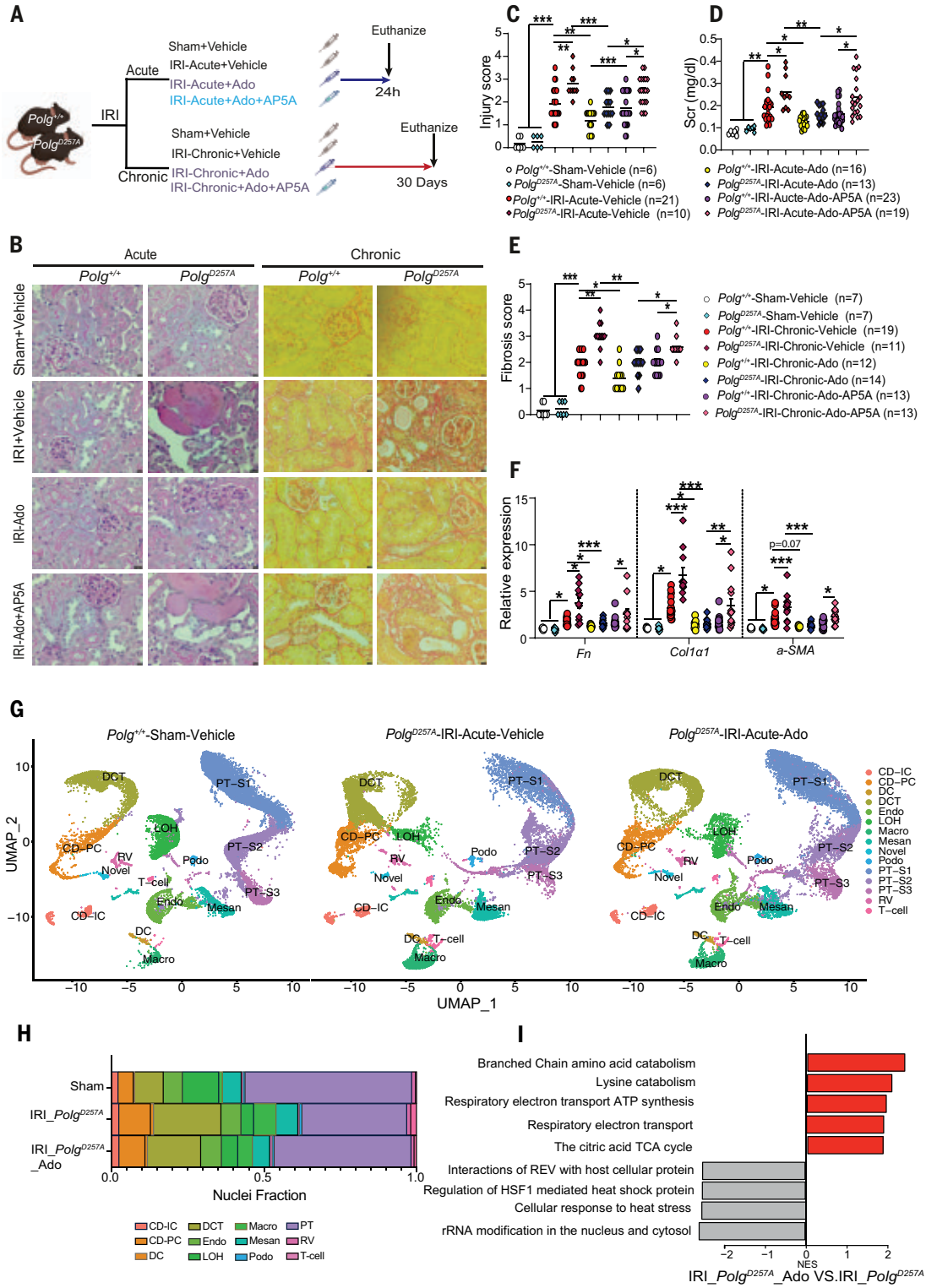


Fig. 4. Adenosine restores injury resistance in mtDNA mutated animals through adenylate kinase. (**A**) Schematic depicting time points for evaluation after kidney IRI in *Polg*^{D257A} mice versus littermate wild-type control *Polg*$^{+/+}$ mice receiving adenosine (Ado, 17.5 mg/kg ip × 1) ± adenylate kinase inhibitor (AP5A, 5 mg/kg ip × 1) at the time of surgery. (**B**) PAS-stained (left two columns) and picrosirius red–stained (right two columns) representative photomicrographs of kidney cortex from indicated conditions. Scale bar, 50 μm. Blinded quantification of (**C**) histological tubular injury, (**D**) serum creatinine, and (**E**) histological fibrosis. (**F**) PCR of kidney cortex mRNA for fibrosis markers *Fn*, *Col1α1*, and *α-SMA*. (**G**) UMAP (uniform manifold approximation and projection) plots of single-nucleus RNA-seq from the following kidneys: *Polg*$^{+/+}$ undergoing sham surgery and treated with vehicle (left); *Polg*^{D257A} undergoing IRI and treated with vehicle (middle); and *Polg*^{D257A} undergoing IRI and treated with adenosine (right). (**H**) Cell population proportions from (G): CD, collecting duct; IC intercalated cell; PC principal cell; DCT, distal convoluted tubule; Endo, endothelial cell; LOH, loop of Henle; Macro, macrophage; Mesan, mesangial; Podo, podocyte; PT, proximal tubule; RV, renal vesicle. (**I**) Pathway analysis results with net enrichment score (NES) PT population from kidneys: *Polg*^{D257A} undergoing IRI and treated with adenosine versus *Polg*^{D257A} undergoing IRI and treated with vehicle. **P* < 0.05, ***P* < 0.01, ****P* < 0.001, as indicated.

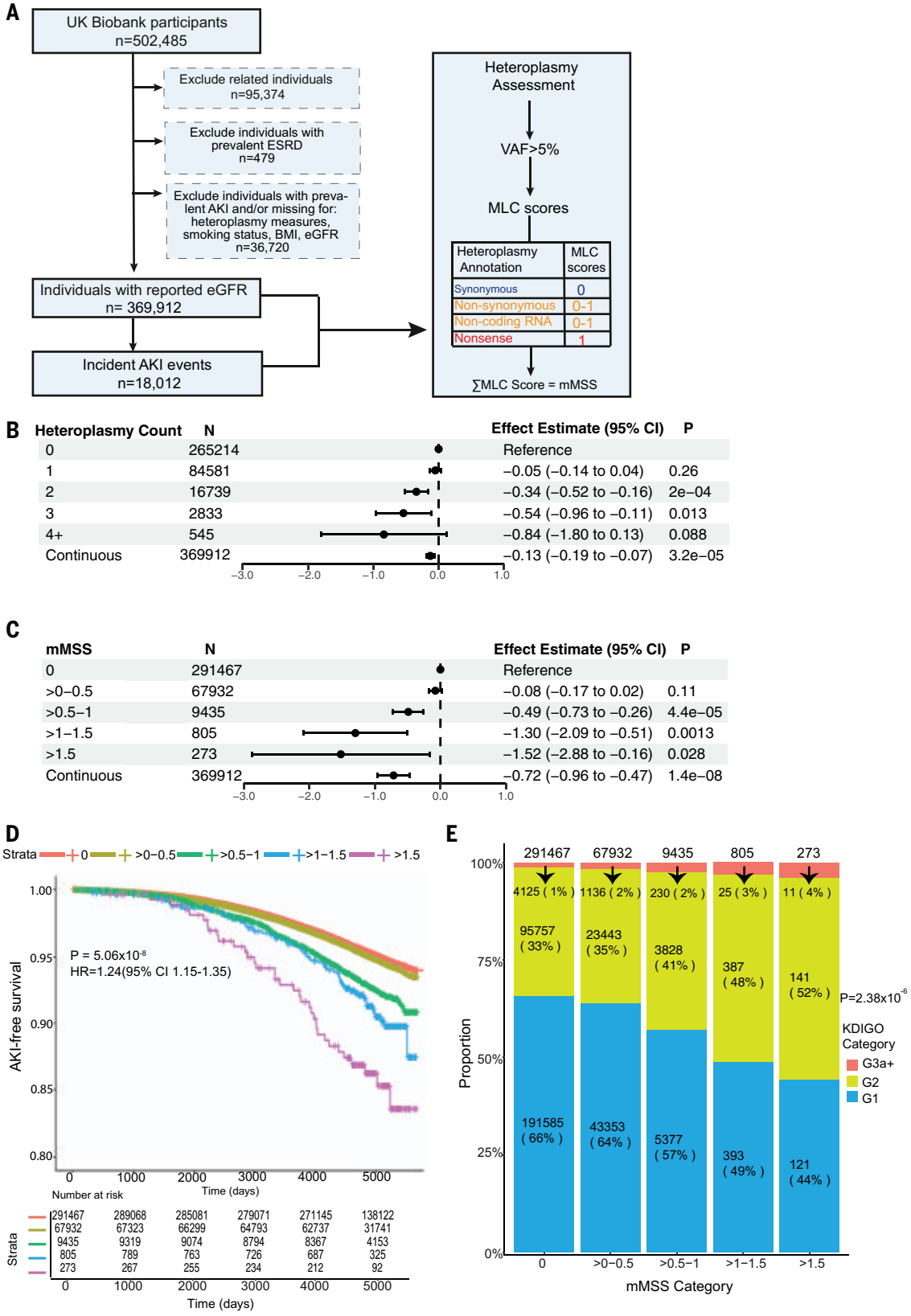


Fig. 5. mtDNA mutations in humans increase the risk of future acute kidney injury and are independently associated with CKD severity. (**A**) Flowchart illustrating application of MLC model in UK Biobank (n = 369,912 with 18,012 incident AKI events). (**B** and **C**) Forest plots showing the association of mtDNA heteroplasmy count (B) and mMSS (C) with eGFR, respectively. (**D**) Kaplan-Meier survival curves for association between mMSS and AKI. (**E**) Proportion of participants with same mMSS at different increasingly severe clinical categories of CKD: G1 (normal), G2 (mild), G3+ (moderate to advanced). $P = 5.83 \times 10^{-6}$. Adjusted for sex, age, BMI, assessment center, and smoking status.

To determine the impact of mitochondrial heteroplasmy on AKI, we performed Cox proportional hazards models adjusted for assessment center, age, sex, body mass index, and smoking status. The mMSS was associated with a 1.25-fold increased hazard ratio (HR) for incident AKI (95% CI 1.15 to 1.35, $P = 4.50 \times 10^{-8}$; Fig. 5D). Including the number of heteroplasmies in the model only minimally attenuated the result (HR = 1.23, 95% CI 1.12 to 1.36, $P = 1.13 \times 10^{-5}$). Because mtDNA mutation burden was associated with both eGFR—a measure of persistent kidney impairment—and risk of future AKI, these findings support the observation that persistent GFR impairment is among the strongest risk factors for AKI (*22*). To determine whether the association of mtDNA heteroplasmy with AKI is independent of reduced eGFR, we then included both mMSS and eGFR in the same model. The mMSS was still associated with incident AKI ($P = 1.70 \times 10^{-6}$), with only modest attenuation of the effect estimate after inclusion of eGFR (HR = 1.21, 95% CI 1.12 to 1.31 versus 1.25, 95% CI 1.15 to 1.35; fig. S13). When we adjusted separately for major risk factors and characteristics of chronic impairment—including type 2 diabetes, hypertension, and albumin-to-creatinine ratio—we found very modest attenuation of the effect of mMSS on AKI risk (HR = 1.21, 95% CI 1.11 to 1.32). These analyses indicated that mMSS is associated with risk of AKI even after adjusting for severity of CKD.

We also grouped patients by different levels of mMSS and categorized them within each group on the basis of the clinical grades proposed by the clinical guidelines: G1 (normal), G2 (mildly decreased), and G3a+ (ranging from mild decrease to kidney failure). Individuals with higher mMSS levels exhibited more severe kidney function decline, with the proportion of G2 increasing from 33% to 52% and G3a+ from 1% to 4% ($P = 5.83 \times 10^{-6}$, adjusted for sex, age, BMI, assessment center, and smoking status; Fig. 5E). Together, these findings suggest that mtDNA mutational burden is independently and proportionally associated with both the risk for future AKI and severity of CKD.

Discussion

Here we have shown that unrelated transient insults lead to a burst of randomly distributed and persistent mutations throughout the mitochondrial genome that reduce gene expression, oxidative metabolism, and resistance to oxidative injury while increasing expression of fibrosis genes. A large human cohort study identified mtDNA burden as a proportional risk factor for future AKI as well as severity of CKD, and additional human results confirmed a relationship between in situ mtDNA mutations and CKD severity.

These results suggest a feed-forward loop in which initial injury leads to persistent mtDNA mutations, which in turn enhance susceptibility to future injury, culminating in irreversible fibrosis. Both in cells and in animals bearing mtDNA mutations, supplementation of adenosine, but not other nucleotide metabolites, acted through adenylate kinase to enhance resistance to early and late adverse sequelae of transient insults.

Overall, 1 out of 5000 adults are diagnosed with mitochondrial disease caused by a homoplasmic mtDNA mutation (*23*). Somatic mtDNA mutations—typically heteroplasmic—are present in ~30% of the adult population (*24*) and have been linked to the development of highly prevalent human conditions as well as overall mortality (*20*, *25*–*27*). These mutations lead to biochemical defects within individual cells. Persistence of mtDNA mutations after transient stress implies an imperfect cellular machinery for monitoring and maintaining wild-type mtDNA genomes.

A recent study of >250,000 individuals suggested roles for multiple nuclear-encoded genes in the regulation of maternally inherited mtDNA indel burden, including the mitochondrial DNA polymerase mutated in this study, *POLG2*, and *AK3*, a paralog of *AK4* described herein (*2*). They also showed that heteroplasmic mutations appear to accumulate somatically with older age rather than as a quantitatively inherited feature. This aligns with the present thesis that mtDNA somatic mutations may be induced by transient stressors throughout life. It remains an open question whether common variation in nuclear-encoded loci such as *POLG2* can control somatic mtDNA mutation load. The kidney may be a model organ to explore this phenomenon, as suggested by a carefully conducted organ-based survey of mtDNA mutation burden across the life span (*3*).

Just as the mtDNA SNV burden is high in the kidney and rises with age (*2*, *3*), there is a sharp rise in the risk of AKI with older age (*28*). A high mtDNA mutation burden may also contribute to adverse long-term outcomes after other age-associated transient insults such as stroke and myocardial infarction. These hypotheses need further study. Our results raise the possibility that variation in normal kidney aging reflects a complex interplay between repeated subclinical injuries and inherited or acquired changes in mtDNA mutation burden.

Both metabolomics and RNA-seq identified defects in nucleotide metabolism arising from increased mtDNA mutations, aligning with recent reports linking mtDNA heteroplasmy with nucleotide balance (*29*, *30*). For both pyrimidine and purine biosynthesis, intact mitochondrial form and function are necessary in at least three ways: (i) provision of sufficient ATP to drive energetically costly reactions necessary for nucleotide synthesis; (ii) localization of individual biosynthetic enzymes or enzyme complexes on or in mitochondria (*31*); and (iii) availability of mitochondrially generated amino acid building blocks for nucleobases (*13*). Purine biosynthesis bears an additional relationship by furnishing the precursor AMP necessary for AKs to generate ADP, which, in turn, undergoes phosphorylation to ATP in the mitochondrion. We found that adenosine required AK4 to restore ATP in cells bearing excess mtDNA mutations, suggesting a reciprocal relationship of mtDNA mutations with *AK* loci. How mtDNA mutations affect purine biosynthesis requires further investigation, although one tracer study has shown that amino acid metabolism may be important (*32*).

Several areas for future investigation should be noted. First, mtDNA mutations could themselves be causal, but also likely indicate the extent of mtDNA damage, including indels, that together impair cellular metabolism and physiological resilience to stressors (*6*, *10*). Second, the polyploid nature of mtDNA permits both inherited and acquired mutations (*33*). Whether both classes of variants are regulated through similar mechanisms merits further study. Third, adenosine can act in multiple ways and is unlikely to protect the kidney solely through substrate-level transformation to ATP. Finally, mtDNA mutation burden reflects a combination of factors favoring the development and persistence of alternative mtDNA clones over the elimination of such clones within a cell's mitochondria or elimination of the cells bearing such clones (*34*). For example, differences in mitophagy may contribute. More frequent sampling may help describe the temporal dynamics of mtDNA mutation appearance after cell injury, particularly with single-cell resolution (*35*). Such methods may also describe tissue-, age-, and disease-related variation of mtDNA mutation burden in humans.

In summary, the present results reveal a burst of acquired mtDNA mutations arising after acute injury that persist to impair cellular metabolic health while promoting fibrosis. In animals, mtDNA mutation burden compromises responses to unrelated acute stressors. In humans, mtDNA mutation burden is independently and quantitatively associated with risk of future AKI and severity of CKD. A high burden of mtDNA mutation reduces nucleotide metabolism, whereas adenosine administration restores cellular metabolic functions and injury resistance through adenylate kinase action. These results reveal mtDNA mutation burden as a genetic and tissue-based indicator of organ health and a nucleotide-dependent mechanism to enhance organ resilience. Considered broadly, the results suggest a means to assess the interaction of genetics and injury at the level of individual tissues in a quantifiable and targetable fashion.

REFERENCES AND NOTES

1. W. Wei *et al.*, *Science* **364**, eaau6520 (2019).
2. R. Gupta *et al.*, *Nature* **620**, 839–848 (2023).

3. M. Sanchez-Contreras *et al.*, *eLife* **12**, e83395 (2023).
4. A. W. Linnane, S. Marzuki, T. Ozawa, M. Tanaka, *Lancet* **1**, 642–645 (1989).
5. Y. Michikawa, F. Mazzucchelli, N. Bresolin, G. Scarlato, G. Attardi, *Science* **286**, 774–779 (1999).
6. A. Trifunovic *et al.*, *Nature* **429**, 417–423 (2004).
7. M. Vermulst *et al.*, *Nat. Genet.* **39**, 540–543 (2007).
8. C. López-Otín, G. Kroemer, *Cell* **184**, 33–63 (2021).
9. S. S. David, V. L. O'Shea, S. Kundu, *Nature* **447**, 941–950 (2007).
10. G. C. Kujoth *et al.*, *Science* **309**, 481–484 (2005).
11. M. T. Tran *et al.*, *Nature* **531**, 528–532 (2016).
12. H. M. Kang *et al.*, *Nat. Med.* **21**, 37–46 (2015).
13. A. N. Lane, T. W. Fan, *Nucleic Acids Res.* **43**, 2466–2485 (2015).
14. S. J. Kerns *et al.*, *Nat. Struct. Mol. Biol.* **22**, 124–131 (2015).
15. N. J. Lanning *et al.*, *Cell Rep.* **7**, 907–917 (2014).
16. V. K. Mootha *et al.*, *Nat. Genet.* **34**, 267–273 (2003).
17. K. M. Dwyer, B. K. Kishore, S. C. Robson, *Nat. Rev. Nephrol.* **16**, 509–524 (2020).
18. S. L. Battle *et al.*, *NAR Genom. Bioinform.* **4**, lqac034 (2022).
19. S. L. Battle *et al.*, medRxiv 2022.09.20.22280151 [Preprint] (2022); https://doi.org/10.1101/2022.09.20.22280151.
20. Y. S. Hong *et al.*, *Nat. Commun.* **14**, 6113 (2023).
21. N. J. Lake *et al.*, *Nature* **635**, 390–397 (2024).
22. L. S. Chawla, P. W. Eggers, R. A. Star, P. L. Kimmel, *N. Engl. J. Med.* **371**, 58–66 (2014).
23. G. S. Gorman *et al.*, *Ann. Neurol.* **77**, 753–759 (2015).
24. K. M. Laricchia *et al.*, *Genome Res.* **32**, 569–582 (2022).
25. M. Corral-Debrinski *et al.*, *Genomics* **23**, 471–476 (1994).
26. J. B. Stewart, P. F. Chinnery, *Nat. Rev. Genet.* **16**, 530–542 (2015).
27. A. Bender *et al.*, *Nat. Genet.* **38**, 515–517 (2006).
28. R. Saran *et al.*, *Am. J. Kidney Dis.* **71** (suppl. 1), A7 (2018).
29. J. Nikkanen *et al.*, *Cell Metab.* **23**, 635–648 (2016).
30. J. Shintaku *et al.*, *J. Clin. Invest.* **132**, e145660 (2022).
31. J. B. French *et al.*, *Science* **351**, 733–737 (2016).
32. E. W. Lim *et al.*, *Sci. Adv.* **7**, eabj4077 (2021).
33. E. A. Schon, S. DiMauro, M. Hirano, *Nat. Rev. Genet.* **13**, 878–890 (2012).
34. Y. Kirita, H. Wu, K. Uchimura, P. C. Wilson, B. D. Humphreys, *Proc. Natl. Acad. Sci. U.S.A.* **117**, 15874–15883 (2020).
35. L. S. Ludwig *et al.*, *Cell* **176**, 1325–1339.e22 (2019).

ACKNOWLEDGMENTS

We thank M. Pollak and M. Brown for advice and support. **Funding:** This work was supported by awards from the National Heart, Lung, and Blood Institute, the National Institute on Aging, and the National Institute of Diabetes and Digestive and Kidney Disease: R01HL144569 (D.E.A., W.S., D.P.), R01AG085753 (D.E.A., W.S., Y.S.H.), R01AG027002 (M.G.S., M.J.S., S.M.P.), U01DK04308 (S.S.W.), and R01DK095072 (S.M.P.). **Author contributions:** H.H. and S.M.P. conceptualized the primary experiments. H.H. conducted the experiments, with support from Y.W., Z.K.Z., J.M.G., V.V., A.J.C., H.P., and J.M.D. V.J., M.G.S., M.J.S., S.S.W., C.R.P., H.T.-P., R.K., J.G.S., D.E.A., and S.M.P. designed the human tissue and genetic studies. D.E.A., Y.S.H., W.S., D.P., N.J.L., and M.L. conducted the UK Biobank analysis. H.H. and S.M.P. led the writing of this manuscript, with contributions from all authors. **Competing interests:** The authors declare that they have no competing interests. **Data and materials availability:** Requests for resources and reagents should be directed to and will be fulfilled by the lead contact, S.M.P. (samir.parikh@utsouthwestern.edu). Reagents and methods in this study will be made available by S.M.P. upon request. UK Biobank analyses were conducted using the UK Biobank Resource under application number 17731. The next-generation sequencing datasets generated during this study are available through the BioSample database (NCBI). RNA-seq raw data are available in the Gene Expression Omnibus (GEO) (GSE239772). The mt-DNA sequencing raw data are available in Sequence Read Archive (SRA) (PRJNA1002252) Metabolomics peak data are available in table S3. Analysis details are provided in the materials and methods section of the supplementary materials. Any additional information is available from S.M.P. upon request. **License information:** Copyright © 2025 the authors, some rights reserved; exclusive licensee American Association for the Advancement of Science. No claim to original US government works. https://www.science.org/about/science-licenses-journal-article-reuse

SUPPLEMENTARY MATERIALS

science.org/doi/10.1126/science.adk7978
Materials and Methods; Figs. S1 to S13; Tables S1 to S13; References (*36*–*74*); MDAR Reproducibility Checklist

Submitted 24 September 2023; resubmitted 1 March 2025; accepted 10 July 2025; published online 4 September 2025

10.1126/science.adk7978

OPTICS

Wavefront shaping enables high-power multimode fiber amplifier with output focus

Stefan Rothe[1]†, Chun-Wei Chen[1,2]†, Peyman Ahmadi[1,3]†, KyeoReh Lee[1]†, Kabish Wisal[4], Mert Ercan[1], Nathan Vigne[1], A. Douglas Stone[1], Hui Cao[1]*

High-power fiber lasers are powerful tools used in science, industry, and defense. A major roadblock for further power scaling of single-frequency fiber laser amplifiers is stimulated Brillouin scattering. Efforts have been made to mitigate this nonlinear process, but these were mostly limited to single-mode or few-mode fiber amplifiers, which have good beam quality. Here, we explored a highly multimode fiber amplifier in which stimulated Brillouin scattering was greatly suppressed due to a reduction of light intensity in a large fiber core and a broadening of the Brillouin scattering spectrum by multimode excitation. By applying a spatial wavefront shaping technique to the input light of a nonlinear amplifier, the output beam was focused to a diffraction-limited spot. Our multimode fiber amplifier can operate at high power with high efficiency and narrow linewidth, which ensures high coherence. Optical wavefront shaping enables coherent control of multimode laser amplification, with potential applications in coherent beam combining, large-scale interferometry and directed energy delivery.

High-power lasers have enabled a wide range of applications such as laser machining, metrology, and directed energy delivery (*1*–*4*). The ultimate limit on power scaling of such lasers are the nonlinear effects and/or material damage encountered during light amplification inside the lasers. An important technique to overcome such detrimental effects in short-pulse amplifiers is chirped pulse amplification, in which laser pulses are stretched temporally, then amplified, and finally compressed (*5*). A similar technique for continuous-wave (CW) amplifiers is the spatial spread of light, for example, by increasing the core area of a fiber amplifier. However, a fiber of larger core tends to support more guided modes, and the interference of light in these modes will generate a pseudorandom spatial field distribution, leading to poor output beam quality. Because high beam quality is needed for many applications, there have been extensive efforts to increase the core area by reducing the numerical aperture (NA) (*6*–*15*) or to explore microstructured fibers while maintaining single-mode amplification (*16*). However, further power scaling is still limited by optical nonlinearities and instabilities [see the supplementary materials, section 3 (*17*)].

The lowest-power nonlinear limit in power scaling of narrow-band fiber amplifiers typically arises from stimulated Brillouin scattering (SBS) of light mediated by acoustic waves (*18*, *19*). This effect scatters the forward-propagating signal to backward-propagating Stokes light, thus limiting the amplifier output power. Moreover, intense Stokes pulses might be generated that could damage upstream lasers. Various techniques have been developed to mitigate SBS, mostly in single-mode or few-mode fibers, to maintain high output-beam quality. One method used to increase the SBS threshold is to increase the signal linewidth to tens of gigahertz to effectively broaden the Brillouin scattering spectrum and thereby lower the peak gain for SBS (*20*). However, this approach greatly reduces temporal coherence, which is required for applications such as metrology and gravitational wave detection (*21*, *22*). To suppress SBS in the single-frequency (linewidth <100 kHz) regime, different approaches have been explored [see the supplementary materials, section 3 (*17*)], such as tailoring acoustic and gain properties, applying differential strain and/or temperature gradients, tapering fiber core diameter, and tight coiling short fibers (*10*, *16*, *23*–*30*). However, SBS remains the major obstacle to power-scale, single-frequency, single-mode fiber (SMF) amplifiers (*31*).

Optical wavefront shaping has become a powerful technique for controlling light propagation in complex media including multimode fibers (MMFs) (*32*). For example, it has been found in previous studies that tailoring the incident wavefront of light to an MMF with a spatial light modulator (SLM) can create any spatial pattern of transmitted field that is a superposition of the fiber modes (*33*–*35*). However, most of these studies were conducted on passive MMFs with linear light propagation or on low-power MMF amplifiers with weak nonlinearity (*36*, *37*). Adaptive mode control through a photonic lantern front end has been used to maintain single-mode operation in a few-mode fiber amplifier (*38*), but this scheme is difficult to extend to the highly multimode regime. Although large-scale wavefront shaping has been used to control nonlinear optical processes in passive MMFs (*39*–*41*), it has not been applied to high-power MMF amplifiers with strong nonlinearity, so its ability, efficacy, and robustness for controlling complex, unstable multimode amplification are not yet known.

Here, we simultaneously suppressed detrimental SBS and focused the output beam in a highly multimode nonlinear fiber amplifier using input wavefront shaping. Our MMF amplifier is free of SBS up to 503 W output power, which is ~30 times higher than the SBS limit in a standard SMF of same length. The slope efficiency is 82%, comparable to SMF amplifiers. The output of our MMF amplifier has a 20-dB linewidth of 18 kHz, corresponding to a 3-dB linewidth of 1 kHz. This linewidth is six orders of magnitude narrower than that of spectrally broadened SMF amplifiers, leading to six orders of magnitude longer temporal coherence length.

We addressed the main concern with using such an MMF amplifier, output beam quality, by focusing the output beam with input wavefront shaping. The beam propagation factor for the focal spot is $M^2 \leq 1.35$. The ability to control the output beam shape, together with the high temporal coherence of our MMF amplifier, will greatly facilitate coherent combining of output beams from multiple amplifiers.

SBS

In our master oscillator power amplifier configuration (Fig. 1), the linearly polarized CW output of a single-frequency laser oscillator at wavelength $\lambda_S = 1064$ nm was preamplified by two-stage Yb-doped SMF preamplifiers. Using a liquid-crystal SLM, we applied phase-only modulation to the linearly polarized signal before coupling it to a Yb-doped MMF amplifier that supports 76 spatial modes. The doped fiber was cladding pumped by five diode lasers in the wavelength range of 966 to 971 nm to amplify the signal through stimulated emission of Yb ions [see the materials and methods for more details (*17*)].

In the fiber amplifier, the signal being amplified acted as a pump for SBS, generating a backward-propagating Stokes field by emitting forward-propagating acoustic waves. The Stokes field was amplified by both SBS and stimulated emission of excited Yb ions as it propagated backward through the fiber. With increasing pump power, the time trace of the backscattered light intensity showed random spikes of duration ~10 to 100 ns (left inset of Fig. 1). These sharp intensity fluctuations are attributed to an SBS-induced dynamic instability (*42*–*45*) and represent a precursor for the onset of SBS (*19*). Here, we

[1]Department of Applied Physics, Yale University, New Haven, CT, USA. [2]Edward L. Ginzton Laboratory, Stanford University, Stanford, CA, USA. [3]Coherent, Bloomfield, CT, USA. [4]Department of Physics, Yale University, New Haven, CT, USA. ***Corresponding author. Email: hui.cao@yale.edu** †These authors contributed equally to this work.

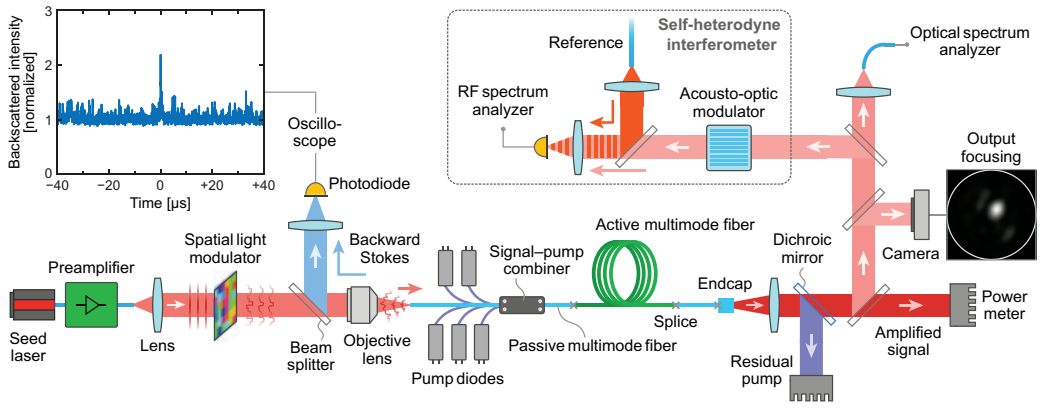


Fig. 1. Schematic of our MMF amplifier with input wavefront shaping to focus output beam. A single-frequency seed laser at wavelength $\lambda_S = 1064$ nm was preamplified to 10 W. The CW beam was expanded and wavefront shaped by an SLM before coupling to a Yb-doped MMF amplifier pumped by five laser diodes. The amplified signal and residual pump were separated by a dichroic mirror, and their powers were measured by power meters. A camera recorded the near-field intensity distribution of the amplified signal outside of the MMF facet. The optical spectrum and linewidth of the output signal were measured with an optical spectrum analyzer and a heterodyne interferometer. The SLM shaped the input wavefront to focus the output beam to a diffraction-limited spot. The right inset shows the focal spot at an output power of 503 W. The left inset is the time trace of total backscattered intensity (normalized to its Rayleigh-scattering component), exhibiting a large spike due to SBS. RF, radiofrequency.

define the SBS instability threshold as the output signal power at which the maximum height of Stokes spikes is 1.5 times that of the continuous background from Rayleigh scattering in the backward intensity trace. This level is well below the conventional SBS threshold that is typically set by the condition that the reflected power equals a small percentage of the transmitted signal power (*46*).

Compared with the standard SMF amplifier, the large cross-section of our MMF amplifier lowers the signal intensity within the fiber core, thus reducing SBS. Similar to the conventional SBS threshold, the SBS instability threshold is expected to scale quadratically with the fiber core diameter [see the supplementary materials, section 2 (*17*)]. If only the fundamental mode (FM) was excited in our MMF with a 42-μm core, the SBS threshold was about eight times that in a large-mode-area SMF amplifier with a 15-μm core (*19*). From the previously measured SBS instability threshold in the SMF amplifier (*45*), we estimated the SBS instability threshold for FM-only excitation in our MMF amplifier to be 24 W, as shown in Fig. 2A.

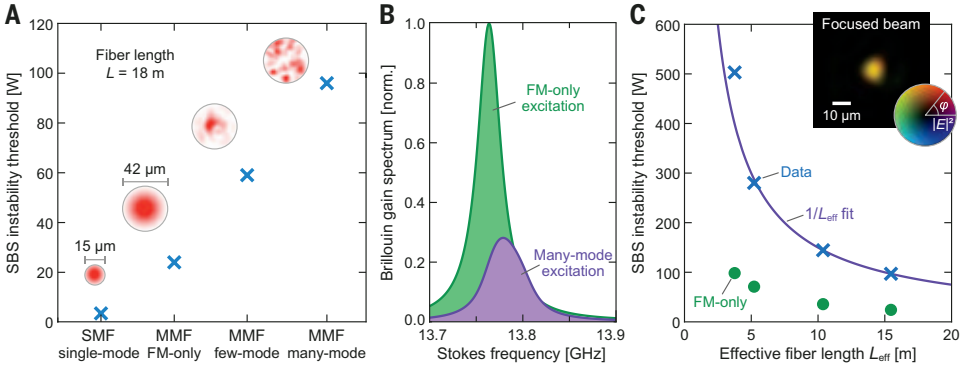


Fig. 2. SBS in single-frequency fiber amplifiers. (**A**) Output signal power at the SBS instability threshold estimated for a 15-μm-core SMF amplifier and compared with a 42-μm-core MMF amplifier under FM-only excitation. Inset shows the calculated intensity profile of the FM. SBS instability thresholds for the MMF amplifier were measured with few-mode and multimode excitations. Inset shows the output intensity distributions. Both SMF and MMF were 18 m long. (**B**) Brillouin gain spectrum calculated with equal excitation of all modes (purple) was broader than FM-only excitation (green) in the MMF amplifier. (**C**) SBS instability threshold as a function of effective fiber length $1/L_{\text{eff}}$ for the 42-μm-core MMF with multimode excitation. Blue crosses are experimental data, and purple solid curve shows the $1/L_{\text{eff}}$ scaling. All data points were taken with the output beam focused to a diffraction-limited spot. Green circles represent the estimated SBS instability thresholds under FM-only excitation at corresponding lengths. The inset shows intensity and phase distributions across the focal spot at output signal power of 173 W. Seventy-six percent of total output power was concentrated inside the focus. Color represents phase and brightness represents the intensity.

Experimentally, it was difficult to realize FM-only excitation in the MMF amplifier because of the inevitable mode coupling in the fiber. When we used a lens of NA ≈ 0.03 to launch the signal into the MMF, the output beam was distorted from a smooth, symmetric profile (inset of Fig. 2A), indicating that both FM and a few high-order modes (HOMs) were excited. The measured SBS instability threshold for the few-mode excitation was 59 W. To excite more HOMs in the MMF amplifier, we replaced the lens with a microscope objective of NA = 0.13, slightly larger than the fiber NA = 0.1. With the input signal tightly focused onto the front facet of the MMF, the output beam was speckled, as seen in the inset of Fig. 2A. The measured SBS instability threshold for multimode excitation was 97 W.

Multimode SBS theory

The fourfold increase of the SBS instability threshold (24 to 97 W) by multimode excitation within the same MMF can be explained by our semianalytic theory of SBS in the MMF amplifier (*46*–*48*). When the input light is distributed over multiple fiber modes, the forward-propagating signal in each mode will be Brillouin scattered to backward-propagating Stokes in all modes. This process is mediated by acoustic modes in the fiber, and the Stokes is frequency downshifted from the signal by the acoustic frequency Ω. The scattering coefficient for signal in the l-th mode and Stokes in the m-th mode, $g_B^{(m,l)}(\Omega)$, depends on the spatial overlap of the signal and Stokes mode profiles with various acoustic modes in the fiber. Each mode

pair of l and m typically has the largest spatial overlap with a single acoustic mode, meaning that $g_B^{(m,l)}$ peaked at this acoustic mode frequency Ω. The total Brillouin gain at axial position z in the m-th mode due to signals in all fiber modes is:

$$G_B^{(m)}(z) = \sum_l g_B^{(m,l)}(\Omega) P_S^{(l)}(z) \quad (1)$$

where $P_S^{(l)}$ is the signal power in the l-th mode. The growth rate of Stokes power in the m-th mode $P_B^{(m)}$ is determined by $G_B^{(m)}$

$$\frac{dP_B^{(m)}}{-dz} = G_B^{(m)} P_B^{(m)}(z) \quad (2)$$

Because of the exponential nature of growth, the total Stokes power, $P_B = \sum_m P_B^{(m)}$, is dominated by the mode m that has the maximum value of $G_B^{(m)}$.

$G_B^{(m)}$ depends on the signal power distribution among the fiber modes. We consider three cases below. First, all of the signal power is in the FM, meaning $l = 1$. $g_B^{(l,l)}$ is larger than $g_B^{(m,l)}$ for any $m > 1$ because of better spatial overlap between optical and acoustic modes. Thus, Brillouin scattering is strongest for the Stokes field in the FM ($m = 1$), mediated by the lowest-order acoustic mode in the fiber. Second, consider when a single HOM $l > 1$ is excited. Because of larger acousto-optic overlap, intramodal Brillouin scattering ($m = l$) is stronger than intermodal scattering ($m \neq l$), $g_B^{(l,l)} > g_B^{(m,l)}$ for any $m \neq l$. However, smaller acousto-optic overlap makes $g_B^{(l,l)} < g_B^{(1,1)}$, and the SBS threshold for $l > 1$ is higher than that with FM-only excitation. Third, if input power is distributed among all fiber modes, then $G_B^{(m)}$ is a sum of intramodal and intermodal scattering coefficients weighted by the signal power $P_S^{(l)}$ in individual modes, which is much less than the total power. Because $g_B^{(m,l)}$ for different mode pairs peaked at varying frequencies Ω, $G_B^{(m)}$ is spectrally broadened and has a notably lower peak value than single-mode excitation (Fig. 2B). Because the peak value dictates the exponential growth of Stokes power, the SBS threshold is appreciably higher for multimode excitation than for the excitation of any single mode.

Pump depletion and gain saturation

In a high-power MMF amplifier such as ours, gain saturation and pump depletion are strong. These effects determine the signal power distribution throughout the fiber, which affects the Stokes growth rate. To include these effects in our theory, we extended our earlier model (*46*) as follows. We first calculated the signal power in each mode $P_S^{(l)}(z)$ throughout the fiber, taking into account gain saturation and pump depletion in the MMF amplifier (*49*). At or below the SBS instability threshold, the Stokes power is much lower than the signal power, so feedback due to SBS was neglected when computing the signal power and pump power distribution in the MMF amplifier [see the supplementary materials, section 2 (*17*)].

Numerical simulation of our MMF amplifier using the improved model [with parameters listed in table S1 (*17*)] revealed that the pump power (at wavelength $\lambda_P = 971$ nm) was mostly absorbed in the first 6 m of the Yb-doped fiber. Beyond this distance, the signal power did not grow appreciably [fig. S6 (*17*)]. To investigate the scaling of SBS instability threshold with fiber length, we started with a long fiber and gradually cut it back in Fig. 2C. From the physical fiber length L and total signal power $P_S(z) = \sum_l P_S^{(l)}(z)$, we computed the effective fiber length for SBS as follows: $L_{eff} = \int_0^L P_S(z)dz / P_S(L)$. Figure 2C shows that the measured SBS instability threshold increased rapidly as L_{eff} decreased (blue crosses). The blue curve shows that SBS threshold scaled inversely with L_{eff}, as expected from our theory [see the supplementary materials, section 2 (*17*)]. To illustrate the enhancement by multimode excitation, the green circles show the estimated thresholds with FM-only excitation at fiber lengths corresponding to experimental values. At the shortest length $L_{eff} = 3.7$ m, the measured SBS instability threshold reached 503 W, ~5 times higher than the FM-only threshold.

Output beam shaping

All data points in Fig. 2C were taken with the output beam focused to a chosen spot outside of the distal facet of the MMF by optimizing the input phase front with the SLM [see the materials and methods (*17*)]. The inset in Fig. 2C is an optical image of focal spot taken at 173 W output signal power. With phase-only modulation of the input signal, 76% of total output power was concentrated within the focal area. We obtained similar focusing efficiencies at higher powers [fig. S7 (*17*)]. The near-field focusing of the output beam was achieved through interference of signal in many fiber modes, so the SBS instability threshold was enhanced by multimode excitation in the amplifier.

To control the output beam profile by input wavefront shaping, the signal bandwidth must be narrower than the spectral correlation width of a MMF amplifier. The latter characterizes how fast the output field pattern decorrelates with frequency detuning for a fixed input wavefront. Despite gain saturation and pump depletion in our MMF amplifier, its spectral correlation width barely changed from that of the passive MMF (*50*). With increasing fiber length, the spectral correlation width decreased, but even for the longest MMF of our amplifier, the correlation width exceeded 1 GHz, which is well above the signal bandwidth (see the next section). The amplified signal was spatially coherent; that is, the relative phase of output fields between any two positions was time invariant. Therefore, the speckle pattern created by multimode interference at any frequency within the signal bandwidth was almost identical, leading to the high-intensity contrast seen in the inset of Fig. 2A.

The spatial coherence of the amplified signal allowed us to generate the same output pattern, e.g., focusing to a chosen location, for all frequency components by imposing a single wavefront on the input beam. To measure the phase of the output field, we performed an interferometric experiment [see the materials and methods (*17*)]. The inset of Fig. 2C shows that the measured phase was constant across the focal spot, confirming diffraction-limited focusing.

To track axial evolution of a focal spot, we imaged the transverse intensity distribution at different axial planes. Three exemplary images are presented in Fig. 3, A to C, revealing that the spot radius increases

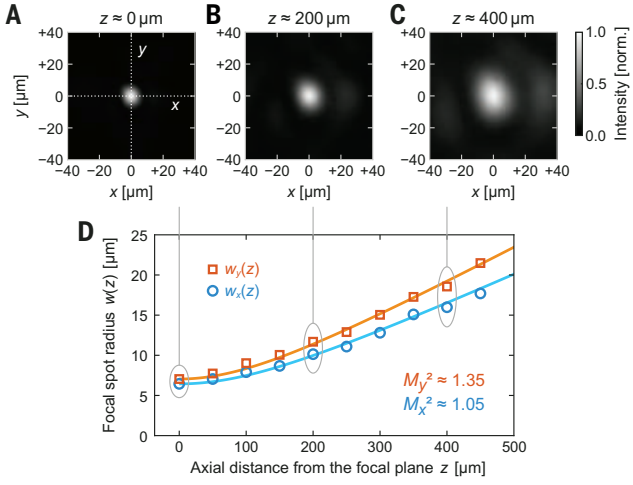


Fig. 3. Beam propagation factor of a focal spot at the MMF amplifier output. (**A**) Intensity profile of a diffraction-limited spot created 300 μm from the MMF distal facet by shaping phase front of input signal; 76% of total output power was concentrated inside the focal area. (**B** and **C**) Output beam profiles recorded at axial distance $z \approx 200$ μm (B) and 400 μm (C) from the focal plane, respectively. (**D**) Focal spot radii along x and y axes (perpendicular to fiber axis z), w_x and w_y, increased with axial distance z. Squares and circles mark experimental data, solid curves represent the fit with Eq. 3 that gives $M_x^2 \approx 1.05$ and $M_y^2 \approx 1.35$.

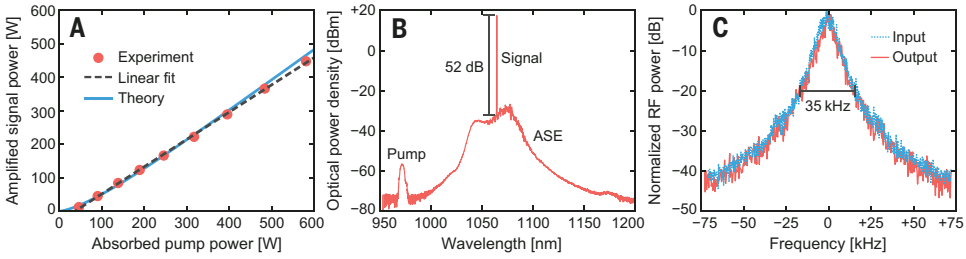


Fig. 4. High-power MMF amplifier with narrow linewidth. The fiber core diameter was 42 μm and the effective length L_{eff} was 3.7 μm. (**A**) Amplified signal power as a function of absorbed pump power gives a slope efficiency of 82%. Red circles are experimental data, black dashed line is a linear fit of data, and blue curve is from our theoretical model. (**B**) Optical spectrum of amplifier output at 453 W power showing the amplified signal peak at 1064 nm on top of a broad amplified ASE band. The signal-to-ASE peak ratio was 52 dB. The small peak centered at 971 nm is from the residual pump. (**C**) Heterodyne spectra for input (blue) and output (red) signals of the MMF amplifier at an output signal power of 503 W. The sweep time was 41 ms. Full width at −20 dB of maximum was 35 kHz for both input and output signals, indicating no detectable spectral broadening by the MMF amplifier. After subtracting the reference linewidth, the 20-dB width of input/output signal was 18 kHz.

with axial distance z from the focal plane. We extracted the intensity profiles in the x and y axes and fit them with a Gaussian envelope to obtain the spot radius w_x and w_y [see the materials and methods (*17*)]. Figure 3D shows the growth of w_x and w_y with z. We fit the z dependence as follows:

$$w(z) = w(0)\sqrt{1+\left(\frac{M^2\lambda_S z}{\pi n[w(0)]^2}\right)^2} \quad (3)$$

where $w(0)$ is the focused spot radius at the focal plane ($z = 0$), λ_S is the signal wavelength in vacuum, and $n \approx 1.45$ is the refractive index of the glass endcap in which the output beam is focused and further propagates. Equation 3 fits the data well and gives the beam propagation factors $M_x^2 \approx 1.05$ and $M_y^2 \approx 1.35$.

Efficiency and linewidth

We further characterized the performance of our high-power MMF amplifier with the shortest $L_{eff} = 3.7$ μm. First, we measured the output signal power and residual pump power. The power of the amplified signal is given by the difference between input and output signal power, $P_S^{(amp)} = P_S^{(out)} - P_S^{(in)}$. The absorbed pump power was obtained by subtracting the residual pump power at the amplifier output from the pump power launched into the MMF, $P_P^{(abs)} = P_P^{(in)} - P_P^{(out)}$. Figure 4A shows that $P_S^{(amp)}$ increased almost linearly with $P_P^{(abs)}$. A linear fitting gives a slope efficiency of 82%. The experimental data agreed with the theoretical prediction of our model.

We also measured the output spectrum of the MMF amplifier with an optical spectrum analyzer. In Fig. 4B, the signal appears as a narrow peak at $\lambda_S = 1064$ nm. It sits on top of a broad amplified spontaneous emission (ASE) band. The peak ratio of amplified signal to ASE was 52 dB.

The signal linewidth, which was too narrow to be resolved by the optical spectrum analyzer, was measured by a heterodyne interferometer [see the materials and methods (*17*)]. Figure 4C shows the heterodyne peak resulting from beating of the amplified signal and a reference (red curve). The full width at −20 dB of the maximum was $\Delta\nu_M = 35$ kHz. Subtracting the reference width of $\Delta\nu_R = 17$ kHz (fig. S6), the 20-dB width of the output signal was $\Delta\nu_S = \Delta\nu_M - \Delta\nu_R = 18$ kHz, corresponding to a Lorentzian line of 3-dB bandwidth (full width at half maximum) ~1 kHz.

For comparison, we measured the linewidth of input signal to the MMF amplifier using the same method. As shown by the blue curve in Fig. 4C, the input signal had nearly identical width as the output (red curve), so optical wavefront shaping and coherent multimode amplification do not cause detectable spectral broadening of the signal. As mentioned earlier, a common approach to mitigating SBS in SMF amplifiers is by broadening the input signal linewidth to tens of gigahertz. In our scheme, the 3-dB signal linewidth was six orders of magnitude narrower, and thus the temporal coherence length was six orders of magnitude longer in the MMF amplifier.

Discussion and conclusions

Input wavefront shaping allowed us to simultaneously mitigate SBS in the MMF amplifier and control the output beam profile. Although an SLM placed at the fiber amplifier output end could shape the amplified beam and allow another SLM at the input end to optimize multimode excitation for maximal SBS suppression (*50*), we chose here to shape the low-power seed to avoid high-power handling. In the current experiment, phase-only modulation of the input wavefront limited output focusing efficiency such that ~20 to 30% of power was outside of the focal spot. Complete focusing can be achieved with both amplitude and phase modulation of the input signal (*35*). Full-field modulation will also generate an output beam with M^2 closer to unity (*50*). In addition to output focusing, input wavefront shaping can generate different output profiles of the MMF amplifier, which will be useful for laser welding and material processing. Even in the presence of strong nonlinearity, gain saturation, and pump depletion, as long as the amplifier operates below the instability threshold, optimal input wavefront can be found by minimizing the difference between the measured output beam shape and the target (*51*). In this work, the spatial profile of a single linear polarization of the output beam was controlled by input wavefront shaping. Although the input signal was linearly polarized, polarization mixing in the MMF caused depolarization. However, it was possible to control output beam profiles for two orthogonal polarizations by shaping both input polarizations. This could be done by separating two orthogonal polarizations of the input signal and shaping their field patterns separately before combining them and coupling them to the MMF (*50*).

An instability-free increase of the power in a MMF amplifier beyond the level demonstrated here will be possible by enlarging the fiber core to further suppress SBS. Even if only the FM is excited, the SBS threshold will scale quadratically with the core diameter [see the supplementary materials, section 2 (*17*)]. With multimode excitation, Brillouin spectrum broadening was more pronounced, because additional modes could be excited in an MMF with a larger core, leading to higher enhancement of the SBS threshold. Although our scheme does not rely on specialty fibers, wavefront shaping can be applied to specialized MMFs with lower optical nonlinearity and to microstructured fibers with a large cross-section for higher-power operation.

More generally, our method can be extended to mitigating other detrimental nonlinear effects in high-power fiber amplifiers, such as transverse mode instability, stimulated Raman scattering, and modulation instability, and also to other types of high-power lasers, such as solid-state and semiconductor optical amplifiers. Our scheme of spatial and modal spread of the signal may be combined with a temporal stretch of optical pulses for high-peak-power amplification.

REFERENCES AND NOTES

1. D. J. Richardson, J. Nilsson, W. A. Clarkson, *J. Opt. Soc. Am. B* **27**, B63–B92 (2010).
2. J. Nilsson, D. N. Payne, *Science* **332**, 921–922 (2011).
3. C. Jauregui, J. Limpert, A. Tünnermann, *Nat. Photonics* **7**, 861–867 (2013).
4. M. N. Zervas, C. A. Codemard, *IEEE J. Sel. Top. Quantum Electron.* **20**, 0904123 (2013).
5. D. Strickland, G. Mourou, *Opt. Commun.* **55**, 447–449 (1985).

6. Y. Jeong, J. Sahu, D. Payne, J. Nilsson, *Opt. Express* **12**, 6088–6092 (2004).
7. L. Huang *et al.*, *Appl. Opt.* **56**, 5412–5417 (2017).
8. F. Beier *et al.*, *Opt. Express* **25**, 14892–14899 (2017).
9. R. Sidharthan *et al.*, *Opt. Lett.* **45**, 3828–3831 (2020).
10. C. Dixneuf *et al.*, *Opt. Express* **28**, 10960–10969 (2020).
11. K.-J. Lim *et al.*, *Photon. Res.* **8**, 1599–1604 (2020).
12. Y. Midilli, B. Ortaç, *J. Lightwave Technol.* **38**, 1915–1920 (2020).
13. Y. Chen *et al.*, *Chin. Opt. Lett.* **22**, 041404 (2024).
14. J. W. Nicholson *et al.*, in *Proc. SPIE 12400, Fiber Lasers XX: Technology and Systems, 1240002 (8 March 2023)* (SPIE, 2023); https://doi.org/10.1117/12.2649969.
15. M. Cui *et al.*, *IEEE Photonics J.* **17**, 1–7 (2025).
16. F. Stutzki *et al.*, *Opt. Lett.* **36**, 689–691 (2011).
17. Supplementary materials are available online.
18. A. Kobyakov, M. Sauer, D. Chowdhury, *Adv. Opt. Photonics* **2**, 1–59 (2010).
19. Y. Panbhiharwala, A. V. Harish, D. Venkitesh, J. Nilsson, B. Srinivasan, *Opt. Express* **26**, 33409–33417 (2018).
20. A. Flores, C. Robin, A. Lanari, I. Dajani, *Opt. Express* **22**, 17735–17744 (2014).
21. M. Steinke *et al.*, *IEEE J. Sel. Top. Quantum Electron.* **24**, 1–13 (2017).
22. A. Buikema, F. Jose, S. J. Augst, P. Fritschel, N. Mavalvala, *Opt. Lett.* **44**, 3833–3836 (2019).
23. P. D. Dragic, C.-H. Liu, G. C. Papen, A. Galvanauskas, in *(CLEO). Conference on Lasers and Electro-Optics, 2005* (IEEE, 2005); https://doi.org/10.1109/CLEO.2005.202342.
24. A. Liu, *Opt. Express* **15**, 977–984 (2007).
25. C. Robin, I. Dajani, B. Pulford, *Opt. Lett.* **39**, 666–669 (2014).
26. L. Huang *et al.*, *Opt. Lett.* **42**, 1–4 (2017).
27. S. Hochheim *et al.*, *J. Lightwave Technol.* **40**, 2136–2143 (2021).
28. T. Hawkins *et al.*, *J. Opt. Soc. Am. B* **38**, F38–F49 (2021).
29. W. Jiang *et al.*, *Photonics* **9**, 518 (2022).
30. C. Shi *et al.*, *Front. Phys.* **10**, 982900 (2022).
31. C. Li *et al.*, *Chin. Opt. Lett.* **21**, 090002 (2023).
32. H. Cao, A. P. Mosk, S. Rotter, *Nat. Phys.* **18**, 994–1007 (2022).
33. I. N. Papadopoulos, S. Farahi, C. Moser, D. Psaltis, *Opt. Express* **20**, 10583–10590 (2012).
34. A. M. Caravaca-Aguirre, E. Niv, D. B. Conkey, R. Piestun, *Opt. Express* **21**, 12881–12887 (2013).
35. A. D. Gomes, S. Turtaev, Y. Du, T. Čižmár, *Opt. Express* **30**, 10645–10663 (2022).
36. R. Florentin *et al.*, *Light Sci. Appl.* **6**, e16208 (2017).
37. R. Florentin, V. Kermene, A. Desfarges-Berthelemot, A. Barthelemy, *Opt. Express* **27**, 32638–32648 (2019).
38. J. Montoya *et al.*, *Opt. Express* **25**, 27543–27550 (2017).
39. O. Tzang, A. M. Caravaca-Aguirre, K. Wagner, R. Piestun, *Nat. Photonics* **12**, 368–374 (2018).
40. E. Deliancourt *et al.*, *Opt. Express* **27**, 17311–17321 (2019).
41. L. G. Wright, W. H. Renninger, D. N. Christodoulides, F. W. Wise, *Optica* **9**, 824–841 (2022).
42. R. G. Harrison, J. S. Uppal, A. Johnstone, J. V. Moloney, *Phys. Rev. Lett.* **65**, 167–170 (1990).
43. A. L. Gaeta, R. W. Boyd, *Phys. Rev. A* **44**, 3205–3209 (1991).
44. G. P. Agrawal, *Nonlinear Fiber Optics* (Academic Press, 4 ed., 2006); https://doi.org/10.1016/b978-0-12-369516-1.x5000-6.
45. Y. Panbiharwala, A. Ghosh, J. Nilsson, D. Venkitesh, B. Srinivasan, in *Proc. SPIE 10512, Fiber Lasers XV: Technology and Systems, 105122X (26 February 2018)* (SPIE, 2018); https://doi.org/10.1117/12.2291462.
46. K. Wisal, S. C. Warren-Smith, C.-W. Chen, H. Cao, A. D. Stone, *Phys. Rev. X* **14**, 031053 (2024).
47. C.-W. Chen *et al.*, *Nat. Commun.* **14**, 7343 (2023).
48. K. Wisal *et al.*, *Optica* **11**, 1663–1672 (2024).
49. K. Wisal, C.-W. Chen, H. Cao, A. D. Stone, *APL Photonics* **9**, 066114 (2024).
50. S. Rothe *et al.*, *Opt. Commun.* **577**, 131405 (2025).
51. C.-W. Chen, K. Wisal, M. Fink, A. D. Stone, H. Cao, *Nat. Phys.* **21**, 839–845 (2025).
52. S. Rothe *et al.*, Data for: Wavefront shaping enables high-power multimode fiber amplifier with output focus, Zenodo (2025); https://doi.org/10.5281/zenodo.16651538.

ACKNOWLEDGMENTS

We thank F. M. Ferreira, N. Bender, O. D. Miller, O. Henderson-Sapir, S. C. Warren-Smith, D. L. Smith, L. V. Nguyen, D. J. Ottaway, H. Ebendorff-Heidepriem, M. J. F. Digonnet, and J. Ballato for fruitful discussions; N. Bernardo and V. Bernardo at Yale University for technical assistance; and AFL, Thorlabs, Lightel, and NP Photonics for support. **Funding:** This work was supported by the Air Force Office of Scientific Research (AFOSR grant FA9550-24-1-0182 to H.C. and A.D.S.) and the German Research Foundation (DFG grant RO 7348/1-1 to S.R.).
Author contributions: H.C. proposed the idea and initiated the project. S.R., C.-W.C., P.A., and K.L. designed and built the MMF amplifier system, performed the experiments in collaboration with M.E. and N.V, and analyzed the data in collaboration with K.W. under the supervision of H.C. K.W. developed the theory and numerical simulations under the supervision of A.D.S. S.R., C.-W.C., K.W., A.D.S., and H.C. wrote the manuscript with input from all authors. **Competing interests:** The authors declare no competing interests. **Data and materials availability:** All data needed to evaluate the conclusions in the study are present in the main text or the supplementary materials. The data for all figures are archived in Zenodo (*52*). **License information:** Copyright © 2025 the authors, some rights reserved; exclusive licensee American Association for the Advancement of Science. No claim to original US government works. https://www.science.org/about/science-licenses-journal-article-reuse

SUPPLEMENTARY MATERIALS

science.org/doi/10.1126/science.ady2226
Materials and Methods; Figs. S1 to S6; Tables S1 to S3; References (*53*–*72*)

Submitted 14 April 2025; accepted 13 August 2025

10.1126/science.ady2226

PREDATION

Greater noctule bats prey on and consume passerines in flight

L. Stidsholt[1,2]*†, E. Tena[3]*†, I. Foskolos[1,4], J. Nogueras[3], I. de la Hera[5,6,7], S. Sánchez-Navarro[3], J. L. García-Mudarra[3], C. Ibáñez[3]

Despite billions of passerines seasonally migrating during the night at high altitudes, only three bat species have been found to consistently tap into this rich prey resource. However, it remains unknown where and how these bats locate, catch, and ingest relatively large passerine prey. Here, we used high-resolution biologging tags to reveal that greater noctule bats (*Nyctalus lasiopterus*) ascend to high altitudes, engage in long echo-guided chases, and consume migrating passerines in flight. By using a private sensory channel through ultrasonic echolocation, prolonged chasing, and mid-air prey consumption, these predators can hunt nocturnally migrating passerines at high altitudes and therefore exploit a rich food resource that remains largely inaccessible to most predators.

Tapping into the massive organismal biomass of passerine nocturnal migration (*1*) poses a challenge for predators, yet a few species have evolved ways to opportunistically exploit this food resource (*2*). Based on passerine remains in their feces, it has been suggested that three species of large, fast-flying echolocating bats seasonally catch passerines on the wing at night (*3*–*5*). However, these passerine species are capable of sustained sprinting and evasive maneuvers against diurnal predators (*6*) and their body mass may be more than 50% the body mass of the bat (*7*, *8*). This presents sensory-motor challenges for fast but poorly maneuverable bats (*5*) during aerial capture and handling, raising the question of where and how these bats locate, catch, and ingest passerines. To investigate this, we recorded the flight altitude and fine-scale foraging behavior of greater noctule bats [*Nyctalus lasiopterus* (Schreber, 1780)] ($n = 14$ bats; table S1) with high-resolution multisensor tags (*9*) (Fig. 1G) during spring passerine migration in southern Spain. We complemented tagging efforts with data from DNA metabarcoding of bat feces ($n = 98$ fecal pellets), x-ray scans ($n = 11$ wings), and predator DNA barcoding ($n = 3$ wings) of passerine wings found at hunting grounds of greater noctule bats. Here, we hypothesized that greater noctule bats (i) capture and consume migrating passerines in flight, (ii) use similar sensory strategies when capturing insects and passerines, and (iii) handle and consume passerines in flight similarly to large winged insects.

Greater noctule bats hunt and consume migrating passerines on the wing

To test the hypothesis that greater noctule bats catch passerines in flight, we quantified their foraging behavior with biologging tags. The tags constituted up to 8% of the bats' body mass, and we did not find evidence of long-term effects on tagged bats (table S2). By grouping consecutive buzzes (i.e., a series of high-repetition, frequency-modulated echolocation calls, indicative of a prey capture attempt) that occurred within a 4-s period into a single attack, we found that tagged greater noctule bats attacked, in total, 611 prey items. Of these attacks, 609 were characterized by few buzzes (95% included <5 buzzes), short chases (95% lasted <10 s), and low heights above ground level {hereafter termed "altitude," average value of 53 m [interquartile range (IQR): 38 m]; we deemed an altitude as relatively low when <100 m, following (*10*)} (Fig. 1, A to D). These attacks thus resembled those of most European bats hunting aerial insects (*11*–*13*) and were likely directed toward small-sized prey (e.g., insects) given the short median mastication duration of 11 s [which is less than the 20-s mastication duration for large moths in greater mouse-eared bats (*Myotis myotis*) (*14*); IQR: 32 s; Fig. 1E].

In contrast to these more common attacks, which are likely directed toward insects, two attacks stood out (Figs. 1, A to J, and 2 and fig. S1), where the bats performed climbing flights of >400-m altitude while searching for prey. Upon prey detection, these bats sprinted vertically downward for 30 to 176 s by flapping their wings faster (from 7.2 to 8.5 Hz) and three times stronger (a mean z-axis acceleration increase from 10 to 29 m/s^2) than during ascending flights. The bats continuously chased their prey by buzzing more than 40 times (Figs. 1 and 2, fig. S1, and movie S1), with a median interbuzz interval of 1.4 s (IQR: 1.2 s; Fig. 2D). These two attacks were therefore markedly longer, included more energetic chases, started at higher altitudes, and contained >25 times more buzzes than all other insect attacks (Figs. 1 and 3 and movie S1). The consecutive buzzes during these extended attacks, with short interbuzz intervals and continuous prey echo streams from the bat's sensory scene (Figs. 2D and 3A), suggest that these attacks were directed toward a single prey item despite their extended duration. In one of these long attacks, the bat aborted its pursuit and resumed search flight after the prey likely escaped because no mastication sounds were detected in the audio recordings (fig. S1). In the other event (Figs. 1 and 2 and movie S1), the bat caught its prey close to the ground, with 21 distress calls from the prey recorded immediately afterward (Fig. 1, H and J, and audio S1) followed by mastication sounds for 23 min while in flight. We identified the prey as a European robin [*Erithacus rubecula* (Linnaeus, 1758)] based on a comparison with an audio collection of distress calls from 19 passerine species that have previously been identified in feces of greater noctule bats (*7*) (fig. S2 and tables S3 and S4). Our data are therefore compatible with greater noctule bats being avivores, capable of locating, tracking, and subduing nocturnally migrating passerines on the wing by using their biosonar. The capture and consumption of passerines on the wing therefore do not support the hypothesis that greater noctule bats primarily capture passerines within shared roosts (*15*), which had been refuted before by Ibáñez and Juste (*16*) and Russo *et al.* (*17*).

Greater noctule bats use similar sensory-motor strategies to catch insects and passerines

Because greater noctule bats use echolocation calls of long duration, low frequency, and long intervals to catch insects, their biosonar is suited for long-range detection of prey in open air (*5*). We therefore hypothesized that the tagged bats would use similar sensory strategies when capturing insects and passerines, but that pursuit of faster and more energetic passerines would require prolonged chases. Indeed, while tracking passerines, the bats used buzz durations [median: 184 ms (IQR: 209) versus 189 ms (IQR: 147) for attacks on insects and passerines] and buzz call intervals [median: 7.7 ms (IQR: 3.8) versus 8.7 ms (IQR: 3.1)] similar to those used during insect attacks (Fig. 3, E and F) while also relying on similar pitch [median: 23° (IQR: 29) versus 23° (IQR: 14)], roll [median: 23° (IQR: 47) versus 16° (IQR: 20)], and turn angles [a median tortuosity index of 0.19

[1]Section of Zoophysiology, Department of Biology, Aarhus University, Aarhus, Denmark. [2]Department of Evolutionary Ecology, Leibniz Institute for Zoo and Wildlife Research, Berlin, Germany. [3]Department of Ecology and Evolution, Doñana Biological Station, CSIC, Seville, Spain. [4]Section of Wildlife Ecology, Department of Ecoscience, Aarhus University, Aarhus, Denmark. [5]Environmental Monitoring Team, Birds (ICTS-Doñana), Doñana Biological Station, CSIC, Seville, Spain. [6]Ecology in the Anthropocene, Associated Unit CSIC-UEx, Faculty of Sciences, Extremadura University, Badajoz, Spain. [7]Department of Functional and Evolutionary Ecology, Experimental Station of Arid Zones, CSIC, Almeria, Spain. ***Corresponding author. Email: laura.stidsholt@bio.au.dk (L.S.); etenalopez@gmail.com (E.T.)** †These authors contributed equally to this work.

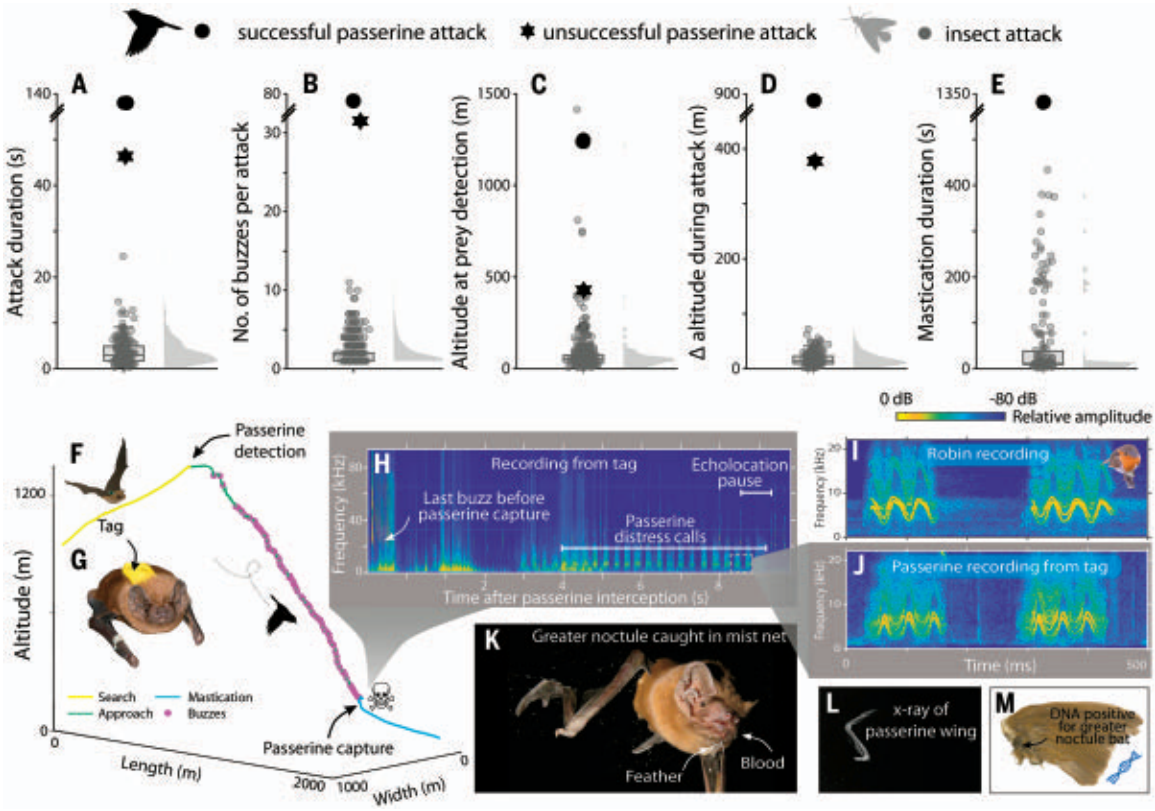
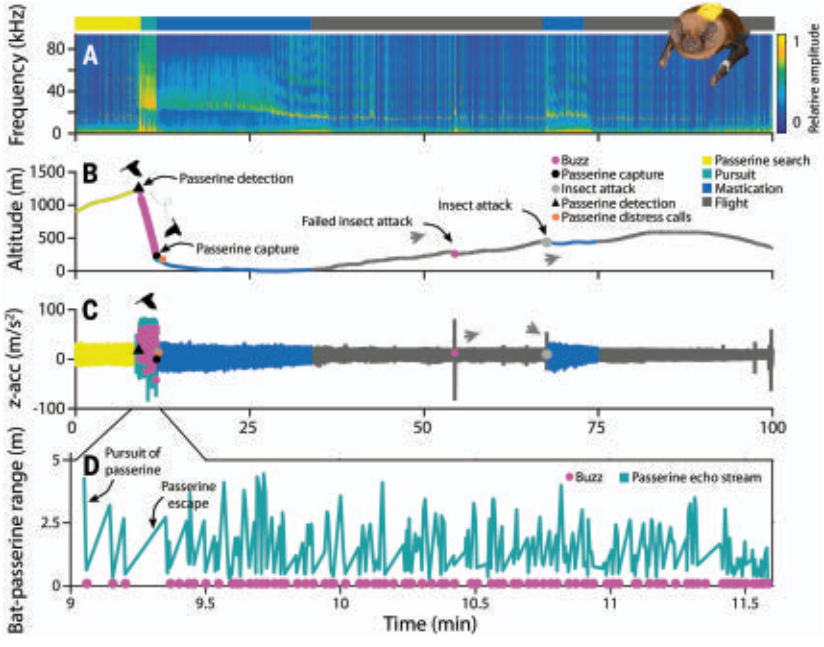


Fig. 1. Greater noctule bats hunt and consume passerines on the wing. (**A** to **E**) Attacks on passerines (black) were much longer (A), contained >25 times more buzzes (B), started at higher altitudes (C), took place over a larger range of altitudes (D), and led to longer mastication durations than insect attacks (gray) (E) (n = 609 insect and 2 passerine attacks from 14 bats). The center line represents the median, box limits are upper and lower quartiles, and whiskers are minimum and maximum values. (**F** and **G**) The dead-reckoning track of the successful passerine attack shows how the bat maneuvered in three-dimensional space. (**H** and **J**) Distress calls emitted by the captured passerine at different timescales. (**I**) The recorded calls match the distress calls of a European robin (*E. rubecula*). (**K**) A greater noctule bat was caught with a passerine feather in its mouth. (**L** and **M**) A wing of a melodious warbler (*Hippolais polyglotta*) was found bitten at the humerus and tested positive for greater noctule bat DNA. [Photo (K) credit: J. Sereno]

Fig. 2. Greater noctule bats pursue migrating passerines through prolonged sprinting and their high-frequency biosonar. (**A**) The echolocation activity during foraging is visualized in a long-term spectral average plot. (**B**) The altitude in meters above the bat roost (i.e., ~10 m above sea level) shows how the bat ascended to 1200 m, where it detected (black triangle), pursued (cyan), and caught (black circle) the robin. (**C**) The oscillations in the z-axis acceleration dimension (z-acc) show the wingbeats (gray) color-coded according to the search (yellow), the pursuit (cyan), and the prey handling (blue) phases. Wingbeat amplitude increased during pursuit and passerine capture. (**D**) During the entire pursuit, interbuzz intervals were short and the interpolated echo stream of the passerine was continuously present in the echograms of the bat's sensory scene.



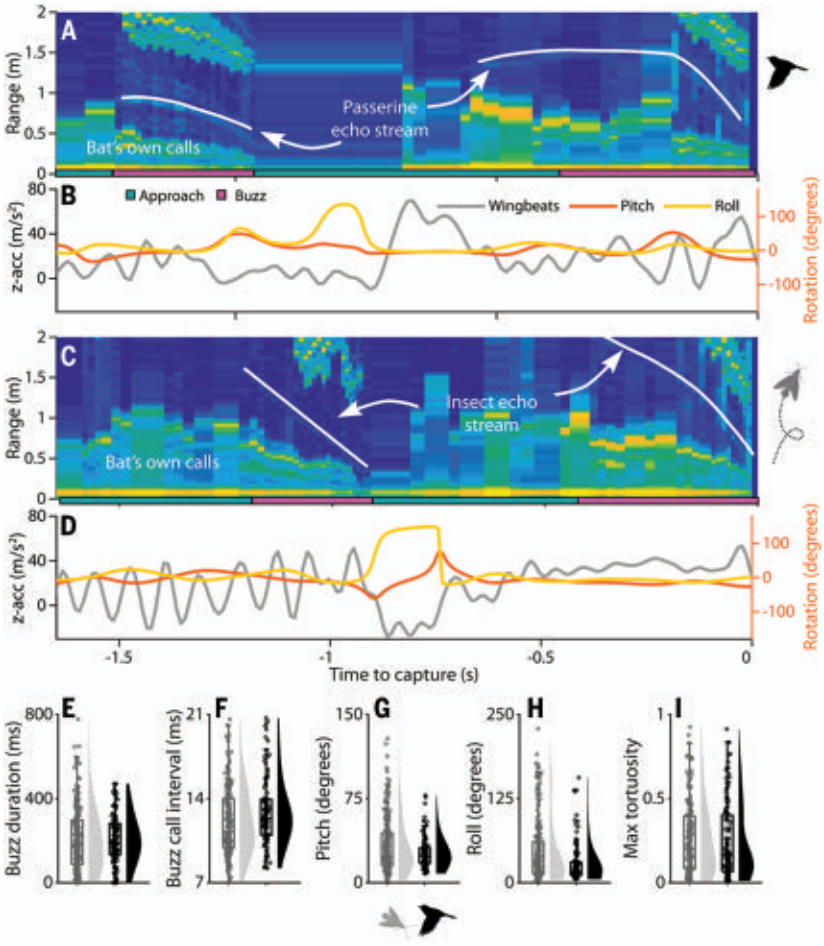


Fig. 3. Greater noctule bats use similar sensory-motor strategies during the last stage of hunting passerines and insects. (**A** and **C**) The sensory scenes of the hunting bats are visualized in echograms (*28*, *29*) for a passerine (black) attack and for an insect (light gray) attack. Echograms are visual representations of the returning echoic scenes over time. This enables tracking of prey echo streams of a passerine (A) and an insect (C), which are highlighted to aid visualization (white, solid lines). (**B** and **D**) The movement is depicted as wingbeats (gray) derived from the oscillations in the *z*-axis acceleration and as pitch and roll estimated from triaxial acceleration data low-pass filtered at 5 Hz for a passerine (B) and an insect (D) attack. (**E** to **I**) Summarized sensory [(E) and (F)] and motor data [(G) to (I)] during the last 2 s of a subset of insect attacks and of all buzzes from the passerine attacks ($n = 249$ insect and 2 passerine attacks from 14 bats; table S1). Buzz duration and mean buzz call interval [(E) and (F)] are depicted for each capture. The center line represents the median, box limits are upper and lower quartiles, and whiskers are minimum and maximum values.

(IQR: 0.31) versus 0.16 (IQR: 0.33)] during the last 2 s of maneuvering before attacking the prey (Fig. 3, G to I). The consistent buzz structure (Fig. 3, E and F), motor patterns (Fig. 3, G to I), and sensory scenes (Fig. 3, A and C) during insect and passerine attacks indicate that the bats use similar sensory-motor strategies despite the large difference in prey size and endurance. Instead, these bats engaged in markedly longer chases to catch their endothermic, metabolically active passerine prey (Fig. 1D). Passerine echo streams (Fig. 3A) revealed that in response to bat predation, targeted passerines exhibited evasive behavior through vertical escapes likely similar to those seen against predators such as Eleonora's falcons during diurnal migration (*6*). Because of the lack of high-frequency hearing in passerines (*18*), the prey may accommodate for the stealthy approaches of the bats by listening to the bats' wingbeats at close range or by using touch from the bats to initiate such last-minute escape responses (*19*, *20*). Thus, prolonged sprinting and the private sensory channel through ultrasonic echolocation, which passerines cannot detect, have allowed greater noctule bats to exploit the vast and largely unexploited niche of nocturnally migrating passerines without competition from diurnal birds, akin to how echolocating toothed whales access dark and murky waters that visual predators cannot tap into (*21*).

Greater noctule bats use an effective technique to handle large passerine prey

Because most bats typically hunt aerial insects of less than 5% of their body mass (*22*), we next hypothesized that greater noctule bats would handle prey constituting up to 50% of their body mass similarly to how they hunt the largest winged insects. According to an alternative hypothesis, the bats may overpower their passerine prey at high altitudes and then use the free fall to handle and consume it while avoiding collision with the ground (*8*, *16*). Instead, the bird-hunting bat caught its prey close to the ground during an interaction that lasted 9 s from the final buzz to the last passerine distress call and consisted of fast and powerful acceleration changes (Figs. 2 and 3). To get hold of the robin while in flight, the bat could have used its feet together with its uropatagium (*23*). An echolocation pause of ~1 s just before the passerine's last distress call (Fig. 1H) suggests that the bat likely used its mouth to deliver a lethal bite. After the kill, mastication sounds, recorded between echolocation calls, confirmed that the bat was eating continuously during flight for 23 min without losing altitude (Fig. 2B and movie S1) and without attempting to attack other prey items (*14*, *24*). Predator DNA barcoding and x-ray analyses of passerine wings collected beneath the hunting grounds of these bats (Fig. 1, L and M; fig. S3; and table S5) revealed distinct bite marks from greater noctule bats. This suggests that the bats, while in flight, bite off the wings to immobilize the passerine, reduce drag, and facilitate handling, a strategy similar to that of aerial-hawking bats that target large insects (*25*). Thus, this bird-handling technique might not be a previously uncharacterized strategy but rather a co-option from the ancestral aerial-hawking of large insects that are prey of greater noctule bats (up to 4 g; table S6). This is in stark contrast with birds of prey and other carnivorous bats that save energy by handling their large prey while being perched (*26*, *27*). Because up to 30% of greater noctule bats may consume passerines each night during spring migration (*5*), we cannot conclude whether the low incidence of bird hunting events in our dataset is related to tagging effects, suboptimal weather for spring passerine migration, or a higher relative abundance of insects when tagging occurred. Future studies could probe the role that this dietary shift may play in the energy budgets of these elusive bats. Additionally, exciting avenues for future research could include the fine-scale foraging behavior of the two other aerial-hawking bird-eating bat species, the antipredator behavior of the targeted passerines, or how changes in timing and intensity of bird migration could affect the diet and population dynamics of these avivorous bats.

Conclusions

We show that greater noctule bats hunt and consume relatively large, agile, and energetic passerines in flight through echolocation. By using prolonged sprinting and similar sensory-motor strategies as when

hunting insects, these bats have tapped into the abundant resource of nocturnally migrating passerines, thereby acting as a rare nocturnal predator in this part of the troposphere.

REFERENCES AND NOTES

1. S. Hahn, S. Bauer, F. Liechti, *Oikos* **118**, 624–626 (2009).
2. R. Buij, M. Gschweng, *Acta Ornithol.* **52**, 35–49 (2017).
3. A. Thabah *et al.*, *J. Mammal.* **88**, 728–735 (2007).
4. D. Fukui, H. Dewa, S. Katsuta, A. Sato, *J. Mammal.* **94**, 657–661 (2013).
5. C. Ibáñez, J. Juste, J. L. García-Mudarra, P. T. Agirre-Mendi, *Proc. Natl. Acad. Sci. U.S.A.* **98**, 9700–9702 (2001).
6. A. Hedenström, M. Rosén, *Behav. Ecol.* **12**, 150–156 (2001).
7. C. Ibáñez, A. G. Popa-Lisseanu, D. Pastor-Beviá, J. L. García-Mudarra, J. Juste, *Mol. Ecol.* **25**, 5254–5263 (2016).
8. C. Ibáñez, J. Juste, J. L. Garcia-Mudarra, P. T. Agirre-Mendi, *Funct. Ecol.* **17**, 143–145 (2003).
9. L. Stidsholt *et al.*, *Methods Ecol. Evol.* **10**, 48–58 (2019).
10. G. F. McCracken, Y. Lee, E. H. Gillam, W. Frick, J. Krauel, in *50 Years of Bat Research: Foundations and New Frontiers*, B. K. Lim *et al.*, Eds. (Springer, 2021), pp. 189–205.
11. J. Rydell, D. P. McNeill, J. Eklöf, *J. Zool.* **256**, 379–381 (2002).
12. H.-U. Schnitzler, E. K. V. Kalko, *Bioscience* **51**, 557–569 (2001).
13. A. R. C. Britton, G. Jones, *J. Exp. Biol.* **202**, 1793–1801 (1999).
14. L. Stidsholt *et al.*, *eLife* **12**, e84190 (2023).
15. G. Dondini, S. Vergari, *J. Zool.* **251**, 233–236 (2000).
16. C. Ibáñez, J. Juste, in *Chiroptera, Handbook of the Mammals of Europe*, D. Russo, Ed. (Springer, 2023), pp. 439–462.
17. D. Russo, A. Mäenurm, A. Martinoli, L. Cistrone, *Ecol. Evol.* **14**, e11098 (2024).
18. O. Gleich, R. J. Dooling, G. A. Manley, *Naturwissenschaften* **92**, 595–598 (2005).
19. D. J. Shearer, E. A. Beilke, *Anim. Cogn.* **26**, 357–367 (2023).
20. L. Gong *et al.*, *Integr. Zool.* **19**, 524–537 (2024).
21. P. T. Madsen, A. Surlykke, *Physiology* **28**, 276–283 (2013).
22. M. B. Fenton, *Can. J. Zool.* **68**, 411–422 (1990).
23. E. K. Kalko, *Anim. Behav.* **50**, 861–880 (1995).
24. K. Krivoruchko *et al.*, *Proc. Natl. Acad. Sci. U.S.A.* **121**, e2321724121 (2024).
25. T. H. Kunz, J. O. Whitaker Jr., M. D. Wadanoli, *Oecologia* **101**, 407–415 (1995).
26. L. Brown, D. Amadon, *Eagles, Hawks and Falcons of the World*, vol. 2 (Country Life Books, ed. 1, 1968).
27. F. Gual-Suárez, R. A. Medellín, *Mammal Rev.* **51**, 540–558 (2021).
28. L. Stidsholt *et al.*, *Sci. Adv.* **7**, eabf1367 (2021).
29. M. Johnson, P. T. Madsen, W. M. X. Zimmer, N. A. de Soto, P. L. Tyack, *Proc. Biol. Sci.* **271**, S383–S386 (2004).
30. L. Stidsholt, Data for: "Greater noctule bats prey on and consume passerines in flight." Mendeley Data (2025); https://doi.org/10.17632/9gnxdgxm95.4.

ACKNOWLEDGMENTS

We thank M. Johnson and S. Nahnsen for designing and preparing tags; J. Juste, D. Dechmann, D. Gálvez, and C. Camacho for help during fieldwork and discussions; and P. T. Madsen for feedback on the manuscript, discussions, and providing tags. We also thank ICTS-Doñana and the Ministry of Science and Innovation for logistic and technical support; the Molecular Ecology Laboratory of the Estación Biológica de Doñana (LEM-EBD) for logistic support; L. Ibáñez from Mascotasalud veterinary hospital for the x-rays of the passerine wings; J. Sereno for the photograph of the greater noctule bat in Fig. 1K; and J. Juste, D. Kelm, D. Pastor, and the staff of the General Directorate of Natural Environment of the Government of La Rioja for providing the passerine wings. Lastly, we thank J. L. Arroyo, R. Rodríguez (Manecorro), B. Martínez-Miranzo (Jardín Botánico Alfonso XIII-UCM), and J. Gómez (Garaio-Txepetxa) for support while recording passerine distress calls. **Funding:** This work was funded by VILLUM FONDEN (grant no. 41386) (L.S.); the Spanish Ministry of Science and Innovation through the European Regional Development Fund SUMHAL project LIFEWATCH-2019-09-CSIC-4, POPE 2014-2020 (E.T., S.S.-N., C.I.); and Spanish Ministry of Science and Innovation ULTIMATE project TED2021-131835B-I00 (E.T., S.S.-N., C.I.). **Author contributions:** Conceptualization: L.S., E.T., I.F., C.I.; Methodology: L.S., E.T., J.N., I.d.l.H., S.S.-N., J.L.G.-M., C.I.; Investigation: L.S., E.T., J.N., I.d.l.H., S.S.-N., C.I.; Visualization: L.S., E.T., J.N., C.I.; Funding acquisition: L.S., C.I.; Project administration: L.S., E.T., C.I.; Supervision: L.S., E.T., C.I.; Writing – original draft: L.S., I.F.; Writing – review & editing: All authors. **Competing interests:** The authors declare that they have no competing interests. **Data and materials availability:** All data and code to reconstruct the figures of this paper are available at Mendeley Data Repository (*30*).

License information: Copyright © 2025 the authors, some rights reserved; exclusive licensee American Association for the Advancement of Science. No claim to original US government works. https://www.science.org/about/science-licenses-journal-article-reuse

SUPPLEMENTARY MATERIALS

science.org/doi/10.1126/science.adr2475
Materials and Methods; Figs. S1 to S3; Tables S1 to S6; References (*31–52*); MDAR Reproducibility Checklist; Movie S1; Audio S1

Submitted 21 June 2024; resubmitted 29 March 2025; accepted 31 July 2025
10.1126/science.adr2475

CARBON OFFSETS

Tropical forest carbon offsets deliver partial gains amid persistent over-crediting

Yuzhi Tang[1,2], Chao Yang[2,3]*, Haishan Wu[4,5], Zihao Xu[1,6], Linlin Tan[1,4], Wei Tu[2,3], Bowen Li[7], Zhaopeng Li[1,4], Zhijun Wang[1], Kai Guo[1], Siting Xiong[1], Shoubin Chen[1], Bo Zhang[1], Jindong Tian[1,8], Yu Hu[1], Zhipeng Chen[2,3], Jonathan M. Chase[9,10], Qingquan Li[2]*

REDD+ (Reducing Emissions from Deforestation and Degradation Plus) projects generate carbon credits to offset emissions, but recent studies have questioned their effectiveness. We evaluated 52 voluntary REDD+ projects across 12 tropical countries using synthetic control methods. Only a minority of project units showed statistically significant reductions in deforestation, and just 19% met their reported emissions targets. Nonetheless, many underperforming projects still delivered partial climate benefits, with an estimated 13.2% of tradable credits supported by counterfactual analysis. Effectiveness varied by region, with stronger performance in Brazil and Africa. Although systematic over-crediting remains a concern, our results suggest greater climate benefits than previous assessments. Improving baseline methodologies and strengthening verification frameworks will be essential for enhancing the credibility and impact of forest carbon offsets.

Tropical forests play a crucial role in supporting biodiversity and ecosystem services (*1*–*3*), and their conservation is critical for sustainable development and nature-based climate solutions (*4*). Unfortunately, forest loss and degradation is intense (*5*–*7*), leading to the emission of ~5 billion metric tons of carbon dioxide annually—second only to fossil fuel use (*8*). The REDD+ (Reducing Emissions from Deforestation and Degradation Plus) program is an international initiative aimed at reducing greenhouse gas emissions by offering economic incentives to developing countries to maintain forest cover, enhance carbon stocks, and promote human well-being (*9*, *10*).

There are currently more than 350 voluntary REDD+ projects operating worldwide (*11*), many of which are funded through the sale of carbon offsets. After their initial development, REDD+ credits gained considerable popularity; by 2021, they accounted for two-thirds of the 227.7 million offsets traded in carbon markets from the land-use sector (excluding agriculture), with a total market value of $1.3 billion (*12*). However, since their inception, the efficacy of REDD+ projects has been a subject of debate (*13*–*16*). Over time, this scrutiny has led to a series of quantitative studies that have challenged the claimed climate benefits of many projects (*17*–*20*). These critiques have shaken confidence in the voluntary carbon market (*21*, *22*), leading to a 62% drop in the value of REDD+ carbon offsets between 2022 and 2023 (*23*). To restore trust and accurately assess the climate benefits of REDD+ projects, there is an urgent need for more robust evaluation methodologies that incorporate adequate controls, sufficient sample sizes, and transparent analytical approaches (*24*–*29*).

In this work, we assessed the climate change mitigation potential of voluntary REDD+ projects certified by Verra's Verified Carbon Standard (VCS) across several tropical regions worldwide. We focused on Avoided Unplanned Deforestation (AUD) projects, which are a crucial component of REDD+ efforts in many developing countries (*15*, *30*), that aim to protect forests from localized deforestation driven by small-scale land uses, such as subsistence agriculture, illegal logging, and fuelwood collection (*31*–*33*). We screened VCS AUD projects (*34*) for those that provided the necessary geospatial and landscape data to apply forest loss baseline comparison methods based on synthetic control models [see (*35*); table S1 and table S2]. In total, we analyzed 54 REDD+ projects across half of the countries where such projects are implemented, including those in South America (Brazil, Colombia, and Peru), Africa (Central African Republic, Democratic Republic of Congo, Madagascar, Mozambique, Sierra Leone, Tanzania, and Zambia), and Southeast Asia (Cambodia and Laos) (Fig. 1). Some projects encompassed geographically dispersed sites, which we treated as separate project units, resulting in 69 distinct project units for our analyses [(*35*); fig. S1]. Although we could not analyze several projects that were included in prior evaluations owing to the inapplicable data or undisclosed results, we did incorporate data from many (31) of the same projects previously assessed (*17*, *20*) as well as from many projects that had not previously been subjected to synthetic analyses (*35*).

We quantified the climate mitigation effectiveness of REDD+ projects at both individual project and regional scales. To do so, we estimated the potential impact of each REDD+ project by constructing a synthetic counterfactual using a weighted average of nearby synthetic control areas selected to match the project's preintervention deforestation trends and key biophysical and socioeconomic conditions [(*35*); fig. S2 and table S3]. In the absence of intervention, the project area should exhibit a similar level of forest loss to its synthetic controls (*36*, *37*). We selected control areas within the REDD+ project buffer zone (table S4), excluding nonnational territory and leakage buffers (figs. S3 to S6), and chose a majority of time-variant key geospatial predictors of deforestation risk for control matching (*35*). For within-study analyses, we generated multiple donor pools after similarity screening using Earth Mover's Distance (*38*), selecting the most representative subsets of control areas (*35*). To establish the forest loss counterfactual for each sample pool, we used the penalized synthetic control method (PSCM), which balances pairwise and overall matching discrepancies (*39*). We applied the PSCM to annual forest loss to match preintervention annual trends. We eliminated project units (1953-1, 1953-2, and 1748) that performed poorly in the model fitting and validation test to ensure adequate test causality (giving us a total sample of 66 units within 52 projects). Next, we evaluated average cross-project impacts when data were aggregated at larger scales using the generalized synthetic control method (GSCM), which incorporates interactive fixed effects to account for preexisting differences and trends between treatment and control groups (*33*). We applied this approach to countries or regions with sufficient project units: (i) each of three countries in South America, Brazil ($N = 28$), Colombia ($N = 12$), and Peru ($N = 13$); (ii) regional or continental scales in Africa ($N = 10$) and Southeast Asia ($N = 3$); and (iii) all pantropical sites combined ($N = 66$). We cross-validated these results with synthetic difference-in-differences (SDID) modeling, which evaluates treatment effects by optimizing the weights of control units over time. Lastly, we estimated the potential over-crediting of REDD+ projects by contrasting forest loss baselines derived from synthetic controls with those reported in project documents, which is crucial for assessing carbon credit reliability.

[1]Guangdong Laboratory of Artificial Intelligence and Digital Economy (SZ), Shenzhen, China. [2]MNR Key Laboratory for Geo-Environmental Monitoring of Great Bay Area & Guangdong Key Laboratory of Urban Informatics, Shenzhen University, Shenzhen, China. [3]School of Architecture and Urban Planning, Shenzhen University, Shenzhen, China. [4]Xcarbon AI, Shenzhen, China. [5]Zand Bank PJSC, Dubai, The United Arab Emirates. [6]College of Computer Science and Software Engineering, Shenzhen University, Shenzhen, China. [7]Department of Geographic Resource Management, The Chinese University of Hong Kong, Hong Kong, China. [8]College of Physics and Optoelectronic Engineering, Shenzhen University, Shenzhen, China. [9]German Centre for Integrative Biodiversity Research (iDiv) Halle-Jena-Leipzig, Germany. [10]Department of Computer Science, Martin Luther University Halle-Wittenberg, Halle (Saale), Germany. ***Corresponding author. Email: yangchao161@szu.edu.cn (C.Y.); liqq@szu.edu.cn (Q.L.)**

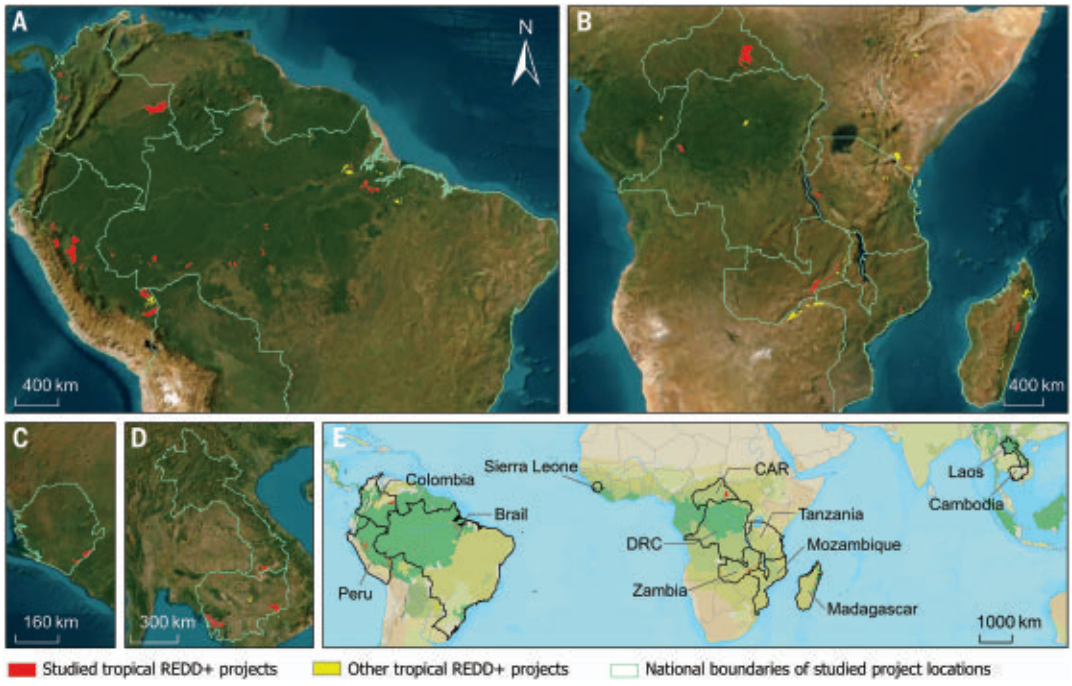


Fig. 1. Distribution map of certified pantropical REDD+ projects in the AUD category during 2001 to 2023. (**A**) Latin America, including Brazil, Colombia, and Peru. (**B**) Most of the studied countries in Africa, including Central African Republic (CAR), the Democratic Republic of Congo (DRC), Madagascar, Mozambique, Tanzania, and Zambia. (**C**) Sierra Leone. (**D**) Southeast Asia, including Cambodia and Laos. (**E**) Global view. The base map data is from Esri.

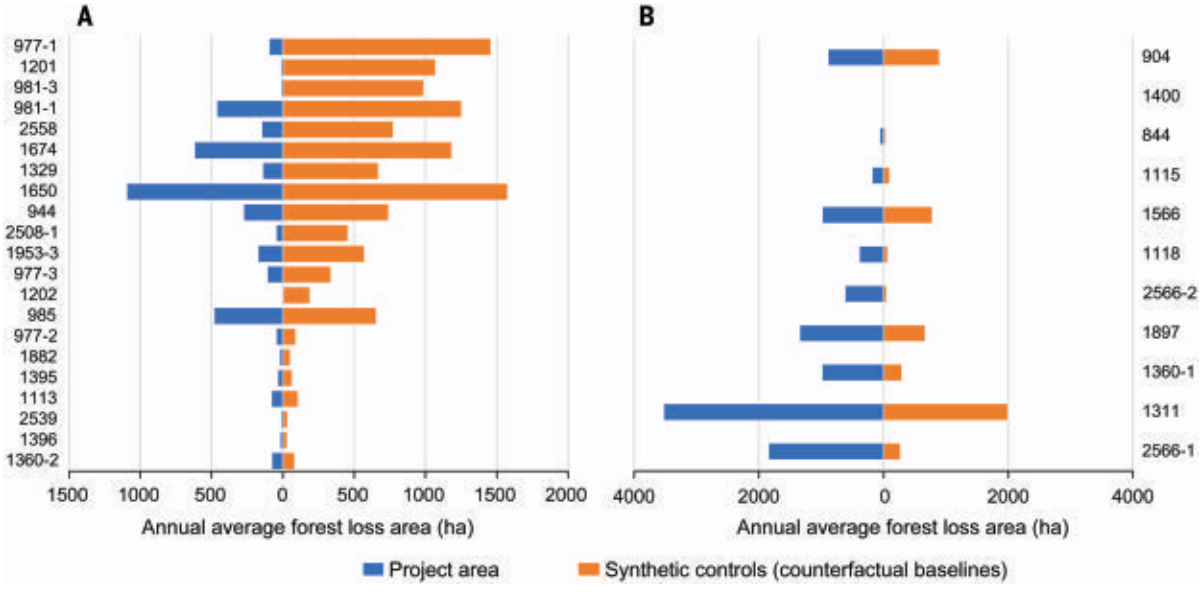


Fig. 2. Post-REDD+ annual average forest loss in project areas versus that of their synthetic controls (counterfactual baselines), shown for the 32 project units with statistically significant differences. (**A**) Effective projects with significant forest loss reduction (climate benefit). (**B**) Ineffective projects with significant forest loss increase (no climate benefit). Results for 34 of 66 total project units with insignificant differences are not shown. For project ID descriptions and geographical locations, see table S1 and fig. S3.

REDD+ project effectiveness

Nearly one-third of the project units (21/66) experienced significantly lower forest loss than expected, suggesting likely successful climate mitigation (Fig. 2A, figs. S7 and S8, and table S5). Of these, one unit of the Portel-Pará REDD+ project (977-1) in the Brazilian Amazon had the greatest reduction in forest loss area compared with that of its control (a decrease of 1362.5 ha year^{-1} after REDD+ implementation, totaling 19.1 thousand ha saved by 2022). Likewise, a unit in the Pacajai REDD+ Project (981-3), also in the Brazilian Amazon, had the largest percentage decrease of forest loss (a 99% reduction). However, 17% (11/66) of the project units actually had higher losses of forests designated in the REDD+ area compared to that of its control (Fig. 2B). Of these, the Brazilian Serra do Amolar project (2566-1) and the Ankeniheny-Zahamena Corridor project (1311) in Madagascar both experienced the highest forest loss (loss of >1500 ha year^{-1}) in project sites compared with that of their controls.

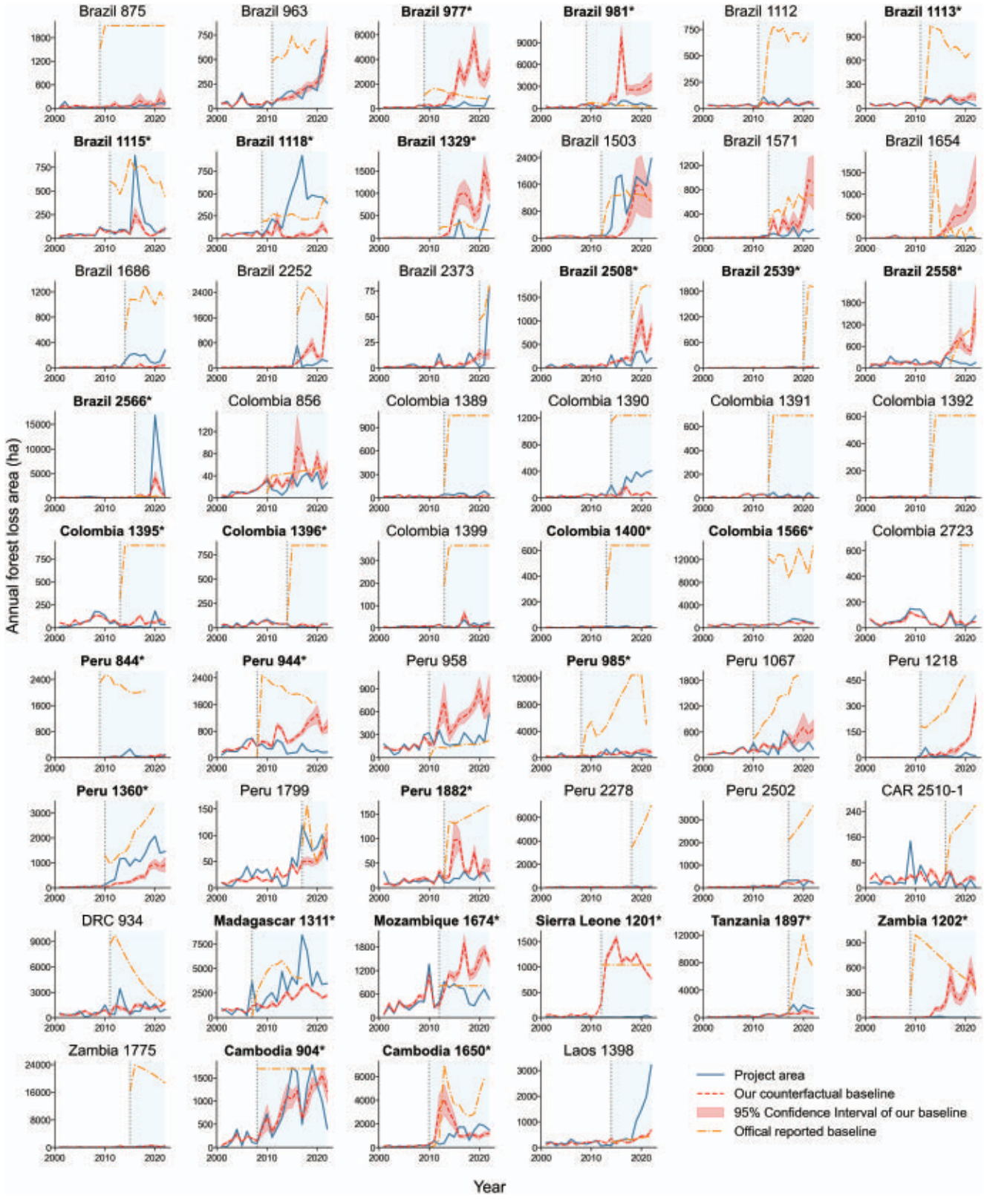


Fig. 3. Annual post-2000 forest loss in studied REDD+ project areas versus that of their synthetic controls and official reported baseline deforestation. Blue lines represent the annual observed forest loss area in project areas, whereas dashed red lines represent that in synthetic controls. Shaded red areas indicate 95% confidence intervals around our baseline deforestation averages, determined from 10 qualified synthetic control models for each individual project. Dash-dotted yellow lines demonstrate the official baseline annual deforestation curves. Dotted black lines indicate the REDD+ project implementation year, and the light blue panel demonstrates the implementation period. Bold subplot titles with asterisks indicate a significant change in deforestation in the project areas compared with that of their synthetic controls, according to the placebo tests and 95% confidence intervals. For project ID descriptions and geographical locations, see table S1 and fig. S3.

The levels of baseline deforestation risks reported in the REDD+ project description documents were substantially different than those that we observed. About 35% (18/52) of the projects had official baselines more than 10 times higher than our estimates, causing substantial overestimation of the forest loss reductions caused by REDD+ projects. Colombia is a hotspot, where 10/12 projects reported more than 10-fold–higher baselines than we estimated. By contrast, ~19% (10/52) of the projects had substantially less deforestation than expected, implying that the deforestation risk of these projects were conservatively estimated (Fig. 3, fig. S9, and table S6).

When we combined results of individual project units into a synthetic analysis based on the GSCM, we found overall decreases of deforestation rate brought by the REDD+ implementation across the whole pantropical region (−0.16%); likewise, we found rate decreases in the regions encompassing Brazil (−0.33%) and Africa (−0.19%) (Fig. 4 and table S7). However, when we used a different synthetical analytical approach (SDID), we found results that were no longer significant at the $P = 0.05$ threshold ($P = 0.09$) (table S7). In this case, we favor stronger inference from the GCSM, which offers analytical flexibility by accommodating time-varying unobserved confounders, whereas the SDID relies on an assumption of parallel trends (i.e., treated and control groups follow similar trajectories without intervention). Nevertheless, using both synthetic approaches can yield a more comprehensive understanding of the effectiveness of REDD+, which, in this case, indicates some uncertainty.

Carbon credit reassessment

To reassess the tradable carbon credits generated by REDD+ projects, we compared the amount of forest loss reduction derived from our counterfactual baseline with the official reported baselines in 48 of the 52 projects that had publicly available data from Verra on Verified Carbon Units (VCU). In the voluntary carbon market, carbon credits are tradable certificates representing the avoidance of one metric ton of carbon dioxide emissions. These credits enable purchasers to offset their own emissions by investing in verified climate projects. Of the potential 264 million tradable carbon credits that these 48 REDD+ projects could have generated by 2022, only 73 million (28%, considering only projects with significant climate benefits) are likely to emerge from the avoided unplanned deforestation activities. We estimated that ~34.8 million carbon credits from these 48 REDD+ projects could genuinely offset emissions, representing 13.2% of the total tradable carbon credits (Fig. 5 and table S8). However, by December 2022 (when the last publicly available data were reported), these projects had issued up to 228.4 million tradable carbon credits (95% of which were sold), with 127 million (55%) used by companies or individuals to offset their greenhouse gas emissions (tables S9 and S10). This represents a 5.6-fold increase over our estimate of genuinely additional credits, highlighting a significant discrepancy that raises concerns about the integrity of the current carbon credit system.

Robustness tests

To ensure that our findings were robust to key assumptions, we conducted additional tests, varying concession data inclusion, forest loss datasets, and leakage buffer widths (supplementary materials, section S5). Incorporating concession covariates modestly reduced the proportion of effective credits but did not alter overall conclusions (fig. S10 and tables S11 and S12). We also compared results using the JRC Tropical Moist Forest dataset versus the Global Forest Change

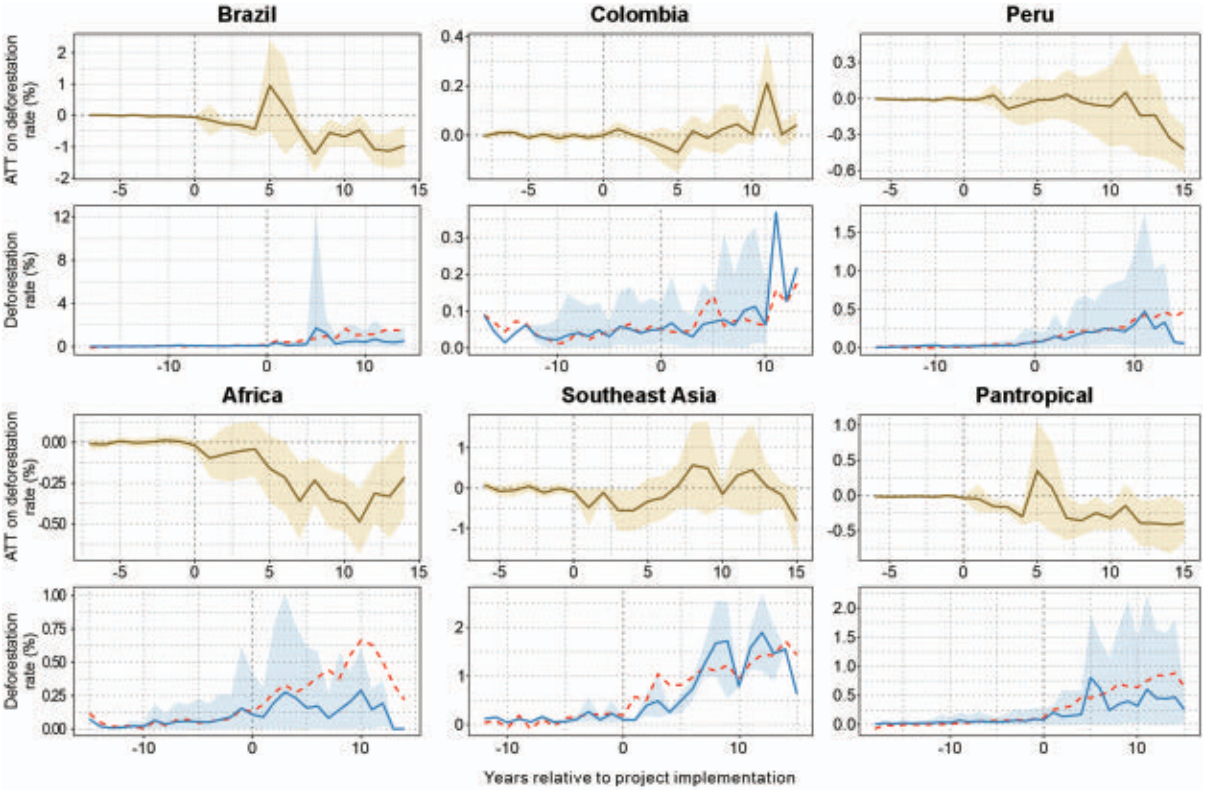


Fig. 4. Estimated average impacts of REDD+ projects on annual deforestation at the country or regional scale, including Brazil, Colombia, Peru, Africa, Southeast Asia, and the whole pantropical region, based on GCSM. (**Top**) The average treatment effect on treated (ATT) units on deforestation rate. (**Bottom**) Average deforestation rates for projects (solid blue line) and counterfactual baselines (dashed red line). The shaded blue areas represent the bootstrapped 95% confidence intervals around the project deforestation averages, estimated by the GSCM.

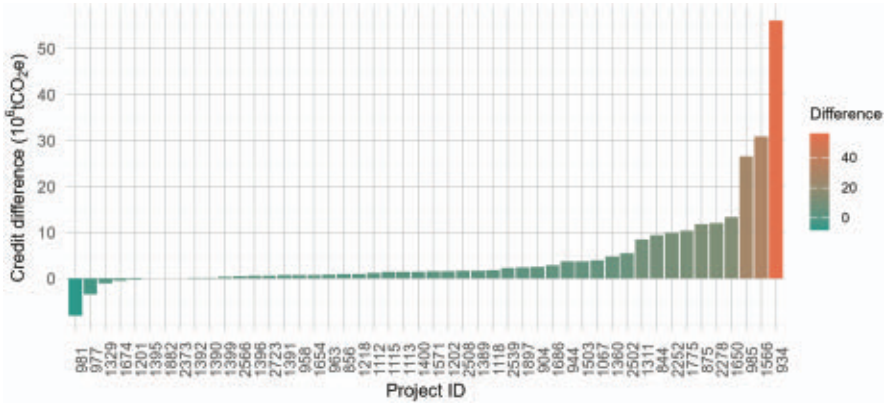


Fig. 5. Comparison of the differences in tradable carbon credits predicted in official project reports and those reassessed on the basis of our counterfactual baseline by 2022. Differences greater than zero indicate over-crediting (the claimed carbon credits exceeds the actual reductions by our counterfactual baseline) by the developers. For project ID descriptions and geographical locations, see table S1 and fig. S3.

dataset, finding highly consistent additionality assessments despite definitional differences (fig. S11 and table S13). Lastly, adjusting leakage buffer widths from 5 to 20 km produced only minor shifts in forest loss estimates (figs. S12 and S13 and table S14).

Discussion

REDD+ has played a prominent, though often contested, role in nature-based climate policy and voluntary carbon markets. Our study offers one of the most comprehensive evaluations to date, analyzing 52 voluntary REDD+ projects (66 units) across the tropics. Only a minority achieved statistically significant reductions in deforestation, and just 19% met their reported emissions targets. We evaluated these data in several ways to access whether alternative assumptions, analyses or data sources would qualitatively alter our conclusions, finding that our results are largely robust to these changes. At the same time, many of these underperforming projects still delivered partial climate benefits, contributing to an estimated 13.2% of tradable carbon credits. As a result, despite the limited effectiveness of many ongoing projects, there is still a high potential for climate impact when REDD+ is implemented and evaluated rigorously.

Our findings that variable but generally low numbers of REDD+ sites effectively reduce forest loss, coupled with limited credible carbon offsets, is consistent with those of previous work (*19*, *40*, *41*), though we found greater mitigation potential. Specifically, by adding more robust analytical procedures and including a broader and more recent set of REDD+ projects while excluding those with incomplete data or spatial inconsistencies, we were able to estimate a nearly twofold increase in the percentage of tradable carbon credits, demonstrating genuine additionality in a larger portion of projects [i.e., 13.2% compared with the 6 to 7% reported in earlier studies (*17*, *42*)]. This includes stronger performance in specific regions: nearly 40% of Brazilian project units and several African projects showed significant reductions (figs. S14 and S15), highlighting the potential for success when implementation is robust. Even when we compared our results with those of previous work, using only sites that are shared between studies (*17*, *20*), we identified more than twice as many with significant positive impacts (15% versus 6%). Two methodological advances (detailed in table S15) likely explain our findings: (i) the use of ecologically matched control areas combined with annual-scale synthetic control models incorporating enhanced covariates and (ii) the exclusion of avoided degradation when reassessing carbon credits.

Despite more optimism for tropical voluntary REDD+ projects that emerges from our results, we also confirm that many projects substantially over-credit their climate benefits. This overestimation is often linked to the selection of inappropriate reference regions that are typically large tracts of land that maintain overall similarity to the conditions in the project area but also include heavily human-impacted lands that have high historical deforestation rates (fig. S16) (*17*, *40*, *43*). To address this, we advocate for stricter limits on the size of baseline reference areas and alignment with pre-REDD+ deforestation trends. Specifically, we recommend adopting more robust counterfactual construction methods, such as the SCM, which explicitly match project and control areas based on preintervention trends while maintaining ecological and socioeconomic comparability. This approach should include generating donor pools within spatially and ecologically constrained buffers, using multiround random sampling to reduce selection bias, and incorporating covariates that capture the key spatiotemporal characteristics of the project area. These refinements would produce more credible and manipulation-resistant counterfactual baselines while remaining compatible with REDD+ monitoring requirements.

Another source of over-crediting lies in the assumption that historical deforestation trends can reliably forecast future risk. In reality, deforestation is influenced by shifting socioeconomic and political conditions (*44*, *45*). In some cases, high deforestation rates can decrease with economic growth (*41*), whereas in other cases, the relationship between per capita income and deforestation is more complex (*46*). In either case, historical deforestation data can sometimes poorly forecast future trends. Political shifts can also trigger abrupt changes. For example, deforestation rates in the Brazilian Amazon more than doubled from 2019 to 2021 under President Bolsonaro (*47*, *48*), a pattern reflected in our findings from Brazil (fig. S7). Explicitly incorporating country-specific governmental cycles into Verra's methods (*49*) along with integrating counterfactual-based approaches could enhance the accuracy of REDD+ forecasts.

Project-level emission-reduction estimates and forecasts remain highly uncertain, especially in tracking forest area change over time, quantifying carbon stored in forest biomass, and estimating emissions per unit of forest lost or degraded (*13*, *14*, *50*). However, these errors tend to cancel out when assessed across larger portfolios, reducing the risk of overestimating total climate benefits (*51*). Individual REDD+ projects may overstate their impact because of measurement imitations or even intentional manipulation, but diversified portfolios help offset this by combining projects with demonstrably reliable additionality. Given growing public concern over the use of low-cost, high-risk carbon credits by high-emitting corporations (*52*), we recommend applying discount factors to single-project offsets to reflect those uncertainties and prioritizing the use of diversified credit portfolios. Recent efforts to improve carbon market quality and third-party ratings are important steps toward increasing transparency, reliability, and standardization in how credits are assessed and valued (*53*, *54*). Our findings also underscore the need for targeted reform for REDD+ projects, rather than complete rejection. Priorities include improving baseline methodologies, increasing transparency in certification, and strengthening accountability to reduce over-crediting. Focusing on areas with strong, long-term carbon storage potential paired with stronger oversight could improve both credibility and outcomes.

REFERENCES AND NOTES

1. A. Goldstein *et al.*, *Nat. Clim. Chang.* **10**, 287–295 (2020).
2. J. Barlow *et al.*, *Nature* **559**, 517–526 (2018).
3. O. L. Phillips, S. L. Lewis, *Glob. Chang. Biol.* **20**, 2039–2041 (2014).

54. B. W. Griscom *et al.*, *Philos. Trans. R. Soc. Lond. B Biol. Sci.* **375**, 20190126 (2020).
5. P. G. Curtis, C. M. Slay, N. L. Harris, A. Tyukavina, M. C. Hansen, *Science* **361**, 1108–1111 (2018).
6. D. M. Lapola *et al.*, *Science* **379**, eabp8622 (2023).
7. Z. Z. Zeng *et al.*, *Nat. Geosci.* **11**, 556–562 (2018).
8. P. Friedlingstein *et al.*, *Earth Syst. Sci. Data* **14**, 4811–4900 (2022).
9. A. Agrawal, D. Nepstad, A. Chhatre, *Annu. Rev. Environ. Resour.* **36**, 373–396 (2011).
10. A. A. Bernstein, *N. Engl. J. Public Policy* **35**, 1 (2023).
11. S. S. Atmadja *et al.*, *Environ. Res. Lett.* **17**, 044038 (2022).
12. M. P. S. Donofrio, C. Daley, C. Calderon, K. Lin, The Art of Integrity: State of the Voluntary Carbon Markets 2022 Q3 (Forest Trends' Ecosystem Marketplace, 2022).
13. B. J. Butler *et al.*, *Carbon Balance Manag.* **19**, 22 (2024).
14. R. D. Yanai *et al.*, *Environ. Res. Lett.* **15**, 124002 (2020).
15. J. Weatherley-Singh, A. Gupta, *Environ. Sci. Policy* **54**, 97–105 (2015).
16. E. O. Sills *et al.*, *Glob. Environ. Change* **43**, 148–160 (2017).
17. T. A. P. West *et al.*, *Science* **381**, 873–877 (2023).
18. A. Guizar-Coutiño, J. P. G. Jones, A. Balmford, R. Carmenta, D. A. Coomes, *Conserv. Biol.* **36**, e13970 (2022).
19. G. Badgley *et al.*, *Glob. Chang. Biol.* **28**, 1433–1445 (2022).
20. T. A. P. West, J. Börner, E. O. Sills, A. Kontoleon, *Proc. Natl. Acad. Sci. U.S.A.* **117**, 24188–24194 (2020).
21. R. Pande, *Science* **384**, eadp5223 (2024).
22. J. P. G. Jones, S. L. Lewis, *Science* **381**, 830–831 (2023).
23. A. Procton, *State of the Voluntary Carbon Market 2024* (Forest Trends Association, 2024).
24. E. T. A. Mitchard *et al.*, Serious errors impair an assessment of forest carbon projects: A rebuttal of West *et al*. arXiv:2312.06793 [econ.GN] (2023).
25. M. Pauly *et al.*, *Environ. Res. Lett.* **19**, 124096 (2024).
26. Verra Response to Guardian Article on Carbon Offsets (2023); https://verra.org/verra-response-guardian-rainforest-carbon-offsets.
27. A. Furey, Sylvera response to The Guardian's Analysis of Rainforest Offsets (2023); https://www.sylvera.com/blog/guardian-offsets-response#sylveras-research-shows-30percent-are-high-quality.
28. A. E. Duchelle, G. Simonet, W. D. Sunderlin, S. Wunder, *Curr. Opin. Environ. Sustain.* **32**, 134–140 (2018).
29. C. Pa *et al.*, *J. For. Res.* **33**, 1109–1122 (2022).
30. VM0015, Methodology for Avoided Unplanned Deforestation (2012); https://verra.org/methodologies/vm0015-methodology-for-avoided-unplanned-deforestation-v1-2/.
31. J. Busch, K. Ferretti-Gallon, *Rev. Environ. Econ. Policy* **11**, 3–23 (2017).
32. G. Kissinger, M. Herold, V. De Sy, Drivers of Deforestation and Forest Degradation: A Synthesis Report for REDD+ Policymakers (Lexeme Consulting, 2012); https://www.forestcarbonpartnership.org/sites/fcp/files/DriversOfDeforestation.pdf_N_S.pdf.
33. J. Andoh, K. A. Oduro, J. Park, Y. H. Lee, *Front. For. Glob. Change* **5**, 957550 (2022).
34. Verified Carbon Standard (2025); https://registry.verra.org/app/search/VCS.
35. Y. Tang, Code data for Tropical forest carbon offsets deliver partial gains amid persistent over-crediting, Zenodo (2025); https://doi.org/10.5281/zenodo.15475925.
36. A. Abadie, A. Diamond, J. Hainmueller, *Am. J. Pol. Sci.* **59**, 495–510 (2015).
37. A. Roopsind, B. Sohngen, J. Brandt, *Proc. Natl. Acad. Sci. U.S.A.* **116**, 24492–24499 (2019).
38. M. Wichterich, I. Assent, P. Kranen, T. Seidl, Efficient EMD-based similarity search in multimedia databases via flexible dimensionality reduction, *Proceedings of the 2008 ACM SIGMOD International Conference on Management of Data*, Vancouver, Canada, 10 to 13 June 2008. (ACM, 2008), pp. 199-211.
39. A. Abadie, J. L'Hour, *J. Am. Stat. Assoc.* **116**, 1817–1834 (2021).
40. B. K. Haya *et al.*, Quality assessment of REDD+ carbon credit projects (Berkeley Carbon Trading Project, 2023).
41. C. Dezécache, J.-M. Salles, B. Hérault, *Carbon Balance Manag.* **13**, 21 (2018).
42. M. Cames *et al.*, How additional is the Clean Development Mechanism? (Institute for Applied Ecology, 2016); https://climate.ec.europa.eu/system/files/2017-04/clean_dev_mechanism_en.pdf.
43. M. Ehara *et al.*, *For. Policy Econ.* **129**, 102474 (2021).
44. H. J. Geist, E. F. Lambin, *Bioscience* **52**, 143–150 (2002).
45. P. Prochazka *et al.*, *Front. For. Glob. Change* **6**, 957550 (2023).
46. J. Crespo Cuaresma *et al.*, *Sci. Rep.* **7**, 40678 (2017).
47. F. Bispo, L. Chaves, Four years of Bolsonaro's Amazon destruction, in satellite imagery. (2022); https://infoamazonia.org/en/2022/10/28/four-years-of-bolsonaros-amazon-destruction-in-pictures/.
48. D. Roy, Deforestation of Brazil's Amazon Has Reached a Record High. What's Being Done? (2022); https://www.cfr.org/in-brief/deforestation-brazils-amazon-has-reached-record-high-whats-being-done/.
49. Verra, Setting the Standard: Verra's Revolutionary New REDD Methodology (2023); https://verra.org/program-notice/setting-the-standard-verras-revolutionary-new-redd-methodology.
50. E. McGlynn, S. Li, M. F. Berger, M. Amend, K. L. Harper, *Clim. Change* **170**, 5 (2022).
51. T. Neeff, *Clim. Change* **166**, 26 (2021).
52. G. Trencher, S. Nick, J. Carlson, M. Johnson, *Nat. Commun.* **15**, 6863 (2024).
53. H. M. Ahonen, K. Möllersten, R. Spalding-Fecher, *Voluntary compensation of greenhouse gas emissions: International guidance and initiatives* (Nordic Council of Ministers, 2024).
54. Carbon Market Watch, Rating the raters: Assessing the quality of carbon credit rating agencies (2023); https://carbonmarketwatch.org/wpcontent/uploads/2023/09/CMW_Policybriefing_rating_raters-v2.pdf.

ACKNOWLEDGMENTS

We express our gratitude to all reviewers for their constructive suggestions. We thank WeBank and many students and colleague (X. Li, M. Wang, and X. Han) for their help. We also thank all the institutions and platforms for providing data and support, such as Global Forest Watch, World Wildlife Fund, World Database on Protected Areas, US Geological Survey, the European Space Agency, OpenStreetMap, and Esri. **Funding:** This study was supported by the National Natural Science Foundation of China (nos. 42306245, 42471312, and 42201319), the National Key Research and Development Program of China (no. 2024YFF0617900), the Shenzhen Outstanding Talents Training Fund, the Shenzhen Major Science and Technology Project (no. KCXFZ20240903093000002), the Open Research Fund Program of MNR Key Laboratory for Geo-Environmental Monitoring of Great Bay Area (no. GEMLab-2023015), and the discipline breakthrough pioneer project of the Ministry of Education of the People's Republic of China. **Author contributions:** Conceptualization: Y.T., C.Y., H.W., K.G., Y.H., and Q.L.; Methodology: Y.T., C.Y., H.W., L.T., W.T., and J.T.; Data processing, programming, validation, and formal analysis: Y.T., C.Y., H.W., Z.X., L.T., W.T., Z.L., Z.W., K.G., S.X., S.C., B.Z., J.T., Y.H., Z.C., J.M.C., and Q.L.; Visualization: Y.T., Z.L., and B.Z.; Writing - original draft: Y.T. and C.Y.; Writing – review & editing: J.M.C., C.Y., Y.T., H.W., B.L., K.G., and Y.H.; Resources support: Y.T., Z.W., Z.C., and Q.L.; Supervision: C.Y., Q.L., and H.W.; Funding acquisition: Q.L., Y.T., and C.Y. All authors contributed to the results. **Competing interests:** The authors declare that they have no competing interests. **Data and materials availability:** The data and all computer codes used in this study are publicly available in Zenodo (*35*). **License information:** Copyright © 2025 the authors, some rights reserved; exclusive licensee American Association for the Advancement of Science. No claim to original US government works. https://www.science.org/about/science-licenses-journal-article-reuse

SUPPLEMENTARY MATERIALS

science.org/doi/10.1126/science.adw4094
Materials and Methods; Figs. S1 to S82; Tables S1 to S82; References (*55–86*)

Submitted 31 January 2025; accepted 30 July 2025

10.1126/science.adw4094

HORMONE SENSORS

SALICYLIC ACID SENSOR1 reveals the propagation of an SA hormone surge during plant pathogen advance

Bijun Tang[1], Jing Lu[1], Hana Leontovyčová[2], Gesa Hoffmann[3], James H. Rowe[1,4], Sacha Fouquay O'Donnell[1], Mathieu Grangé-Guermente[1], Bo Larsen[1], Rinukshi Wimalasekera[1]†, Philip Carella[5], Marco Incarbone[3], Tetiana Kalachova[2], Alexander M. Jones[1]*

Salicylic acid (SA) is a key phytohormone that orchestrates immune responses against pathogens, including *Pseudomonas syringae* bacteria. The timing and extent of SA accumulation are tightly controlled by plants but can be suppressed by pathogens to overcome immunity. Understanding SA dynamics at high spatiotemporal resolution remains challenging owing to limitations in existing detection methods that are indirect, destructive, or lacking in cellular precision and temporal resolution. We developed SalicS1, a genetically encoded fluorescence resonance energy transfer (FRET) biosensor specific to SA. SalicS1 enables real-time, reversible monitoring of SA levels in vivo with minimal perturbation of endogenous signaling. We reveal the propagation of an SA surge spreading from bacterial infection sites with spatiotemporal fidelity. SalicS1 unlocks precise understanding of SA dynamics underpinning crop resilience to pathogens.

Salicylic acid (SA) is a phytohormone that is critical for plant defenses but is also involved in regulating physiological processes during development and responses to abiotic stress (*1*–*3*). Used widely as a topical medicine and as the feedstock for commercial acetylsalicylate (aspirin) production, SA is an indispensable component of the plant immune system, acting to promote resistance induced by the pattern-triggered immunity (PTI) and effector-triggered immunity (ETI) pathways (*1*, *4*, *5*). In compatible interactions in which plant immunity fails to prevent disease, for example *Pseudomonas syringe* pv. *tomato* DC3000 (*Pst* DC3000) infection of *Arabidopsis thaliana*, SA accumulation slows bacterial growth and pathogenesis but does not ultimately prevent infection. By comparison, incompatible interactions generally promote high levels of SA that are associated with resistance. SA and its methylated form are also central to the systemic acquired resistance (SAR) response that confers broad-spectrum pathogen protection across plant organs (*6*–*9*).

SA biosynthesis in plants is mediated by two pathways named from chorismate utilizing enzymes ISOCHORISMATE SYNTHASE (ICS) and PHENYLALANINE AMMONIA-LYASE (PAL), with the ICS pathway being dominant in *Arabidopsis* (*10*, *11*). Key regulators include AtICS1, the transporter ENHANCED DISEASE SUSCEPTIBILITY 5 (AtEDS5), the avrPphB SUSCEPTIBLE 3 (AtPBS3) enzyme (*11*–*15*), and transcriptional regulators such as SAR DEFICIENT 1 (SARD1) and CALMODULIN BINDING PROTEIN 60g (CBP60g) (*16*) that control ICS1, EDS5, and PBS3 induction. SA accumulation triggers transcriptional networks via NONEXPRESSOR OF PATHOGENESIS-RELATED GENES (NPR) receptors. NPR1, also known as NONINDUCIBLE IMMUNITY 1 (NIM1), is the central regulator of SA signaling that translocates to the nucleus upon SA binding and interacts with TGACG-binding TGA transcription factors to reprogram transcription and strengthen immune responses (*17*–*19*). Further modulation of SA signaling occurs through protein-protein interactions among NPR proteins (*17*), NPR1 posttranslational modifications (*20*, *21*), and NPR1 interaction with NIM1-INTERACTING (NIMIN) proteins, adding additional layers of complexity to SA regulation. Pathogens have also evolved strategies to inhibit SA-mediated immunity, including directly lowering SA levels through the *nahG*-encoded salicylate hydroxylase catabolic enzyme (*22*, *23*). Despite considerable advancements in understanding the molecular pathways governing SA biosynthesis, modification, and catabolism, SA dynamics across cells and subcellular compartments during infection—a crucial battleground in the evolutionary arms race between plant and pathogen—remain unknown.

Traditional SA detection methods such as high-performance liquid chromatography (HPLC) (*24*, *25*) provide quantitative information but are destructive and lack the spatial and temporal resolution needed to track SA dynamics at the cellular level. Indirect methods, including *PATHOGENESIS-RELATED PROTEIN 1* (*PR1*) promoter–based reporters (*26*), improve spatiotemporal resolution but provide only semi-quantitative data on SA activity and are sensitive to non-SA–regulated signaling events. Bacteria engineered to respond to SA with luminescence reporters can be deployed to apoplasmic spaces but cannot report intracellular SA levels or temporal dynamics (*27*). Electrochemical and nanotube-based SA sensing technologies have shown promise for use in vivo and do not require transgenic plants, but they do require creation and application of devices or chemical probes and lack specificity for bioactive SA (*28*, *29*). Only protein-based fluorescence resonance energy transfer (FRET) biosensors that co-opt sensory domains adapted to ligand perception, once expressed in the organism of interest, can offer the combination of minimally invasive, specific, quantitative, and spatially resolved analyte detection over time (*30*, *31*).

To address the need for real-time, high-resolution monitoring of SA, we developed SALICYLIC ACID SENSOR1 (SalicS1), a genetically encoded FRET-based biosensor specific for SA. SalicS1 enables direct, reversible detection of SA within the *Arabidopsis* physiological range, providing a precise tool for tracking SA dynamics in response to biotic stresses. SalicS1 revealed accumulation of micromolar levels of exogenous SA in yeast and in *Arabidopsis* root nuclei, as well as biologically relevant induction of endogenous SA in nuclei of *Arabidopsis* leaves under bacterial, fungal, and insect attack.

Results

Engineering SalicS1 with an accelerated FRET-based biosensor screening platform

FRET biosensors for the hormones abscisic Acid and gibberellin—ABAleon, ABACUS, and GPS—co-opted hormone-induced protein-protein interactions into sensory modules by sandwiching two-part hormone binding domains between fluorescent proteins (FPs) of a FRET pair (*32*–*36*). In the latter biosensors, ligand binding promotes an intramolecular interaction that increases the energy transfer between the donor and acceptor FPs, which is quantified by measuring a positive change in fluorescence emission ratio after excitation of the donor (*33*, *36*). We envisioned SalicS1 as a negative ratio change sensor designed to co-opt the SA-induced disruption of NPR-NIMIN protein interactions previously discovered in yeast two-hybrid assays of *Nicotiana tabacum* proteins (Fig. 1A and fig. S1) (*37*, *38*).

We initially screened biosensor designs using high-affinity AtNPR3 (*17*) fused with AtNIMIN1 as the sensory domain using a two-part combinatorial Gateway-based engineering platform previously used to develop several FRET biosensors (*33*, *34*, *39*–*41*). Sensor candidates were expressed in protease-deficient yeast (*42*) and screened in whole

[1]Sainsbury Laboratory, University of Cambridge, Cambridge, UK. [2]Institute of Experimental Botany of the Czech Academy of Science, Prague, Czech Republic. [3]Max Planck Institute of Molecular Plant Physiology, Potsdam, Germany. [4]Plants, Photosynthesis and Soil, School of Biosciences, University of Sheffield, Sheffield, UK. [5]Cell and Developmental Biology, John Innes Centre, Norwich, UK. ***Corresponding author. Email: alexander.jones@slcu.cam.ac.uk** †Present address: Department of Botany, University of Sri Jayewardenepura, Nugegoda, Sri Lanka.

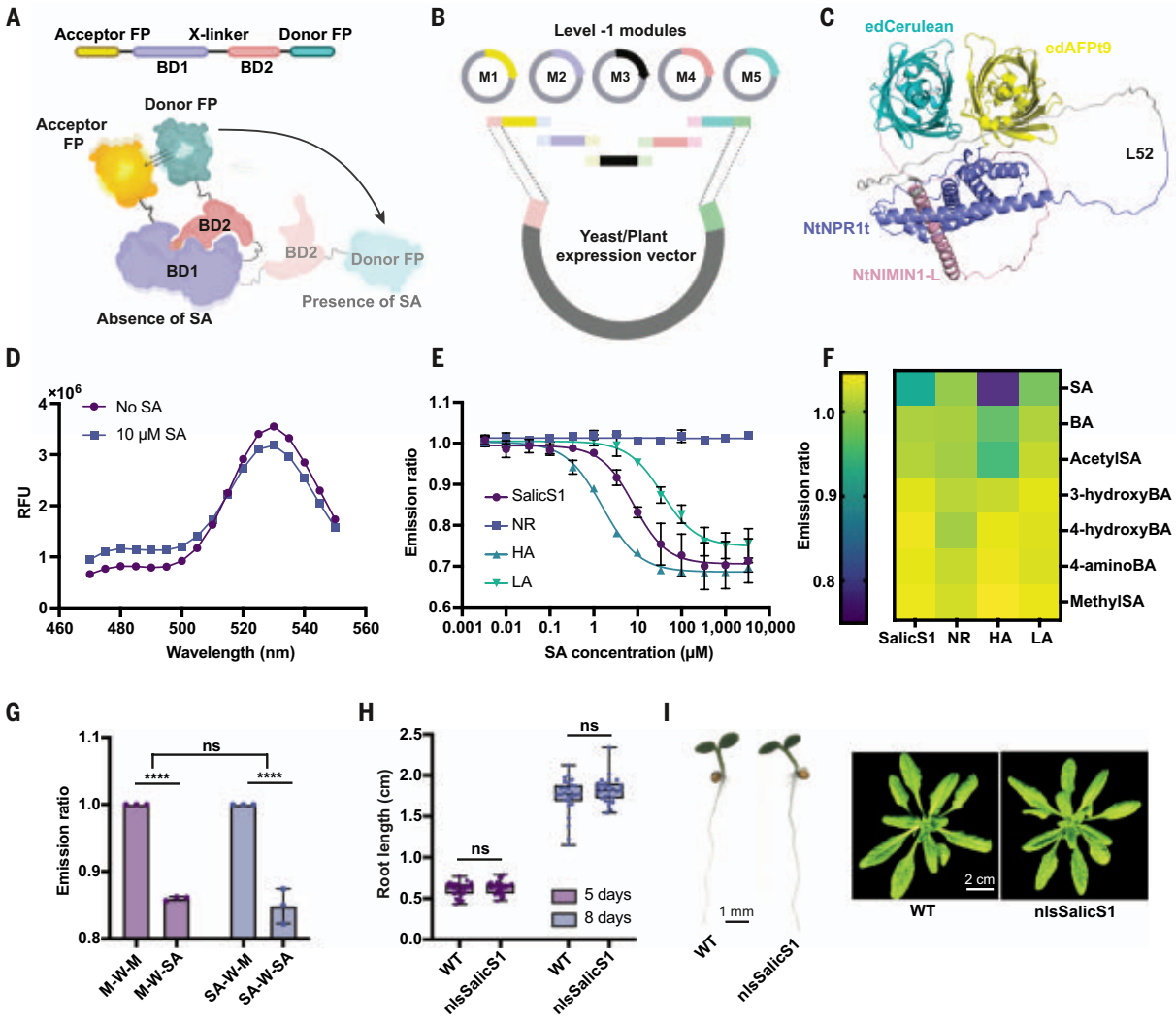


Fig. 1. Design and engineering of SalicS1 and their variants. (**A**) SalicS1 is a negative ratio change sensor consisting of four main domains—binding domain 1 and 2 (BD1 and 2), fluorescent proteins 1 and 2 (FP1 and 2)—and three key linkers. In the absence of SA, there is more FRET between the donor FP and the acceptor FP, whereas in the presence of SA, the conformational change of the sensory domain results in less FRET, therefore lower emission ratio. (**B**) The Golden Gate–based screening platform was built for FRET-based sensor screening in a high-throughput manner. The platform consists of five main modules (M1 to M5), which are donor and acceptor FPs, two components of the sensory domain, and the X-linker. (**C**) AlphaFold3 predicted the structure for SalicS1, shown here. Predicted local distance difference test confidence score: 0.61 (**D**) Emission spectrum of the determined SalicS1 with and without SA ($n = 5$ independent biological replicates). RFU, relative fluorescence unit. (**E**) Dose-response curve of SalicS1, -NR, -HA, and -LA with K_d^{SA} values of 8.1 μM, NA, 1.6 μM, and 36.0 μM from one representative experiment ($n = 3$). Experiments were independently performed three times. (**F**) Specificity test of SalicS1 and its variants to 10 μM of SA and structurally related chemicals from one representative experiment ($n = 3$). The experiment was independently performed three times. (**G**) Reversibility test for SalicS1. Error bars represent SD. M, mock, W, wash; SA: 10 μM ($n = 3$). One representative experiment was analyzed with two-way analysis of variance (ANOVA) and uncorrected Fisher's least significant difference (LSD) test; ****$P < 0.0001$, ns = not significant. Experiments were independently performed two times. (**H**) Phenotyping experiment for 5- and 8-day-old seedlings of *Arabidopsis* (WT versus nlsSalicS1, $n = 29, 27, 27, 28$). One representative experiment was analyzed with two-way ANOVA and uncorrected Fisher's LSD test; ns = not significant. A root-length comparison between Col-0 WT and nlsSalicS1 at 5 days and 8 days shows no significant difference. Each point indicates the length of an individual root. For box plots, center line indicates median; box limits indicate upper and lower quartiles; and whiskers indicate the upper and lower adjacent values. (**I**) (Left) Representative images of 5-day-old seedling stages between Col-0 WT versus nlsSalicS1. (Right) Representative images of 4-week-old rosette stages between Col-0 WT versus nlsSalicS1 ($n = 15$). Experiments were independently performed three times. (G and H) Exact *P* values for all comparisons, *F* values, and degrees of freedom are provided in data S1.

cells or lysates. A slight emission ratio change was observed using AtNPR3-AtNIMIN in combination with several FRET pairs when analyzed in whole cells (fig. S2A and table S1). However, analysis of yeast cell lysates showed loss of FRET while maintaining fluorescence, indicating cleavage of the sensory domain (fig. S2B). On the basis of NtNPR1 and NtNIMIN interaction studies (*38*), we reasoned that retaining only the SA-binding C terminus of NPR1 may stabilize the protein, avoid posttranslational modifications (*21*, *43*) (fig. S1C), and retain SA-sensitive NIMIN interaction while reducing interaction with other endogenous components (*44*) (fig. S1, D and E). Together, these changes would result in a more orthogonalized biosensor with reduced likelihood of causing phenotypes (*36*, *45*) or being sensitive to nonspecific signaling events when expressed in planta. Truncated AtNPR1t and NtNPR1t linked with AtNIMIN1 and NtNIMIN1-L, respectively, were screened in both orientations with a series of FRET pairs (fig. S2C and table S1). The NPR1 truncations successfully enabled screening of SA-induced emission ratio change in yeast cell lysates, and NtNPR1t and NtNIMIN1-L were selected as sensory domains for further optimization.

We next established an accelerated five-part combinatorial Golden Gate–based platform (Fig. 1B and table S2) to improve the FRET biosensor screening process (fig. S1B). Modeled after our Gateway platform, Golden-Gate modules encoding for NtNPR1t–NtNIMIN1-L—NtNPR1t–NtNIMIN1-L linkers (X-linkers) of different lengths and flexibilities—were synthesized (table S3). The linker between FP and sensory domains is an important target for optimizing FRET biosensor signal-to-noise ratio (*46*), and a series of FRET pair FPs was also generated (table S2). A total of 62 variant combinations were screened in yeast cell lysates (fig. S2D and table S4). The optimized SalicS1 biosensor consists of an N-terminal edAFPt9 (enhanced dimer Aphrodite with nine–amino acid C-terminal truncation) linked via a serine-proline linker to NtNPR1t, connected by X-linker 52 (L52) to NtNIMIN1-L, and finally linked via a proline-leucine linker to edCerulean (Fig. 1C). AlphaFold predicted that in the absence of SA, α helix 3 of NtNPR1t would interact with an α helix of NtNIMIN1-L (fig. S1E). Upon SA binding, we predicted that the interaction between NtNPR1t and NtNIMIN1-L would be disrupted, causing an opening of the sensory domain that reduces FRET and lowers the emission ratio (Fig. 1D).

Engineering of SalicS1 variants

A series of nonresponsive (NR) and low-affinity (LA) SalicS1 variant candidates were designed based on mutation of highly conserved or possible SA binding NtNPR1t residues from previous structural analysis of AtNPR4 (*47*) (fig. S3, A to C). High-affinity (HA) candidates were designed based on mutation of NtNPR1t residues to corresponding residues in HA AtNPR3 and AtNPR4 (*17*) (fig. S3, A and C). The dissociation constants (K_d^{SA}) and dynamic range of 21 variants were determined for purified biosensors in vitro (table S5 and fig. S3D). The final selected variants—SalicS1, SalicS1-NR (R431Q) (Arg431→Gln), SalicS1-HA (K424R) (K, Lys), and SalicS1-LA (F508A) (F, Phe; A, Ala)—had K_d^{SA} values of 8.1 μM, not applicable (NA), 1.6 μM, and 36.0 μM, respectively (Fig. 1E). In a specificity test against SA derivatives, precursors, and metabolites, purified SalicS1 responded specifically to SA (fig. S4A), whereas SalicS1-HA also responded to acetylsalicylate with lower emission ratio change than for SA (Fig. 1F and fig. S4, A and B). SalicS1 was also determined to be rapidly reversible, suggesting that it could report both accumulation and depletion of SA (Fig. 1G and fig. S4C).

In planta validation of SalicS

Stable transgenic *Arabidopsis* lines were generated using the constitutive p16 promoter (*48*) and *Agrobacterium tumefaciens* nopaline synthase Tnos terminator. An N-terminal nuclear-localization sequence (nls) was fused to SalicS1 and variants to facilitate image analysis of nuclear patterns across neighboring cells and to measure SA levels in a highly relevant subcellular compartment. Expression of nlsSalicS1 did not cause detectable phenotypic changes in roots or rosette leaves compared with wild-type (WT) Col-0 (Fig. 1, H and I).

When imaged in roots, hypocotyls, cotyledons, and mature leaves, nlsSalicS1 indicated cellular SA levels in living plants, although basal SA levels might fall near or below nlsSalicS1 detection range (see below and Fig. 2A and fig. S5A). A predicted reduction in nlsSalicS1, -HA, and -LA variant emission ratio—but not nlsSalicS1-NR variant emission ratio—was observed with exogenous 10-μM SA treatments in roots, cotyledons, and mature leaves (Fig. 2, B to E, fig. S5, B to C; and fig. S6, A to C). Similarly to in vitro experiments, nlsSalicS1 biosensor responses were dose-dependent in planta with response to submicromolar exogenous SA (fig. S6D) and reversible with ability to detect repeat treatment after a buffer wash (fig S6E). Based on the highest expression level in T2 seedlings and the maximum SA response (SalicS1, -HA, and -LA) or minimum nonresponse in planta, transgenic lines were selected for further experiments (fig. S7, A and B). Taken together, these results suggested that nlsSalicS1 was not saturated for SA detection in the organs studied, but they also confirmed the ability of plant cells to accumulate and deplete exogenous SA and indicated that nlsSalicS1-NR can serve as a negative control for detection of nonspecific biosensor responses.

A gradient of biosensor emission ratio was observed in roots expressing both nlsSalicS1 and nlsSalicS1-NR variants, indicating artifact arising from non-SA mediated biosensor dynamics (e.g., interaction between NtNIMIN1-L and endogenous components such as NPR1, NPR3, or NPR4 proteins). To exclude the possibility that SA-induced emission ratio changes of nlsSalicS1 in vivo results from interaction with endogenous NPR proteins and not SA binding, we generated *npr* mutant lines [*npr1-1* and *npr3-2, npr4-3* double mutant (*49*)], expressing nlsSalicS1. The pattern of SA distribution and emission ratio change upon exogenous SA application was similar in WT and mutants, indicating that nlsSalicS1 response is not dependent on endogenous NPR proteins (Fig. 2F and fig. S8A).

To further validate the sensor, nlsSalicS1 lines overexpressing the *nahG* (*22*) SA catabolic enzyme (nlsSalicS1-pUBQ10::NahG) were generated (fig. S8B). Before SA treatment, nlsSalicS1 emission ratios were comparable between WT and NahG overexpression lines, possibly indicating low basal SA levels in roots (Fig. 2, G and H, and fig. S5D). As anticipated, NahG overexpression prevented both biosensor responses to exogenous SA, as well as exogenous SA accumulation, as detected by an SA-responsive bacterial bioassay (*50*) (Fig. 2, G and H, and fig. S8C). Additionally, *eds5-1* and *pbs3* biosynthesis mutants expressing nlsSalicS1 also showed SA levels comparable to those of untreated WT, which is consistent with low basal SA levels in roots and mature leaves being at or below the detection range of nlsSalicS1 in the cell types analyzed (fig. S9, A to C). As expected, these mutants were still responsive to exogenous SA (fig. S9, A to C). In both NahG overexpression and the biosynthetic mutants, the gradient of emission ratio is again observed in roots before and after exogenous SA, suggesting an artifact that is unrelated to SA levels as observed in nlsSalicS1-NR lines.

To check whether expression of nlsSalicS1 could affect immunity negatively, whether by overexpression of the tobacco NIMIN1-L moiety or through buffering of SA, we tested bacterial growth and SA content measured with bacterial bioassay (*50*) in WT Col-0, nlsSalicS1, PR1::GUS, PR1::Venus, and NahG overexpression lines. In both assays, NahG but not nlsSalicS1 overexpression resulted in decreased immunity (fig. S10). To assess the relative sensitivity of in vivo SA detection by SalicS1 versus destructive SA quantification by bacterial bioassay (*50*), we compared seedlings exposed to 0.5 μM and 1 μM exogenous SA and found that nlsSalicS1 was more sensitive to submicromolar levels (fig. S10, C and D).

Validation of nlsSalicS1 dynamics under biotic stress

Using nlsSalicS1, we observed SA induction in *Arabidopsis* in response to diverse biotic invaders, including the bacterium *Pst* DC3000, the nonadapted fungus *Blumeria graminis f. sp. hordei* (*Bgh*), and the specialized aphid *Brevicoryne brassicae* (*B. brassicae*) (Fig. 3A and fig. S11, A to E) at varying concentrations after 1 or 2 days postinfection. *Pst* infiltration ensured relatively homogenous colonization of the leaf, and significant increases in bioassay quantified SA levels (*50*) (Fig. 3B) alongside downstream signaling induction detected by pPR1-GUS and pPR1-Venus reporter lines (*51*, *52*). The fungus *Bgh* is not adapted to *Arabidopsis*, so SA increased locally where spores germinated but failed to invade epidermal cells, producing patchy responses across the leaf that were detectable by SalicS1 and other reporters in the groups of cells surrounding the infected cell (fig. S12, A to C). *B. brassicae* aphids preferentially inject stylets into the veins (*53*), and although SA induction or responses were not detected through destructive quantification in total leaf extracts, SA responses were detected in the cells directly surrounding the puncture site by pPR1::GUS and pPR1::Venus reporters. Overall, these results with semiquantitative SA signaling reporters were comparable to SA accumulation quantified by nlsSalicS1 (Fig. 3A). In the case of *B. brassicae*, only SalicS1 and pPR1-GUS were sensitive enough to detect significant increases in SA.

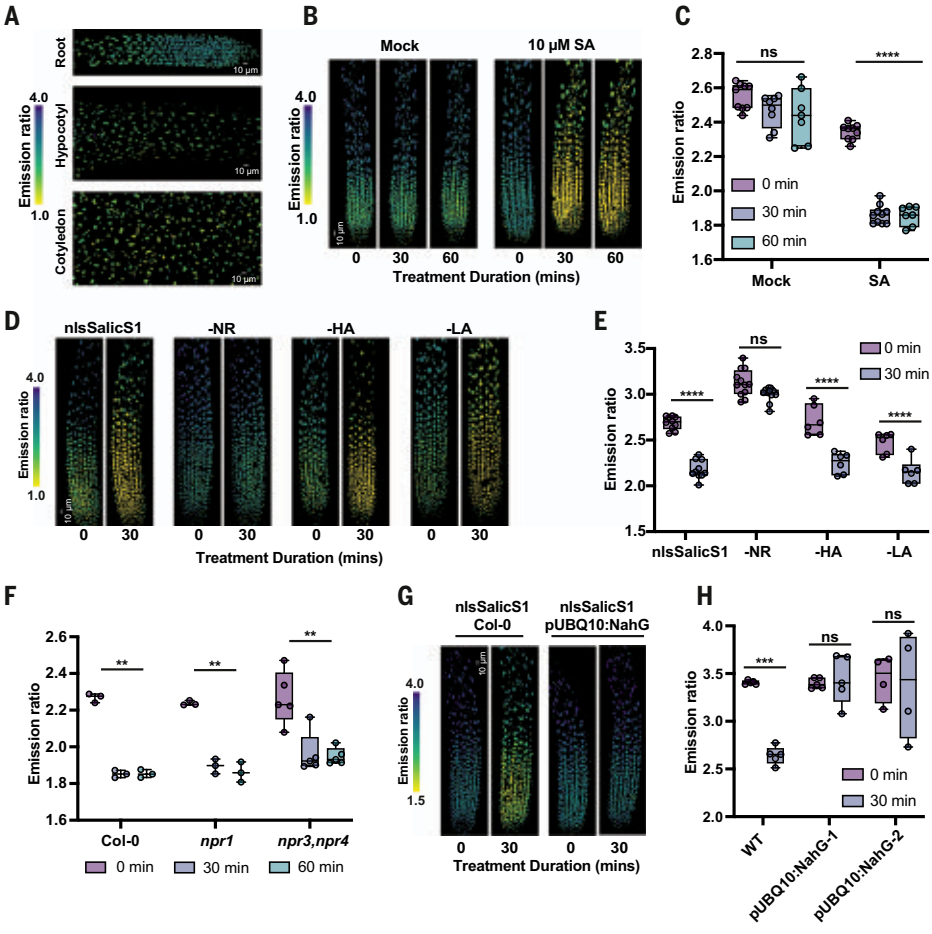


Fig. 2. In planta validation for nlsSalicS1 in stably transformed *Arabidopsis*. (**A**) Endogenous pattern of SA reported by nlsSalicS1 in 5-day-old seedlings at root, hypocotyl, and cotyledon [look-up table (LUT): 1.0 to 4.0; $n = 10$]. (**B**) nlsSalicS1 reported increased SA after exogenous 10-µM SA application. False-color images of roots before and after mock or 10-µM SA treatment (LUT: 1.0 to 4.0). (**C**) Significant reduction of emission ratio was observed in the treatment group, whereas no significant difference was observed in the mock treatment group. Each dot represents the average of all nuclei in one sample (n = 9, 8, 7, 9, 10, 7). Repeated measures two-way ANOVA and Sidak's multiple comparisons test were performed; ****$P < 0.0001$; ns = not significant, $P > 0.05$. The sample size for individual data points was 440 to 820 nuclei in an image of 581.82 by 145.45 µm. (**D**) Representative images of nlsSalicS1, -HA, -LA, and -NR reported different levels of emission ratio change when 10 µM exogenous SA was applied (LUT: 1.0 to 4.0). (**E**) Significant differences in emission ratio after 10 µM of SA application were observed in nlsSalicS, -HA, and -LA, whereas no significant difference was reported in -NR ($n = 10, 10, 12, 10, 6, 6, 6, 6$). Repeated measures two-way ANOVA and Sidak's multiple comparisons test were performed; ****$P < 0.0001$; ns = not significant, $P > 0.05$. The sample size for individual data points was 360 to 940 nuclei in an image of 581.82 by 145.45 µm. (**F**) Significant differences were reported by nlsSalicS1 in Col-0 WT, *npr1* mutant, and *npr3, npr4* double mutants ($n = 3, 3, 5$). Repeated measures two-way ANOVA and Tukey's multiple comparisons test were performed; **$P < 0.01$. The sample size for individual data points was 530 to 1100 nuclei in an image of 581.82 by 145.45 µm. (**G**) Representative images of nlsSalicS1 when 10 µM SA was applied to pUBQ10::NahG (overexpressed NahG) mutant (LUT: 1.5 to 4.0). (**H**) Quantification of emission ratio of nlsSalicS1 in WT Col-0 versus pUBQ10::NahG ($n = 5, 5, 4$). Repeated measures two-way ANOVA and Sidak's multiple comparisons test were performed; ***$P = 0.0002$; ns = not significant, $P > 0.05$. The sample size for individual data points was 360 to 560 nuclei in an image of 581.82 by 145.45 µm. (B to H) Experiments were repeated three times independently. Each point indicates the mean nuclear emission ratio for an individual root *z*-stack. For box plots, center line indicates median; box limits indicate upper and lower quartiles; and whiskers indicate the upper and lower adjacent values. An analysis test was performed on one representative repeat; exact *P* values, *F* values, and degrees of freedom are provided in data S1.

nlsSalicS1 reveals the propagation of SA surge during pathogen advance

To interrogate local responses to infection, we introduced bacteria into *Arabidopsis* by piercing a single area of the leaf with a fine-point needle carrying *Pst* DC3000. In response to the localized application of *Pst* DC3000, we observed strong SA accumulation at the inoculation site at 20 hours but also broad SA accumulation, which even crossed the midvein (Fig. 3C and fig. S13A). A detailed cellular analysis of nlsSalicS1 versus nlsSalicS1-NR revealed that both epidermal and stomatal cells accumulate SA where no significant change of SA accumulation is reported by nlsSalicS1-NR (fig. S14). As anticipated, reduced SA induction was observed in both the *eds5* mutant and *pUBQ10::NahG* plants, with *pUBQ10::NahG* showing lower basal SA levels compared with WT and *eds5* leaves (Fig. 3, D and E, and fig. S13B). nlsSalicS1-NR does not respond to *Pst* DC3000 with lowered emission ratios (Fig. 3, D and E, and fig. S13B).

Using in planta nlsSalicS1, we detected differences in SA induction in WT *Pst* DC3000 and a series of mutants with altered immune induction; for example, infection with the polyeffector mutant D36E (Asp36→Glu) (*54*) or the type III secretion system mutant *hrpA*− (*55*) did not lead to significant SA induction at 20 hours after needle inoculation (Fig. 4, A and B, and fig. S15A). In comparison, two avirulent *Pst* DC3000 strains (avrRpm1 and avrRpt2) (*56*, *57*) expected to induce high levels of SA after activation of ETI showed high but spatially restricted SA induction at 20 hours (Fig. 4, A and B, and fig. S15A). The distribution of SA accumulation differed between ETI-activating avrRpm1 or avrRpt2 carrying *Pst* DC3000 relative to the WT control, with avirulent strains inducing SA accumulation nearer to the infection site, whereas the WT strain promoted a more widespread distribution (Fig. 4C and fig. S16A). Thus, nlsSalicS1 revealed both absolute and spatial differences in SA accumulation during interactions with immune activating or disease-promoting *Pst* strains. Taken together, these results validate nlsSalicS1 for minimally invasive, high-resolution quantification of SA levels in vivo. Time series analysis revealed SA induction around 14 to 17 hours after infection in response to local application with *Pst* DC3000 (Fig. 4, D and E, and fig. S15B). SA levels are thought to quantitatively affect the outcome of infection, ranging from full resistance to susceptibility, yet the specific relationship between SA level and bacterial spread remains unclear. Key questions include whether high local SA concentration limits pathogen spread or whether *Pst* DC3000 actively reduces SA levels in infected regions. To begin to explore these questions, we used *Pst* DC3000 expressing mCherry to track bacterial dissemination relative to SA distribution visualized by the nlsSalicS1 biosensor. *Pst* DC3000-mCherry and WT *Pst* DC3000 induced similar levels of SA, and red fluorescence was only detected in *Pst* DC3000–mCherry infections (fig. S16, B and C). We used mCherry fluorescence to categorize *Arabidopsis* cell nuclei into groups that are proximal or distal to bacterial infection sites. Proximal cells more directly exposed to bacteria exhibited higher SA levels from 11 to 20 hours, whereas distal cells were

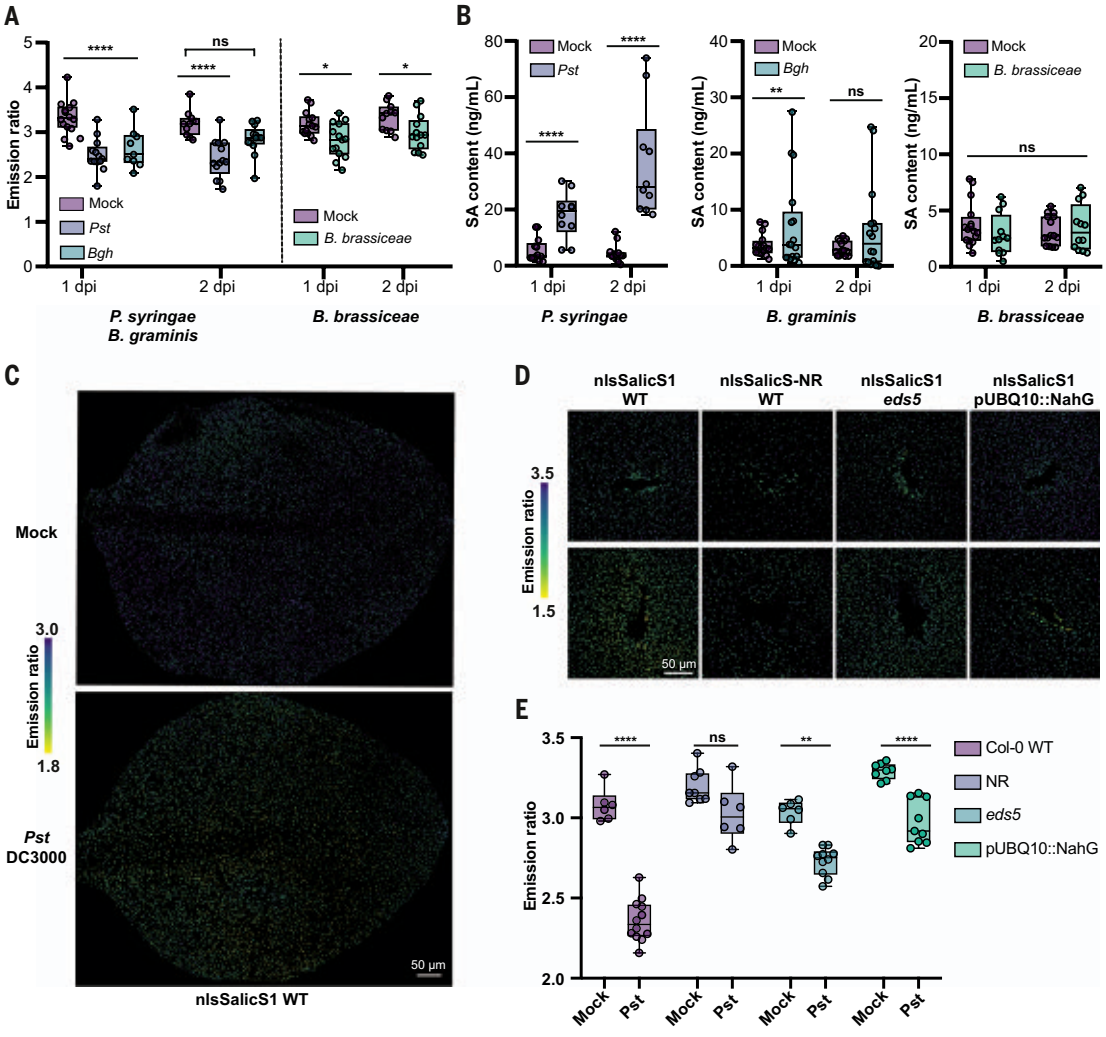


Fig. 3. nlsSalicS1 reported SA accumulation under biotic stress. (**A**) Emission ratio reported by nlsSalicS1 upon *P. syringae* pv. *tomato* DC3000 (*Pst*), *B. graminis* (*Bgh*), and *B. brassiceae* (*Bb*) infection 1 and 2 days postinfection (dpi). Two-way ANOVA with Sidak's multiple comparisons test was performed; ****$P < 0.0001$, *P is provided in data S1; ns = not significant in all comparisons, $P > 0.05$. Mock ($n = 14, 11$), *Pst* ($n = 13$), *Bgh* ($n = 9$), *Bb* infested ($n = 14, 11$). The sample size for individual data points was 1500 to 2800 nuclei in an image of 1553.04 by 1553.04 µm. (**B**) SA quantification by *Acinetobacter* sp. *ADPWH_lux* luminescence 1 and 2 dpi. Two-way ANOVA with Sidak's multiple comparisons test was performed; ****$P < 0.0001$, **$P < 0.01$; ns = not significant in all comparisons, $P > 0.05$. Mock ($n = 13, 14$), *Pst* ($n = 10$), *Bgh* ($n = 6, 16$), *Bb* infested ($n = 12, 12$). (**C**) Represented images of 3-week-old nlsSalicS1mature leaves under mock versus *Pst* DC3000 infection 20 hours after infection ($n = 3$, LUT: 1.8 to 3.0). (**D**) Representative images for nlsSalicS1 WT Col-0 ($n = 6$), nlsSalicS-NR WT Col-0 ($n = 6$), nlsSalicS1 *eds5* ($n = 6$), and nlsSalicS1 pUBQ10::NahG ($n = 8$) upon mock (top panels) versus *Pst* DC3000 (bottom panels) inoculation 20 hours after infection. LUT: 1.5 to 3.5. (**E**) Quantification of emission ratio of nlsSalicS1 in different background after mock versus *Pst* DC3000 infection. Two-way ANOVA with Sidak multiple comparisons test was performed; ****$P < 0.0001$, **$P = 0.0027$; ns = not significant, $P > 0.05$. The sample size for individual data points was 1100 to 2800 nuclei in an image of 1553.04 by 1553.04 µm. Analysis was performed on one representative experiment. Experiments were repeated two times independently. Each point indicates the mean nuclear emission ratio for an individual root *z*-stack. For box plots, center line indicates median; box limits indicate upper and lower quartiles; and whiskers indicate the upper and lower adjacent values. Exact *P* values, *F* values, and degrees of freedom are provided in data S1.

slower and accumulated SA after 17 hours postinfection (Fig. 4, F and G, and fig. S15C). A time series showed the cellular basis of a surge of SA spreading from the *Pst* inoculation site (Fig. 4H, fig. S15D, movie S1, and fig. S16D). Furthermore, during a 7-day systemic infection with turnip mosaic virus expressing 6K2:Scarlet, known to trigger a systemic SA response in *Arabidopsis* (*58*), SA levels increased in WT but not in *pUBQ10::NahG* leaves with the invading virus (fig. S17, A and B).

Discussion

Pathogens suppress plant immune responses to proliferate within host tissues, while plants use SA as a critical defense signal to limit infection. High-resolution detection of SA-related immune events during *Pst* DC3000 infection, such as NPR1 condensate formation (*59*) and single-cell RNA sequencing of defense-associated gene expression (*60*), revealed the localized nature of plant immunity. However, the nucleus-by-nucleus nature of SA dynamics determining the balance between infection and immunity remained unclear. When expressed in *Arabidopsis* nuclei, nlsSalicS1 revealed high-resolution SA dynamics in living organs in a minimally invasive manner.

Although previous studies demonstrated that ETI-inducing strains of *Pst* DC3000 provoke higher SA levels than WT (*61*), whole-leaf infiltrations and bulk SA quantification fail to account for the spatial organization of immunity. For example, spatially restricted *Arabidopsis* infection assays with *Pst* carrying avrRpt2 demonstrated *PR1* gene expression only in cell layers immediately surrounding infection sites (*62*), which is broadly consistent with our direct visualization of SA accumulation

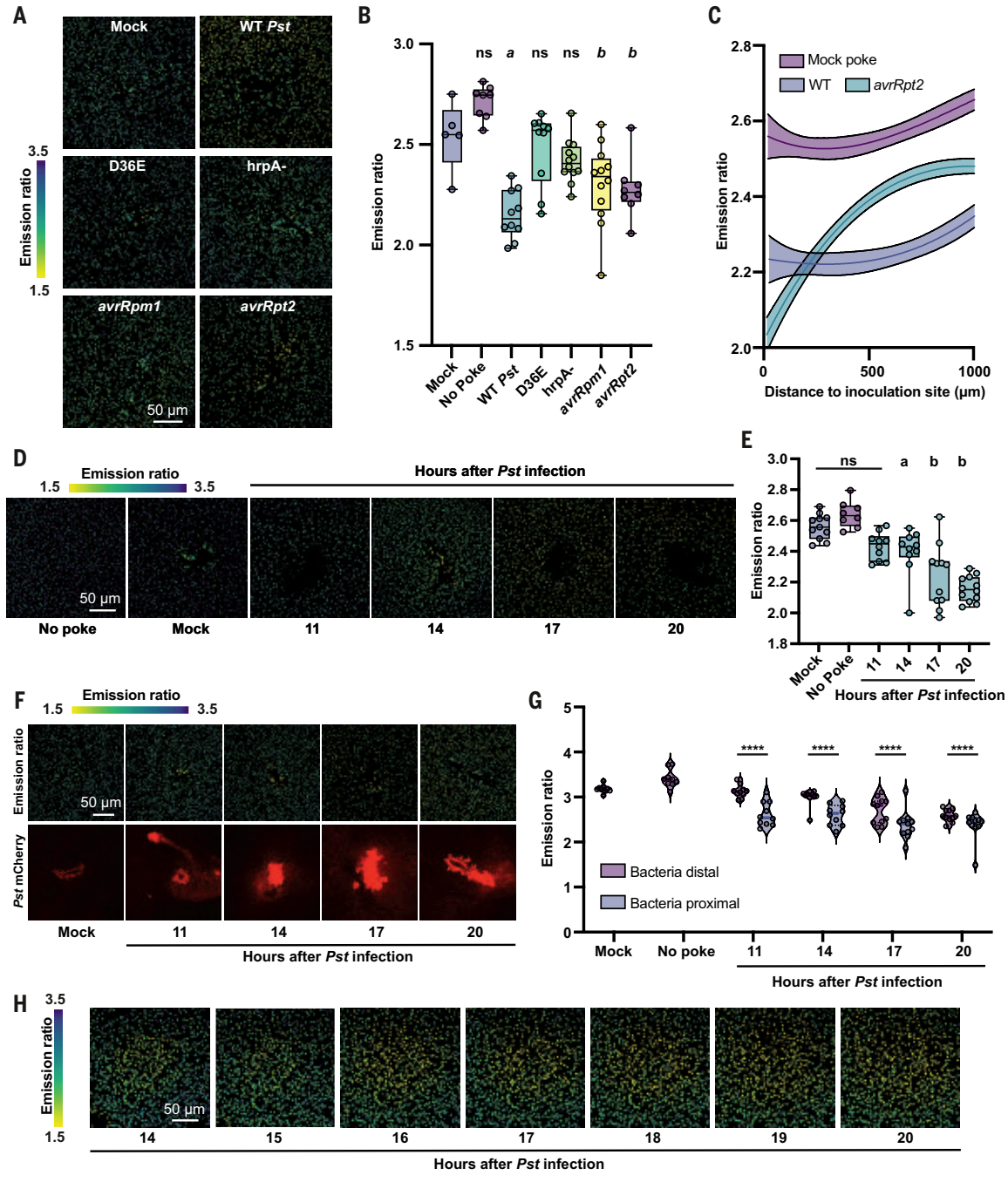


Fig. 4. nlsSalicS1 reported SA in high spatiotemporal manner under *Pst* DC3000 infection. (**A**) Representative images of nlsSalicS1 reported different emission ratio changes upon different *Pst* DC3000 mutant strains infection 20 hours after infection. Mock poke ($n = 5$), no poke ($n = 8$), WT *Pst* DC3000 ($n = 9$), D36E ($n = 8$), *hrpA*− ($n = 9$), *avrRpm1* ($n = 10$), *avrRpt2* ($n = 10$, LUT: 1.5 to 3.5). (**B**) Quantification of emission ratio under *Pst* mutants' infection. One-way ANOVA analysis was performed against the mock control *a*: $P < 0.001$; *b*: $P = 0.0172$ (*avrRpm1*), $P = 0.0138$ (*avrRpt2*); ns = not significant, $P > 0.05$. (**C**) Emission ratio of nlsSalicS1 under mock poke, WT *Pst* DC3000, and *avrRpt2* variants treatment 20 hours after infection against the distance of nucleus to inoculation site. Nonlinear third-order polynomial fit; shaded area represents confidence interval = 95% ($n = 8$). (**D**) Pseudotime course of representative images for nlsSalicS1 in 3-week-old mature leaves after infection. (**E**) Quantification of emission ratio under *Pst* DC3000 infection in pseudotime course. No poke ($n = 8$), mock ($n = 11$), 11 hours ($n = 10$), 14 hours ($n = 10$), 17 hours ($n = 11$), 20 hours ($n = 12$). One-way ANOVA and Dunnett's multiple comparisons test were performed against the mock control, *a*: $P = 0.0329$; *b*: $P < 0.0001$; ns = not significant. (**F**) Representative images reported by nlsSalicS1 versus *Pst* DC3000-mCherry in pseudotime course (LUT: 1.5 to 3.5). (**G**) Significant difference was reported between nonbacteria touching nucleus versus bacteria touching nucleus during the pseudotime course. Two-way ANOVA and Tukey's multiple comparisons test were performed; ****$P < 0.0001$ ($n = 10$). (**H**) nlsSalicS1 reported a surge of SA in *Arabidopsis* leaves spreading out from the infection site in a time course ($n = 3$). After analysis, nuclei were dilated to allow easy visual discrimination at this magnification (LUT: 1.5 to 3.5). In (B), (E), and (G), the sample size for individual data points was 900 to 2900 nuclei in an image of 1553.04 by 1553.04 μm. In (A) to (F), analysis was performed on one representative experiment. Experiments were performed three times independently. Each point indicates the mean nuclear emission ratio for an individual root *z*-stack. For box plots, center line indicates median; box limits indicate upper and lower quartiles; and whiskers indicate the upper and lower adjacent values. Exact *P* values, *F* values, and degrees of freedom are provided in data S1.

using SalicS1. The SA antagonist jasmonic acid (JA) is likely responsible for tightly constraining SA signaling because it similarly accumulates to high levels (*63*, *64*), and the JA marker *VSP1* encircles *PR1*-responding cells during ETI responses associated with immune-related cell death (*62*). A precise mapping of the quantitative relationship between cellular SA accumulation, PR1 gene activation, and JA marker gene activation during localized ETI awaits further study. Such future research leveraging spatially aware technologies such as SalicS1 can reveal how plants control SA to promote a robust local immune response while also maintaining cell survival in adjacent cells and tissues.

Tracking nlsSalicS1 emission ratios in combination with mCherry-expressing *Pst* DC3000 during infection, we found that a surge of SA accumulation begins at proximal cells exposed to bacteria and extends outwards to distal cells over time. This distal SA accumulation adds defense hormone context to the discovery of distinct immune transcriptomes in multiple leaf-cell populations during *Pst* DC3000 infection (*60*). It remains to be determined whether this SA surge results from local synthesis in distal cells or from translocation of the SA hormone itself, although the progression over hours suggests that SA depletion mechanisms are sufficient to limit simple diffusive spread (*61*). It will also be important to decipher how broad-based SA accumulation quantitatively affects not only pathogen spread and systemic acquired resistance induction but also stomatal aperture and plant growth, which are also regulated by SA (*65*, *66*). Future biosensor engineering efforts could also further optimize SalicS1 to detect higher concentrations of SA or to reveal the source of and avoid the root gradient artifact of the present biosensors. Furthermore, as a transferable genetically encoded part (*67*, *68*), the SalicS1 FRET biosensor has the potential to be adapted for use in additional subcellular compartments (e.g., with chloroplast transit peptides) and diverse taxa (e.g., aspirin fluxes in human cells), as well as in crop plants where SA is a conserved determinant of disease and immunity.

REFERENCES AND NOTES

1. R. F. White, *Virology* **99**, 410–412 (1979).
2. I. Raskin, *Plant Physiol.* **99**, 799–803 (1992).
3. S. H. Spoel, X. Dong, *Plant Cell* **36**, 1451–1464 (2024).
4. C. Zipfel, *Trends Immunol.* **35**, 345–351 (2014).
5. J. Malamy, J. P. Carr, D. F. Klessig, I. Raskin, *Science* **250**, 1002–1004 (1990).
6. J. P. Métraux *et al.*, *Science* **250**, 1004–1006 (1990).
7. W. E. Durrant, X. Dong, *Annu. Rev. Phytopathol.* **42**, 185–209 (2004).
8. C. An, Z. Mou, *J. Integr. Plant Biol.* **53**, 412–428 (2011).
9. J. D. G. Jones, R. E. Vance, J. L. Dangl, *Science* **354**, aaf6395 (2016).
10. C. Nawrath, J.-P. Métraux, *Plant Cell* **11**, 1393–1404 (1999).
11. H. Lefevere, L. Bauters, G. Gheysen, *Front. Plant Sci.* **11**, 338 (2020).
12. M. C. Wildermuth, J. Dewdney, G. Wu, F. M. Ausubel, *Nature* **414**, 562–565 (2001).
13. D. Rekhter *et al.*, *Science* **365**, 498–502 (2019).
14. C. Nawrath, S. Heck, N. Parinthawong, J. P. Métraux, *Plant Cell* **14**, 275–286 (2002).
15. M. P. Torrens-Spence *et al.*, *Mol. Plant* **12**, 1577–1586 (2019).
16. L. Wang *et al.*, *Plant J.* **67**, 1029–1041 (2011).
17. Y. Ding *et al.*, *Cell* **173**, 1454–1467.e15 (2018).
18. W. Fan, X. Dong, *Plant Cell* **14**, 1377–1389 (2002).
19. A. Rochon, P. Boyle, T. Wignes, P. R. Fobert, C. Després, *Plant Cell* **18**, 3670–3685 (2006).
20. Y. Tada *et al.*, *Science* **321**, 952–956 (2008).
21. A. Saleh *et al.*, *Cell Host Microbe* **18**, 169–182 (2015).
22. L. Friedrich, B. Vernooij, T. Gaffney, A. Morse, J. Ryals, *Plant Mol. Biol.* **29**, 959–968 (1995).
23. T. P. Delaney *et al.*, *Science* **266**, 1247–1250 (1994).
24. I. Raskin, I. M. Turner, W. R. Melander, *Proc. Natl. Acad. Sci. U.S.A.* **86**, 2214–2218 (1989).
25. G. Marek *et al.*, *Plant Methods* **6**, 21 (2010).
26. T. Pečenková, R. Pleskot, V. Žárský, *Int. J. Mol. Sci.* **18**, 825 (2017).
27. W. E. Huang *et al.*, *Plant J.* **46**, 1073–1083 (2006).
28. A. H. Bukhamsin *et al.*, *Sci. Adv.* **11**, eads8733 (2025).
29. M. C. Y. Ang *et al.*, *Nat. Commun.* **15**, 2943 (2024).
30. A. Miyawaki *et al.*, *Nature* **388**, 882–887 (1997).
31. J. H. Rowe, M. Josse, B. Tang, A. M. Jones, *Annu. Rev. Plant Biol.* **76**, 285–315 (2025).
32. R. Waadt *et al.*, *eLife* **3**, e01739 (2014).
33. A. M. Jones *et al.*, *eLife* **3**, e01741 (2014).
34. A. Rizza, A. Walia, V. Lanquar, W. B. Frommer, A. M. Jones, *Nat. Plants* **3**, 803–813 (2017).
35. A. Rizza *et al.*, *Proc. Natl. Acad. Sci. U.S.A.* **118**, e1921960118 (2021).
36. J. Rowe *et al.*, *Nat. Plants* **9**, 1103–1115 (2023).
37. R. R. Weigel, C. Bäuscher, A. J. P. Pfitzner, U. M. Pfitzner, *Plant Mol. Biol.* **46**, 143–160 (2001).
38. M. Hermann *et al.*, *Front. Plant Sci.* **4**, 88 (2013).
39. C. H. Ho, W. B. Frommer, *eLife* **3**, e01917 (2014).
40. C. L. Cuevas-Velazquez *et al.*, *Nat. Commun.* **12**, 5438 (2021).
41. Y.-N. Chen, H. N. Cartwright, C.-H. Ho, *Sci. Adv.* **8**, eabq4915 (2022).
42. E. W. Jones, *Methods Enzymol.* **194**, 428–453 (1991).
43. S. H. Spoel *et al.*, *Cell* **137**, 860–872 (2009).
44. S. Kumar *et al.*, *Nature* **605**, 561–566 (2022).
45. J. Griffiths, A. Rizza, B. Tang, W. B. Frommer, A. M. Jones, *Plant Cell* **36**, 4426–4441 (2024).
46. M. Balcerowicz, K. N. Shetty, A. M. Jones, *Plant Physiol.* **187**, 590–602 (2021).
47. W. Wang *et al.*, *Nature* **586**, 311–316 (2020).
48. C. Schuster *et al.*, *Dev. Cell* **28**, 438–449 (2014).
49. Z. Q. Fu *et al.*, *Nature* **486**, 228–232 (2012).
50. C. T. DeFraia, E. A. Schmelz, Z. Mou, *Plant Methods* **4**, 28 (2008).
51. A. D. Shapiro, C. Zhang, *Plant Physiol.* **127**, 1089–1101 (2001).
52. L. Poncini *et al.*, *PLOS ONE* **12**, e0185808 (2017).
53. N. Rubil, T. Kalachova, T. P. Hauser, L. Burketová, *Mol. Plant-Microbe Interact.* **35**, 119–124 (2022).
54. H. L. Wei *et al.*, *Cell Host Microbe* **17**, 752–762 (2015).
55. W. Wei *et al.*, *Proc. Natl. Acad. Sci. U.S.A.* **97**, 2247–2252 (2000).
56. Z. Nimchuk *et al.*, *Cell* **101**, 353–363 (2000).
57. H. S. Kim *et al.*, *Proc. Natl. Acad. Sci. U.S.A.* **102**, 6496–6501 (2005).
58. M. Incarbone *et al.*, *Proc. Natl. Acad. Sci. U.S.A.* **120**, e2302069120 (2023).
59. R. Zavaliev, R. Mohan, T. Chen, X. Dong, *Cell* **182**, 1093–1108.e18 (2020).
60. T. Nobori *et al.*, Time-resolved single-cell and spatial gene regulatory atlas of plants under pathogen attack. bioRxiv 2023.04.10.536170 [Preprint] (2023). https://doi.org/10.1101/2023.04.10.536170.
61. J. L. Carviel *et al.*, *PLOS ONE* **9**, e88608 (2014).
62. S. Betsuyaku *et al.*, *Plant Cell Physiol.* **59**, 8–16 (2018).
63. L. Liu *et al.*, *Nat. Commun.* **7**, 13099 (2016).
64. S. H. Spoel *et al.*, *Plant Cell* **15**, 760–770 (2003).
65. M. Rivas-San Vicente, J. Plasencia, *J. Exp. Bot.* **62**, 3321–3338 (2011).
66. L. Xu *et al.*, *New Phytol.* **238**, 1420–1430 (2023).
67. C. Drapek *et al.*, *Plant Cell* **36**, 4442–4456 (2024).
68. S. Zhang *et al.*, *New Phytol.* **234**, 1817–1831 (2022).
69. B. Tang, Raw data for SALICYLIC ACID SENSOR1 reveals the propagation of an SA hormone surge during pathogen advance, Apollo – University of Cambridge Repository (2025); https://doi.org/10.17863/CAM.119273.
70. J. H. Rowe, JimageJ/FRETENATOR2: FRETENATOR2 alpha for Tang et al 2025, Version 2.0-alpha_Tang2025, Zenodo (2025); https://doi.org/10.5281/zenodo.16843696.

ACKNOWLEDGMENTS

We thank M. C. Wildermuth for kindly providing *eds5* and *pbs3* seeds used in this study, M. Wrzaczek and M. Janda for kindly providing *Acinetobacter* sp. *ADPWH_lux* strain, and S. Schornack and A. Walia for helpful comments on the manuscript. We thank all staff of the SLCU for lab support and horticulture support, and especially R. Wightman and G. Evans from the Core Microscopy Unit for supporting the confocal imaging experiments. H.L. and T.K. acknowledge IEB Imaging Facility and support by a project of the Ministry of Education, Youth and Sports, "National Infrastructure for Biological and Medical Imaging (Czech-BioImaging – LM2023050)." **Funding:** This work was supported by the Gatsby Charitable Foundation (GAT3395) (A.M.J.), the European Research Council [H2020-EU.1.1. - EXCELLENT SCIENCE - European Research Council (ERC) agreement no. 759282] (A.M.J.), and Czech-BioImaging – LM2023050 (T.K.). M.I. acknowledges research group funding from the Max Planck Society, and G.H. acknowledges funding by an EMBO postdoctoral fellowship (ALTF 929-2023). **Author contributions:** Conceptualization: B.T., A.M.J.; Funding acquisition: T.K., A.M.J.; Methodology: B.T., J.L., H.L., G.H., S.O., M.G., B.L., R.W., P.C., T.K., M.I.; Supervision: A.M.J.; Visualization: B.T., T.K., A.M.J.; Writing – original draft: B.T., A.M.J.; Writing – review & editing: B.T., J.L., J.R., P.C., T.K., A.M.J. **Competing interests:** The authors declare that they have no competing interests. **Data and materials availability:** *Arabidopsis* transgenic lines with nlsSalicsS1, nlsSalicS1-NR, and nlsSalicS1-pUBQ10::NahG are deposited to Nottingham *Arabidopsis* Stock Centre (NASC IDs N2112676, N2112677, and N2112678). Plasmids with nlsSalicsS1 and nlsSalicS1-NR are deposited to Addgene (Plasmids 232190 and 232192). All other transgenic plant lines and plasmids are available upon request. All data in this manuscript are available at the Apollo Open Access Cambridge Data Repository (*69*). Code is available at Zenodo (*70*). **License information:** Copyright © 2025 the authors, some rights reserved; exclusive licensee American Association for the Advancement of Science. No claim to original US government works. https://www.science.org/about/science-licenses-journal-article-reuse. This research was funded in whole or in part by the European Research Council (agreement no. 759282), a cOAlition S organization. The author will make the Author Accepted Manuscript (AAM) version available under a CC BY public copyright license.

SUPPLEMENTARY MATERIALS

science.org/doi/10.1126/science.adw7650
Materials and Methods; Figs. S1 to S17; Tables S1 to S6; References (*71*–*88*); Movie S1; Data S1 and S2; MDAR Reproducibility Checklist

Submitted 20 February 2025; accepted 15 August 2025

10.1126/science.adw7650

FERROIC MATERIALS

Photo-induced nonvolatile rewritable ferroaxial switching

Z. Zeng[1,2], M. Först[1], M. Fechner[1], D. Prabhakaran[2], P. G. Radaelli[2], A. Cavalleri[1,2]*

Ultrafast switching of ferroic phases is an active research area with technological potential. Yet, some key challenges remain, ranging from limited speeds in ferromagnets to intrinsic volatility of switched domains owing to depolarizing fields in ferroelectrics. Unlike these ferroic systems, ferroaxial materials host bistable states that preserve spatial-inversion and time-reversal symmetry and are therefore immune to depolarizing fields but also difficult to manipulate with conventional methods. We demonstrate photo-induced switching of ferroaxial order by engineering an effective axial field composed of circularly driven terahertz phonon modes. A switched ferroaxial domain remains stable for many hours and can be reversed back with a second terahertz pulse of opposite helicity. The effects demonstrated in this work may lead to the development of a robust platform for ultrafast information storage.

Ferroic orders in solids exhibit pairs of energetically degenerate macroscopic states that can be switched by the application of a corresponding conjugate field. Well-known examples are ferromagnetism and ferroelectricity, which break time-reversal and spatial-inversion symmetry, respectively, and are used in memories, sensors, actuators, and spintronic devices (*1*, *2*). Ferroaxiality is a distinct type of ferroic order, characterized by a rotational texture that hosts vortices of electric dipoles, which preserves both time-reversal and spatial-inversion symmetry (*3*, *4*). Because no net polarization or net magnetization is present, ferroaxials are free from depolarizing or stray fields (*5*), making them promising candidates for stable, nonvolatile data storage. Furthermore, ferroaxial order provides a symmetry channel that mediates the coupling between chiral magnetic texture and electric polarization (*6*–*9*) and is of interest to research in multiferroics. These functional properties have driven rapid advances in both the exploration of ferroaxial materials (*10*–*12*) and the development of techniques for probing their domain structures (*13*, *14*).

Rubidium iron dimolybdate, $RbFe(MoO_4)_2$, is a prototypical ferroaxial system with a transition temperature T_C of about 190 K (*15*–*17*). At temperatures greater than (above) T_C, the material crystallizes in a high-symmetry para-axial state of space group $P\bar{3}m1$. Cooling through the transition temperature spontaneously breaks the mirror symmetries, lowering the crystal symmetry to $P\bar{3}$ and resulting in two opposite ferroaxial domains, A+ and A−, which correspond to clockwise and counterclockwise rotations of the FeO_6 octahedra, respectively (Fig. 1A).

This type of symmetry breaking is invisible to linear optical probes but gives rise to circular dichroism in electric quadrupole second-harmonic generation (SHG-CD) (*18*), providing a sensitive measure of the ferroaxial domain state (*14*). The emergence of ferroaxial order in $RbFe(MoO_4)_2$ is evidenced by temperature-dependent SHG-CD, which displays a sharp increase to a finite value at T_C (Fig. 1B). Notably, the SHG-CD signal is either positive or negative for the two ferroaxial domains (*14*), enabling direct optical identification of their orientation [see the supplementary materials (*19*)]. Spatial mapping resolves the multidomain structure at temperatures less than (below) T_C, with domain sizes of about 100 μm (inset, Fig. 1B) (*20*).

Ferroaxial conjugate field engineering

The ferroaxial order parameter is a time-reversal invariant axial vector (*3*), defined as $\vec{A} = \vec{r} \times \vec{P}$, the cross product of the position vector $\vec{r}$ and the local electric dipole moment $\vec{P}$. Direct external control of this order requires a conjugate field that transforms in the same way as the order parameter under all symmetry operations of the system (*21*). This can be realized by the cross product of two different polar fields, $\vec{X} \times \vec{Y}$, applied simultaneously along two different directions (*21*–*24*). However, combining conventional fields, such as electric fields $\vec{E}$, thermal gradients ∇T, or longitudinal strain gradients $\partial_i \varepsilon_{ii}$, in a well-controlled configuration is experimentally challenging.

In certain systems, where the ferroaxial transition is accompanied by ferroelasticity, uniaxial strain has been used to control the crystallographic axis along which the ferroaxial order develops (*25*). However, this approach does not set the direction of the axial vector $\vec{A}$; therefore, it cannot be used for ferroaxial domain switching to its opposite state. Switching of ferroaxial order by an electric field was reported in a charge density wave material (*24*), though the observed effect was attributed to the response of local electric dipoles at domain walls rather than a direct coupling to the ferroaxial order parameter.

In this work, we constructed a ferroaxial conjugate field $\vec{F} = \vec{Q} \times \vec{E}$ by a terahertz light field $\vec{E}$ and the displacement $\vec{Q}$ of an infrared-active phonon resonantly driven by this field (*26*–*37*). Linearly polarized terahertz pulses, which excite atomic motions parallel to the terahertz electric field, do not couple to the ferroaxial order because the field $\vec{F} = \vec{Q} \times \vec{E}$ vanishes. By contrast, circularly polarized terahertz pulses drive circular atomic motions when resonantly exciting a pair of degenerate phonon modes (*38*–*41*). In this dynamical setting, both the

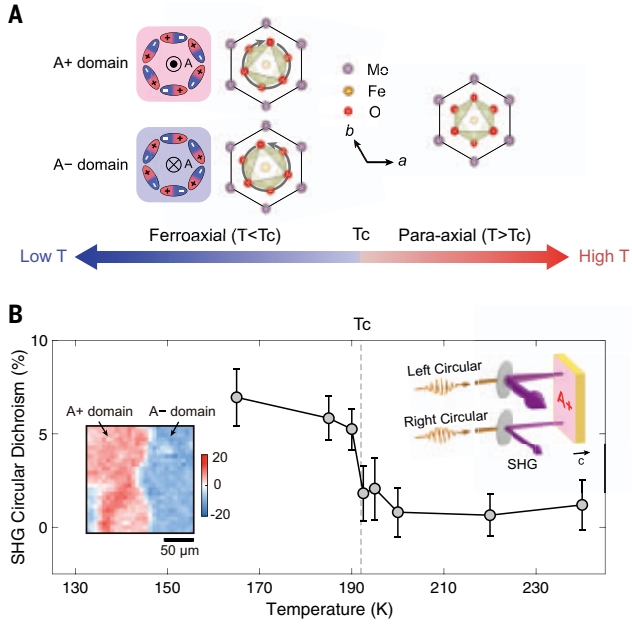


Fig. 1. Ferroaxial order in $RbFe(MoO_4)_2$. (**A**) Crystal structure of $RbFe(MoO_4)_2$ viewed along the crystal *c* axis, above and below the structural phase transition temperature T_C. Below T_C, two ferroaxial domains exist (A+ and A−), corresponding to clockwise and counterclockwise rotations of the FeO_6 octahedra, respectively. (**B**) Ferroaxial transition characterized by SHG-CD. Error bars represent the standard error of the mean. (Right inset) Schematic of the SHG-CD measurement. In the A+ ferroaxial domain, the SHG intensity is higher for the left-circularly polarized probe than for the right-circularly polarized probe. (Left inset) SHG-CD domain mapping at 170K (below T_C).

[1]Max Planck Institute for the Structure and Dynamics of Matter, Hamburg, Germany.
[2]Department of Physics, Clarendon Laboratory, University of Oxford, Oxford, UK.
*Corresponding author. Email: andrea.cavalleri@mpsd.mpg.de

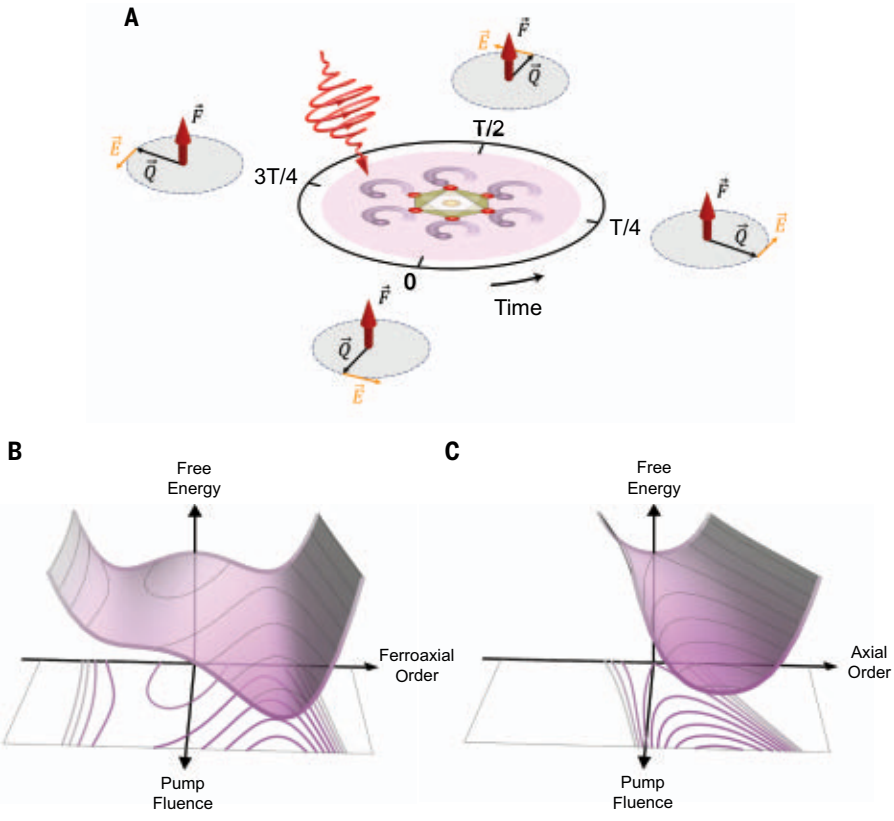


Fig. 2. Circular phonon excitation as a conjugate field of axial order. (**A**) A circularly polarized terahertz pulse, resonant with a doubly degenerate infrared-active phonon, excites circular phonon motion. At each moment during the drive, the electric field $\vec{E}$ and the phonon displacement $\vec{Q}$ are orthogonal, and the direction of the cross product of $\vec{E} \times \vec{Q}$ remains fixed. (**B**) Potential energy landscape of axial order under circular pump below T_C. A circularly polarized terahertz pump biases the double-well potential, favoring one domain over the other, as shown here for a left-circularly polarized terahertz pulse. (**C**) Potential energy landscape of axial order under circular pump in the para-axial state above T_C. A circularly polarized pump shifts the potential energy minimum from zero to a finite value of the axial order parameter, shown here again for a left-circularly polarized terahertz pulse.

electric field and the phonon displacement rotate continuously, where the cross product of the two fields $\vec{F} = \vec{Q} \times \vec{E}$ remains directionally fixed (Fig. 2A). This configuration offers an experimentally accessible conjugate field to ferroaxial order (*42*), with its direction determined by the helicity of the terahertz electric field.

In $RbFe(MoO_4)_2$, the ferroaxial order develops along the crystal c axis and is characterized by the axial mode Q_A subject to a temperature-dependent potential $U(Q_A, T)$. Dynamically, the axial mode couples to the z-component of the conjugate field $\left(\vec{Q} \times \vec{E}\right)_z$ through the interaction potential $\Delta U = \alpha\left(\vec{Q} \times \vec{E}\right)_z Q_A$. Below T_C, the potential $U(Q_A, T)$ takes the form of a symmetric double well, with each well corresponding to one of the two ferroaxial domains. A circular phonon excitation lifts the degeneracy between the two domains by lowering the energy of one well relative to the other (Fig. 2B). Above T_C, $RbFe(MoO_4)_2$ is in a para-axial state with a single-well potential. Here, a circular phonon excitation shifts the minimum of the well, transiently inducing an axially polarized state (Fig. 2C). In both cases, the direction of the torque applied to the ferroaxial soft mode is controlled by the helicity of the terahertz excitation pulse.

Single-shot switching of ferroaxial order below T_C

Ferroaxial switching by the terahertz pulse below T_C is expected owing to the transient asymmetric lowering of the double-well potential [see the supplementary materials (*19*)]. This process is captured by the following equations of motion:

$$\frac{\partial^2}{\partial t^2}\overline{Q}_{E_u} + \gamma_{E_u}\frac{\partial}{\partial t}\overline{Q}_{E_u} + \omega_{E_u}^2\overline{Q}_{E_u} = Z_{E_u}^*\vec{E}(t) \quad (1)$$

$$\frac{\partial^2}{\partial t^2}Q_A + \gamma_A\frac{\partial}{\partial t}Q_A + \frac{\partial}{\partial Q_A}U(Q_A) = \alpha\left[\overline{Q}_{E_u}(t) \times \vec{E}(t)\right]_z \quad (2)$$

Here, $\overline{Q}_{E_u}$ is the displacement vector of the in-plane E_u symmetry phonon mode, γ_A and γ_{E_u} are the damping coefficients, and ω_{E_u} is the frequency of the driven phonon modes. $Z_{E_u}^*$ is the effective charge that couples $\overline{Q}_{E_u}$ to the pulsed terahertz electric field $\vec{E}(t) = E_0\begin{bmatrix}\cos(\omega_{E_u}t)\\ \cos(\omega_{E_u}t + \phi)\end{bmatrix}e^{-\frac{t^2}{2\tau^2}}$, where $\phi = +\frac{\pi}{2}$ and $-\frac{\pi}{2}$ correspond to left and right circular polarization, respectively. Numerical solutions of these equations reveal the evolution of the ferroaxial order as a function of the terahertz pulse excitation fluence, showing that a single pulse induces a reversal of the order parameter above a switching threshold, which is analogous to the coercive field of a ferroelectric. Similar switching behavior is obtained when starting in the opposite domain by changing the helicity of the terahertz excitation pulse [see the supplementary materials (*19*)].

To validate this approach, we used an optical setup (Fig. 3A) to excite the doubly degenerate E_u symmetry phonon at 24 THz frequency in the ab plane of $RbFe(MoO_4)_2$ with resonant, circularly polarized terahertz pulses and probed the ferroaxial state with SHG-CD measurements [see the supplementary materials (*19*)]. First, we applied a single right-circularly polarized terahertz pulse with a fluence of 20 mJ/cm^2 at normal incidence to an A+ domain at 180 K lattice temperature (below T_C), identified by its positive static SHG-CD. Following this single-pulse excitation, the static SHG-CD at the excited sample spot was measured again and showed a negative static SHG-CD of approximately the same magnitude, indicating that the A+ state was locally switched to an A− state (Fig. 3B). In a second step, a single left-circularly polarized terahertz pulse with the same fluence but opposite helicity illuminated the same spot. Following this second pulse, the static SHG-CD reverted to a positive value, evidencing that the system switched back to the A+ state.

A sequence of terahertz pulses with alternating helicities was then applied to the same sample spot, with static SHG-CD measurements performed between pulses to monitor the ferroaxial state. The signal was observed to alternate between positive and negative values, demonstrating reversible optical switching between A+ and A− ferroaxial states (Fig. 3B).

We investigated the fluence dependence of the ferroaxial state switching, aiming to map a "hysteresis loop" of the ferroaxial order under circular phonon excitation. The experiment was performed with single, right-circularly polarized terahertz pulses of increasing fluence, with static SHG-CD measured for about 20 min after each excitation pulse. Single terahertz pulses up to an excitation fluence of 12.5 mJ/cm^2 left the A+ ferroaxial state unaffected, with a positive static SHG-CD (Fig. 4A). A subsequent terahertz pulse with a fluence of 14 mJ/cm^2 inverted the static SHG-CD signal to a negative

value, evidencing the ferroaxial state switching above this threshold. On the same sample spot, now in the A– ferroaxial state, this protocol was repeated by using left-circularly polarized terahertz pulses, i.e., those of opposite helicity. The SHG-CD signal returned to a positive value, characteristic of the A+ state, at the same excitation fluence of 14 mJ/cm^2 (Fig. 4B). The observed threshold behavior is in qualitative agreement with the predictions from the equations of motion in our circular phonon excitation model. According to this model, the switching is expected to occur on a picosecond timescale; however, additional lattice degrees of freedom associated with the equilibrium para-to-ferroaxial phase transition may slow down the material response.

Notably, the rewritable domain remained in the switched state for more than 6 hours, which is the duration between switching from A+ state to A– state and back to the A+ state in the measurement shown in Fig. 4B. At a lower temperature (170 K), ferroaxial domain switching was not observed up to an excitation fluence of ~20 mJ/cm^2, likely as a result of the hardening of the ferroaxial soft mode.

Polarizing the para-axial state above T_C

We further explored the possibility of using circular phonon excitation to induce a transient axial polarization in para-axial $RbFe(MoO_4)_2$ above T_C. A left-circularly polarized terahertz pulse centered at 24 THz—as above, in resonance with the in-plane infrared-active E_u-symmetry phonons—is expected to transiently shift the single-well potential of the para-axial state, centered at $Q_A = 0$, to an A+ axial state. Conversely, a transient A– axial state is expected for excitation with a right-circularly polarized terahertz pulse.

In the time-resolved SHG-CD signal induced by excitation with a 600-fs, left-circularly polarized terahertz pulse at a fluence of 6 mJ/cm^2 at 200 K (above T_C), the short-lived, positive signal refers to the emergence of a transient A+ axial polarization (Fig. 5A). Its lifetime suggests that the duration of the axial conjugate field is determined by the temporal overlap between the terahertz pulse and the resonantly driven phonon. Excitation with a right-circularly polarized terahertz pulse induced a short-lived negative SHG-CD signal (Fig. 5B), evidencing a transient A– axial polarization. The helicity-dependent response above T_C is consistent with the model in which circular phonon excitation serves as the conjugate field for axial order. Excitation with linearly polarized terahertz pulses did not show detectable SHG-CD, confirming that the conjugate field requires circularly polarized excitation [see the supplementary materials (*19*)].

In the temperature dependence of the photo-induced axial state above T_C (Fig. 5C), the amplitude of the transient SHG-CD signal, measured under left-circularly polarized excitation at a fixed fluence of 6 mJ/cm^2, increases as the sample temperature approaches T_C. This response of the axial order parameter is characteristic of ferroic systems, which exhibit increased susceptibility near phase transitions.

The frequency dependence of the photo-induced axial state as a function of the center frequency of the terahertz excitation pulses, measured at 200 K and a constant excitation fluence of 6 mJ/cm^2, is shown in Fig. 5D. We found a resonant enhancement in the transient SHG-CD response at the 24-THz frequency of the doubly degenerate in-plane E_u symmetry phonon mode, which verifies the essential role of resonant phonon excitation when inducing the axial order by light [see the supplementary materials (*19*)].

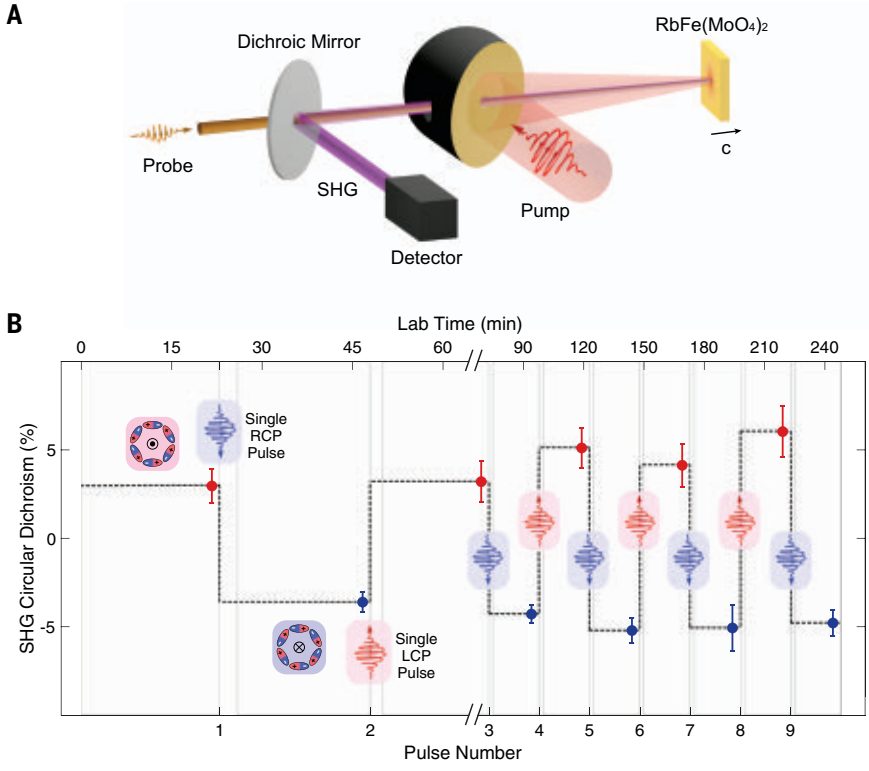


Fig. 3. Demonstration of single-shot switching of ferroaxial order below T_C. (**A**) Schematic of the experimental setup. A circularly polarized terahertz excitation pulse, polarized in the *ab* plane, drives circular motion of the doubly degenerate E_u symmetry phonons in $RbFe(MoO_4)_2$. SHG-CD monitors the ferroaxial state at the excited position. (**B**) Measurement of the ferroaxial domain state at 180 K lattice temperature between single terahertz excitation pulses. The SHG-CD measurement averages over the shaded time windows. Error bars represent the standard error of the mean. RCP, right-circularly polarized; LCP, left-circularly polarized.

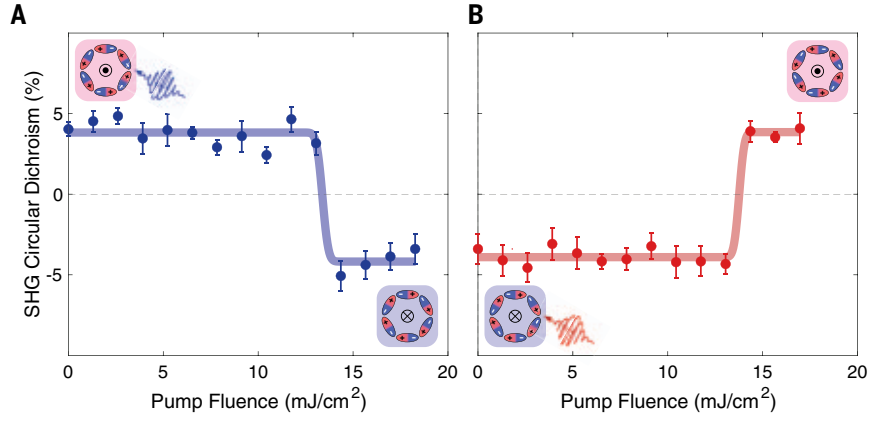


Fig. 4. Fluence-dependent single-shot switching of the ferroaxial order below T_C. (**A**) Measurement of the SHG-CD at 180 K lattice temperature, probing the ferroaxial order after each of the single, right-circularly polarized terahertz excitation pulses of increasing fluence. (**B**) Same measurement for left-circularly polarized single-shot pump pulses, taken on the same sample spot after the measurements shown in (A). Error bars represent the standard error of the mean.

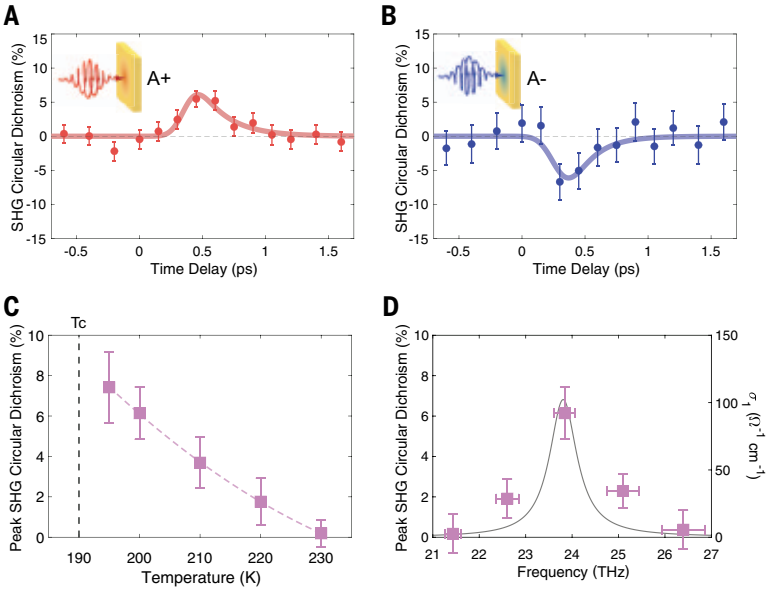


Fig. 5. Photo-induced axial order in the para-axial state above T_C. (**A**) Time delay–dependent SHG-CD measurement for left-circularly polarized excitation. (**B**) Time delay–dependent SHG-CD measurement for right-circularly polarized excitation. (**C**) Peak amplitude of the transient SHG-CD response as a function of temperature above T_C. The dashed pink curve is a guide to the eye. (**D**) Peak amplitude of the transient SHG-CD response as a function of the center frequency of the excitation pulse. The gray curve corresponds to the real part of the optical conductivity. Vertical error bars represent the standard error of the mean. Horizontal error bars in (D) represent the 1σ confidence interval of the center frequency of the excitation pulses.

Discussion and conclusions

We experimentally demonstrated the generation of a photo-phonon conjugate field for ferroaxial order (*23*) in the prototypical ferroaxial system $RbFe(MoO_4)_2$. This protocol is expected to be broadly applicable across a wide range of ferroaxial materials (*11*, *23*, *43*, *44*). Switching the ferroaxial order represents a distinct advantage over earlier attempts to reverse ferroelectric polarization in $LiNbO_3$ with light, where excitation of an auxiliary high-frequency infrared-active mode was nonlinearly coupled to the ferroelectric soft mode (*28*, *36*). In that case, a complete reversal of the ferroelectric polarization was inhibited, likely owing to the buildup of a depolarizing field at the driven region, which destabilized the switched state (*45*). The control of the ferroaxial state opens opportunities for applications in data storage and next-generation electronic and magnetic devices (*11*, *46*, *47*), flanking the field of optically controlled ferro- and ferrimagnetic order (*48*–*50*). Moreover, the emergence of axiality in the para-axial state above the critical temperature highlights the strength of coherent electromagnetic fields to engineer functionality of complex materials that have no equilibrium counterparts.

REFERENCES AND NOTES

1. A. MacDonald, P. Schiffer, N. Samarth, *Nat. Mater.* **4**, 195–202 (2005).
2. L. W. Martin, A. M. Rappe, *Nat. Rev. Mater.* **2**, 16087 (2016).
3. V. Dubovik, L. Tosunyan, V. Tugushev, *J. Exp. Theor. Phys.* **90**, 590–605 (1986).
4. S. Bhowal, N. A. Spaldin, *Phys. Rev. Res.* **6**, 043141 (2024).
5. M. Dawber, P. Chandra, P. Littlewood, J. Scott, *J. Phys. Condens. Matter* **15**, L393–L398 (2003).
6. R. D. Johnson *et al.*, *Phys. Rev. Lett.* **107**, 137205 (2011).
7. R. D. Johnson *et al.*, *Phys. Rev. Lett.* **108**, 067201 (2012).
8. A. J. Hearmon *et al.*, *Phys. Rev. Lett.* **108**, 237201 (2012).
9. J. Yang *et al.*, *Adv. Sci. (Weinh.)* **11**, e2402048 (2024).
10. T. Nagai, Y. Mochizuki, S. Yoshida, T. Kimura, *J. Am. Chem. Soc.* **145**, 8090–8098 (2023).
11. J. Yang, F.-T. Huang, S.-W. Cheong, *J. Phys. Condens. Matter* **37**, 195801 (2025).
12. Y. Kajita, T. Hayashida, S. Yamagishi, K. Kimura, T. Kimura, *J. Phys. Soc. Jpn.* **94**, 063702 (2025).
13. T. Hayashida *et al.*, *Nat. Commun.* **11**, 4582 (2020).
14. H. Yokota, T. Hayashida, D. Kitahara, T. Kimura, *NPJ Quantum Mater.* **7**, 106 (2022).
15. A. Waśkowska *et al.*, *J. Phys. Condens. Matter* **22**, 055406 (2010).
16. W. Jin *et al.*, *Nat. Phys.* **16**, 42–46 (2020).
17. R. Owen *et al.*, *Phys. Rev. B* **103**, 054104 (2021).
18. M. Fiebig, D. Fröhlich, B. B. Krichevtsov, R. V. Pisarev, *Phys. Rev. Lett.* **73**, 2127–2130 (1994).
19. Materials, methods, and additional information are available in the supplementary materials.
20. T. Hayashida *et al.*, *Phys. Rev. Mater.* **5**, 124409 (2021).
21. S.-W. Cheong, S. Lim, K. Du, F.-T. Huang, *NPJ Quantum Mater.* **6**, 58 (2021).
22. J. Hlinka, J. Privratska, P. Ondrejkovic, V. Janovec, *Phys. Rev. Lett.* **116**, 177602 (2016).
23. S.-W. Cheong, D. Talbayev, V. Kiryukhin, A. Saxena, *NPJ Quantum Mater.* **3**, 19 (2018).
24. G. Liu *et al.*, *Nat. Nanotechnol.* **18**, 1–7 (2023).
25. R. Yuan, L. Duan, X. Du, Y. Li, *Phys. Rev. B Condens. Matter Mater. Phys.* **91**, 054102 (2015).
26. M. Först *et al.*, *Nat. Phys.* **7**, 854–856 (2011).
27. D. Fausti *et al.*, *Science* **331**, 189–191 (2011).
28. R. Mankowsky, A. von Hoegen, M. Först, A. Cavalleri, *Phys. Rev. Lett.* **118**, 197601 (2017).
29. P. G. Radaelli, *Phys. Rev. B* **97**, 085145 (2018).
30. T. F. Nova, A. S. Disa, M. Fechner, A. Cavalleri, *Science* **364**, 1075–1079 (2019).
31. X. Li *et al.*, *Science* **364**, 1079–1082 (2019).
32. A. S. Disa *et al.*, *Nat. Phys.* **16**, 937–941 (2020).
33. A. Stupakiewicz *et al.*, *Nat. Phys.* **17**, 489–492 (2021).
34. D. Afanasiev *et al.*, *Nat. Mater.* **20**, 607–611 (2021).
35. A. S. Disa, T. F. Nova, A. Cavalleri, *Nat. Phys.* **17**, 1087–1092 (2021).
36. M. Henstridge, M. Först, E. Rowe, M. Fechner, A. Cavalleri, *Nat. Phys.* **18**, 457–461 (2022).
37. Z. Zeng *et al.*, *Science* **387**, 431–436 (2025).
38. D. M. Juraschek, M. Fechner, A. V. Balatsky, N. A. Spaldin, *Phys. Rev. Mater.* **1**, 014401 (2017).
39. J. Luo *et al.*, *Science* **382**, 698–702 (2023).
40. M. Basini *et al.*, *Nature* **628**, 534–539 (2024).
41. C. S. Davies *et al.*, *Nature* **628**, 540–544 (2024).
42. Z. He, G. Khalsa, *Phys. Rev. Res.* **6**, 043220 (2024).
43. Y. Wang *et al.*, *Nature* **606**, 896–901 (2022).
44. Y. Kajita *et al.*, *Chem. Mater.* **36**, 7451–7458 (2024).
45. V. A. Abalmasov, *Phys. Rev. B* **101**, 014102 (2020).
46. S. Hayami, R. Oiwa, H. Kusunose, *Phys. Rev. B* **108**, 085124 (2023).
47. E. Day-Roberts, R. M. Fernandes, T. Birol, *Phys. Rev. Lett.* **134**, 016401 (2025).
48. A. V. Kimel *et al.*, *Nature* **435**, 655–657 (2005).
49. C. D. Stanciu *et al.*, *Phys. Rev. Lett.* **99**, 047601 (2007).
50. A. Stupakiewicz, K. Szerenos, D. Afanasiev, A. Kirilyuk, A. V. Kimel, *Nature* **542**, 71–74 (2017).

ACKNOWLEDGMENTS

We thank M. Buzzi for valuable discussions. A. Liu and T.-H. Chou are acknowledged for their help with the optical setup. We thank D. Nicoletti for help with the Fourier transform infrared characterization, P. Licht for technical assistance, and J. Harms for help with graphics. **Funding:** Cluster of Excellence "CUI: Advanced Imaging of Matter" of the Deutsche Forschungsgemeinschaft (DFG) (EXC 2056, project ID 390715994) (A.C.). **Author contributions:** A.C., P.G.R., and Z.Z. conceived the project. Z.Z. and M.Fö. designed and performed the experiments. P.D. grew the $RbFe(MoO_4)_2$ sample. M.Fe. performed the DFT calculations and the simulations of the coupled light-phonon dynamics. Z.Z. analyzed the data with help from M.Fö., M.Fe., and P.G.R. Z.Z., M.Fö., and A.C. wrote the manuscript with contributions from all other authors. **Competing interests:** The authors declare that they have no competing interests. **Data and materials availability:** The data supporting the findings of this study are provided in the main text or the supplementary materials. **License information:** Copyright © 2025 the authors, some rights reserved; exclusive licensee American Association for the Advancement of Science. No claim to original US government works. https://www.science.org/about/science-licenses-journal-article-reuse

SUPPLEMENTARY MATERIALS

science.org/doi/10.1126/science.adz5230
Materials and Methods; Supplementary Text; Figs. S1 to S9; Tables S1 to S2; References (*51*–*61*)

Submitted 4 June 2025; accepted 18 August 2025

10.1126/science.adz5230

BATTERIES

Anion sublattice design enables superionic conductivity in crystalline oxyhalides

Feipeng Zhao[1]†‡, Shumin Zhang[1,2]†§, Shuo Wang[3]†, Joel W. Reid[4]†, Wei Xia[1], Jue Liu[5], Graham King[4], James A. Kaduk[6,7], Jianwen Liang[1], Jing Luo[1], Yingjie Gao[1], Feipeng Yang[8], Yang Zhao[1], Weihan Li[1], Sandamini H. Alahakoon[2], Jinghua Guo[8], Yining Huang[2], Tsun-Kong Sham[2], Yifei Mo[3]*, Xueliang Sun[1,9,10]*

Solid-state batteries are attractive energy storage systems as a result of their inherent safety, but their development hinges on advanced solid-state electrolytes (SSEs). Most SSEs remain largely confined to single-anion systems (e.g., sulfides, oxides, halides, and polymers). Through mixed-anion design strategy, we develop crystalline $Li_3Ta_3O_4Cl_{10}$ (LTOC) and its derivatives with excellent ionic conductivities (up to 13.7 millisiemens per centimeter at 25°C) and electrochemical stability. The LTOC structure features mixed-anion spiral chains, consisting of corner-shared oxygen and terminal chlorine atoms, which induces continuous "tetrahedron-tetrahedron" Li-ion migration pathways with low energy barriers. Additionally, LTOC demonstrates holistic cathode compatibility, enabling solid-state batteries operation at 4.9 volts versus Li/Li^+ and low temperature, down to –50°C. These findings describe a promising class of superionic conductors for high-performance solid-state batteries.

Solid-state electrolytes (SSEs) are a core component in all-solid-state Li-ion batteries (ASSLBs) (*1*–*3*). There are generally three categories of SSEs: inorganic (including oxides, sulfides, halides, and others), organic polymers [such as the popular poly(ethylene) oxide electrolytes], and hybrids of the two (*4*–*6*). Inorganic SSEs provide advantages such as high ionic conductivity, excellent thermal stability, and high Li-ion transference number (*4*). Therefore, the inorganic SSEs have attracted increasing attention and have been viewed as the cornerstone of hybrid SSE development (*5*).

Ionic conductivity is a key property of SSEs, followed by the interfacial compatibility between SSEs and electrode materials (*7*, *8*). Sulfide-based inorganic SSEs [i.e., $Li_{10}GeP_2S_{12}$ (LGPS) type (*9*, *10*) and Li argyrodites (*11*, *12*)] possess an ionic conductivity of 10^{-2} S cm^{-1} level at room temperature (RT), which can compete with conventional liquid electrolytes. However, the sulfides inherently suffer from moisture sensitivity and poor electrode incompatibility (*4*, *5*). Oxide SSEs show much better (electro)chemical stability compared with sulfides, but their insufficient RT ionic conductivities (10^{-4} ~ 10^{-3} S cm^{-1}) and required high-temperature processes make them challenging to be used solely to support ASSLBs (*4*–*6*). There is renewed interest in halide-based SSEs, particularly chlorides, as a result of their decent ionic conductivity (10^{-3} S cm^{-1} level) and good compatibility with layered oxide cathode active materials (*13*, *14*). Inspired by Panasonic's Li_3YX_6 (X = Cl, Br) work (*15*), several Li-M-Cl (M = In, Sc, Zr, La, Ta) halide systems have been reported to show good ionic conductivities (cold-pressing max. 6.05×10^{-3} S cm^{-1} at 25°C) and promising electrochemical stability at RT (*16*–*22*). Given the distinct advantages of different anion chemistries in ionic conductivity and (electro)chemical stabilities, mixed-anion chemistry has been a promising yet underexplored opportunity to improve SSEs. This approach offers the potential to replace liquid electrolytes while maintaining high ionic conductivity and enhancing (electro) chemical stability (*23*, *24*).

Lithium-ion transport in solids is determined by the anion framework and Li-coordinated environment. Wang *et al.* showed that the ultrahigh ionic conductivities in sulfides (e.g., LGPS and $Li_7P_3S_{11}$) originate from the body-centered cubic (bcc)–like anion sublattice with the face-sharing "tetrahedral-to-tetrahedral" ("tet-tet") Li-ion migration pathway (*25*). However, the desirable "tet-tet" pathway is rarely reported in other anion frameworks of SSEs, neither in halides nor oxides. Chloride SSEs typically crystallize in either a close-packed anion sublattice (hexagonal or cubic close-packing) or a non–close-packed (e.g., zeolite-like) anion framework. These halide structures feature Li-ion diffusion channels composed of octahedral (oct) and tetrahedral (tet) sites (Fig. 1A) (*21*, *26*). By contrast, in oxide SSEs, the anion framework established through the oxygen corner-sharing manner shows a high degree of freedom, which has been demonstrated to form a distorted Li-coordinated environment and flatten the energy landscape for fast Li-ion migration (*27*, *28*). Therefore, we envision a mixed-anion strategy to design an oxygen corner-sharing oxychloride anion framework to induce the distinct "tet-tet" Li-ion migration channels (Fig. 1B), which were limited to bcc-like anion sublattice and absent in oxide and halide chemistries. As illustrated in Fig. 1C, compared with the "oct-involved" pathways, the continuous "tet-tet" Li-ion migration pathway shows the lowest activation energy and benefits ion transport.

Tanaka *et al.* (*23*) reported $LiMOCl_4$ (M = Nb, Ta) superionic conductors with an ionic conductivity up to 12.4 mS cm^{-1}. However, the crystal structures of these compounds have not been fully resolved. The proposed ordered Li sublattice in their structures cannot account for the high ionic conductivity observed (*29*, *30*), and the considerable number of amorphous phases in these materials as synthesized further complicates efforts to understand the structural origin of high ionic conductivity (*20*, *31*). Therefore, the superior Li-ion conduction mechanism in these oxyhalides is not fully understood.

Crystalline $Li_3Ta_3O_4Cl_{10}$

Leveraging anion sublattice design, we developed a crystalline lithium superionic conductor $Li_3Ta_3O_4Cl_{10}$ (LTOC) with a conventional co-melting synthesis method (see methods for details). The primary LTOC particle size can be reduced from micron-size crystallites to 100 to 200 nm after simple hand-grinding with an agate mortar (figs. S1 and S2), which is beneficial for dry mixing with cathode active materials in providing sufficient interfacial contact and Li-ion percolating networks. The basic coordination environment of the LTOC material around Ta was analyzed by x-ray absorption spectroscopy (XAS) of Ta L_3-edge (fig. S3). A combination of Ta-O

[1]Department of Mechanical and Materials Engineering, Western University, London, ON, Canada. [2]Department of Chemistry, Western University, London, ON, Canada. [3]Department of Materials Science and Engineering, University of Maryland, College Park, MD, USA. [4]Canadian Light Source Inc., Saskatoon, SK, Canada. [5]Neutron Scattering Division, Oak Ridge National Laboratory, Oak Ridge, TN, USA. [6]Illinois Institute of Technology, 3101 S. Dearborn St., Chicago, IL, USA. [7]North Central College, 131 S. Brainard St., Naperville, Illinois, USA. [8]Advanced Light Source, Lawrence Berkeley National Laboratory, Berkeley, CA, USA. [9]Eastern Institute for Advanced Study, Ningbo Institute of Digital Twin, Eastern Institute of Technology, Ningbo, Zhejiang, P. R. China. [10]Zhejiang Key Laboratory of All-Solid-State Battery, Ningbo Key Laboratory of All-Solid-State Battery, Ningbo, Zhejiang, P. R. China. ***Corresponding author. Email: yfmo@umd.edu (Y.M.); xsun9@uwo.ca (X.S.)** †These authors contributed equally to this work. ‡Present address: Institute of Functional Nano and Soft Materials (FUNSOM), Jiangsu Key Laboratory for Advanced Negative Carbon Technologies, Soochow University, Suzhou, P. R. China. §Present address: School of Physical Science and Technology, Jiangsu Key Laboratory of Frontier Material Physics and Devices, Suzhou Key Laboratory of Intelligent Photoelectric Perception, Jiangsu Key Laboratory of Advanced Negative Carbon Technologies, Center for Energy Conversion Materials & Physics (CECMP), Soochow University, Suzhou, P. R. China.

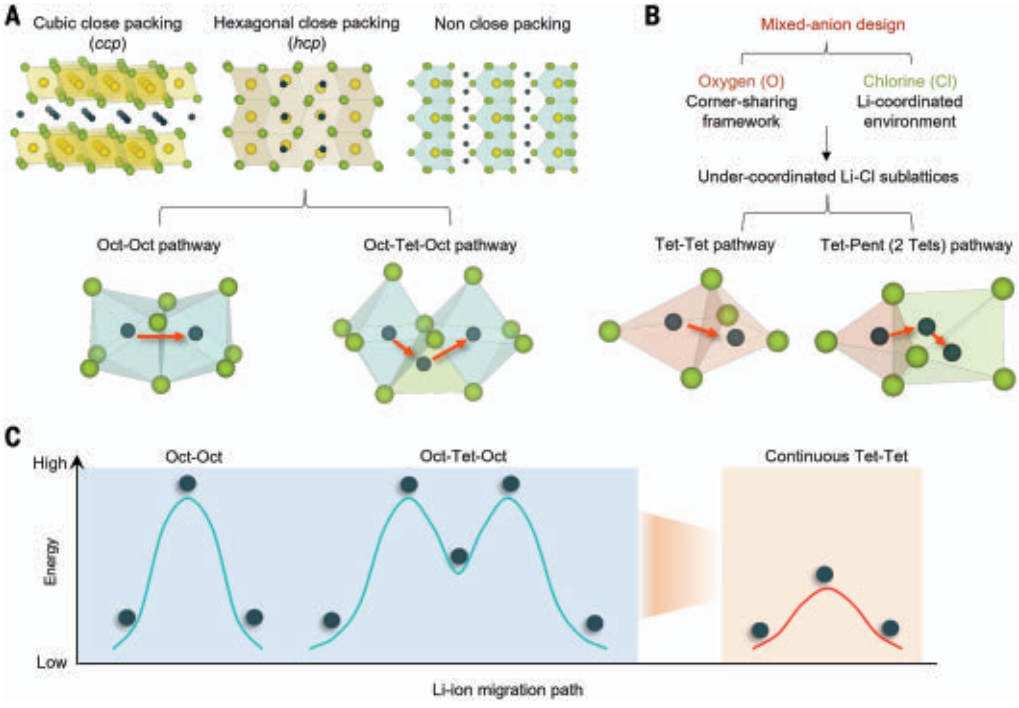


Fig. 1. Anion sublattice design toward low-energy–barrier Li-ion migration pathways. (**A**) Anion packing of known halide SSEs, in which the octahedral (oct) lithium sites are the most common and the Li migration pathways occur through said oct sites. (**B**) Mixed-anion strategy enabling anion framework with corner-sharing O to induce a low-coordinated Li-Cl environment [e.g., tetrahedral (tet), pentahedral (pent)] for desirable low-energy pathways. A pentahedron can be viewed as two split face-sharing tetrahedrons. (**C**) Schematic illustration of Li-ion migration energy in the pathways with different local anion coordination.

and Ta-Cl bonds was found to construct Ta-O/Cl coordination in the LTOC, which was also reflected by the XAS results of O K-edge and Cl K-edge (fig. S4), as well as the Raman spectrum of the LTOC SSE (fig. S5). The crystal structure of LTOC was solved using a combination of synchrotron powder x-ray diffraction (PXRD) and neutron powder diffraction (NPD) (figs. S6 and S7). As displayed in Fig. 2A, LTOC shows a large monoclinic cell in the space group of I2/a (see table S1 for the cell parameters and analysis details of synchrotron PXRD refinement). Three-dimensional (3D) spiral Ta-O/Cl chains run along the *a*-axis and Li ions are located among the intercolumnar Ta-O/Cl framework. The typical Ta-O/Cl chain is extracted from the unit cell, as shown in Fig. 2B. All O atoms (four crystallographic sites) are at the junction sites to link the four types of Ta-O/Cl oct (two TaO_2Cl_4 and two TaO_4Cl_2), and all oct terminal sites are completely occupied by Cl atoms. As a result, the long Ta-O/Cl chain is constructed based on the bridging Ta-O-Ta skeleton that is connected by corner-sharing O. Fourier difference map from the NPD data showed that Li ions were distributed in a very dispersive manner, which was also confirmed by the Li probability from ab initio molecular dynamics (AIMD) simulations of the crystal structure of LTOC (fig. S8). These results suggested high mobility of Li ions in the LTOC but also indicated the difficulties in defining all specific Li sites in the unit cell of LTOC. For simplicity, we determined five plausible Li sites (all are at 8f), and atomic coordinates are displayed in table S2. Induced by the high-degree-of-freedom Ta-O/Cl long chain (constructed through O sharing), the Li-Cl environment in the LTOC appears distorted and undercoordinated. The $LiCl_x$ (x = 4, 5) polyhedra (fig. S9) are connected to each other as displayed in Fig. 2C. ^{6}Li magic angle spinning nuclear magnetic resonance (MAS-NMR) spectroscopy was also used to prove that there were two kinds of Li-Cl coordination environment (tet and pent) in the crystal structure of LTOC (fig. S10). The anion framework and Li sublattice of LTOC fulfill our rational design strategy regarding use of mixed-anion chemistry toward ultrafast Li-ion conduction.

The LTOC exhibits 3D ionic conduction pathways in the crystal structure, as confirmed by the Li-ion probability density in the AIMD simulations (figs. S11 and S12). The dispersed and continuous distribution of Li-ion probability density indicates a flat energy landscape that facilitates fast Li^+ migration. Specifically, Li-ion migrates among these $LiCl_x$ (x = 4, 5) polyhedral sites to form a continuous Li-ion diffusion channel along the *c*-axis and in the *ab* plane, as shown in Fig. 2, D and E, respectively. Using nudged elastic band (NEB) calculations, we analyzed the energy landscape of the ionic diffusion along the pathways observed in the AIMD simulations (Fig. 2, F and G). We found that the highly distorted $LiCl_5$ polyhedral sites split into two neighboring tet sites with similar energies, forming a "tet-tet" diffusion pathway with a flat energy landscape. The calculated barriers of ionic migration in the "tet-tet" diffusion pathways are as low as ~0.2 to 0.3 eV (Fig. 2, H and I), which are consistent with the activation energy calculated by the the AIMD simulations. The isotropic 3D Li-ion migration feature was also verified by analyzing the variable-temperature ^{7}Li spin-lattice relaxation time as shown in fig. S13. The "tet-tet" Li-ion diffusion channels is highly desirable as it is the key feature of the low migration barrier in the bcc-type anion framework, which was only reported in sulfide SSEs with RT ionic conductivity above 10^{-2} S cm^{-1}, including LGPS and $Li_7P_3S_{11}$ (*25*). In LTOC, the mixed halogen-oxygen sublattice enables "tet-tet" diffusion channels, demonstrating the key advantage of mixed-anion chemistry in broadening the possible structures in designing novel Li-ion conductors.

High ionic conductivity and integrated properties derived from anion sublattice designs

The ionic conductivity of the LTOC SSE was experimentally obtained from calculating the impedance of the Nyquist plots obtained through electrochemical impedance spectroscopy (EIS) measurements at various temperatures (fig. S14). As shown in Fig. 3A, the ionic conductivity of LTOC has reached as high as 1.10×10^{-2} S cm^{-1} at RT with a low activation energy (Ea) of 0.241 eV. The data were obtained based on the cold-pressed LTOC pellet during the EIS measurements. The ionic conductivity of the LTOC remained over 10^{-3} S cm^{-1} at low temperatures down to −35°C (1.30×10^{-3} S cm^{-1}). At −65°C, the ionic conductivity remained at 2.42×10^{-4} S cm^{-1}. As shown in Fig. 3B, the AIMD simulations also confirmed the fast Li-ion conduction in LTOC. The predicted RT ionic conductivity is 1.96×10^{-2} S cm^{-1} with an error bound of 1.01×10^{-2}

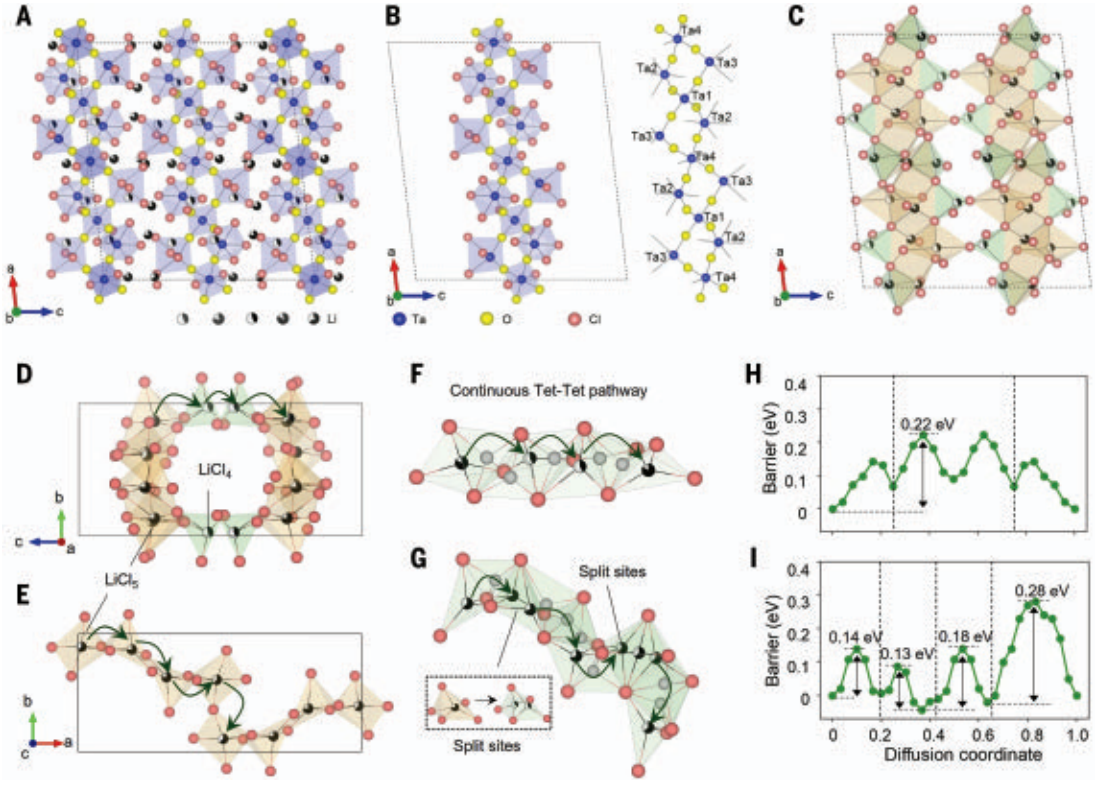


Fig. 2. Unique crystal structure and desirable Li-ion migration pathways in the $Li_3Ta_3O_4Cl_{10}$ (LTOC) SSE. (**A**) Crystal structure of the LTOC along the *b*-axis. (**B**) One Ta-O/Cl long chain extracted from the crystal structure, showing Ta-O-Ta connections with Ta-Cl branches; the simplified Ta-O-Ta long chains running parallel to the *a*-axis are shown on the right. (**C**) Continuous $LiCl_x$ (x = 4, 5) polyhedra constitutes the Li sublattices in the LTOC. (**D** and **E**) $LiCl_x$ (x = 4, 5) coordination environment observed along the *a*- and *c*-axes, respectively. (**F** and **G**) The local coordination environments of representative diffusion pathways along the *c*-axis and within the *ab* plane, respectively, observed from AIMD simulations. The highly distorted $LiCl_5$ polyhedra is split into tetrahedral sites for ionic migration, forming continuous "tet-tet" diffusion channels. (**H** and **I**) The calculated energy landscape of ionic diffusion along the *c*-axis and within the *ab* plane, respectively, by NEB method.

to 3.41×10^{-2} S cm^{-1}, and the activation energy is 0.20 ± 0.02 eV, which agrees well with our experimental results. Direct current (DC) polarization was used to derive an electronic conductivity of 7.79×10^{-9} S cm^{-1} at RT for the LTOC SSE (fig. S15). The electronic conductivity of LTOC was seven orders of magnitude lower than the value of ionic conductivity, fulfilling the requirements of electrolyte materials for fast Li-ion conduction and electronic insulation. Sintering the LTOC pellet (see fig. S16 for the SEM images) was verified to increase the relative density of LTOC pellet and improve the ionic conductivity to 1.37×10^{-2} S cm^{-1} at RT, and the delivered Ea accordingly dropped to 0.228 eV over a temperature range of −65 to 70°C (see fig. S17 for the Nyquist plots). The ionic conductivity of LTOC has overtaken the conventional liquid electrolytes (1.15×10^{-2} S cm^{-1} at 25°C for 1 M $LiPF_6$ in carbonate), which is one of the highest in the recent wave of reviving halide-based SSEs (Fig. 3C and table S3), rivaling the state-of-the-art sulfide SSEs (table S4).

Another advantage of LTOC is the improved moisture stability. As shown in fig. S18, because of the enhanced bonding energy of metal-coordination involving oxygen, the LTOC shows relatively stable structure and superior ionic conductivity retention compared with the typical halide (Li_3YCl_6) and sulfide (Li_6PS_5Cl) SSEs. Furthermore, based on mixed-anion chemistry, we designed and realized high moisture stability for the lithium tantalum oxyfluoride SSE (fig. S19), which exhibits a negligible change in ionic conductivity after exposure to a dry-room atmosphere for 12 hours. The universal applicability of the mixed-anion strategy to design oxychloride SSEs has been validated using Nb (fig. S20) and other cost-effective or earth-abundant elements (fig. S21). Through the co-melting method, 50% of the Ta sites in the LTOC crystal structure can be replaced by Fe, Al, V, or Zr, showing ionic conductivities at a high level (0.4 to 4.3×10^{-3} S cm^{-1}). Moreover, Ta-free SSEs based on Nb, Fe, and Al, as well as high-entropy (equal molarity of Ta, Fe, Al, V, and Zr) oxychloride SSEs, were realized with an ionic conductivity up to 7.7×10^{-3} S cm^{-1}. These results demonstrate that replacing precious metals in mixed-anion frameworks provides a promising alternative route toward enhancing the sustainability of this class of SSEs.

Electrochemical performance

A high-Ni cathode, $LiNi_{0.83}Co_{0.11}Mn_{0.06}O_2$ (NCM83), was chosen as the cathode active material to work with the LTOC SSE to construct the ASSLBs. As shown in Fig. 4A, at a low current density of 0.1 C, the reversible capacity was 213 mAh g^{-1}. At higher rates of 0.2, 0.5, and 1 C, the reversible capacities were retained for 205, 185, and 163 mAh g^{-1}, respectively. Even at high current densities of 2 C and 3 C, effective Li (de)intecalation processes still took place, as indicated by the charge/discharge curves in Fig. 4B. The charge/discharge curves showed sloppy redox plateaus between 2.5 and 4.3 V (versus Li/Li^+, the same hereafter), which were similar to the NCM83 cells

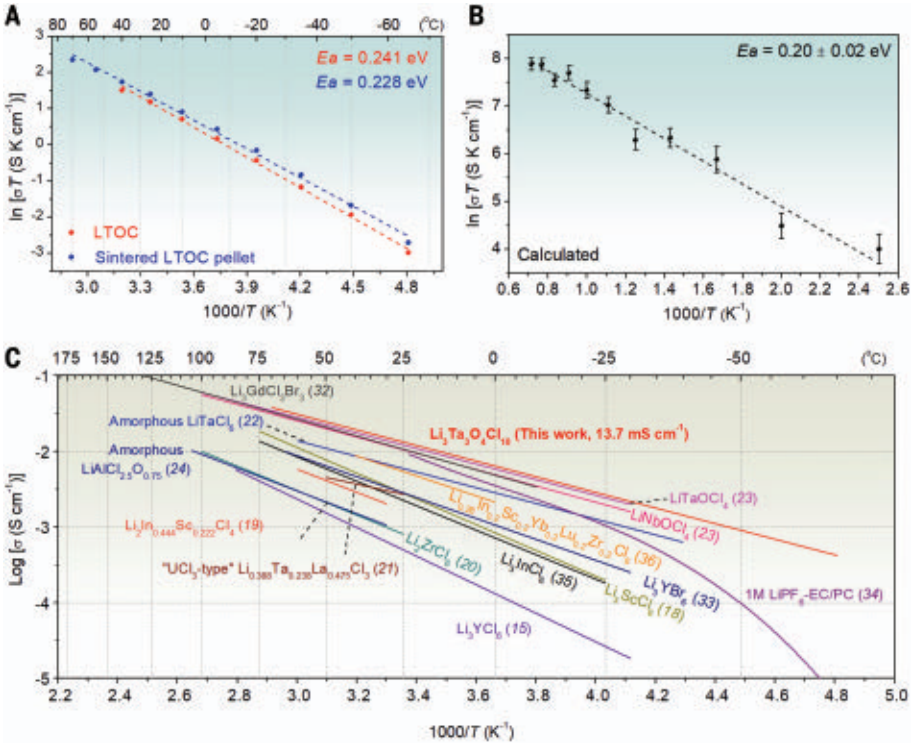


Fig. 3. Li-ion conduction properties of the LTOC SSE. (**A**) Arrhenius plots of Li-ion transport in the LTOC SSE (cold-pressed) and sintered LTOC pellet obtained from EIS measurements. (**B**) Arrhenius plot of Li-ion transport in the LTOC SSE based on AIMD simulations. The calculation of the error bars is described in the methods. (**C**) Comparison of the ionic conductivity of representative halide-based SSEs (*15*,*18*–*24*,*35*–*39*). The lines were plotted according to the reported ionic conductivity at RT; the activation energy, detailed data, and references are summarized as table S3 in the supplementary materials.

using the conventional liquid electrolyte (fig. S22). We further increased the ratio of cathode active materials up to 90% and excellent cycling performances were obtained at 2 C (fig. S23), indicating that the nanosized LTOC particles coupled well with the microsized NCM83 cathodes to form highly effective ion/electron percolating networks. As a result of the good oxidation limit of the LTOC SSE—confirmed by the linear scanning voltammetry (LSV) measurements (fig. S24)—we extended the charging cutoff voltage from 4.3 to 4.6, 4.8, and 4.9 V to examine the high-voltage durability of the NCM83 cells. As shown in Fig. 4C and fig. S25, the reversible capacity at a high rate of 2 C increased with elevated cutoff voltages, although the polarization and cycling stability deteriorated accordingly. Despite this, the NCM83 cell exhibited a very promising high-voltage durability at 4.9 V, and the capacity retention was ~87% after 200 cycles. Long-term cycling stability of the NCM83 cell (2.5 ~ 4.3 V) was evaluated at various current densities (Fig. 4D and fig. S26). At a high rate of 3 C, there was a negligible capacity decay during 2000-time continuous charging and discharging, exhibiting a capacity of approximately 100 mAh g^{-1} and an ideal Coulombic efficiency of ~100%. Even after extending to 4200 cycles, the capacity retention was still maintained at ~75%. The cycling performance of the liquid cell was not as good as that in the solid counterpart (fig. S27). This phenomenon was probably caused by continuous electrolyte consumption at the cathode/liquid electrolyte interface at high voltages, which was also observed in Nazar's work (*19*).

Our solid-cell performances were achieved under an applied stack pressure of 80 MPa during cycling. Leveraging the flexible mixed-anion design, we reduced the crystallinity of LTOC (fig. S28) by optimizing the synthesis process (see methods). This allowed us to lower the stack pressure to 10 MPa without compromising rate capability or cycling stability (fig. S29). As widely recognized, developing an ideal SSE with simultaneous compatibility for anode and cathode materials is highly challenging (*32*). In the case of LTOC, compared with the excellent oxidation stability, the cathodic stability (stability to reduction reaction) is relatively low as a result of the high reduction potential of Ta^{5+}. However, this can be alleviated by doping low-valence elements (e.g., La or Zn) or inserting protective interlayer SSEs (e.g., $Li_{5.3}PS_{4.3}ClBr_{0.7}$) in the construction of Li-metal solid cells (fig. S30). Furthermore, we employed dry-film fabrication to prepare free-standing cathode and SSE layers, which can be used to fabricate a lab-scale pouch cell (area capacity: 4.4 mAh cm^{-2}), showing a capacity retention of 89.8% after 50 cycles at 0.1 C (fig. S31).

The solid-state configuration is regarded as an advantage to realize high performance at low temperatures, as superionic conductors can show superior continuous and fast Li-ion conduction when compared with liquid electrolytes at low temperatures (*9*). We systematically studied the low-temperature performance of the ASSLBs using LTOC. At −10°C, the reversible capacity of the NCM83 cell at various current densities (Fig. 4E) dropped accordingly compared with the results at RT. However, a reversible capacity of ~89 mAh g^{-1} was still achieved at a relatively high rate of 1 C, and the effective (de)lithiation processes (~100% Coulombic efficiency) were performed at each current density (Fig. 4F). The cycling stability was verified at a relatively high rate of 1 C (Fig. 4G), which showed a marginal capacity decay with a cycle number >720. At −30°C, ultrastable cycling was also exhibited at 0.2 C, showing no capacity decay after 400 cycles as shown in Fig. 4H and ~80% retention after 1000 cycles (fig. S32). Cycling stability of the NCM83 cell at other current densities at −10 or −30°C is presented in fig. S33. We further examined the solid cell at −50°C. As depicted in Fig. 4I, the NCM83 solid cell operated fully reversibly over 2000 cycles at 0.1 C and sustained a capacity of ~80 mAh g^{-1} (Fig. 4J). Imaging and spectroscopy characterization (fig. S34) of the cycled NCM83 cathode materials indicated that the cathode particle was free of cracks but subject to chemical reduction of metal elements (e.g., Ni) at the interface. Nevertheless, the nanosized LTOC particles still covered the cathode surface as a sheath to prevent further chemical decomposition. Low temperature was also demonstrated in ASSLBs using a $LiCoO_2$ (LCO) cathode (fig. S35 and fig. S36). These battery performances at RT and low temperatures are compared with those in the literature in tables S5 and S6 and fig. S37 (*33*, *34*).

In summary, the anion sublattice design has proven effective in achieving high ionic conductivity, reaching up to 13.7 mS cm^{-1} in the crystalline LTOC SSE. The LTOC crystal structure features corner-sharing O atoms and terminal Cl atoms that form a 3D spiral Ta-O/Cl framework, combined with an undercoordinated Li sublattices. This arrangement enables desirable "tet-tet" Li-ion migration pathways, leading to the superionic conduction properties of LTOC

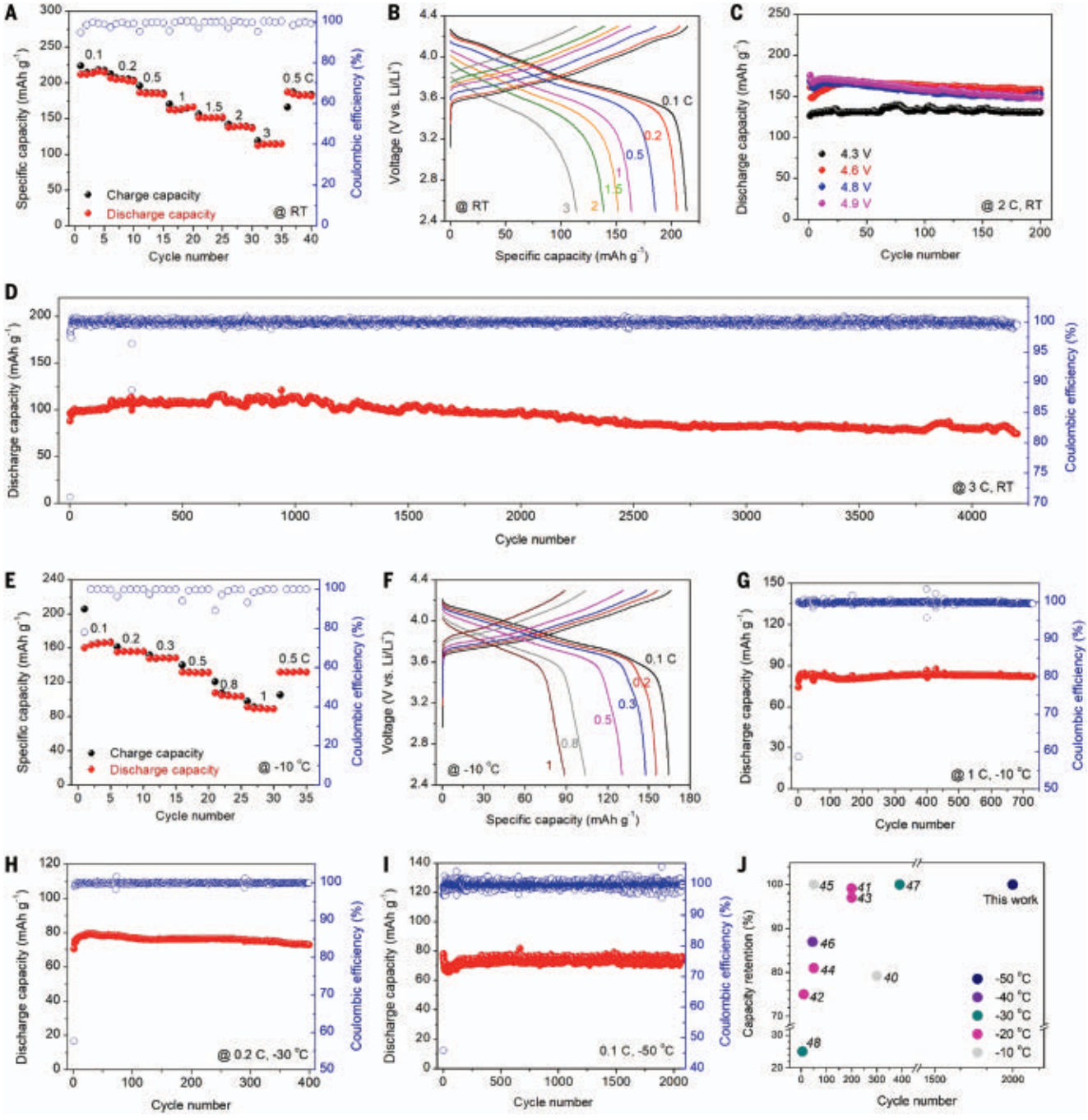


Fig. 4. Electrochemical performance of LTOC-based ASSLBs using the NCM83 cathode. (**A**) Rate capability (from 0.1 C to 3 C) of the NCM83 cell achieved at RT. (**B**) Charge/discharge curves of the NCM83 cell at various current densities (RT). (**C**) Cycling stability of the NCM83 cell at various cutoff voltages obtained at a high rate of 2 C and at RT. (**D**) Long-term cycling performance of the NCM83 cell at a high rate of 3 C (cutoff voltage: 4.3 V, RT). (**E**) Rate capability (from 0.1 C to 1 C) of the NCM83 cell achieved at −10°C. (**F**) Charge/discharge curves of the NCM83 cell at various current densities (−10°C). (**G**) Long-term cycling performance of the NCM83 cell at 1 C (−10°C). (**H**) Long-term cycling performance of the NCM83 cell achieved at 0.2 C and −30°C. (**I**) Long-term cycling performance of the NCM83 cell at 0.1 C and −50°C. (**J**) Comparison of the low-temperature performance of the NCM83 cells with the literature (*40*–*48*). The ionic conductivities of LTOC are 3.57×10^{-3} S cm^{-1}, 1.61×10^{-3} S cm^{-1}, and 5.68×10^{-4} S cm^{-1} at −10°C, −30°C, and −50°C, respectively.

materials. In addition, LTOC-based SSEs exhibit key properties such as cathode compatibility, moisture stability, Li-metal compatibility, low-pressure operation, and economic viability. The application of LTOC has been demonstrated in NCM83 and LCO solid cells, operating at room temperature and low temperatures (as low as −50°C) over thousands of stable cycles. Overall, our LTOC-based oxychloride SSEs exemplify how anion sublattice design can overcome the structural limitations of single-anion chemistry, enabling enhanced structural functionality and major improvements in material properties.

REFERENCES AND NOTES

1. Q. Zhao, S. Stalin, C.-Z. Zhao, L. A. Archer, *Nat. Rev. Mater.* **5**, 229–252 (2020).
2. A. M. Abakumov, S. S. Fedotov, E. V. Antipov, J. M. Tarascon, *Nat. Commun.* **11**, 4976 (2020).
3. D. H. S. Tan *et al.*, *Science* **373**, 1494–1499 (2021).
4. Z. Zhang *et al.*, *Energy Environ. Sci.* **11**, 1945–1976 (2018).
5. A. Manthiram, X. Yu, S. Wang, *Nat. Rev. Mater.* **2**, 16103 (2017).
6. R. Chen, Q. Li, X. Yu, L. Chen, H. Li, *Chem. Rev.* **120**, 6820–6877 (2020).
7. Y. Xiao *et al.*, *Nat. Rev. Mater.* **5**, 105–126 (2019).
8. A. M. Nolan, Y. Zhu, X. He, Q. Bai, Y. Mo, *Joule* **2**, 2016–2046 (2018).
9. Y. Kato *et al.*, *Nat. Energy* **1**, 16030 (2016).
10. N. Kamaya *et al.*, *Nat. Mater.* **10**, 682–686 (2011).
11. P. Adeli *et al.*, *Angew. Chem. Int. Ed.* **58**, 8681–8686 (2019).
12. L. Zhou, A. Assoud, Q. Zhang, X. Wu, L. F. Nazar, *J. Am. Chem. Soc.* **141**, 19002–19013 (2019).
13. J. Liang, X. Li, K. R. Adair, X. Sun, *Acc. Chem. Res.* **54**, 1023–1033 (2021).
14. X. N. Li *et al.*, *Energy Environ. Sci.* **13**, 1429–1461 (2020).
15. T. Asano *et al.*, *Adv. Mater.* **30**, e1803075 (2018).
16. X. N. Li *et al.*, *Energy Environ. Sci.* **12**, 2665–2671 (2019).
17. L. D. Zhou *et al.*, *Energy Environ. Sci.* **13**, 2056–2063 (2020).
18. J. Liang *et al.*, *J. Am. Chem. Soc.* **142**, 7012–7022 (2020).
19. L. Zhou *et al.*, *Nat. Energy* **7**, 83–93 (2022).
20. K. Wang *et al.*, *Nat. Commun.* **12**, 4410 (2021).
21. Y.-C. Yin *et al.*, *Nature* **616**, 77–83 (2023).
22. F. Li *et al.*, *J. Am. Chem. Soc.* **145**, 27774–27787 (2023).
23. Y. Tanaka *et al.*, *Angew. Chem. Int. Ed.* **62**, e202217581 (2023).
24. T. Dai *et al.*, *Nat. Energy* **8**, 1221–1228 (2023).
25. Y. Wang *et al.*, *Nat. Mater.* **14**, 1026–1031 (2015).
26. S. Wang *et al.*, *Angew. Chem. Int. Ed.* **58**, 8039–8043 (2019).
27. K. Jun *et al.*, *Nat. Mater.* **21**, 924–931 (2022).
28. D. Di Stefano *et al.*, *Chem* **5**, 2450–2460 (2019).
29. B. Singh *et al.*, *J. Am. Chem. Soc.* **146**, 17158–17169 (2024).
30. S. Adams, *Energy Storage Mater.* **68**, 103359 (2024).
31. Y. Hu *et al.*, *Matter* **7**, 1018–1034 (2024).
32. K. Jun, Y. Chen, G. Wei, X. C. Yang, G. Ceder, *Nat. Rev. Mater.* **9**, 887–905 (2024).
33. N. Zhang *et al.*, *Adv. Mater.* **34**, e2107899 (2022).
34. P. S. Lu *et al.*, *Joule* **8**, 635–657 (2024).
35. Z. Liu *et al.*, *Nat. Chem.* **16**, 1584–1591 (2024).
36. C. Yu *et al.*, *Nano Energy* **77**, 105097 (2020).
37. P. E. Stallworth *et al.*, *J. Power Sources* **81**, 739–747 (1999).
38. X. Li *et al.*, *Angew. Chem. Int. Ed.* **58**, 16427–16432 (2019).
39. Q. Wang *et al.*, *Nat. Commun.* **15**, 1050 (2024).
40. S. Zhang *et al.*, *Nat. Commun.* **14**, 3780 (2023).
41. Z. Li *et al.*, *Nat. Commun.* **14**, 482 (2023).
42. A. X. Wang, S. X. Geng, Z. F. Zhao, Z. L. Hu, J. Y. Luo, *Adv. Funct. Mater.* **32**, 2201861 (2022).
43. L. F. Peng *et al.*, *Chem. Eng. J.* **430**, 132896 (2022).
44. L. Peng *et al.*, *Energy Storage Mater.* **43**, 53–61 (2021).
45. T. Kwon, I. Choi, M. J. Park, *ACS Appl. Mater. Interfaces* **9**, 24250–24258 (2017).
46. X. Li *et al.*, *Angew. Chem. Int. Ed.* **62**, e202306433 (2023).
47. S. Choi, M. Jeon, B. K. Kim, B. I. Sang, H. Kim, *Chem. Commun.* **54**, 14116–14119 (2018).
48. P. S. Lu *et al.*, *Nano Energy* **118**, 109029 (2023).

ACKNOWLEDGMENTS

The authors thank L.-Y. Chang for collecting the XAS data of Ta L-edge at Taiwan Photon Source and M. Shakouri for collecting XAS data of Cl K-edge at the Canadian Light Source (CLS). Authors acknowledge support from Western University. The synchrotron PXRD was completed at the CLS, which is supported by the Canada Foundation for Innovation, the National Research Council, the Canadian Institutes of Health Research, the Government of Saskatchewan, and the University of Saskatchewan. **Funding:** X.S. acknowledges support from the Natural Sciences and Engineering Research Council of Canada, the Canada Research Chair Program, the Canada Foundation for Innovation, and funding support from the National Natural Science Foundation of China (grant W2441017). Y.M. acknowledges funding support from National Science Foundation under awards 1940166 and 2118838, the computational facilities from the University of Maryland supercomputing resources, and the Maryland Advanced Research Computing Center. This research was conducted at the NOMAD beamlines (Spallation Neutron Source of Oak Ridge National Laboratory) and was sponsored by the Scientific User Facilities Division, Office of Basic Sciences, US Department of Energy (DOE). J.L. was partially supported by ORNL-LDRD 10761. This research used resources of the Advanced Light Source, which is a DOE Office of Science User Facility under contract DE-AC02-05CH11231. **Author contributions:** X.S. and F.Z. conceived the project. F.Z. and S.Z. performed the electrolyte synthesis and electrochemical performance characterizations. S.W. performed computational simulations (under the supervision of Y.M.) J.R. performed the synchrotron PXRD data collection and structural analysis. Jue L. performed neutron data collection and analysis. W.X., G.K., and J.K. helped to solve the crystal structure. Jianwen L., Jing L., Y.G., Y.Z., S.A., and Y.H. helped with physical characterizations and analyses. S.Z., F.Y., W.L., J.G., and T.S. helped with the synchrotron XAS data analysis. F.Z. and S.Z. interpreted the data and wrote the manuscript. X.S. supervised the project. All the authors commented on the final manuscript. **Competing interests:** The authors declare that they have no competing interests. **Data and materials availability:** All data are available in the manuscript or the supplementary materials. **License information:** Copyright © 2025 the authors, some rights reserved; exclusive licensee American Association for the Advancement of Science. No claim to original US government works. https://www.science.org/content/page/science-licenses-journal-article-reuse

SUPPLEMENTARY MATERIALS

science.org/doi/10.1126/science.adt9678
Materials and Methods; Supplementary Text; Figs. S1 to S37; Tables S1 to S7; References (*49*–*85*); CIF file for $Li_3Ta_3O_4Cl_{10}$

Submitted 24 Jun 2022; resubmitted 18 October 2024; accepted 20 August 2025
10.1126/science.adt9678

Unifying Healthcare, Research, Innovation and Education: A Blueprint for Africa from UM6P's Faculty of Medical Sciences & Hospitals



How can African countries simultaneously address the challenge of delivering quality healthcare while conducting research that tackles local disease burdens and contributes to global medical knowledge?

The UM6P Faculty of Medical Sciences (FMS), together with its affiliated UM6P Hospitals, offer a groundbreaking solution with the creation of an integrated ecosystem where education, research, and clinical care reinforce each other in real time with a vision centered on innovation. The established research environment is built on state-of-the-art infrastructures including molecular and cellular platforms, advanced imaging cores, accredited animal facility, cutting-edge medical equipment, and a biobank designed to collect and preserve locally relevant samples, and a forthcoming center for clinical trials. A robust information system supports secure, standardized clinical data collection, empowering large-scale epidemiological and genomic studies on Moroccan and African populations groups often underrepresented in global datasets.



Complementing these facilities, FMS places a strong focus on developing human capacity. Undergraduate students, including those from across Africa, gain early exposure to scientific methods, mentorship, AI and evidence-based medicine training with full access to the hospital, research laboratories and a simulation center to enhance clinical reasoning before patient contact. In addition, students can enroll in an integrated and innovative MD/PharmD-PhD program that offers a unique pathway to careers bridging basic research and clinical practice, enabling them to develop critical thinking skills, formulate their own research questions, and translate discoveries into practice. By uniting advanced research capabilities, innovation with a dedicated Bio-Park, clinical care, and education within one framework, FMS UM6P Hospitals may offer a replicable model for African countries seeking to build sustainable health innovation systems. To pursue its development, the institution actively recruits international scientists, especially from the African diaspora, catalyzing technology transfer and fostering international collaborations. This strategy helps counter brain drains and strengthens national capacity to respond to emerging health threats with homegrown expertise. In doing so, it not only improves patient outcomes but also contributes to training the next generation of scientists and healthcare leaders, ensuring that discoveries made in Morocco can benefit both the local population and the broader global community.



UHN Princess Margaret Cancer Centre

Principal Investigator – Cancer Biology
Princess Margaret Cancer Centre at the UHN

The Princess Margaret Cancer Centre at the University Health Network (UHN) is seeking an outstanding early-career faculty Scientist (full time Assistant Professor level) to establish an independent world-class research program in Cancer Biology. Successful candidate must have a PhD and/or MD or equivalent designation; extensive experience in one or more functional and cancer biology fields; exceptional track record evidenced by high impact discoveries (publications and/or intellectual properties or patents); dissemination of research at formal scientific meetings, and participation in the education and supervision of students and trainees. Applications across the spectrum of cancer biology are encouraged, with emphasis on functional and mechanistic research towards development of future therapies. Examples include but are not limited to aging, inflammation, cellular stress, functional genomics, structural biology, and chemical biology. Use of novel research platforms and technologies will be prioritized, complementing institutional expertise and resources in genomics, proteomics, computational and structural biology, immunology and high-throughput biology, supported by cutting-edge research core facilities.

Successful candidate will be supported by a generous start-up package, independent modern laboratory space and extensive institutional expertise and resources in genomics, proteomics, computational and structural biology, cutting-edge high-throughput and research core facilities, full salary and assistance in obtaining cross-appointments to the University of Toronto. PM appointment is expected at the rank of Scientist, on a career path to Senior Scientist over a six-year period (tenure-track-equivalent). funded research program of international caliber and will be supported by a generous start-up package complemented by independent modern laboratory space.

The Faculty Search Committee recognizes that scholars have varying career paths and that career interruptions due to personal circumstances can be part of an excellent academic record. Committing to an inclusive recruitment process, the Committee will shortlist applications based on the applicant's scientific excellence, alignment with Princess Margaret research programs, and with an aim to correct conditions of disadvantage in employment experienced by the four designated groups in Canada's Employment Equity Act (women, Indigenous peoples, persons with disabilities, and members of visible minorities). UHN is a respectful, caring, and inclusive workplace. We are committed to championing accessibility, diversity and equal opportunity. All qualified candidates are encouraged to apply.

Interested candidates can obtain more information and follow the instructions to apply via UHN webpage:
https://jobs.smartrecruiters.com/UniversityHealthNetwork/744000084918171-scientist-cancer-biology

ScienceCareers.org
ScienceCareers



YOUR NEXT BIG SCIENTIFIC DISCOVERY: A NEW JOB.

Find your next job at ScienceCareers.org

The relevance of science is at an all-time high these days. For anyone who's looking to get ahead in—or just plain get into—science, there's no better, more trusted resource or authority on the subject than *Science* Careers. Here you'll find opportunities and savvy advice across all disciplines and levels. There's no shortage of global problems today that science can't solve. Be part of the solution.

ScienceCareers
FROM THE JOURNAL SCIENCE AAAS

Massachusetts Institute of Technology

Tenure-Track Faculty Positions
Institute for Medical Engineering and Science (IMES)

The Institute for Medical Engineering and Science (IMES) http://imes.mit.edu/ at the Massachusetts Institute of Technology (MIT), in Cambridge, Massachusetts, invites applicants to apply for tenure-track faculty positions in all areas of science and engineering with application to health sciences to begin July 1, 2026 or on a mutually agreed date thereafter. Established in 2012, IMES is an inclusive community of students, administrative staff, research staff, and faculty who research, work, educate, and learn, at the convergence of engineering, science, and medicine to transform human health for all.

Appointment will be at the assistant professor level. In special cases, however, an untenured associate or senior faculty appointment may be possible, commensurate with experience. The appointment will be made in partnership with a relevant science or engineering department. The position will have equal academic responsibilities in IMES and the partner department. Applicants must hold an MD or a PhD in a science or engineering field related to health sciences by the beginning of employment. While all research areas are of interest, IMES encourages applications from candidates whose research and teaching interests would be enhanced and accelerated through deep engagement with both basic and clinical partners, and whose research program intimately involves the development and/or application of advanced computational methods. Examples include, but are not limited to:

- Clinical data generation, analysis, and sharing to improve health care delivery;
- The development, testing, and analysis of devices, sensors, & interfaces (mechanical, optical, electrical, chemical), and their products, to advance health care and its delivery;;
- Methods and modeling to understand the impact of environmental shifts on human health;
- Deriving insights into human diseases through epidemiological research and mechanistic modeling;
- Improving our ability to understand, predict, and manipulate human immune responses (e.g., in the context of infectious diseases, neuro-immune interactions, or women's health)

The successful candidate will be expected to fulfill all teaching, research, and service obligations of a tenure-track faculty member at MIT. Faculty duties include teaching courses in both the candidate's home science/engineering department and in Health Science & Technology at the undergraduate and graduate levels, advising students, conducting original scholarly research, developing course materials at the graduate and undergraduate levels, and service to MIT and the profession.

Interested candidates should submit application materials electronically at https://faculty-searches.mit.edu/imes-search/. Each application must include: a curriculum vitae; the names and addresses of three or more references; a strategic statement of research interests; a statement of teaching interests; and three representative recent publications. It is the responsibility of the candidate to arrange for reference letters to be uploaded at http://imes-search.mit.edu/letters.

Please address questions to imes-search@mit.edu. Complete application materials received by December 1, 2025 will be given priority.

MIT is an equal employment opportunity employer. We value diversity and strongly encourage applications from individuals from all identities and background. All qualified applicants will receive equitable consideration for employment based on their experience and qualifications and will not be discriminated against on the basis of race, color, sex, sexual orientation, gender identity, pregnancy, religion, disability, age, genetic information, veteran status, ancestry, or national or ethnic origin. See MIT's full policy on Nondiscrimination (https://policies.mit.edu/policies-procedures/90-relations-and-responsibilities-within-mit-community/92-nondiscrimination). Know your rights: see https://www.eeoc.gov/sites/default/files/2022-10/EEOC_KnowYourRights_screen_reader_10_20.pdf.

Employment is contingent upon the completion of a satisfactory background check, including possible verification of any finding of misconduct (or pending investigation) from prior employers.

The pay range for a 9-month academic appointment at the entry-level Assistant Professor rank (excluding summer salary): $140,000 – $150,000.

The pay offered to a selected candidate during hiring will be based on factors such as (but not limited to) the scope and responsibilities of the position, the candidate's work experience and education/training, internal peer equity, and applicable legal requirements. This pay range represents base pay only and does not include any other benefits or compensation.

TENURE-TRACK POSITIONS
DEPARTMENT OF PHYSIOLOGY

UT Southwestern Medical Center

The Department of Physiology invites outstanding scientists with Ph.D., M.D., or equivalent degrees to apply for tenure-track faculty positions at the level of Assistant Professor. Exceptional candidates at the Associate Professor level will also be considered. Candidates who bring innovative approaches to the study of any under-explored or unexplored questions broadly related to physiology are encouraged to apply. The scientific excellence of the candidates is more important than the specific area of research. These positions are part of the continuing growth of the Department at one of the country's leading academic medical centers. They will be supported by significant laboratory space, competitive salaries, state-of-the-art core facilities, and exceptional start-up packages. The University of Texas Southwestern Medical Center is the scientific home to six Nobel Prize laureates since 1985, 25 members of the National Academy of Sciences, 23 members of the National Academy of Medicine, and 14 Howard Hughes Medical Institute Investigators. UT Southwestern conducts more than 5,800 research projects annually, totaling more than $719 million. Additional information about the Department of Physiology can be found at utsouthwestern.edu/education/medical-school/departments/physiology/index.html.

Applicants should submit a CV, a brief statement of current and proposed research, a summary of their two most significant publications (100-150 words each), and should arrange to have three letters of reference sent to: Physiology search, Tenure Track Faculty job at UT Southwestern Medical Center, Dallas, TX. Completed applications will be reviewed starting November 1, 2025. For questions, please email Priya Thevar at priya.thevar@utsouthwestern.edu.

UT Southwestern Medical Center is committed to an educational and working environment that provides equal opportunity to all members of the University community. In accordance with federal and state law, the University prohibits unlawful discrimination, including harassment, on the basis of race, color, religion, national origin, sex (including sexual harassment), age, disability, genetic information, citizenship status, and protected veteran status. In addition, it is UT Southwestern policy to prohibit discrimination on the basis of sexual orientation, gender identity, or gender expression.

Faculty Positions
Yale Stem Cell Center
Yale University School of Medicine

The Yale Stem Cell Center invites applications for faculty positions at the rank of Assistant, Associate, or full Professor. Rank and tenure will be commensurate with experience. Applicants should have a Ph.D. and/or M.D. degree. Each successful candidate will be expected to develop a vigorous, externally funded research program on fundamental questions related to the biology of embryonic or adult stem cells. Preference will be given to research on neural stem cells and neural regeneration, cancer stem cells and related therapy, and cardiac repair and regeneration. Investigators will establish labs in a state-of-the-art new building and will join a vibrant stem cell research community at Yale with over 100 labs working on various aspects of stem cell biology and medicine. Investigators will also contribute to teaching graduate and/or medical students as well as shaping stem cell research at Yale.

Applicants must apply and submit all application materials electronically to https://apply.interfolio.com/173430 by December 15, 2025. Inquiries about the position may be sent to Dr. Haifan Lin, Director of the Yale Stem Cell Center, c/o Vanessa Woolley vanessa.woolley@yale.edu.

Yale Equal Opportunity and Nondiscrimination Statement
The University is committed to basing judgments concerning the admission, education, and employment of individuals upon their qualifications and abilities and seeks to attract to its faculty, staff, and student body qualified persons from a broad range of backgrounds and perspectives.

U.S. POSTAL SERVICE

Statement required by the Act of 12 August 1970, Section 3685, Title 39, United States Code, showing the ownership, management, and circulation of:
1–9. *Science*, Publication No. 0036-8075, is published weekly on Friday, except the last week in December, at 1200 New York Avenue, N.W., Washington, DC 20005. Date of filing: 25 September 2025. This is also the address of the publisher, the editor, and the managing editor, who are, respectively, Bill Moran, Holden Thorp, and Valda Vinson.
10. The owner is the American Association for the Advancement of Science, 1200 New York Avenue, N.W., Washington, DC 20005. Stockholders: None.
11. Known bondholders, mortgages, and other security holders owning or holding 1 percent or more of total amount of bonds, mortgages, or other securities: None.
12. The purpose, function, and nonprofit status of this organization and the exempt status for federal income tax purposes have not changed during the preceding 12 months.
13–15. The average number of copies of each issue during the preceding 12 months is (A) Total number of copies printed: 33,819; (B) Paid circulation: 27,250; (1) Paid/Requested outside-county mail subscriptions stated on form 3541: 27,250; (2) Paid/Requested in-county subscriptions stated on form 3541: 0; (3) Sales through dealers and carriers, street vendors, counter sales: 3,436. (4) Other classes mailed through USPS: 4; (C) Total paid circulation: 30,689 ; (D) Free distribution: samples, complimentary, and other free copies: 2,227; (1) Outside-county as stated on form 3541: 2,227; (2) In-county as stated on form 3541: 0; (3) Other classes mailed through the USPS: 0; (4) Free distribution outside of mail carrier or other means: 257; (E) Total free distribution: 2,484; (F) Total distribution: 33,173; (G) Copies not distributed: 576; (H) Total: 33,749; (I) Percent paid and/or Requested Circulation: 92.51%.
Actual number of copies of single issue (9/18/2025) published nearest to filing date are (A) Total number of copies printed: 32,261; (B) Paid circulation: 26,385; (1) Paid/Requested outside-county mail subscriptions stated on form 3541: 26,385; (2) Paid/Requested in-county subscriptions stated on form 3541: 0; (3) Sales through dealers and carriers, street vendors, counter sales: 2,850; (4) Other classes mailed through USPS: 3; (C) Total paid circulation: 29,238; (D) Free distribution: Samples, complimentary, and other free copies: 2,268; (1) Outside-county as stated on form 3541: 2,268; (2) In-county as stated on form 3541: 0; (3) Other classes mailed through the USPS: 0; (4) Free distribution outside of mail: Carrier or other means: 185; (E) Total free distribution: 2,453; (F) Total distribution: 31,691; (G) Copies not distributed: 570; (H) Total: 32,261; (I) Percent paid and/or Requested Circulation: 92.26%.
I certify that the statements made above are correct and complete. (signed) Bill Moran, Publisher.

Search more jobs online

Access hundreds of job postings on ScienceCareers.org.

Expand your search today.





myIDP ScienceCareers
INDIVIDUAL DEVELOPMENT PLAN

Features in myIDP include:

- Exercises to help you examine your skills, interests, and values.
- 20 career paths with a prediction of which ones best fit your skills and interests.
- A tool for setting strategic goals with optional reminders to keep you on track.
- Articles and resources to guide you through the process.
- Options to save materials online and print them for further review and discussion.
- A certificate of completion for users that finish myIDP.

Start planning your future today!
myIDP.sciencecareers.org

In partnership with:

UCSF University of California San Francisco
UIC
BURROUGHS WELLCOME FUND
FASEB Federation of American Societies for Experimental Biology
UMASS University of Massachusetts Medical School



THE UNIVERSITY OF TENNESSEE HEALTH SCIENCE CENTER

Associate Professor or Assistant Professor

The Department of Anatomy and Neurobiology at the University of Tennessee Health Science Center seeks outstanding researchers to **fill two tenure-track positions at the level of Assistant Professor and Associate Professor**. We seek candidates to complement and extend departmental and campus-wide research in neural circuits of mental health, neurodegeneration/Alzheimer's Disease, and related areas. Research incorporating state-of-the-art in vivo approaches to study neural circuits is encouraged, including optogenetics, chemogenetics, electrophysiology and imaging.

Basic Qualifications:
Applicants must have a PhD, MD, or equivalent degree and excellent oral and written communication skills. Candidates at the assistant professor level are expected t:o demonstrate strong potential for establishing a rigorous, independent, and federally-funded research program. Appointment as an Associate Professor requires demonstrated sustained extramural grant support, and research and scholarship that are consistent with an appointment to that rank at a research-intensive university.
Applications must be submitted through https://fa-ewlq-saasfaprod1.fa.ocs.oraclecloud.com/hcmUI/CandidateExperience/en/sites/CX_1/jobs/preview/1331/?keyword=neuroscience&location=Memphis%2C+TN%2C+United+States&locationId=3000000104681 93&locationLevel=city&mode=location&radius=25&radiusUnit=MI

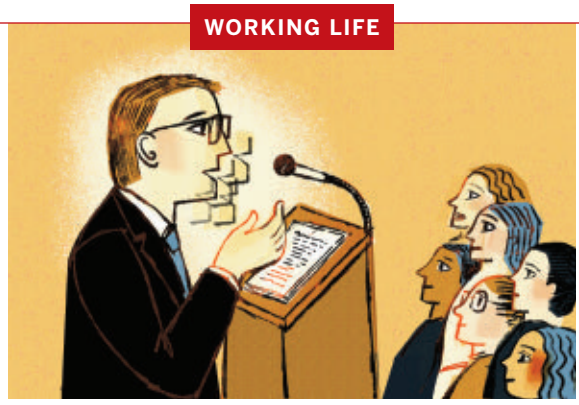
What's Your Next Career Move?

From networking to mentoring to evaluating your skills, find answers to your career questions on *Science* Careers

To view the complete collection, visit
ScienceCareers.org/booklets



ScienceCareers
FROM THE JOURNAL SCIENCE AAAS



Learning from my stutter

Peter Deak

"My name is ..." The words stick in my throat, obstinately refusing to yield. The silence stretches on as I shake a stranger's hand. Consciously relaxing my jaw, I breathe in and manage to release my name in a breathy tone, "Pppeeeettterr." Typical responses range from awkward pauses to the joking "Are you sure?" or, in the worst case, "I'm sorry, what did you say?" As a child, I would imagine I just made myself look stupid. Now, I see it differently. My stutter is an invitation to humility.

I have been a stutterer since I was about 7 years old. It had no obvious cause; even the most current literature on the topic will admit the pathology of stuttering is "enigmatic." When I was young, I avoided speaking. I learned speech therapy techniques, methods of breathing and forming my words, but I was comfortable in my own mind and didn't really need to share my thoughts. When I couldn't avoid speaking, my go-to strategy was to replace words with synonyms when I felt a block coming. Then I fell in love with science, where precision mattered not only in benchwork, but also in terminology. So, while in graduate school, I restarted speech therapy, worked on new strategies, and began to gain confidence in my own voice. I thought I had my stutter under control.

One postdoc and many job interviews later, I became an assistant professor, facing the standard challenges of starting a research group—and my speech was regressing. Using speech strategies is taxing: To avoid stammering on tricky words I must be aware of how I breathe, form words on my lips, and move my mouth. But between grants, papers, project management, paperwork, other principal investigator stresses, and being a father of four (soon to be five) young children, I had too little intellectual space left to devote to preparing to speak. In addition, the transition from the few planned and prepared speaking opportunities I had as a postdoc to endless obligatory communication overwhelmed my coping strategies. I have been so preoccupied with what I am saying that I cannot focus on how I say it.

The regression was gradual, and I didn't notice it until one day, a few months ago, I was teaching my thermodynamics class and found myself unable to say "equilibrium." Later that day I struggled to tell a colleague the name of my newborn daughter. The students seemed to shrug off my difficulty, and my colleague changed the subject after a brief awkward moment. Still, a feeling of humiliation remained, clashing with my self-image as a capable scientist. I began to wonder how anyone could respect me or my work if I was unable to communicate clearly.

A few weeks later, I found myself nervously ruminating on a commitment I had made to introduce a speaker at an upcoming conference. I began dwelling on worst-case scenarios in which I humiliated myself in front of my peers. This anxiety over 30 seconds of public speaking months in the future was not healthy. I began to wonder whether I had subconsciously begun to avoid speaking roles again, as in my childhood. I thought back to a conference opportunity I had passed up, telling myself I was too busy to apply. Maybe I just didn't want to give a talk.

Eventually I came to a realization: I will probably never be free of my stutter. I will always face the burden of coaxing my body to do what comes naturally and effortlessly for most. The thought was both depressing and exhausting. At the same time, I began to wonder whether I can gain some good from this burden. If radiation can be used to cure cancer, why can't my stutter make me better, too?

I have decided to reject feelings of humiliation and instead embrace humility; to accept my vulnerabilities and my limitations and welcome the new perspectives they provide. When my voice sticks and refuses to cooperate, I can't force it. And I can't control how others perceive me. Instead, I can choose to relax, breathe, and coax each syllable, gently yet diligently. This mindset can help my work as well. I can employ similar strategies when I receive grant rejections or belittling paper reviews. I am not in control, but I can, with proper effort, participate in the conversation. □

Peter Deak is an assistant professor at Drexel University. Send your career story to SciCareerEditor@aaas.org.

ILLUSTRATION: ROBERT NEUBECKER



myIDP ScienceCareers
INDIVIDUAL DEVELOPMENT PLAN

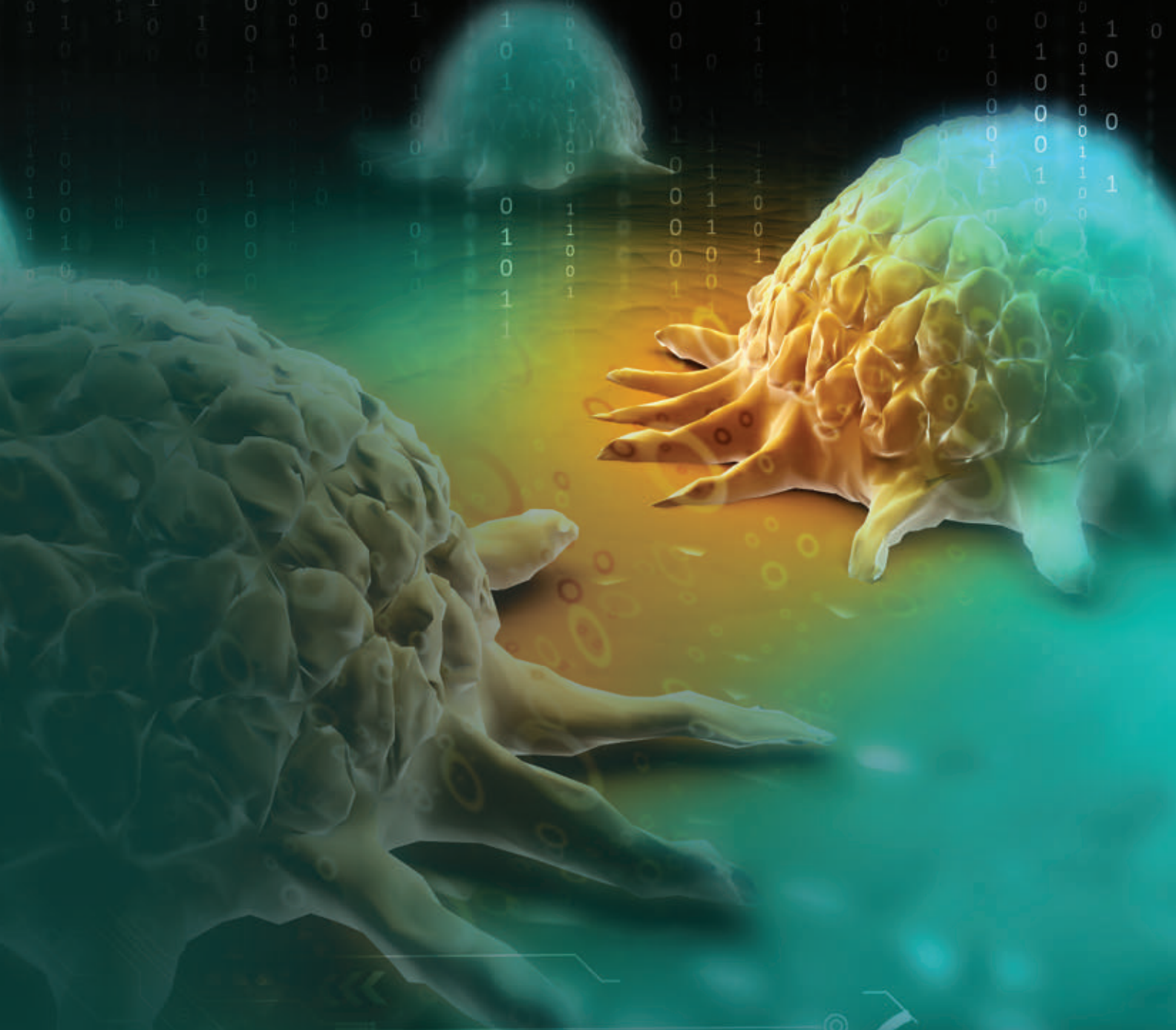
Features in myIDP include:

- Exercises to help you examine your skills, interests, and values.
- 20 career paths with a prediction of which ones best fit your skills and interests.
- A tool for setting strategic goals with optional reminders to keep you on track.
- Articles and resources to guide you through the process.
- Options to save materials online and print them for further review and discussion.
- A certificate of completion for users that finish myIDP.

Start planning your future today!
myIDP.sciencecareers.org

In partnership with:

FASEB Federation of American Societies for Experimental Biology
UMASS University of Massachusetts Medical School
UCSF University of California San Francisco
UIC
BURROUGHS WELLCOME FUND



2026

AAAS MARTIN AND ROSE WACHTEL CANCER RESEARCH AWARD

Recognizing the work of an early career scientist who has performed outstanding research in the field of cancer. Award nominees must have received their Ph.D. or M.D. within the last 10 years. The winner will deliver a public lecture on their research, receive a cash award of **$25,000**, and publish a Focus article on their award-winning research in *Science Translational Medicine*.

For more information visit
www.aaas.org/aboutaaas/awards/wachtel
or e-mail wachtelprize@aaas.org.
Deadline for submission: **February 1, 2026**.

AAAS Science Translational Medicine